

School of Electrical Engineering, Computing
and Mathematical Sciences

Wave-Packet Convergent Close-Coupling Approach to Ion
Collisions with Atoms and Molecules

Corey Thomas Plowman
0000-0001-8224-7143

This thesis is presented for the degree of
Doctor of Philosophy
of
Curtin University

November 2023

Declaration

To the best of my knowledge and belief this thesis contains no material previously published by any other person except where due acknowledgement has been made.

This thesis contains no material which has been accepted for the award of any other degree or diploma in any university.

Portions of this thesis contain extracts from my own published work in which the copyright is held by the publisher. In each case the publishers provide the right to use an article or a portion of an article in a thesis or dissertation without requesting permission.


Corey T. Plowman

November 10, 2023

Summary

This thesis is devoted to extending and applying the wave-packet convergent close-coupling (WP-CCC) approach to ion-atom and ion-molecule collisions. In this method the total scattering wave function is expanded in terms of bound states and wave-packet pseudostates that represent the continuum of both the target and projectile atoms. This expansion is substituted into the full time-independent Schrödinger equation for the total scattering wave function and the semiclassical approximation is used to derive the two-centre close-coupling equations. Numerical solution of the close-coupling equations yields the expansion coefficients in the final channel, from which the transition amplitudes for all single-electron processes are determined. The method is applied to calculate integrated and differential cross sections important for modelling fusion plasmas, ion-beam transport through matter, and interactions between solar wind ions and planetary atmospheres. The results are compared to experimental and theoretical data where available. For some collision systems and processes the present results are the first available data.

First, an extensive set of integrated cross sections for electron capture, ionisation, and target excitation for Li^{3+} , Be^{4+} , and Ne^{10+} collisions with atomic hydrogen is calculated over a wide range of incident energies relevant to fusion-plasma modelling. These, and results for Be^{4+} scattering on initially excited hydrogen atoms, represent the most comprehensive data for the investigated systems to date. The speed up obtained from utilising graphics processing unit (GPU) accelerators is essential for enabling the use of sufficiently large bases for

the calculations to converge.

Then, the method is applied to calculate all types of singly differential cross sections in the fundamental three-body $p + H$ collision system. The results are the first coupled-channel calculations of the singly differential cross sections for all interconnected processes occurring in proton-hydrogen collisions. Excellent agreement with experimental data and improvement over previously available calculations is found.

A novel approach to calculating electron capture within the single-centre close-coupling formalism is developed. Results are compared to full two-centre calculations for $p + H$ collisions, finding very good agreement for all integrated cross sections. The method is applied to calculate integrated cross sections for ionisation, electron capture, and target excitation in $p + Li$ collisions. Accounting for capture of both K- and L-shell electrons using the independent-event model, good agreement is found with the experimental data.

An effective one-electron approach to ion collisions with multielectron targets is developed and applied to proton scattering on alkali metal atoms. The multi-electron wave function calculated from multiconfigurational Hartree-Fock theory is summed over the spin variables of all electrons and integrated over the spatial variables of all but one electron. The resulting wave function is used to reverse-solve the one-electron Schrödinger equation to obtain an effective pseudopotential that can be used to generate effective one-electron excited states and the continuum solution. Total electron-capture cross sections for proton collisions with Li, Na, and K atoms agree well with the experimental data, especially at energies where the inner-shell electrons contribute significantly to the overall results. This approach is readily scalable to larger atoms and pioneers the way for performing detailed close-coupling calculating ion collisions with many electron targets.

Furthermore, the four-body WP-CCC approach that accounts for electron-exchange and correlation effects throughout the collision is applied to calculate singly differential cross sections for $p + He$ collisions. Comparison with the ef-

fective one-electron method reveals that, in most cases, the effective one-electron method is sufficient to provide a satisfactory description of the experimental data. Both approaches are also applied to calculate integrated cross sections for elastic scattering, excitation, electron capture, and ionisation in $\text{He}^{2+} + \text{He}$ collisions. It is found that electron-exchange and electron-correlation effects are more important for the He^{2+} projectile compared to protons.

An effective one-electron approach to proton collisions with molecular hydrogen is also developed. This approach uses a model potential that represents the field of the H_2^+ core averaged over all orientations. Then, integrated cross sections for all one-electron processes occurring in $p + \text{H}_2$ collisions are calculated using the three-body WP-CCC method. Good agreement with experiment is found, suggesting this approach is suitable for intermediate- and high-energy collisions. Next the method is applied to calculate singly differential cross sections for elastic scattering, target excitation, electron capture, and ionisation. The results agree very well with experiment, especially for ionisation where significant improvement over previously available theories is observed. Finally, the doubly differential cross sections for ionisation in $p + \text{H}_2$ collisions are calculated. The results provide the first accurate description of the energy and angular distribution of emitted electrons. The present calculations for $p + \text{H}_2$ collisions are the first two-centre close-coupling results for this system.

Main Results

- The two-centre WP-CCC method is extended to use GPU accelerators allowing for significantly larger calculations to be performed:
 - Offloading calculations of the scattering equations to GPU accelerators provided a speed up of over two orders of magnitude. This significantly increased the throughput of calculations and maximum practical basis size.
 - The method is applied to calculate integrated cross sections for total

electron capture, ionisation and state-selective electron capture into all 2ℓ - and 3ℓ -states for $\text{Li}^{3+} + \text{H}(1s)$ collisions in the energy range from 1 keV to 1 MeV.

- Integrated cross sections for total electron capture, ionisation, target excitation and state-selective electron capture into all $n\ell$ -states up to $5g$ are calculated for $\text{Be}^{4+} + \text{H}(1s)$ collisions from 1 keV to 1 MeV.
- Integrated cross sections for total electron capture, ionisation, electron loss, target excitation into the $n = 3, 4,$ and 5 states, and state-selective electron capture into projectile states up to $8j$ for Be^{4+} collisions with $\text{H}(2s), \text{H}(2p_0),$ and $\text{H}(2p_1)$ are calculated from 1 to 500 keV.
- Integrated cross sections for total electron capture, ionisation, and state-selective electron capture into all $n\ell$ -states up to $10m$ are calculated for $\text{Ne}^{10+} + \text{H}(1s)$ collisions from 1 keV to 1 MeV.
- The method is applied to calculate differential cross sections for the three-body $p + \text{H}$ collision system:
 - Angular differential cross sections for elastic scattering, $n = 2$ target excitation, and total electron capture are calculated.
 - Singly differential cross sections for ionisation as functions of the energy of the and angle of the ejected electron are also calculated, finding significantly improved agreement with experiment compared to other theoretical results.
- A method is developed for extracting integrated cross sections for electron-capture from the single-centre WP-CCC approach:
 - Cross sections for total electron capture, state-selective capture, and total ionisation are compared to results from the two-centre version of the WP-CCC method, finding perfect agreement for $p + \text{H}$ collisions.

-
- The approach is applied to calculate cross sections for total electron capture, total electron loss, and $2p$ -excitation in $p + \text{Li}$ collisions using the independent-event model to account for capture from both the L- and K-shells.
 - An effective one-electron description of multielectron atoms that accounts for the electron-electron correlations in the target structure without using the independent-event model is developed:
 - Total electron-capture and ionisation cross sections are calculated for $p + \text{Li}$, $p + \text{Na}$, and $p + \text{K}$ collisions. Good agreement with experimental data is observed, particularly for high-energy capture where inner-shell electrons play an important role.
 - The method is applied to calculate all types of singly differential cross sections for $p + \text{He}$ collisions and the results are compared to those from the four-body WP-CCC approach. It is found that the effective one-electron approach is capable of accurately describing the experimental data in most cases, only for the singly differential cross section for ionisation as a function of the angle of the ejected electron are notable differences with the four-body WP-CCC results observed.
 - The four-body WP-CCC approach is extended to collisions of multiply charged ions with helium atoms:
 - Cross sections for total electron capture, state-selective electron capture up to $3d$, elastic scattering, state-selective target excitation up to $3d$, and total ionisation are calculated for $\text{He}^{2+} + \text{He}$ collisions.
 - Results are also compared to those obtained using the effective one-electron approach. It is found that direct-scattering cross sections are very sensitive to the accuracy of the target description.

- An effective one-electron approach to $p + H_2$ collisions within the WP-CCC framework is developed:
 - Cross sections are calculated for total single-electron capture, single ionisation, elastic scattering, target excitation, and state-selective electron capture up to $3d$ for non-dissociative collisions.
 - All types of singly differential cross sections for one-electron processes are calculated, significantly improved agreement with the experimental data for ionisation compared to previously available calculations is observed.
 - The doubly differential cross section for ionisation as a function of the energy and angle of the ejected electron is calculated, providing the first accurate description of the energy and angular distribution of electrons emitted in $p + H_2$ collisions.
 - The doubly differential cross sections for ionisation as a function of the scattering angle of the projectile and energy of the ejected electron and as a function of the scattering angle of the projectile and angle of the ejected electron are also calculated.

Acknowledgements

This PhD project would not have been possible without the innumerable contributions of many individuals. I am extremely grateful for all the support and encouragement I have received. It is impossible to name everyone who enabled me to pursue this successfully. Below I offer my thanks to those who played the most influential roles.

First and foremost I express my deepest thanks to my primary supervisor, Prof. Alisher Kadyrov, for his unwavering support throughout this project. His guidance and mentorship have been invaluable to me since I began working with him over five years ago. Alisher's incredible knowledge, commitment to science, and approachability make it a pleasure to work with him. I offer my thanks for the extensive time and effort he has committed towards my education and his patience when I inevitably make mistakes. Finally, I am very grateful for his balanced approach to supervision, providing me with the autonomy to investigate problems on my own while still knowing when to re-direct my attention when I become stuck.

Next, I need to thank Dr. Ilkhom Abdurakhmanov for introducing me to the computer codes necessary for this project and teaching me how to use them. His guidance in code development and optimisation were invaluable. I am also very grateful for his mentorship and supervision during his time at Curtin.

To my associate supervisor, Prof. Igor Bray, I offer my sincerest thanks for his continuing encouragement and support as well as his infectious enthusiasm for physics that helped inspire me to come to Curtin in the first place.

I am thankful to all members of the Institute of Theoretical Physics for making me feel welcome and providing a positive, friendly, and supportive work environment. In particular, I must thank Kade Spicer and Nick Antonio for many stimulating discussions. Their input has played an essential role in developing my understanding of the underlying physics and code. Furthermore, as undergraduate students, under the guidance and supervision of Alisher and myself, Nick Antonio, Kade Spicer, and Aks Kotian performed a number of the calculations that form parts of this project. For this I am very grateful.

To Grace, Sandro, Matt, Arni, Chris, and Rachel, with whom I traversed the gauntlet of undergraduate physics, I could not have done this without your support. The many banterous gatherings and games have helped keep me sane throughout this endeavour. In particular, I offer my sincerest thanks to Grace for her friendship and emotional support as well as listening to me talk about all the esoteric problems I encountered during my research.

I am also eternally grateful to my family for their continuing support and encouragement. I thank my sister, Jade, for fostering a motivational competitiveness within me that can only come from a sibling. Finally, without the incredible efforts of my mum and dad I would never have been able to achieve so much. They have taught me countless skills that have been essential throughout my educational journey.

This research was supported by an Australian Government Research Training Program Scholarship. Parts of this work were supported by the Pawsey Supercomputing Centre, and the National Computational Infrastructure.

Some of the work presented herein was performed as part of the Coordinated Research Project on Data for Atomic Processes of Neutral Beams in Fusion Plasma carried out under the sponsorship of the International Atomic Energy Agency.

To everyone who played a part in enabling this PhD project, thank you.

Acknowledgement of country

We acknowledge the Aboriginal and Torres Strait Islander people as the Traditional Custodians of the lands and waters of Australia. The work contained in this thesis was performed on the land of the Nyoongar Whadjuk people upon which Curtin University's Bentley campus resides. We pay our respects to their elders past, present, and emerging.

List of publications

During the course of this PhD project, 19 papers were published in peer-reviewed journals. Following is a list of these publications in reverse-chronological order. Specific author contribution statements for each paper are given in App. C.

The content of publications 3, 4, and 6 was created in collaboration with other PhD students at Curtin University and is not claimed towards this PhD.

1. C. T. Plowman, K. H. Spicer, M. Schulz, and A. S. Kadyrov, “Scattering-angle dependence of doubly differential cross sections for ionization in proton collisions with molecular hydrogen”, [Phys. Rev. A **108**, 052809 \(2023\)](#)
2. C. T. Plowman, K. H. Spicer, and A. S. Kadyrov, “Calculation of energy and angular distributions of electrons produced in intermediate-energy $p + H_2$ collisions”, [Atoms **11**, 112 \(2023\)](#)
3. A. M. Kotian, C. T. Plowman, and A. S. Kadyrov, “Electron capture and ionisation in He^{2+} collisions with H_2 ”, [Eur. Phys. J. D **77**, 163 \(2023\)](#)
4. K. H. Spicer, C. T. Plowman, M. Schulz, and A. S. Kadyrov, “Doubly differential ionization in proton-helium collisions at intermediate energies: Energy distribution of emitted electrons as a function of scattered-projectile angle”, [Phys. Rev. A **108**, 022803 \(2023\)](#)

-
5. K. H. Spicer, C. T. Plowman, Sh. U. Alladustov, I. B. Abdurakhmanov, I. Bray, and A. S. Kadyrov, “Doubly differential cross sections for ionisation in proton-helium collisions at intermediate energies: energy and angular distribution of emitted electrons”, [Eur. Phys. J. D **77**, 131 \(2023\)](#)
 6. C. T. Plowman, I. B. Abdurakhmanov, I. Bray, and A. S. Kadyrov, “Energy and angular distributions of electrons emitted in proton collisions with molecular hydrogen”, [Phys. Rev. A **107**, 032824 \(2023\)](#)
 7. Sh. U. Alladustov, C. T. Plowman, I. B. Abdurakhmanov, I. Bray, and A. S. Kadyrov, “Wave-packet continuum discretization approach to He^{2+} -He collisions”, [Phys. Rev. A **106**, 062819 \(2022\)](#)
 8. A. M. Kotian, C. T. Plowman, I. B. Abdurakhmanov, I. Bray, and A. S. Kadyrov, “Electron capture and ionisation in collisions of Ne^{10+} and Li^{3+} with atomic hydrogen”, [Atoms **10**, 144 \(2022\)](#)
 9. N. W. Antonio, C. T. Plowman, I. B. Abdurakhmanov, I. Bray, and A. S. Kadyrov, “Fully-stripped beryllium-ion collisions with $2\ell m$ states of atomic hydrogen: target excitation and ionisation cross sections”, [Atoms **10**, 137 \(2022\)](#)
 10. N. W. Antonio, C. T. Plowman, I. B. Abdurakhmanov, I. Bray, and A. S. Kadyrov, “Fully-stripped-beryllium-ion collisions with $2\ell m$ states of atomic hydrogen: Total and state-selective electron-capture cross sections”, [Phys. Rev. A **106**, 012822 \(2022\)](#)
 11. C. T. Plowman, I. B. Abdurakhmanov, I. Bray, and A. S. Kadyrov, “Differential scattering in proton collisions with molecular hydrogen”, [Eur. Phys. J. D **76**, 129 \(2022\)](#)

-
12. A. M. Kotian, C. T. Plowman, I. B. Abdurakhmanov, I. Bray, and A. S. Kadyrov, “State-selective electron capture in collisions of fully stripped neon ions with ground-state hydrogen”, *J. Phys. B* **55**, 115201 (2022)
 13. C. T. Plowman, I. B. Abdurakhmanov, I. Bray, and A. S. Kadyrov, “Effective one-electron approach to proton collisions with molecular hydrogen”, *Eur. Phys. J. D* **76**, 31 (2022)
 14. K. H. Spicer, C. T. Plowman, I. B. Abdurakhmanov, Sh. U. Alladustov, I. Bray, and A. S. Kadyrov, “Proton-helium collisions at intermediate energies: Singly differential ionization cross sections”, *Phys. Rev. A* **104**, 052815 (2021)
 15. I. B. Abdurakhmanov, C. T. Plowman, K. H. Spicer, I. Bray, and A. S. Kadyrov, “Effective single-electron treatment of ion collisions with multielectron targets without using the independent-event model”, *Phys. Rev. A* **104**, 042820 (2021)
 16. N. W. Antonio, C. T. Plowman, I. B. Abdurakhmanov, I. Bray, and A. S. Kadyrov, “Integrated total and state-selective cross sections for bare beryllium ion collisions with atomic hydrogen”, *J. Phys. B* **54**, 175201 (2021)
 17. K. H. Spicer, C. T. Plowman, I. B. Abdurakhmanov, A. S. Kadyrov, I. Bray, and Sh. U. Alladustov, “Differential study of proton-helium collisions at intermediate energies: Elastic scattering, excitation, and electron capture”, *Phys. Rev. A* **104**, 032818 (2021)
 18. C. T. Plowman, K. H. Spicer, I. B. Abdurakhmanov, A. S. Kadyrov, and I. Bray, “Singly differential cross sections for direct scattering, electron capture, and ionization in proton-hydrogen collisions”, *Phys. Rev. A* **102**, 052810 (2020)

19. I. B. Abdurakhmanov, C. T. Plowman, A. S. Kadyrov, I. Bray, and A. M. Mukhamedzhanov, “One-center close-coupling approach to two-center rearrangement collisions”, *J. Phys. B* **53**, 145201 (2020)

Conference presentations

The work undertaken during this PhD project has been presented by the candidate at a number of national and international conferences. Following is a list of these conferences in reverse chronological order.

1. C. T. Plowman, K. H. Spicer, I. B. Abdurakhmanov, I. Bray and A. S. Kadyrov, “Differential ionisation in proton collisions with molecular hydrogen”, *Contributed poster*, XXXIII International Conference on Photonic, Electronic and Atomic Collisions, (2023), Ottawa, Canada
2. C. T. Plowman, K. H. Spicer, M. Schulz, and A. S. Kadyrov, “Differential study of ionisation in $p + H_2$ collisions”, *Invited talk*, XXVIII International Symposium on Ion-Atom Collisions, (2023), Rolla, MO, USA
3. C. T. Plowman, I. B. Abdurakhmanov, I. Bray, and A. S. Kadyrov, “Coupled-Channel Approach to Proton Scattering on Molecular Hydrogen Using an Effective One-Electron Model”, *Contributed talk*, XXIV Australian Institute of Physics Congress, (2022), Adelaide, Australia
4. C. T. Plowman, K. H. Spicer, I. B. Abdurakhmanov, A. S. Kadyrov, and I. Bray, “Calculation of singly differential cross sections for binary and breakup processes in proton-hydrogen collisions”, *Contributed poster*, XXII Gaseous Electronics Meeting, (2022), Sydney, Australia

5. C. T. Plowman, K. H. Spicer, I. B. Abdurakhmanov, A. S. Kadyrov, and I. Bray, “Calculation of singly differential cross sections in proton collisions with atomic hydrogen”, *Contributed talk*, III Australian Institute of Physics Summer Meeting, (2021), Brisbane, Australia
6. C. T. Plowman, K. H. Spicer, I. B. Abdurakhmanov, I. Bray and A. S. Kadyrov, “Differential studies of proton-hydrogen collisions”, *Contributed poster*, XXXII International Conference on Photonic, Electronic and Atomic Collisions, (2021), virtual
7. C. T. Plowman, K. H. Spicer, I. B. Abdurakhmanov, I. Bray and A. S. Kadyrov, “Calculation of differential cross sections in proton-hydrogen collisions”, *Contributed poster*, XXVII International Symposium on Ion-Atom Collisions, (2021), virtual

Statement of contribution of others

This thesis is based on the work contained in a number of joint publications created through individual and collaborative efforts. Signed statements by all co-authors specifying the contribution of the candidate to each publication are given in App. C.

The theory of the wave-packet convergent close-coupling method and associated computer codes were originally developed by A. S. Kadyrov and his team of students and postdocs at Curtin University over a number of years. The candidate further developed and optimised the code for the various types of calculations and collision systems considered herein and generalised the code to different types of computational architectures and compilers.

Calculation of the angular differential cross sections for proton collisions with H, He, and H₂ presented in Ch. 5, 8, and 10, respectively, was performed with post-processing code developed by the candidate. The candidate also developed substantial parts of the theory and code to calculate the singly and doubly differential cross sections for ionisation in the two-centre approach. The stability and numerical accuracy of the code for calculating differential cross sections was significantly improved by the candidate through implementation of various interpolation algorithms and numerical subroutines.

Calculations of multiply charged ion collisions with hydrogen presented in Ch. 4 were performed by honours students Nick Antonio and Aks Kotian under the supervision of both the candidate and A. S. Kadyrov. The results presented in Ch. 5 were calculated by the candidate. The single-centre approach to rear-

rangement processes presented in Ch. 6 and effective one-electron description of multielectron atoms presented in Ch. 7 were developed by A. S. Kadyrov and I. B. Abdurakhmanov and the computer code was optimised by the candidate. The Hartree-Fock code for the lithium structure used in Ch. 6 was developed by I. Bray. Calculations for differential cross sections in $p + \text{He}$ collisions presented in Ch. 8 were performed by honours student Kade Spicer under the supervision of A. S. Kadyrov and the candidate. The results in Ch. 9 were calculated by Sh. U. Alladustov and the candidate. The theory and code for the effective one-electron approach to H_2 targets was developed and implemented by the candidate. All results presented in Ch. 10 were performed by the candidate.

Signature of candidate:



Signature of supervisor:



Contents

Frontmatter	i
Summary	ii
Acknowledgements	viii
Acknowledgement of country	x
List of publications	xi
Conference presentations	xv
Statement of contribution of others	xvii
Contents	xix
List of Figures	xx
List of Tables	xxi
1 Introduction	1
1.1 Physics of atomic collisions	3
1.2 Applications	4
1.2.1 Fusion plasmas	4
1.2.2 Hadron therapy	5
1.2.3 Astrophysics	7
1.3 Aims of this work	8
2 Overview of existing theoretical methods	11
2.1 Classical methods	12
2.1.1 Classical trajectory Monte Carlo method	12
2.1.2 Gryziński method	13

2.2	Quantum-mechanical methods	14
2.2.1	First-order Born approximation	14
2.2.2	Second-order Born approximation	15
2.2.3	Distorted-wave Born method	16
2.2.4	Continuum-distorted-wave approach	16
2.2.5	Partial-wave approach	17
2.2.6	Lattice-based methods	18
2.2.7	Molecular-orbital close-coupling method	18
2.2.8	Atomic-orbital close-coupling method	19
2.2.9	Basis-generator method	20
2.2.10	Optical-potential method	21
2.2.11	Impact-parameter Faddeev approach	21
2.2.12	Convergent close-coupling approach	22
3	Two-centre wave-packet convergent close-coupling method	24
3.1	Two-centre scattering equations	27
3.2	Target structure	36
3.2.1	Wave-packet pseudostates	37
3.3	Evaluation of matrix elements	40
3.3.1	Direct-scattering matrix elements	40
3.3.2	Overlap matrix elements	42
3.3.3	Exchange matrix elements	46
3.4	Probability amplitudes and cross sections	51
3.4.1	Integrated cross sections	54
3.4.2	Differential cross sections	57
3.4.3	Ionisation amplitudes	58
3.4.4	Differential cross sections for ionisation	59
3.5	Computational implementation	63
3.6	Chapter summary	66

4	Multiply charged ion scattering on atomic hydrogen	67
4.1	Li ³⁺ +H collisions	69
4.2	Be ⁴⁺ +H collisions	73
4.2.1	Scattering on ground-state hydrogen	74
4.2.2	Scattering on excited hydrogen	84
4.3	Ne ¹⁰⁺ +H collisions	93
4.4	Chapter summary	104
5	Proton scattering on atomic hydrogen	106
5.1	Angular differential cross sections for p+H collisions	107
5.2	Singly differential cross sections for ionisation in p+H collisions	112
5.3	Chapter summary	118
6	Single-centre approach to rearrangement collisions	119
6.1	Electron-capture probabilities	119
6.2	Hartree-Fock method for lithium structure	121
6.3	Calculations of integrated cross sections	123
6.3.1	Proton scattering on atomic hydrogen	124
6.3.2	Proton scattering on lithium	130
6.4	Chapter summary	135
7	Proton scattering on alkali metals	137
7.1	Structure of multielectron atoms	138
7.2	Proton collisions with Li, Na, and K atoms	144
7.2.1	Overview of previous works	145
7.2.2	Single-electron-capture cross sections	145
7.2.3	Single-ionisation cross sections	149
7.3	Chapter summary	151
8	Proton scattering on helium	153
8.1	Two-electron WP-CCC approach to ion collisions with helium	154

8.1.1	Four-body scattering equations	154
8.1.2	Two-electron helium structure	158
8.2	Effective one-electron description of helium	159
8.3	Angular differential cross sections for p+He collisions	161
8.4	Singly differential cross sections for ionisation in p+He collisions .	174
8.5	Chapter summary	184
9	Fully stripped helium-ion scattering on helium	186
9.1	Overview of previous work	187
9.2	Calculations of integrated cross sections	188
9.2.1	Single-electron-capture cross section	189
9.2.2	State-selective electron-capture cross sections	191
9.2.3	Elastic-scattering cross section	195
9.2.4	State-selective target-excitation cross sections	196
9.2.5	Single-ionisation cross section	199
9.3	Chapter summary	200
10	Proton scattering on molecular hydrogen	202
10.1	Overview of previous work	203
10.1.1	Experimental data	203
10.1.2	Theoretical methods	206
10.2	Effective one-electron description of H ₂	211
10.2.1	Matrix elements in E1E approach to H ₂	213
10.2.2	Probabilities and cross sections for single-electron processes	215
10.3	Calculations of integrated cross sections	216
10.3.1	Electron loss in \bar{p} +H ₂ collisions	216
10.3.2	Integrated cross sections for p+H ₂ collisions	218
10.4	Angular differential cross sections for p+H ₂ collisions	227
10.5	Singly differential cross sections for ionisation in p+H ₂ collisions .	232
10.6	Doubly differential cross sections for ionisation in p+H ₂ collisions	242

10.6.1	DDCS as functions of the electron energy and the electron angle	242
10.6.2	DDCS as functions of the projectile scattering angle and the electron energy	253
10.6.3	DDCS as functions of the projectile scattering angle and the electron angle	261
10.7	Chapter summary	262
11	Conclusion and outlook	265
	Appendices	272
A	Momentum-transfer algebra	273
A.1	$\alpha \rightarrow \alpha'$ channel	273
A.2	$\beta \rightarrow \beta'$ channel	274
A.3	$\beta \rightarrow \alpha'$ channel	274
A.4	$\alpha \rightarrow \beta'$ channel	278
B	Frames of reference transformations	279
B.1	Rotating molecular frame	279
B.2	The laboratory and centre-of-mass frames of reference	284
C	Statements of contribution to published works	287
D	Abbreviations	304
	Bibliography	332

List of Figures

1.1	Neutral beam system for the ITER tokamak	5
1.2	Comparison of dose distributions of photons, protons, and carbon ions	6
3.1	Three-body collision system	25
3.2	Two-centre Jacobi coordinates	26
3.3	Rotating molecular frame	43
3.4	Collision momenta	60
4.1	Total electron-capture cross section for $\text{Li}^{3+} + \text{H}(1s)$ collisions . . .	71
4.2	Partial 2ℓ and 3ℓ electron-capture cross sections for $\text{Li}^{3+} + \text{H}(1s)$ collisions	71
4.3	Total ionisation cross section for $\text{Li}^{3+} + \text{H}(1s)$ collisions	73
4.4	Total electron-capture cross section for $\text{Be}^{4+} + \text{H}(1s)$ collisions . . .	75
4.5	Total ionisation cross section for $\text{Be}^{4+} + \text{H}(1s)$ collisions	75
4.6	Partial n -resolved cross sections for electron capture in $\text{Be}^{4+} + \text{H}(1s)$ collisions	76
4.7	n -partial cross sections for electron capture in $\text{Be}^{4+} + \text{H}(1s)$ collisions	78
4.8	Partial 2ℓ partial cross sections for electron capture in $\text{Be}^{4+} + \text{H}(1s)$ collisions	79
4.9	Partial 3ℓ cross sections for electron capture in $\text{Be}^{4+} + \text{H}(1s)$ collisions	80
4.10	Partial 4ℓ cross sections for electron capture in $\text{Be}^{4+} + \text{H}(1s)$ collisions	81
4.11	Partial 5ℓ cross sections for electron capture in $\text{Be}^{4+} + \text{H}(1s)$ collisions	82
4.12	Total electron-capture cross section for $\text{Be}^{4+} + \text{H}(2\ell m)$ collisions . .	85

4.13	n -partial cross sections for electron capture in $\text{Be}^{4+} + \text{H}(2\ell m)$ collisions	86
4.14	Partial 3ℓ and 4ℓ cross sections for electron capture in $\text{Be}^{4+} + \text{H}(2\ell m)$ collisions	88
4.15	Partial 5ℓ and 6ℓ cross sections for electron capture in $\text{Be}^{4+} + \text{H}(2\ell m)$ collisions	89
4.16	Partial 7ℓ and 8ℓ cross sections for electron capture in $\text{Be}^{4+} + \text{H}(2\ell m)$ collisions	90
4.17	Cross sections for excitation in $\text{Be}^{4+} + \text{H}(2\ell m)$ collisions	91
4.18	Cross sections for ionisation and electron loss in $\text{Be}^{4+} + \text{H}(2\ell m)$ collisions	92
4.19	Total electron-capture cross section for $\text{Ne}^{10+} + \text{H}(1s)$ collisions	94
4.20	Total ionisation cross section for $\text{Ne}^{10+} + \text{H}(1s)$ collisions	95
4.21	Partial n -resolved cross sections for electron capture in $\text{Ne}^{10+} + \text{H}(1s)$ collisions	96
4.22	Partial $1s$, 2ℓ and 3ℓ cross sections for electron capture in $\text{Ne}^{10+} + \text{H}(1s)$ collisions	96
4.23	Partial 4ℓ cross sections for electron capture in $\text{Ne}^{10+} + \text{H}(1s)$ collisions	98
4.24	Partial 5ℓ cross sections for electron capture in $\text{Ne}^{10+} + \text{H}(1s)$ collisions	99
4.25	Partial 6ℓ cross sections for electron capture in $\text{Ne}^{10+} + \text{H}(1s)$ collisions	100
4.26	Partial 7ℓ cross sections for electron capture in $\text{Ne}^{10+} + \text{H}(1s)$ collisions	101
4.27	Partial 8ℓ cross sections for electron capture in $\text{Ne}^{10+} + \text{H}(1s)$ collisions	102
4.28	Partial 9ℓ cross sections for electron capture in $\text{Ne}^{10+} + \text{H}(1s)$ collisions	103
4.29	Partial 10ℓ cross sections for electron capture $\text{Ne}^{10+} + \text{H}(1s)$ collisions	104
5.1	Angular differential cross sections for 25 keV $p + \text{H}$ collisions	108
5.2	Angular differential cross sections for 60 keV $p + \text{H}$ collisions	110
5.3	Angular differential cross sections for 125 keV $p + \text{H}$ collisions	111
5.4	Singly differential cross sections for ionisation in 20 keV $p + \text{H}$ collisions as functions of the electron energy and electron angle	113

5.5	Singly differential cross sections for ionisation in 48 keV p + H collisions as functions of the electron energy and electron angle	114
5.6	Singly differential cross sections for ionisation in 67 keV p + H collisions as functions of the electron energy and electron angle	115
5.7	Singly differential cross sections for ionisation in 95 keV p + H collisions as functions of the electron energy and electron angle	116
5.8	Singly differential cross sections for ionisation in 114 keV p + H collisions as functions of the electron energy and electron angle	117
6.1	Convergence of integrated cross sections with respect to the maximum included angular momentum for p + H collisions	124
6.2	Total electron-capture cross section for p + H collisions	126
6.3	Total electron-loss cross section for p + H collisions	127
6.4	Total ionisation cross section for p + H collisions	128
6.5	State-resolved cross sections for excitation and electron-capture in p + H collisions	129
6.6	Integrated elastic, excitation, and electron-capture cross sections for p + H collisions	130
6.7	Total electron-capture cross section for p + Li collisions	132
6.8	Total electron-loss cross section for p + Li collisions	133
6.9	2 <i>p</i> -excitation cross section for p + Li collisions	134
7.1	Effective one-electron pseudopotentials and reduced radial wave functions for Li, Na, and K	142
7.2	Total single-electron-capture cross section for p + Li collisions	146
7.3	Total single-electron-capture cross section for p + Na collisions	147
7.4	Total single-electron-capture cross section for p + K collisions	148
7.5	Total ionisation cross section for p + Li collisions	149
7.6	Total ionisation cross section for p + Na collisions	150
7.7	Total ionisation cross section for p + K collisions	150

8.1	Effective one-electron pseudopotential and reduced radial wave function for He	160
8.2	Angular differential cross sections for 75 keV p + He collisions . . .	164
8.3	Angular differential cross sections for 100 keV p + He collisions . . .	165
8.4	Angular differential cross sections for 150 keV p + He collisions . . .	166
8.5	Angular differential cross sections for 300 keV p + He collisions . . .	167
8.6	State-resolved angular differential cross sections for 75 keV p + He collisions	168
8.7	State-resolved angular differential cross sections for 100 keV p + He collisions	170
8.8	State-resolved angular differential cross sections for 150 keV p + He collisions	171
8.9	State-resolved angular differential cross sections for 300 keV p + He collisions	172
8.10	Singly differential cross sections for ionisation in p + He collisions as functions of the electron energy	175
8.11	DI and ECC components for the singly differential cross sections for ionisation in p + He collisions as functions of the electron energy . .	178
8.12	Singly differential cross sections for ionisation in p + He collisions as functions of the electron angle	179
8.13	DI and ECC components for the singly differential cross sections for ionisation in p + He collisions as functions of the electron angle . . .	181
8.14	Singly differential cross sections for ionisation in p + He collisions as functions of the scattering angle of the projectile	182
8.15	DI and ECC components for the singly differential cross sections for ionisation in p + He collisions as functions of the scattering angle of the projectile	183
9.1	Single-electron-capture cross section for $\text{He}^{2+} + \text{He}$ collisions	190
9.2	Partial 1s cross section for electron capture in $\text{He}^{2+} + \text{He}$ collisions .	191

9.3	Partial 2ℓ cross sections for electron capture in $\text{He}^{2+} + \text{He}$ collisions	192
9.4	Partial 3ℓ cross sections for electron capture in $\text{He}^{2+} + \text{He}$ collisions	194
9.5	State-selective electron-capture cross sections for $\text{He}^{2+} + \text{He}(1s^2)$ collisions	195
9.6	Elastic scattering cross section for $\text{He}^{2+} + \text{He}$ collisions	196
9.7	Partial 2ℓ cross sections for target excitation in $\text{He}^{2+} + \text{He}$ collisions	197
9.8	Partial 3ℓ cross sections for target excitation in $\text{He}^{2+} + \text{He}$ collisions	198
9.9	Single-ionisation cross section for $\text{He}^{2+} + \text{He}$ collisions	199
10.1	Single-electron-loss cross section for $\bar{p} + \text{H}_2$ collisions	217
10.2	Single-electron-loss cross section for $p + \text{H}_2$ collisions	220
10.3	Single-electron-capture cross section for $p + \text{H}_2$ collisions	221
10.4	Single-ionisation cross section for $p + \text{H}_2$ collisions	221
10.5	Elastic-scattering cross section for $p + \text{H}_2$ collisions	222
10.6	Net target-excitation cross section for $p + \text{H}_2$ collisions	223
10.7	Partial $1s$ cross section for electron capture in $p + \text{H}_2$ collisions . . .	224
10.8	Partial 2ℓ cross sections for electron capture in $p + \text{H}_2$ collisions . .	225
10.9	Partial 3ℓ cross sections for electron capture in $p + \text{H}_2$ collisions . .	226
10.10	Angular differential cross sections for 25 keV $p + \text{H}_2$ collisions . . .	228
10.11	Angular differential cross sections for 75 keV $p + \text{H}_2$ collisions . . .	229
10.12	Angular differential cross sections for 100 keV $p + \text{H}_2$ collisions . . .	230
10.13	Angular differential cross sections for 300 keV $p + \text{H}_2$ collisions . . .	231
10.14	Singly differential cross sections for ionisation in $p + \text{H}_2$ collisions as functions of the electron energy	233
10.15	DI and ECC components for the singly differential cross sections for ionisation in $p + \text{H}_2$ collisions as functions of the electron energy . .	235
10.16	Singly differential cross sections for ionisation in $p + \text{H}_2$ collisions as functions of the electron angle	237
10.17	DI and ECC components for the singly differential cross sections for ionisation in $p + \text{H}_2$ collisions as functions of the electron angle . . .	239

10.18	Singly differential cross sections for ionisation in $p + H_2$ collisions as functions of the scattering angle of the projectile	241
10.19	Doubly differential cross sections for ionisation in 48 keV $p + H_2$ collisions as functions of electron energy at various emission angles .	243
10.20	Doubly differential cross sections for ionisation in 67 keV $p + H_2$ collisions as functions of electron energy at various emission angles .	244
10.21	Doubly differential cross sections for ionisation in 75 keV $p + H_2$ collisions as functions of electron energy at various emission angles .	245
10.22	Doubly differential cross sections for ionisation in 95 keV $p + H_2$ collisions as functions of electron energy at various emission angles .	246
10.23	Doubly differential cross sections for ionisation in 100 keV $p + H_2$ collisions as functions of electron energy at various emission angles .	247
10.24	Doubly differential cross sections for ionisation in 114 keV $p + H_2$ collisions as functions of electron energy at various emission angles .	249
10.25	Doubly differential cross sections for ionisation in 200 keV $p + H_2$ collisions as functions of electron energy at various emission angles .	250
10.26	Doubly differential cross sections for ionisation in 300 keV $p + H_2$ collisions as functions of electron energy at various emission angles .	251
10.27	Doubly differential cross sections for ionisation in 75 keV $p + H_2$ collisions as functions of the scattering angle of the projectile at various ejected-electron energies	255
10.28	DI and ECC components for the doubly differential cross sections for ionisation in 75 keV $p + H_2$ collisions as functions of the scattering angle of the projectile at various ejected-electron energies	258
10.29	Doubly differential cross sections for ionisation in 100 keV $p + H_2$ collisions as functions of the scattering angle of the projectile at various ejected-electron energies	259

10.30	Doubly differential cross sections for ionisation in 200 keV $p + H_2$ collisions as functions of the scattering angle of the projectile at various ejected-electron energies	260
10.31	Doubly differential cross sections for ionisation in 75 keV $p + H_2$ collisions as functions of the scattering angle of the projectile at various emission angles	262
B.1	Prolate spheroidal coordinates	281

List of Tables

6.1	Binding energies for Li subshells generated using multiconfigura- tional Hartree-Fock theory	123
6.2	Convergence with respect to the number of continuum bins for p+H collisions	125
8.1	Energy levels of He calculated from two-electron and effective one- electron structure models	161

Chapter 1

Introduction

Ion collisions with atoms and molecules represent one of the most fundamental physical processes and play an essential role in developing our understanding of the structure of matter and its interactions. Investigations of atomic collisions have resulted in a number of significant advancements in our understanding of the physical universe. For example, experimental measurements of ion-atom collisions lead Rutherford [1] to the development of the nuclear model of the atom and later Chadwick [2] to the discovery of the neutron. Collisions between ions, atoms, and molecules also occur in many natural environments such as planetary atmospheres. A spectacular example of this are the *aurora borealis* and *aurora australis* which Birkeland [3] discovered are caused by emission of energy transferred in collisions of solar-wind ions with atoms and molecules in the Earth's upper atmosphere. The most powerful aurorae in the solar system were observed on Jupiter by the Hubble Space Telescope [4]. Studies of X-rays emitted as a result of ion collisions with atoms and molecules in extraterrestrial environments provide insight into the composition and atmospheric dynamics of other planets [5].

In addition to enhancing our understanding of fundamental physics, atomic collisions underpin several state-of-the-art technologies such as nuclear fusion reactors and hadron therapy. Fusion energy is capable of providing abundant

clean power using the same mechanism as the sun to generate energy. Monte Carlo (MC) simulations essential for diagnostics and control of the fusion plasma rely on accurate data for collisions of injected atoms with various fuel and impurity ions [6]. Hadron therapy is a major cancer treatment modality that uses ions to bombard tumours very precisely. It was first proposed by Wilson [7] based on Bragg's [8] observations that ion beams travelling through matter deposit most of their energy at the end of their path just before coming to a stop. This technique spares far more healthy tissue than traditional X-ray therapy and can be an effective alternative where surgical removal is not recommended [9]. Treatment plans are developed with MC simulations of ion transport through biological material. Accurate data for collisions between the beam ions and target atoms and molecules is essential to ensure radiation is delivered to the correct location.

Predicting the various outcomes of atomic collisions has been a major focus of scientific investigation since the inception of quantum mechanics [10, 11]. Often, researchers face unique challenges and some types of collisions that are easier to investigate in the laboratory are very difficult to calculate, and vice-versa. For example, it is easier to prepare H_2 targets experimentally than H atoms [12], however theoretical modelling of collisions with molecules is a significantly more challenging task than those involving atomic targets. Furthermore, some types of atoms which are involved in important collisions, such as beryllium, are toxic. Therefore, experiments may not be able to be safely performed, necessitating the development of accurate theories capable of providing the required collision data instead.

In this thesis we will investigate ion-atom and ion-molecule collisions with state-of-the-art theoretical methods to provide the data essential for MC modelling in fusion energy, hadron therapy, and astrophysical research. The theoretical methods developed and results will further our understanding of the underlying physics and provide the most accurate description of the studied collision systems.

1.1 Physics of atomic collisions

On the energy scale in which atomic and molecular collisions occur the dynamics of scattering is described by quantum mechanics. This means that the outcome of a given collision is not exactly determined by the initial conditions of the particles. Rather, there may be a number of possible outcomes, called reaction channels, each of which has an associated probability. These probabilities are quantified by the scattering cross section, a measure of the number of outgoing scattered particles resulting from a particular reaction channel to the incoming particle flux.

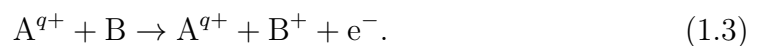
Consider a three-body collision system consisting of an ionic projectile colliding with a one-electron atom, denoted as A^{q+} and B, respectively. The incoming projectile has electronic charge $q+$. The simplest mechanism is elastic scattering, where the incident particle may be deflected but there is no transfer of energy between the projectile and target,



On the other hand, inelastic collisions involve energy transfer. They may be caused by a number of different mechanisms. Target excitation occurs if the target electron gains energy less than the ionisation energy of the atom,



Ionisation occurs if the electron is given sufficient energy to leave the collision system unbound to either the target or projectile,



For collisions involving positively charged projectiles, electron capture may occur

where the target electron forms a bound state with the projectile ion,



For multielectron targets, these mechanisms can occur simultaneously for different electrons. However, for the collision systems considered herein single-electron processes are typically at least an order of magnitude more likely. Therefore, we consider only single-electron processes in this work.

1.2 Applications

Cross sectional data for various outcomes of atomic collisions is used in a number of active fields of research [13, 14]. In this section we outline three areas in which accurate data is required.

1.2.1 Fusion plasmas

The ITER (formerly the International Thermonuclear Experimental Reactor) project aims to fuse hydrogen isotopes and harness the energy released to produce electricity. This large-scale, decades-long, international project should demonstrate the possibility of producing energy that is millions of times more efficient than burning coal, with no pollution and significantly less radioactive waste than traditional fission reactors [15]. The ITER project is an ambitious feat of engineering, demanding state-of-the-art scientific knowledge to succeed. Activating hot fusion reactions requires carefully controlled heating of plasma fuel to a temperature of millions of degrees. One method used by the ITER project for heating and diagnostics of the fusion plasma is the injection of beams of neutral atoms, in particular atomic hydrogen [16]. The neutral-beam injection system for the ITER tokamak is illustrated in Fig. 1.1. Injected beam atoms collide with various fully and partially stripped impurity ions present in the plasma and transfer their energy [17]. Plasma diagnostics are performed using charge-

exchange spectroscopy (CXS) [18]. The CXS technique is based on emission, usually in the visible spectrum, of the excited one-electron or multielectron ions resulting from electron capture. The application of the CXS technique requires knowledge of state-resolved electron-capture cross sections. Therefore, accurate data for collisions of ions with hydrogen is essential for precise monitoring and control of the fusion plasma [6].

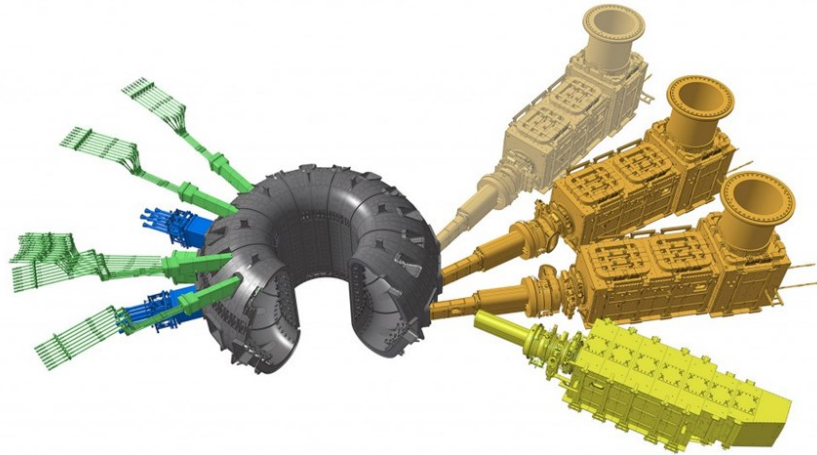


Figure 1.1: Neutral-beam injection system for the ITER tokamak. The grey torus is the tokamak reactor and the locomotive-sized orange apparatus on the right is the neutral beam injection system. Image courtesy of ITER [19].

1.2.2 Hadron therapy

Radiotherapy is an important method used in the treatment of cancer, particularly for deep-seated tumours where surgical methods pose significant risks [20]. Traditional radiotherapy bombards cancerous cells with high-energy X-rays which causes significant damage to healthy tissues, not only around the tumour site but also along the beam path [21]. In fact, this technique delivers the maximum radiation dose to the healthy cells near the surface of the skin. Furthermore, successful X-ray treatment still carries a high risk of long-term complications including recurrences and the development of secondary cancers. Hadron (or ion) therapy offers an alternative where, instead of photons, ions are used to deliver energy to the tumour site [7]. In contrast to X-rays, ion beams travelling through matter deposit most of their energy in a small region toward the end of their

path. This appears as a sharp peak in the depth-dose profile, known as the Bragg peak [8], where the ions come to a full stop. Compared to X-rays, much less energy is delivered to healthy tissue along the path and more to the cancerous tissue [22].

The most commonly used projectiles in hadron therapy are protons. Heavier ions like C^{6+} have several advantages such as a narrower Bragg peak and reduced spreading of the incoming beam [23]. However, one disadvantage is that composite particles can fragment, leading to a small number of lighter ions that can penetrate beyond the target site. Efforts are currently underway to determine if helium ions may provide a useful compromise [24].

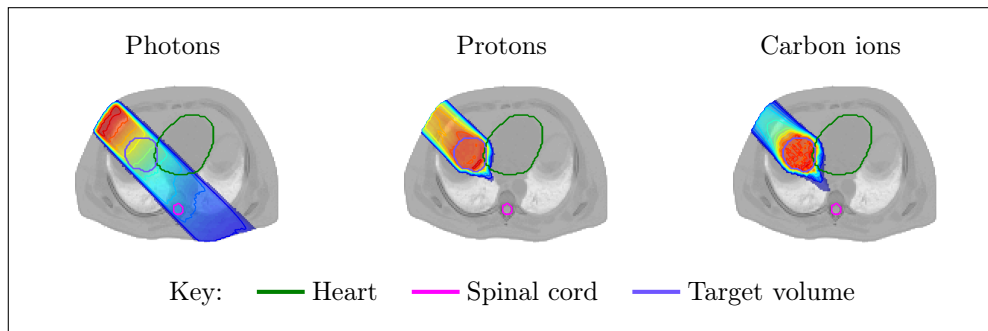


Figure 1.2: Simulated dose distribution for irradiation of a liver tumour using photons, protons, and carbon ions. With the photon beam the majority of energy is deposited in the healthy tissue in the incoming channel, whereas the ion beams deliver the majority of their energy to the target volume, sparing the heart and spinal cord. Simulation created with MATRAD [25].

Figure 1.2 shows the simulated dose distribution for photon, proton, and carbon-ion irradiation of a liver tumour. For the photon beam the majority of energy is delivered in the entrance channel and significant amounts of radiation penetrate beyond the target site, putting the sensitive spinal cord at risk. In contrast, both the proton and carbon beams deliver the majority of their energy near the end of their path. The carbon ions provide the most focussed energy deposition at the tumour, doing the least damage in the entrance channel. A small amount of energy is distributed in the distal region, but significantly less than for the photon beam.

The intensity and position of the Bragg peak depend on the type of ion, beam

energy, and type of target [21]. MC depth-dose simulations predict the Bragg peak position using the stopping power data. The stopping power is a measure of the energy lost by particles as they travel through matter. Therefore, accurate knowledge of the various mechanisms responsible for energy loss is required to generate stopping power data used to model beam transport through biological media. However, current MC simulation packages are based on the Bethe-Bloch stopping power formula [26]. This model is only accurate at very high energies. Important processes such as electron capture and coupling between reaction channels, as well as the atomic and molecular target structure, are ignored. Furthermore, experiments showed that cell destruction is mostly caused by secondary electrons rather than by the original ionising radiation directly [27]. Therefore, modelling the energy and angular distribution of the secondary electrons emitted when beam ions collide with target atoms and molecules is very important.

1.2.3 Astrophysics

Astrophysical phenomena occurring in space present a natural laboratory for atomic collision physics. Scattering occurs in various astrophysical events such as collisions of solar wind ions with planetary atmospheres [28] and charge transfer between stellar remnants of distant supernovae [29]. Such systems provide observational experiments for obtaining very accurate and important information for research in atomic collision physics that may otherwise not be attainable in a laboratory. Conversely, improved knowledge of collision processes can help solve outstanding problems in astrophysics.

Observations have found that several solar system objects shine in the X-ray spectrum [30]. Depending on the properties of the X-ray radiation, it is possible to determine characteristics of the emitter environment. Two of the main mechanisms that result in the production of X-rays from solar system objects are charge exchange between solar-wind ions and neutral atoms, and charge exchange between the neutral atoms and energetic heavy ions of planetary atmospheric and

magnetospheric origin [31]. X-ray observations of spontaneous de-excitation following charge exchange between ions, atoms, and molecules in Jupiter's upper atmosphere provide evidence of ion precipitation which is responsible for the creation of currents that drive atmospheric dynamics [28]. Furthermore, collisions of keV to MeV energy protons, present in the Jovian atmosphere [32], with molecular hydrogen contribute significantly to the ion and electron currents through ionisation and stripping processes. Currently there is a lack of detailed experimental and theoretical data for both single and double-electron processes involved in these collisions [28].

1.3 Aims of this work

The overall aim of this project is to extend and apply the highly successful wave-packet convergent close-coupling (WP-CCC) approach to ion-atom collisions, important for modelling in fusion plasma science, hadron therapy, and astrophysics. We intend to calculate differential cross sections, which provide a more detailed description of the collision, for all single-electron processes, including ionisation. Currently, the experimental data for relatively simple processes, like the ionisation of atomic hydrogen by proton impact, are inconsistently described by available theories. Furthermore, those calculations that are available consider different scattering outcomes independently, without accounting for coupling between reaction channels. We will calculate the differential cross sections for all (binary and breakup) single-electron processes occurring in p+H collisions within a single theoretical framework. The WP-CCC approach was recently applied to calculate integrated cross sections for proton scattering on helium, taking into account electron-electron correlations [33]. We also plan to calculate differential cross sections in collisions of protons and alpha particles on He.

For the purposes of fusion plasma modelling, data on the state-resolved charge-transfer cross sections for collisions of various ions with atomic hydrogen are required by the ITER project. Previously, the WP-CCC method was successfully

applied to $\text{He}^{2+} + \text{H}$ collisions [34] and $\text{C}^{6+} + \text{H}$ collisions [35]. In this work we will consider collisions of Li^{3+} , Be^{4+} , and Ne^{10+} ions with hydrogen, for which data is urgently needed for fusion plasma modelling [36]. These ion species are expected to be present in the ITER tokamak where they will interact with neutral hydrogen atoms. However, for many of the relevant inelastic processes no experimental and little theoretical data is available. In this work we will provide accurate collision data to fulfil this requirement.

In treatment planning for hadron therapy the water molecule is used as a reference target for modelling ion transport through biological media [21]. Hence, there is an urgent need for accurate stopping power cross sections on proton collisions with H_2O . The path to developing theories that can accurately calculate cross sections for ion collisions with water starts with the simplest molecular target, H_2 . However, even for simple molecules, currently available theoretical data is based on the Bragg summation rule in which cross sections for the constituent atoms are simply added together. This crude approximation is known to be inaccurate at intermediate and low projectile energies. Previously, the convergent close-coupling (CCC) method was used to calculate the integrated cross sections in $\bar{p} + \text{H}_2$ collisions, providing the most accurate theory for the total ionisation cross section (TICS) to-date [37]. In this project we will extend the two-centre WP-CCC method to tackle collisions of protons and positively charged ions with H_2 .

A significant obstacle in the path of applying advanced scattering theory and computer codes to generate cross sectional data is the increase in theoretical complexity and computational requirements when considering molecules or multi-electron atoms. To address this we intend to (i) implement GPU acceleration to increase the computational efficiency of the WP-CCC code, (ii) develop a simpler single-centre method to calculate electron-capture, and (iii) create an effective one-electron approach to multi-electron targets that will allow the three-body WP-CCC method to be applied to more complex systems. These developments

will pave the way towards application of the two-centre WP-CCC approach to ion-atom and ion-molecule collisions relevant to the areas outlined in Sect. 1.2.

The layout of this thesis is as follows. First, an overview of existing theoretical methods for ion-atom collisions is given in Ch. 2 before detailing the three-body WP-CCC approach in Ch. 3. After this the method is applied to collisions of Li^{3+} , Be^{4+} , and Ne^{10+} ions with hydrogen in Ch. 4. In Ch. 5 we calculate, for the first time, all types of singly differential cross sections in $\text{p} + \text{H}$ collisions within a single theoretical framework. The following chapter presents a novel approach for determining integrated electron-capture cross sections within the single-centre WP-CCC method. The idea is tested against the full two-centre approach for $\text{p} + \text{H}$ collisions before being applied to study proton scattering on lithium atoms. In Ch. 7 we demonstrate a new method for calculating proton scattering on alkali metals by developing a pseudopotential description of the multielectron target that treats all electron on an equal footing. Then we apply the WP-CCC approach to $\text{p} + \text{He}$ collisions to calculate differential cross sections in Ch. 8. The WP-CCC approach is applied to $\text{He}^{2+} + \text{He}$ collisions in Ch. 9. Extension of the present method to the molecular hydrogen target is considered in Ch. 10 where we calculate integrated and differential cross sections for all single-electron processes. Finally, Ch. 11 summarises the results of this work and discusses the future outlook.

Atomic units are used throughout, unless otherwise stated.

Chapter 2

Overview of existing theoretical methods

Many approaches have been developed to model ion-atom collisions. For low-energy collisions, where the probability of ionisation of a target electron is negligible, methods based on expanding the scattering wave function in terms of molecular orbitals provide accurate results. At high energies, ionisation plays an integral role in the collision, becoming the dominant electron-loss mechanism. Here perturbative methods can provide an accurate description of the experimental data. The intermediate-energy region lies between these two extremes where the projectile speed is comparable to the orbital speed of the target electron. Here the total ionisation cross section maximises and there are many competing reaction channels. As a result, accurate modelling of intermediate-energy ion-atom collisions represents a challenging theoretical problem. For ionic projectiles, the intermediate-energy region spans from approximately 1 keV/u to several MeV/u. The projectile speed is of the order 10^6 m s^{-1} and the collision timescale is very short. However, the speed of the particles involved is sufficiently less than the speed of light that non-relativistic mechanics provide a suitable description of scattering.

This chapter provides an overview of the various methods developed for cal-

culating ion collisions with atoms and molecules. Theories may be categorised as either classical or quantum-mechanical. Classical approaches describe the collision system entirely using classical equations of motion. In contrast, quantum-mechanical methods are based on the Schrödinger equation. For atomic hydrogen and hydrogen-like atoms the Schrödinger equation can be solved exactly. However, when additional particles are added the equations become significantly more complex and exact solution becomes impossible. Therefore, carefully considered approximations must be made in order to ensure sufficiently accurate solution of the quantum-mechanical equations of motion.

2.1 Classical methods

Methods based on a purely classical description of the scattering dynamics provide a relatively simpler alternative to more sophisticated quantum-mechanical approaches. However, as the underlying physics is governed by the latter, the classical picture cannot be considered a complete description of the collision system. Nonetheless, classical methods have seen widespread use and at sufficiently high collision energies can provide a simpler alternative to more sophisticated methods, generally finding agreement with experimental data [38].

2.1.1 Classical trajectory Monte Carlo method

The classical trajectory Monte Carlo (CTMC) approach to ion-atom collisions is based on the assumption that the scattering dynamics are entirely governed by Newtonian physics. First, the initial impact parameter of the projectile as well as the position and momentum of the target electrons are chosen randomly using a Monte Carlo technique. Then, starting with the projectile and target far apart, the classical Hamilton equations are solved numerically. This is repeated for many randomly chosen initial conditions. Integrated and differential cross sections are obtained from the calculated trajectories. The accuracy of the results depends

on the number of trajectories used and the associated statistical uncertainty [39].

The advantages of this approach is that it can provide a kinematically complete picture of the collision and the computations are relatively easy to perform. Application to multielectron targets is also straightforward. However, the main disadvantage is the omission of quantum-mechanical effects that are known to play an important role in collisional dynamics. Furthermore, calculating a sufficiently large number of trajectories to ensure statistical reliability of the results can be computationally very expensive. However, the CTMC method has been applied to many collision systems, often providing a reasonably accurate description of the experimental data [38].

2.1.2 Gryziński method

Gryziński [40] proposed a method for calculating the energy and angular distribution of electrons produced in ionising collisions using a fully classical description of the dynamics. In the so-called binary-encounter approximation the scattering system is reduced to a simple two-body classical collision between the projectile and target electron. Conservation of momentum leads to the result that the electron should be emitted with approximately twice the speed of the incoming projectile. One advantage of this approach is that the resulting analytical expression for the ionisation cross section is easy to compute. However, the binary-encounter mechanism is only responsible for fast electrons and cannot describe the cross section for electrons emitted with small energies. Furthermore, whilst it can provide reasonable results for the energy distribution of emitted electrons, the angular distribution is strongly influenced by the target nucleus [40]. Therefore, application of the approach to calculate the angular distribution of emitted electrons yields very poor results.

2.2 Quantum-mechanical methods

Methods that describe part or all of the collisional dynamics with the Schrödinger equation fall into this category. Quantum-mechanical methods may be further divided into two types: perturbative or non-perturbative. In the former approach, the interaction between the projectile and target is treated as a small perturbation to the Hamiltonian of the isolated system. The scattering wave function is then expanded as an infinite series where each successive term corresponds to a higher-order correction to the approximate solution [41]. In practice, the series is often truncated to only one or two terms that can be evaluated analytically. Including additional terms makes analytical solution prohibitively difficult very quickly. However, higher-order terms correspond to important physical processes and, especially at low collision energies, cannot be neglected [42].

Non-perturbative methods attempt to solve the problem directly. This way higher-order processes are intrinsically included in the solution. Typically, these approaches make use of well-justified approximations to write the Schrödinger equation in a form more amenable to numerical solution. The robustness of the solution can be verified by performing calculations with increasing numerical accuracy until the results converge to a constant value. The main obstacle with non-perturbative approaches is the complexity of the equations and large computational requirements. However, non-perturbative quantum-mechanical methods provide the most detailed description of the underlying physics and, consequently, often describe the available experimental data very well.

2.2.1 First-order Born approximation

The Born perturbation series has been used to describe ion-atom collisions since the inception of quantum mechanics. Electron capture in $p + H$ collisions was studied by Oppenheimer [11] and Brinkman and Kramers [43] using what is now known as the Oppenheimer-Brinkman-Kramers (OBK) method. This approach

used the first term of the Born series but neglected the interaction between the heavy particles as this was believed to make no contribution [44]. Subsequent experimental measurements revealed that this approximation provided an inaccurate description of the differential cross section for electron capture. Jackson and Schiff [45] and Bates and Dalgarno [46] included the interaction between the two protons and found improved agreement with the experimental data. This approach could not, however, accurately describe scattering between other types of ions and targets. This was later determined to be caused by incorrect description of the Coulomb boundary conditions [47]. The first-order boundary-corrected Born (CB1) approximation remedies this shortcoming [48] and provides a reasonably accurate description of the integrated cross section for electron capture [49]. However, even with the correct boundary conditions the method still remains first-order and is incapable of reproducing features caused by higher-order processes [50].

2.2.2 Second-order Born approximation

In many cases the first term of the Born series is insufficient to accurately describe the collision. The second-order boundary-corrected Born (CB2) approximation incorporates the first two terms of the perturbation expansion [51]. However, the second-order term is considerably more difficult to calculate due to the presence of an infinite sum over intermediate bound states and integration over the infinite continuum [47]. A significant simplification based on replacing the correct Green's functions with the phase-modified free-particle Green's functions was thus developed. This is known as the second-order boundary-corrected Born approximation with simplified Green's functions (B2B0) [52]. The second-order method has been considerably more successful in describing the experimental data for the differential electron-capture cross section [50]. However, as with methods based on the first-order term in the Born expansion, this approach is only accurate at high energies and moreover extension to higher-order terms is prohibitively difficult.

2.2.3 Distorted-wave Born method

In an attempt to improve the accuracy of the Born approximation the asymptotic wave functions upon which the perturbation expansion is based can be replaced by *distorted* waves. These may be chosen in infinitely many ways and are typically selected to describe certain physical features of the scattering system [47]. However, there is no way of knowing which distorted waves will yield the best results before comparison with experiment. Nonetheless, both first- and second-order calculations based on the distorted-wave Born (DWB) approximation were found to provide a reasonably accurate description of electron capture in $p + H$ collisions [53].

2.2.4 Continuum-distorted-wave approach

The previously discussed perturbative methods rapidly become inaccurate at intermediate projectile energies and are typically only reliable for fast projectiles. To address this shortcoming, Cheshire [54] developed the continuum-distorted-wave (CDW) method which accounts for the distortion of the target wave function through inclusion of the effect of the interaction potentials in the unperturbed basis [47]. The first term in the CDW approach effectively includes some contributions from the second-order term in the Born expansion, resulting in more rapid convergence of the perturbation series. A commonly used approximation to the CDW method is to replace the distorted wave with the semiclassical eikonal approximation [55]. In the continuum-distorted-wave eikonal-initial-state (CDW-EIS) method the eikonal wave function is employed in the initial channel whereas in the continuum-distorted-wave eikonal-final-state (CDW-EFS) method the eikonal wave function is employed in the final channel.

Overall, methods based on the CDW approach provide some of the most accurate results within the perturbative approximation. Furthermore, the utility of an analytical expression makes it straightforward to perform calculations.

However, for some processes, such as the fully differential cross section (FDCS) for ionisation in $p + H_2$ collisions, there exist significant discrepancies between experimental data and currently available calculations based on the CDW-EIS method [56, 57].

All of the methods discussed so far suffer from two major shortcomings. First, higher-order terms in the perturbative expansion are too difficult to calculate, making the methods inaccurate at low and intermediate impact energies. Second, coupling between reaction channels, which is very important at intermediate energies, is not accounted for. As a result, perturbative methods cannot in practice be considered as capable of providing an accurate description of the underlying physics in the intermediate energy region.

2.2.5 Partial-wave approach

A common technique used in calculating electron collisions with atoms is to expand the projectile wave function in terms of partial waves. The accuracy of the solution can be tested by systematically including additional terms in the expansion. However, for collisions of heavy projectiles a very large number of partial waves are required, making practical calculation prohibitively difficult [47]. Therefore, it is common for intermediate- and high-energy ionic projectiles to use a semiclassical approximation where the projectile is assumed to move along a straight-line trajectory. This is a reasonable approximation to make provided that the speed of the projectile is comparable to or greater than the orbital speed of the electrons. In such cases the scattering angle is very small and the projectile can be modelled as a plane wave. There have been some attempts at applying the partial-wave method to ion-atom collisions. In particular, Wong *et al.* [58] showed that with modern computer technology it is possible to obtain convergent results within the partial-wave formalism for proton scattering on both hydrogen and helium atoms. However, there were discrepancies between the results and the experimental data for angular differential cross sections.

2.2.6 Lattice-based methods

The most direct method to solving the Schrödinger equation for a collision system is to discretise the total scattering wave function and operators over a large grid (lattice). The time-dependent Schrödinger equation (TDSE) is then solved numerically at every point on the grid and cross sections are recovered from the total scattering wave function [59]. Such methods are very accurate and applicable at all collision energies, but extremely demanding computationally and therefore only recently have become possible. The main utility of such approaches is to provide a benchmark for other methods as the computational requirements can make lattice-based direct solution impractical.

2.2.7 Molecular-orbital close-coupling method

If the collision energy is sufficiently low, e.g. no more than about 1 keV, then the probability of ionisation is negligible in comparison to direct scattering (either elastic scattering or target excitation) and electron capture. If this is the case, then molecular-orbital close-coupling (MOCC) approaches provide very accurate results. The idea is that the total scattering wave function can be expanded in terms of molecular orbitals constructed by considering the electron in the field of both the target and projectile nuclei [60]. The expansion is inserted into the Schrödinger equation for the scattering system and a set of coupled differential equations results. These are then solved numerically to determine the expansion coefficients from which the cross sections are calculated. This sophisticated approach provides a detailed description of the underlying physics, accounting for coupling effects between the various reaction channels.

The main drawback with this method is the omission of the continuum which prohibits application at intermediate and high energies where ionisation plays a significant role. Compared to perturbative methods, it is also much more computationally difficult and in practice the number of states used in the close-coupling

expansion is restricted by the available computational resources. However, for slow projectiles the MOCC method provides very accurate results [61–63] and as a close-coupling method it is straightforward to determine state-resolved cross sections as well as total cross sections, all within a single calculation.

2.2.8 Atomic-orbital close-coupling method

If the projectile speed is comparable to or greater than the orbital speed of the electron then it is reasonable to assume that the projectile and target will not form quasi-molecular orbitals, due to the speed at which scattering takes place. The atomic-orbital close-coupling (AOCC) method expands the total scattering wave function in terms of atomic orbitals. For collisions where electron capture is unlikely (e.g. fast antiproton scattering on hydrogen) atomic orbitals centred about the target are sufficient to describe all possible electronic configurations. However, for positively charged projectiles, two sets of atomic orbitals are required: one centred on the target and the other on the projectile representing the atom formed by electron capture. Even with very few states, accurate results can be obtained if the dominant coupling is between the included channels [64].

The accuracy of the results obtained from close-coupling approaches depends on the choice of basis functions used in the expansion of the total scattering wave function. For hydrogen-like atoms, eigenfunctions can be used to describe negative-energy states. However, for atomic systems in which the analytic functions are unknown, alternative bases may be employed. Furthermore, at intermediate and high energies coupling to the continuum plays an important role in the collisional dynamics. Therefore, positive-energy electronic states must be incorporated into the close-coupling expansion. However, unlike bound-state eigenfunctions, continuum solutions for atomic systems are non-normalisable. A solution to this is to construct normalisable *pseudostates* that effectively represent the continuum of the target. This can be done by diagonalising the target Hamiltonian in terms of a set of square-integrable basis functions [38], effectively

discretising the continuum. As the number of states included in the basis increases, the discretisation becomes more dense. Some commonly used basis types include Sturmian functions [65, 66], Slater-type orbitals [67], Gaussian-type orbitals (GTO) [68], B -splines [69], and Laguerre polynomials [70, 71].

Bates [44] first used the AOCC method within a simple two-state approximation to calculate electron-capture cross sections in $p + H$ collisions. Subsequent calculations with more basis functions enabled determination of the cross section for target excitation [72, 73]. Positive-energy pseudostates were used by Cheshire *et al.* [72], Gallaher and Wilets [74] and Shakeshaft [75] to calculate the TICS using the AOCC method. Toshima and Eichler [76] used a large set of GTO basis functions to accurately describe the experimental data for the differential cross section for electron capture in collisions of MeV-energy protons with H. Their methodology allowed for analytical evaluation of the matrix elements, significantly reducing computational requirements that would otherwise have made calculations with large basis expansions impossible at the time. The fully quantal AOCC results by Kadyrov *et al.* [77] provided a good description of the experimental data for the angular differential cross section for electron capture in $p + H$ collisions.

Overall, agreement between close-coupling calculations and experimental data is quite good. However, due to limited computational resources it has historically not been possible to perform thorough convergence studies to determine if a sufficiently large number of states were included in the calculations. Furthermore, while the traditional AOCC method can be used to calculate the TICS, the scattering amplitudes for ionisation are unknown, making calculations of differential cross sections for ionisation impossible.

2.2.9 Basis-generator method

One drawback with close-coupling approaches is that a large number of states may be required to obtain accurate results. Kroneisen *et al.* [78] proposed an

alternative implementation whereby the basis is dynamically generated in such a way that the most important channels are incorporated, while states that are only weakly coupled are omitted. This allows the close-coupling equations to be solved with a minimal number of states, simplifying computational requirements. The two-centre basis generator method (TC-BGM) was used by Zapukhlyak *et al.* [79] to calculate the total integrated cross section for single-electron capture and single ionisation in $p + \text{Na}$ collisions. The multielectron target was described using the independent-event model (IEM). Collisions of Li^{3+} , C^{3+} , and O^{3+} with hydrogen atoms were investigated using the TC-BGM by Leung and Kirchner [80].

2.2.10 Optical-potential method

In the limit of an infinite number of terms in the expansion of the total scattering wave function, the close-coupling solution is exact. However, this is practically impossible. Truncating the expansion with a finite number of basis states effectively attempts to solve the collision problem over a finite-dimensional subspace. If this subspace is sufficiently large then coupling to the excluded channels becomes small and the results converge to the exact solution. The optical-potential approach was introduced to account for the coupling between the finite subspace and the complementary infinite-dimensional Hilbert space [81]. This is achieved through the introduction of an imaginary, non-local potential and a perturbative expansion of the resulting close-coupling equations [47]. Second-order calculations using this approach have demonstrated good agreement with experimental data for elastic-scattering, target-excitation, and electron-capture differential cross sections in proton collisions with atomic hydrogen [82].

2.2.11 Impact-parameter Faddeev approach

This alternative approach to quantum scattering is based on solving the three-particle Faddeev integral equations [83]. The impact-parameter Faddeev ap-

proach (IPFA) was pioneered by Avakov *et al.* [84] and successfully applied to calculate charge-exchange cross sections in proton collisions with H and He in Ref. [85] and proton collisions with alkali atoms in Ref. [86]. The method is based on the Alt-Grassberger-Sandhas approach [87, 88] which reduces the three-particle Faddeev equations into effective two-particle Lippmann-Schwinger type equations. Application of the IPFA to angular differential cross sections for elastic scattering and electron capture resulted in good agreement with the experimental data [89].

A drawback of this approach is that it cannot be applied to ionising collisions because the Faddeev equations become non-compact. Macek [90] attempted to overcome this problem using the first term in the Neuman expansion of the Faddeev integral equations to calculate differential cross sections for ionisation in $p + H_2$ collisions. However, the results, while qualitatively reasonable, quantitatively disagreed with the experimental data.

2.2.12 Convergent close-coupling approach

The CCC method was originally developed for electron scattering on atoms [70, 91]. This fully quantal approach solves the multichannel Lippmann-Schwinger equation using the method of partial waves. An orthogonal basis of both negative- and positive-energy pseudostates is constructed by diagonalising the target Hamiltonian with orthonormal Laguerre functions. The resulting set of pseudostates forms a quadrature rule for the summation over the countably infinite space of bound states and the integration over the uncountably infinite space of positive-energy continuum solutions. With increasing basis size the negative-energy pseudostates converge to the true eigenstates of the bound spectrum of the target. The positive-energy pseudostates discretise the continuum of the target with increasing density as the size of the basis is enlarged. Convergence in the results is obtained by systematically increasing the basis size. The method was extended to heavy projectiles by Abdurakhmanov *et al.* [71] and used to calculate integrated

and differential [92] cross sections in $\bar{p} + \text{H}$ collisions, demonstrating very good agreement with the experimental data. The approach was applied to $\bar{p} + \text{He}$ collisions in Ref. [93]. A semiclassical version was developed for antiproton collisions with molecular hydrogen, providing the first theoretical description of the experimentally observed target-structure induced suppression of the orientation-averaged TICS [37, 94].

The CCC approach to antiproton collisions with hydrogen was applied to calculate differential ionisation by Abdurakhmanov *et al.* [95]. This work introduced two important developments into the heavy-projectile CCC formalism. First, following the ideas developed by Kadyrov *et al.* [96], they calculated the momentum-space amplitudes for ionisation, allowing determination of all types of differential cross sections within the close-coupling approach. Second, the use of stationary wave-packet pseudostates to describe the target continuum afforded a fine degree of control over the continuum discretisation that was not possible with a Laguerre-type basis. Furthermore, comparison between fully quantal and semiclassical versions showed that for intermediate- and high-energy projectiles there is practically no difference between the two approaches.

A two-centre version of the semiclassical wave-packet CCC method was developed to tackle collisions involving positively charged projectiles by Avazbaev *et al.* [97] and Abdurakhmanov *et al.* [98]. The method was applied to fully stripped helium and carbon ions by Faulkner *et al.* [34] and Abdurakhmanov *et al.* [35], respectively. Proton collisions with initially excited hydrogen atoms were studied in Ref. [99]. The two-centre approach was applied to $p + \text{He}$ collisions, accounting for electron-electron correlations, by Alladustov *et al.* [33]. In all cases thorough convergence studies were performed, leading to some of the most reliable results to date for the studied systems.

Chapter 3

Two-centre wave-packet convergent close-coupling method

In this chapter, the two-centre wave-packet convergent close-coupling approach is formulated. We consider collisions of ions with one and quasi-one electron targets. Initially, the electron is in a bound state of the target atom. The momentum of the projectile relative to the target atom in the initial channel, i , and final channel, f , is denoted as \mathbf{q}_i and \mathbf{q}_f , respectively. The kinetic energy of the projectile in the laboratory frame is denoted E_i . The projectile ion has charge Z_P and the target nucleus has charge Z_T .

The WP-CCC method is based on the semiclassical impact-parameter formalism. In this framework the electrons are treated fully quantum-mechanically and the relative motion of the heavy particles is treated classically. It has been shown [100] that results obtained in the semiclassical method are very close to those obtained using the fully quantum theory, if the following conditions hold:

1. The momentum of the projectile relative to the target is large $|\mathbf{q}_i| \gg 1$.
2. The kinetic energy of the projectile motion is much larger than the energy lost by the projectile during the collision, $|\mathbf{q}_i| \approx |\mathbf{q}_f| \gg (2\mu_T \Delta E)^{1/2}$, where ΔE is the energy transfer.

3. The scattering angle of the projectile is very small, $\arccos(\hat{\mathbf{q}}_i \cdot \hat{\mathbf{q}}_f) \ll 1$.

For the projectile energies considered herein, these conditions are satisfied and the semiclassical approximation can be employed [47]. Under this approximation, the electronic part of the wave function changes much more rapidly than the nuclear part. The electrons are assumed to be able to arrange into a stationary state effectively instantaneously in response to a change in the relative positions of the target and projectile nuclei.

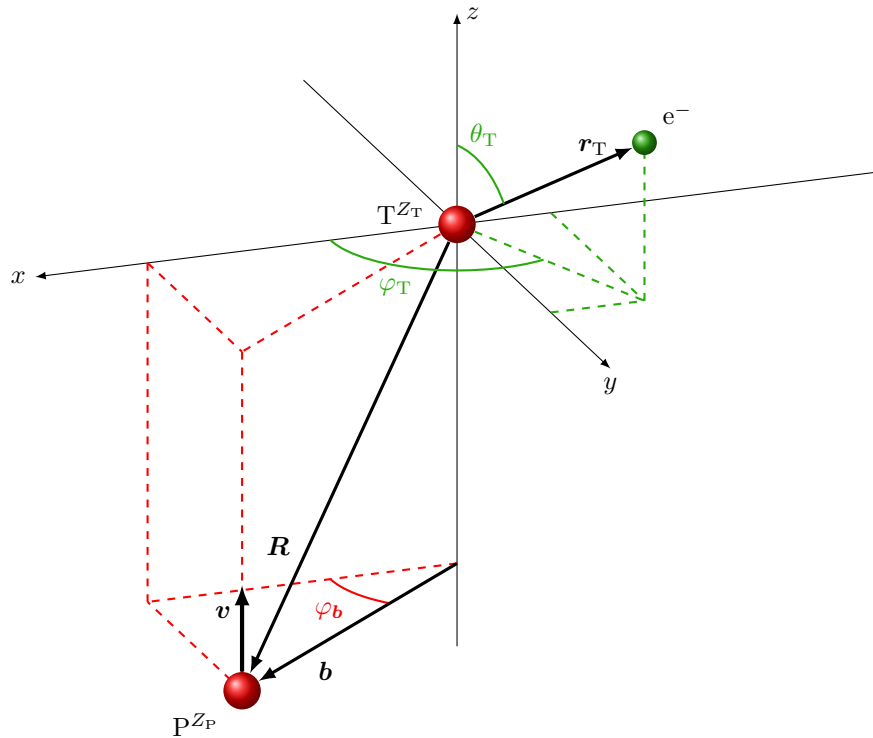


Figure 3.1: Three-body collision system in the laboratory frame.

The three-body collision system is shown in Fig. 3.1. The target is at rest with respect to the laboratory frame and the origin is located at the target nucleus. The projectile is incident parallel to the z -axis with velocity \mathbf{v} and impact parameter \mathbf{b} such that $\mathbf{v} \cdot \mathbf{b} = 0$. The semiclassical approximation effectively parameterises the relative position of the projectile in terms of time t according to

$$\mathbf{R}(t) = \mathbf{b} + \mathbf{v}t, \quad (3.1)$$

with φ_b being the azimuthal angle of the projectile. Therefore, the position of the

3.1 Two-centre scattering equations

The exact, non-relativistic, time-independent Schrödinger equation for the collision system is

$$(H - E)\Psi_i^+ = 0, \quad (3.2)$$

where Ψ_i^+ is the total scattering wave function subject to the outgoing-wave boundary conditions, H is the Hamiltonian and E is the total energy. The total Hamiltonian may be written in two equivalent forms,

$$\begin{cases} H = -\frac{1}{2\mu_T}\nabla_{\sigma_T}^2 + H_T + \bar{V}_T, \\ H = -\frac{1}{2\mu_P}\nabla_{\sigma_P}^2 + H_P + \bar{V}_P, \end{cases} \quad (3.3)$$

where μ_T is the reduced mass of the projectile and target atom, and μ_P is the reduced mass of the projectile atom formed by electron capture and the residual target ion. The Hamiltonians of the target and projectile atoms are

$$\begin{cases} H_T = -\frac{1}{2}\nabla_{r_T}^2 + V_T, \\ H_P = -\frac{1}{2}\nabla_{r_P}^2 + V_P, \end{cases} \quad (3.4)$$

respectively, where

$$\begin{cases} V_T = -\frac{Z_T}{r_T}, \\ V_P = -\frac{Z_P}{r_P}. \end{cases} \quad (3.5)$$

The interactions between the projectile and target atom, and between the projectile atom and residual target ion are

$$\begin{cases} \bar{V}_T = \frac{Z_T Z_P}{R} - \frac{Z_P}{|\mathbf{r}_T - \mathbf{R}|}, \\ \bar{V}_P = \frac{Z_T Z_P}{R} - \frac{Z_T}{|\mathbf{r}_P - \mathbf{R}|}. \end{cases} \quad (3.6)$$

The total scattering wave function is expanded as

$$\Psi_i^+ = \sum_{\alpha=1}^{\infty} F_{\alpha}(\boldsymbol{\sigma}_T) e^{i\mathbf{q}_{\alpha} \cdot \boldsymbol{\sigma}_T} \psi_{\alpha}^T(\mathbf{r}_T) + \sum_{\beta=1}^{\infty} G_{\beta}(\boldsymbol{\sigma}_P) e^{i\mathbf{q}_{\beta} \cdot \boldsymbol{\sigma}_P} \psi_{\beta}^P(\mathbf{r}_P), \quad (3.7)$$

where $e^{i\mathbf{q}_{\alpha} \cdot \boldsymbol{\sigma}_T}$ is a plane wave describing the projectile motion relative to the target atom, $e^{i\mathbf{q}_{\beta} \cdot \boldsymbol{\sigma}_P}$ is a plane wave describing the motion of the projectile atom relative to the target nucleus, $\psi_{\alpha}^T(\mathbf{r}_T)$ are target pseudostates, $\psi_{\beta}^P(\mathbf{r}_P)$ are projectile pseudostates, and $F_{\alpha}(\boldsymbol{\sigma}_T)$ and $G_{\beta}(\boldsymbol{\sigma}_P)$ are unknown expansion coefficients. The target pseudostates form an orthonormal set

$$\langle \psi_{\alpha}^T | \psi_{\alpha'}^T \rangle = \delta_{\alpha\alpha'}, \quad (3.8)$$

that diagonalises the target Hamiltonian,

$$\langle \psi_{\alpha}^T | H_T | \psi_{\alpha'}^T \rangle = \varepsilon_{\alpha}^T \delta_{\alpha\alpha'}. \quad (3.9)$$

Similarly, the projectile pseudostates form an orthonormal set

$$\langle \psi_{\beta}^P | \psi_{\beta'}^P \rangle = \delta_{\beta\beta'}, \quad (3.10)$$

that diagonalises the projectile Hamiltonian,

$$\langle \psi_{\beta}^P | H_P | \psi_{\beta'}^P \rangle = \varepsilon_{\beta}^P \delta_{\beta\beta'}. \quad (3.11)$$

Expansion coefficients $F_{\alpha}(\boldsymbol{\sigma}_T)$ and $G_{\beta}(\boldsymbol{\sigma}_P)$ contain all information about the state of the system at a given time. In the limit as $t \rightarrow -\infty$, the expansion coefficients describe the system in the initial channel and in the limit as $t \rightarrow +\infty$, they describe the system in the final channel.

To form the two-centre scattering equations we substitute Eq. (3.7) into

Eq. (3.2), to get

$$\begin{aligned} & \left(-\frac{1}{2\mu_T} \nabla_{\sigma_T}^2 + H_T + \bar{V}_T - E \right) \sum_{\alpha=1}^{\infty} F_{\alpha}(\sigma_T) e^{i\mathbf{q}_{\alpha} \cdot \sigma_T} \psi_{\alpha}^T(\mathbf{r}_T) \\ & + \left(-\frac{1}{2\mu_P} \nabla_{\sigma_P}^2 + H_P + \bar{V}_P - E \right) \sum_{\beta=1}^{\infty} G_{\beta}(\sigma_P) e^{i\mathbf{q}_{\beta} \cdot \sigma_P} \psi_{\beta}^P(\mathbf{r}_P) = 0. \end{aligned} \quad (3.12)$$

In the α channel the total energy is the sum of the energy of the target bound state α and the energy of the relative motion of the projectile, $E = \varepsilon_{\alpha}^T + q_{\alpha}^2/(2\mu_T)$. In the β channel the total energy is the sum of the energy of the projectile atom bound state β and the relative motion of the residual target ion, $E = \varepsilon_{\beta}^P + q_{\beta}^2/(2\mu_P)$. Next we act with $-\nabla_{\sigma_T}^2/2\mu_T$ on $e^{i\mathbf{q}_{\alpha} \cdot \sigma_T} F_{\alpha}(\sigma_T)$ and use the fact that

$$\nabla_{\sigma_T}^2 (F_{\alpha}(\sigma_T)) \ll \nabla_{\sigma_T}^2 (e^{i\mathbf{q}_{\alpha} \cdot \sigma_T}) \quad (3.13)$$

to simplify the result. We are left with

$$-\frac{\nabla_{\sigma_T}^2}{2\mu_T} (F_{\alpha}(\sigma_T) e^{i\mathbf{q}_{\alpha} \cdot \sigma_T}) = -\frac{1}{2\mu_T} [2i\mathbf{q}_{\alpha} \cdot \nabla_{\sigma_T} (F_{\alpha}(\sigma_T)) e^{i\mathbf{q}_{\alpha} \cdot \sigma_T} - q_{\alpha}^2 F_{\alpha}(\sigma_T) e^{i\mathbf{q}_{\alpha} \cdot \sigma_T}]. \quad (3.14)$$

Now consider the first term on the RHS of Eq. (3.14). We can write

$$\frac{\mathbf{q}_{\alpha}}{\mu_T} \cdot \nabla_{\sigma_T} = \mathbf{v} \cdot \nabla_{\sigma_T}, \quad (3.15)$$

since $\mathbf{q}_{\alpha} = \mu_T \mathbf{v}$. Furthermore, since ∇_{σ_T} is the differential operator with respect to σ_T , and \mathbf{v} is the time-derivative of σ_T , we see that

$$\mathbf{v} \cdot \nabla_{\sigma_T} = \frac{d}{dt}. \quad (3.16)$$

This means Eq. (3.14) reduces to

$$-\frac{\nabla_{\sigma_T}^2}{2\mu_T} (F_{\alpha}(\sigma_T) e^{i\mathbf{q}_{\alpha} \cdot \sigma_T}) = -i\dot{F}_{\alpha}(\sigma_T) e^{i\mathbf{q}_{\alpha} \cdot \sigma_T} + \frac{q_{\alpha}^2}{2\mu_T} F_{\alpha}(\sigma_T) e^{i\mathbf{q}_{\alpha} \cdot \sigma_T}, \quad (3.17)$$

where \dot{F}_α denotes the time derivative of F_α . Similarly, acting with $-\nabla_{\sigma_P}^2/2\mu_P$ on $G_\beta(\sigma_P)e^{i\mathbf{q}_\beta \cdot \sigma_P}$ results in

$$-\frac{\nabla_{\sigma_P}^2}{2\mu_P}(G_\beta(\sigma_P)e^{i\mathbf{q}_\beta \cdot \sigma_P}) = -i\dot{G}_\beta(\sigma_P)e^{i\mathbf{q}_\beta \cdot \sigma_P} + \frac{q_\beta^2}{2\mu_P}G_\beta(\sigma_P)e^{i\mathbf{q}_\beta \cdot \sigma_P}. \quad (3.18)$$

where \dot{G}_β is the time derivative of G_β .

Therefore, Eq. (3.12) becomes

$$\begin{aligned} & i \sum_{\alpha=1}^{\infty} \dot{F}_\alpha(\sigma_T)e^{i\mathbf{q}_\alpha \cdot \sigma_T} + i \sum_{\beta=1}^{\infty} \dot{G}_\beta(\sigma_P)e^{i\mathbf{q}_\beta \cdot \sigma_P} \\ &= (H_T + \bar{V}_T - \varepsilon_\alpha^T) \sum_{\alpha=1}^{\infty} \psi_\alpha^T(\mathbf{r}_T)F_\alpha(\sigma_T)e^{i\mathbf{q}_\alpha \cdot \sigma_T} \\ &+ (H_P + \bar{V}_P - \varepsilon_\beta^P) \sum_{\beta=1}^{\infty} \psi_\beta^P(\mathbf{r}_P)G_\beta(\sigma_P)e^{i\mathbf{q}_\beta \cdot \sigma_P}. \end{aligned} \quad (3.19)$$

Next we multiply Eq. (3.19) on the left by $\psi_{\alpha'}^{T*}(\mathbf{r}_T)e^{-i\mathbf{q}_{\alpha'} \cdot \sigma_T}$ and integrate over \mathbf{r}_T , to get

$$\begin{aligned} & i \sum_{\alpha=1}^{\infty} \dot{F}_\alpha(\sigma_T) \langle \psi_{\alpha'}^T | \psi_\alpha^T \rangle e^{i(\mathbf{q}_\alpha - \mathbf{q}_{\alpha'}) \cdot \sigma_T} \\ &+ i \sum_{\beta=1}^{\infty} \dot{G}_\beta(\sigma_P) \langle \psi_{\alpha'}^T | e^{i(\mathbf{q}_\beta \cdot \sigma_P - \mathbf{q}_{\alpha'} \cdot \sigma_T)} | \psi_\beta^P \rangle \\ &= \sum_{\alpha=1}^{\infty} F_\alpha(\sigma_T) \langle \psi_{\alpha'}^T | (H_T + \bar{V}_T - \varepsilon_\alpha^T) | \psi_\alpha^T \rangle e^{i(\mathbf{q}_\alpha - \mathbf{q}_{\alpha'}) \cdot \sigma_T} \\ &+ \sum_{\beta=1}^{\infty} G_\beta(\sigma_P) \langle \psi_{\alpha'}^T | (H_P + \bar{V}_P - \varepsilon_\beta^P) e^{i(\mathbf{q}_\beta \cdot \sigma_P - \mathbf{q}_{\alpha'} \cdot \sigma_T)} | \psi_\beta^P \rangle. \end{aligned} \quad (3.20)$$

Since the centre-of-mass of the target atom is very close to the target nucleus and the centre-of-mass of the projectile atom is very close to the projectile nucleus, we make the approximation $\sigma_T \approx \mathbf{R}$ and $\sigma_P \approx \mathbf{R}$. Therefore, $F_\alpha(\sigma_T) \approx F_\alpha(\mathbf{R})$ and $G_\beta(\sigma_P) \approx G_\beta(\mathbf{R})$. Consider the exponential term appearing in the sum over α in Eq. (3.20). Writing the momentum transfer as $\mathbf{q}_T \equiv \mathbf{q}_\alpha - \mathbf{q}_{\alpha'}$ we obtain

$$(\mathbf{q}_\alpha - \mathbf{q}_{\alpha'}) \cdot \sigma_T \approx (\mathbf{q}_\alpha - \mathbf{q}_{\alpha'}) \cdot \mathbf{R} = \mathbf{q}_T \cdot \mathbf{R}, \quad (3.21)$$

where

$$\mathbf{q}_T \cdot \mathbf{R} = q_T^{\parallel} z + \mathbf{q}_T^{\perp} \cdot \mathbf{b}. \quad (3.22)$$

In App. A it is shown that

$$\mathbf{q}_T \cdot \mathbf{R} = (\varepsilon_{\alpha'}^T - \varepsilon_{\alpha}^T)t + \mathbf{q}_T^{\perp} \cdot \mathbf{b}. \quad (3.23)$$

Now consider the other exponential term appearing in Eq. (3.20). We define the momentum transfer vectors

$$\begin{cases} \mathbf{p}_{\beta} = \gamma_P \mathbf{q}_{\beta} - \mathbf{q}_{\alpha'}, \\ \mathbf{p}_{\alpha'} = \mathbf{q}_{\beta} - \gamma_T \mathbf{q}_{\alpha'}, \end{cases} \quad (3.24)$$

where

$$\begin{cases} \gamma_T \equiv \frac{M_T - 1}{M_T}, \\ \gamma_P \equiv \frac{M_P}{M_P + 1}. \end{cases} \quad (3.25)$$

Here M_T is the mass of the target atom and M_P is the mass of the projectile ion.

Then we use the following results from App. A:

$$\mathbf{q}_{\beta} \cdot \boldsymbol{\sigma}_P - \mathbf{q}_{\alpha'} \cdot \boldsymbol{\sigma}_T = p_{\beta}^{\parallel} z + \mathbf{p}_{\beta}^{\perp} \cdot \mathbf{b} + \mathbf{v} \cdot \mathbf{r}_T, \quad (3.26)$$

and

$$p_{\beta}^{\parallel} = -\frac{v}{2} - \frac{(\varepsilon_{\beta}^P - \varepsilon_{\alpha'}^T)}{v}. \quad (3.27)$$

Combining Eqs. (3.23), (3.26), and (3.27) we write Eq. (3.20) as

$$\begin{aligned}
& i e^{i \mathbf{q}_T^\perp \cdot \mathbf{b}} \sum_{\alpha=1}^{\infty} \dot{F}_\alpha(\boldsymbol{\sigma}_T) \langle \psi_{\alpha'}^T | \psi_\alpha^T \rangle e^{i(\varepsilon_{\alpha'}^T - \varepsilon_\alpha^T)t} \\
& + i e^{i \mathbf{p}_\beta^\perp \cdot \mathbf{b}} \sum_{\beta=1}^{\infty} \dot{G}_\beta(\boldsymbol{\sigma}_P) \langle \psi_{\alpha'}^T | e^{i \mathbf{v} \cdot \mathbf{r}_T} | \psi_\beta^P \rangle e^{i((\varepsilon_{\alpha'}^T - \varepsilon_\beta^P) - v^2/2)t} \\
& = e^{i \mathbf{q}_T^\perp \cdot \mathbf{b}} \sum_{\alpha=1}^{\infty} F_\alpha(\mathbf{R}) \langle \psi_{\alpha'}^T | (H_T + \bar{V}_T - \varepsilon_\alpha^T) | \psi_\alpha^T \rangle e^{i(\varepsilon_{\alpha'}^T - \varepsilon_\alpha^T)t} \\
& + e^{i \mathbf{p}_\beta^\perp \cdot \mathbf{b}} \sum_{\beta=1}^{\infty} G_\beta(\mathbf{R}) \langle \psi_{\alpha'}^T | (H_P + \bar{V}_P - \varepsilon_\beta^P) e^{i \mathbf{v} \cdot \mathbf{r}_T} | \psi_\beta^P \rangle e^{i((\varepsilon_{\alpha'}^T - \varepsilon_\beta^P) - v^2/2)t}. \quad (3.28)
\end{aligned}$$

Since the momentum of the projectile in the incident channels, \mathbf{q}_α and \mathbf{q}_β , is along the direction of the z -axis, we have that $\mathbf{q}_T^\perp = -\mathbf{q}_{\alpha'}^\perp$ and $\mathbf{p}_\beta^\perp = -\mathbf{q}_{\alpha'}^\perp$. Removing these common terms from both sides we arrive at the first set of coupled-channel equations in the two-centre formalism,

$$\begin{aligned}
& i \dot{F}_\alpha(\boldsymbol{\sigma}_T) + i \sum_{\beta=1}^{\infty} \dot{G}_\beta(\boldsymbol{\sigma}_P) \langle \psi_{\alpha'}^T | e^{i \mathbf{v} \cdot \mathbf{r}_T} | \psi_\beta^P \rangle e^{i((\varepsilon_{\alpha'}^T - \varepsilon_\beta^P) - v^2/2)t} \\
& = \sum_{\alpha=1}^{\infty} F_\alpha(\mathbf{R}) \langle \psi_{\alpha'}^T | H_T + \bar{V}_T - \varepsilon_\alpha^T | \psi_\alpha^T \rangle e^{i(\varepsilon_{\alpha'}^T - \varepsilon_\alpha^T)t} \\
& + \sum_{\beta=1}^{\infty} G_\beta(\mathbf{R}) \langle \psi_{\alpha'}^T | (H_P + \bar{V}_P - \varepsilon_\beta^P) e^{i \mathbf{v} \cdot \mathbf{r}_T} | \psi_\beta^P \rangle e^{i((\varepsilon_{\alpha'}^T - \varepsilon_\beta^P) - v^2/2)t}. \quad (3.29)
\end{aligned}$$

Returning to Eq. (3.19) we now multiply on the left by $\psi_{\beta'}^{P*}(\mathbf{r}_P) e^{-i \mathbf{q}_{\beta'} \cdot \boldsymbol{\sigma}_P}$ and integrate over \mathbf{r}_P to get

$$\begin{aligned}
& i \sum_{\alpha=1}^{\infty} \dot{F}_\alpha(\boldsymbol{\sigma}_T) \langle \psi_{\beta'}^P | e^{i(\mathbf{q}_\alpha \cdot \boldsymbol{\sigma}_T - \mathbf{q}_{\beta'} \cdot \boldsymbol{\sigma}_P)} | \psi_\alpha^T \rangle \\
& + i \sum_{\beta=1}^{\infty} \dot{G}_\beta(\boldsymbol{\sigma}_P) \langle \psi_{\beta'}^P | \psi_\beta^P \rangle e^{i(\mathbf{q}_\beta - \mathbf{q}_{\beta'}) \cdot \mathbf{r}_P} \\
& = \sum_{\alpha=1}^{\infty} F_\alpha(\boldsymbol{\sigma}_T) \langle \psi_{\beta'}^P | (H_T + \bar{V}_T - \varepsilon_\alpha^T) e^{i(\mathbf{q}_\alpha \cdot \boldsymbol{\sigma}_T - \mathbf{q}_{\beta'} \cdot \boldsymbol{\sigma}_P)} | \psi_\alpha^T \rangle \\
& + \sum_{\beta=1}^{\infty} G_\beta(\boldsymbol{\sigma}_P) \langle \psi_{\beta'}^P | (H_P + \bar{V}_P - \varepsilon_\beta^P) | \psi_\beta^P \rangle e^{i(\mathbf{q}_\beta - \mathbf{q}_{\beta'}) \cdot \boldsymbol{\sigma}_P}. \quad (3.30)
\end{aligned}$$

We again use the semiclassical approximation to write $F_\alpha(\boldsymbol{\sigma}_T) \approx F_\alpha(\mathbf{R})$ and

$G_\beta(\boldsymbol{\sigma}_P) \approx G_\beta(\mathbf{R})$. We also make the approximation $\boldsymbol{\sigma}_P \approx \mathbf{R}$ in the exponential terms containing momentum transfer between two projectile channels. This allows us to write

$$(\mathbf{q}_\beta - \mathbf{q}_{\beta'}) \cdot \boldsymbol{\sigma}_P \approx (\mathbf{q}_\beta - \mathbf{q}_{\beta'}) \cdot \mathbf{R} = \mathbf{q}_P \cdot \mathbf{R}, \quad (3.31)$$

where $\mathbf{q}_P \equiv \mathbf{q}_\beta - \mathbf{q}_{\beta'}$ and

$$\mathbf{q}_P \cdot \mathbf{R} = q_P^\parallel z + \mathbf{q}_P^\perp \cdot \mathbf{b}. \quad (3.32)$$

It is shown in App. A that

$$\mathbf{q}_P \cdot \mathbf{R} = (\varepsilon_{\beta'}^P - \varepsilon_\beta^P)t + \mathbf{q}_P^\perp \cdot \mathbf{b}. \quad (3.33)$$

For the other exponential term in Eq. (3.30), we define the momentum transfer vectors

$$\begin{cases} \mathbf{p}_\alpha = \gamma_T \mathbf{q}_\alpha - \mathbf{q}_{\beta'}, \\ \mathbf{p}_{\beta'} = \mathbf{q}_\alpha - \gamma_P \mathbf{q}_{\beta'}. \end{cases} \quad (3.34)$$

This allows us to write (see App. A for details)

$$\mathbf{q}_\alpha \cdot \boldsymbol{\sigma}_T - \mathbf{q}_{\beta'} \cdot \boldsymbol{\sigma}_P = p_\alpha^\parallel z + \mathbf{p}_\alpha^\perp \cdot \mathbf{b} - \mathbf{v} \cdot \mathbf{r}_P, \quad (3.35)$$

where

$$p_\alpha^\parallel = -\frac{v}{2} - \frac{\varepsilon_\alpha^T - \varepsilon_{\beta'}^P}{v}. \quad (3.36)$$

With this, Eq. (3.30) becomes

$$\begin{aligned}
& i e^{i \mathbf{p}_\alpha^\perp \cdot \mathbf{b}} \sum_{\alpha=1}^{\infty} \dot{F}_\alpha(\boldsymbol{\sigma}_T) \langle \psi_{\beta'}^P | e^{-i \mathbf{v} \cdot \mathbf{r}_P} | \psi_\alpha^T \rangle e^{i((\varepsilon_{\beta'}^P - \varepsilon_\alpha^T) - v^2/2)t} \\
& + i e^{i \mathbf{q}_{\mathbb{P}}^\perp \cdot \mathbf{b}} \sum_{\beta=1}^{\infty} \dot{G}_\beta(\boldsymbol{\sigma}_P) \langle \psi_{\beta'}^P | \psi_\beta^P \rangle e^{i(\varepsilon_{\beta'}^P - \varepsilon_\beta^P)t} \\
& = e^{i \mathbf{p}_\alpha^\perp \cdot \mathbf{b}} \sum_{\alpha=1}^{\infty} F_\alpha(\mathbf{R}) \langle \psi_{\beta'}^P | (H_T + \bar{V}_T - \varepsilon_\alpha^T) e^{-i \mathbf{v} \cdot \mathbf{r}_P} | \psi_\alpha^T \rangle e^{i((\varepsilon_{\beta'}^P - \varepsilon_\alpha^T) - v^2/2)t} \\
& + e^{i \mathbf{q}_{\mathbb{P}}^\perp \cdot \mathbf{b}} \sum_{\beta=1}^{\infty} G_\beta(\mathbf{R}) \langle \psi_{\beta'}^P | (H_P + \bar{V}_P - \varepsilon_\beta^P) | \psi_\beta^P \rangle e^{i(\varepsilon_{\beta'}^P - \varepsilon_\beta^P)t} \tag{3.37}
\end{aligned}$$

Considering that \mathbf{q}_α and \mathbf{q}_β are directed along the z -axis, we find that, $\mathbf{q}_P^\perp = -\mathbf{q}_{\beta'}^\perp$ and $\mathbf{p}_\alpha^\perp = -\mathbf{q}_{\beta'}^\perp$. With this we arrive at the second set of coupled-channel equations in the two-centre formalism,

$$\begin{aligned}
& i \sum_{\alpha=1}^{\infty} \dot{F}_\alpha(\boldsymbol{\sigma}_T) \langle \psi_{\beta'}^P | e^{-i \mathbf{v} \cdot \mathbf{r}_P} | \psi_\alpha^T \rangle e^{i((\varepsilon_{\beta'}^P - \varepsilon_\alpha^T) - v^2/2)t} + i \dot{G}_\beta(\boldsymbol{\sigma}_P) \\
& = \sum_{\alpha=1}^{\infty} F_\alpha(\mathbf{R}) \langle \psi_{\beta'}^P | (H_T + \bar{V}_T - \varepsilon_\alpha^T) e^{-i \mathbf{v} \cdot \mathbf{r}_P} | \psi_\alpha^T \rangle e^{i((\varepsilon_{\beta'}^P - \varepsilon_\alpha^T) - v^2/2)t} \\
& + \sum_{\beta=1}^{\infty} G_\beta(\mathbf{R}) \langle \psi_{\beta'}^P | H_P + \bar{V}_P - \varepsilon_\beta^P | \psi_\beta^P \rangle e^{i(\varepsilon_{\beta'}^P - \varepsilon_\beta^P)t} \tag{3.38}
\end{aligned}$$

Combined, Eq. (3.29) and Eq. (3.38) form a set of equations that couples together all of the expansion coefficients:

$$\begin{cases} i \dot{F}_{\alpha'} + i \sum_{\beta=1}^{\infty} \dot{G}_\beta K_{\alpha'\beta}^T = \sum_{\alpha=1}^{\infty} F_\alpha D_{\alpha'\alpha}^T + \sum_{\beta=1}^{\infty} G_\beta Q_{\alpha'\beta}^T, \\ i \sum_{\alpha=1}^{\infty} \dot{F}_\alpha K_{\beta'\alpha}^P + i \dot{G}_{\beta'} = \sum_{\alpha=1}^{\infty} F_\alpha Q_{\beta'\alpha}^P + \sum_{\beta=1}^{\infty} G_\beta D_{\beta'\beta}^P. \end{cases} \tag{3.39}$$

Note that in Eq. (3.39) we omit the functional dependence of the expansion coefficients and matrix elements on \mathbf{R} for conciseness. The direct-scattering matrix

elements are

$$\begin{cases} D_{\alpha'\alpha}^{\text{T}}(\mathbf{R}) = e^{i(\varepsilon_{\alpha'}^{\text{T}} - \varepsilon_{\alpha}^{\text{T}})t} \mathcal{D}_{\alpha'\alpha}^{\text{T}}(\mathbf{R}), \\ D_{\beta'\beta}^{\text{P}}(\mathbf{R}) = e^{i(\varepsilon_{\beta'}^{\text{P}} - \varepsilon_{\beta}^{\text{P}})t} \mathcal{D}_{\beta'\beta}^{\text{P}}(\mathbf{R}), \end{cases} \quad (3.40)$$

where

$$\begin{cases} \mathcal{D}_{\alpha'\alpha}^{\text{T}}(\mathbf{R}) \equiv \langle \psi_{\alpha'}^{\text{T}} | \bar{V}_{\text{T}} | \psi_{\alpha}^{\text{T}} \rangle, \\ \mathcal{D}_{\beta'\beta}^{\text{P}}(\mathbf{R}) \equiv \langle \psi_{\beta'}^{\text{P}} | \bar{V}_{\text{P}} | \psi_{\beta}^{\text{P}} \rangle. \end{cases} \quad (3.41)$$

The overlap matrix elements are defined as

$$\begin{cases} K_{\beta'\alpha}^{\text{P}}(\mathbf{R}) = e^{i(\varepsilon_{\beta'}^{\text{P}} - \varepsilon_{\alpha}^{\text{T}})t} \mathcal{K}_{\beta'\alpha}^{\text{P}}(\mathbf{R}), \\ K_{\alpha'\beta}^{\text{T}}(\mathbf{R}) = e^{i(\varepsilon_{\alpha'}^{\text{T}} - \varepsilon_{\beta}^{\text{P}})t} \mathcal{K}_{\alpha'\beta}^{\text{T}}(\mathbf{R}), \end{cases} \quad (3.42)$$

where

$$\begin{cases} \mathcal{K}_{\beta'\alpha}^{\text{P}}(\mathbf{R}) \equiv e^{-iv^2t/2} \langle \psi_{\beta'}^{\text{P}} | e^{-i\mathbf{v}\cdot\mathbf{r}_{\text{P}}} | \psi_{\alpha}^{\text{T}} \rangle, \\ \mathcal{K}_{\alpha'\beta}^{\text{T}}(\mathbf{R}) \equiv e^{-iv^2t/2} \langle \psi_{\alpha'}^{\text{T}} | e^{i\mathbf{v}\cdot\mathbf{r}_{\text{T}}} | \psi_{\beta}^{\text{P}} \rangle. \end{cases} \quad (3.43)$$

The exchange matrix elements are

$$\begin{cases} Q_{\beta'\alpha}^{\text{P}}(\mathbf{R}) = e^{-iv^2t/2 + i(\varepsilon_{\beta'}^{\text{P}} - \varepsilon_{\alpha}^{\text{T}})t} \mathcal{Q}_{\beta'\alpha}^{\text{P}}(\mathbf{R}), \\ Q_{\alpha'\beta}^{\text{T}}(\mathbf{R}) = e^{-iv^2t/2 + i(\varepsilon_{\alpha'}^{\text{T}} - \varepsilon_{\beta}^{\text{P}})t} \mathcal{Q}_{\alpha'\beta}^{\text{T}}(\mathbf{R}), \end{cases} \quad (3.44)$$

where

$$\begin{cases} \mathcal{Q}_{\beta'\alpha}^{\text{P}}(\mathbf{R}) \equiv \langle \psi_{\beta'}^{\text{P}} | e^{-i\mathbf{v}\cdot\mathbf{r}_{\text{P}}} (H_{\text{T}} + \bar{V}_{\text{T}} - \varepsilon_{\alpha}^{\text{T}}) | \psi_{\alpha}^{\text{T}} \rangle, \\ \mathcal{Q}_{\alpha'\beta}^{\text{T}}(\mathbf{R}) \equiv \langle \psi_{\alpha'}^{\text{T}} | e^{i\mathbf{v}\cdot\mathbf{r}_{\text{T}}} (H_{\text{P}} + \bar{V}_{\text{P}} - \varepsilon_{\beta}^{\text{P}}) | \psi_{\beta}^{\text{P}} \rangle. \end{cases} \quad (3.45)$$

The set of equations in Eq. (3.39) is solved subject to the initial condition

$$F_{\alpha}(-\infty, \mathbf{b}) = \delta_{\alpha i}, \quad G_{\beta}(-\infty, \mathbf{b}) = 0, \quad (3.46)$$

i.e. the active electron is initially in the state $\alpha = i$ of the target atom. The expansion of the total scattering wave function is limited to finite size. Equation (3.39) is exact.¹ However, for practical calculations the size of the basis must be finite. Therefore, the infinite summations over α and β are truncated by limiting the number of basis states used in the expansion in Eq. (3.7). The total number of target states is $N^T = N_b^T + N_c^T$, where N_b^T is the number of bound states and N_c^T is the number of pseudostates representing the continuum of the target. The total number of projectile states is $N^P = N_b^P + N_c^P$, where N_b^P is the number of bound states and N_c^P is the number of pseudostates representing the continuum of the projectile. The final results converge as the number of included basis states increases. If N^P is set to zero then Eq. (3.39) reduces to

$$i\dot{F}_{\alpha'}(\mathbf{R}) = \sum_{\alpha=1}^{\infty} F_{\alpha}(\mathbf{R}) D_{\alpha'\alpha}(\mathbf{R}), \quad (3.47)$$

and we recover the single-centre scattering equations.

3.2 Target structure

In this section we describe our method for constructing orthonormal basis states that diagonalise the Hamiltonian of the hydrogen atom and hydrogen-like ions. That is, systems consisting of a single electron and a Coulombic interaction between the electron and nucleus such as H, He⁺, Li²⁺, etc. We describe the structure of a hydrogen-like target but the same approach is used to construct pseudostates for the hydrogen-like projectile atom formed by electron capture. The interaction between the nucleus and electron is spherically symmetric. Therefore, the radial and angular parts of the target-atom (or projectile-atom) wave function are separable. The radial part of the target wave function varies depending on the target species. However, the solution to the angular part for spherically symmetric potentials is always given by the spherical harmonic functions. We

¹within the semiclassical approximation

write

$$\psi_{n\ell m}(\mathbf{r}_T) \equiv \frac{\phi_{n\ell}(r_T)}{r_T} Y_{\ell m}(\hat{\mathbf{r}}_T), \quad (3.48)$$

where $\phi_{n\ell}(r_T)$ is the reduced radial wave function and n , ℓ , and m are the principal, orbital angular momentum, and magnetic quantum numbers, respectively. The bound-state wave functions for hydrogen-like systems are the eigenfunctions, $\psi_\alpha^T(\mathbf{r}_T)$, of the Schrödinger equation,

$$H_T \psi_\alpha(\mathbf{r}_T) = \varepsilon_\alpha \psi_\alpha(\mathbf{r}_T), \quad (3.49)$$

where ε_α is the energy of the state $\alpha = \{n\ell m\}$ and the target Hamiltonian is defined as in Sect. 3.1. The radial wave equation is

$$-\frac{d^2 \phi_{n\ell}}{dr_T^2} + \left[\frac{\ell(\ell+1)}{r_T^2} - \frac{2Z_T}{r_T} - 2\varepsilon_\alpha \right] \phi_{n\ell}(r_T) = 0. \quad (3.50)$$

Equation (3.50) is solved in the standard way [101], leading to an analytical expression for the radial wave functions,

$$\phi_{n\ell}(r_T) = Z_T^{3/2} \frac{2r_T}{n^2} \sqrt{\frac{(n-\ell-1)!}{[(n+\ell)!]^3}} \left(\frac{2r_T}{Z_T n} \right)^\ell e^{-Z_T r_T/n} L_{n-\ell-1}^{2\ell+1} \left(\frac{2r_T}{Z_T n} \right) \quad (3.51)$$

where $L_{n-\ell-1}^{2\ell+1}(x)$ are the associated Laguerre polynomials. The eigenvalues of Eq. (3.49) are

$$\varepsilon_\alpha = -\frac{Z_T^2}{2n^2}. \quad (3.52)$$

3.2.1 Wave-packet pseudostates

Solution of the Schrödinger equation for a hydrogen-like atom is possible for both negative and positive energy eigenvalues. However, while it is possible to obtain a normalisable set of orthogonal solutions when $\varepsilon_\alpha < 0$, the positive-energy solution

is unbounded and extends to infinity. This makes it unsuitable for scattering calculations since it is not square-integrable. Instead we take the approach of constructing a finite set of orthonormal stationary wave packets to represent the continuum. This is done by first discretising the electron momentum κ into a finite set of n_{pos} intervals, $[k_N, k_{N+1}]$, where $N \in [1, n_{\text{pos}}]$. Within each interval we construct stationary wave-packet pseudostates for different orbital angular momentum ℓ and angular momentum projection m according to

$$\psi_{\alpha}^{\text{WP}}(\mathbf{r}_{\text{T}}) \equiv \psi_{n\ell m}^{\text{WP}}(\mathbf{r}_{\text{T}}) = \frac{\phi_{n\ell}^{\text{WP}}(r_{\text{T}})}{r_{\text{T}}} Y_{\ell m}(\hat{\mathbf{r}}_{\text{T}}). \quad (3.53)$$

The reduced radial wave function, $\phi_{n\ell}^{\text{WP}}(r_{\text{T}})$, in Eq. (3.53) is determined by integrating the true continuum-wave solution over the bin,

$$\phi_{n\ell}^{\text{WP}}(r_{\text{T}}) = \mathcal{N}_n \int_{k_N}^{k_{N+1}} d\kappa \sqrt{\kappa} \phi_{\kappa\ell}(r_{\text{T}}), \quad (3.54)$$

where \mathcal{N}_n is the normalisation constant, and $\phi_{\kappa\ell}(r_{\text{T}})$ is defined in terms of the pure Coulomb wave as

$$\phi_{\kappa\ell}(r_{\text{T}}) = \sqrt{\frac{2}{\pi}} F_{\ell\kappa}(r_{\text{T}}). \quad (3.55)$$

The partial-wave expansion of the incoming Coulomb wave function is written as [101]

$$\psi_{\kappa}^{-}(\mathbf{r}_{\text{T}}) = \frac{4\pi}{\kappa r_{\text{T}}} \sum_{\lambda\mu} i^{\lambda} e^{-i\sigma_{\lambda}^{\text{T}}(\kappa)} F_{\kappa\lambda}^{*}(r_{\text{T}}) Y_{\lambda\mu}^{*}(\hat{\mathbf{r}}_{\text{T}}) Y_{\lambda\mu}(\hat{\mathbf{k}}), \quad (3.56)$$

where

$$F_{\kappa\ell}(r_{\text{T}}) = 2^{\ell} (\kappa r_{\text{T}})^{\ell+1} \exp\left(\frac{\pi}{2\kappa}\right) \frac{|\Gamma(\ell+1-i/\kappa)|}{(2\ell+1)!} \\ \times \exp(i\kappa r_{\text{T}}) {}_1F_1(\ell+1-i/\kappa, 2\ell+2, -2i\kappa r), \quad (3.57)$$

and for conciseness we have introduced the notation

$$\sum_{\lambda\mu} = \sum_{\lambda=0}^{\infty} \sum_{\mu=-\lambda}^{\lambda}. \quad (3.58)$$

The wave functions in Eqs. (3.55) and (3.56) are normalised according to

$$\int_0^{\infty} dr_{\text{T}} \phi_{\kappa\ell}(r_{\text{T}}) \phi_{\kappa'\ell}(r_{\text{T}}) = \delta(\kappa' - \kappa), \quad (3.59)$$

and

$$\int d\mathbf{r}_{\text{T}} \psi_{\boldsymbol{\kappa}}^{-*}(\mathbf{r}_{\text{T}}) \psi_{\boldsymbol{\kappa}'}^{-}(\mathbf{r}_{\text{T}}) = (2\pi)^3 \delta(\boldsymbol{\kappa} - \boldsymbol{\kappa}'), \quad (3.60)$$

respectively.

The normalisation, \mathcal{N}_n , is defined such that the wave-packet pseudostates are orthonormal, i.e.

$$1 = \langle \psi_{n\ell m}^{\text{WP}} | \psi_{n\ell m}^{\text{WP}} \rangle = \int_0^{\infty} dr_{\text{T}} r_{\text{T}}^2 \frac{\phi_{n\ell}^{\text{WP}*}}{r_{\text{T}}} \frac{\phi_{n\ell}^{\text{WP}}}{r_{\text{T}}} \int d\hat{\mathbf{r}}_{\text{T}} Y_{\ell m}^*(\hat{\mathbf{r}}_{\text{T}}) Y_{\ell m}(\hat{\mathbf{r}}_{\text{T}}) \quad (3.61)$$

The angular integral can be taken trivially. Then we substitute the integral definition of the reduced radial wave function and rearrange to find that

$$\mathcal{N}_n = \sqrt{\frac{2}{k_{N+1}^2 - k_N^2}} \equiv \frac{1}{\sqrt{E_{N+1} - E_N}}, \quad (3.62)$$

where E_N is the energy corresponding to the momentum bin limit k_N .

To find the energy of the wave-packet pseudostate we diagonalise the Hamiltonian,

$$\varepsilon_n \equiv \langle \psi_{n'\ell'm'}^{\text{WP}} | H_{\text{T}} | \psi_{n\ell m}^{\text{WP}} \rangle. \quad (3.63)$$

After inserting Eqs. (3.54), (3.59), and (3.62), it is easy to see that

$$\langle \psi_{n'\ell'm'}^{\text{WP}} | H_{\text{T}} | \psi_{n\ell m}^{\text{WP}} \rangle = \delta_{n'n} \frac{k_{N+1}^2 + k_N^2}{4}. \quad (3.64)$$

Thus, the energy of the wave packet is in fact defined as the midpoint between the energies corresponding to k_{N+1} and k_N . We also introduce the momentum of the electron corresponding to the N^{th} wave packet:

$$\kappa_n = \sqrt{2\varepsilon_n}. \quad (3.65)$$

Combined, the negative-energy eigenstates given in Eq. (3.51) and the wave-packet pseudostates defined by Eq. (3.53) form an orthonormal basis that diagonalises the target Hamiltonian.

3.3 Evaluation of matrix elements

3.3.1 Direct-scattering matrix elements

To evaluate the direct-scattering matrix elements we separate the radial and angular parts of the target states and substitute Eq. (3.6) into Eq. (3.41). For the first set of matrix elements this results in

$$\mathcal{D}_{\alpha'\alpha}^{\text{T}} = \int d\mathbf{r}_{\text{T}} \frac{\phi_{\alpha'}^{\text{T}}(r_{\text{T}})}{r_{\text{T}}} Y_{\ell_{\alpha'} m_{\alpha'}}^*(\hat{\mathbf{r}}_{\text{T}}) \left(\frac{Z_{\text{T}} Z_{\text{P}}}{R} - \frac{Z_{\text{P}}}{|\mathbf{r}_{\text{T}} - \mathbf{R}|} \right) \frac{\phi_{\alpha}^{\text{T}}(r_{\text{T}})}{r_{\text{T}}} Y_{\ell_{\alpha} m_{\alpha}}(\hat{\mathbf{r}}_{\text{T}}). \quad (3.66)$$

The Coulomb potential in the second term can be expanded in terms of spherical harmonics [102], leading to

$$\begin{aligned} \mathcal{D}_{\alpha'\alpha}^{\text{T}} &= 4\pi \sum_{\lambda\mu} \frac{Y_{\lambda\mu}^*(\hat{\mathbf{R}})}{2\lambda + 1} \int dr_{\text{T}} \phi_{\alpha'}^{\text{T}}(r_{\text{T}}) \phi_{\alpha}^{\text{T}}(r_{\text{T}}) \mathcal{U}_{\lambda}(R, r_{\text{T}}) \\ &\quad \times \int d\hat{\mathbf{r}}_{\text{T}} Y_{\ell_{\alpha'} m_{\alpha'}}^*(\hat{\mathbf{r}}_{\text{T}}) Y_{\ell_{\alpha} m_{\alpha}}(\hat{\mathbf{r}}_{\text{T}}) Y_{\lambda\mu}(\hat{\mathbf{r}}_{\text{T}}), \end{aligned} \quad (3.67)$$

where we define

$$\mathcal{U}_\lambda(R, r_T) \equiv \begin{cases} \frac{\delta_{\lambda 0} Z_P}{R} - \frac{Z_P R^\lambda}{r_T^{\lambda+1}}, & R \leq r, \\ \frac{\delta_{\lambda 0} Z_P}{R} - \frac{Z_P r_T^\lambda}{R^{\lambda+1}}, & R > r. \end{cases} \quad (3.68)$$

Taking the angular integral analytically results in

$$\begin{aligned} \mathcal{D}_{\alpha'\alpha}^T &= \sum_{\lambda\mu} \sqrt{\frac{4\pi[\ell_\alpha]}{[\ell_{\alpha'}][\lambda]}} C_{\ell_\alpha 0 \lambda 0}^{\ell_{\alpha'} 0} C_{\ell_\alpha m_\alpha \lambda \mu}^{\ell_{\alpha'} m_{\alpha'}} Y_{\lambda\mu}^*(\hat{\mathbf{R}}) \\ &\times \int dr_T \phi_{\alpha'}^T(r_T) \phi_\alpha^T(r_T) \mathcal{U}_\lambda(R, r_T), \end{aligned} \quad (3.69)$$

where $[\ell] \equiv 2\ell + 1$. This can be further simplified since the Clebsch-Gordan coefficients are only non-zero if $|\ell_{\alpha'} - \ell_\alpha| \leq \lambda \leq \ell_{\alpha'} + \ell_\alpha$ and $m_{\alpha'} = m_\alpha + \mu$. Additionally, the upper limits for $\ell_{\alpha'}$ and ℓ_α are set by the size of the basis used in the expansion of the total scattering wave function. Hence, the infinite summation over λ is truncated at $\lambda_{\max} = \ell_{\alpha'} + \ell_\alpha$, and the summation over μ is removed since only the term in which $\mu = m_{\alpha'} - m_\alpha$ is non-zero. The final form of the direct-scattering matrix elements is therefore

$$\begin{aligned} \mathcal{D}_{\alpha'\alpha}^T &= \sum_{\lambda=|\ell_{\alpha'}-\ell_\alpha|}^{\ell_{\alpha'}+\ell_\alpha} \sqrt{\frac{4\pi[\ell_\alpha]}{[\ell_{\alpha'}][\lambda]}} C_{\ell_\alpha 0 \lambda 0}^{\ell_{\alpha'} 0} C_{\ell_\alpha m_\alpha \lambda (m_{\alpha'}-m_\alpha)}^{\ell_{\alpha'} m_{\alpha'}} Y_{\lambda(m_{\alpha'}-m_\alpha)}^*(\hat{\mathbf{R}}) \\ &\times \int dr_T \phi_{\alpha'}^T(r_T) \phi_\alpha^T(r_T) \mathcal{U}_\lambda(R, r_T). \end{aligned} \quad (3.70)$$

The integral over r_T is evaluated numerically.

For the second set of matrix elements in Eq. (3.41), we obtain

$$\begin{aligned} \mathcal{D}_{\beta'\beta}^P &= \sum_{\lambda=|\ell_{\beta'}-\ell_\beta|}^{\ell_{\beta'}+\ell_\beta} \sqrt{\frac{4\pi[\ell_\beta]}{[\ell_{\beta'}][\lambda]}} C_{\ell_\beta 0 \lambda 0}^{\ell_{\beta'} 0} C_{\ell_\beta m_\beta \lambda (m_{\beta'}-m_\beta)}^{\ell_{\beta'} m_{\beta'}} Y_{\lambda(m_{\beta'}-m_\beta)}^*(\hat{\mathbf{R}}) \\ &\times \int dr_P \phi_{\beta'}^P(r_P) \phi_\beta^P(r_P) \mathcal{U}_\lambda(R, r_P). \end{aligned} \quad (3.71)$$

3.3.2 Overlap matrix elements

Defining the electron position vector, $\mathbf{r} = (r, \theta_e, \varphi_e)$, from the midpoint of \mathbf{R} we have

$$\begin{cases} \mathbf{r}_T = \mathbf{r} + \frac{\mathbf{R}}{2}, \\ \mathbf{r}_P = \mathbf{r} - \frac{\mathbf{R}}{2}. \end{cases} \quad (3.72)$$

Using Eqs. (3.72), we can write the matrix elements in Eq. (3.43) as

$$\begin{cases} \mathcal{K}_{\beta'\alpha}^P = e^{-iv^2t/2} \int d\mathbf{r} \psi_{\beta'}^{P*}(\mathbf{r} - \mathbf{R}/2) e^{-i\mathbf{v}\cdot(\mathbf{r}-\mathbf{R}/2)} \psi_{\alpha}^T(\mathbf{r} + \mathbf{R}/2), \\ \mathcal{K}_{\alpha'\beta}^T = e^{-iv^2t/2} \int d\mathbf{r} \psi_{\alpha'}^{T*}(\mathbf{r} + \mathbf{R}/2) e^{i\mathbf{v}\cdot(\mathbf{r}+\mathbf{R}/2)} \psi_{\beta}^P(\mathbf{r} - \mathbf{R}/2). \end{cases} \quad (3.73)$$

Using the fact that²

$$\mathbf{v} \cdot \frac{\mathbf{R}}{2} = \frac{vR}{2} \cos(\theta_{\mathbf{v}\mathbf{R}}) = \frac{v^2t}{2}, \quad (3.74)$$

where $\theta_{\mathbf{v}\mathbf{R}}$ is the angle between the vectors \mathbf{v} and \mathbf{R} , we obtain

$$\begin{cases} \mathcal{K}_{\beta'\alpha}^P = \int d\mathbf{r} \psi_{\beta'}^{P*}(\mathbf{r} - \mathbf{R}/2) e^{-i\mathbf{v}\cdot\mathbf{r}} \psi_{\alpha}^T(\mathbf{r} + \mathbf{R}/2), \\ \mathcal{K}_{\alpha'\beta}^T = \int d\mathbf{r} \psi_{\alpha'}^{T*}(\mathbf{r} + \mathbf{R}/2) e^{i\mathbf{v}\cdot\mathbf{r}} \psi_{\beta}^P(\mathbf{r} - \mathbf{R}/2). \end{cases} \quad (3.75)$$

Taking the complex conjugate of $\mathcal{K}_{\beta'\alpha}^P$ yields

$$\mathcal{K}_{\beta'\alpha}^{P*} = \int d\mathbf{r} \psi_{\beta'}^P(\mathbf{r} - \mathbf{R}/2) e^{i\mathbf{v}\cdot\mathbf{r}} \psi_{\alpha}^{T*}(\mathbf{r} + \mathbf{R}/2) = \mathcal{K}_{\alpha\beta'}^T. \quad (3.76)$$

Thus, we see that the target and projectile overlap matrix elements are in fact complex conjugates of one another. Therefore, it is sufficient to calculate only the first of Eqs. (3.75) and use Eq. (3.76) to recover $\mathcal{K}_{\alpha'\beta}^T$. For the remainder of this section we make the replacement $\beta' \rightarrow \beta$ and consider the overlap matrix

²The vector \mathbf{v} is directed along the z -axis so the angle between \mathbf{R} and \mathbf{v} is simply the polar angle of \mathbf{R} , i.e. vt/R .

element for transition from an arbitrary channel α to arbitrary channel β .

It is convenient to calculate the integral entering the overlap matrix elements in the rotating molecular frame. Coordinates in the molecular frame are denoted

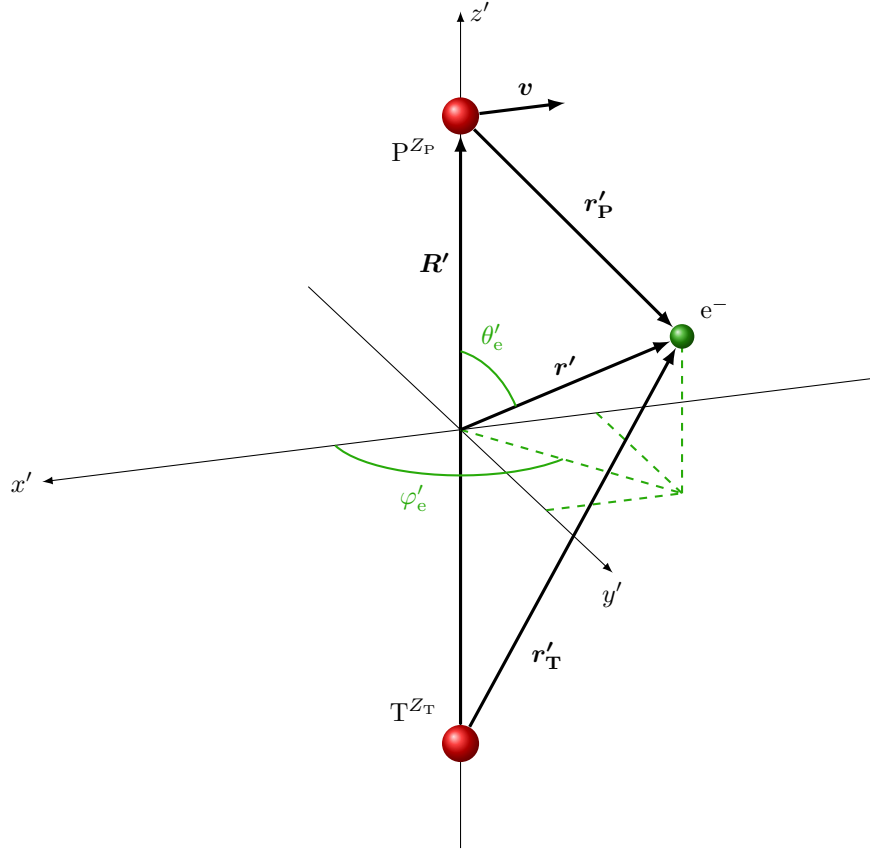


Figure 3.3: Spherical coordinates of the electron in the rotating molecular frame. Shown here the projectile ion is at the position of closest approach, i.e. v' is perpendicular to the z' -axis.

with primes. The molecular frame is defined such that the z' -axis is oriented along the vector \mathbf{R} , and the origin is at the midpoint between the target and projectile nuclei, as illustrated in Fig. 3.3. The target is positioned at $-\mathbf{R}'/2$ and the projectile is positioned at $\mathbf{R}'/2$, where \mathbf{R}' is directed along the z' -axis from the target nucleus to the projectile nucleus. Details of the transformation from laboratory frame to rotating molecular frame are given in App. B.

We separate the target and projectile wave functions in terms of radial and angular components. In the rotated frame the magnitudes r_T and r_P remain unchanged so the radial wave functions are the same in both frames of reference. To

express the angular parts in the rotated frame, we expand the spherical harmonics in terms of Wigner- D rotation matrices [102],

$$\begin{cases} Y_{\ell_\alpha m_\alpha}(\hat{\mathbf{r}}_T) = \sum_{\mu_\alpha=-m_\alpha}^{m_\alpha} D_{m_\alpha \mu_\alpha}^{\ell_\alpha*}(\varphi_{\mathbf{b}}, \theta_{\mathbf{R}}, 0) Y_{\ell_\alpha \mu_\alpha}(\hat{\mathbf{r}}'_T), \\ Y_{\ell_\beta m_\beta}(\hat{\mathbf{r}}_P) = \sum_{\mu_\beta=-m_\beta}^{m_\beta} D_{m_\beta \mu_\beta}^{\ell_\beta*}(\varphi_{\mathbf{b}}, \theta_{\mathbf{R}}, 0) Y_{\ell_\beta \mu_\beta}(\hat{\mathbf{r}}'_P). \end{cases} \quad (3.77)$$

Using the identity

$$D_{m\mu}^\ell(\alpha, \beta, \gamma) = e^{-im\alpha} d_{m\mu}^\ell(\beta) e^{-i\mu\gamma}, \quad (3.78)$$

and symmetry property

$$d_{m\mu}^\ell(-\beta) = (-1)^{m-\mu} d_{m\mu}^\ell(\beta), \quad (3.79)$$

we write Eqs. (3.77) in terms of the real-valued (small) Wigner- d matrices as

$$\begin{cases} Y_{\ell_\alpha m_\alpha}(\hat{\mathbf{r}}_T) = \sum_{\mu_\alpha=-m_\alpha}^{m_\alpha} (-1)^{m_\alpha-\mu_\alpha} e^{im_\alpha\varphi_{\mathbf{b}}} d_{\mu_\alpha m_\alpha}^{\ell_\alpha}(\theta_{\mathbf{R}}) Y_{\ell_\alpha \mu_\alpha}(\hat{\mathbf{r}}'_T), \\ Y_{\ell_\beta m_\beta}(\hat{\mathbf{r}}_P) = \sum_{\mu_\beta=-m_\beta}^{m_\beta} (-1)^{m_\beta-\mu_\beta} e^{im_\beta\varphi_{\mathbf{b}}} d_{\mu_\beta m_\beta}^{\ell_\beta}(\theta_{\mathbf{R}}) Y_{\ell_\beta \mu_\beta}(\hat{\mathbf{r}}'_P), \end{cases} \quad (3.80)$$

respectively. Furthermore, we write the spherical harmonic functions in terms of the associated Legendre polynomials [102] so that Eqs. (3.80) become

$$\begin{cases} Y_{\ell_\alpha m_\alpha}(\hat{\mathbf{r}}_T) = e^{im_\alpha\varphi_{\mathbf{b}}} \sqrt{\frac{[\ell_\alpha]}{4\pi}} \sum_{\mu_\alpha=-m_\alpha}^{m_\alpha} (-1)^{m_\alpha-\mu_\alpha} d_{\mu_\alpha m_\alpha}^{\ell_\alpha}(\theta_{\mathbf{R}}) \\ \quad \times \sqrt{\frac{(\ell_\alpha - \mu_\alpha)!}{(\ell_\alpha + \mu_\alpha)!}} P_{\ell_\alpha}^{\mu_\alpha}(\cos \theta'_T) e^{i\mu_\alpha\varphi_T}, \\ Y_{\ell_\beta m_\beta}(\hat{\mathbf{r}}_P) = e^{im_\beta\varphi_{\mathbf{b}}} \sqrt{\frac{[\ell_\beta]}{4\pi}} \sum_{\mu_\beta=-m_\beta}^{m_\beta} (-1)^{m_\beta-\mu_\beta} d_{\mu_\beta m_\beta}^{\ell_\beta}(\theta_{\mathbf{R}}) \\ \quad \times \sqrt{\frac{(\ell_\beta - \mu_\beta)!}{(\ell_\beta + \mu_\beta)!}} P_{\ell_\beta}^{\mu_\beta}(\cos \theta'_P) e^{i\mu_\beta\varphi_P}, \end{cases}$$

respectively. The azimuthal angle of the electron in the target and projectile frames is the same since the axis of quantisation is the same in both frames (parallel to \mathbf{v}) and the orientation of the xy -plane may be chosen identically. Therefore, $\varphi_T = \varphi_P = \varphi_e$, and consequently upon rotation $\varphi'_T = \varphi'_P = \varphi'_e$.

Next we make the transformation from spherical to prolate spheroidal coordinates, (η, τ, φ_e) , where $1 \leq \eta \leq \infty$, $-1 \leq \tau \leq 1$, and $0 \leq \varphi_e \leq 2\pi$. Details of the transformation are given in App. B. We also define the radial wave function $\mathcal{R}_{n\ell}(r) \equiv \phi_{n\ell}(r)/r$. Then, the overlap matrix element is written in the rotating molecular frame as

$$\begin{aligned} \mathcal{K}_{\beta\alpha} = & e^{i(m_\alpha - m_\beta)\varphi_b} (-1)^{m_\alpha + m_\beta} \frac{R^3}{32\pi} \sqrt{[\ell_\alpha][\ell_\beta]} \\ & \times \sum_{\mu_\alpha \mu_\beta} (-1)^{-\mu_\alpha - \mu_\beta} d_{\mu_\alpha m_\alpha}^{\ell_\alpha}(\theta_R) d_{\mu_\beta m_\beta}^{\ell_\beta}(\theta_R) \sqrt{\frac{(\ell_\alpha - \mu_\alpha)! (\ell_\beta - \mu_\beta)!}{(\ell_\alpha + \mu_\alpha)! (\ell_\beta + \mu_\beta)!}} \\ & \times \int_1^\infty d\eta \int_{-1}^1 d\tau (\eta^2 - \tau^2) e^{-i\frac{v^2 t}{2} \eta \tau} \mathcal{R}_{n_\beta \ell_\beta}^P \left(\frac{R(\eta - \tau)}{2} \right) \mathcal{R}_{n_\alpha \ell_\alpha}^T \left(\frac{R(\eta + \tau)}{2} \right) \\ & \times P_{\ell_\beta}^{\mu_\beta} \left(\frac{\eta\tau - 1}{\eta - \tau} \right) P_{\ell_\alpha}^{\mu_\alpha} \left(\frac{\eta\tau + 1}{\eta + \tau} \right) \int_0^{2\pi} d\varphi_e e^{i(\mu_\alpha - \mu_{\beta'})\varphi_e} e^{i\frac{vb}{2} \sqrt{(\eta^2 - 1)(1 - \tau^2)} \cos(\varphi_e)}. \end{aligned} \quad (3.81)$$

Using the integral definition of the Bessel functions [103] the integral over φ_e can be taken analytically, resulting in

$$\begin{aligned} \mathcal{K}_{\beta\alpha} = & e^{i(m_\alpha - m_\beta)\varphi_b} (-1)^{m_\alpha + m_\beta} \frac{R^3}{16} \sqrt{[\ell_\alpha][\ell_\beta]} \\ & \times \sum_{\mu_\alpha \mu_\beta} (-1)^{-\mu_\alpha - \mu_\beta} i^{\mu_\alpha - \mu_\beta} d_{\mu_\alpha m_\alpha}^{\ell_\alpha}(\theta_R) d_{\mu_\beta m_\beta}^{\ell_\beta}(\theta_R) \sqrt{\frac{(\ell_\alpha - \mu_\alpha)! (\ell_\beta - \mu_\beta)!}{(\ell_\alpha + \mu_\alpha)! (\ell_\beta + \mu_\beta)!}} \\ & \times \int_1^\infty d\eta \int_{-1}^1 d\tau (\eta^2 - \tau^2) e^{-i\frac{v^2 t}{2} \eta \tau} \mathcal{R}_{n_\beta \ell_\beta}^P \left(\frac{R(\eta - \tau)}{2} \right) \mathcal{R}_{n_\alpha \ell_\alpha}^T \left(\frac{R(\eta + \tau)}{2} \right) \\ & \times P_{\ell_\beta}^{\mu_\beta} \left(\frac{\eta\tau - 1}{\eta - \tau} \right) P_{\ell_\alpha}^{\mu_\alpha} \left(\frac{\eta\tau + 1}{\eta + \tau} \right) J_{\mu_\alpha - \mu_\beta} \left(\frac{vb}{2} \sqrt{(\eta^2 - 1)(1 - \tau^2)} \right). \end{aligned} \quad (3.82)$$

Explicit expressions for both $\mathcal{K}_{\beta'\alpha}^P$ and $\mathcal{K}_{\alpha'\beta}^T$ are obtained from Eq. (3.82) as follows. For $\mathcal{K}_{\beta'\alpha}^P$, we first swap $\beta \rightarrow \beta'$. Then, we replace $\tau \rightarrow -\tau$ in the integral

and use the parity relation for the associated Legendre polynomials to get

$$\begin{aligned}
\mathcal{K}_{\beta'\alpha}^{\text{P}} &= e^{i(m_\alpha - m_{\beta'})\varphi_{\mathbf{b}}} (-1)^{\ell_\alpha + \ell_{\beta'} + m_\alpha + m_{\beta'}} \frac{R^3}{16} \sqrt{[\ell_\alpha][\ell_{\beta'}]} \\
&\times \sum_{\mu_\alpha \mu_{\beta'}} i^{\mu_\alpha - \mu_{\beta'}} d_{\mu_\alpha m_\alpha}^{\ell_\alpha}(\theta_R) d_{\mu_{\beta'} m_{\beta'}}^{\ell_{\beta'}}(\theta_R) \sqrt{\frac{(\ell_\alpha - \mu_\alpha)! (\ell_{\beta'} - \mu_{\beta'})!}{(\ell_\alpha + \mu_\alpha)! (\ell_{\beta'} + \mu_{\beta'})!}} \\
&\times \int_1^\infty d\eta \int_{-1}^1 d\tau (\eta^2 - \tau^2) e^{i\frac{v^2 t}{2} \eta \tau} \mathcal{R}_{n_{\beta'} \ell_{\beta'}}^{\text{P}} \left(\frac{R(\eta + \tau)}{2} \right) \mathcal{R}_{n_\alpha \ell_\alpha}^{\text{T}} \left(\frac{R(\eta - \tau)}{2} \right) \\
&\times P_{\ell_{\beta'}}^{\mu_{\beta'}} \left(\frac{\eta\tau + 1}{\eta + \tau} \right) P_{\ell_\alpha}^{\mu_\alpha} \left(\frac{\eta\tau - 1}{\eta - \tau} \right) J_{\mu_\alpha - \mu_{\beta'}} \left(\frac{vb}{2} \sqrt{(\eta^2 - 1)(1 - \tau^2)} \right). \quad (3.83)
\end{aligned}$$

The other overlap matrix element is found by taking the complex conjugate of Eq. (3.82), replacing α with α' , and applying the parity relation for the Bessel functions,

$$\begin{aligned}
\mathcal{K}_{\alpha'\beta}^{\text{T}} &= e^{i(m_\beta - m_{\alpha'})\varphi_{\mathbf{b}}} (-1)^{m_\beta + m_{\alpha'}} \frac{R^3}{16} \sqrt{(2\ell_{\alpha'} + 1)(2\ell_\beta + 1)} \\
&\times \sum_{\mu_{\alpha'} \mu_\beta} i^{\mu_\beta - \mu_{\alpha'}} d_{\mu_{\alpha'} m_{\alpha'}}^{\ell_{\alpha'}}(\theta_R) d_{\mu_\beta m_\beta}^{\ell_\beta}(\theta_R) \sqrt{\frac{(\ell_{\alpha'} - \mu_{\alpha'})! (\ell_\beta - \mu_\beta)!}{(\ell_{\alpha'} + \mu_{\alpha'})! (\ell_\beta + \mu_\beta)!}} \\
&\times \int_1^\infty d\eta \int_{-1}^1 d\tau (\eta^2 - \tau^2) e^{i\frac{v^2 t}{2} \eta \tau} \mathcal{R}_{n_{\alpha'} \ell_{\alpha'}}^{\text{P}} \left(\frac{R(\eta - \tau)}{2} \right) \mathcal{R}_{n_\beta \ell_\beta}^{\text{T}} \left(\frac{R(\eta + \tau)}{2} \right) \\
&\times P_{\ell_\beta}^{\mu_\beta} \left(\frac{\eta\tau - 1}{\eta - \tau} \right) P_{\ell_{\alpha'}}^{\mu_{\alpha'}} \left(\frac{\eta\tau + 1}{\eta + \tau} \right) J_{\mu_\beta - \mu_{\alpha'}} \left(\frac{vb}{2} \sqrt{(\eta^2 - 1)(1 - \tau^2)} \right). \quad (3.84)
\end{aligned}$$

3.3.3 Exchange matrix elements

To calculate the exchange matrix elements we express the electron position vectors in terms of \mathbf{r} and use Eq. (3.74) to obtain

$$\begin{cases} \mathcal{Q}_{\beta'\alpha}^{\text{P}} = \int d\mathbf{r} \psi_{\beta'}^{\text{P}*}(\mathbf{r} - \mathbf{R}/2) e^{-i\mathbf{v}\cdot\mathbf{r}} (H_{\text{T}} + \bar{V}_{\text{T}} - \varepsilon_\alpha^{\text{T}}) \psi_\alpha^{\text{T}}(\mathbf{r} + \mathbf{R}/2), \\ \mathcal{Q}_{\alpha'\beta}^{\text{T}} = \int d\mathbf{r} \psi_{\alpha'}^{\text{T}*}(\mathbf{r} + \mathbf{R}/2) e^{i\mathbf{v}\cdot\mathbf{r}} (H_{\text{P}} + \bar{V}_{\text{P}} - \varepsilon_\beta^{\text{P}}) \psi_\beta^{\text{P}}(\mathbf{r} - \mathbf{R}/2). \end{cases} \quad (3.85)$$

Consider the action of H_{T} on the target-atom basis state in Eq. (3.85). For negative-energy states the result is the eigenvalue of the target-atom Schrödinger equation. Thus, $(H_{\text{T}} - \varepsilon_\alpha^{\text{T}}) \psi_\alpha^{\text{T}} = 0$ when $\varepsilon_\alpha^{\text{T}} < 0$. However, for the wave-packet pseudostates this is not the case. Instead, we insert the integral definition in

Eq. (3.54) and operate the Hamiltonian on the Coulomb wave function,

$$H_{\text{T}}\psi_{n\ell m}^{\text{WP}}(\mathbf{r}_{\text{T}}) = \mathcal{N}_n \int_{k_n}^{k_{n+1}} d\kappa \sqrt{\kappa} \left(\frac{\kappa^2}{2} \right) \frac{\phi_{\kappa\ell}(r_{\text{T}})}{r_{\text{T}}} Y_{\ell m}(\hat{\mathbf{r}}_{\text{T}}). \quad (3.86)$$

In this case we define the function

$$\xi_{n\alpha\ell\alpha}^{\text{T}}(r_{\text{T}}) \equiv \frac{\mathcal{N}_n}{r_{\text{T}}} \int_{k_n}^{k_{n+1}} d\kappa \sqrt{\kappa} \left(\frac{\kappa^2}{2} \right) \phi_{\kappa\alpha\ell\alpha}^{\text{T}}(r_{\text{T}}), \quad (3.87)$$

where $\phi_{\kappa\alpha\ell\alpha}^{\text{T}}(r_{\text{T}})$ is the radial part of the true continuum-wave solution to the target-atom Schrödinger equation for an electron with momentum $\kappa = \sqrt{2\varepsilon_{\alpha}^{\text{T}}}$ relative to the target nucleus. We also define the function

$$\Xi_{\alpha}^{\text{T}}(\mathbf{r}_{\text{T}}) \equiv \xi_{n\alpha\ell\alpha}^{\text{T}}(r_{\text{T}}) Y_{\ell\alpha m_{\alpha}}(\hat{\mathbf{r}}_{\text{T}}). \quad (3.88)$$

In Eq. (3.85) we find an analogous result when considering the action of H_{P} on $\psi_{\beta}^{\text{P}}(\mathbf{r}_{\text{P}})$. Consequently, we define the functions

$$\xi_{n\beta\ell\beta}^{\text{P}}(r_{\text{P}}) \equiv \frac{\mathcal{N}_n}{r_{\text{P}}} \int_{k_n}^{k_{n+1}} d\kappa \sqrt{\kappa} \left(\frac{\kappa^2}{2} \right) \phi_{\kappa\beta\ell\beta}^{\text{P}}(r_{\text{P}}), \quad (3.89)$$

and

$$\Xi_{\beta}^{\text{P}}(\mathbf{r}_{\text{P}}) \equiv \xi_{n\beta\ell\beta}^{\text{P}}(r_{\text{P}}) Y_{\ell\beta m_{\beta}}(\hat{\mathbf{r}}_{\text{P}}), \quad (3.90)$$

where $\phi_{\kappa\beta\ell\beta}^{\text{P}}(r_{\text{P}})$ is the radial part of the true continuum-wave solution to the projectile-atom Schrödinger equation for an electron with momentum $\kappa = \sqrt{2\varepsilon_{\beta}^{\text{P}}}$ relative to the projectile nucleus. Thus, we express the exchange matrix elements as

$$\begin{cases} \mathcal{Q}_{\beta'\alpha}^{\text{P}} = \left(\frac{Z_{\text{T}}Z_{\text{P}}}{R} - \varepsilon_{\alpha}^{\text{T}} \right) \mathcal{K}_{\beta'\alpha}^{\text{P}} - \mathcal{X}_{\beta'\alpha}^{\text{P}} + \mathcal{Z}_{\beta'\alpha}^{\text{P}}, \\ \mathcal{Q}_{\alpha'\beta}^{\text{T}} = \left(\frac{Z_{\text{T}}Z_{\text{P}}}{R} - \varepsilon_{\beta}^{\text{P}} \right) \mathcal{K}_{\alpha'\beta}^{\text{T}} - \mathcal{X}_{\alpha'\beta}^{\text{T}} + \mathcal{Z}_{\alpha'\beta}^{\text{T}}. \end{cases} \quad (3.91)$$

In writing Eqs. (3.91) we introduced shorthand notations for the matrix elements

$$\begin{cases} \mathcal{X}_{\beta'\alpha}^{\text{P}}(\mathbf{R}) = \int d\mathbf{r} \psi_{\beta'}^{\text{P}*}(\mathbf{r} - \mathbf{R}/2) e^{-i\mathbf{v}\cdot\mathbf{r}} \frac{Z_{\text{P}}}{|\mathbf{r} - \mathbf{R}/2|} \psi_{\alpha}^{\text{T}}(\mathbf{r} + \mathbf{R}/2), \\ \mathcal{X}_{\alpha'\beta}^{\text{T}}(\mathbf{R}) = \int d\mathbf{r} \psi_{\alpha'}^{\text{T}*}(\mathbf{r} + \mathbf{R}/2) e^{i\mathbf{v}\cdot\mathbf{r}} \frac{Z_{\text{T}}}{|\mathbf{r} + \mathbf{R}/2|} \psi_{\beta}^{\text{P}}(\mathbf{r} - \mathbf{R}/2), \end{cases} \quad (3.92)$$

and

$$\begin{cases} \mathcal{Z}_{\beta'\alpha}^{\text{P}}(\mathbf{R}) = \int d\mathbf{r} \psi_{\beta'}^{\text{P}*}(\mathbf{r} - \mathbf{R}/2) e^{-i\mathbf{v}\cdot\mathbf{r}} \Xi_{\alpha}^{\text{T}}(\mathbf{r} + \mathbf{R}/2), \\ \mathcal{Z}_{\alpha'\beta}^{\text{T}}(\mathbf{R}) = \int d\mathbf{r} \psi_{\alpha'}^{\text{T}*}(\mathbf{r} + \mathbf{R}/2) e^{i\mathbf{v}\cdot\mathbf{r}} \Xi_{\beta}^{\text{P}}(\mathbf{r} - \mathbf{R}/2). \end{cases} \quad (3.93)$$

These four matrix elements are evaluated using a similar procedure to the overlap matrix elements. Close inspection reveals that $\mathcal{X}_{\beta'\alpha}^{\text{P}}$ differs from $\mathcal{K}_{\beta'\alpha}^{\text{P}}$ only by an additional factor of $Z_{\text{T}}/|\mathbf{r} - \mathbf{R}/2|$ in the integrand and $\mathcal{X}_{\alpha'\beta}^{\text{T}}$ differs from $\mathcal{K}_{\alpha'\beta}^{\text{T}}$ only by an additional factor of $Z_{\text{P}}/|\mathbf{r} + \mathbf{R}/2|$ in the integrand. Therefore, we find that

$$\begin{aligned} \mathcal{X}_{\beta'\alpha}^{\text{P}} &= e^{i(m_{\alpha}-m_{\beta'})\varphi_{\mathbf{b}}} (-1)^{\ell_{\alpha}+\ell_{\beta'}+m_{\alpha}+m_{\beta'}} \frac{R^2}{8} \sqrt{[\ell_{\alpha}][\ell_{\beta'}]} \\ &\times \sum_{\mu_{\alpha}\mu_{\beta'}} i^{\mu_{\alpha}-\mu_{\beta'}} d_{\mu_{\alpha}m_{\alpha}}^{\ell_{\alpha}}(\theta_R) d_{\mu_{\beta'}m_{\beta'}}^{\ell_{\beta'}}(\theta_R) \sqrt{\frac{(\ell_{\alpha}-\mu_{\alpha})!(\ell_{\beta'}-\mu_{\beta'})!}{(\ell_{\alpha}+\mu_{\alpha})!(\ell_{\beta'}+\mu_{\beta'})!}} \\ &\times \int_1^{\infty} d\eta \int_{-1}^1 d\tau (\eta+\tau) e^{i\frac{v^2 t}{2}\eta\tau} \mathcal{R}_{n_{\beta'}\ell_{\beta'}}^{\text{P}}\left(\frac{R(\eta+\tau)}{2}\right) \mathcal{R}_{n_{\alpha}\ell_{\alpha}}^{\text{T}}\left(\frac{R(\eta-\tau)}{2}\right) \\ &\times P_{\ell_{\beta'}}^{\mu_{\beta'}}\left(\frac{\eta\tau+1}{\eta+\tau}\right) P_{\ell_{\alpha}}^{\mu_{\alpha}}\left(\frac{\eta\tau-1}{\eta-\tau}\right) J_{\mu_{\alpha}-\mu_{\beta'}}\left(\frac{vb}{2}\sqrt{(\eta^2-1)(1-\tau^2)}\right), \end{aligned} \quad (3.94)$$

and

$$\begin{aligned} \mathcal{X}_{\alpha'\beta}^{\text{T}} &= e^{i(m_{\beta}-m_{\alpha'})\varphi_{\mathbf{b}}} (-1)^{m_{\beta}+m_{\alpha'}} \frac{R^2}{8} \sqrt{[\ell_{\alpha'}][\ell_{\beta}]} \\ &\times \sum_{\mu_{\alpha'}\mu_{\beta}} i^{\mu_{\beta}-\mu_{\alpha'}} d_{\mu_{\alpha'}m_{\alpha'}}^{\ell_{\alpha'}}(\theta_R) d_{\mu_{\beta}m_{\beta}}^{\ell_{\beta}}(\theta_R) \sqrt{\frac{(\ell_{\alpha'}-\mu_{\alpha'})!(\ell_{\beta}-\mu_{\beta})!}{(\ell_{\alpha'}+\mu_{\alpha'})!(\ell_{\beta}+\mu_{\beta})!}} \\ &\times \int_1^{\infty} d\eta \int_{-1}^1 d\tau (\eta-\tau) e^{i\frac{v^2 t}{2}\eta\tau} \mathcal{R}_{n_{\beta}\ell_{\beta}}^{\text{P}}\left(\frac{R(\eta-\tau)}{2}\right) \mathcal{R}_{n_{\alpha'}\ell_{\alpha'}}^{\text{T}}\left(\frac{R(\eta+\tau)}{2}\right) \\ &\times P_{\ell_{\beta}}^{\mu_{\beta}}\left(\frac{\eta\tau-1}{\eta-\tau}\right) P_{\ell_{\alpha'}}^{\mu_{\alpha'}}\left(\frac{\eta\tau+1}{\eta+\tau}\right) J_{\mu_{\beta}-\mu_{\alpha'}}\left(\frac{vb}{2}\sqrt{(\eta^2-1)(1-\tau^2)}\right). \end{aligned} \quad (3.95)$$

The matrix elements $\mathcal{Z}_{\beta'\alpha}^P$ are expressed in terms of prolate spheroidal coordinates in the rotating molecular frame by making the replacement

$$\mathcal{R}_{n_\alpha \ell_\alpha}^T \left(\frac{R(\eta - \tau)}{2} \right) \longrightarrow \xi_{n_\alpha \ell_\alpha}^T \left(\frac{R(\eta - \tau)}{2} \right) \quad (3.96)$$

in Eq. (3.83). The matrix elements $\mathcal{Z}_{\alpha'\beta}^T$ are expressed in terms of prolate spheroidal coordinates in the rotating molecular frame by making the replacement

$$\mathcal{R}_{n_\beta \ell_\beta}^P \left(\frac{R(\eta - \tau)}{2} \right) \longrightarrow \xi_{n_\beta \ell_\beta}^P \left(\frac{R(\eta - \tau)}{2} \right) \quad (3.97)$$

in Eq. (3.84). Therefore,

$$\begin{aligned} \mathcal{Z}_{\beta'\alpha}^P &= e^{i(m_\alpha - m_{\beta'})\varphi_b} (-1)^{\ell_\alpha + \ell_{\beta'} + m_\alpha + m_{\beta'}} \frac{R^3}{16} \sqrt{[\ell_\alpha][\ell_{\beta'}]} \\ &\times \sum_{\mu_\alpha \mu_{\beta'}} i^{\mu_\alpha - \mu_{\beta'}} d_{\mu_\alpha m_\alpha}^{\ell_\alpha}(\theta_R) d_{\mu_{\beta'} m_{\beta'}}^{\ell_{\beta'}}(\theta_R) \sqrt{\frac{(\ell_\alpha - \mu_\alpha)! (\ell_{\beta'} - \mu_{\beta'})!}{(\ell_\alpha + \mu_\alpha)! (\ell_{\beta'} + \mu_{\beta'})!}} \\ &\times \int_1^\infty d\eta \int_{-1}^1 d\tau (\eta^2 - \tau^2) e^{i\frac{v^2 t}{2} \eta \tau} \mathcal{R}_{n_{\beta'} \ell_{\beta'}}^P \left(\frac{R(\eta + \tau)}{2} \right) \xi_{n_\alpha \ell_\alpha}^T \left(\frac{R(\eta - \tau)}{2} \right) \\ &\times P_{\ell_{\beta'}}^{\mu_{\beta'}} \left(\frac{\eta\tau + 1}{\eta + \tau} \right) P_{\ell_\alpha}^{\mu_\alpha} \left(\frac{\eta\tau - 1}{\eta - \tau} \right) J_{\mu_\alpha - \mu_{\beta'}} \left(\frac{vb}{2} \sqrt{(\eta^2 - 1)(1 - \tau^2)} \right) \quad (3.98) \end{aligned}$$

and

$$\begin{aligned} \mathcal{Z}_{\alpha'\beta}^T &= e^{i(m_\beta - m_{\alpha'})\varphi_b} (-1)^{m_\beta + m_{\alpha'}} \frac{R^3}{16} \sqrt{[\ell_{\alpha'}][\ell_\beta]} \\ &\times \sum_{\mu_{\alpha'} \mu_\beta} i^{\mu_\beta - \mu_{\alpha'}} d_{\mu_{\alpha'} m_{\alpha'}}^{\ell_{\alpha'}}(\theta_R) d_{\mu_\beta m_\beta}^{\ell_\beta}(\theta_R) \sqrt{\frac{(\ell_{\alpha'} - \mu_{\alpha'})! (\ell_\beta - \mu_\beta)!}{(\ell_{\alpha'} + \mu_{\alpha'})! (\ell_\beta + \mu_\beta)!}} \\ &\times \int_1^\infty d\eta \int_{-1}^1 d\tau (\eta^2 - \tau^2) e^{i\frac{v^2 t}{2} \eta \tau} \xi_{n_\beta \ell_\beta}^P \left(\frac{R(\eta - \tau)}{2} \right) \mathcal{R}_{n_{\alpha'} \ell_{\alpha'}}^T \left(\frac{R(\eta + \tau)}{2} \right) \\ &\times P_{\ell_\beta}^{\mu_\beta} \left(\frac{\eta\tau - 1}{\eta - \tau} \right) P_{\ell_{\alpha'}}^{\mu_{\alpha'}} \left(\frac{\eta\tau + 1}{\eta + \tau} \right) J_{\mu_\beta - \mu_{\alpha'}} \left(\frac{vb}{2} \sqrt{(\eta^2 - 1)(1 - \tau^2)} \right). \quad (3.99) \end{aligned}$$

The dependence on φ_b in the direct-scattering matrix elements in Eqs. (3.70) and (3.71) is contained entirely in the spherical harmonic of $\hat{\mathbf{R}}$. Therefore, we define direct-scattering matrix elements $\tilde{D}_{\alpha'\alpha}^T$ and $\tilde{D}_{\beta'\beta}^P$ independent of φ_b according

to

$$\begin{cases} D_{\alpha'\alpha}^{\text{T}}(\mathbf{R}) = e^{i(m_\alpha - m_{\alpha'})\varphi_{\mathbf{b}}} \tilde{D}_{\alpha'\alpha}^{\text{T}}(t, b), \\ D_{\beta'\beta}^{\text{P}}(\mathbf{R}) = e^{i(m_\beta - m_{\beta'})\varphi_{\mathbf{b}}} \tilde{D}_{\beta'\beta}^{\text{P}}(t, b). \end{cases} \quad (3.100)$$

Examination of Eqs. (3.83), (3.94), and (3.98) reveals that the functional dependence on $\varphi_{\mathbf{b}}$ is contained entirely within the factor $e^{i(m_\alpha - m_{\beta'})\varphi_{\mathbf{b}}}$. Therefore, we define the matrix elements $\tilde{K}_{\beta'\alpha}^{\text{P}}$, $\tilde{K}_{\alpha'\beta}^{\text{T}}$, $\tilde{Q}_{\beta'\alpha}^{\text{P}}$, and $\tilde{Q}_{\alpha'\beta}^{\text{T}}$ such that

$$\begin{cases} K_{\beta'\alpha}^{\text{P}}(\mathbf{R}) = e^{i(m_\alpha - m_{\beta'})\varphi_{\mathbf{b}}} \tilde{K}_{\beta'\alpha}^{\text{P}}(t, b), \\ K_{\alpha'\beta}^{\text{T}}(\mathbf{R}) = e^{i(m_\beta - m_{\alpha'})\varphi_{\mathbf{b}}} \tilde{K}_{\alpha'\beta}^{\text{T}}(t, b), \end{cases} \quad (3.101)$$

and

$$\begin{cases} Q_{\beta'\alpha}^{\text{P}}(\mathbf{R}) = e^{i(m_\alpha - m_{\beta'})\varphi_{\mathbf{b}}} \tilde{Q}_{\beta'\alpha}^{\text{P}}(t, b), \\ Q_{\alpha'\beta}^{\text{T}}(\mathbf{R}) = e^{i(m_\beta - m_{\alpha'})\varphi_{\mathbf{b}}} \tilde{Q}_{\alpha'\beta}^{\text{T}}(t, b). \end{cases} \quad (3.102)$$

Since the collision system is cylindrically symmetric with respect to the z -axis, we make the assumption that the expansion coefficients are separable with respect to $\varphi_{\mathbf{b}}$,

$$\begin{cases} F_{\alpha'}(\mathbf{R}) = e^{i(m_i - m_{\alpha'})\varphi_{\mathbf{b}}} \tilde{F}_{\alpha'}(t, b), \\ G_{\beta'}(\mathbf{R}) = e^{i(m_i - m_{\beta'})\varphi_{\mathbf{b}}} \tilde{G}_{\beta'}(t, b). \end{cases} \quad (3.103)$$

Using these definitions, the first set of coupled equations in Eq. (3.39) can be written as

$$\begin{aligned} & i e^{i(m_i - m_{\alpha'})\varphi_{\mathbf{b}}} \dot{\tilde{F}}_{\alpha'} + i \sum_{\beta=1}^{\infty} e^{i(m_i - m_\beta)\varphi_{\mathbf{b}}} \dot{\tilde{G}}_{\beta} e^{i(m_\beta - m_{\alpha'})\varphi_{\mathbf{b}}} \tilde{K}_{\alpha'\beta}^{\text{T}} \\ &= \sum_{\alpha=1}^{\infty} e^{i(m_i - m_\alpha)\varphi_{\mathbf{b}}} \tilde{F}_{\alpha} e^{i(m_\alpha - m_{\alpha'})\varphi_{\mathbf{b}}} \tilde{D}_{\alpha'\alpha}^{\text{T}} \\ &+ \sum_{\beta=1}^{\infty} e^{i(m_i - m_\beta)\varphi_{\mathbf{b}}} \tilde{G}_{\beta} e^{i(m_\beta - m_{\alpha'})\varphi_{\mathbf{b}}} \tilde{Q}_{\alpha'\beta}^{\text{T}}. \end{aligned} \quad (3.104)$$

Simplifying, leads to

$$\begin{aligned} e^{i(m_i-m_{\alpha'})\varphi_b} i\dot{\tilde{F}}_{\alpha'} + e^{i(m_i-m_{\alpha'})\varphi_b} i \sum_{\beta=1}^{\infty} \dot{\tilde{G}}_{\beta} \tilde{K}_{\alpha'\beta}^T \\ = e^{i(m_i-m_{\alpha'})\varphi_b} \sum_{\alpha=1}^{\infty} \tilde{F}_{\alpha} \tilde{D}_{\alpha'\alpha}^T + e^{i(m_i-m_{\alpha'})\varphi_b} \sum_{\beta=1}^{\infty} \tilde{G}_{\beta} \tilde{Q}_{\alpha'\beta}^T. \end{aligned} \quad (3.105)$$

Since $e^{i(m_i-m_{\alpha'})\varphi_b}$ is always non-zero, we may cancel this common factor from all terms, resulting in

$$i\dot{\tilde{F}}_{\alpha'} + i \sum_{\beta=1}^{\infty} \dot{\tilde{G}}_{\beta} \tilde{K}_{\alpha'\beta}^T = \sum_{\alpha=1}^{\infty} \tilde{F}_{\alpha} \tilde{D}_{\alpha'\alpha}^T + \sum_{\beta=1}^{\infty} \tilde{G}_{\beta} \tilde{Q}_{\alpha'\beta}^T. \quad (3.106)$$

For the second set of equations in Eq. (3.39) we find

$$i \sum_{\alpha=1}^{\infty} \dot{\tilde{F}}_{\alpha} \tilde{K}_{\beta'\alpha}^P + i\dot{\tilde{G}}_{\beta'} = i \sum_{\alpha=1}^{\infty} \tilde{F}_{\alpha} \tilde{Q}_{\beta'\alpha}^P + \sum_{\beta=1}^{\infty} \tilde{G}_{\beta} \tilde{D}_{\beta'\beta}^P. \quad (3.107)$$

Combined, Eqs. (3.106) and (3.107) form the two-centre close coupling equations that are independent of the azimuthal angle of the impact parameter. The fact that the coupled-channel equations can be written in a form that is independent of the azimuthal angle of the impact parameter should not be surprising. Due to the azimuthal symmetry of the potential, the result of scattering should be the same regardless of the initial value of φ_b . Therefore, the solution should be independent of φ_b .

3.4 Probability amplitudes and cross sections

In general, the post form of the on-shell T -matrix element is given by [104]

$$T_{fi}(\mathbf{q}_f, \mathbf{q}_i) = \langle \Phi_f^- | \overleftarrow{H} - E | \Psi_i^+ \rangle, \quad (3.108)$$

where \mathbf{q}_f and \mathbf{q}_i are the relative momenta in the final and initial channels, respectively, and Φ_f^- is the asymptotic state corresponding to the final channel.

The arrow over the Hamiltonian indicates that it acts on the bra state $\langle \Phi_f^- |$. We introduce the following projection operators formed by the outer product of our complete set of target- and projectile-pseudostates

$$\begin{cases} I_T = \sum_{\alpha=1}^{N^T} |\psi_\alpha^T\rangle \langle \psi_\alpha^T|, \\ I_P = \sum_{\beta=1}^{N^P} |\psi_\beta^P\rangle \langle \psi_\beta^P|. \end{cases} \quad (3.109)$$

Equations (3.109) are inserted into Eq. (3.108), resulting in

$$\begin{aligned} T_{fi}(\mathbf{q}_f, \mathbf{q}_i) &= \langle \Phi_f^- (I_T + I_P) | \overleftarrow{H} - E | \Psi_i^+ \rangle \\ &= \langle \Phi_f^- I_T | \overleftarrow{H} - E | \Psi_i^+ \rangle + \langle \Phi_f^- I_P | \overleftarrow{H} - E | \Psi_i^+ \rangle. \end{aligned} \quad (3.110)$$

This splits the amplitude into two parts. In both parts the final state is projected onto the orthogonal basis states (either target- or projectile-centred). The action of the operator I_T leads to limiting the target subspace by replacing the full set of the target states (including non- L^2 continuum) with a set of L^2 pseudostates. This effectively screens the interaction between the projectile and target constituents even in the continuum. Likewise, the action of the operator I_P limits the projectile subspace by replacing the full set of projectile states (including non- L^2 continuum) with a set of L^2 pseudostates. This effectively screens the interaction between the target and projectile constituents even in the continuum.

If the collision results in elastic scattering or excitation of the target, then the final-state wave function is given by a plane wave representing the relative motion of the projectile ion and a bound-state of the target, ψ_f^T . Therefore, we define the direct scattering (DS) amplitude as

$$T_{fi}^{\text{DS}}(\mathbf{q}_f, \mathbf{q}_i) \equiv \langle \mathbf{q}_f \psi_f^T | \overleftarrow{H}_T + \bar{V}_T - \varepsilon_f^T | \Psi_i^+ \rangle. \quad (3.111)$$

Furthermore, if $\varepsilon_f^T < 0$ then $\langle \psi_f^T | \overleftarrow{H}_T = \langle \psi_f^T | \varepsilon_f^T$. Hence, for negative-energy

target states we obtain the standard definition of the T -matrix elements for elastic scattering and excitation,

$$T_{fi}^{\text{DS}}(\mathbf{q}_f, \mathbf{q}_i) = \langle \mathbf{q}_f \psi_f^{\text{T}} | \bar{V}_{\text{T}} | \Psi_i^+ \rangle. \quad (3.112)$$

If scattering results in electron capture (EC), then the final state is given by a plane wave representing the motion of the projectile-atom system relative to the residual target ion and an eigenstate solution to the projectile Schrödinger equation, ψ_f^{P} . Writing the full Hamiltonian in terms of the projectile Hamiltonian, we have

$$T_{fi}^{\text{EC}}(\mathbf{q}_f, \mathbf{q}_i) \equiv \langle \mathbf{q}_f \psi_f^{\text{P}} | \overleftarrow{H}_{\text{P}} + \bar{V}_{\text{P}} - \varepsilon_f^{\text{P}} | \Psi_i^+ \rangle. \quad (3.113)$$

Furthermore, if $\varepsilon_f^{\text{P}} < 0$ then $\langle \psi_f^{\text{P}} | \overleftarrow{H}_{\text{P}} = \langle \psi_f^{\text{P}} | \varepsilon_f^{\text{P}}$. Therefore, for negative-energy projectile states we obtain the standard definition of the T -matrix elements for electron capture,

$$T_{fi}^{\text{EC}}(\mathbf{q}_f, \mathbf{q}_i) = \langle \mathbf{q}_f \psi_f^{\text{P}} | \bar{V}_{\text{P}} | \Psi_i^+ \rangle. \quad (3.114)$$

If scattering results in ionisation, then the final state is given by the three-body asymptotic wave that represents the three unbound particles. However, after inserting $I_{\text{T}} + I_{\text{P}}$ into Eq. (3.108) the amplitude is split into two parts. For ionisation, the first part corresponds to ejection of the electron into the target continuum, we call this direct ionisation (DI). The second part corresponds to electron capture into the continuum (ECC) of the projectile. The DI amplitude is written as

$$T_{fi}^{\text{DI}}(\boldsymbol{\kappa}, \mathbf{q}_f, \mathbf{q}_i) = \sum_{\alpha=1}^{N^{\text{T}}} \langle \psi_{\boldsymbol{\kappa}}^{\text{T}} | \psi_{\alpha}^{\text{T}} \rangle \langle \mathbf{q}_f \psi_{\alpha}^{\text{T}} | \overleftarrow{H} - E | \Psi_i^+ \rangle. \quad (3.115)$$

For direct ionisation, the only surviving term in Eq. (3.115) is the wave packet that corresponds to the interval that contains the momentum $\boldsymbol{\kappa}$. All other pseu-

dostates do not overlap with ψ_{κ}^T , by construction. The overlapping wave-packet pseudostate may have any ℓ and m , within the size of the basis. Consequently, the summation over all pseudostates $\alpha = \{n_{\alpha}, \ell_{\alpha}, m_{\alpha}\}$ reduces to a summation over only ℓ_{α} and m_{α} within the single momentum-bin that contains κ . So, we are left with

$$T_{fi}^{\text{DI}}(\boldsymbol{\kappa}, \mathbf{q}_f, \mathbf{q}_i) = \sum_{\ell_{\alpha} m_{\alpha}} \langle \psi_{\kappa}^T | \psi_{\alpha}^T \rangle T_{fi}^{\text{DS}}(\mathbf{q}_f, \mathbf{q}_i), \quad (3.116)$$

where $T_{fi}^{\text{DS}}(\mathbf{q}_f, \mathbf{q}_i)$ is the T -matrix element for excitation into the positive-energy pseudostates within the bin corresponding to $n_{\alpha} = n_f$.

In the case of electron capture into the continuum of the projectile, we write the amplitude as

$$T_{fi}^{\text{ECC}}(\boldsymbol{\varkappa}, \mathbf{q}_f, \mathbf{q}_i) = \sum_{\beta=1}^{N^{\text{P}}} \langle \psi_{\boldsymbol{\varkappa}}^{\text{P}} | \psi_{\beta}^{\text{P}} \rangle \langle \mathbf{q}_f \psi_{\beta}^{\text{P}} | \overleftarrow{H} - E | \Psi_i^+ \rangle. \quad (3.117)$$

Here, the only surviving term in Eq. (3.117) is the wave-packet pseudostate of the projectile basis that corresponds to the interval that contains the energy $\boldsymbol{\varkappa}^2/2$. The result is analogous to that for the DI amplitude. In the end we are left with

$$T_{fi}^{\text{ECC}}(\boldsymbol{\varkappa}, \mathbf{q}_f, \mathbf{q}_i) = \sum_{\ell_{\beta} m_{\beta}} \langle \psi_{\boldsymbol{\varkappa}}^{\text{P}} | \psi_{\beta}^{\text{P}} \rangle T_{fi}^{\text{EC}}(\mathbf{q}_f, \mathbf{q}_i), \quad (3.118)$$

where $T_{fi}^{\text{EC}}(\mathbf{q}_f, \mathbf{q}_i)$ is the T -matrix element for electron capture into the positive-energy pseudostates within the bin corresponding to $n_{\beta} = n_f$.

3.4.1 Integrated cross sections

For elastic scattering, target excitation, or electron capture into a bound state of the projectile atom, the integrated cross section is given by [101]

$$\sigma_{fi}^{\text{DS(EC)}} = \frac{\mu_{\text{T}} \mu_f}{(2\pi^2)} \frac{q_f}{q_i} \int d\Omega_f \left| T_{fi}^{\text{DS(EC)}}(\mathbf{q}_i, \mathbf{q}_f) \right|^2, \quad (3.119)$$

where $d\Omega_f$ is the solid angle of the scattered projectile, $\mu_f = \mu_T$ for direct scattering, and $\mu_f = \mu_P$ for electron capture. The T -matrix elements in momentum space are found from the impact-parameter probability amplitudes according to

$$T_{fi}^{\text{DS(EC)}}(\mathbf{q}_f, \mathbf{q}_i) = iv \int d\mathbf{b} e^{i\mathbf{q}_{T(P)}^\perp \cdot \mathbf{b}} A_{fi}^{\text{DS(EC)}}(\mathbf{b}), \quad (3.120)$$

where $\mathbf{q}_{T(P)}^\perp$ is the perpendicular momentum transfer,³ and $A_{fi}^{\text{DS(EC)}}(\mathbf{b})$ is the probability amplitude for transition into final state f , defined as

$$\begin{cases} A_f^{\text{DS}}(\mathbf{b}) = \lim_{t \rightarrow \infty} [F_f(t, \mathbf{b}) - \delta_{fi}], \\ A_f^{\text{EC}}(\mathbf{b}) = \lim_{t \rightarrow \infty} [G_f(t, \mathbf{b})]. \end{cases} \quad (3.121)$$

Inserting Eq. (3.120) into Eq. (3.119) and applying the rectilinear approximation leads to

$$\sigma_{fi}^{\text{DS(EC)}} = \frac{1}{(2\pi)^2} \int d\mathbf{q}_{T(P)}^\perp \int d\mathbf{b}' e^{-i\mathbf{q}_{T(P)}^\perp \cdot \mathbf{b}'} A_{fi}^{\text{DS(EC)*}}(\mathbf{b}') \int d\mathbf{b} e^{i\mathbf{q}_{T(P)}^\perp \cdot \mathbf{b}} A_{fi}^{\text{DS(EC)}}(\mathbf{b}). \quad (3.122)$$

For collisions of ions with energies of several keV and higher the upper limit on $q_{T(P)}^\perp$ is very large and may be taken as approaching infinity [105]. Therefore, the integral over $\mathbf{q}_{T(P)}^\perp$ is simply the definition of the delta function in two-dimensions,

$$\int d\mathbf{q}_{T(P)}^\perp e^{i\mathbf{q}_{T(P)}^\perp \cdot (\mathbf{b} - \mathbf{b}')} = (2\pi)^2 \delta(\mathbf{b} - \mathbf{b}'). \quad (3.123)$$

The resulting delta function effectively takes the integral over \mathbf{b}' and we are left with

$$\sigma_{fi}^{\text{DS(EC)}} = \int d\mathbf{b} \left| A_{fi}^{\text{DS(EC)}}(\mathbf{b}) \right|^2. \quad (3.124)$$

³It is worth noting that for direct scattering we have $f = \alpha'$ so $\mathbf{q}_T^\perp = -\mathbf{q}_{\alpha'}^\perp$ and for electron capture we have $f = \beta'$ so $\mathbf{q}_P^\perp = -\mathbf{q}_{\beta'}^\perp$.

The differential element can be explicitly written in terms of the magnitude of the impact parameter and the azimuthal angle, resulting in

$$\sigma_{fi}^{\text{DS(EC)}} = \int_0^{2\pi} d\varphi_{\mathbf{b}} \int_0^\infty db b \left| A_{fi}^{\text{DS(EC)}}(\mathbf{b}) \right|^2. \quad (3.125)$$

Furthermore, the dependence on the azimuthal angle $\varphi_{\mathbf{b}}$ may be explicitly factored out of the expansion coefficients according to Eq. (3.103). Therefore, the probability amplitudes are also separable with respect to $\varphi_{\mathbf{b}}$. We define probability amplitudes independent of the azimuthal angle of the projectile, $\tilde{A}_{fi}^{\text{DS(EC)}}(b)$, such that

$$A_{fi}^{\text{DS(EC)}}(\mathbf{b}) = e^{i(m_f - m_i)\varphi_{\mathbf{b}}} \tilde{A}_{fi}^{\text{DS(EC)}}(b). \quad (3.126)$$

The integral over $\varphi_{\mathbf{b}}$ in Eq. (3.125) yields 2π and we are left with the following final expression for the integrated cross section

$$\sigma_{fi}^{\text{DS(EC)}} = 2\pi \int_0^\infty db b \left| \tilde{A}_{fi}^{\text{DS(EC)}}(b) \right|^2. \quad (3.127)$$

This result says two important things. First, for the purpose of determining the integrated cross sections, the values of the expansion coefficients in the final channel are sufficient and there is no need to compute either the scattering amplitude or the total scattering wave function. Second, the square of the magnitude of $\tilde{A}_{fi}^{\text{DS(EC)}}(b)$ is the probability for the transition to the final channel f and it is independent of $\varphi_{\mathbf{b}}$. The probabilities for direct scattering and electron capture are therefore given by

$$\begin{cases} P_{fi}^{\text{DS}}(b) = \left| \tilde{A}_{fi}^{\text{DS}}(b) \right|^2 = \left| \tilde{F}_f(t, b) - \delta_{fi} \right|^2, \\ P_{fi}^{\text{EC}}(b) = \left| \tilde{A}_{fi}^{\text{EC}}(b) \right|^2 = \left| \tilde{G}_f(t, b) \right|^2, \end{cases} \quad (3.128)$$

respectively. When f is a target channel, then if $f = i$ Eq. (3.127) corresponds to elastic scattering. For $f \neq i$ and $\varepsilon_f^{\text{T}} < 0$ it is the cross section for excitation

into the bound target state with quantum numbers $\{n_f, \ell_f, m_f\}$. When $\varepsilon_f^T > 0$ the result is the integrated cross section for excitation into the corresponding positive-energy pseudostate. When f is a projectile channel, $\varepsilon_f^P < 0$ this is the cross section for electron capture into the bound target state with quantum numbers $\{n_f, \ell_f, m_f\}$. When $\varepsilon_f^P > 0$ the result is the integrated cross section for electron capture into the corresponding continuum pseudostate of the projectile.

3.4.2 Differential cross sections

We have shown that the integrated cross sections can be determined directly from the expansion coefficients. However, the momentum-space scattering amplitude must be explicitly evaluated in order to calculate differential cross sections. Starting from Eq. (3.120), we separate the angular part of the integral by writing the scalar product of the perpendicular momentum transfer and impact parameter as

$$\mathbf{q}_{T(P)}^\perp \cdot \mathbf{b} = q_{T(P)}^\perp b \cos(\varphi_f - \varphi_b), \quad (3.129)$$

where φ_f is the azimuthal angle of the projectile in the final stationary state. Additionally, we factorise the azimuthal part of the probability amplitude using Eq. (3.126). Then, using Eq. (3.129) and $d\mathbf{b} = b db d\varphi_b$ the transition amplitude is written as

$$T_{fi}^{\text{DS(EC)}}(\mathbf{q}_f, \mathbf{q}_i) = iv \int_0^\infty db b \tilde{A}_{fi}^{\text{DS(EC)}}(b) \int_0^{2\pi} d\varphi_b e^{iq_{T(P)}^\perp b \cos(\varphi_f - \varphi_b)} e^{i(m_i - m_f)\varphi_b}. \quad (3.130)$$

Making the substitution $u = \varphi_f - \varphi_b$ and writing $d\varphi_b = du$ ⁴ this becomes

$$T_{fi}^{\text{DS(EC)}}(\mathbf{q}_f, \mathbf{q}_i) = 2\pi i^{m_f - m_i + 1} e^{i(m_i - m_f)\varphi_f} v \int_0^\infty db b \tilde{A}_{fi}^{\text{DS(EC)}}(b) J_{m_f - m_i}(q_{T(P)}^\perp b). \quad (3.131)$$

⁴since $d\varphi_f = 0$

For collisions resulting in elastic scattering, excitation, or electron capture into a bound state of the projectile atom, the differential cross section is given by

$$\frac{d\sigma_{fi}^{\text{DS(EC)}}}{d\Omega_f} = \frac{\mu_T \mu_f q_f}{(2\pi)^2 q_i} \left| T_{fi}^{\text{DS(EC)}}(\mathbf{q}_i, \mathbf{q}_f) \right|^2. \quad (3.132)$$

Substituting Eq. (3.131) into Eq. (3.132), leads to

$$\begin{aligned} \frac{d\sigma_f^{\text{DS(EC)}}}{d\Omega_f} &= \frac{\mu_T \mu_f q_f}{(2\pi)^2 q_i} \left| 2\pi i^{m_f - m_i + 1} e^{i(m_i - m_f)\varphi_f} \nu \int_0^\infty db b \tilde{A}_{fi}^{\text{DS(EC)}}(b) J_{m_f - m_i}(q_{\text{T(P)}}^\perp b) \right|^2 \\ &= q_f q_i \left| \int_0^\infty db b \tilde{A}_{fi}^{\text{DS(EC)}}(b) J_{m_f - m_i}(q_{\text{T(P)}}^\perp b) \right|^2, \end{aligned} \quad (3.133)$$

where we made the approximation that the reduced mass in the initial and final channels is the same.⁵ The differential cross section for elastic scattering is given by Eq. (3.133) when $f = i$. The differential cross section for target excitation is given by the sum of the result in Eq. (3.133) for all $f \in \{\alpha\}_{N_{\text{b}}^{\text{T}}}$. The differential cross section for electron capture is given by the sum of the result in Eq. (3.133) for all $f \in \{\beta\}_{N_{\text{b}}^{\text{P}}}$.

3.4.3 Ionisation amplitudes

Before we can evaluate the differential cross section for ionisation, we must calculate both $T_{fi}^{\text{DI}}(\boldsymbol{\kappa}, \mathbf{q}_f, \mathbf{q}_i)$ and $T_{fi}^{\text{ECC}}(\boldsymbol{\chi}, \mathbf{q}_f, \mathbf{q}_i)$. To do this, we must evaluate the overlap of the continuum-wave solution and wave packet appearing in Eqs. (3.116) and (3.118). Using Eqs. (3.56) and (3.55), we find that the overlap of a wave-packet pseudostate with the continuum-wave can be expressed as

$$\langle \psi_{\boldsymbol{\kappa}}^- | \psi_{n\ell m}^{\text{WP}} \rangle = \frac{(2\pi)^{3/2}}{\kappa} (-i)^\ell e^{i\sigma_\ell^{\text{T}}(\kappa)} Y_{\ell m}(\hat{\boldsymbol{\kappa}}) \int dr \phi_{\kappa\ell}(r) \phi_{n\ell}^{\text{WP}}(r), \quad (3.134)$$

⁵Since $1/M_{\text{P}}$ and $1/M_{\text{T}} \ll 1$, it is reasonable to assume $\mu_i \approx \mu_f$.

where

$$\int dr \phi_{\kappa\ell}(r) \phi_{n\ell}^{\text{WP}}(r) = \mathcal{N}_n \sqrt{\kappa}. \quad (3.135)$$

So the final form of the overlap is

$$\langle \psi_{\kappa}^- | \psi_{n\ell m}^{\text{WP}} \rangle = \frac{(2\pi)^{3/2} \mathcal{N}_n}{\sqrt{\kappa}} (-i)^\ell e^{i\sigma_\ell^{\text{T}}(\kappa)} Y_{\ell m}(\hat{\boldsymbol{\kappa}}). \quad (3.136)$$

This result is valid for both target and projectile basis functions, provided the appropriate continuum wave is used. With this result, the amplitude in Eq. (3.116) becomes

$$T_{fi}^{\text{DI}}(\boldsymbol{\kappa}, \mathbf{q}_f, \mathbf{q}_i) = \frac{(2\pi)^{3/2} \mathcal{N}_{n_\alpha}}{\sqrt{\kappa}} \sum_{\ell_\alpha m_\alpha} (-i)^{\ell_\alpha} e^{i\sigma_{\ell_\alpha}^{\text{T}}(\kappa)} Y_{\ell_\alpha m_\alpha}(\hat{\boldsymbol{\kappa}}) T_{fi}^{\text{DS}}(\mathbf{q}_f, \mathbf{q}_i). \quad (3.137)$$

Similarly, the amplitude in Eq. (3.118) becomes

$$T_{fi}^{\text{ECC}}(\boldsymbol{\varkappa}, \mathbf{q}_f, \mathbf{q}_i) = \frac{(2\pi)^{3/2} \mathcal{N}_{n_\beta}}{\sqrt{\varkappa}} \sum_{\ell_\beta m_\beta} (-i)^{\ell_\beta} e^{i\sigma_{\ell_\beta}^{\text{P}}(\varkappa)} Y_{\ell_\beta m_\beta}(\hat{\boldsymbol{\varkappa}}) T_{fi}^{\text{EC}}(\mathbf{q}_f, \mathbf{q}_i). \quad (3.138)$$

3.4.4 Differential cross sections for ionisation

For ionising collisions, the fully differential cross section is not only a function of the solid angle of the scattered projectile, but also of the solid angle of the ejected electron Ω_e and the energy of the ejected electron E_e . Figure 3.4 shows the coordinate system used to describe the fully differential cross section. The z -axis is given by the momentum of the incoming projectile and we define the x -axis by the projection of the post-collision momentum of the projectile onto the plane orthogonal to the direction of incidence.

In the laboratory frame, the fully differential cross section for ionisation in the two-centre WP-CCC approach is given by the incoherent sum of the direct

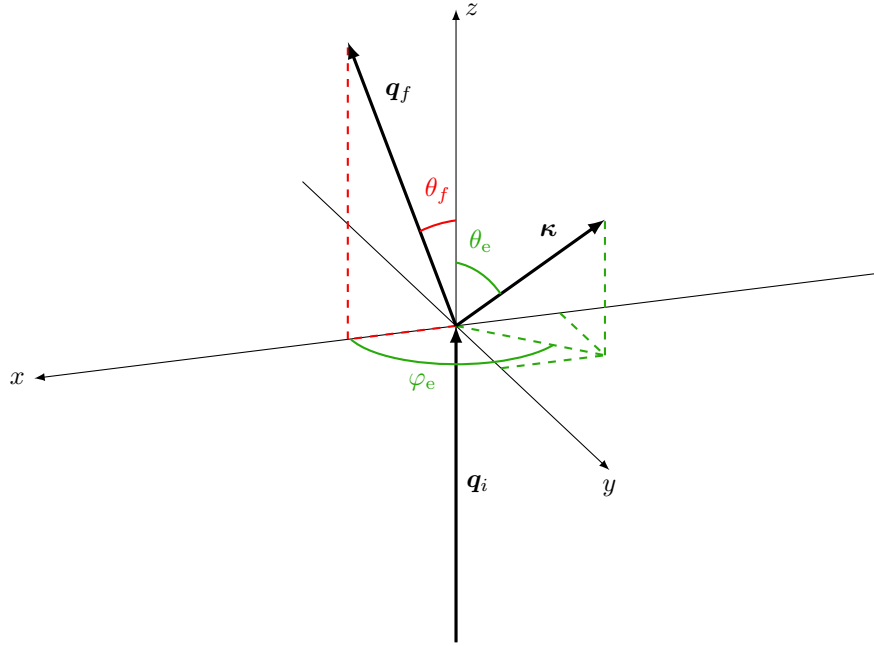


Figure 3.4: Geometry of the momenta of the projectile and electron in ionising collisions. The origin is positioned at the scattering centre.

ionisation and electron capture into continuum components [98],

$$\frac{d^3\sigma_N^{\text{ion}}}{dE_e d\Omega_e d\Omega_f} = \frac{\mu_T^2}{(2\pi)^5} \frac{\kappa q_f}{q_i} \left(|T_{fi}^{\text{DI}}(\boldsymbol{\kappa}, \mathbf{q}_i, \mathbf{q}_f)|^2 + |T_{fi}^{\text{ECC}}(\boldsymbol{\kappa} - \mathbf{v}, \mathbf{q}_i, \mathbf{q}_f)|^2 \right), \quad (3.139)$$

Before combining, the ECC component must be transformed into a common frame of reference with the DI part. We choose the laboratory frame as a common coordinate system. Therefore, the DI amplitude given by Eq. (3.116) does not need to be transformed since it is defined in the laboratory frame. However, the ECC amplitude given by Eq. (3.118) is defined in the projectile frame and must, therefore, be converted into the laboratory frame of reference. To do this, we substituted $\boldsymbol{\kappa} - \mathbf{v}$ for $\boldsymbol{\kappa}$ and $(\mathbf{q}_{\text{T(P)}} - \boldsymbol{\kappa})^\perp$ for $\mathbf{q}_{\text{T(P)}}^\perp$ in Eq. (3.118) (see also Eq. (3.131)) to obtain (after integration) the amplitudes for charge transfer into the projectile continuum with electron momentum $\boldsymbol{\kappa}$. This provides amplitudes for specific electron momenta determined by the distribution of the continuum bins. Therefore, the result in Eq. (3.139) represents the fully differential cross section for ionisation leading to electron emission with momentum $\boldsymbol{\kappa} \in [k_N, k_{N+1}]$ in the target frame, where an electron is ejected with energy $E_e = \kappa^2/2$ into the

solid angle Ω_e which corresponds to $\hat{\boldsymbol{\kappa}}$. It is important to note that this cross section is for ionisation into the N^{th} bin only, i.e.

$$E_e \in \left[\frac{k_N^2}{2}, \frac{k_{N+1}^2}{2} \right]. \quad (3.140)$$

To obtain the cross section across all ejection energies this quantity must be calculated for each wave-packet pseudostate. Each wave packet will result in a single non-zero overlap with the Coulomb wave, providing the FDCS at a discrete number of energy points given by the energy of the wave-packet pseudostate.

To evaluate the FDCS we substitute Eqs. (3.137) and (3.138) into Eq. (3.139),

$$\begin{aligned} \frac{d^3\sigma_N^{\text{ion}}}{dE_e d\Omega_e d\Omega_f} &= \frac{\mu_T^2}{(2\pi)^2} \frac{q_f \kappa}{q_i} \left(\left| \frac{\mathcal{N}_{n_\alpha}}{\sqrt{\kappa}} \sum_{\ell_\alpha m_\alpha} (-i)^{\ell_\alpha} e^{i\sigma_{\ell_\alpha}^T(\kappa)} Y_{\ell_\alpha m_\alpha}(\hat{\boldsymbol{\kappa}}) T_{fi}^{\text{DS}}(\mathbf{q}_f, \mathbf{q}_i) \right|^2 \right. \\ &\quad \left. + \left| \frac{\mathcal{N}_{n_\beta}}{\sqrt{\boldsymbol{\varkappa}}} \sum_{\ell_\beta m_\beta} (-i)^{\ell_\beta} e^{i\sigma_{\ell_\beta}^P(\boldsymbol{\varkappa})} Y_{\ell_\beta m_\beta}(\hat{\boldsymbol{\varkappa}}) T_{fi}^{\text{EC}}(\mathbf{q}_f, \mathbf{q}_i) \right|^2 \right), \quad (3.141) \end{aligned}$$

where $\boldsymbol{\varkappa} = \boldsymbol{\kappa} - \mathbf{v}$. The doubly and singly differential cross section for ionisation is obtained by integrating the result in Eq. (3.141) over the desired variables. This can be performed numerically. However, we also calculate the integrals for some types of doubly differential cross section (DDCS) analytically. Comparison of results obtained using both approaches provides a useful self-consistency check.

Inserting Eq. (3.131) into Eq. (3.141) and integrating over the azimuthal angle and perpendicular momentum transfer yields

$$\begin{aligned} \frac{d^2\sigma_N^{\text{ion}}}{dE_e d\Omega_e} &= 2\pi \left(\mathcal{N}_{n_\alpha}^2 \sum_{\ell_\alpha=0}^{\ell_\alpha^{\max}} \sum_{\ell'_\alpha=0}^{\ell'_\alpha^{\max}} \sum_{m_\alpha=-\ell_\alpha}^{\ell_\alpha} Y_{\ell_\alpha m_\alpha}^*(\hat{\boldsymbol{\kappa}}) Y_{\ell'_\alpha m_\alpha}(\hat{\boldsymbol{\kappa}}) e^{i(\sigma_{\ell'_\alpha}^T(\kappa) - \sigma_{\ell_\alpha}^T(\kappa))} \right. \\ &\quad \times (-i)^{\ell'_\alpha - \ell_\alpha} \int db b \tilde{A}_{n_\alpha \ell_\alpha m_\alpha}^{\text{DS}*}(b) \tilde{A}_{n \ell'_\alpha m_\alpha}^{\text{DS}}(b) \\ &\quad + \mathcal{N}_{n_\beta}^2 \sqrt{\frac{\kappa}{\boldsymbol{\varkappa}}} \sum_{\ell_\beta=0}^{\ell_\beta^{\max}} \sum_{\ell'_\beta=0}^{\ell'_\beta^{\max}} \sum_{m_\beta=-\ell_\beta}^{\ell_\beta} Y_{\ell_\beta m_\beta}^*(\hat{\boldsymbol{\varkappa}}) Y_{\ell'_\beta m_\beta}(\hat{\boldsymbol{\varkappa}}) e^{i(\sigma_{\ell'_\beta}^P(\boldsymbol{\varkappa}) - \sigma_{\ell_\beta}^P(\boldsymbol{\varkappa}))} \\ &\quad \left. \times (-i)^{\ell'_\beta - \ell_\beta} \int db b \tilde{A}_{n_\beta \ell_\beta m_\beta}^{\text{EC}*}(b) \tilde{A}_{n \ell'_\beta m_\beta}^{\text{EC}}(b) \right), \quad (3.142) \end{aligned}$$

where $\tilde{A}_{n_\beta \ell'_\beta m_\beta}^{\text{EC}}(b)$ denotes the probability amplitude for ECC after the transformation $\boldsymbol{\kappa} \rightarrow \boldsymbol{\kappa} - \boldsymbol{v}$. Equation (3.142) is the DDCS for ionisation resulting in electron emission along the surface of a cone at an angle of θ_e to the z -axis with a momentum between the boundaries of the N^{th} target-centred continuum bin. The singly differential cross section (SDCS) for ionisation as a function of the ejected-electron energy and the SDCS for ionisation as a function of the emission angle of the ejected electron can both be obtained by numerically integrating Eq. (3.142) over the desired variables.

To calculate the TICS, the FDCS for ionisation must be integrated over all variables. First, consider only the integrated cross section for DI into the bin N . Starting with the first term in Eq. (3.142) we integrate over Ω_e . Due to the orthogonality of spherical harmonic functions, this results in a factor of $\delta_{\ell_\alpha \ell'_\alpha}$. Therefore, we are left with

$$\begin{aligned} \frac{d\sigma_N^{\text{DI}}}{dE_e} &= 2\pi \mathcal{N}_{n_\alpha}^2 \sum_{\ell_\alpha m_\alpha} \int db b \left| \tilde{A}_{n_\alpha \ell_\alpha m_\alpha}^{\text{DS}}(b) \right|^2 \\ &= \mathcal{N}_{n_\alpha}^2 \sum_{\ell_\alpha m_\alpha} \sigma_{n_\alpha \ell_\alpha m_\alpha}^{\text{DS}}. \end{aligned} \quad (3.143)$$

Integrating this result with respect to E_e over the width of the N^{th} bin trivially results in

$$\sigma_N^{\text{DI}} = \mathcal{N}_{n_\alpha}^2 \sum_{\ell_\alpha m_\alpha} \sigma_{n_\alpha \ell_\alpha m_\alpha}^{\text{DS}} \frac{k_{N+1}^2 - k_N^2}{2}, \quad (3.144)$$

where we used the fact that $\sigma_{n_\alpha \ell_\alpha m_\alpha}^{\text{DS}}$ is the integrated cross section for the *fixed* energy representing the N^{th} bin and is therefore not a function of E_e . Substituting Eq. (3.62) into Eq. (3.144) we get

$$\sigma_N^{\text{DI}} = \sum_{\ell_\alpha m_\alpha} \sigma_{n_\alpha \ell_\alpha m_\alpha}^{\text{DS}}. \quad (3.145)$$

To evaluate the ECC contribution, we apply the same approach to the second

term in Eq. (3.142). However, since integrated cross sections are frame-invariant, there is no need to transform the DI and ECC amplitudes into a common frame in order to calculate it. Therefore, we integrate the second term in Eq. (3.142) over Ω_e in the projectile frame without including the factor of $\sqrt{\kappa/\varkappa}$ that appears from transforming into the laboratory frame. The result is

$$\sigma_N^{\text{ECC}} = \sum_{\ell_\beta m_\beta} \sigma_{n_\beta \ell_\beta m_\beta}^{\text{EC}}. \quad (3.146)$$

Therefore, the TICS is given by Eqs. (3.145) and (3.146) summed over the number of target- and projectile-centred bins, $n_{\text{pos}}^{\text{T}}$ and $n_{\text{pos}}^{\text{P}}$, respectively,

$$\sigma^{\text{ion}} = \sum_{N=1}^{n_{\text{pos}}^{\text{T}}} \sigma_N^{\text{DI}} + \sum_{N=1}^{n_{\text{pos}}^{\text{P}}} \sigma_N^{\text{ECC}}. \quad (3.147)$$

3.5 Computational implementation

The set of two-centre equations for $\tilde{F}_{\alpha'}(t, b)$ and $\tilde{G}_{\beta'}(t, b)$ is written in matrix form as

$$i \begin{pmatrix} \mathbf{I} & \tilde{\mathbf{K}}^{\text{T}} \\ \tilde{\mathbf{K}}^{\text{P}} & \mathbf{I} \end{pmatrix} \begin{pmatrix} \dot{\tilde{\mathbf{F}}} \\ \dot{\tilde{\mathbf{G}}} \end{pmatrix} = \begin{pmatrix} \tilde{\mathbf{D}}^{\text{T}} & \tilde{\mathbf{Q}}^{\text{T}} \\ \tilde{\mathbf{Q}}^{\text{P}} & \tilde{\mathbf{D}}^{\text{P}} \end{pmatrix} \begin{pmatrix} \tilde{\mathbf{F}} \\ \tilde{\mathbf{G}} \end{pmatrix}, \quad (3.148)$$

where \mathbf{I} is the identity matrix. Solution of the coupled equations is achieved using the fourth-order Runge-Kutta approach. The axis of propagation is discretised into N_z exponentially-spaced points that are symmetric about the origin where the distribution is most dense. In this approach, z_{min} corresponds to the limit as $t \rightarrow -\infty$ and z_{max} corresponds to the limit as $t \rightarrow \infty$. The values of z_{min} and z_{max} as well as the number of time-steps are chosen to be sufficiently large that the results of interest converge. At each time-step the value of the expansion coefficients are calculated using a weighted average of their values at the previous

step as

$$\tilde{F}_{\alpha'}^{i+1} = \tilde{F}_{\alpha'}^i + \frac{(z_{i+1} - z_i)}{6}(k_1 + 2k_2 + 2k_3 + k_4), \quad (3.149)$$

where $\tilde{F}_{\alpha'}^i$ is the time-discretised expansion coefficient for the channel α' at the i^{th} time-step,⁶ $z_{i+1} - z_i$ is the width of the discretisation grid, and

$$\begin{cases} k_1 = f\left(z_i, \tilde{F}_{\alpha'}^i\right), \\ k_2 = f\left(z_i + \frac{(z_{i+1} - z_i)}{2}, \tilde{F}_{\alpha'}^i + (z_{i+1} - z_i)\frac{k_1}{2}\right), \\ k_3 = f\left(z_i + \frac{(z_{i+1} - z_i)}{2}, \tilde{F}_{\alpha'}^i + (z_{i+1} - z_i)\frac{k_2}{2}\right), \\ k_4 = f\left(z_i + (z_{i+1} - z_i), \tilde{F}_{\alpha'}^i + (z_{i+1} - z_i)k_3\right). \end{cases} \quad (3.150)$$

At each time step, the integrals appearing in the direct-scattering, overlap, and exchange matrix elements are evaluated numerically. Then, the solution of the generalised eigenvalue problem in Eq. (3.148) at $t = z_i/v$ is offloaded to GPU accelerators using the CUSOLVERDN library [106]. This greatly reduces the computational time required and allows us to investigate problems requiring very large basis sizes that would otherwise be prohibitively large for traditional CPU-based computation. With this we can calculate the expansion coefficients using Eqs. (3.149) and (3.150). The coupling of reaction channels is evident here since calculation of each expansion coefficient at the next point in time depends on the values of all (both target and projectile) expansion coefficients. According to the boundary condition stated in Eq. (3.46) the only non-zero coefficient at the initial step in the Runge-Kutta propagation is the one corresponding to the state of the target in the initial channel. Probability flux flows from this coefficient to all others throughout the propagation, effectively representing intermediate-state coupling. Far from the scattering centre in the asymptotic limit, provided z_{max}

⁶i.e. $\tilde{F}_{\alpha'}^i = \tilde{F}_{\alpha'}(z_i v, b)$.

is sufficiently large, the value of $\tilde{F}_{\alpha'}^{i+1}$ differs little from that of $\tilde{F}_{\alpha'}^i$, i.e.

$$\tilde{F}_{\alpha'}(\infty, b) = \lim_{z_{\max} \rightarrow \infty} \tilde{F}_{\alpha'}^{Nz}. \quad (3.151)$$

The projectile-centred expansion coefficients are evaluated in the same way.

So far we have considered only the z -dimension. However, the expansion coefficients depend also on the impact parameter. In Sect. 3.4 it was shown that the expansion coefficients determine the scattering probabilities entirely. However, we must still solve the coupled equations for all values of b . Since the value of $F_{\alpha'}(t, b)$ at a given impact-parameter point is independent of all other impact-parameter values, we can straightforwardly discretise the impact-parameter space and solve the coupled equations for each discrete value of b independently. We choose an optimal distribution that accurately discretises $bP(b)$. The integration in Eq. (3.127) is performed using the trapezoidal rule.

Throughout the calculation the norm of the total scattering wave function is monitored to verify the accuracy of the solution. All results presented herein were obtained while preserving the unitarity of the total scattering wave function.

The integrated cross sections are then recovered from the values of the expansion coefficients according to the method outlined in Eq. (3.4). To calculate differential cross sections, the momentum-space amplitudes are calculated from the expansion coefficients using Eq. (3.131). Numerical evaluation of the integral in Eq. (3.131) is difficult due to the oscillatory nature of the integrand. One method for dealing with this is to interpolate the calculated expansion coefficients onto a very dense impact-parameter grid before integration. This saves significant time by not having to compute the expansion coefficients for a very large number of impact-parameter points. However, for some types of differential cross sections for ionisation, very large values of perpendicular momentum transfer are required. This makes the Bessel functions highly oscillatory and a more accurate approach to evaluating the integral in Eq. (3.131) is required. Therefore, we use the fast Hankel transform algorithm developed by Anderson [107]. This algorithm takes

advantage of the fact that the Hankel transform can be expressed as a convolution and evaluated using a set of pre-calculated filter weights, removing the need to evaluate any Bessel functions during the calculation. We find that this method is capable of calculating T_{fi}^{DS} and T_{fi}^{EC} accurately for large values of $q_{\text{T(P)}}^{\perp}$ and is approximately an order of magnitude faster than direct numerical integration.

Having obtained the momentum-space scattering amplitudes, the FDCS for ionisation is calculated according to Eq. (3.141). The doubly and singly differential cross sections for ionisation are obtained either from the analytical formulas derived in Sect. 3.4 or direct numerical integration of the FDCS. The SDCS obtained from numerically integrating the FDCS is also integrated to check that the total ionisation cross section agrees with the TICS calculated directly from the impact-parameter amplitudes according to Eq. (3.147). In practice the TICS differ by roughly 1%.

3.6 Chapter summary

In this chapter the two-centre semiclassical WP-CCC approach to positively charged projectile collisions with hydrogen-like atoms was derived. First, the total scattering wave function was expanded in terms of two sets of orthonormal pseudostates. The first set diagonalises the target-atom Hamiltonian and the second set diagonalises the projectile-atom Hamiltonian. Inserting this into the Schrödinger equation for the three-body scattering system and applying the semiclassical approximation led to the coupled-channel equations for the unknown expansion coefficients. Then, we detailed how the matrix elements are evaluated, and showed that the dependence on the azimuthal angle of the projectile could be factorised from the scattering equations. Next, the probability amplitudes and integrated cross sections were given in terms of the expansion coefficients corresponding to the final channel. We then described the way in which differential cross sections are calculated for binary and ionisation processes. Finally, the computational implementation of the method was outlined.

Chapter 4

Multiply charged ion scattering on atomic hydrogen*

In this chapter we apply the WP-CCC approach to calculate integrated cross sections in collisions of Li^{3+} , Be^{4+} , and Ne^{10+} with atomic hydrogen. Previously, the approach has been used to study $\text{He}^{2+} + \text{H}$ collisions, resulting in the most accurate calculations to date of the integrated cross sections for target excitation, electron capture, and ionisation [34]. Here we consider three additional ion species of relevance to the ITER project. Plasma diagnostic techniques [113] require accurate knowledge of the n - and $n\ell$ -resolved integrated cross sections for electron capture and target excitation in collisions between the various impurity ions and atoms present in the plasma. However, experimental data for these collision systems are sparse and theoretical calculations are only available for certain cross sections in limited energy regions. Therefore, we apply the two-centre WP-CCC method to provide an accurate and comprehensive set of data for the aforementioned processes over a wide energy range, all within a single theoretical framework.

Integrated cross sections in collisions of fully stripped lithium ions with atomic

* This chapter is adapted from works published by the candidate [108–112]. The publishers (IOP Publishing, MDPI, and the American Physical Society) provide the author with the right to use the articles, or parts thereof, in a thesis or dissertation without requesting permission.

hydrogen were measured by Shah *et al.* [114], Seim *et al.* [115], and Shah and Gilbody [116]. Shah *et al.* [114] recorded the total electron-capture cross section (TECS) at projectile energies between 14 and 300 keV/u. Shah and Gilbody [116] performed measurements for the TICS at projectile energies between 50 and 400 keV/u. The TECS measurements by Shah *et al.* [114] have an average uncertainty of 20% and the TICS measurements by Shah and Gilbody [116] have an average uncertainty of 4.9%. Seim *et al.* [115] also performed measurements for the TECS at projectile energies between 1 and 6 keV/u with an average uncertainty of 15%. Due to the toxicity of beryllium, there exist no experimental data for comparison. Experimental data for collisions of fully stripped neon ions with atomic hydrogen is only available for the TECS. These data are by Panov *et al.* [117] and Meyer *et al.* [118]. Both sets of measurements have an uncertainty of about 17%. They made measurements at energies between 0.1 and 10 keV/u, however, there is poor agreement between the two sets of data over this energy range. Furthermore, for CXS, n -resolved cross sections are required instead of the total cross section and the typical energy of the hydrogen beam in fusion plasma is between 10 and 100 keV/u, limiting the applicability of the available experimental data.

A number of theoretical methods have been employed to calculate cross sections for collisions of Li^{3+} , Be^{4+} , and Ne^{10+} ions with ground-state hydrogen [119]. Perturbative methods applied to the problem include the first-order Born approximation (FBA), the CB1 method [49], the three-body boundary-corrected continuum-intermediate-state (BCIS-3B) method [120], the CDW method [121], the CDW-EIS method [122], the eikonal impulse approximation (EIA) [123], and the three-body eikonal approach (TBEA) [89]. Both atomic [62, 124–132] and molecular orbital [61, 63] close-coupling approaches have also been used. The CTMC method has been extensively applied to collisions of fully stripped ions with hydrogen [63, 133–136]. There are also results from the lattice numerical solution to the time-dependent Schrödinger equation (LTDSE) method [137, 138], the advanced adiabatic (AA) method [139], and the TC-BGM [80]. However,

significant differences exist between the various approaches and between theory and experiment.

We also consider collisions of the Be^{4+} ions with hydrogen atoms in the $2\ell m$ initially excited states. Although these targets are expected to be present in relatively small quantities in the ITER plasma, it has been shown that charge exchange cross sections for impurity ions colliding with $\text{H}(2s, 2p_0, 2p_1)$ are expected to be at least an order of magnitude larger than that for collisions with $\text{H}(1s)$ [140]. Therefore, contributions to formation of the Be^{3+} ions in the reactor due to scattering on excited hydrogen atoms cannot be neglected. There are no experimental data for $\text{Be}^{4+} + \text{H}(2\ell m)$ collisions and very few calculations are available. These are the CTMC method [141–143], the MOCC method [62, 144], the AOCC method [128, 130], and the numerical grid approach to solving the time-dependent Schrödinger equation for the total scattering wave function (GTDSE) [141].

The two-centre wave-packet convergent close-coupling method can be used to evaluate the total and n - and $n\ell$ -resolved partial integrated cross sections for all of the aforementioned processes. For these calculations, we used a symmetric basis when expanding the total scattering wave function. To ensure the results presented are accurate we establish convergence with respect to the parameters used to model the collisions, including the number of basis functions that describe the electronic states on each centre.

4.1 $\text{Li}^{3+} + \text{H}$ collisions

In this section we present calculations of integrated cross sections for electron capture and ionisation in $\text{Li}^{3+} + \text{H}(1s)$ collisions. We found that a symmetric basis containing $10 - \ell$ bound states and 20 continuum bins up to $\ell_{\text{max}} = 5$ was sufficient to obtain convergence to within 1% in the present results. In Fig. 4.1 we present our results for the TECS alongside the existing experimental data and other theoretical calculations. We find good agreement with both sets of experimental

data [117, 118], which span most of the energy range considered in this work. Our results are somewhat higher than the experimental measurements by Shah *et al.* [114] at intermediate energies, which, however, is the case for most of the available theoretical methods. We get good agreement with two sets of the CTMC results by Errea *et al.* [63] at high energies. The microcanonical distribution for the initial electron cloud yields a spatial density which is too compact, whereas the hydrogenic distribution provides a better representation of the spatial density. Therefore, the hydrogenic classical trajectory Monte Carlo (hCTMC) method is expected to be more reliable than the microcanonical classical trajectory Monte Carlo (mCTMC) one. Nevertheless, at intermediate energies, the hCTMC results are also larger than the experimental measurements by Shah *et al.* [114]. Furthermore, within this energy region, the hCTMC calculations are in poor agreement with the MOCC ones by the same authors. Fritsch and Lin [124] calculated the TECS at low energies using the AOCC approach, however, the size of their basis was too small to give convergent results. The AA calculations by Janev *et al.* [139] are also available only at low energies. Both sets of results disagree with the experimental measurements by Seim *et al.* [115] and the other theoretical calculations available at these energies, including ours. The TBEA calculations by Alt *et al.* [89] disagree with both sets of experimental measurements over the entire energy range. In their calculations, Alt *et al.* [89] neglected the second- and higher-order terms in the quasi-Born expansion of their effective potential. This was suggested as a possible reason for disagreement with the experimental data. Our results are in good agreement with the TC-BGM results by Leung and Kirchner [80] and the AOCC results by Liu *et al.* [132] over the entire 1–1000 keV/u energy range. The CDW calculations by Datta *et al.* [121] and the BCIS-3B calculations by Delibašić *et al.* [120] significantly overestimate the data at intermediate energies, but we see better agreement at high energies. This is as expected, since both methods are perturbative approaches and accurate at sufficiently high energies. Overall, the present results are in excellent agreement

with the experimental data at low and high energies with slight disagreement near the peak of the cross section.

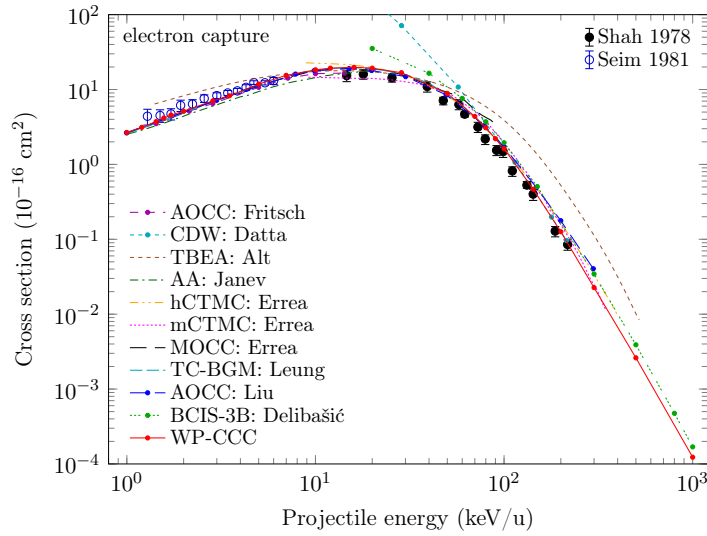


Figure 4.1: Total electron-capture cross section for $\text{Li}^{3+} + \text{H}(1s)$ collisions. Experimental data are by Shah *et al.* [114] and Seim *et al.* [115]. The theoretical results are: present WP-CCC approach, AOCC method by Fritsch and Lin [124], CDW method by Datta *et al.* [121], TBEA by Alt *et al.* [89], AA method by Janev *et al.* [139], hCTMC, mCTMC, and MOCC methods by Errea *et al.* [63], TC-BGM by Leung and Kirchner [80], AOCC method by Liu *et al.* [132], and BCIS-3B method by Delibašić *et al.* [120].

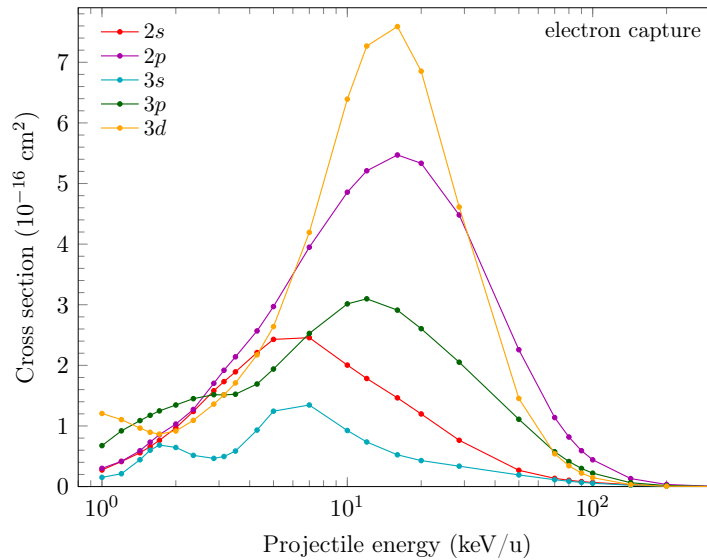


Figure 4.2: Partial 2ℓ and 3ℓ electron-capture cross sections for $\text{Li}^{3+} + \text{H}(1s)$ collisions.

In Fig. 4.2, we plot the partial cross sections for electron capture into 2ℓ and 3ℓ states in collisions of fully stripped lithium ions with atomic hydrogen. We present results for these states in particular because we find that capture into these states have the largest contribution towards the TECS. Noticeable

oscillations are observed in the $3s$ EC cross section at low energies. However, since the magnitude of this cross section is small compared to the 2ℓ and the other 3ℓ electron-capture cross sections, these oscillations are not visible in the TECS. Generally, this oscillatory behaviour is seen in all n and $n\ell$ cross sections for $n > 3$ as well.

Figure 4.3 shows the TICS obtained with the WP-CCC method alongside the existing experimental data by Shah and Gilbody [116] and previous theoretical results. We observe that our calculations overestimate the experimental measurements, especially in the region of the peak. Though the AOCC and TC-BGM calculations appear to better agree with the experiment, it is unclear if these cross sections are convergent in terms of the included states given that our smaller-size, i.e., non-convergent, calculations (not shown) also appear to better agree with the experiment. The WP-CCC results lie between the hCTMC and mCTMC calculations over the entire energy range under consideration. At low energies the AA calculations by Janev *et al.* [139] and the AOCC calculations by Toshima [68] are quite similar to the MOCC calculations by Errea *et al.* [63], but our results appear to be smaller. However, at these energies, we get good agreement with the AOCC calculations by Agueny *et al.* [131] and the TC-BGM calculations by Leung and Kirchner [80]. The AA and AOCC methods are expected to be reliable at low energies since they incorporate molecular features. The AOCC and TC-BGM results are the most recent set of calculations performed for this system. All the aforementioned calculations peak at practically the same projectile energy, however, the respective peaks have different magnitudes. The CDW-EIS results by Crothers and McCann [122] underestimate the TICS at intermediate energies, but we get good agreement with their calculations at high energies. More experimental measurements at intermediate energies could help resolve the disparity between the theoretical methods.

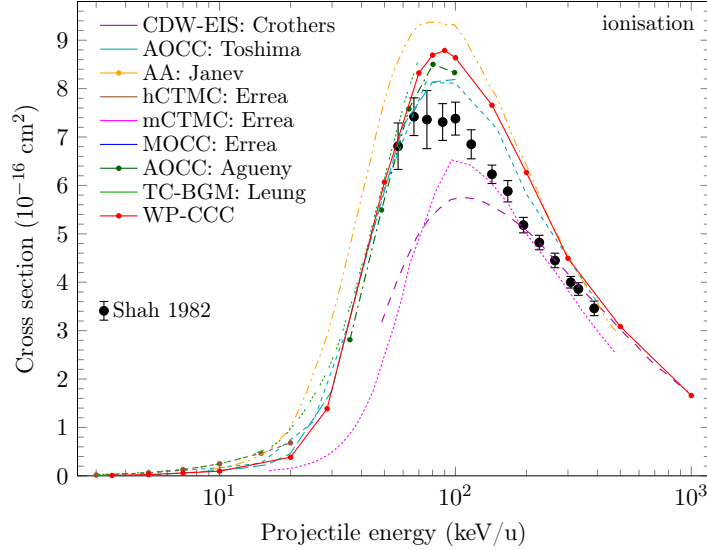


Figure 4.3: Total ionisation cross section for $\text{Li}^{3+} + \text{H}(1s)$ collisions. Experimental data are by Shah and Gilbody [116]. The theoretical results are: present WP-CCC approach, CDW-EIS method by Crothers and McCann [122], AOCC method by Toshima [68], AA method by Janev *et al.* [139], hCTMC, mCTMC, and MOCC methods by Errea *et al.* [63], AOCC method by Agueny *et al.* [131], and TC-BGM by Leung and Kirchner [80].

4.2 $\text{Be}^{4+} + \text{H}$ collisions

In this section we apply the WP-CCC approach to collisions of fully stripped beryllium ions with atomic hydrogen. These collisions are very relevant for fusion plasma modelling for ITER. In particular, beryllium metal is used in some plasma-facing components in the ITER tokamak and, as a result, beryllium impurity ions are expected to make their way into the plasma. We investigate the collision processes leading to ionisation and electron capture in the energy region between 1 keV/u and 1 MeV/u, which is most relevant to fusion plasma modelling. The wide energy range considered covers the lower energies in which electron capture is dominant through to higher energies where excitation and ionisation prevail. There are no experimental data for $\text{Be}^{4+} + \text{H}$ collisions. Instead, we compare our results with other calculations where available. First we present results for scattering on hydrogen atoms initially in the ground ($1s$) state. Then we apply the approach to beryllium scattering on hydrogen atoms in the lowest excited levels ($2\ell m$).

4.2.1 Scattering on ground-state hydrogen

In Fig. 4.4 we present our WP-CCC results for the TECS as a function of incident energy alongside previous theoretical works. The present FBA results are also shown. A symmetric basis containing $n_{\text{neg}} = 10 - \ell$ bound states and $n_{\text{pos}} = 20$ bins with $\ell_{\text{max}} = 5$ was found to be sufficient to obtain convergence within 1%. For the EC channel, the FBA greatly disagrees with the more sophisticated WP-CCC approach at the lower energies but does begin to improve in accuracy as the energy increases. However, even at 1 MeV/u the percentage difference between the FBA and WP-CCC results is 60% for EC. This leads to the conclusion that for $\text{Be}^{4+} + \text{H}(1s)$ collisions, either non-perturbative approaches are needed or higher order terms are required in the perturbation series to obtain accurate electron capture cross sections at and below 1 MeV/u. We see overall good agreement between the WP-CCC results and the AOCC method used by Igenbergs *et al.* [130] across the energy range between 1 to 750 keV/u considered in their work. The maximum difference between the WP-CCC and AOCC calculations is about 2%. At energies greater than 25 keV/u we see the AOCC method employed by Toshima [126] deviates from our results. A possible reason for this discrepancy is the fact that the authors only included bound states of Be^{3+} up to $n = 5$, whereas in our calculations we used bound states up to $n_{\text{neg}} = 10$ to obtain converged results. Another possibility could be the Gaussian type orbitals used to expand the total scattering wave function. These are not true eigenstates of the system and thus only provide approximations to bound state energy values. In Fig. 4.4 we also see two calculations done by Ziaeian and Tórkési [134] using the CTMC and quasi-classical trajectory Monte Carlo (QTMC-KW) approaches. The standard CTMC method shows relatively good agreement with the WP-CCC results in the higher energy range (≥ 100 keV/u), however, below this we see large differences between the two calculations (100%). The reason for this is at lower projectile energies the Coulomb interaction between the target electron and projectile is more significant than at a higher projectile energy, thus a quantum mechanical description is re-

quired in order to calculate accurate channel transitions into different eigenstates. The QTMC-KW calculation corrects this issue of disagreement at lower energies, however above 200 keV/u we see a deviation in results.

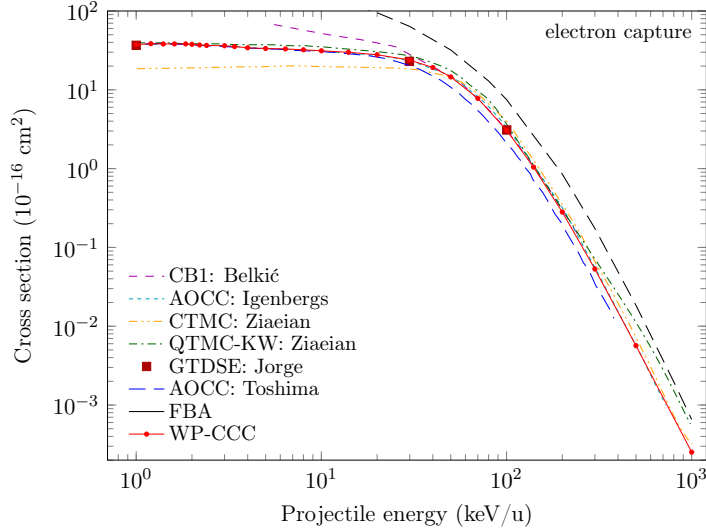


Figure 4.4: Total electron-capture cross section for $\text{Be}^{4+} + \text{H}(1s)$ collisions. The theoretical results are: present WP-CCC and FBA results, CB1 method by Belkić *et al.* [49], AOCC method by Igenbergs *et al.* [130], CTMC and QTMC-KW methods by Ziaean and Tókési [134], GTDSE method by Jorge *et al.* [138], and AOCC method by Toshima [126].

Figure 4.5 shows the TICS as a function of projectile energy. We can again see the FBA results differ from the WP-CCC calculations drastically, deviating by orders of magnitude at low energies. Nonetheless, just as for the EC cross section, the FBA to the ionisation cross section displays improvement in accuracy, albeit slower, towards the upper energy limit. It is clear that, except for the FBA, all calculations display the same maximum TICS around the 100 keV/u region. In this energy region all calculations, excluding the CTMC results [134], agree within a maximum of 10% difference of the WP-CCC results. The agreement between the WP-CCC, QTMC-KW [134] and AOCC [126] continues into the high energy region. However, towards the lower energy region the results begin to diverge from one another. At 20 keV/u the WP-CCC results appear to agree with those of the CTMC approach.

Figure 4.6 shows the partial n -resolved (summed over the orbital angular mo-

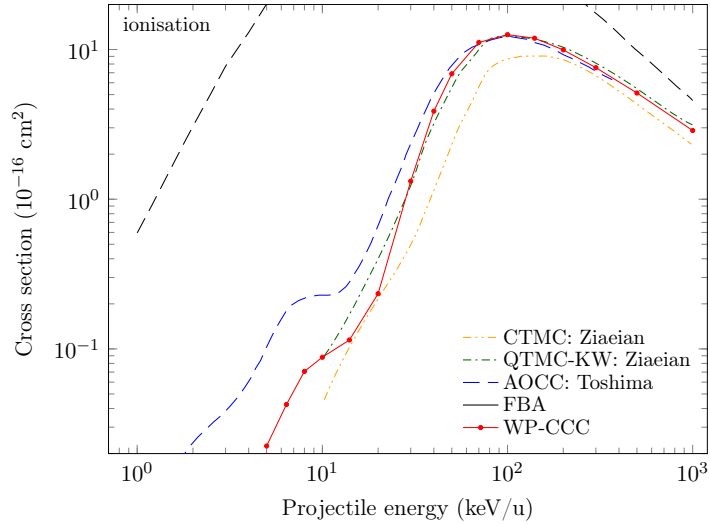


Figure 4.5: Total ionisation cross section for $\text{Be}^{4+} + \text{H}(1s)$ collisions. The theoretical results are: present WP-CCC and FBA results, CTMC and QTMC-KW methods by Ziaecian and Tórkési [134], and AOCC method by Toshima [126].

mentum and magnetic quantum numbers) cross sections as functions of incident projectile energy. We can see that $n = 3$ and $n = 4$ states dominate the TECS presented in Fig. 4.4, below 100 keV/u. For $n > 4$ we can see a systematic decrease in the contributions for the electron transfer process. For $n = 2$, as the projectile energy increases above 100 keV/u the cross section for this state begins to dominate. The $n = 1$ state is negligible for incident energies below 100 keV/u but further towards the upper energy limit (1 MeV/u) its contribution becomes the primary EC channel into the Be^{3+} states. This result is a known characteristic for highly charged projectile collisions with hydrogen [47].

Figure 4.7 shows the distribution of the n -resolved cross sections for EC at incident projectile energies of 20, 100, and 500 keV/u. The present WP-CCC results are compared with the AOCC calculations by Fritsch and Lin [125] and Igenbergs *et al.* [130] as well as the CTMC and GTDSE calculations by Jorge *et al.* [138], and EIA calculations by Jorge *et al.* [123]. At 20 keV we see that there is excellent agreement between the WP-CCC and AOCC results of Fritsch and Lin [125] for the $n = 2$ and $n = 3$ partial cross sections. However, for $n = 4$ we see considerable disagreement between the two approaches. A possible reason for this discrepancy could be the limited size of the basis functions ($2 \leq n \leq 4$)

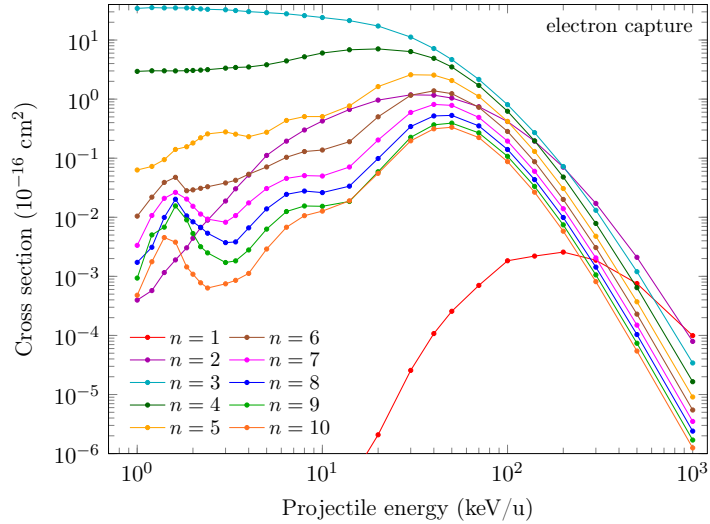


Figure 4.6: Partial n -resolved cross sections for electron capture in $\text{Be}^{4+} + \text{H}(1s)$ collisions.

used in the scattering wave function expansion on the Be^{4+} centre in the AOCC calculations. One can see from Fig. 4.6 that at 20 keV/u the $n = 5$ contribution to EC transitions is greater than the $n = 2$ and $n = 6$ states. Thus the $n > 4$ states should be taken into account at 20 keV/u to obtain accurate distributions of the n -resolved cross sections. For 100 keV projectiles, the WP-CCC results agree with the shape of the calculations by Jorge *et al.* [138] across all values of n shown. Returning to Fig. 4.7, for $n > 5$ the AOCC results by Igenbergs *et al.* [130] show an unphysical rise that is not supported by any of the other methods, and is perhaps a numerical problem. At 500 keV we see that the numerical issues present in the AOCC calculations have lessened. However, the difference at $n = 8$ seems to indicate that the error present at 100 keV/u may still be present at this higher energy. We do, however, see at smaller n states improved agreement with the AOCC results, excluding $n = 1$ where the largest difference between the two calculations is seen. Comparing the WP-CCC and GTDSE calculations, we find very good agreement at the energies where results are available. The maximum difference between the GTDSE results and our own is 4%. However, to achieve this high density lattice meant only presenting up to $n = 3$ due to memory limitations that are associated with this method. We see that the WP-CCC calculations result in slightly smaller n -resolved cross sections in comparison to

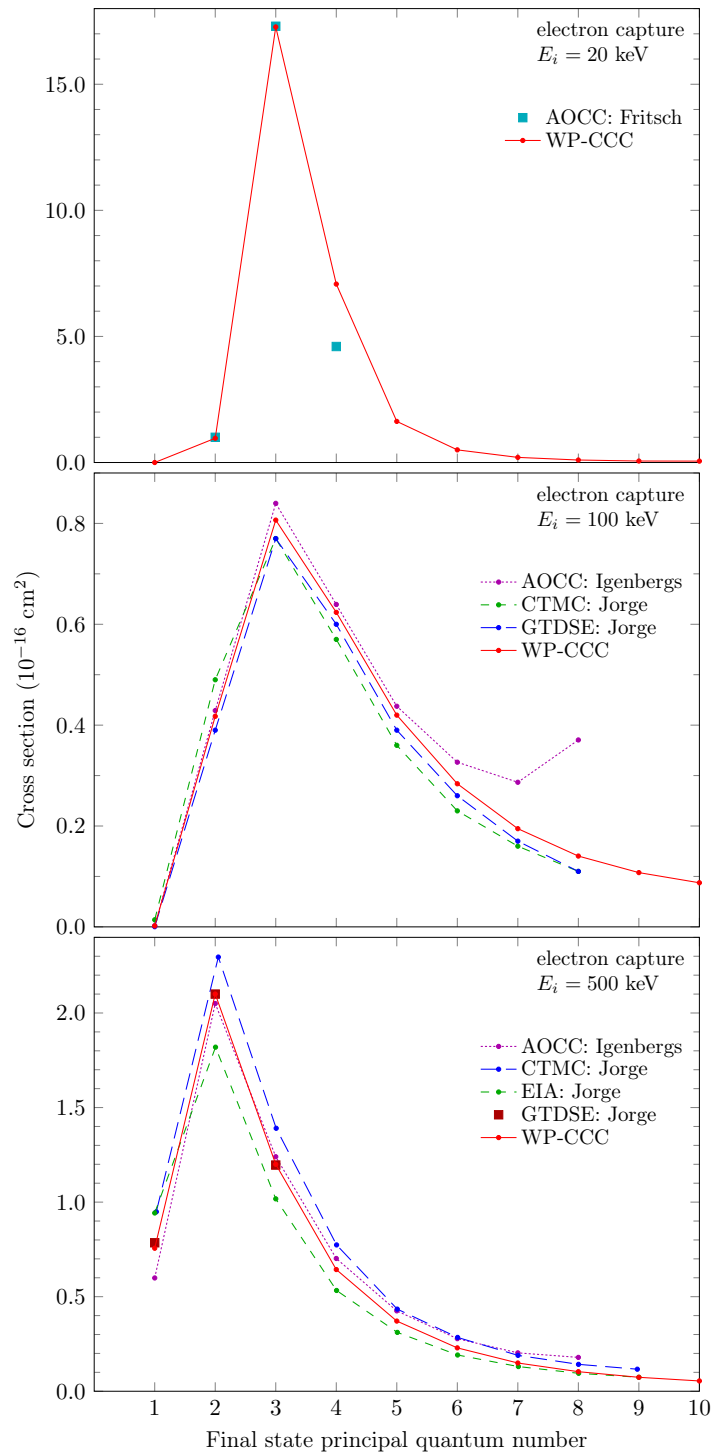


Figure 4.7: n -partial cross sections for electron capture in $\text{Be}^{4+} + \text{H}(1s)$ collisions at 20, 100, and 500 keV/u. The theoretical results are: present WP-CCC approach, AOCC method by Fritsch and Lin [125] and Igenbergs *et al.* [130], CTMC and GTDSE methods by Jorge *et al.* [138], and EIA method by Jorge *et al.* [123].

the CTMC approach for all n considered in Ref. [138]. The largest disagreement between these two approaches occurs at $n = 2$, but improves in comparison for $n > 2$. Regarding the EIA calculations by Jorge *et al.* [123], we see that the WP-CCC method produces larger n -resolved cross sections at 500 keV/u. This is especially noticeable at $n = 2$. As n increases, however, agreement between the two calculations improves. This is especially evident for $n > 7$ where the results practically coincide.

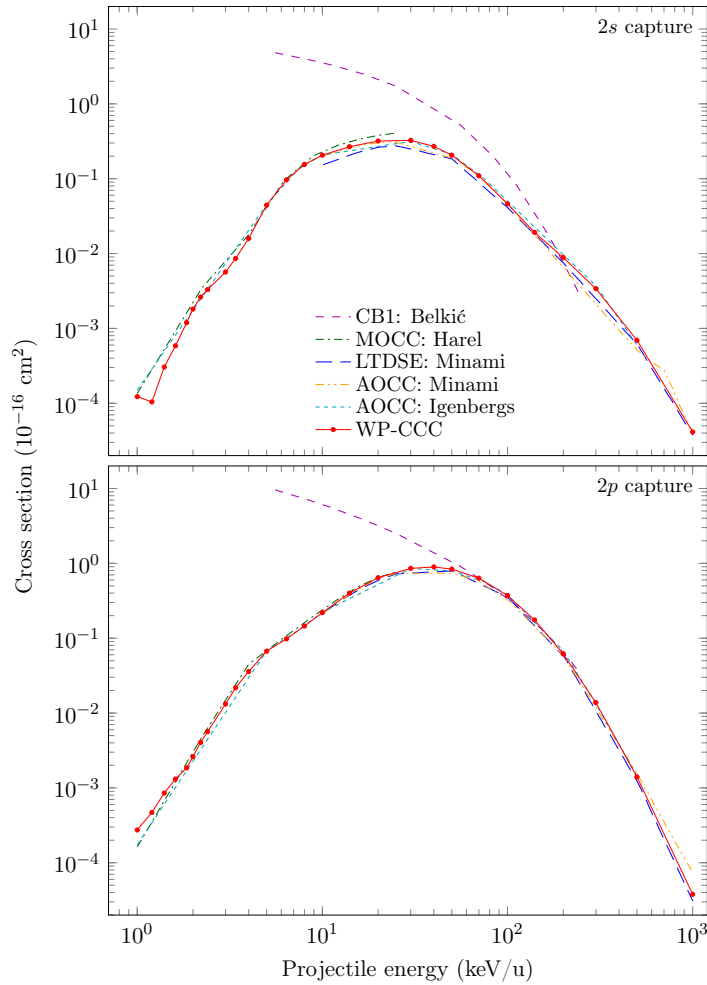


Figure 4.8: Partial 2ℓ cross sections for electron capture in $\text{Be}^{4+} + \text{H}(1s)$ collisions. The theoretical results are: present WP-CCC approach, CB1 method by Belkić *et al.* [49], MOCC method by Harel *et al.* [61], LTDSE and AOCC methods by Minami *et al.* [137], and AOCC method by Igenbergs *et al.* [130]. The key in the upper panel applies to both panels.

In Figs. 4.8–4.11 we show the present WP-CCC results for the partial 2ℓ , 3ℓ , 4ℓ , and 5ℓ EC cross sections. Comparison is made with the CB1 results by Belkić *et al.* [49], AOCC results by Igenbergs *et al.* [130], LTDSE and AOCC results

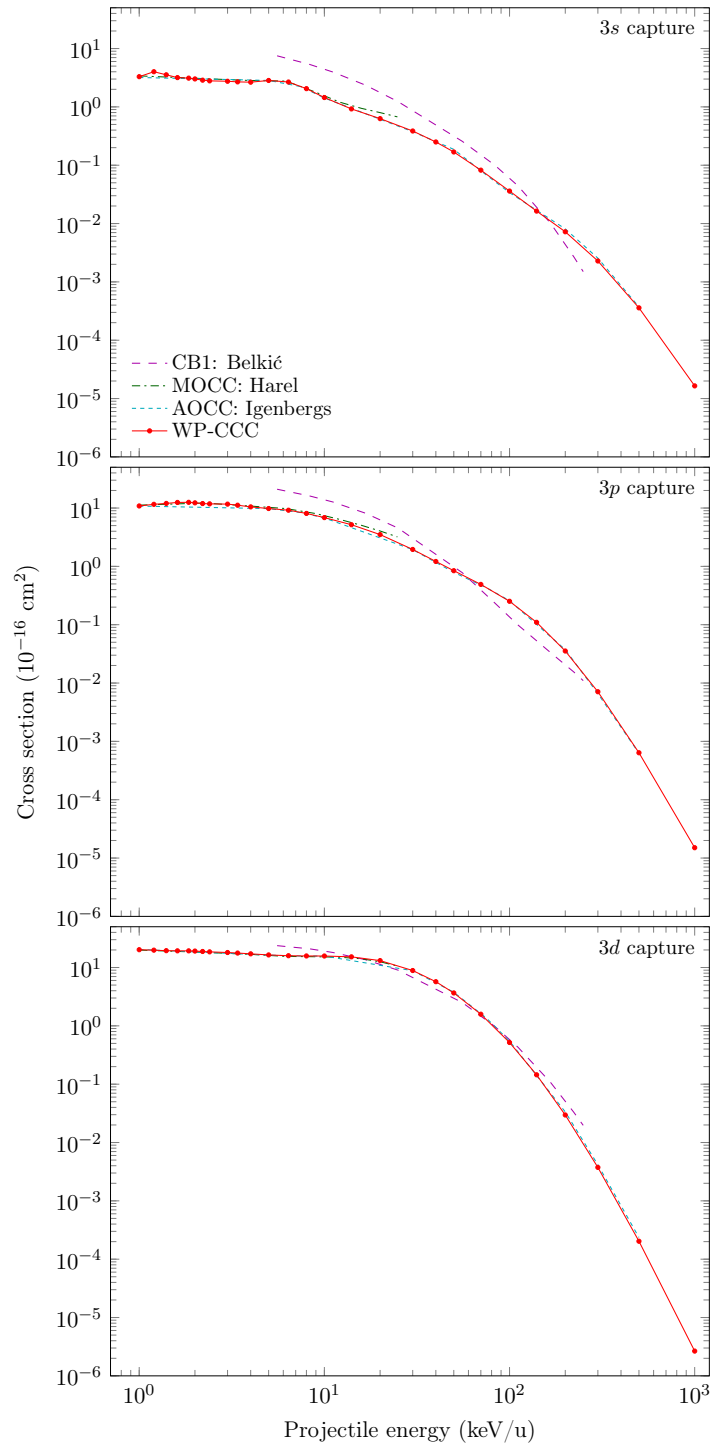


Figure 4.9: Partial 3ℓ cross sections for electron capture in $\text{Be}^{4+} + \text{H}(1s)$ collisions. The theoretical results are: present WP-CCC approach, CB1 method by Belkić *et al.* [49], MOCC method by Harel *et al.* [61], and AOCC method by Igenbergs *et al.* [130]. The key in the upper panel applies to all panels.

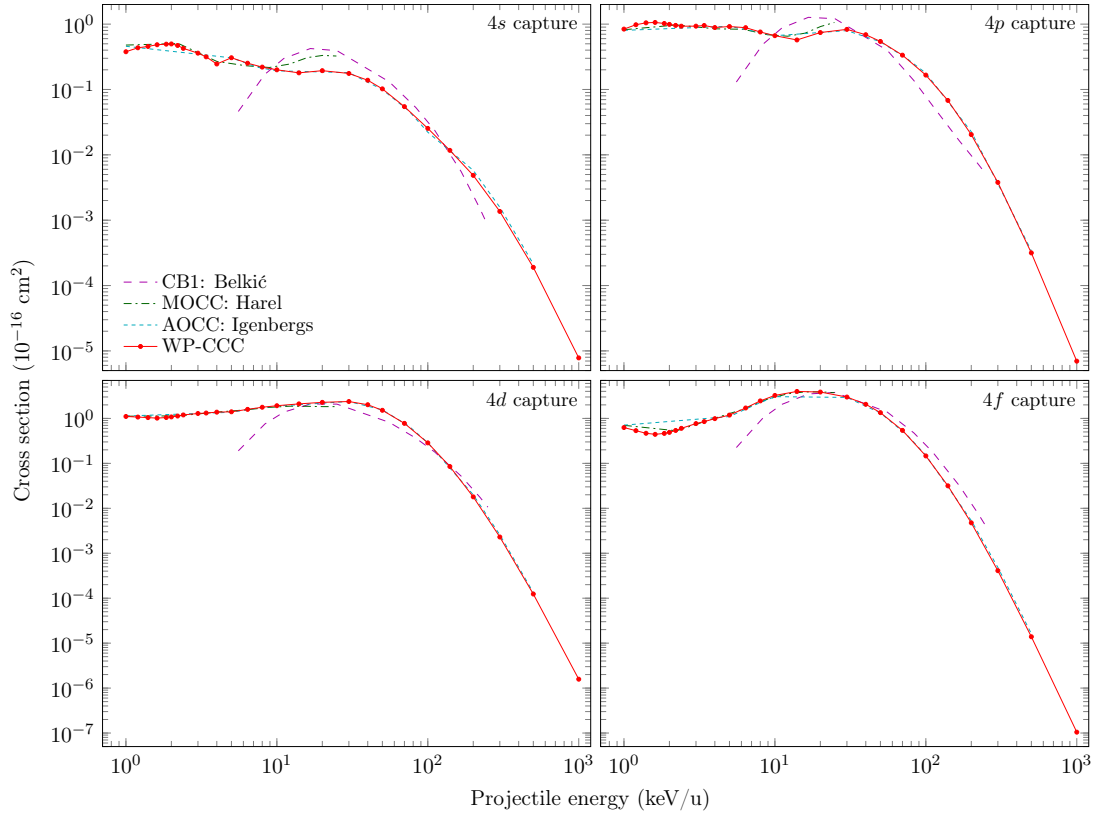


Figure 4.10: Partial 4ℓ cross sections for electron capture in $\text{Be}^{4+} + \text{H}(1s)$ collisions. The theoretical results are: present WP-CCC approach, CB1 method by Belkić *et al.* [49], MOCC method by Harel *et al.* [61], and AOCC method by Igenbergs *et al.* [130]. The key in the upper-left panel applies to all panels.

by Minami *et al.* [137], and the MOCC results by Harel *et al.* [61], where available. Overall, the present WP-CCC results agree very closely with the LTDSE and AOCC calculations as well as the MOCC calculations. However, the cross sections obtained by Belkić *et al.* [49] using the CB1 method sit above the aforementioned calculations at low energies for capture into the $2s$, $2p$, $3s$, and $3p$ states. This is expected for a first-order perturbation calculation as it neglects higher-order terms important at these lower projectile energies. Nevertheless, we see reasonably good agreement at higher projectile energies. For the $3d$ state we see fairly good agreement with the CB1 calculations across the entire projectile energy range considered in Ref. [49].

For the $4s$ -partial cross sections, there is some disagreement between the present results and MOCC calculations by Minami *et al.* [137] at energies between 10 and 25 keV/u. The WP-CCC calculations for the 4ℓ cross sections suggest that

in this energy region there is an oscillatory behaviour with increasing ℓ . Thus, denser energy points are required in order to capture these oscillations. For 4ℓ and 5ℓ partial cross sections, the CB1 results display a slightly different behaviour at lower projectile energies than what is shown in Figs. 4.8 and 4.9. The CB1 method predicts significantly lower cross sections than the AOCC and WP-CCC approaches at small energies. We do see improved agreement, however, for the $4d$ and $4f$ cross sections at higher energies.

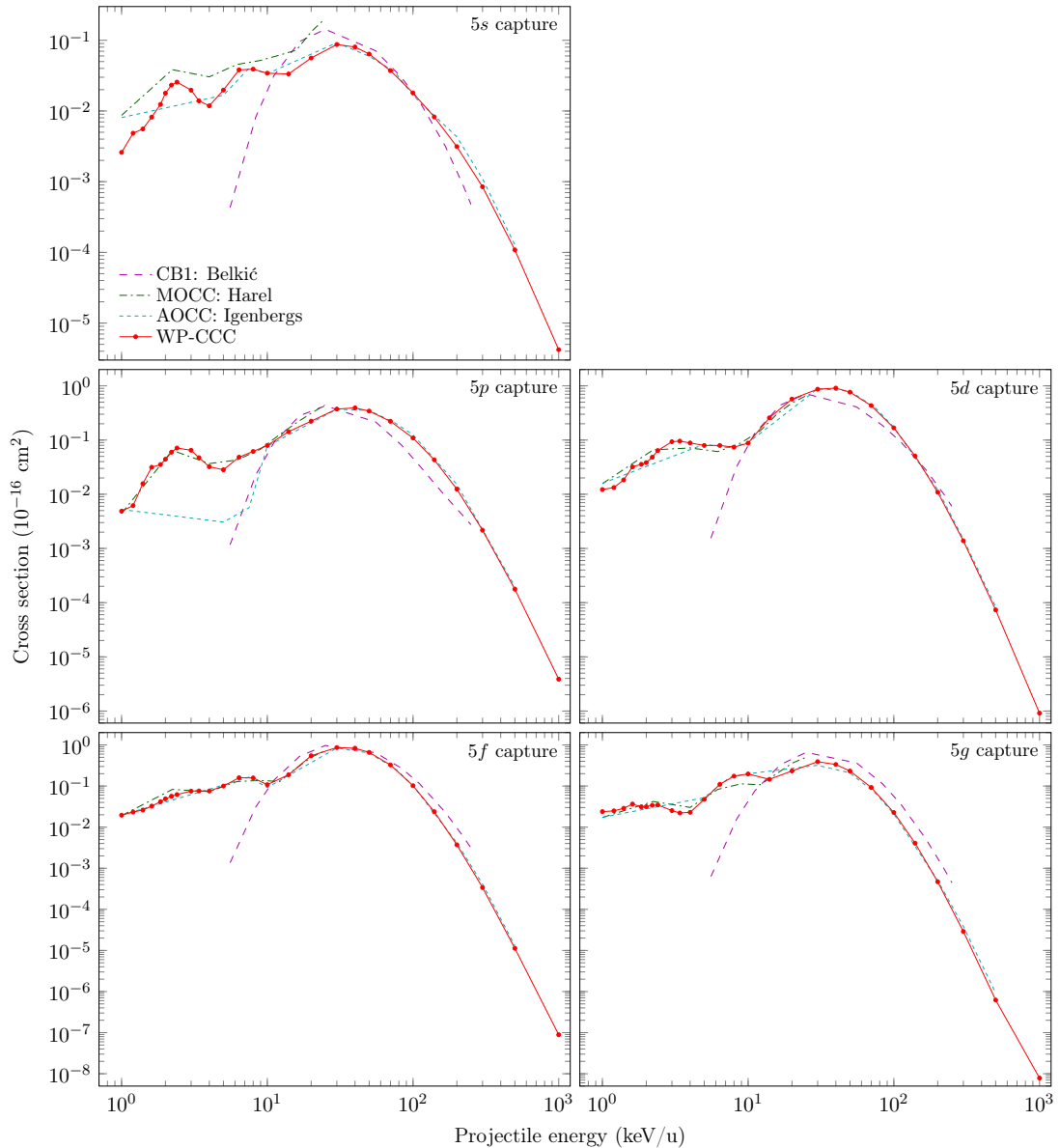


Figure 4.11: Partial 5ℓ cross sections for electron capture in $\text{Be}^{4+} + \text{H}(1s)$ collisions. The theoretical results are: present WP-CCC approach, CB1 method by Belkić *et al.* [49], MOCC method by Harel *et al.* [61], and AOCC method by Igenbergs *et al.* [130]. The key in the upper-left panel applies to all panels.

Results for the 5ℓ -partial cross sections show the most deviation between theoretical methods. In our calculations for all 5 states we see oscillatory behaviour, at low incident energies. For the $5s$ cross section we see the WP-CCC results are in good agreement with the AOCC calculation at energies greater than 5 keV/u. However, at 1 keV/u the calculations differ significantly. Due to the lack of energy points between 1 and 5 keV/u for the AOCC approach, it is difficult to conclude where the WP-CCC results start deviating. It is apparent, however, that we have captured the aforementioned oscillatory behaviour of the $5s$ cross section in this energy range that was not seen in Ref. [130]. We observe quantitative disagreement between the MOCC and WP-CCC results for the $5s$ cross section, however, the oscillatory nature of the cross section is similar for both calculations. For the $5p$ cross section, between 1 and 10 keV/u we observe nearly an order of magnitude disagreement between the WP-CCC and the AOCC results. Nonetheless, we still see excellent agreement between the WP-CCC and MOCC results here. Apart from this energy region, the WP-CCC and AOCC calculations appear to be in excellent agreement with each other.

The present calculations have been performed on a fine energy mesh to identify oscillatory structures in the n - and $n\ell$ -resolved capture cross sections in the low-energy region. Oscillations start to appear in the $n = 4$ partial cross sections becoming pronounced for $n > 4$ below 20 keV/u. Similar oscillations were also seen in target excitation and electron capture in proton-hydrogen [97, 145] and $\text{He}^{2+} + \text{H}(1s)$ [34] collisions. The structures appearing in the cross sections for target excitation, capture into excited states and for ionisation in collisions of multiply charged ions with $\text{H}(1s)$ at low collision energies were discussed by Schultz *et al.* [146]. They have a physical origin and are associated with the number of swaps that the electron undergoes during the collision. As described above we have used symmetric bases on both centres. We have also performed calculations using asymmetric bases where the wave-packet bin states are placed solely on the target or on the projectile centre. However, our calculations showed that the

symmetric basis is optimal for achieving convergent results in all channels. The TICS did not converge when the positive-energy pseudostates were only included in the projectile basis. Nevertheless the symmetric and two types of asymmetric bases gave practically the same EC cross sections across all projectile energies.

4.2.2 Scattering on excited hydrogen

Here, we extend this research to bare beryllium ion scattering on hydrogen in its lowest excited states within the projectile-energy domain between 1 and 500 keV/u. Specifically, this includes collisions with the hydrogen target initially in the $2s$, $2p_0$, and $2p_1$ states. Note that the cross sections for scattering on $H(2p_{-1})$ are identical to the cross sections for scattering on $H(2p_1)$. Therefore, we present results for $H(2p_1)$ but they are applicable also to $H(2p_{-1})$.

Figure 4.12 displays the total EC cross sections for $\text{Be}^{4+} + H(2\ell m)$ collisions. The present WP-CCC results for scattering on hydrogen in the $2s$, $2p_0$ and $2p_1$ states are shown alongside our calculations for hydrogen in the $1s$ state for comparison. We also show theoretical results from other methods were available. We find that in the energy range between 1 and 10 keV/u, the total EC cross section is approximately an order of magnitude larger for the initially excited target. However, for projectile energies > 40 keV/u, the situation is reversed. The reason for this is the difference in the radial probability distribution for finding the electron at a certain distance from the target nucleus in the $1s$ and $2s$ states. In the $1s$ state, the electron is most likely to be found closer to the nucleus. At sufficiently high energies, the projectile can approach the target nucleus much closer. This is why we see the total cross section for EC from $H(1s)$ to be larger in comparison to that from $H(2s)$ at high projectile energies. Our calculations for $\text{Be}^{4+} + H(2s)$ collisions are in excellent agreement with the CTMC results by Ziaeeian and Tókési [142], below 10 keV/u we also agree with the MOCC calculations by Errea *et al.* [62]. However, above 10 keV/u the two sets of results deviate, possibly because the energy becomes too high for a MOCC-type approach. The MOCC results by

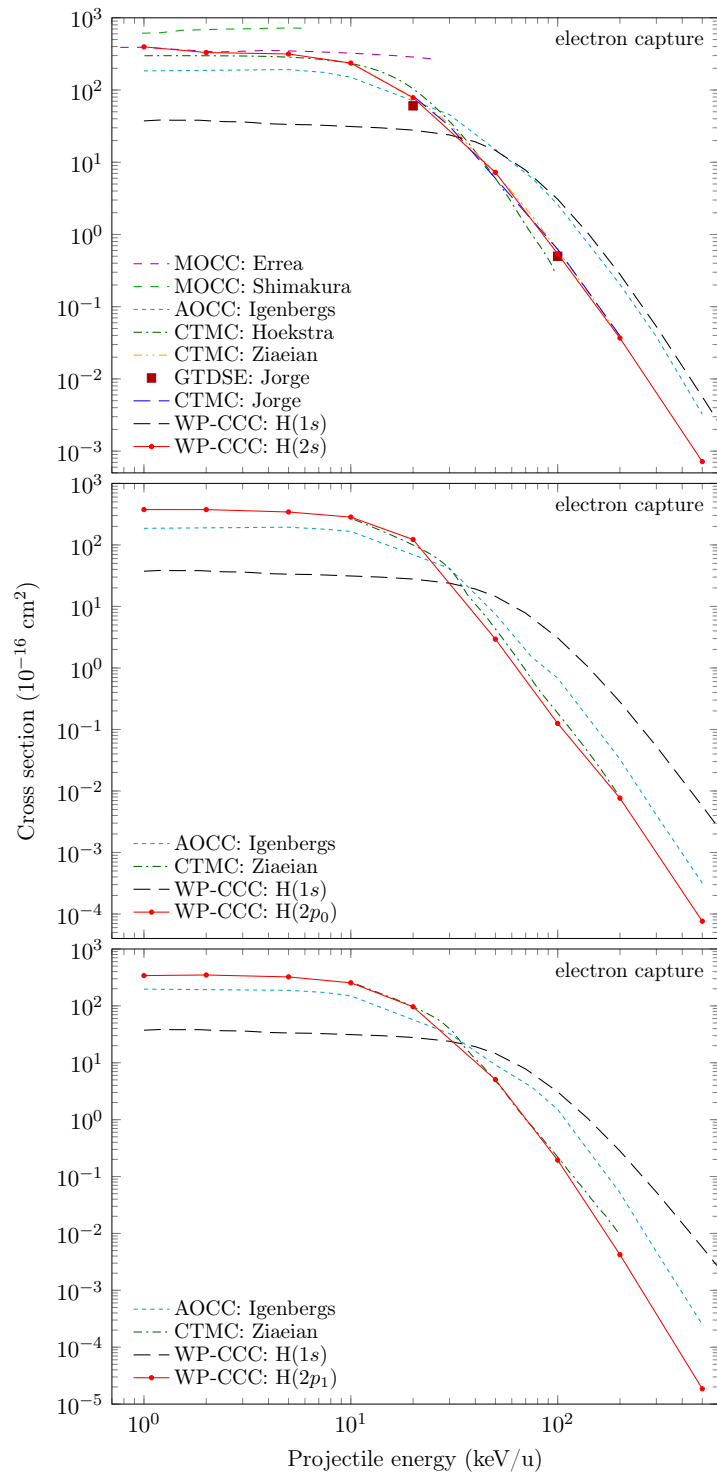


Figure 4.12: Total electron-capture cross section for $\text{Be}^{4+} + \text{H}(2\ell m)$ collisions. The theoretical results are: present WP-CCC approach, MOCC method by Errea *et al.* [62] and Shimakura *et al.* [144], AOCC method by Igenbergs [128], CTMC method by Hoekstra *et al.* [143], Ziaecian and Tórkési [142], and Jorge *et al.* [141], and GTDSE method by Jorge *et al.* [141].

Shimakura *et al.* [144] are substantially different at all energies. This contrasts with the clear agreement found with the work by Errea *et al.* [62] also using the same MOCC method. Our calculations also disagree with the results by Igenbergs [128] obtained using the AOCC approach across the entire energy domain. Interestingly, at high energies, the AOCC results replicate the WP-CCC ones for H(1s), while substantially overestimating the H(2s) results. The reason for such a big deviation in the results from the two similar semiclassical approaches remains to be understood. We find reasonable agreement with both the CTMC and GTDSE calculations by Jorge *et al.* [141] at the projectile energies 20 and 200 keV/u. For scattering on H(2p₀) and H(2p₁) we also find notable disagreements with the AOCC approach. Also, the WP-CCC EC cross sections display good agreement with the CTMC ones.

Figure 4.13 shows the WP-CCC results for the n -partial EC cross sections for Be⁴⁺ collisions with H(2s) (top), H(2p₀) (centre), and H(2p₁) (bottom). The left, centre, and right columns are for collision energies of 20, 100, and 500 keV, respectively. We compare our results with the MOCC calculations by Errea *et al.* [62], GTDSE and CTMC calculations by Jorge *et al.* [141], and AOCC calculations by Igenbergs [128]. As far as we are aware, these are the only other data available for these processes. At 20 keV, the WP-CCC cross sections are in complete agreement with the CTMC and GTDSE ones but not with the MOCC calculations. Also, the MOCC results suggest the dominant n -partial EC cross section for 20 keV Be⁴⁺ + H(2s) collisions occurs at $n = 8$. However, it is worth noting that the MOCC approach is only applicable at low incident energies, and 20 keV/u could be too high. For 100 keV projectiles, our results again agree very well with the GTDSE and CTMC results by Jorge *et al.* [141] for all n . However, there is significant disagreement with the AOCC calculations by Igenbergs [128] for capture from all three of the considered initially excited states of the target. In terms of the distribution of the n -partial EC cross sections, the AOCC calculations also display unphysical peaks at $n = 8$, where we expect the results to be steadily

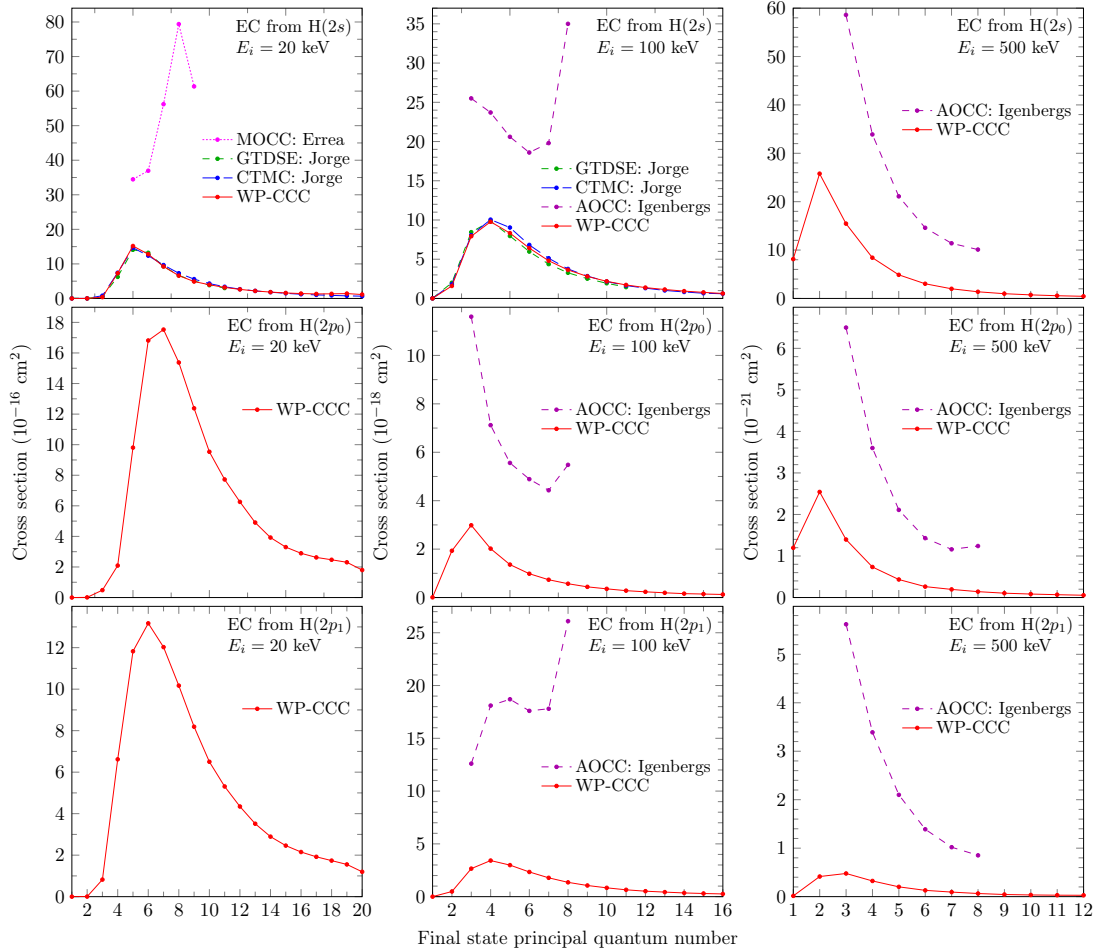


Figure 4.13: n -partial cross sections for electron capture in $\text{Be}^{4+} + \text{H}(2\ell m)$ collisions at 20, 100, and 500 keV/u. The theoretical results are: present WP-CCC approach, AOCC method by Igenbergs [128], MOCC method by Errea *et al.* [62], and CTMC and GTDSE methods by Jorge *et al.* [141].

declining. The AOCC calculations use an asymmetric basis on both centres where only eight hydrogen states are included. In our convergence studies, we apply a symmetric basis expansion. We also tested an asymmetric approach to investigate the contribution the target centred states have on the n -partial EC cross sections. Our analysis showed that a large and nearly symmetric basis expansion is required to obtain stable state-selective EC cross sections. Comparison between the WP-CCC results and AOCC calculations by Igenbergs [128] at 500 keV/u is similar to the situation at 100 keV/u. We find large discrepancies between the two results. Specifically, the minimum difference between our two sets of results is 92%. More calculations using alternative methods would help resolve the discrepancy.

State-resolved $n\ell$ -partial electron-capture cross sections, represent a particular

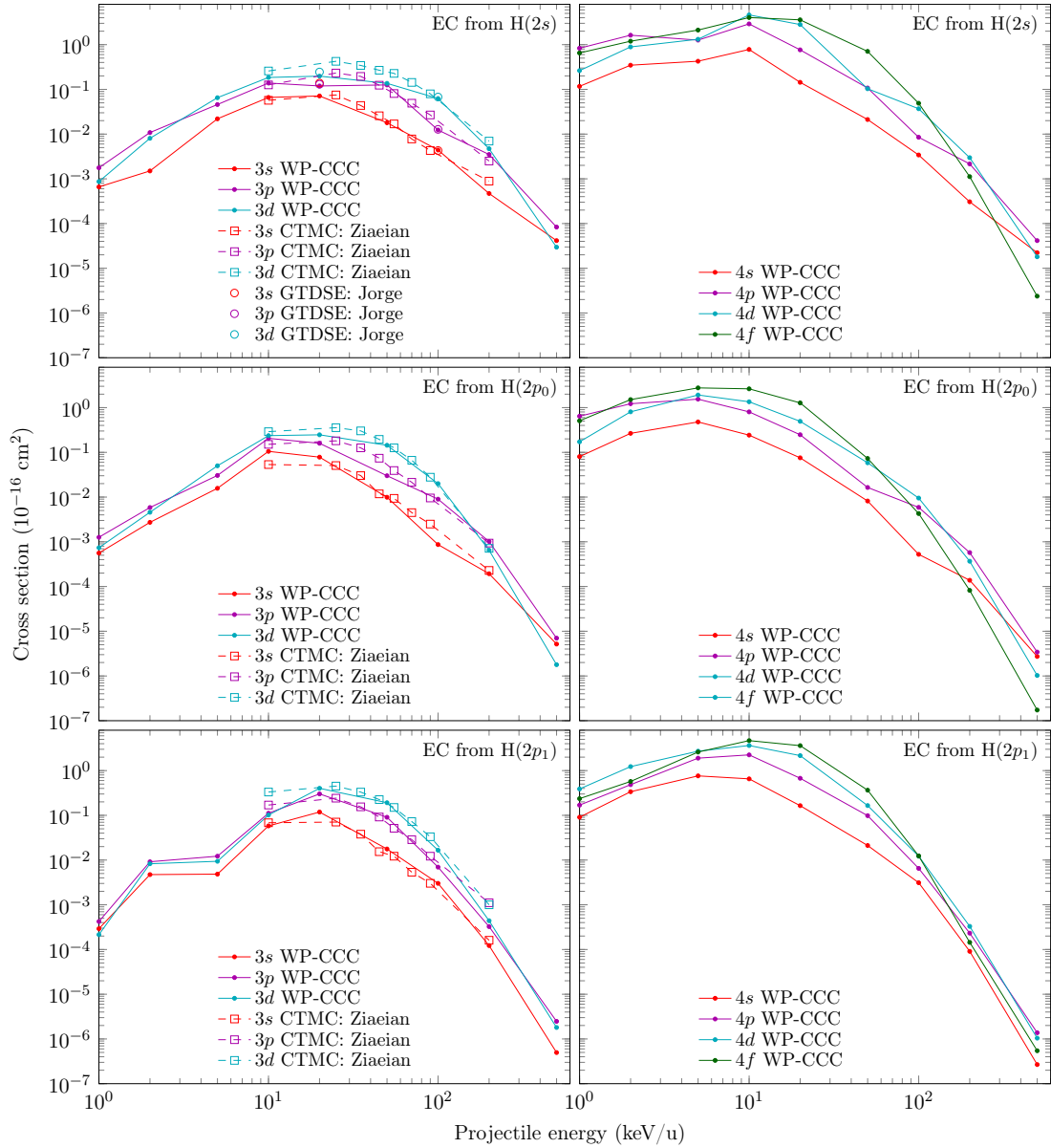


Figure 4.14: Partial 3ℓ and 4ℓ cross sections for electron capture in $\text{Be}^{4+} + \text{H}(2\ell m)$ collisions. The theoretical results are: present WP-CCC approach, CTMC method by Ziaecian and Tókési [142], and GTDSE method by Jorge *et al.* [141].

interest for plasma diagnostics. In Figs. 4.14–4.16 we present results for the $n\ell$ -partial EC cross sections in Be^{4+} collisions with $\text{H}(2s)$, $\text{H}(2p_0)$, and $\text{H}(2p_1)$. We compare to other theoretical results where available. The largest cross sections are convergent within a few percent; however, the smallest ones are converged only within $\approx 8\%$. For capture from $\text{H}(2p_0)$ and $\text{H}(2p_1)$, the WP-CCC results for the 3ℓ -partial cross sections appear to agree reasonably well with the CTMC results by Ziaecian and Tókési [142] across the majority of the overlapping energy range. However, we do notice significant discrepancies when comparing our $3d$ -

partial cross sections from H($2s$) to the CTMC ones below 100 keV/u. Also, for capture from H($2s$), our 3ℓ - and 6ℓ -partial cross sections show excellent agreement with the GTDSE calculations by Jorge *et al.* [141] at the two projectiles energies reported in their work. This is excluding the results for capture into the $3s$ state at 20 keV/u, where we find noticeable differences between our results and theirs.

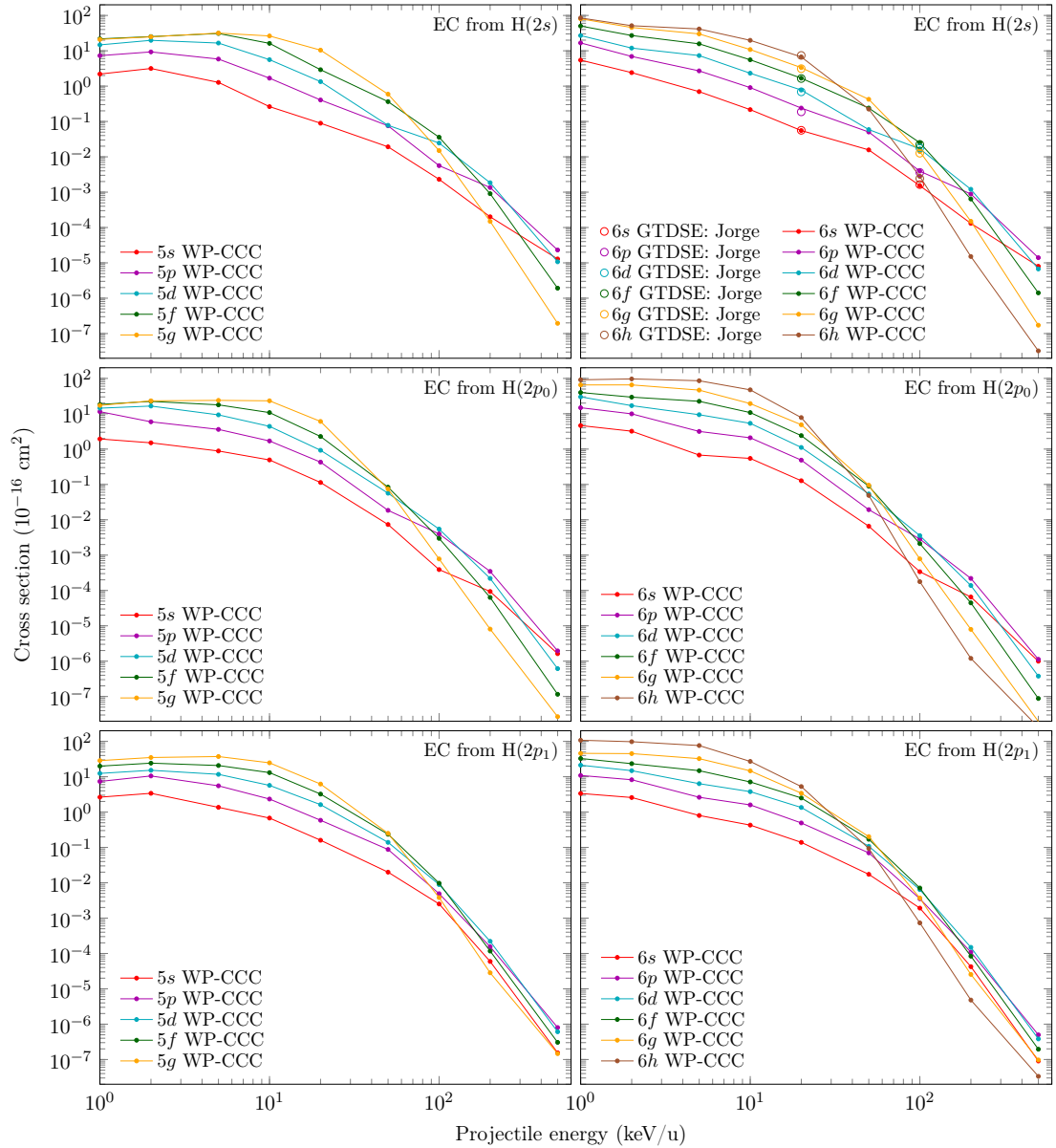


Figure 4.15: Partial 5ℓ and 6ℓ cross sections for electron capture in $\text{Be}^{4+} + \text{H}(2\ell m)$ collisions. The theoretical results are: present WP-CCC approach and GTDSE method by Jorge *et al.* [141].

Overall we find that within each set of results for the 3ℓ - to 5ℓ -partial EC cross sections, in the energy region between 5 and 50 keV/u, the dominant n state for

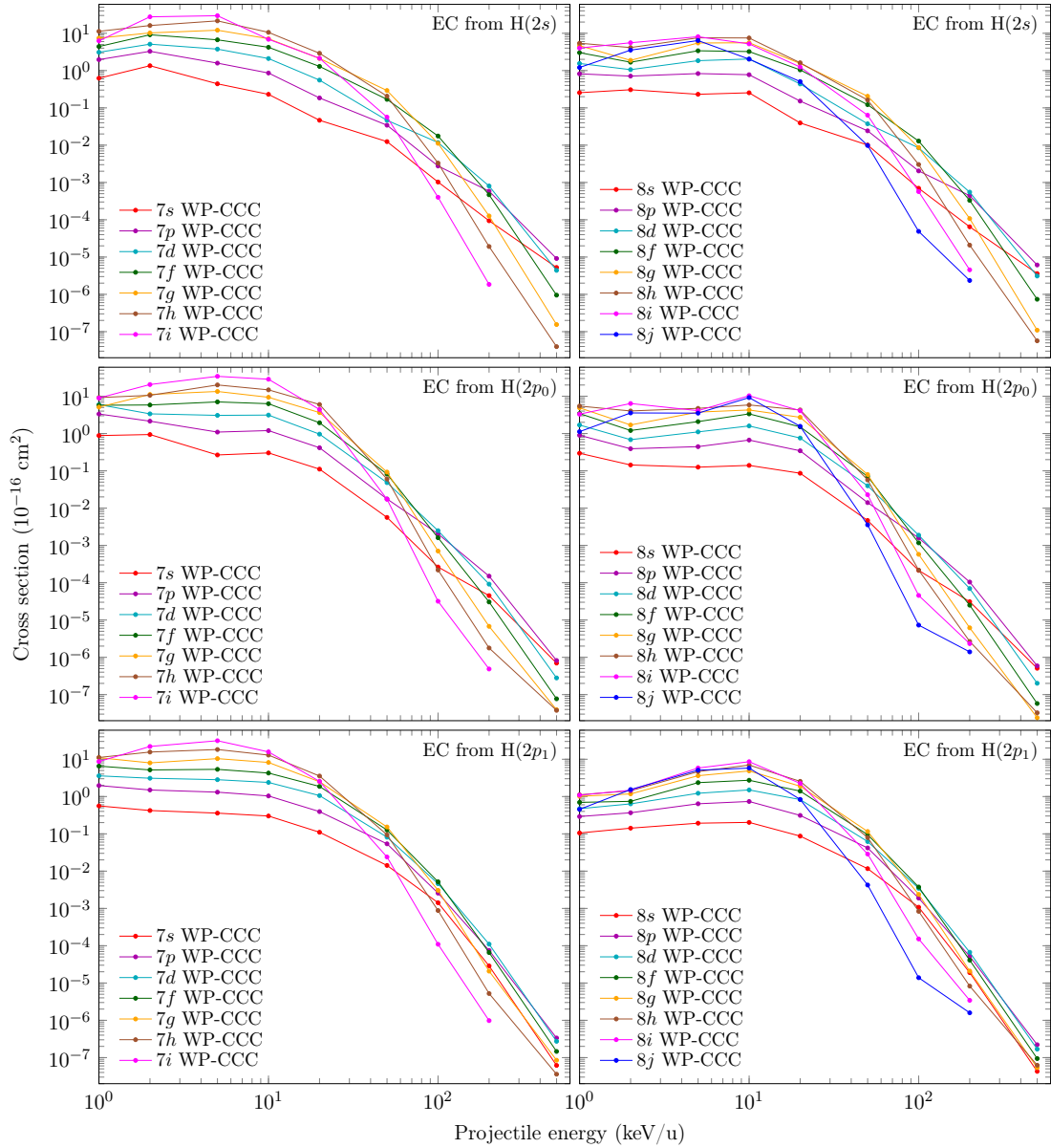


Figure 4.16: Partial 7ℓ and 8ℓ cross sections for electron capture in $\text{Be}^{4+} + \text{H}(2\ell m)$ collisions.

capture is the one with the largest allowed orbital angular momentum within the shell, i.e., $\ell = n - 1$. In the same energy region, the dominant contribution comes from capture into the state with $\ell \approx Z_P^{3/4}$ in the 6ℓ - to 8ℓ -partial cross sections. This is in agreement with the findings of Olson [147].

We also calculate the n -partial excitation cross sections in $\text{Be}^{4+} + \text{H}(2\ell m)$ collisions in Fig. 4.17. To obtain these results a combination of single-centre (denoted as 1c) and two-centre (denoted as 2c) calculations were performed. This is done to establish the internal consistency of both calculations. For all

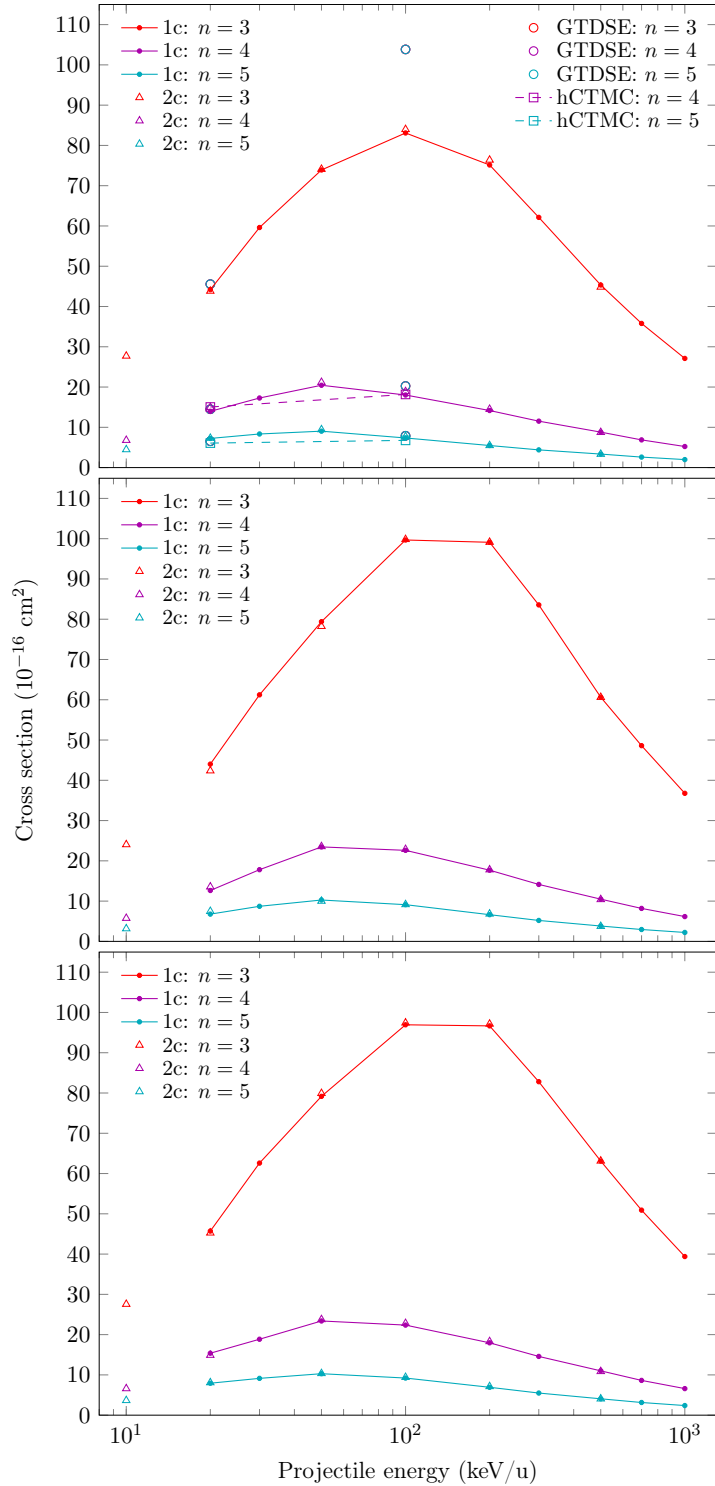


Figure 4.17: Cross sections for target excitation into the $n = 3, 4,$ and 5 states in $\text{Be}^{4+} + \text{H}(2\ell m)$ collisions. The theoretical results are: present single-centre (1c) and two-centre (2c) WP-CCC approaches and GTDSE and hCTMC methods by Jorge *et al.* [141].

overlapping projectile energies, excellent agreement between the two sets of the WP-CCC results is found. This suggests that, at least starting from 20 keV/u, the target excitation cross sections for $\text{Be}^{4+} + \text{H}(2\ell m)$ collisions can be obtained

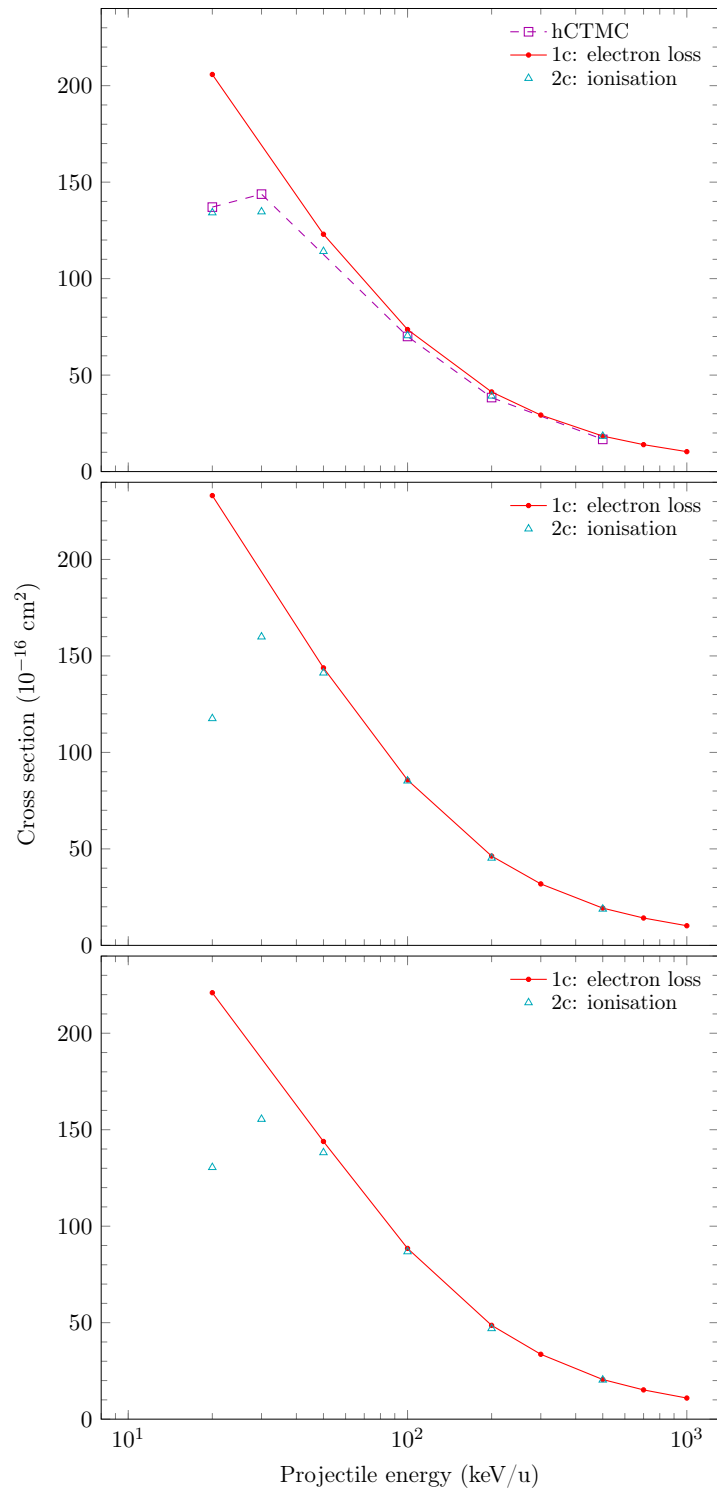


Figure 4.18: Cross sections for ionisation and electron loss in $\text{Be}^{4+} + \text{H}(2lm)$ collisions. The theoretical results are: present single-centre (1c) and two-centre (2c) WP-CCC approaches and hCTMC method by Jorge *et al.* [141].

through purely single-centre calculations. Figure 4.17 also shows that the $n = 3$ states represent dominant excitation channels across the entire projectile energy range. Furthermore, we see the excitation cross sections decrease significantly

with increasing n . Also shown in Fig. 4.17 are the GTDSE and hCTMC results for collisions with H(2s) by Jorge *et al.* [141], available at 20 and 100 keV/u. The WP-CCC cross-sections are in excellent agreement with the GTDSE ones at 20 keV/u. This level of agreement is also found at 100 keV/u with the exception of the dominant excitation cross-section into the $n = 3$ states. Here, we find the WP-CCC results to be approximately 25% smaller than the GTDSE ones. The reason for this disagreement is undetermined. We also find the WP-CCC results to be in excellent agreement with the hCTMC ones for excitations into the $n = 4$ and $n = 5$ states. However, the hCTMC results for the $n = 3$ target excitation cross section [141] (not shown) are significantly larger than the present ones.

Figure 4.18 shows the TICS, obtained using the two-centre WP-CCC method, and total electron loss (TEL) cross sections, obtained using the single-centre WP-CCC method, for $\text{Be}^{4+} + \text{H}(2\ell m)$ collisions. For the H(2s) target we compare our results with the hCTMC results by Jorge *et al.* [141]. For both H(2p₀) and H(2p₁) targets the present WP-CCC calculations are the first available data for these cross sections. As one-centre calculations cannot distinguish electron capture from ionisation, the TEL cross section represents these two processes together. However, for collisions with excited state H, we found that the TECS becomes considerably smaller than the ionisation cross section above 100 keV/u. Therefore, we conclude that the TEL cross section accurately represents the TICS above 100 keV/u. Clearly, this is not the case at lower projectile energies, where we see considerable differences between the electron-loss and ionisation cross sections. Note that the WP-CCC and hCTMC ionisation cross sections are in excellent agreement with each other at all projectile energies where the hCTMC results are available.

4.3 $\text{Ne}^{10+} + \text{H}$ collisions

In this section we use the WP-CCC method to calculate integrated cross sections for electron capture in Ne^{10+} collisions with H(1s). Cross sections for n - and

$n\ell$ -resolved EC are required for plasma modelling and, as with the other ions considered thus far, very little experimental data is available. Therefore, accurate theoretical results are essential. Furthermore, obtaining converged results for more highly charged projectiles is significantly more difficult due to the large number of reaction channels that play important roles in the collisional dynamics. Therefore, successful application of the WP-CCC method to $\text{Ne}^{10+} + \text{H}$ collisions also acts as a proof-of-concept for less highly charged ions that have yet to be considered, such as B^{5+} and N^{7+} .

For this collision system we found that a very large number of states were required to obtain convergence in the electron-capture cross sections. Therefore, we used an asymmetric set of basis states allowing us to omit unnecessary states from the target side, optimising the computations. For the electron-capture cross sections we include on the target side $n_{\text{neg}}^{\text{T}} = 11 - \ell^{\text{T}}$ bound states and $n_{\text{pos}}^{\text{T}} = 10$ continuum bins with $\ell_{\text{max}}^{\text{T}} = 7$. On the projectile side we used $n_{\text{neg}}^{\text{P}} = 15 - \ell^{\text{P}}$ and $n_{\text{pos}}^{\text{P}} = 10$ with $\ell_{\text{max}}^{\text{P}} = 9$. For the TICS calculations we used a basis containing $n_{\text{neg}}^{\text{T}} = 7 - \ell^{\text{T}}$ and $n_{\text{pos}}^{\text{T}} = 20$ with $\ell_{\text{max}}^{\text{T}} = 5$ states on the target side. On the projectile side we used $n_{\text{neg}}^{\text{P}} = 10 - \ell^{\text{P}}$ and $n_{\text{pos}}^{\text{P}} = 20$ with $\ell_{\text{max}}^{\text{P}} = 8$. These bases were sufficient for the present results to converge to within 3%.

The calculated total electron-capture cross section is shown in Fig. 4.19 alongside experimental data and other theoretical results over an energy range of 1–1000 keV/u. In their analysis, Meyer *et al.* [118] estimated the relative uncertainties in their experimental data taking repeated measurements and using counting statistics. They used the larger of the two for each measurement and with an estimated 90% confidence level, most points typically have a relative uncertainty of $\pm 8\%$ – 12% . The quadrature sum of the relative uncertainty with the absolute systematic uncertainty of $\pm 13.5\%$ then yields the total uncertainty which is close to 17% for most measurements. In general, our results are in good agreement with the hCTMC Errea *et al.* [63], AOCC [128] and two-centre atomic-orbital close-coupling (TC-AOCC) Leung and Kirchner [80] results over

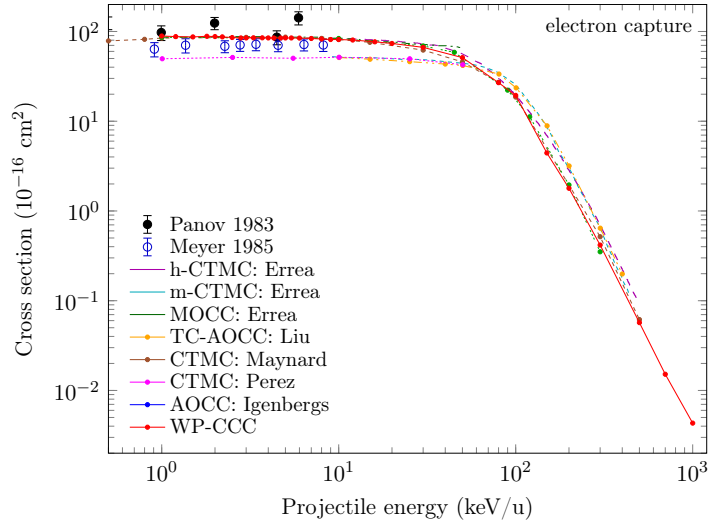


Figure 4.19: Total electron-capture cross section for $\text{Ne}^{10+} + \text{H}(1s)$ collisions. Experimental data are by Panov *et al.* [117] and Meyer *et al.* [118]. The theoretical results are: present WP-CCC approach, hCTMC, mCTMC, and MOCC methods by Errea *et al.* [63], TC-AOCC method by Liu *et al.* [132], CTMC method by Perez *et al.* [136] and Maynard *et al.* [135], and AOCC method by Igenbergs [128].

the entire considered energy range and with the MOCC results [63] at the low energies. From the discrepancy between the experimental and theoretical works it is evident that there is some systematic error in the experiment or the theory which is leading to a consistent under or over estimation of the cross section at the lower energies. The fact that calculations from multiple theoretical approaches yield similar results suggests that the experiment by Meyer *et al.* [118] might be underestimating the cross section. A new set of experimental data could help alleviate this discrepancy. Within the existing data there was a large discrepancy between the hCTMC results by Errea *et al.* [63] and the older CTMC results at projectile energies less than 100 keV/u. The AOCC calculations by Igenbergs [128] and Liu *et al.* [132] agree with the hCTMC results and we find that our results do the same. This is similar to the situation for Be^{4+} projectiles where we saw that the hCTMC method generally provided more accurate results than the older mCTMC approach.

In Fig. 4.20 we present the calculated TICS and compare to the existing theoretical data. We find that our results better agree with the hCTMC ones by Errea *et al.* [63] while slightly underestimating them. At the same time, the

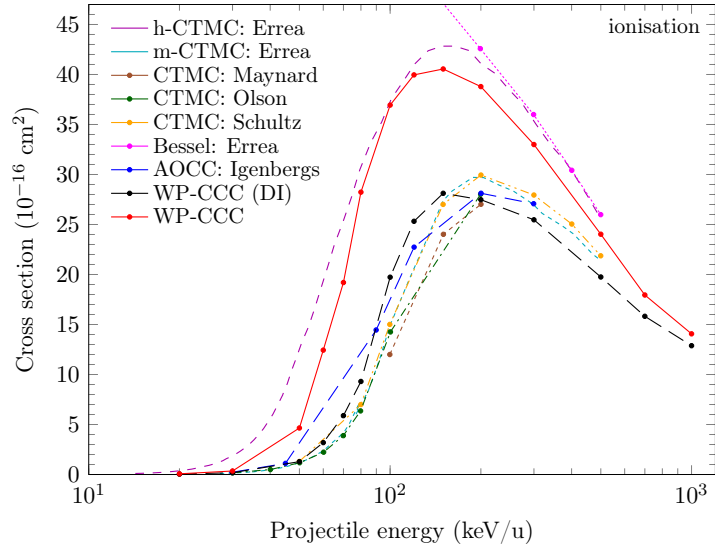


Figure 4.20: Total ionisation cross section for $\text{Ne}^{10+} + \text{H}(1s)$ collisions. The theoretical results are: present WP-CCC results, hCTMC, mCTMC, and spherical Bessel monocentric expansion methods by Errea *et al.* [63], other (older) CTMC methods by Maynard *et al.* [135], Olson and Salop [148], and Schultz and Krstic [149], and AOCC method by Igenbergs [128]. Also shown is the DI component of the total two-centre WP-CCC calculations.

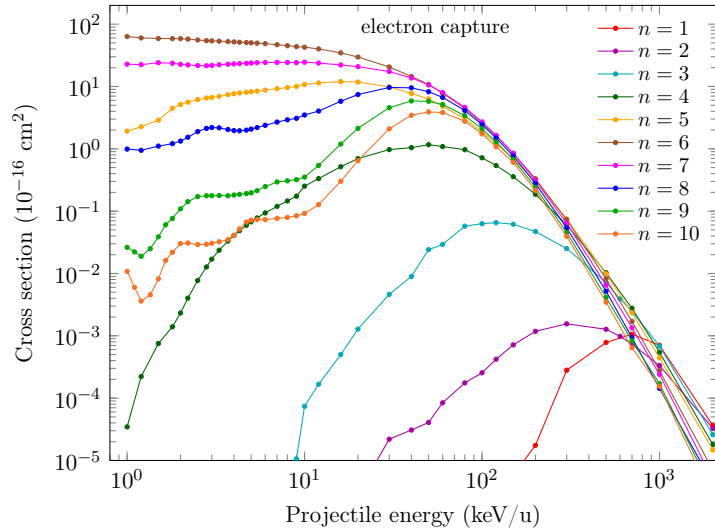


Figure 4.21: Partial n -resolved cross sections for electron capture in $\text{Ne}^{10+} + \text{H}(1s)$ collisions.

present results significantly overestimate the mCTMC results [63], older CTMC results [135, 148, 149] and the AOCC calculations [128]. In addition to the CTMC calculations, Errea *et al.* [63] also used a basis of spherical Bessel functions to perform single-centre close-coupling calculations. Above 200 keV/u, there is good agreement between the Bessel and hCTMC calculations, but at low energies the Bessel approach significantly overestimates the TICS. This is because the Bessel

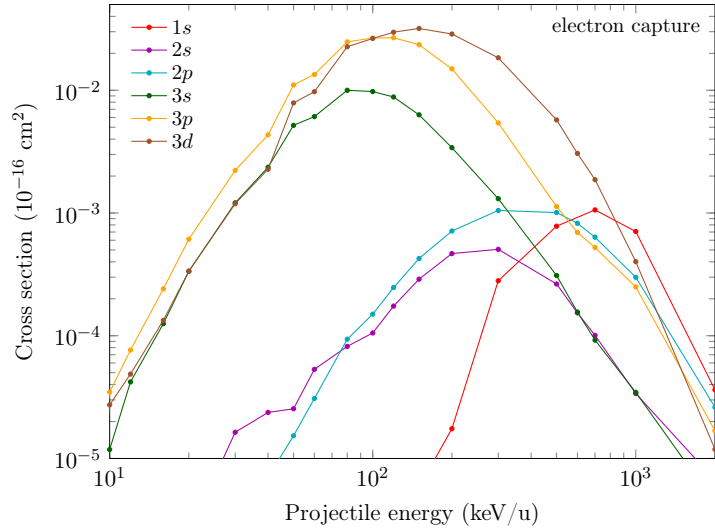


Figure 4.22: Partial $1s$, 2ℓ and 3ℓ cross sections for electron capture in $\text{Ne}^{10+} + \text{H}(1s)$ collisions.

approach gives the electron-loss cross section, which includes EC and ionisation processes. Thus the ionisation cross section from the Bessel approach is accurate only at sufficiently high energies, where ionisation dominates the total electron loss cross section. In their AOCC calculations, Igenbergs [128] included pseudostates representing a united atom and placed them on the target centre. This means that they do not account for the EC into continuum component of the TICS. This explains why their TICS is consistently lower than ours over the entire energy range. To illustrate this, in Fig. 4.20 we show the DI component of the TICS result from our calculations. Indeed, our DI cross section better agrees with the AOCC calculations by Igenbergs [128]. However, agreement between the present DI results and the mCTMC results is more difficult to explain. The agreement is most likely coincidental since the present close-coupling method and CTMC approach are fundamentally very different. The present approach can be concluded to provide the most accurate TICS available for $\text{Ne}^{10+} + \text{H}(1s)$ collisions. The classical calculations disagree with one another and previously available quantum results either over or underestimate the TICS because, unlike the WP-CCC method, they do not account for both the DI and ECC contributions to the total ionisation cross section.

Partial n -resolved electron-capture cross sections have also been calculated

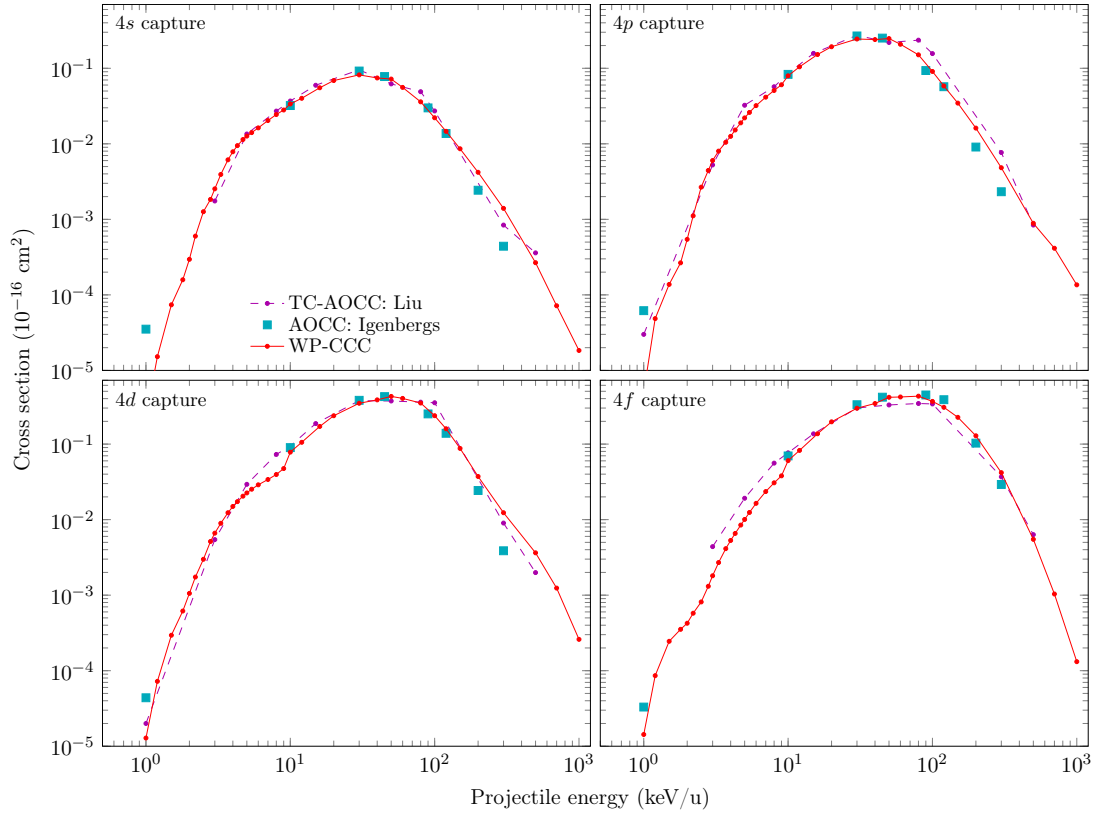


Figure 4.23: Partial 4ℓ cross sections for electron capture in $\text{Ne}^{10+} + \text{H}(1s)$ collisions. The theoretical results are: present WP-CCC approach, TC-AOCC method by Liu *et al.* [132], and AOCC method by Igenbergs [128]. The key in the upper-left panel applies to all panels.

for capture into ground and excited states of the Ne^{9+} ion, up to $n = 10$. These are shown in Fig. 4.21 as functions of the projectile energy. We find $n = 6$ to be the most probable shell for EC at low and intermediate projectile energies. This is in agreement with the hCTMC Errea *et al.* [63], AOCC [128] and TC-AOCC [132] calculations at these impact energies. The older CTMC results, however, predict $n = 5$ to be the dominant state for capture by the projectile. There is no experimental data to shed light on the situation. The most recent calculations predict $n = 6$ to be the dominant state, this suggests that the older CTMC results either overestimate the $n = 5$ cross section or underestimate the $n = 6$ cross sections. Regardless, both results seem to agree with the predictions by Olson [147], which states that at low collision energies, in collisions of highly

charged ions with atomic target, the dominant state is given by

$$n_f = n_i \left(\frac{Z_P}{Z_T} \right)^{3/4}, \quad (4.1)$$

where n_f and n_i are the captured electron's final and initial state quantum numbers, respectively. In our case the formula gives $n_f = 5.6$, suggesting the most likely n -state for capture is either 5 or 6. We find that at projectile energies less than 100 keV/u, for $n \geq 6$ the cross section falls systematically as n increases.

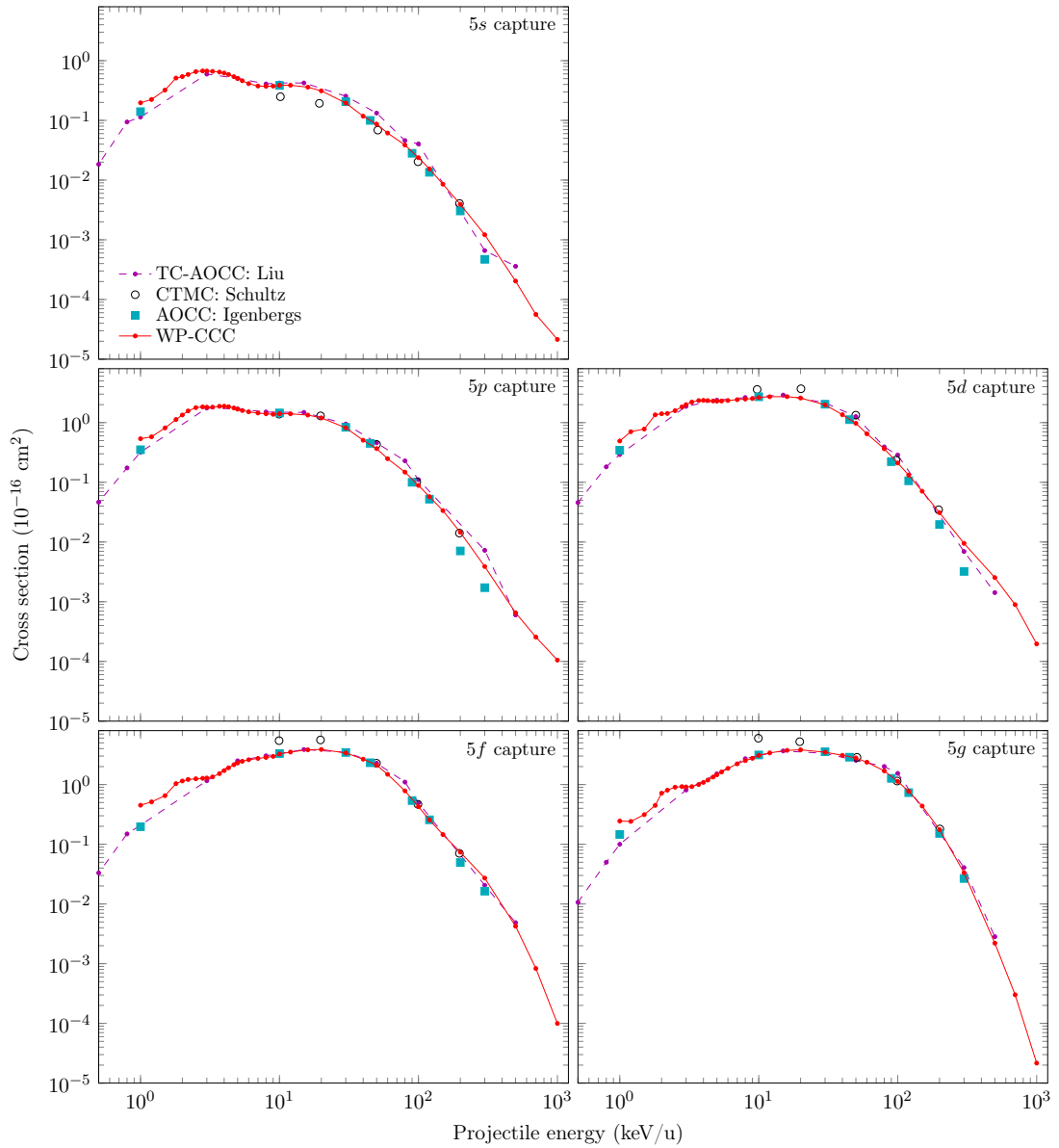


Figure 4.24: Partial 5ℓ cross sections for electron capture in $\text{Ne}^{10+} + \text{H}(1s)$ collisions. The theoretical results are: present WP-CCC approach, TC-AOCC method by Liu *et al.* [132], CTMC method by Schultz and Krstic [149], and AOCC method by Igenbergs [128]. The key in the upper-left panel applies to all panels.

Figure 4.22 shows our results for electron capture into the $1s$, 2ℓ , and 3ℓ states of the Ne^{10+} projectile. There are no other results available for these cross sections. It is very challenging to calculate these cross sections accurately due to their small magnitudes at low energies. Nevertheless, their significance grows with energy with the cross section for EC into the $1s$ state ultimately becoming dominant in the MeV/u region. There are other calculations available for the $n = 4$ to $n = 8$ shell states. We present our results for capture into the 4ℓ and 5ℓ states of Ne^{9+} alongside these other calculations in Fig. 4.23 and Fig. 4.24, respectively. We find very good agreement with the AOCC calculations [128, 132] for projectile energies above 2 keV/u. The 5ℓ partial cross sections are also compared to the CTMC calculations by Schultz and Krstic [149], with which we find good agreement at high energies but there is slight disagreement near 10 keV/u.

In Figs. 4.25–4.27 we present the partial 6ℓ , 7ℓ , and 8ℓ cross sections, respectively. As we saw in Fig. 4.21, below 100 keV/u the dominant contribution to the TECS comes from the $n = 6$ shell. Generally speaking, we find good agreement with the AOCC calculations [128, 132] for all three sets of partial cross sections over the entire energy range considered in this work. The only discrepancy we find is for capture into the s states. At energies below 5 keV/u, our results are significantly larger than the corresponding results from the TC-AOCC calculations by Liu *et al.* [132]. However, we find excellent agreement with the older AOCC calculations by Igenbergs [128].

We also compare our results to the CTMC calculations by Schultz and Krstic [149] available for the $n = 6$ and $n = 7$ shell states. We find good agreement at high energies, however, below 50 keV/u, the CTMC method appears to predict significantly smaller cross sections for capture into all 6ℓ and 7ℓ states except for the $6g$ and $6h$ states. Figure 4.25 also shows the 6ℓ partial cross sections obtained using the one-electron diatomic molecular (OEDM) orbitals method by Salin [150]. These calculations seem to consistently overestimate the cross section

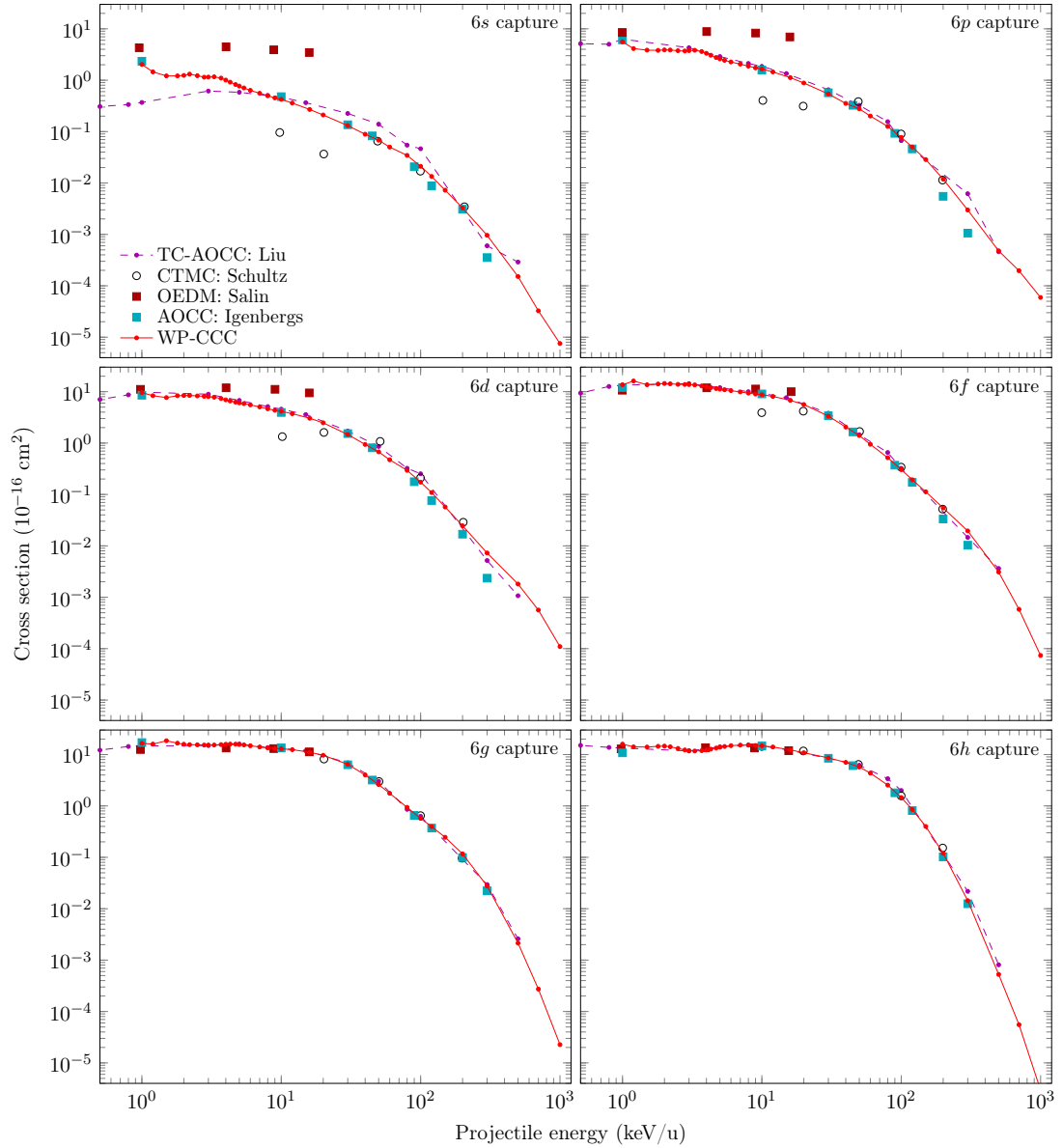


Figure 4.25: Partial 6ℓ cross sections for electron capture in $\text{Ne}^{10+} + \text{H}(1s)$ collisions. The theoretical results are: present WP-CCC approach, TC-AOCC method by Liu *et al.* [132], CTMC method by Schultz and Krstic [149], OEDM method by Salin [150], and AOCC method by Igenbergs [128]. The key in the upper-left panel applies to all panels.

in comparison with our results and all other theoretical calculations for $\ell = 0, 1,$ and 2 . However, agreement is much better for $\ell = 3, 4,$ and 5 . Note that at low energies the OEDM method is believed to be reliable. Our 6ℓ cross sections indeed agree with the OEDM ones at 1 keV/u . The TC-AOCC results by Liu *et al.* [132] for the $6s$ cross section does not tend towards the molecular result at low energies. This suggests that our $6s$ cross section could be more accurate. A similar argument can be applied to the cross sections for capture into the $7s, 8s$

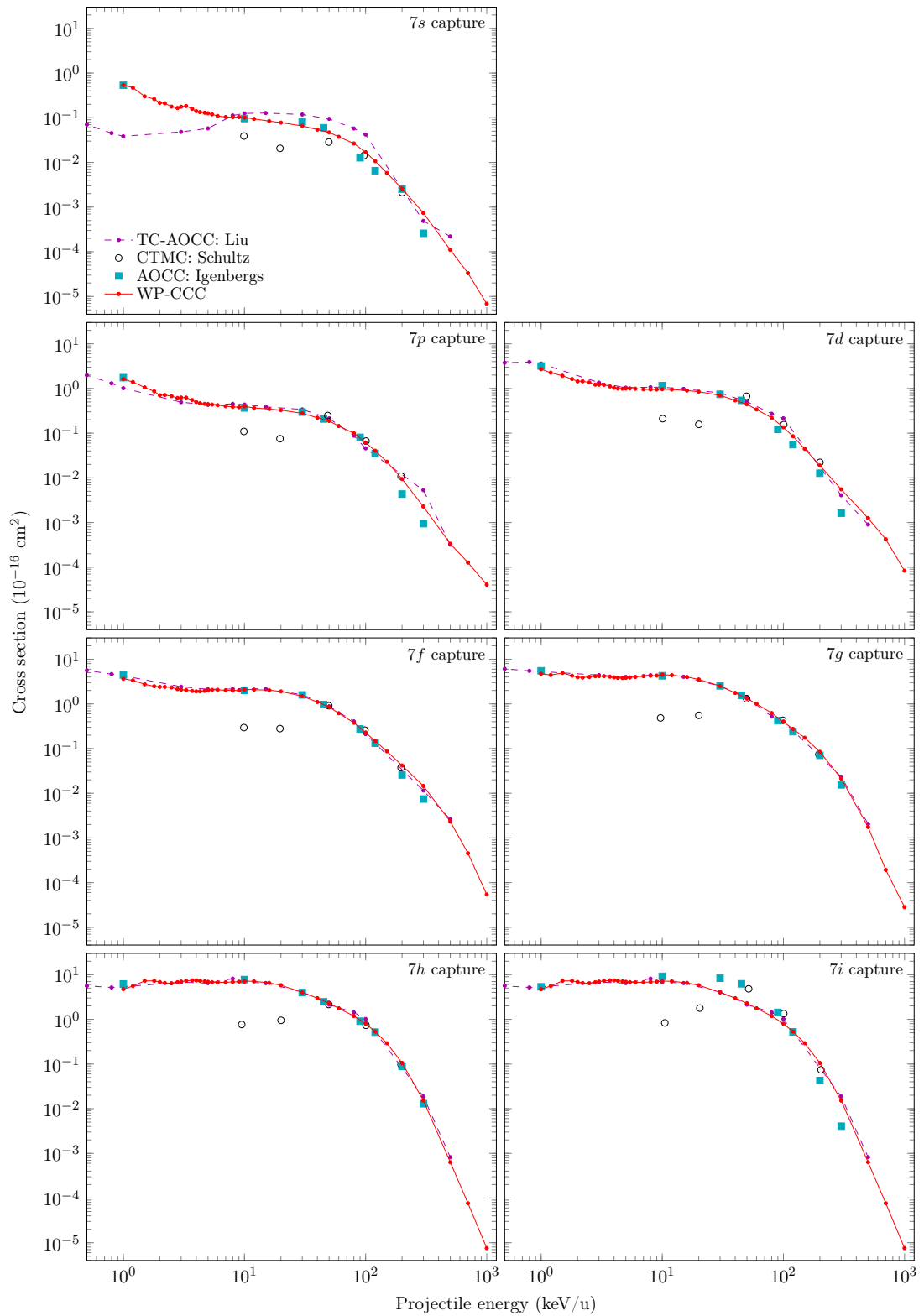


Figure 4.26: Partial $7l$ cross sections for electron capture in $\text{Ne}^{10+} + \text{H}(1s)$ collisions. The theoretical results are: present WP-CCC approach, TC-AOCC method by Liu *et al.* [132], CTMC method by Schultz and Krstic [149], and AOCC method by Igenbergs [128]. The key in the upper-left panel applies to all panels.

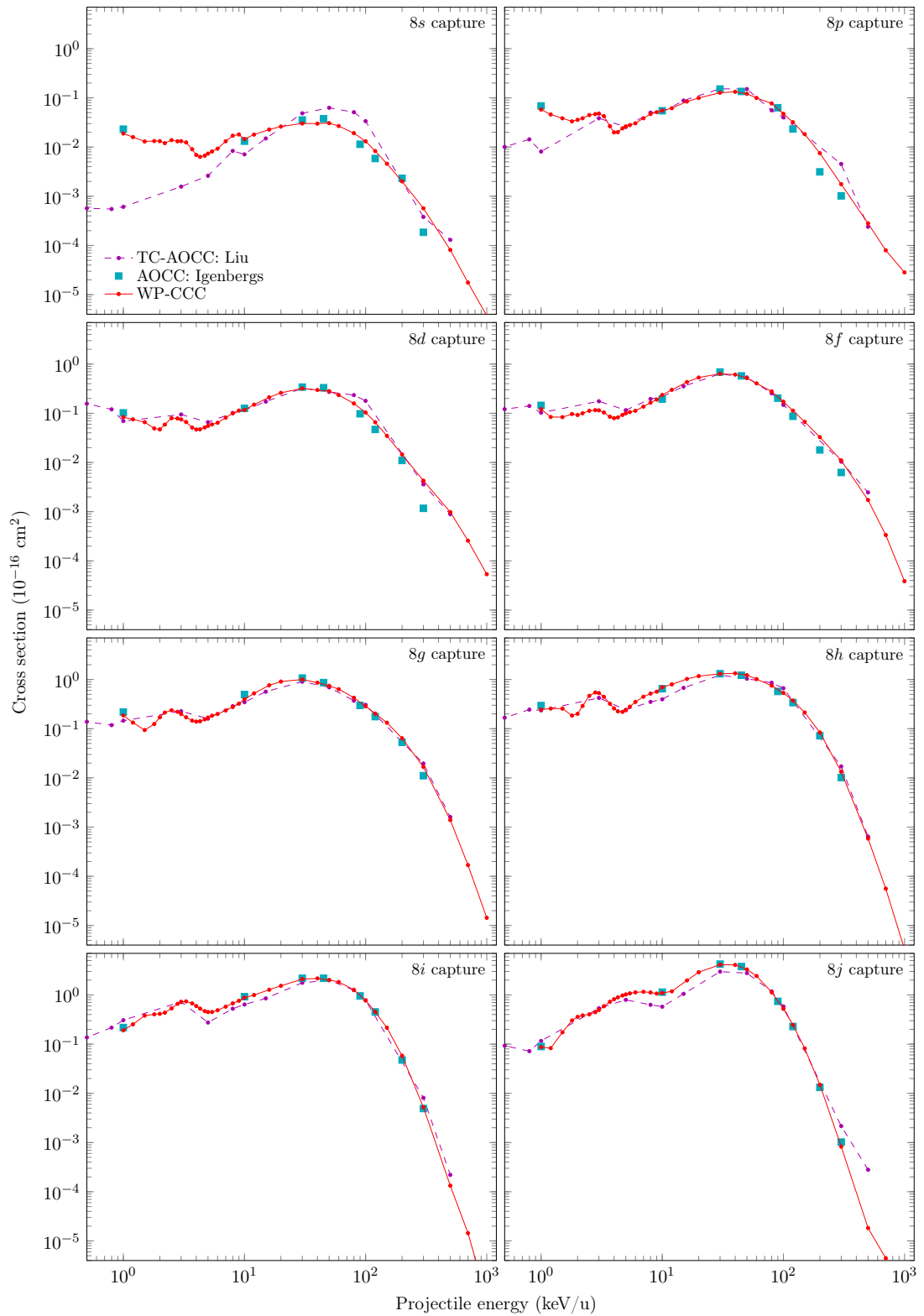


Figure 4.27: Partial 8ℓ cross sections for electron capture in $\text{Ne}^{10+} + \text{H}(1s)$ collisions. The theoretical results are: present WP-CCC approach, TC-AOCC method by Liu *et al.* [132], and AOCC method by Igenbergs [128]. The key in the upper-left panel applies to all panels.

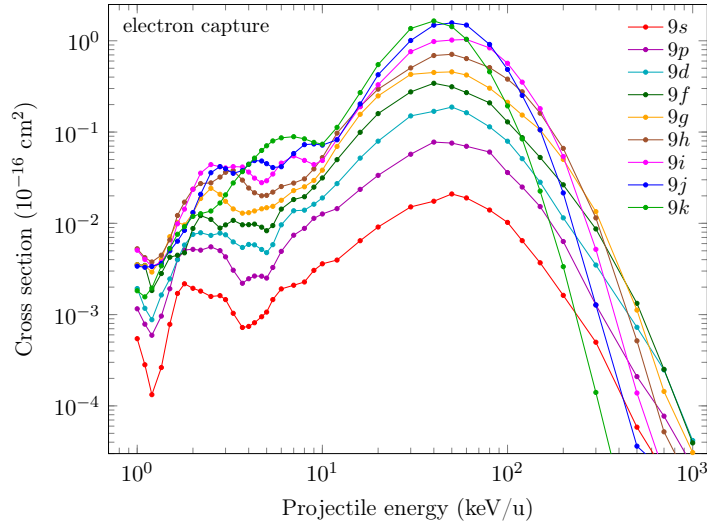


Figure 4.28: Partial 9ℓ cross sections for electron capture in $\text{Ne}^{10+} + \text{H}(1s)$ collisions.

and $8p$ states, where we see disagreement with the TC-AOCC results.

The 9ℓ and 10ℓ cross sections are shown in Figs. 4.28 and 4.29. Interestingly, we observe pronounced oscillations in all the 9ℓ and 10ℓ partial cross sections at energies below 10 keV/u. In fact, such oscillations start to appear in the 8ℓ partial cross sections as well. We note that these oscillations appear only in non-resonant transitions. This is similar to the structures observed in our results for collisions of Li^{3+} and Be^{4+} projectiles with $\text{H}(1s)$. We find that within each shell, the relative contribution of the $n\ell$ cross section grows with increasing ℓ at energies below 100 keV/u. At the same time, we also find that the contribution from the largest allowed ℓ drops significantly at energies above 100 keV/u.

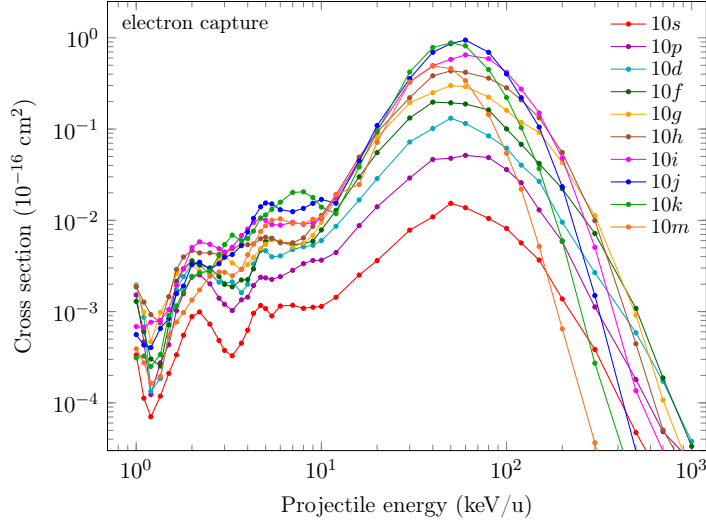


Figure 4.29: Partial 10ℓ cross sections for electron capture in $\text{Ne}^{10+} + \text{H}(1s)$ collisions.

4.4 Chapter summary

In this chapter we applied the WP-CCC approach to calculate integrated cross sections for different processes taking place in collisions of the Li^{3+} , Be^{4+} , and Ne^{10+} ions with atomic hydrogen. For the total cross sections for the lithium and neon ion projectiles we find good agreement with the available experimental data. However, for the Be^{4+} projectiles there are no experimental data to compare to. Furthermore, there are no experimental measurements of the n - and $n\ell$ -partial cross sections for electron capture. Previous calculations are only available over limited energy ranges or for certain processes. We presented calculations for all significant processes over a wide energy range where accurate data are essential for plasma modelling, all within the same theoretical framework and subject to the unitary principle. The results converged within several percent over the entire energy range considered. For $\text{Be}^{4+} + \text{H}(2\ell m)$ collisions, we also performed purely single-centre calculations to check for internal consistency in our results. Overall, we find that the present results agree with the hCTMC calculations in most cases, but differences are observed for the older microcanonical ensemble-based CTMC calculations. In some cases, significant differences with existing AOCC calculations was found, possibly due to numerical inaccuracies in the older AOCC

results. At low energies, the WP-CCC method generally agrees well with the MOCC calculations while at high energies we find agreement with perturbative methods. We also find that our results agree very well with the sophisticated GTDSE and LTDSE methods, where available.

We conclude that the data in this chapter represent the most comprehensive set of state-selective cross sections for the considered collision systems. The data presented in this chapter will be available in due course through the International Atomic Energy Agency (IAEA) repositories within the framework of the IAEA Coordinated Research Project (CRP) on Data for Atomic Processes of Neutral Beams in Fusion Plasma [151].

The results presented in this chapter were performed on massively parallel GPU-based supercomputers using significant computational resources. Obtaining converged results for the presently considered $n\ell$ -resolved cross sections within the two-centre close-coupling framework would not have been possible with CPU-based computing.

Chapter 5

Proton scattering on atomic hydrogen^{*}

The three-body $p+H$ collision system is the simplest ion-atom scattering problem where rearrangement of particles is possible. As such, it provides a useful testing ground for theoretical methods and has been extensively studied. Calculating the angular differential cross section for elastic scattering, target excitation, or electron capture presents a more difficult challenge than the corresponding integrated cross section. Differential cross sections for ionisation are further complicated by the need to accurately represent the state of the electron in the continuum of the target and projectile nuclei. As a result, very few calculations of the SDCS for ionisation in $p+H$ collisions are available and those that are, do not agree with the experimental data in all kinematic regions.

In this chapter the WP-CCC method is applied to calculate all types of singly differential cross sections for $p+H$ collisions. We consider projectile energies from 20 to 125 keV, where experimental data are available. This is a challenging energy region for theoretical methods where coupling between all reaction channels plays an important role in the collision dynamics.

^{*} This chapter is adapted from work published by the candidate [152]. The publishers (the American Physical Society) provide the author with the right to use the articles, or parts thereof, in a thesis or dissertation without requesting permission.

5.1 Angular differential cross sections for p+H collisions

Angular differential cross sections for elastic scattering, excitation into the $n = 2$ states and electron capture (summed over all included projectile bound states) were calculated from the transition amplitudes for the corresponding states for each of these processes. It was found that a basis containing $10 - \ell$ bound states and 20 bin states (for each orbital angular momentum ℓ), on both centres, with the maximum orbital angular momentum $\ell_{\max} = 3$ was sufficient to obtain convergence in the differential cross sections at all three energies considered. The maximum ionisation-state energy was set by momenta $\kappa_{\max} = 5.5$ a.u., which was verified to be sufficient for all the angular differential cross sections considered in this work to converge. The trajectory of the projectile is discretised using 1200 points from $z_{\min} = -300$ to $z_{\max} = 300$ a.u. In calculating the angular differential cross section (DCS) over the range from $\theta_{\min} = 0$ mrad to $\theta_{\max} = 3.5$ mrad, it was found that including additional impact parameters beyond $b_{\max} = 14$ a.u. made no appreciable difference to the SDCS. While 64 impact-parameter points were sufficient for most results, 128 were required to remove unphysical oscillations in the differential cross section for $n = 2$ excitation at 125 keV. To check the robustness of our results we numerically integrated the DCS and compared the resulting values with the elastic, excitation, and electron-capture cross sections obtained directly from the expansion coefficients. Surprisingly, to obtain 99% agreement it was necessary to include scattering angles up to 20 mrad in the integration.

Figure. 5.1 shows the WP-CCC results for the angular DCS for 25 keV p + H collisions. The present results for elastic scattering agree well with the experimental data by Rille *et al.* [153]. The multichannel optical-model (MOM) calculations by Potvliege *et al.* [82] show a similar level of agreement with the experiment. There is significant deviation between the various available theoretical

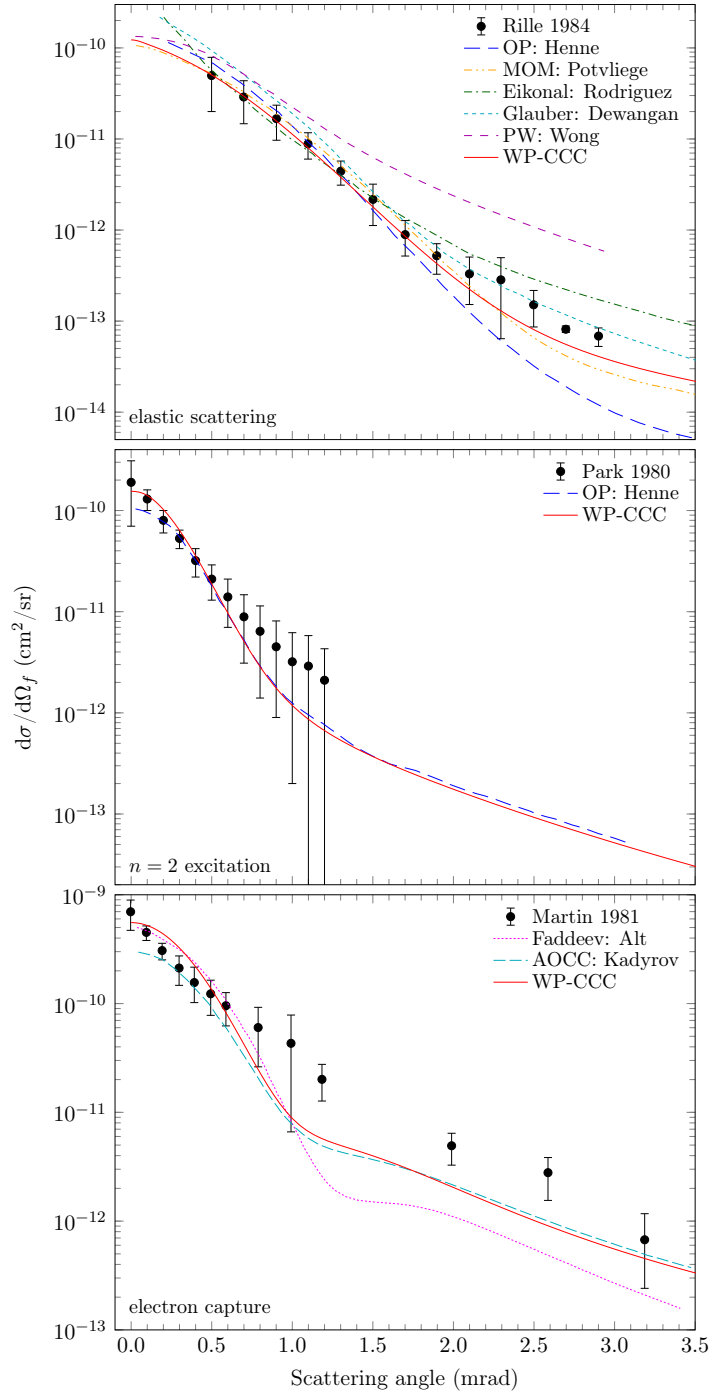


Figure 5.1: Angular differential cross sections (in the centre-of-mass frame) for elastic scattering, excitation into the $n = 2$ target states, and electron capture summed over all projectile states for 25 keV $p + H$ collisions. Experimental data are by Rille *et al.* [153], Park *et al.* [154], and Martin *et al.* [155]. The theoretical results are: present WP-CCC approach, OP method by Henne *et al.* [81], MOM by Potvliege *et al.* [82], Eikonal method by Rodriguez [156], Glauber approximation by Dewangan and Eichler [48], PW approach by Wong *et al.* [58], Faddeev method by Alt *et al.* [157], and AOCC method by Kadyrov *et al.* [77].

approaches. In particular, the elastic-scattering cross section by Wong *et al.* [58], obtained in a partial-wave (PW) approach using only the ground state of

H, substantially overestimates the experimental data above 1 mrad. Results for excitation into the $n = 2$ states of the target atom agree well with experiment, especially in the forward direction. At larger scattering angles the WP-CCC calculations closely follow the results from Ref. [81]. Henne *et al.* [81] used a doorway approximation within the optical potential (OP) method to calculate differential excitation into the $n = 2$ states. Their results tend to underestimate the experiment [154] near the forward direction. This should lead to significant underestimation of the corresponding integrated cross section. The present results for electron capture generally agree well with experiment. However, the WP-CCC differential cross section is noticeably smaller for scattering angles from 1.5 to 2 mrad. The electron capture results agree best with those calculated using a three-dimensional integral equation approach to the AOCC method [77] at 25 keV.

In Fig. 5.2 we present our results at 60 keV. Here there is generally good agreement between the various theoretical results for elastic scattering. The WP-CCC calculations agree well with the experimental data and again most closely follow the MOM calculations of Potvliege *et al.* [82]. However, there is disagreement with the results of the IPFA by Alt *et al.* [157] and the PW approach by Wong *et al.* [58]. The Faddeev approach deviates from other calculations at scattering angles below 0.5 mrad possibly due to insufficient number of channels included in Ref. [157]. For $n = 2$ excitation the situation is the same as at 20 keV, although the WP-CCC results are slightly higher than the OP calculations by Henne *et al.* [81] at the larger scattering angles. The WP-CCC calculations of the angular differential cross sections for electron capture generally agree well with the experimental data by Martin *et al.* [155]. We again find that the electron capture results agree best with those by [77]. A recent extension of the BCIS-3B method to include capture into many bound states by Milojević *et al.* [158] agrees well with our results below 1 mrad. However, between 1 and 1.5 mrad it is smaller and beyond 2 mrad it is larger than the other theoretical results.

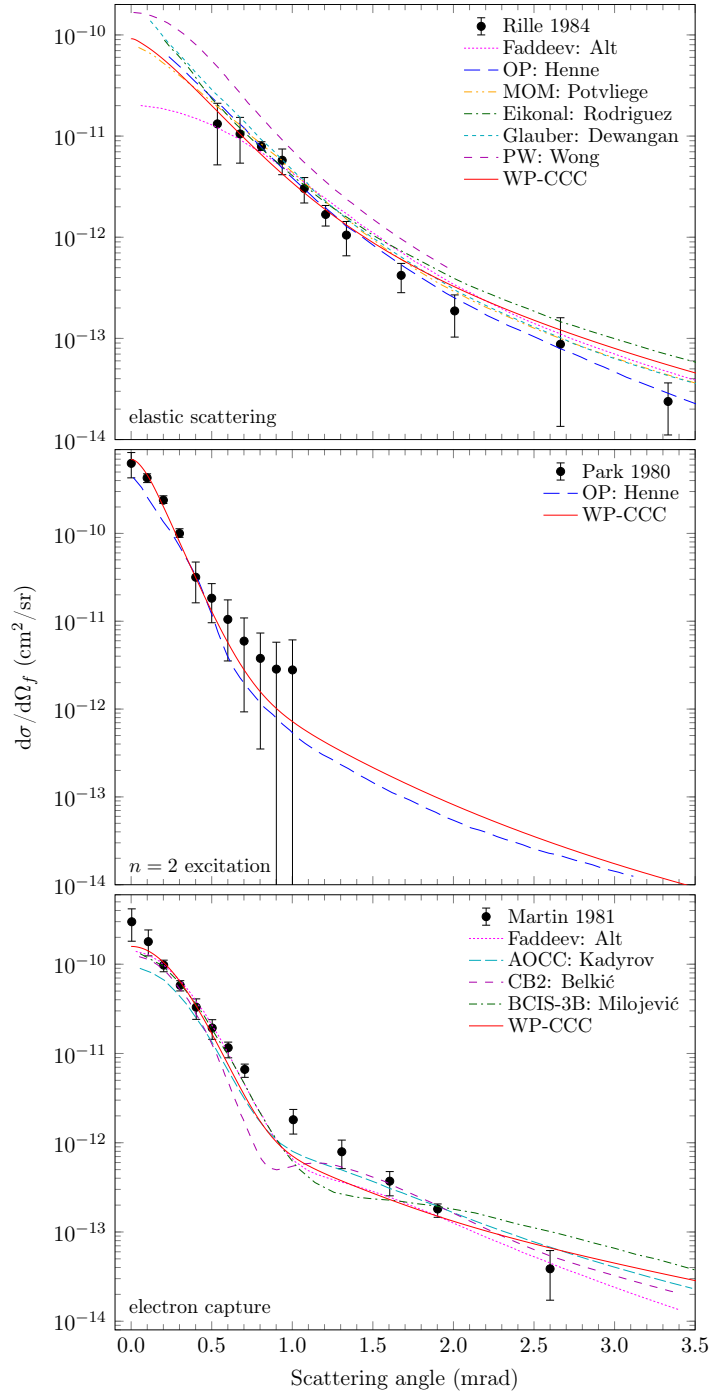


Figure 5.2: Same as Fig. 5.1 but for 60 keV protons. Also shown are the results from the CB2 method by Belkić [50] and BCIS-3B method by Milojević *et al.* [158].

For 125 keV collisions, there is no experimental or theoretical data available for the elastic-scattering differential cross section. Therefore, in Fig. 5.3 we compare our calculations with those obtained using the FBA. Differences between the WP-CCC and FBA results, especially in the forward direction, clearly demonstrate the importance of including the contribution from the many interacting reaction

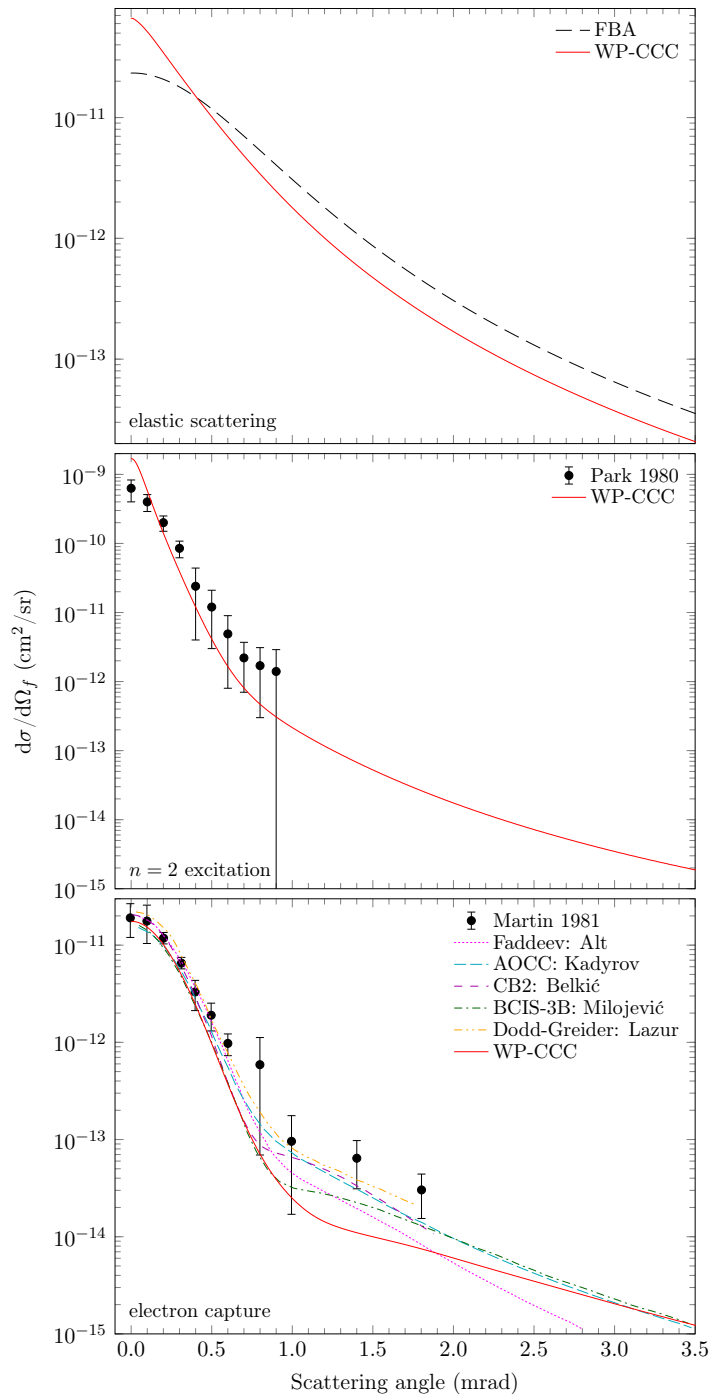


Figure 5.3: Same as Fig. 5.2 but for 125 keV protons. Also shown are the results from the Dodd-Greider approach by Lazur *et al.* [159] and the present FBA results for elastic scattering.

channels. For excitation into the $n = 2$ states the present results overestimate the experimental data of Park *et al.* [154] in the forward direction, but generally agree well at larger scattering angles. For electron capture, we find excellent agreement with the experimental data for small scattering angles. However, the WP-CCC calculations underestimate the experiment from 1.5 to 2 mrad. A

recently developed approach based on the first iteration of the Dodd-Greider equations by Lazur *et al.* [159] appears to perform well for electron capture at 125 keV; however, no results are available at 25 and 60 keV. Also, it is unclear if the approach can provide the cross sections for direct scattering and ionisation. The BCIS-3B calculations by Milojević *et al.* [158] agree well with our results below 1 mrad. From 1 to 2 mrad, the BCIS-3B results are closer to experiment than the WP-CCC results but towards larger angles they converge.

Note that all the theoretical calculations mentioned above, except the present WP-CCC ones and the recent BCIS-3B calculations, are for electron capture into the ground state of hydrogen. These are scaled up by a factor of 1.202 to effectively compensate for the missing excited states. We find that in our calculations the ground-state of the projectile atom contributes 71% of the total electron capture cross section, indicating the inclusion of additional negative-energy exchange channels has a significant effect on the results.

5.2 Singly differential cross sections for ionisation in p+H collisions

For ionisation calculations, the maximum momentum, κ_{\max} , of the included pseudostates was 5.0 a.u. for projectile energies of 20, 48, and 67 keV. For projectile energies of 95 and 114 keV, κ_{\max} was set to 6.6 and 7.6 a.u., respectively. The present results were checked by integrating the SDCS and comparing the resulting TICS with that obtained directly from the expansion coefficients. In all cases, we find 99% or better agreement. A basis of $5 - \ell$ bound states and 30 continuum pseudostates, on both centres, with $\ell_{\max} = 4$ was found to be sufficient to obtain convergence in the results at 25 keV. For higher projectile energies, the same basis as used for the angular DCS in Sect. 5.1 was sufficient.

In Figs. 5.4–5.8 we show our calculations for the singly differential cross sections for ionisation as functions of the energy and angle of the ejected electron

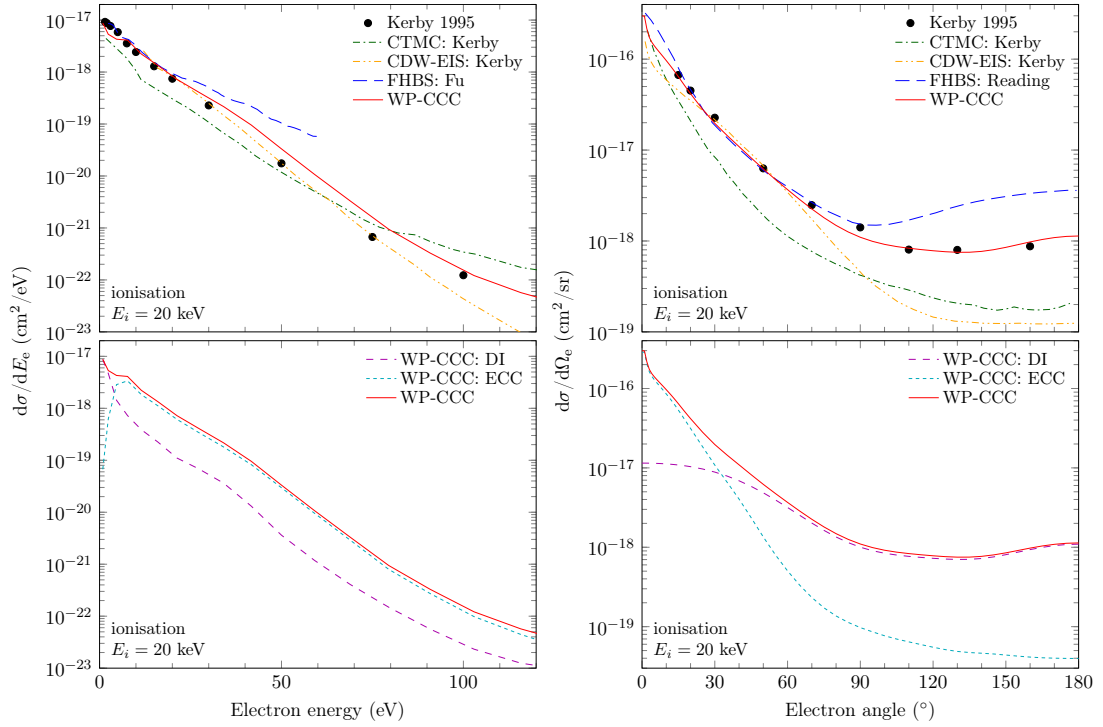


Figure 5.4: Singly differential cross sections (in the laboratory frame) for ionisation in 20 keV $p + H$ collisions as functions of the electron energy (left) and ejection angle (right). Experimental data are by Kerby III *et al.* [160]. The theoretical results are: present WP-CCC approach, CTMC and CDW-EIS methods by Kerby III *et al.* [160] and FHBS method by Fu [161] and Reading *et al.* [162]. The DI and ECC components of the WP-CCC cross sections are shown in the lower panels.

at 20, 48, 67, 95, and 114 keV, respectively. The upper-left panel in each figure shows the ionisation cross section differential in the energy of the electron and the upper-right panel shows the ionisation cross section differential in the emission angle of the electron. The present results are compared with the experimental data by Kerby III *et al.* [160] as well as CTMC and CDW-EIS calculations by Kerby III *et al.* [160] and results obtained using a finite Hilbert basis set (FHBS) method by Fu [161], Fu *et al.* [163], and Reading *et al.* [162]. Experimental uncertainties are not shown because it is difficult to gauge them from Ref. [160]. However, the experimental data on the singly differential cross sections were obtained by numerically integrating the experimental doubly differential cross section over electron angle or electron energy [160]. As mentioned in the associated work [12], the uncertainties in the measured doubly differential cross sections were 26% at 1.5 eV, decreasing to 22% at 10 eV, but then increasing to 50% or more at the

highest electron energies. Consequently, the uncertainties in the SDCS data are expected to be even larger.

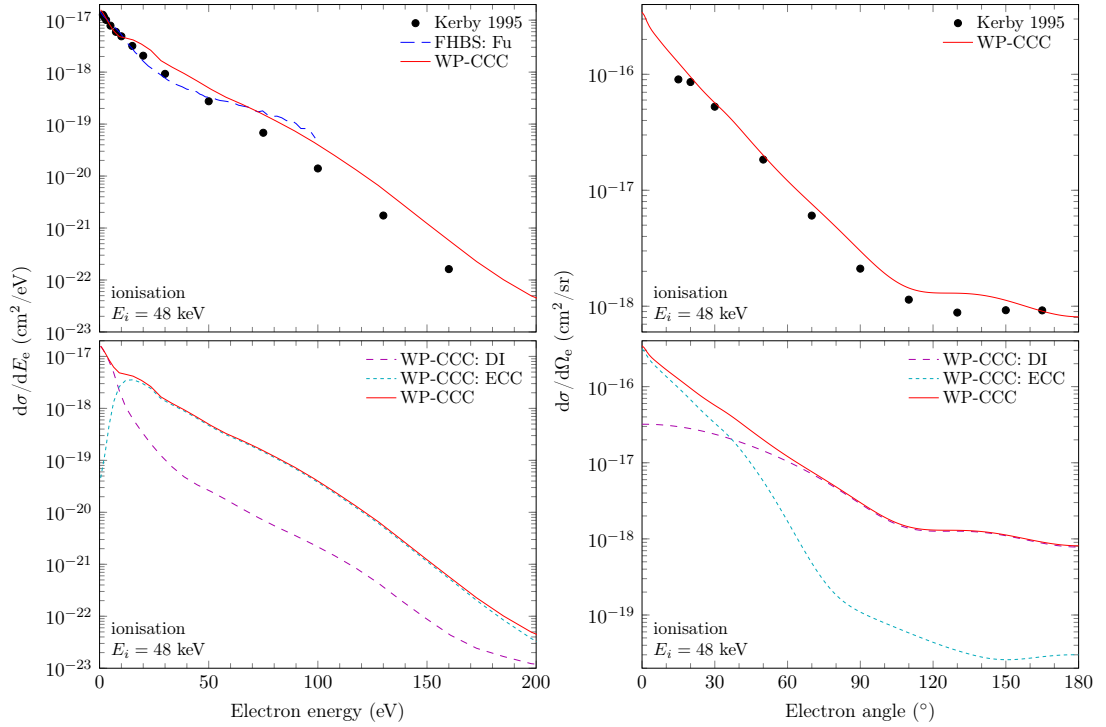


Figure 5.5: Singly differential cross sections (in the laboratory frame) for ionisation in 48 keV $p + H$ collisions as functions of the electron energy (left) and ejection angle (right). Experimental data are by Kerby III *et al.* [160]. The theoretical results are: present WP-CCC approach and FHBS method by Fu *et al.* [163]. The DI and ECC components of the WP-CCC cross sections are shown in the lower panels.

For 20 keV projectiles, the results in Fig. 5.4 show improvement over previously available calculations, especially for the SDCS as a function of the angle of the electron. The FHBS calculations for the energy-differential ionisation cross section by Fu [161] are only available for small ejected electron energies where they agree well with the experimental results. However, they start deviating from the experiment rising too quickly above 20 eV. The calculations of the SDCS differential in the angle of the electron by Reading *et al.* [162] agree well with the experiment and our results for the ejection angles from 20 to 90°. However, beyond 90° the FHBS calculations rise too quickly suggesting they converged to an incorrect result. For the SDCS as a function of the electron energy we find reasonable agreement with the CDW-EIS calculations, but the WP-CCC results tend to slightly overestimate the experiment as energy increases. The CTMC

results underestimate the experimental data up until 70 eV, after which they overestimate it. In contrast, the WP-CCC results are the only calculations that accurately reproduce the experimentally measured cross section for the SDCS as a function of the electron angle at 20 keV.

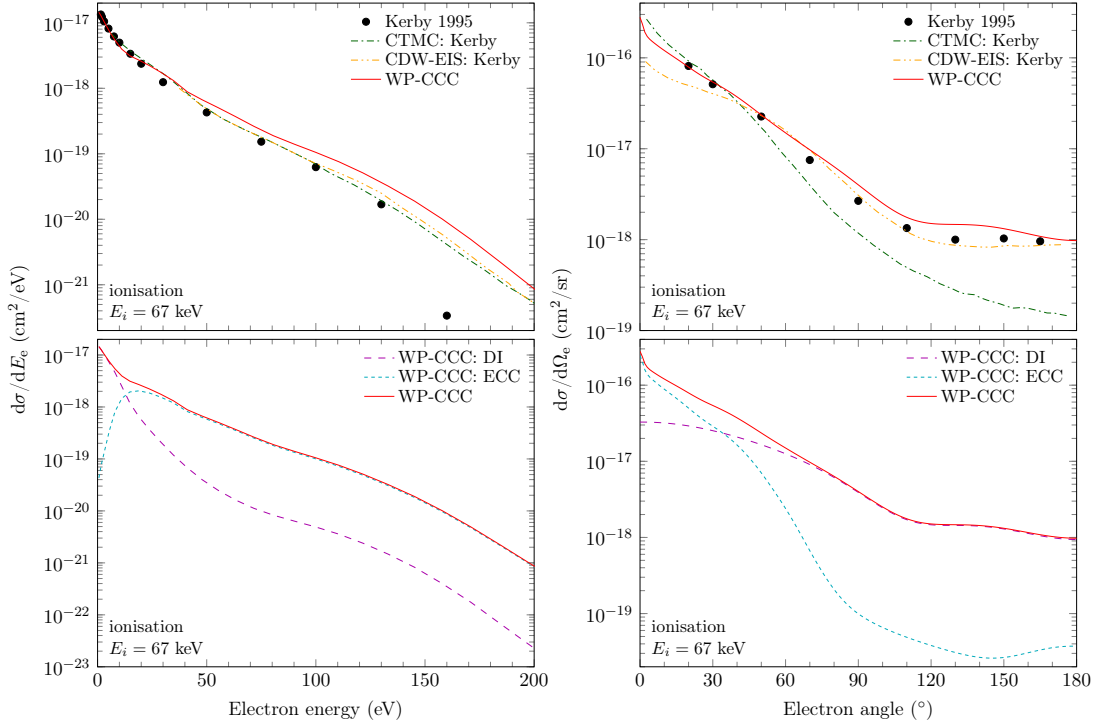


Figure 5.6: Singly differential cross sections (in the laboratory frame) for ionisation in 67 keV $p + H$ collisions as functions of the electron energy (left) and ejection angle (right). Experimental data are by Kerby III *et al.* [160]. The theoretical results are: present WP-CCC approach and CTMC and CDW-EIS methods by Kerby III *et al.* [160]. The DI and ECC components of the WP-CCC cross sections are shown in the lower panels.

Figure 5.5 shows our results at 48 keV. One can see a small bump in the WP-CCC results at the 20 and 48 keV incident energies at small ejection energies. This occurs when the contribution from DI drops sharply as the ejection energy rises while the contribution from ECC increases. This feature washes out as collision energy goes up and is barely noticeable already at 67 keV. The FHBS calculations for the energy-differential ionisation cross section by Fu *et al.* [163] again agree with the experiment for very small emission energies, but begin to deviate above 50 eV. There are no other calculations available at this incident energy. The WP-CCC results agree very well with the experimental data for SDCS as a function of energy for small emission energies where DI is the primary mechanism leading

to ionisation. However, when the ECC component dominates we consistently overestimate the experiment. For the SDCS differential in the emission angle of the electron, we find that our results agree reasonably well with the experimental data, although slightly overestimate it. Unlike for 20 keV protons, here the WP-CCC calculation is somewhat larger than the first experimental point which doesn't seem to follow the trend of the other data. We also observe a small bump at 140° which is not reflected in the experiment.

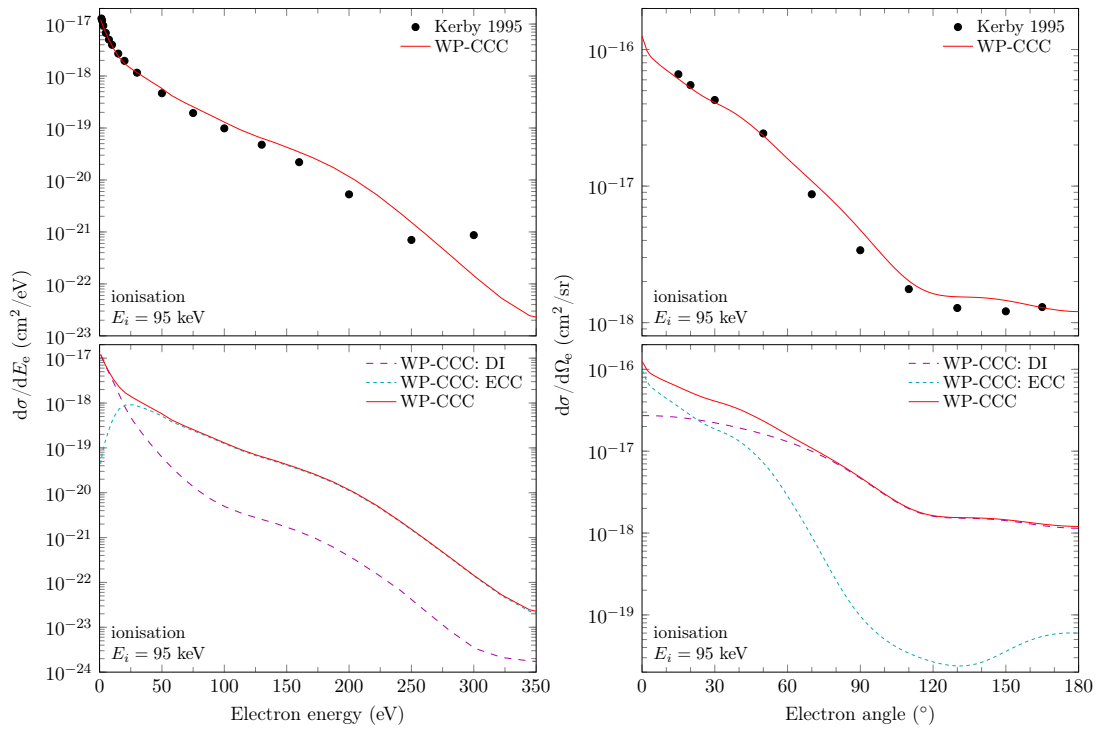


Figure 5.7: Singly differential cross sections (in the laboratory frame) for ionisation in 95 keV $p + H$ collisions as functions of the electron energy (left) and ejection angle (right). Experimental data are by Kerby III *et al.* [160]. The theoretical results are: present WP-CCC approach and DI and ECC components (lower panels).

At 67 keV, the results shown in Fig. 5.6 agree closely with the CDW-EIS calculations by Kerby III *et al.* [160] for the SDCS as a function of the electron energy. We see that all three theoretical methods significantly overestimate the final data point near 160 eV. The reason for this is unknown. For the SDCS as a function of the electron angle, our results agree closely with the experimental data at all angles. In contrast, the CTMC results only agree at small angles and the CDW-EIS calculations deviate from the experiment when $\theta_e < 50^\circ$.

Figure 5.7 shows our results for 95 keV projectiles. We find very good agreement with the experiment for both types of SDCS. However, the last experimental point for ejection of 300 eV electrons in the upper-left panel is larger than the WP-CCC result and does not follow the trend of the other experimental data.

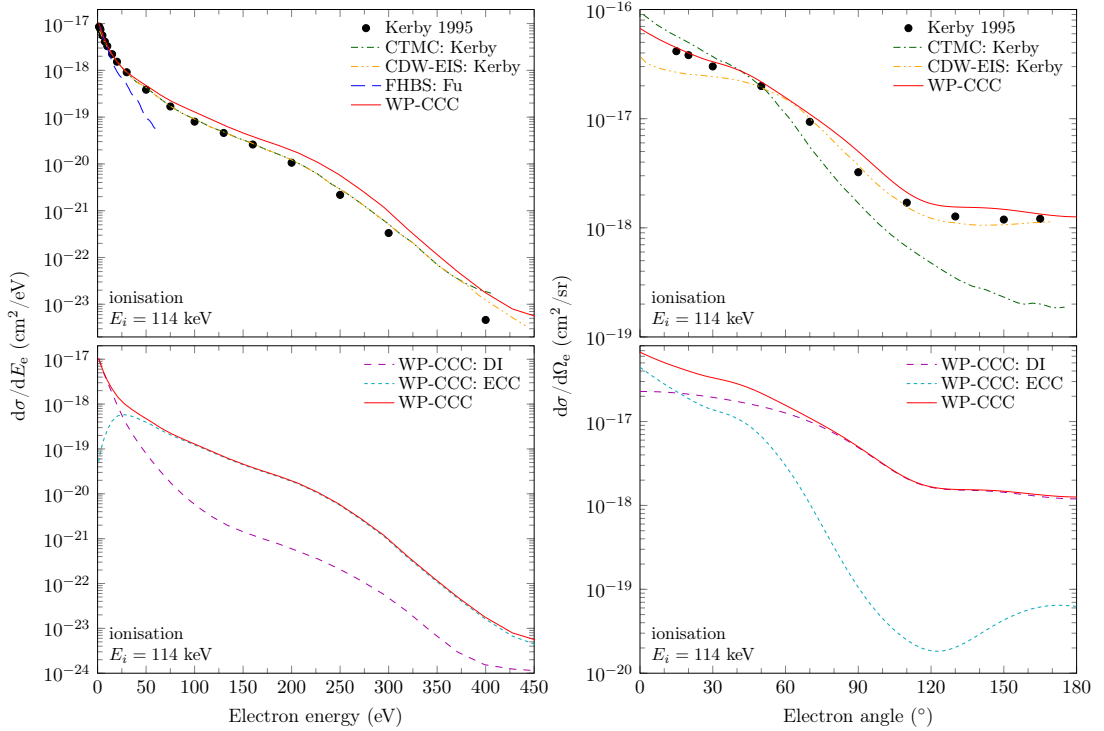


Figure 5.8: Singly differential cross sections (in the laboratory frame) for ionisation in 114 keV $p + H$ collisions as functions of the electron energy (left) and ejection angle (right). Experimental data are by Kerby III *et al.* [160]. The theoretical results are: present WP-CCC approach and FHBS method by Fu *et al.* [163]. The DI and ECC components of the WP-CCC cross sections are shown in the lower panels.

In Fig. 5.8 we show results at 114 keV. We again find very good agreement with the experimental data by Kerby III *et al.* [160]. The FHBS calculations by Fu *et al.* [163] fall off steeply and underestimate all other theoretical methods as well as the experiment, except at very small emission energies. At this energy the CTMC and CDW-EIS results by Kerby III *et al.* [160] agree very well with the experimental data for the SDCS differential in the energy of the electron. However, both methods still show significant discrepancies for the SDCS differential in the ejection angle. The WP-CCC calculation is the only result available that is capable of accurately describing the experimental data for this type of SDCS.

In the lower panels of Figs. 5.4–5.8 we show the DI and ECC contributions to

the total WP-CCC SDCS. Overall we find that SDCS in ejected electron energy is dominated by the DI component when the electron is slow indicating the electron remains close to the target nucleus. However, when the ejected electron is more energetic, the SDCS is dominated by ECC suggesting that the electron travels closer to the scattered projectile. For the SDCS as a function of ejection angle we find that ECC gives a dominant contribution when the electron is ejected in the forward direction indicating the electron travels with the projectile. As the ejection angle grows DI becomes dominant. Furthermore, the significance of ECC drops as the collision energy goes up. This indicates that at higher projectile energies the likelihood of charge-exchange processes decreases.

5.3 Chapter summary

The two-centre wave-packet convergent close-coupling approach was applied to calculate singly differential cross sections for electron capture, direct scattering, and ionisation in proton-hydrogen collisions at intermediate projectile energies. Convergent results obtained for the angular differential cross sections of elastic scattering, excitation, and electron capture agree well with experiment. The convergent singly differential ionisation cross sections in the ejected electron angle and in the ejected electron energy also agree well with available experiment. The present results are the first calculations of all types of angular and singly differential cross sections for $p + H$ collisions performed within a single theoretical framework. Furthermore, we conclude that the WP-CCC method is thus far the only approach capable of consistently reproducing the experimental data for the singly differential cross sections considered in this chapter.

Chapter 6

Single-centre approach to rearrangement collisions*

In this chapter we present a simpler alternative to the full two-centre WP-CCC method that is capable of determining integrated cross sections for electron capture using a single-centre expansion of the total scattering wave function. The method is applied to $p + H$ collisions and compared with the results obtained from the two-centre WP-CCC method. Having established the robustness of the present approach, we then apply the method to proton scattering on lithium atoms.

6.1 Electron-capture probabilities

We insert a single-centre expansion of the total scattering wave function (see e.g. the first set of terms in Eq. (3.7)) into the definition of the electron-capture T -matrix element given by Eq. (3.114), resulting in

$$T_{fi}^{\text{EC}}(\mathbf{q}_f, \mathbf{q}_i) = \int d\boldsymbol{\sigma}_T \sum_{\alpha=1}^{\infty} F_{\alpha}(\boldsymbol{\sigma}_T) \int d\mathbf{r}_P e^{i(\mathbf{q}_{\alpha} \cdot \boldsymbol{\sigma}_T - \mathbf{q}_f \cdot \boldsymbol{\sigma}_P)} \psi_f^{\text{P}*}(\mathbf{r}_P) \bar{V}_P \psi_{\alpha}^{\text{T}}(\mathbf{r}_T). \quad (6.1)$$

* This chapter is adapted from work published by the candidate [164]. The publishers (IOP Publishing) provide the author with the right to use the articles, or parts thereof, in a thesis or dissertation without requesting permission.

It can be shown that (see App. A for details),¹

$$\begin{aligned} \mathbf{q}_\alpha \cdot \boldsymbol{\sigma}_T - \mathbf{q}_f \cdot \boldsymbol{\sigma}_P &= p_\alpha^\parallel z + \mathbf{p}_\alpha^\perp \cdot \mathbf{b} - \mathbf{v} \cdot \mathbf{r}_P \\ &= (\varepsilon_f^P - \varepsilon_\alpha^T)t - \frac{v^2 t}{2} + \mathbf{q}_P^\perp \cdot \mathbf{b} - \mathbf{v} \cdot \mathbf{r}_P, \end{aligned} \quad (6.2)$$

where ε_f^P is the energy of the final state in the rearrangement channel. With this, and writing $F(\boldsymbol{\sigma}_T) \approx F(\mathbf{R})$, we can express Eq. (6.1) as

$$\begin{aligned} T_{fi}^{\text{EC}}(\mathbf{q}_f, \mathbf{q}_i) &= \int d\mathbf{R} \sum_{\alpha=1}^{\infty} F_\alpha(\mathbf{R}) e^{-i\frac{v^2 t}{2}} e^{i\mathbf{q}_P^\perp \cdot \mathbf{b}} \\ &\quad \times \int d\mathbf{r}_P e^{-i\mathbf{v} \cdot \mathbf{r}_P} \psi_f^{P*}(\mathbf{r}_P) \bar{V}_P \psi_\alpha^T(\mathbf{r}_T) e^{i(\varepsilon_f^P - \varepsilon_\alpha^T)t}. \end{aligned} \quad (6.3)$$

Then, using $d\mathbf{R} = v d\mathbf{b} dt$, we obtain

$$\begin{aligned} T_{fi}^{\text{EC}}(\mathbf{q}_f, \mathbf{q}_i) &= v \int d\mathbf{b} \int dt \sum_{\alpha=1}^{\infty} F_\alpha(t, \mathbf{b}) e^{-i\frac{v^2 t}{2}} e^{i\mathbf{q}_P^\perp \cdot \mathbf{b}} \\ &\quad \times \int d\mathbf{r}_P e^{-i\mathbf{v} \cdot \mathbf{r}_P} \psi_f^{P*}(\mathbf{r}_P) \bar{V}_P \psi_\alpha^T(\mathbf{r}_T) e^{i(\varepsilon_f^P - \varepsilon_\alpha^T)t}. \end{aligned} \quad (6.4)$$

We now define the electron-capture matrix element,

$$C_{f\alpha}(t, \mathbf{b}) \equiv e^{i(\varepsilon_f^P - \varepsilon_\alpha^T)t} e^{-i\frac{v^2 t}{2}} \int d\mathbf{r}_P e^{-i\mathbf{v} \cdot \mathbf{r}_P} \psi_f^{P*}(\mathbf{r}_P) \bar{V}_P \psi_\alpha^T(\mathbf{r}_T). \quad (6.5)$$

With this, Eq. (6.4) can be written as

$$\begin{aligned} T_{fi}^{\text{EC}}(\mathbf{q}_f, \mathbf{q}_i) &= v \int d\mathbf{b} \int_{-\infty}^{\infty} dt \sum_{\alpha=1}^{\infty} F_\alpha(t, \mathbf{b}) e^{i\mathbf{q}_P^\perp \cdot \mathbf{b}} C_{f\alpha}(t, \mathbf{b}) \\ &\equiv v \int d\mathbf{b} e^{i\mathbf{q}_P^\perp \cdot \mathbf{b}} A_{fi}(\mathbf{b}), \end{aligned} \quad (6.6)$$

¹Note that the final channel belongs the basis of projectile-atom pseudostates, i.e. $f = \beta'$, and $\mathbf{p}_\alpha^\perp = -\mathbf{q}_{\beta'}^\perp = \mathbf{q}_P^\perp$.

where

$$A_{fi}(\mathbf{b}) \equiv \int_{-\infty}^{\infty} dt \sum_{\alpha=1}^{\infty} F_{\alpha}(t, \mathbf{b}) C_{f\alpha}(t, \mathbf{b}). \quad (6.7)$$

Comparing Eq. (6.7) and Eq. (3.120) we see that $A_{fi}(\mathbf{b})$ is a probability amplitude for electron capture. Therefore, using a single-centre expansion of the total scattering equation, we can calculate the integrated cross section for electron capture by inserting Eq. (6.7) into Eq. (3.124). The matrix element in Eq. (6.5) is evaluated in the same way as the overlap matrix elements in Sect. 3.3. In the single-centre approach, the sum of the partial cross sections for excitation into all positive-energy target pseudostates included in the basis yields the total electron-loss cross section,

$$\sigma^{\text{TEL}} = \sum_{\alpha=N_b^{\text{T}}+1}^{N^{\text{T}}} \sigma_{\alpha i}^{\text{DS}}. \quad (6.8)$$

The total ionisation cross section can be found by subtracting the total electron-capture cross section from the total electron-loss cross section.

6.2 Hartree-Fock method for lithium structure

In this section we develop a self-consistent-field Hartree-Fock method for constructing basis states suitable for single-centre close-coupling calculations. The Hamiltonian of the lithium atom is written as

$$H_{\text{Li}} = -\frac{1}{2} \nabla_{\mathbf{r}_{\text{T}}}^2 + V_{\text{Li}}(r_{\text{T}}), \quad (6.9)$$

where \mathbf{r}_{T} is the position of the active electron relative to the target nucleus, and $V_{\text{Li}}(r_{\text{T}})$ is the interaction of the active electron with the $\text{Li}^+(1s^2)$ core. It is

written as

$$V_{\text{Li}}(r_{\text{T}}) = V_{\text{st}}(r_{\text{T}}) + V_{\text{ex}}(r_{\text{T}}), \quad (6.10)$$

where the static potential of the $\text{Li}(1s^2)$ core can be written as

$$V_{\text{st}}(r_{\text{T}}) = -\frac{3}{r_{\text{T}}} + 2 \int d\mathbf{x} \frac{|\psi_{\text{c}}(\mathbf{x})|^2}{|\mathbf{r}_{\text{T}} - \mathbf{x}|}, \quad (6.11)$$

with $\psi_{\text{c}}(\mathbf{x})$ being the state of the core which is generated by performing the self-consistent-field Hartree-Fock calculations [165]. This potential has the following properties,

$$\lim_{r_{\text{T}} \rightarrow 0} V_{\text{st}}(r_{\text{T}}) = -\frac{3}{r_{\text{T}}}, \quad (6.12)$$

and

$$\lim_{r_{\text{T}} \rightarrow \infty} V_{\text{st}}(r_{\text{T}}) = -\frac{1}{r_{\text{T}}}. \quad (6.13)$$

The limits in Eqs. (6.12) and (6.13) reflect the screening of the Li nucleus by the $1s^2$ electrons. The part of the potential representing exchange between the active electron and the core electrons, $V_{\text{ex}}(r_{\text{T}})$, is taken into account in the framework of the equivalent local-exchange approximation, i.e.

$$V_{\text{ex}}(r_{\text{T}}) = \frac{1}{2} \left(E_{\text{ex}} + V_{\text{st}}(r_{\text{T}}) - \sqrt{(E_{\text{ex}} + V_{\text{st}}(r_{\text{T}}))^2 + \rho(r_{\text{T}})} \right), \quad (6.14)$$

where,

$$\rho(r_{\text{T}}) = \int d\hat{\mathbf{r}}_{\text{T}} |\psi_{\text{c}}|^2, \quad (6.15)$$

is the electron density distribution in the core, and E_{ex} is a potential parameter [166].

The lithium target pseudostates, $\psi_\alpha(\mathbf{r}_T)$, are obtained by diagonalising the target Hamiltonian, H_{Li} , using a square-integrable orthogonal Laguerre basis of the form

$$\xi_{k\ell}(r_T) = \left(\frac{2\lambda_\ell(k-1)!}{(2\ell+1+k)!} \right) (2\lambda_\ell r_T)^{\ell+1} e^{-\lambda_\ell r_T} L_{k-1}^{2\ell+2}(2\lambda_\ell r_T), \quad (6.16)$$

where $L_{k-1}^{2\ell+2}(x)$ is the associated Laguerre polynomial and n ranges from 1 to the basis size N_ℓ for each $\ell = 0, 1, \dots, \ell_{\text{max}}$. The complete set of pseudostates contains both negative- and positive-energy states. Negative-energy states correspond to the bound states of the atomic target, while positive-energy states provide a discretisation of the continuum. The Laguerre fall-off parameter, λ_ℓ , was optimised for each target energy level to ensure alignment with experimentally verified electron binding energies. The resultant energies associated with the pseudostates are shown in Tbl. 6.1. We find that agreement with the experimentally measured values is consistently better than 99%.

Table 6.1: Comparison of calculated pseudostate energies to experimentally determined binding energies of the valence electron for lithium.

Subshell	Binding energy (eV)	Pseudostate energy (eV)	Variance (%)
2s	-5.392	-5.404	-0.23
2p	-3.544	-3.559	-0.42
3s	-2.019	-2.021	-0.14
3p	-1.557	-1.562	-0.30
3d	-1.513	-1.513	-0.01
4s	-1.051	-1.052	-0.10
4p	-0.870	-0.872	-0.23

6.3 Calculations of integrated cross sections

In this section we apply the single-centre approach to electron-capture processes described in Sect. 6.1. First, we test the approach on the well-studied $p + \text{H}$ collision system. Then, we apply it to $p + \text{Li}$ collisions.

6.3.1 Proton scattering on atomic hydrogen

The three-body $p + \text{H}$ collision system represents the simplest ion-atom scattering problem where electron capture processes are significant. This makes it ideal to serve as a testing ground for the present method. Furthermore, we can readily compare the results to those obtained using the two-centre WP-CCC method which provide a reliable foundation to test the single-centre method within the same theoretical framework.

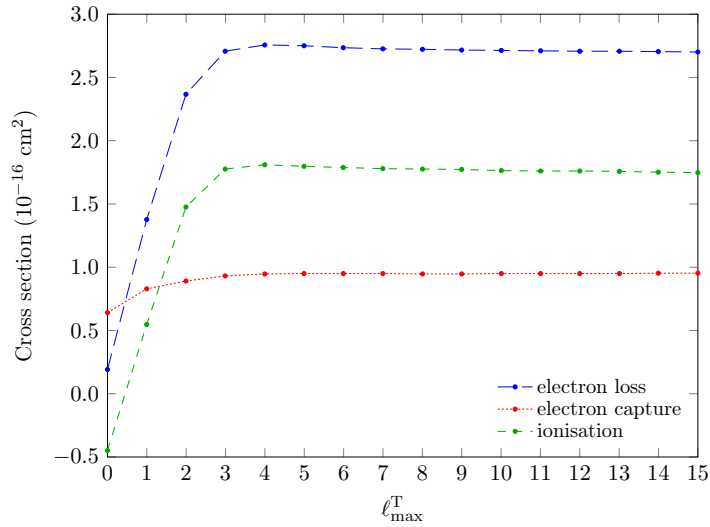


Figure 6.1: Convergence of the integrated cross sections for ionisation, total electron capture, and electron loss with respect to the maximum angular momentum quantum number of included states for 50 keV $p + \text{H}$ collisions. The results are obtained using the single-centre WP-CCC approach to rearrangement.

The number of both negative- and positive-energy target-centred pseudostates used in the expansion of the total scattering wave function has a strong influence on the final results. The fundamental idea behind the convergent close-coupling approach is to increase the basis size until the results of interest converge within a pre-determined tolerance. This ensures that the internal structure of the relevant collision species is described sufficiently accurately. In Fig. 6.1 we investigate the convergence of the of the results with respect to the maximum included angular momentum ℓ_{\max}^T at a representative incident energy of 50 keV. Using $n_{\text{neg}}^T = 10 - \ell^T$ bound target states for each included angular momentum and $n_{\text{pos}}^T = 50$ continuum bins, we systematically increase the value of ℓ_{\max}^T . Note that the

bound states include angular momenta values up to $\ell^T = 9$ due to the restriction on atomic eigenstates that $\ell^T \leq n_{\text{neg}}^T - 1$. However, for wave-packet pseudostates, ℓ^T is under no such restriction and for each bin there are pseudostates for all values of ℓ^T from 0 to ℓ_{max}^T . Altogether, the largest basis used contained 12760 basis states. The projectile-atom basis contained eigenstates with the principal quantum number up to $n_{\text{neg}}^P = 5 - \ell^P$ for each angular momentum up to $\ell_{\text{max}}^P = 4$. The contribution of partial electron-capture cross sections into states with $n^P > 5$ was found to be negligible.

The convergence of all displayed cross sections in Fig. 6.1 is remarkable. One can also see that for $\ell_{\text{max}}^T = 0$ the result for ionisation is negative which is unphysical. This is due to the fact that the total ionisation cross section in the present approach is calculated by subtracting the total electron-capture cross section from the total electron-loss cross section. Therefore, the TICS should be calculated only when a sufficient number of angular momentum states are included and a desirable convergence in the total electron-capture and electron-loss cross sections is achieved.

Table 6.2: Convergence with respect to the number of continuum bins of the integrated cross sections for electron-loss processes in 50 keV p + H collisions using the single-centre WP-CCC approach to rearrangement. Cross sections are presented in units of 10^{-16} cm².

n_{pos}^T	electron loss	electron capture	ionisation
10	2.63	1.27	1.36
20	2.69	1.26	1.43
30	2.70	1.17	1.53
40	2.70	1.00	1.70
48	2.71	0.966	1.74
49	2.71	0.951	1.76
50	2.71	0.951	1.76

Next we demonstrate that the number of bin states representing the continuum, n_{pos}^T , is sufficiently large to ensure convergence of the total electron-loss, electron-capture and ionisation cross sections at $\ell_{\text{max}}^T = 15$ and $n_{\text{neg}}^T = 10 - \ell^T$. Tbl. 6.2 displays a typical example of n_{pos}^T -convergence at a projectile energy of

50 keV. One can see from the table, all the considered cross sections converge well as the number of continuum discretisation bins increases.

Having demonstrated the capability of the presently developed approach to yield convergent results not only for the processes associated with the target, but also for electron capture by the projectile, next we compare one-centre results for all these processes with the corresponding results obtained with the symmetric two-centre WP-CCC approach [99] which explicitly includes identical expansion bases on the target and projectile centres. The two-centre WP-CCC calculations were performed with a total number of 3350 states (1675 on each centre), where for each angular momentum $\ell \in [0, 5]$, $n_{\text{neg}} = 10 - \ell$ bound states and $n_{\text{pos}} = 40$ continuum wave-packet pseudostates were used. For the purpose of illustration we compare the total cross sections for electron capture, electron loss and ionisation, as well as several state-resolved cross sections, obtained using the one-centre (1c) and two-centre (2c) approaches.

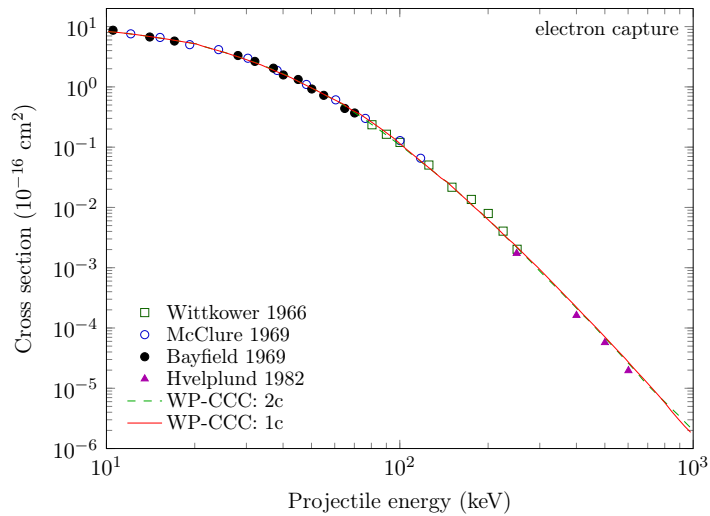


Figure 6.2: Total electron-capture cross section for $p + H$ collisions. Experimental results are by Wittkower *et al.* [167], McClure [168], Bayfield [169], and Hvelplund and Andersen [170]. The theoretical results are: two-centre WP-CCC approach and single-centre WP-CCC approach to rearrangement.

In Fig. 6.2 we show the energy dependence of the total electron-capture cross section. The one-centre WP-CCC results are compared with the experimental data by McClure [168], Bayfield [169], Wittkower *et al.* [167], and the results of the two-centre WP-CCC approach. One can see the present results are in

perfect agreement with the calculations of the more sophisticated approach and the experimental measurements across all considered impact energies.

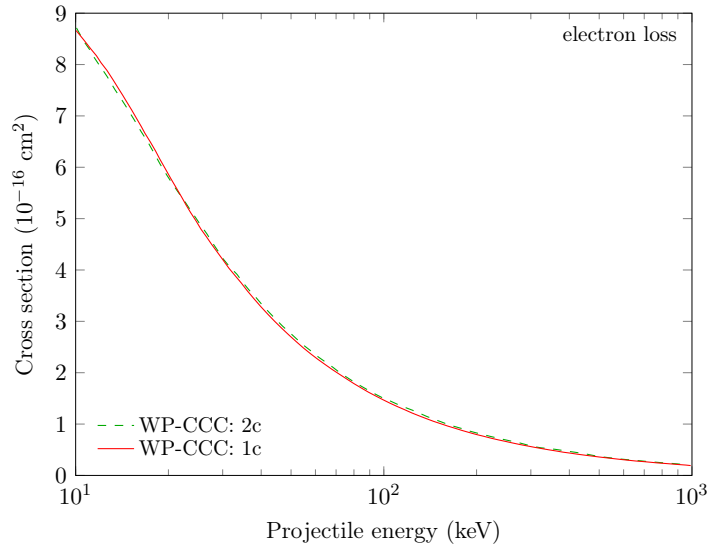


Figure 6.3: Total electron-loss cross section for $p + H$ collisions. The theoretical results are: two-centre WP-CCC approach and single-centre WP-CCC approach to rearrangement.

Figure 6.3 shows the energy dependence of the total electron-loss cross section. In the one-centre WP-CCC approach this cross section is obtained directly by using the time-dependent coefficients representing the excitation of the target electron into the continuum. Unlike the situation with electron-capture cross sections, to obtain the total electron-loss cross section no additional calculations are required after the scattering equations are solved. Here again we can see perfect agreement between the two approaches within the whole energy range considered.

Figure 6.4 compares the total ionisation cross section obtained from the two WP-CCC approaches with the experimental measurements of Shah and Gilbody [171], Shah *et al.* [172], and Kerby III *et al.* [160]. In both calculations this is the most sensitive quantity with respect to the underlying expansion basis and determines the overall accuracy. In the one-centre approach we find the lowest energy region to be the most difficult to deal with. This is because at these energies the total electron-loss and electron-capture cross sections are comparable and an order of magnitude larger than the ionisation cross section, defined as the dif-

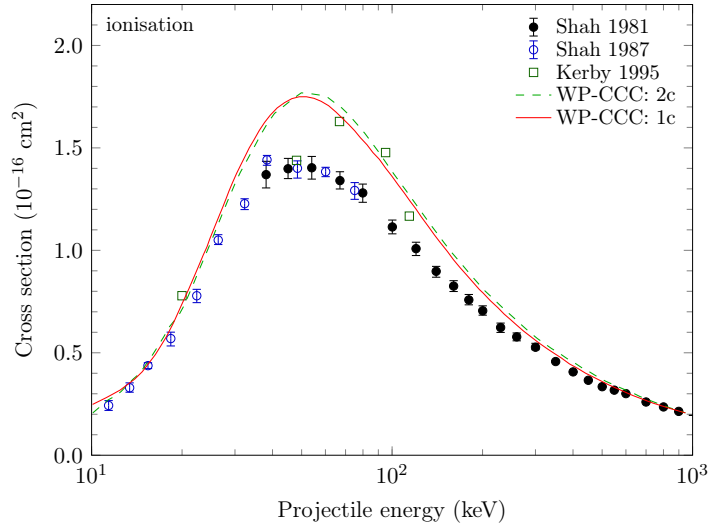


Figure 6.4: Total ionisation cross section for $p + H$ collisions. Experimental results are by Shah and Gilbody [171], Shah *et al.* [172], and Kerby III *et al.* [160]. The theoretical results are: two-centre WP-CCC approach and single-centre WP-CCC approach to rearrangement.

ference between the two. Nevertheless, excellent agreement between the present one-centre and two-centre results has been obtained. There is some disagreement between theory and experiment, and between experiments, at intermediate collision energies. It has been discussed elsewhere, see, e.g. Refs. [173–176]. The strength of the CCC formalism is that once convergence is reached, it should be to the correct result.

Next, to demonstrate the capability of the one-centre method to produce reliable results also for the state-resolved integrated cross sections, we present in Fig. 6.5 the $2s$ and $2p$ (summed over magnetic quantum number m) excitation and electron-capture cross sections for $p + H(1s)$ collisions as a function of the impact energy. For all displayed excitation and electron-capture transitions excellent agreement between the one and two-centre WP-CCC approaches has been obtained over the entire considered energy range.

The elastic scattering, excitation and electron-capture cross sections summed over ℓ and m for the states with the principal quantum number $n = 1$ to $n = 3$ are shown in Fig. 6.6. Here again we can see excellent agreement between one- and two-centre results for all considered cross sections. The experimental data by Park *et al.* [177] for $n = 2$ and $n = 3$ excitation cross sections lie higher than

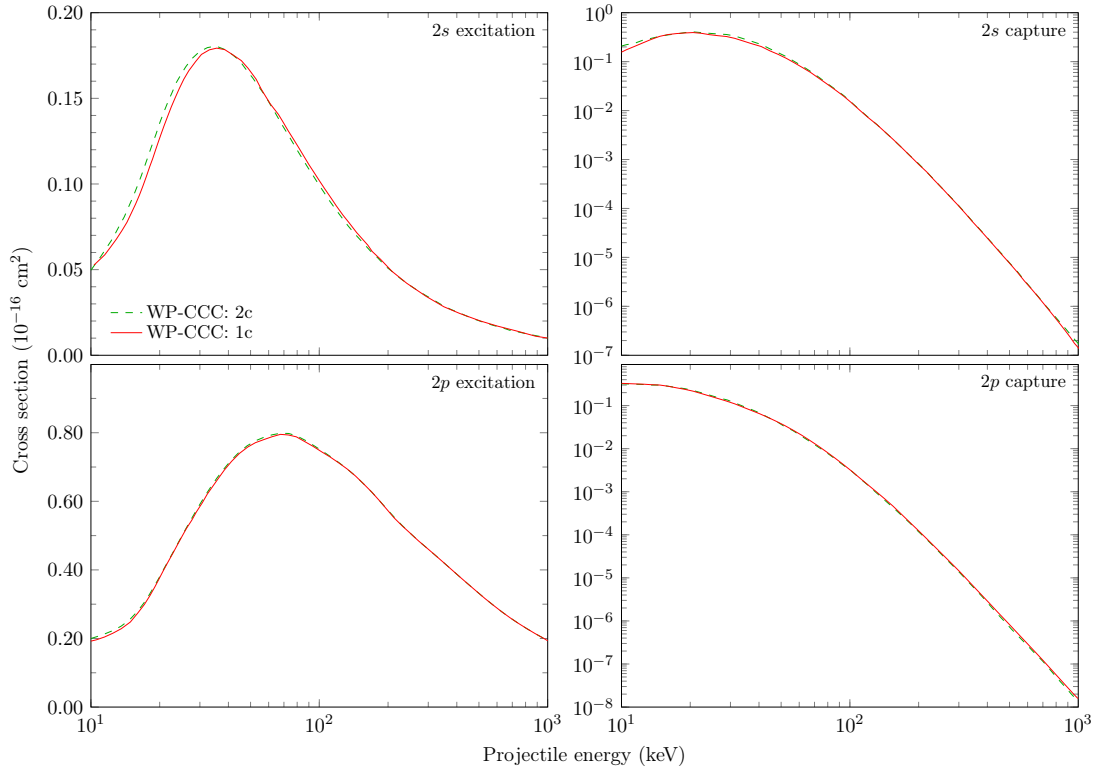


Figure 6.5: Partial 2ℓ and 3ℓ cross sections for excitation and electron capture in $p + \text{H}$ collisions. The theoretical results are: two-centre WP-CCC approach and single-centre WP-CCC approach to rearrangement. The key in the upper-left panel applies to all panels.

our results within the energy region of 50–100 keV, where the cross section peaks. This disagreement was discussed in detail in Ref. [145] but is not the subject of the present work. Here we are interested in agreement between the results of the two different one-centre and two-centre WP-CCC approaches. Their difference is significantly smaller than the relevant experimental error bars. Therefore, for practical applications both approaches can be applied. In terms of computer resources required, the proposed one-centre technique has a significant advantage in calculation time. To be specific, e.g. at 10 keV incident energy, the single-centre calculations are about 30 times faster than the two-centre ones.

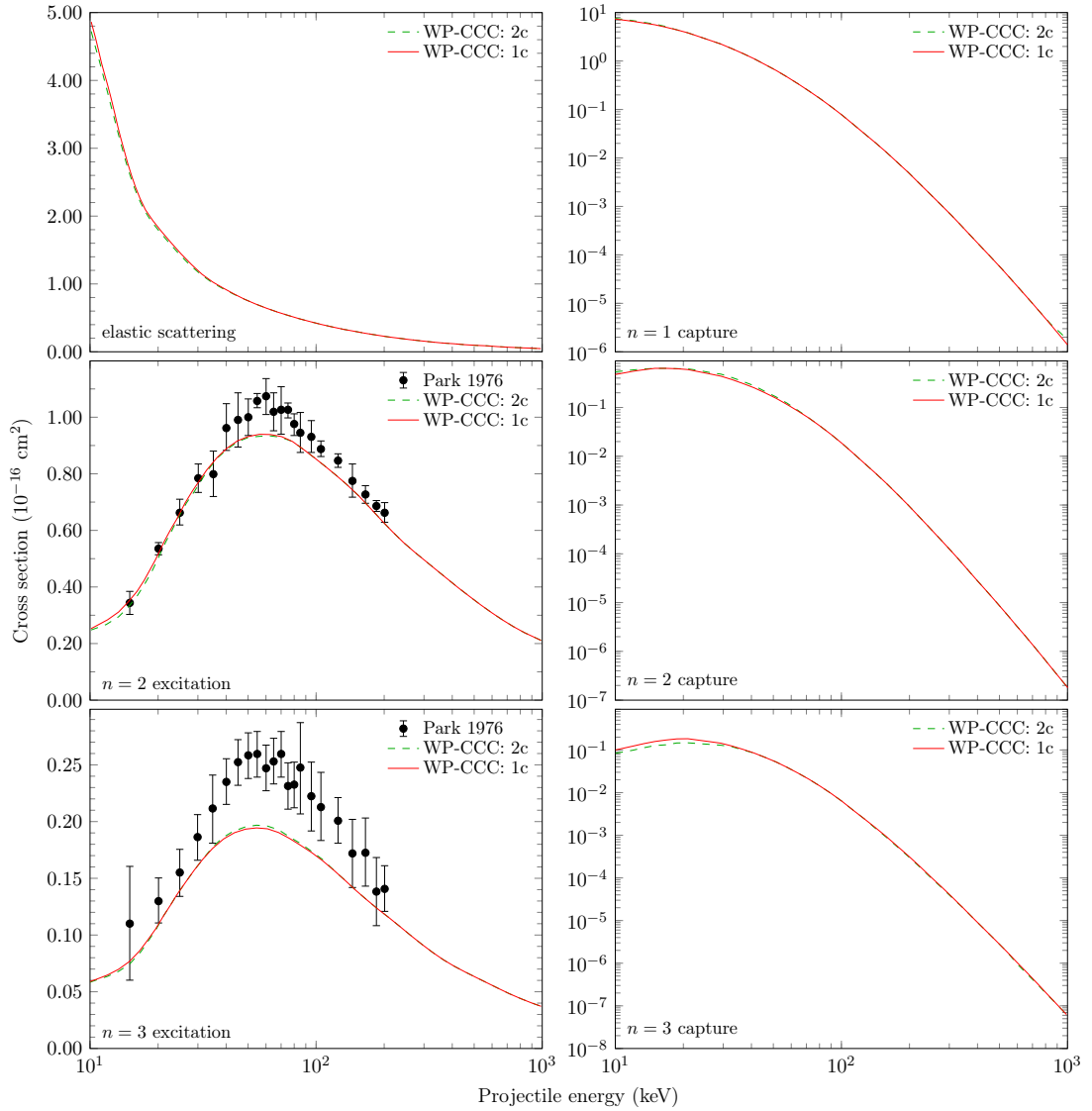


Figure 6.6: Partial n -resolved cross sections for elastic scattering, excitation, and electron capture in $p + H$ collisions. Experimental results are by Park *et al.* [177]. The theoretical results are: two-centre WP-CCC approach and single-centre WP-CCC approach to rearrangement.

6.3.2 Proton scattering on lithium

For proton scattering on lithium, we expand the total scattering wave function in terms of pseudostates obtained by diagonalising the target-atom Hamiltonian, according to the procedure described in Sect. 6.2. The interaction of the incident proton with the lithium target, which enters the scattering equations, is written

as

$$\bar{V}_T(R, r) = -V_{\text{st}}(R) - \frac{1}{r_P}. \quad (6.17)$$

When the target is Li(2s), the interaction of the residual target nucleus with the atom formed by the projectile after electron capture, required for calculating the electron-capture amplitude, reads as

$$\bar{V}_P(R, r) = -V_{\text{st}}(R) + V_{\text{st}}(r_T) + V_{\text{ex}}(r_T). \quad (6.18)$$

With this, the single-centre scattering equations are solved as for the hydrogen target.

Here, convergence in ℓ_{max}^T was established by selecting a maximum principle quantum number $n_{\text{max}}^T = 30$ prior to solving the coupled-equations for values of increasing ℓ_{max}^T . The maximum magnetic quantum numbers, m_{max}^T , for each case was kept equal to ℓ_{max}^T (i.e. the full set of the magnetic quantum numbers is used for each included orbital angular-momentum quantum number). While fixing the fall-off parameter of the Laguerre functions at $\lambda_\ell = 1$, the value for ℓ_{max}^T was incrementally increased until the variance between subsequent runs for a particular projectile energy was below 3%. The cross sections for the projectile energies near 1 keV were found to converge the slowest (especially the total electron-capture cross section) with the results becoming stable only when ℓ_{max}^T reached 10. Increasing ℓ_{max}^T to 11 yielded results which deviated by less than 3% from the $\ell_{\text{max}}^T = 10$ case. As such, the selection of $\ell_{\text{max}}^T = m_{\text{max}}^T = 10$ was deemed acceptable.

In Fig. 6.7 we show the energy dependence of the total electron-capture cross section in p + Li(2s) collisions. The present CCC results are compared with the experimental data from Refs. [178–185] and recent calculations by Mančev *et al.* [187]. In the present approach the cross section is calculated using the amplitude given in Eq. (6.7). One can see that the results are in excellent agreement with

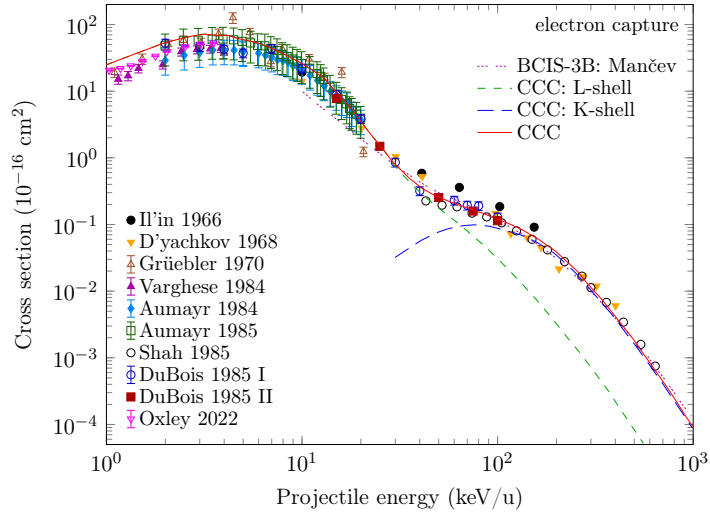


Figure 6.7: Total electron-capture cross section for $p + \text{Li}$ collisions. Experimental results are by D'yachkov [178], Il'in *et al.* [179], Gruebler *et al.* [180], Varghese *et al.* [181], Aumayr *et al.* [182], Aumayr *et al.* [183], Shah *et al.* [184], DuBois and Toburen [185] (I), and DuBois [186] (II). The theoretical results are: present single-centre CCC approach to rearrangement for L-, K-, and both L- and K-shell Li and BCIS-3B method by Mančev *et al.* [187].

the experimental measurements across all considered impact energies. At energies above 30 keV, the measurements of electron-capture cross sections display a shoulder. This feature cannot be reproduced by considering only capture of the valence $2s$ electron. Energetic protons can penetrate the target deeper and there is a possibility of capturing one of the inner, K-shell electrons. Therefore, this channel should be taken into account. We model capture of the K-shell electron by considering proton scattering from the helium-like $\text{Li}^+(1s^2)$ ion with the nuclear charge of 3. This model neglects the influence of the outer electron. It is expected, however, that the loosely-bound L-shell electron cannot significantly influence the state of the tightly-bound K-shell electrons. The problem of $p + \text{Li}^+(1s^2)$ scattering is also solved using the procedures given in Sect. 6.1. The two-electron pseudostates describing the helium-like $\text{Li}^+(1s^2)$ ion are constructed using the configuration-interaction approach in the frozen-core approximation developed in Refs. [33, 188].

The CCC results represent a combination of the cross sections for capture of the L-shell and K-shell electrons. One can see that the treatment described above indeed leads to good agreement with experiment. The contribution of electron

capture from the K-shell is an order of magnitude larger than that from the L-shell at the incident energies above 100 keV. In contrast, at energies below 30 keV capture of the L-shell electron is the dominant process. The three-body Faddeev equation approach of Avakov *et al.* [86] also took into account electron capture from the K- and L-shells of the Li(2s) target. However, in their case overall agreement with experiment was less satisfactory.

Also shown are the results of calculations based on the BCIS-3B method of Mančev *et al.* [187]. The BCIS-3B method is a hybrid formalism, which is the combination of the continuum distorted-wave method in the exit channel and the boundary-corrected first Born method in the entrance channel. The initial ground state of the active electron in the three-electron Li target is described by the Roothaan-Hartree-Fock wave function. Using this method, Mančev *et al.* [187] separately calculated the cross sections for single electron capture from the K-shell and L-shell of the Li(2s) target. The sum of their K- and L-shell electron-capture cross sections are shown in Fig. 6.7. As one can see BCIS-3B results are in good agreement with the experimental data and the present CCC calculations above about 30 keV collision energy. However, at lower energies the BCIS-3B cross sections tend to underestimate the data due to the perturbative nature of the approach.

In Fig. 6.8 we present the energy dependence of the total electron-loss cross section. One can see that above 10 keV the present CCC results are in agreement with the AOCC calculations of Lühr and Saenz [69] and above 100 keV also with the CDW-EIS calculations of McCartney and Crothers [190]. However, below 100 keV the CDW-EIS results start underestimating the total electron-loss cross section since this perturbative model is not applicable at low collision energies. The AOCC calculations of Schweinzer *et al.* [189] are systematically lower than the other calculations above 10 keV. This most likely indicates the lack of convergence in these results. At energies below 10 keV the present results are larger than the AOCC calculations of Schweinzer *et al.* [189] where $\ell_{\max} = 4$

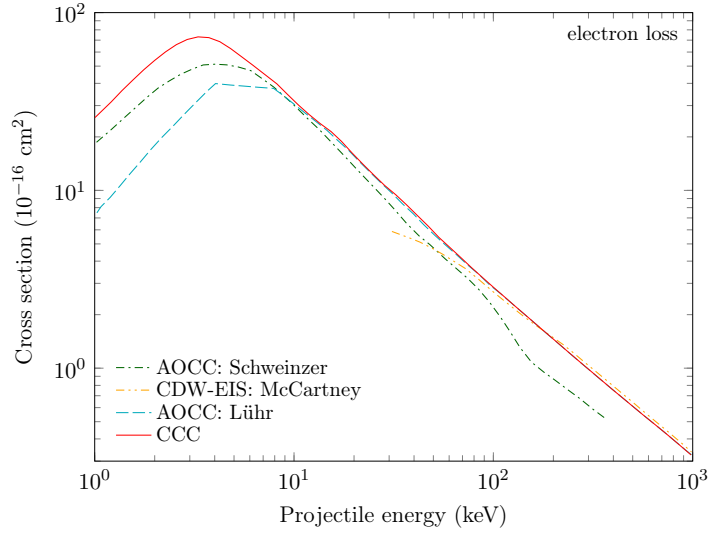


Figure 6.8: Total electron-loss cross section for $p + \text{Li}$ collisions. The theoretical results are: present single-centre CCC approach, AOCC method by Schweinzer *et al.* [189], CDW-EIS method by McCartney and Crothers [190], and AOCC method by Lühr and Saenz [69].

was used and the AOCC calculations of Lühr and Saenz [69] where $\ell_{\max} = 8$ was used. This discrepancy is due to the smaller number of the pseudostates used in the previous close-coupling calculations. At the same time, adequate effective representation of the electron-capture channel demands significantly larger single-centre expansion than those used in the aforementioned approaches. Note that in this low-energy region the electron-loss cross section essentially corresponds to electron capture.

Fig. 6.9 presents the integrated cross section for excitation of the $2p$ subshell states of the Li target. The CCC results are compared with the experimental measurements of Aumayr *et al.* [191] and the theoretical calculations of Lühr and Saenz [69], Pindzola [192], Stary *et al.* [193], Brandenburg *et al.* [194], and Lee and Pindzola [195]. One can see that the present results agree well with the AOCC calculations of Lühr and Saenz [69] in the entire energy range considered. At high energies the results of Stary *et al.* [193] obtained within the framework of the optical potential model significantly deviate from the former two. There is also reasonably good agreement between the present results and the AOCC calculations of Brandenburg *et al.* [194] below 10 keV. However, there is signifi-

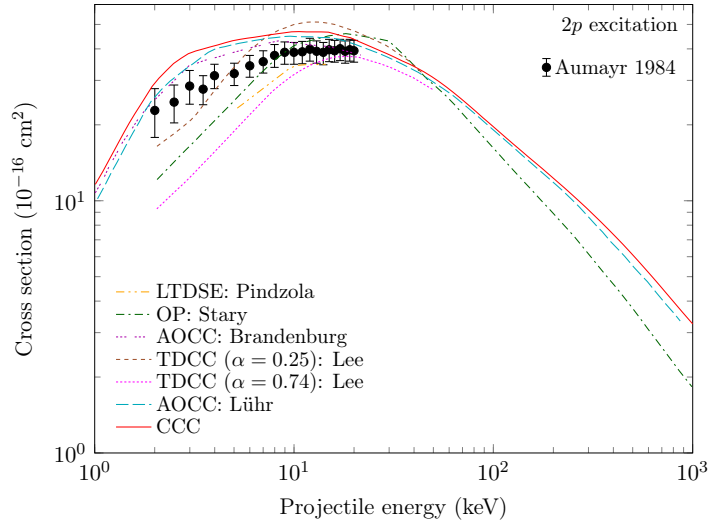


Figure 6.9: $2p$ -excitation cross section for $p + \text{Li}$ collisions. Experimental results are by Aumayr *et al.* [191]. The theoretical results are: present single-centre CCC approach, LTDSE method by Pindzola [192], OP method by Stary *et al.* [193], AOCC method by Brandenburg *et al.* [194], TDCC method by Lee and Pindzola [195], and AOCC method by Lühr and Saenz [69].

cant deviation between the results of the other presented methods. Whereas the present results and the results of two other close-coupling approaches go through the upper edge of the experimental error bars, some of the other calculations are significantly lower than the experiment.

Finally, one has to emphasise that the experimental data for the $2s \rightarrow 2p$ excitation cross section from Ref. [191] shown in Fig. 6.9 were extracted from the data for the $\text{Li } 2p \rightarrow 2s$ emission cross section using cascade contributions estimated from the $\text{Li } 2s \rightarrow 3\ell$ excitation cross sections calculated by Ermolaev [196]. However, since these calculations were performed with a very small basis size (the basis only included $n \leq 3$ states of negative energy on both centres) and did not include any pseudostates to represent the continuum, the accuracy of the resulting $2s \rightarrow 3\ell$ excitation cross sections reported in Ref. [196] is questionable. Thus, possible uncertainties from the calculations of Ermolaev [196] may be imprinted in the experimental data for $2s \rightarrow 2p$ excitation.

6.4 Chapter summary

In this chapter we presented a novel technique for extracting integrated electron-capture cross sections from close-coupling calculations performed using a single-centred expansion of the total scattering wave function. Starting from the general post-form of the T -matrix we inserted a basis of projectile-atom pseudostates for the final-channel and the single-centre expansion in terms of target pseudostates for the initial channel. From this we found that the probability amplitudes for electron capture are given by the time integral of the product of the single-centre expansion coefficients and electron-capture matrix elements. The method was benchmarked against highly accurate two-centre close-coupling calculations for $p + H$ collisions. Remarkable agreement between the single- and two-centred approaches was found for the integrated cross sections for target-excitation, charge-exchange, and ionisation processes. It was found that a much larger basis was required to obtain convergence in the results using the single-centre approach. However, due to the complexity of the two-centre method, the single-centre approach demonstrated a significant reduction in computational time.

Having tested the utility of the method on proton collisions with the one-electron target (hydrogen), we applied the method to study proton scattering on the multielectron $\text{Li}(2s)$ target. The obtained results for the $2s \rightarrow 2p$ excitation and total electron-capture cross sections are in good agreement with corresponding experimental data. At higher collision energies the incident protons can penetrate the target deeper and capture one of the K-shell electrons as well. To calculate the cross section for K-shell electron capture we considered proton scattering from the helium-like $\text{Li}^+(1s^2)$ ion with the nuclear charge of 3, assuming that the loosely bound L-shell electron cannot significantly influence the state of the tightly bound K-shell electrons. Good agreement between the obtained results and experiment shows this assumption to be plausible.

Chapter 7

Proton scattering on alkali metals*

In ion-atom collisions involving multielectron targets the role of inner-shell electrons becomes important with increasing collision energy. Faster projectiles can penetrate further into the target core, interacting with inner-shell electrons. However, only collisions with one- or two-electron targets can be treated without significant approximations. Usually, the contributions of the outer and inner-shell electrons are taken into account using the IEM, where processes involving the outer-shell and inner-shell electrons are separated and treated independently. However, the IEM becomes impractical when the number of shells is more than two.

In this chapter we develop an *ab initio* effective one-electron approach to multielectron atoms that treats all of the electrons on an equal footing. We consider targets with a single valence electron, i.e. alkali metal atoms. These atomic targets contain a single valence electron well isolated from the inner electronic shells. This fact suggests that it may be reasonable to consider the target atom with one active electron in the field of the frozen core. Several previous theoretical approaches used this approximation but they were only able to account for processes involving the valence electron. In Ch. 6 we applied the single-centre

* This chapter is adapted from work published by the candidate [197]. The publishers (the American Physical Society) provide the author with the right to use the articles, or parts thereof, in a thesis or dissertation without requesting permission.

WP-CCC approach to rearrangement collisions to model $p + \text{Li}$ scattering. The target structure was based on the frozen-core approximation, meaning that the projectile can capture only the valence electron. This separation appeared to work well in this case, but may not work for other targets where the ionic core is not well separated and the frozen-core approximation is not applicable. Here we develop a new method that accounts for the multi-core structure of the target.

7.1 Structure of multielectron atoms

Consider an atom with N_e electrons and assume that the nucleus is sufficiently light that a non-relativistic description of the electronic wave function is suitable. The goal is to construct a wave function that represents any one of the electrons subject to the average field of the nucleus and all other electrons. We will call this the active electron and denote its position as \mathbf{r} and spin as s . The position and spin coordinates of the ensemble of all other electrons are \mathbf{r}' and s' , respectively. It is important to note that we do not single-out any particular electron, rather any of the target electrons may be equivalently interchanged with the active electron.

The Schrödinger equation for the atom is

$$H_T \psi_T(\mathbf{r}, \mathbf{r}', s, s') = \varepsilon_T \psi_T(\mathbf{r}, \mathbf{r}', s, s'), \quad (7.1)$$

where H_T is the Hamiltonian of the atom and ε_T is the energy of the ground state multielectron wave function, ψ_T . The Hamiltonian is given by

$$H_T = -\frac{1}{2} \nabla_{\mathbf{r}}^2 - \frac{1}{2} \nabla_{\mathbf{r}'}^2 - \sum_{i=1}^{N_e} \frac{Z_T}{r_i} + \sum_{i=1}^{N_e} \sum_{j=1}^{N_e} \frac{(1 - \delta_{ij})}{|\mathbf{r}_i - \mathbf{r}_j|}, \quad (7.2)$$

where $-\nabla_{\mathbf{r}}^2/2$ is the kinetic-energy operator of the active electron and $-\nabla_{\mathbf{r}'}^2/2$ is the sum of kinetic energy operators for the $N_e - 1$ remaining electrons. The

multielectron wave function is normalised according to

$$\sum_{ss'} \int d\mathbf{r} \int d\mathbf{r}' \psi_{\text{T}}^*(\mathbf{r}, \mathbf{r}', s, s') \psi_{\text{T}}(\mathbf{r}, \mathbf{r}', s, s') = 1, \quad (7.3)$$

and possesses the necessary antisymmetrisation requirements. In order to construct a one-electron wave function that effectively describes any one of the N_e target electrons we make use of the single-electron density function,

$$\rho(\mathbf{r}) \equiv N_e \sum_{ss'} \int d\mathbf{r}' \psi_{\text{T}}^*(\mathbf{r}, \mathbf{r}', s, s') \psi_{\text{T}}(\mathbf{r}, \mathbf{r}', s, s'). \quad (7.4)$$

This represents the probability of finding an electron at position \mathbf{r} and, therefore, contains information about the overall distribution of the remaining electrons. From Eq. (7.4) we can obtain a radial density by averaging over the angular coordinate of the active electron,

$$\rho(r) \equiv \frac{1}{4\pi} N_e \sum_{ss'} \int d\hat{\mathbf{r}} \int d\mathbf{r}' \psi_{\text{T}}^*(\mathbf{r}, \mathbf{r}', s, s') \psi_{\text{T}}(\mathbf{r}, \mathbf{r}', s, s'). \quad (7.5)$$

If we integrate Eq. (7.5) over \mathbf{r} we find that the angular part simply evaluates to 4π and therefore we are left with

$$\int d\mathbf{r} \rho(r) = N_e. \quad (7.6)$$

Taking the square root of the radial density in Eq. (7.5) we can construct a spherically symmetric pseudo-ground-state wave function for the active electron. We define this wave function in a normalised form as

$$\psi_0^{\text{E1E}}(\mathbf{r}) = \sqrt{\frac{\rho(r)}{N_e}} \quad (7.7)$$

Recognising that $Y_{00}(\hat{\mathbf{r}}) = 1/\sqrt{4\pi}$ we define the following effective one-electron

(E1E) ground-state radial wave function,

$$\mathcal{R}_0^{\text{E1E}}(r) = \sqrt{\sum_{ss'} \int d\hat{\mathbf{r}} \int d\mathbf{r}' \psi_{\text{T}}^*(\mathbf{r}, \mathbf{r}', s, s') \psi_{\text{T}}(\mathbf{r}, \mathbf{r}', s, s')}. \quad (7.8)$$

The pseudostate, $\psi_0^{\text{E1E}}(\mathbf{r}) = \mathcal{R}_0^{\text{E1E}}(r)Y_{00}(\hat{\mathbf{r}})$, equivalently represents any one of the target electrons in the ground-state configuration of the multielectron atom. To construct a set of orthogonal pseudostates for scattering calculations we first calculate the effective potential, $U(r)$, experienced by this ground-state wave function, assuming that it satisfies the effective one-electron Schrödinger equation,

$$\left(-\frac{1}{2}\nabla_{\mathbf{r}}^2 + U(r)\right)\psi_0^{\text{E1E}}(\mathbf{r}) = \varepsilon_0^{\text{E1E}}\psi_0^{\text{E1E}}(\mathbf{r}), \quad (7.9)$$

where $\varepsilon_0^{\text{E1E}}$ is the energy of the ground state. We call the potential appearing in Eq. (7.9) a *pseudopotential*. Separating the radial and angular parts results in the following equation for the radial part of the effective one-electron wave function,

$$\left(-\frac{1}{2}\frac{d^2}{dr^2} - \frac{1}{r}\frac{d}{dr} + U(r)\right)\mathcal{R}_0^{\text{E1E}}(r) = \varepsilon_0^{\text{E1E}}\mathcal{R}_0^{\text{E1E}}(r), \quad (7.10)$$

which can be solved for the pseudopotential, yielding

$$U(r) = \varepsilon_0^{\text{E1E}} + \frac{1}{\mathcal{R}_0^{\text{E1E}}(r)}\left(\frac{1}{2}\frac{d^2}{dr^2} + \frac{1}{r}\frac{d}{dr}\right)\mathcal{R}_0^{\text{E1E}}(r). \quad (7.11)$$

Equation (7.11) is solved numerically subject to the conditions,

$$\begin{cases} \lim_{r \rightarrow 0} U(r) = -\frac{Z_{\text{T}}}{r}, \\ \lim_{r \rightarrow \infty} U(r) = -\frac{1}{r}. \end{cases} \quad (7.12)$$

Once the pseudopotential is calculated it can be used to construct wave functions for excited and continuum states using the reduced radial single-electron

Schrödinger equation for arbitrary angular quantum number ℓ ,

$$\left(-\frac{1}{2} \frac{d^2}{dr^2} - \frac{1}{r} \frac{d}{dr} + \frac{\ell(\ell+1)}{2r^2} + U(r)\right) \mathcal{R}_\alpha(r) = \varepsilon_\alpha \mathcal{R}_\alpha(r). \quad (7.13)$$

Here index α corresponds to the set of quantum numbers specifying the single-electron atomic state. Equation (7.13) is solved using a Numerov method. If the energy, ε_α , is negative then solutions only exist for discrete energies with $\alpha = \{n\ell\}$, corresponding to bound states. The resulting states form a set of negative-energy pseudostates approximately representing the target space, including the ground state. The latter, of course, coincides with $\mathcal{R}_0^{\text{E1E}}(r)$ and is accurate by construction. For positive energies, there exists a continuum solution with $\alpha = \{\kappa\ell\}$, where $\kappa = \sqrt{2\varepsilon_\alpha}$. The latter can be used to construct wave-packet pseudostates according to the method outlined in Sect. 3.2.

The question remains, how to construct the multielectron wave function required for this approach? Many methods have been developed for this purpose such as Hartree-Fock (HF), multiconfigurational self-consistent field (MCSCF), and time-dependent density-functional theory (TDDFT). We use the multiconfigurational HF method in which the radial probability density function is given by

$$\rho(r) = \frac{1}{4\pi} \sum_{n\ell} w_{n\ell} |\mathcal{R}_{n\ell}^{\text{HF}}(r)|, \quad (7.14)$$

where $w_{n\ell}$ is the number of electrons in the $n\ell$ orbital and $\mathcal{R}_{n\ell}^{\text{HF}}$ is the radial electron wave function obtained from the HF equations for the orbital with quantum numbers n and ℓ . We note that the standard HF approach does not account for electron-electron correlations. However, for alkali atoms the correlation energy is small.

In Fig. 7.1 we present the radial dependence of the pseudopotential $U(r)$ multiplied by r for the Li, Na, and K atoms. Here $U(r)$ is the potential which is felt by any one of the electrons in the field produced by the nucleus and the

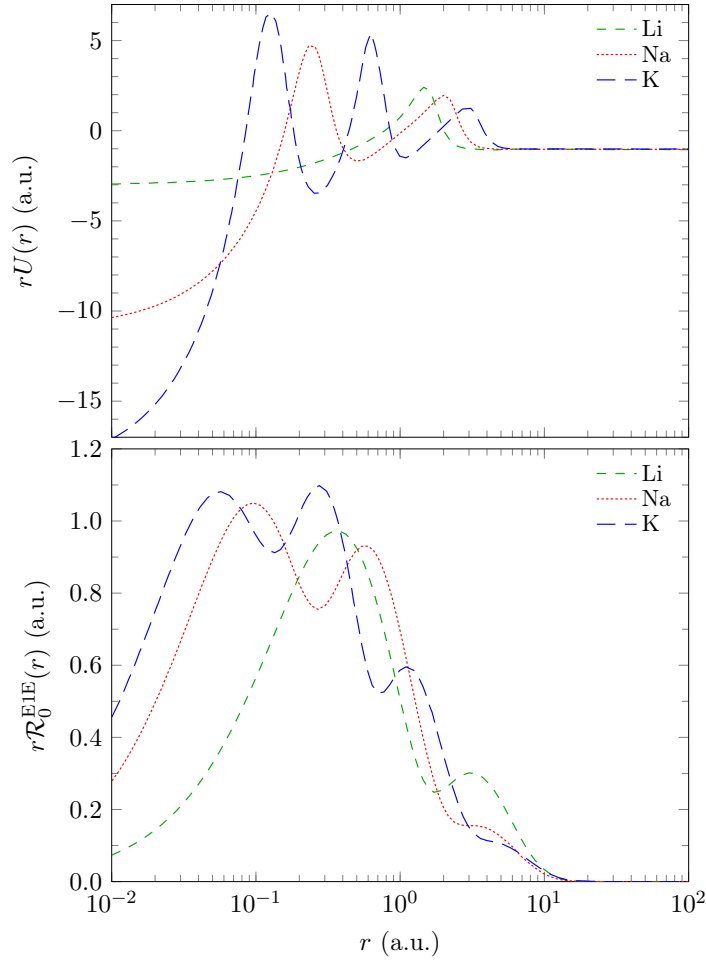


Figure 7.1: The pseudopotential $U(r)$ (upper panel) and effective one-electron ground-state radial wave function (lower panel) weighted by r for Li, Na, and K.

remaining electrons of the atom. We infer from the figure that for all three atoms the pseudopotential tends to the expected functional form of $-Z_T/r$ near the origin and has the asymptotic $-1/r$ tail at large distances. Generally, the pseudopotential is attractive except in the intermediate region where one can see an oscillatory behaviour. This is consistent with the electronic structure of the considered atoms. In particular, for the Li atom with the $1s^2 2s^1$ electronic configuration there is a region around 1.42 a.u. where the pseudopotential becomes repulsive. This is due to the occupied $n = 1$ shell. The states in this shell are on average either unavailable or unlikely to be available for the active electron. Similarly, for the Na atom with the $1s^2 2s^2 2p^6 3s^1$ electronic configuration there are two regions, one around 0.23 a.u. and the other around 1.94 a.u., where the potential is positive. The first peak is due to the complete $n = 1$ shell and the

second is due to the $n = 2$ shell. For the K atom with the $1s^2 2s^2 2p^6 3s^2 3p^6 4s^1$ electronic configuration there are three regions (located around 0.12, 0.62, and 2.83 a.u.) where the pseudopotential turns repulsive, corresponding to the complete $n = 1$, $n = 2$, and $n = 3$ shells, respectively. It is noteworthy to mention that no such oscillatory features in the intermediate region are observed in the model effective potential proposed by Klapisch [198] and employed in proton-alkali atom scattering calculations by Lühr and Saenz [199]. The Klapisch potential based on multiple tuning parameters accurately reproduces the $-Z_T/r$ behaviour near the origin and the asymptotic $-1/r$ tail. However, it goes from one functional behaviour to the other smoothly and monotonically. Our pseudopotentials appear to better reflect the physical situation that the active electron should experience. The presently calculated ionisation potentials of the ground-state Li, Na, and K atoms are 5.34, 4.96, and 4.21 eV, respectively. They compare favourably to the corresponding experimentally measured values of 5.39, 5.14, and 4.34 eV, respectively [200]. This level of agreement with experiment is consistent with the underlying Hartree-Fock approach used in the current model.

The above method reduces the description of the multielectron atom to the effectively two-body system consisting of a core ion and one active electron. The mutual interaction of electrons, the electron-exchange effects and the interaction of multiple electrons with the atomic nucleus are all represented by one pseudopotential for the active electron and the core ion. With this description of the target, the collision system reduces to an effectively three-body scattering problem. Therefore, we can apply the WP-CCC approach to ion collisions with one electron targets from Ch. 3 with necessary modifications which involve introducing pseudopotentials representing interactions of the target core ion with the active electron and the incident proton.

It is worthwhile to emphasise the distinguishing features of the present model from the approaches which are based on the IEM. The ground-state wave function, $\psi_0^{\text{E1E}}(r)$, is obtained from the probability density function, which contains

all necessary information about the electrons in every subshell of the target. Additionally, all other target pseudostates used in expansion of the total scattering wave function also contain this information since they are obtained using the same pseudopotential constructed to describe the ground state of the multielectron target. For this very reason, the present approach is capable of describing the fate of any one of the target electrons on an equal footing. In contrast, the models which are based on the IEM treat the target atom as if it has a frozen core and one electron (which is in the outermost shell of the atom), where the interaction potential between them represents the collective field of all electrons in the frozen core. Therefore, the pseudostates representing the active electron in those models by construction describe only the fate of the electron in the outermost shell of the target.

Within this representation, we effectively split the N_e -electron problem into N_e equivalent single-electron ones. Therefore, the resulting probabilities found from solving Eq. (3.39) are multiplied by a factor of N_e to account for any of the electrons occupying a given final channel.

7.2 Proton collisions with Li, Na, and K atoms

In this section we apply the developed method to calculate the total electron capture and the total ionisation cross sections in proton collisions with Li, Na, and K atoms. A large amount of experimental data [178–186, 201–208] for proton scattering on these targets has been collected for integrated electron-capture and excitation cross sections. These measurements for single electron capture and single electron ionisation only detect an electron without specific information whether it originated from the outermost or inner shells of the target. Therefore, these systems provide an ideal testing ground for the present approach which also does not distinguish which electron is ionised.

7.2.1 Overview of previous works

There have also been a number of theoretical investigations of proton collisions with alkali atoms. Some of the earliest calculations were performed by Stary *et al.* [193] using an optical-potential approach. The CDW-EIS method was used by McCartney and Crothers [190] to calculate the TICS in proton collisions with lithium. Dubois *et al.* [209] used the AOCC approach to investigate differential cross sections, alignment, and orientation effects for electron capture in $p + \text{Na}$ collisions. More recently Lühr and Saenz [199] investigated single-electron loss by alkali atom targets for a wide range of proton projectile energies ranging from 0.25 to 1000 keV. In their method they construct one-electron pseudostates for the valence electron using the model potential of Klapisch [198] to simulate the interaction between the atom's active electron and its frozen-core pseudonucleus. The pseudostates were then constructed using B -spline functions and used to expand the total scattering wave function. While good agreement was found between the obtained results and those presented by McCartney and Crothers [190], notable discrepancies were seen when compared with the results of Stary *et al.* [193]. Another time-dependent close-coupling approach was developed by Pindzola *et al.* [210]. Their method used frozen Hartree-Fock potentials to generate the pseudostates. For the considered projectile energy range (1 to 100 keV), good agreement was found between their results and those presented by Lühr and Saenz [199]. However, all these theoretical studies were not successful in producing accurate total cross sections for single-electron capture at intermediate to high collision energies. The conclusion was that, at these energies, the incident proton is more likely to capture the electron from the inner shells of the atom rather than the valence electron.

7.2.2 Single-electron-capture cross sections

We now present our results for single-electron capture in proton collisions with Li, Na, and K atoms using the pseudopotential method developed in Sect. 7.1. Convergent results were obtained with a symmetric basis for all incident energies with $\ell_{\max} = 4$, $n_{\text{neg}} = 5 - \ell$, $\kappa_{\max} = 5.4$ a.u., and $n_{\text{pos}} = 20$. In our calculations we found the low-energy region (1–10 keV) to be the most challenging. In this region we encountered ill-conditioning problems due to norm unity violation. However, these issues have been successfully mitigated by significantly increasing the number of Runge-Kutta time steps (e.g., at 1 keV it had to be increased to 10000).

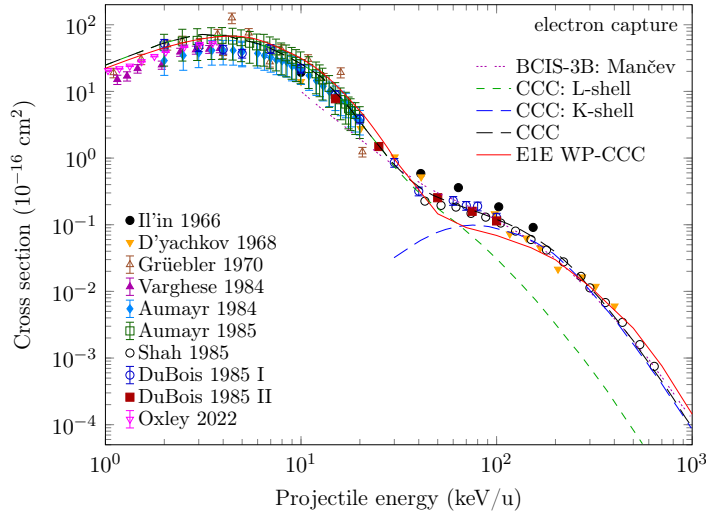


Figure 7.2: Total single-electron-capture cross section for p+Li collisions. Experimental data are by D'yachkov [178], Il'in *et al.* [179], Gruebler *et al.* [180], Varghese *et al.* [181], Aumayr *et al.* [182], Aumayr *et al.* [183], Shah *et al.* [184], DuBois and Toburen [185] (I), and DuBois [186] (II). The theoretical results are: present effective one-electron two-centre WP-CCC approach, BCIS-3B method by Mančev *et al.* [187], and single-centre CCC approach to rearrangement for L-, K-, and both L- and K-shell Li from Ch. 6.

In Fig. 7.2 we show the total single-electron-capture cross section as a function of incident energy in proton-lithium collisions. Our results are displayed in comparison with the experimental data from Refs. [178–186] and theoretical results of Mančev *et al.* [187]. We also show the calculations from Ch. 6 obtained using the frozen-core approximation. Agreement with experimental data is good in the

entire range of impact energies considered in this work. At the energy region of 30 keV and above, the measured total single-electron-capture cross sections display a shoulder-like structure. This behaviour cannot be explained by taking into account only the capture of the outer $2s$ electron of the lithium atom. At high impact energies incident protons can go deeper into the lithium atom and interact with its inner electrons which leads to the capture of K-shell electrons. In Ch. 6 we modelled this process by considering it as a collision of protons with the helium-like $\text{Li}^+(1s^2)$ target. That model neglected the effect of the valence L-shell electron. This is a widely used approximation. The sum of the capture cross sections of the L- and K-shell target electrons indeed displayed good agreement with experiment. Analysing the results one can see that at energies above 100 keV the electron capture from the K shell is significantly more pronounced than that from the L shell. At the same time, at low energies the L-shell electron capture is the main contributor. In a similar way, the BCIS-3B method of Mančev *et al.* [187] also considered the capture of K- and L-shell electrons of the lithium target as two independent processes. The BCIS-3B results are in overall good agreement with experimental data at intermediate and high-energy regions. However, due to the perturbative nature of the BCIS-3B method their results are systematically lower than the measured data below 30 keV.

In our present calculations the Li target is treated using a pseudopotential in a way which takes into account the possibility of K- and L-shell electron capture. Therefore, the final electron-capture cross section already includes their aggregate effect.

In Figs. 7.3 and 7.4 we present our results of the total single-electron-capture cross sections for proton collisions on atomic targets of Na, and K, respectively. Here also the obtained results are in good agreement with available experimental measurements [185, 201–208] across a wide energy range. If considered separately, similarly to the Li case, the contribution of electron capture from the inner shells would dominate over capture from the outermost shell at the incident

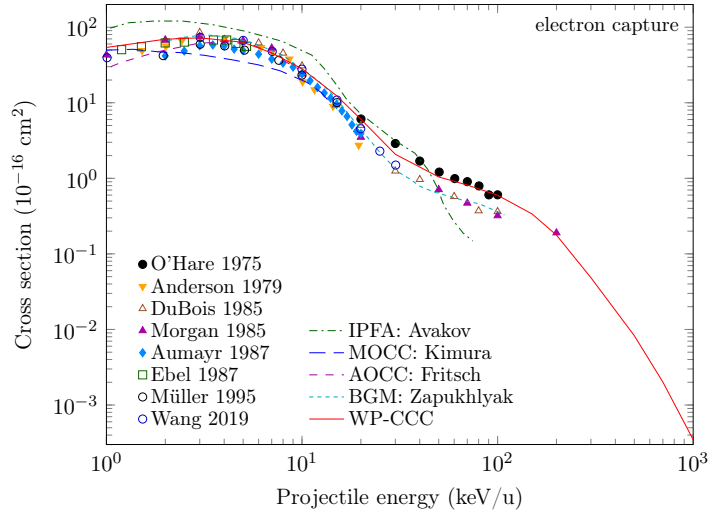


Figure 7.3: Total single-electron-capture cross section for p+Na collisions. Experimental data are by O'Hare *et al.* [204], Anderson *et al.* [206], DuBois and Toburen [185], Morgan *et al.* [205], Aumayr *et al.* [201], Ebel and Salzborn [203], Müller *et al.* [202], and Wang *et al.* [207]. The theoretical results are: present effective one-electron two-centre WP-CCC approach, IPFA by Avakov *et al.* [86], MOCC method by Kimura and Lane [60], AOCC method by Fritsch and Lin [125], and TC-BGM method by Zapukhlyak *et al.* [79].

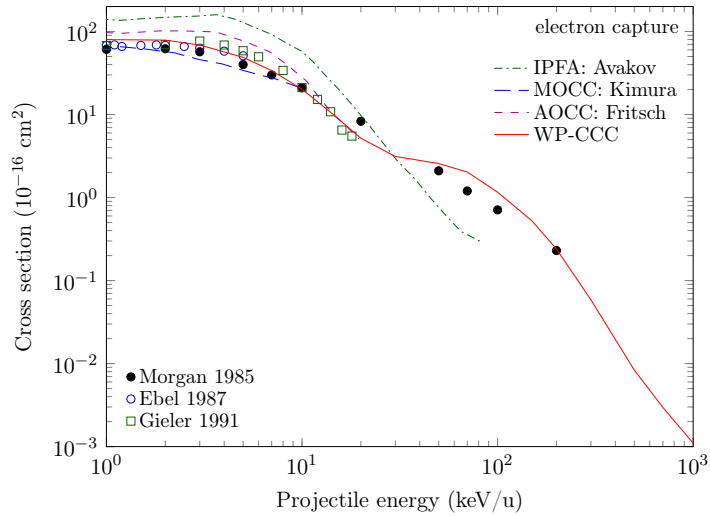


Figure 7.4: Total single-electron-capture cross section for p+K collisions. Experimental data are by Morgan *et al.* [205], Ebel and Salzborn [203], and Gieler *et al.* [208]. The theoretical results are: present effective one-electron two-centre WP-CCC approach, IPFA by Avakov *et al.* [86], MOCC method by Kimura and Lane [60], and AOCC method by Fritsch and Lin [125].

energies above 30 keV. These figures demonstrate a clear advantage of the present method over the IEM. The latter would require combination of the cross sections for three independent events for the Na target and four independent events for the K target. Clearly, the IEM becomes very cumbersome and impractical for

targets with several shells. In addition, it neglects the effect of coupling between the shells of the target to the final results. Instead the IEM introduces several screening parameters corresponding to each target shell. This leads to the final results becoming too sensitive to the choice of these parameters. At the same time we note that the results of Zapukhlyak *et al.* [79] for $p + \text{Na}$ obtained by considering three independent events show good agreement with experiment.

7.2.3 Single-ionisation cross sections

Here we calculate the total cross sections for single ionisation in Li, Na, and K collisions with H. These calculations were performed with the same basis as the calculations of the single-electron-capture cross sections.

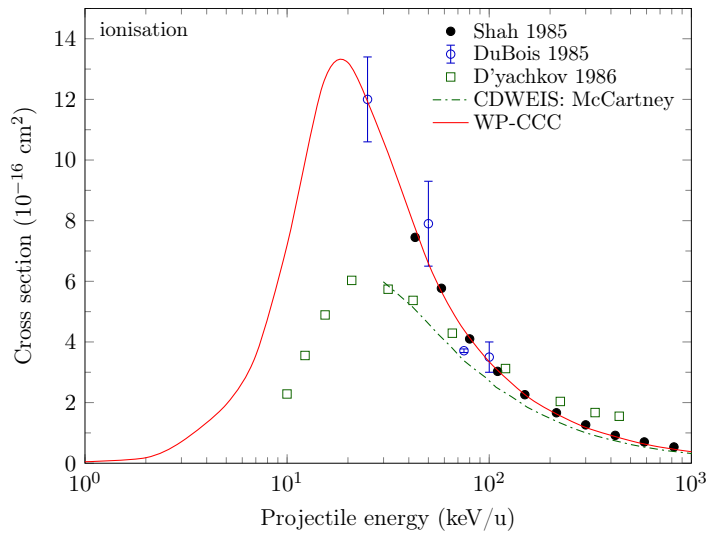


Figure 7.5: Total ionisation cross section for $p + \text{Li}$ collisions. Experimental data are by Shah *et al.* [184], DuBois [186], and D'yachkov [178]. The theoretical results are: present effective one-electron two-centre WP-CCC approach and CDW-EIS method by McCartney and Crothers [190].

Figure 7.5 presents the TICS as a function of incident energy for $p + \text{Li}$ collisions. The obtained results are in excellent agreement with the measurements of Shah *et al.* [184] and DuBois [186], but significantly overestimate the measurements of D'yachkov [178] at collision energies below 70 keV. At the same time, at energies above 100 keV the measurements of D'yachkov [178] are larger than the present calculations and the measurements of Shah *et al.* [184]. One should note that

these single-ionisation cross sections include also the contribution of inner-shell electrons, as in the case with electron capture. The results of CDW-EIS calculations of McCartney and Crothers [190] are generally lower than the present results and in better agreement with the measurements of D'yachkov [178] at 30 and 40 keV. Measurements of DuBois [186] are for multiple ionisation, however here single ionisation is expected to dominate.

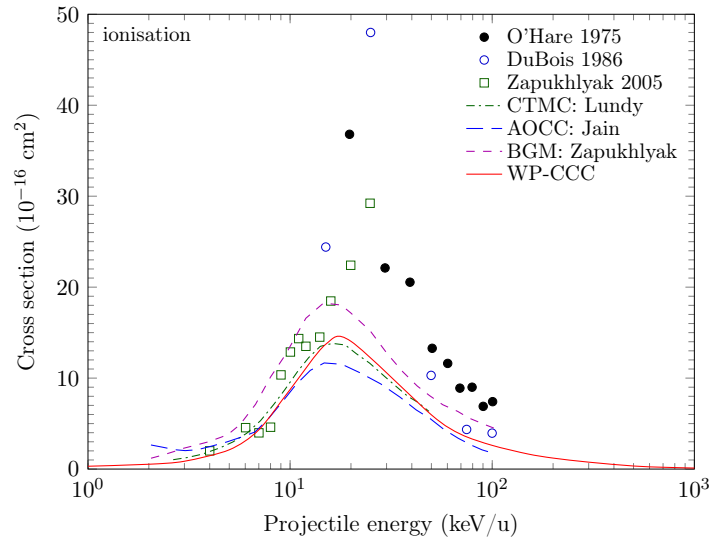


Figure 7.6: Total ionisation cross section for $p + \text{Na}$ collisions. Experimental data are by O'Hare *et al.* [204], DuBois [211], and Zapukhlyak *et al.* [79]. The theoretical results are: present effective one-electron two-centre WP-CCC approach, CTMC method by Lundy and Olson [212], AOCC method by Jain and Winter [213], and TC-BGM by Zapukhlyak *et al.* [79].

The total single-ionisation cross section for $p + \text{Na}$ collisions is shown in Fig. 7.6. The obtained results for $p + \text{Na}$ collisions are in reasonable agreement with the measurements of Zapukhlyak *et al.* [79] but significantly underestimate the measurements of O'Hare *et al.* [204] and DuBois [211]. Again, measurements of DuBois [186] are for multiple ionisation. We should also note overall good agreement of the present results with the CTMC calculations of Lundy and Olson [212]. In general, all the calculations appear to agree in shape but can differ in magnitude up to 60%.

Figure 7.7 presents the total cross section for single ionisation in $p + \text{K}$ collisions. Our results disagree with the measurements of O'Hare *et al.* [204] except at 100 keV. Above 100 keV our results agree well with the measurements of Elliott

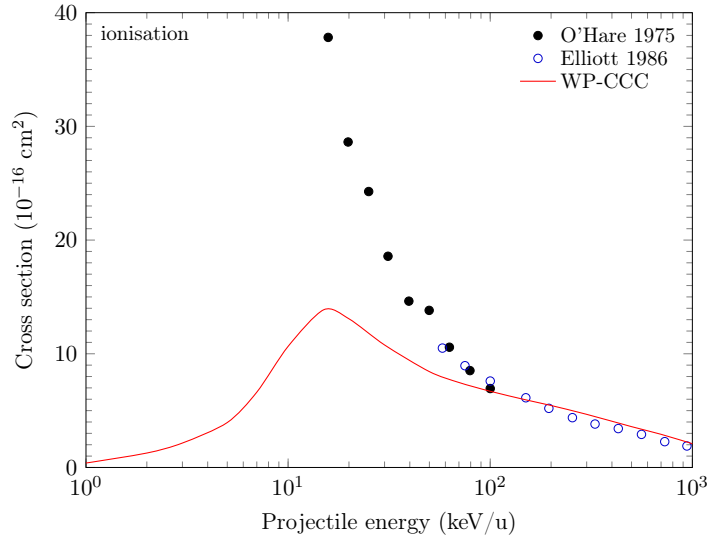


Figure 7.7: Total ionisation cross section for $p + K$ collisions. Experimental data are by O'Hare *et al.* [204] and Elliott *et al.* [214]. The theoretical results are: present effective one-electron two-centre WP-CCC approach.

et al. [214]. To our best knowledge, for the K target there are no other theoretical studies of this process.

Discrepancies between theory and experiment for single ionisation of Na and K around the peak region are striking. Zapukhlyak *et al.* [79] speculated that the experimental $p + Na$ ionisation cross sections might be higher than the theoretical ones possibly due to contributions from autoionising doubly excited states, which were ignored in their calculation. Our effective single-electron approach also neglects such contributions. However, Zapukhlyak *et al.* [79] estimated these contributions to be about two orders of magnitude smaller than the net ionisation cross section over the whole range of impact energies. Indeed this makes sense. We also notice that the disagreement appears to worsen as the projectile energy falls from 100 down to 20 keV. This is counter-intuitive as the likelihood of exciting an inner-shell electron to form an auto-ionising state should fall with energy. This is because the probability of the projectile penetrating deeper into the target atom is smaller at lower energies. Thus, not only do the discrepancies for single-electron ionisation in $p + Na$ collisions above 20 keV still remain unexplained but a similar issue also exists for $p + K$ collisions.

7.3 Chapter summary

In this chapter we developed an effective one-electron approach to proton collisions with alkali atoms. The method allows the calculation of single-ionisation and single-electron capture cross sections taking into account the effect of all the inner- and outer-shell target electrons. The approach does not differentiate which one of the many target electrons is captured or ionised. The ground-state wave function obtained in the multiconfigurational Hartree-Fock approach is used to calculate the probability density averaged over spins and all the configuration-space variables except for the position of one electron from the nucleus. The obtained single-electron probability density is then used to derive a pseudopotential describing the interaction of one electron with the collective field produced by the target nucleus and the other electrons. This pseudopotential is also used to construct the effective three-body Schrödinger equation of the scattering system. This can then be solved using the two-centre WP-CCC formalism developed for one-electron systems. Results for the TECS in proton collisions with Li, Na, and K atoms are in very good agreement with the available experimental measurements. However, considerable disagreement for single ionisation of sodium and potassium has been found. The method has a clear advantage over approaches based on the IEM, especially as the number of target electrons increases.

Chapter 8

Proton scattering on helium*

In this chapter we investigate differential cross sections for proton collisions with helium atoms. This is a four-body problem and presents a significant theoretical challenge. The WP-CCC method was extended to $p + \text{He}$ collisions by Alladustov *et al.* [33]. By freezing one electron in the ground state they were able to generate a correlated two-electron structure for the helium target. The obtained two-electron wave function is then used to expand the total scattering wave function in a similar way to the three-body WP-CCC method. However, the resulting scattering equations are more complex and require significantly more computational resources to solve. Results for integrated cross sections for all interconnected processes occurring in intermediate-energy $p + \text{He}$ collisions demonstrated very good agreement with experiment, even at lower energies where electron correlations are believed to play an important role.

Here we apply the pseudopotential idea from Ch. 7 to the helium atom to develop an effective one-electron description. We then compare the two-electron and E1E versions of the WP-CCC method by calculating singly differential cross sections for direct scattering, electron capture, and ionisation in $p + \text{He}$ collisions.

* This chapter is adapted from works published by the candidate [215, 216]. The publishers (the American Physical Society) provide the author with the right to use the articles, or parts thereof, in a thesis or dissertation without requesting permission.

8.1 Two-electron WP-CCC approach to ion collisions with helium

In this section we give a brief overview of the two-electron WP-CCC approach to ion collisions with helium. Full details of the four-body WP-CCC approach to proton-helium collisions are provided in Refs. [33, 217]. While this chapter is devoted to the study of differential cross sections in $p + \text{He}$ collisions, the method is readily extended to collisions involving multiply charged ions. In Ch. 9 we apply the approach to $\text{He}^{2+} + \text{He}$ collisions. Therefore, to avoid repetition, in this chapter we present equations for scattering of a multiply charged ion P^{Z_P} on He.

8.1.1 Four-body scattering equations

For ion collisions with He, the total scattering wave function Ψ_i^+ is the solution of the Schrödinger equation

$$(H - E)\Psi_i^+ = 0, \quad (8.1)$$

where H is the four-body Hamiltonian. The total energy E can be written in three equivalent forms,

$$\begin{cases} E = \varepsilon_{1s}^{\text{He}^+} + \frac{q_\alpha^2}{2\mu_T} + \varepsilon_\alpha, \\ E = \varepsilon_{1s}^{\text{He}^+} + \frac{q_{\beta_1}^2}{2\mu_P} + \varepsilon_{\beta_1}^P, \\ E = \varepsilon_{1s}^{\text{He}^+} + \frac{q_{\beta_2}^2}{2\mu_P} + \varepsilon_{\beta_2}^P, \end{cases} \quad (8.2)$$

where $\varepsilon_{1s}^{\text{He}^+}$ is the binding energy of the frozen target electron. Here α and β denote the full set of quantum numbers representing states in the $P^{Z_P} + \text{He}$ and $P^{Z_P-1} + \text{He}^+$ channels, respectively. Furthermore, \mathbf{q}_α is the momentum of the projectile relative to the helium atom in the α channel, μ_T is the reduced mass of the $P^{Z_P} + \text{He}$ system, ε_α is the energy of the pseudostate α , \mathbf{q}_{β_1} (and \mathbf{q}_{β_2}) is the

momentum of the formed P^{Z_P-1} ion relative to the residual helium ion in the β_1 (β_2) channel, and μ_P is the reduced mass. The total energy of the helium target in state α is $\varepsilon_\alpha^T = \varepsilon_{1s}^{\text{He}^+} + \varepsilon_\alpha$. Channel β_1 is the same as channel β_2 but with the electron of the residual target and that of the P^{Z_P-1} ion exchanged. Therefore, the energy of the hydrogen-like ion in channel β_1 is the same as in channel β_2 , i.e. $\varepsilon_\beta^P \equiv \varepsilon_{\beta_1}^P = \varepsilon_{\beta_2}^P$.

The four-body Hamiltonian can also be written in three equivalent forms,

$$\begin{cases} H = K_{\sigma_T} + H_{T1} + H_{T2} + \bar{V}_T + V_{12}, \\ H = K_{\sigma_{P1}} + H_{P1} + H_{T2} + \bar{V}_{P1}, \\ H = K_{\sigma_{P2}} + H_{P2} + H_{T1} + \bar{V}_{P2}. \end{cases} \quad (8.3)$$

where the kinetic energy operators are defined as

$$\begin{cases} K_{\sigma_T} = -\frac{\nabla_{\sigma_T}^2}{2\mu_T}, \\ K_{\sigma_{P1}} = -\frac{\nabla_{\sigma_{P1}}^2}{2\mu_P}, \\ K_{\sigma_{P2}} = -\frac{\nabla_{\sigma_{P2}}^2}{2\mu_P} \end{cases} \quad (8.4)$$

and the interaction potentials as

$$\begin{cases} \bar{V}_T = \frac{2Z_P}{R} - \frac{Z_P}{r_{P1}} - \frac{Z_P}{r_{P2}}, \\ \bar{V}_{P1} = \frac{2Z_P}{R} - \frac{2}{r_{T1}} - \frac{Z_P}{r_{P2}}, \\ \bar{V}_{P2} = \frac{2Z_P}{R} - \frac{2}{r_{T2}} - \frac{Z_P}{r_{P1}}, \\ V_{12} = \frac{1}{|\mathbf{r}_1 - \mathbf{r}_2|}. \end{cases} \quad (8.5)$$

Vectors \mathbf{r}_{T1} and \mathbf{r}_{T2} are the position of the two electrons from the target nucleus (located at the origin) and \mathbf{r}_{P1} and \mathbf{r}_{P2} are the positions of the two electrons from the projectile ion. We use σ_{P1} and σ_{P2} to denote the position of the P^{Z_P-1} system relative to the residual helium ion. The Hamiltonians of the He^+ and P^{Z_P-1} ions

are

$$\left\{ \begin{array}{l} H_{T_1} = -\frac{\nabla_{\mathbf{r}_{T1}}^2}{2} - \frac{2}{r_{T1}}, \\ H_{T_2} = -\frac{\nabla_{\mathbf{r}_{T2}}^2}{2} - \frac{2}{r_{T2}}, \\ H_{P_1} = -\frac{\nabla_{\mathbf{r}_{P1}}^2}{2} - \frac{Z_P}{r_{P1}}, \\ H_{P_2} = -\frac{\nabla_{\mathbf{r}_{P1}}^2}{2} - \frac{Z_P}{r_{P2}}. \end{array} \right. \quad (8.6)$$

Therefore, the Hamiltonian of the helium atom can be written as

$$H_T = H_{T_1} + H_{T_2} + V_{12}. \quad (8.7)$$

As in the case of the three-body WP-CCC method, we use the impact-parameter method and write the position of the projectile nucleus relative to the origin as $\mathbf{R} = \mathbf{b} + \mathbf{v}t$. The total scattering wave function is expanded as

$$\begin{aligned} \Psi_i^+ &= \sum_{\alpha=1}^{\infty} F_{\alpha}(\boldsymbol{\sigma}_T) e^{i\mathbf{q}_{\alpha} \cdot \boldsymbol{\sigma}_T} \psi_{\alpha}^{\text{He}}(\mathbf{r}_{T1}, \mathbf{r}_{T2}) \\ &+ \frac{1}{\sqrt{2}} \sum_{\beta=1}^{\infty} G_{\beta}(\boldsymbol{\sigma}_P) [e^{i\mathbf{q}_{\beta 1} \cdot \boldsymbol{\sigma}_{P1}} \psi_{\beta}^{(Z_P)}(\mathbf{r}_{P1}) \psi_{1s}^{\text{He}^+}(\mathbf{r}_{T2}) \\ &+ e^{i\mathbf{q}_{\beta 2} \cdot \boldsymbol{\sigma}_{P2}} \psi_{\beta}^{(Z_P)}(\mathbf{r}_{P2}) \psi_{1s}^{\text{He}^+}(\mathbf{r}_{T1})], \end{aligned} \quad (8.8)$$

where $\psi_{\alpha}^{\text{He}}$ and $\psi_{\beta}^{(Z_P)}$ are the wave functions for the helium atom and the hydrogen-like atom formed through electron capture by the projectile nucleus, respectively. The helium wave functions are constructed according to the method outlined in Sect. 8.1.2 whereas the wave functions for the hydrogen-like ion are made using the approach described in Sect. 3.2. We use the notation $\psi_{1s}^{\text{He}^+}$ to denote the ground-state wave function of He^+ .

Next we insert Eq. (8.8) into Eq. (8.1) and apply the semiclassical approximation. Then, to obtain the first set of coupled equations we pre-multiply by $\psi_{\alpha'}^{\text{He}*}(\mathbf{r}_{T1}, \mathbf{r}_{T2}) e^{-i\mathbf{q}_{\alpha'} \cdot \boldsymbol{\sigma}_T}$ and integrate over \mathbf{r}_{T1} and \mathbf{r}_{T2} . The second set of equa-

tions is obtained by pre-multiplying by

$$1/\sqrt{2}[\psi_{\beta'}^{(Z_P)*}(\mathbf{r}_{P1})\psi_{1s}^{\text{He}^+}(\mathbf{r}_{T2})e^{-i\mathbf{q}_{\beta'}\cdot\boldsymbol{\sigma}_{P1}} + \psi_{\beta'}^{(Z_P)*}(\mathbf{r}_{P2})\psi_{1s}^{\text{He}^+}(\mathbf{r}_{T1})e^{-i\mathbf{q}_{\beta'}\cdot\boldsymbol{\sigma}_{P2}}]$$

and integrating over \mathbf{r}_{T1} and \mathbf{r}_{T2} . Altogether, the four-body scattering equations are

$$\begin{cases} i\dot{F}_{\alpha'} + i\sum_{\beta=1}^{\infty}\dot{G}_{\beta}K_{\alpha'\beta}^{\text{T}} = \sum_{\alpha=1}^{\infty}F_{\alpha}D_{\alpha'\alpha}^{\text{T}} + \sum_{\beta=1}^{\infty}G_{\beta}Q_{\alpha'\beta}^{\text{T}}, \\ i\sum_{\alpha=1}^{\infty}\dot{F}_{\alpha}K_{\beta'\alpha}^{\text{P}} + i\sum_{\beta=1}^{\infty}\dot{G}_{\beta}L_{\beta'\beta}^{\text{P}} = \sum_{\alpha=1}^{\infty}F_{\alpha}Q_{\beta'\alpha}^{\text{P}} + \sum_{\beta=1}^{\infty}G_{\beta}D_{\beta'\beta}^{\text{P}}. \end{cases} \quad (8.9)$$

The direct-scattering matrix elements are given by

$$\begin{cases} D_{\alpha'\alpha}^{\text{T}}(\mathbf{R}) = \langle \mathbf{q}_{\alpha'}\psi_{\alpha'}^{\text{He}} | H_{\text{T}} - \varepsilon_{\alpha}^{\text{T}} + \bar{V}_{\text{T}} | \psi_{\alpha}^{\text{He}} \mathbf{q}_{\alpha} \rangle, \\ L_{\beta'\beta}^{\text{P}}(\mathbf{R}) = \frac{1}{2} \sum_{i,j=1,2} \langle \mathbf{q}_{i\beta'}\psi_{\beta'}^{(Z_P)}\psi_{1s}^{\text{He}^+} | \psi_{\beta}^{(Z_P)}\psi_{1s}^{\text{He}^+} \mathbf{q}_{j\beta} \rangle, \\ D_{\beta'\beta}^{\text{P}}(\mathbf{R}) = \frac{1}{2} \sum_{i,j=1,2} \langle \mathbf{q}_{i\beta'}\psi_{\beta'}^{(Z_P)}\psi_{1s}^{\text{He}^+} | H_{\text{Pi}} - \varepsilon_{\beta}^{\text{P}} | \psi_{\beta}^{(Z_P)}\psi_{1s}^{\text{He}^+} \mathbf{q}_{j\beta} \rangle \\ \quad + \frac{1}{2} \sum_{i,j=1,2} \langle \mathbf{q}_{i\beta'}\psi_{\beta'}^{(Z_P)}\psi_{1s}^{\text{He}^+} | \bar{V}_{\text{Pi}} | \psi_{\beta}^{(Z_P)}\psi_{1s}^{\text{He}^+} \mathbf{q}_{j\beta} \rangle. \end{cases}$$

The overlap matrix elements are

$$\begin{cases} K_{\beta'\alpha}^{\text{P}}(\mathbf{R}) = \frac{1}{\sqrt{2}} \sum_{i=1,2} \langle \mathbf{q}_{i\beta'}\psi_{\beta'}^{(Z_P)}\psi_{1s}^{\text{He}^+} | \psi_{\alpha}^{\text{He}} \mathbf{q}_{\alpha} \rangle, \\ K_{\alpha'\beta}^{\text{T}}(\mathbf{R}) = \frac{1}{\sqrt{2}} \sum_{i=1,2} \langle \mathbf{q}_{\alpha'}\psi_{\alpha'}^{\text{He}} | \psi_{\beta}^{(Z_P)}\psi_{1s}^{\text{He}^+} \mathbf{q}_{i\beta} \rangle. \end{cases} \quad (8.10)$$

The exchange matrix elements are defined as

$$\begin{cases} Q_{\beta'\alpha}^{\text{P}}(\mathbf{R}) = \frac{1}{\sqrt{2}} \sum_{i=1,2} \langle \mathbf{q}_{i\beta'}\psi_{\beta'}^{(Z_P)}\psi_{1s}^{\text{He}^+} | H_{\text{T}} - \varepsilon_{\alpha}^{\text{T}} + \bar{V}_{\text{T}} | \psi_{\alpha}^{\text{He}} \mathbf{q}_{\alpha} \rangle, \\ Q_{\alpha'\beta}^{\text{T}}(\mathbf{R}) = \frac{1}{\sqrt{2}} \sum_{i=1,2} \langle \mathbf{q}_{\alpha'}\psi_{\alpha'}^{\text{He}} | H_{\text{Pi}} - \varepsilon_{\beta}^{\text{P}} + \bar{V}_{\text{Pi}} | \psi_{\beta}^{(Z_P)}\psi_{1s}^{\text{He}^+} \mathbf{q}_{i\beta} \rangle. \end{cases} \quad (8.11)$$

Evaluation of the matrix elements is detailed in Ref. [217]. We follow the same

ideas as for the matrix elements in the three-body WP-CCC method. However, it is worth noting that calculation of the matrix elements is significantly more computationally demanding than in the three-body case. The coupled equations in Eq. (8.9) are solved using the approach outlined in Sect. 3.5. In the final channel, expansion coefficients $F_\alpha(+\infty, \mathbf{b})$ and $G_\beta(+\infty, \mathbf{b})$ are used to calculate the transition probabilities and T -matrix elements for all possible single-electron processes in exactly the way discussed in Sect. 3.4.

8.1.2 Two-electron helium structure

There is no known analytical solution for the Schrödinger equation for the helium atom. Therefore, approximate methods must be employed to calculate the two-electron wave functions. To ensure an accurate description of the electronic wave function both electron-electron correlation as well as electron-exchange effects should be accounted for in the model. The two-electron WP-CCC approach to ion collisions with helium is based on the wave-packet description in the frozen-core approximation. The symmetrised helium wave function is written as

$$\psi_\alpha^{\text{He}}(\mathbf{r}_{\text{T1}}, \mathbf{r}_{\text{T2}}) = \psi_\alpha(\mathbf{r}_{\text{T1}})\psi_{1s}^{\text{He}^+}(\mathbf{r}_{\text{T2}}) + \psi_\alpha(\mathbf{r}_{\text{T2}})\psi_{1s}^{\text{He}^+}(\mathbf{r}_{\text{T1}}), \quad (8.12)$$

where $\psi_{1s}^{\text{He}^+}$ is the ground-state wave function of the hydrogen-like ion, He^+ . We assume that the total spin ($S = 0$) is conserved throughout the collision and therefore use only singlet states in expansion Eq. (8.8). Equation (8.12) is normalised to unity. The two-electron wave function, ψ_α^{He} , is obtained from the Schrödinger equation,

$$H_{\text{T}}\psi_\alpha^{\text{He}}(\mathbf{r}_{\text{T1}}, \mathbf{r}_{\text{T2}}) = \varepsilon_\alpha^{\text{T}}\psi_\alpha^{\text{He}}(\mathbf{r}_{\text{T1}}, \mathbf{r}_{\text{T2}}). \quad (8.13)$$

Here $\varepsilon_\alpha^{\text{T}}$ is the total energy of helium in the α state. The Hamiltonian is given by Eq. (8.7). We substitute Eq. (8.12) into Eq. (8.13) and, after some algebra,

obtain an equation for the reduced radial wave function, $\phi_\alpha(r_{T1})$, of $\psi_\alpha(\mathbf{r}_{T1})$,

$$\begin{aligned} & \left[\frac{d^2 \phi_\alpha}{dr_{T1}^2} - \left(\frac{\ell_\alpha(\ell_\alpha + 1)}{r_{T1}^2} - \frac{4}{r_{T1}} + 2W_0[\phi_{1s}^{\text{He}^+}, \phi_{1s}^{\text{He}^+}] - 2\varepsilon_\alpha \right) \phi_\alpha(r_{T1}) \right] \\ & = \left[\frac{2}{2\ell_\alpha + 1} W_{\ell_\alpha}[\phi_{1s}^{\text{He}^+}, \phi_\alpha] \right. \\ & \quad \left. - 2\delta_{0\ell_\alpha} \int_0^\infty dr_{T2} \phi_{1s}^{\text{He}^+}(r_{T2}) W_0[\phi_{1s}^{\text{He}^+}, \phi_{1s}^{\text{He}^+}] \phi_\alpha(r_{T2}) \right] \phi_{1s}^{\text{He}^+}(r_{T1}), \end{aligned} \quad (8.14)$$

where $\phi_{1s}^{\text{He}^+}(r_{T1}) = 4\sqrt{2}e^{-2r_{T1}}r_{T1}$, and ε_α is the eigenenergy of the state described by ψ_α . In Eq. (8.14) we define the functional

$$W_\ell[f, g] = \frac{1}{r^{\ell+1}} \int_0^r f(t)g(t)t^\ell dt + r^\ell \int_r^\infty \frac{f(t)g(t)}{t^{\ell+1}} dt. \quad (8.15)$$

Equation (8.14) is solved numerically using an iterative Numerov approach. The ground-state energy obtained with this method is very similar to the experimentally measured value, see Tbl. 8.1 for a detailed comparison. Radial wave functions for excited states are obtained by using different values of $\alpha = \{n_\alpha, \ell_\alpha, m_\alpha\}$ when solving Eq. (8.14). For positive energies, Eq. (8.14) can be solved numerically to obtain the continuum wave function from which the positive-energy pseudostates are constructed using the wave-packet discretisation approach.

8.2 Effective one-electron description of helium

Proton scattering on a two-electron system is a complex problem to solve due to the electron-electron correlations and exchange effects between the captured electron and the electron of the residual helium ion which belong to different centres. On the other hand, there are no such complications in the case of bare-ion collisions with a hydrogen-like system. In Ch. 7 we developed an effective one-electron approach to proton collisions with alkali metals that allowed us to utilise existing theoretical techniques and numerical methods for three-body collisions.

Application of the pseudopotential idea to helium is the same as for the alkali metals. First, we generate an accurate two-electron wave function using the

multiconfigurational HF approach, then integrate over the spatial coordinate of one and spin coordinates of both of the two electrons. Averaging over the angular coordinate of the remaining electron yields the single-electron radial density function which is then used to calculate an effective one-electron ground-state. This wave function is used in the one-electron Schrödinger equation to solve for the pseudopotential. Once the pseudopotential has been obtained we can use an iterative Numerov approach to calculate one-electron wave functions for excited and continuum states. Wave-packet pseudostates are constructed from the continuum solution as per the method described in Sect. 3.2.

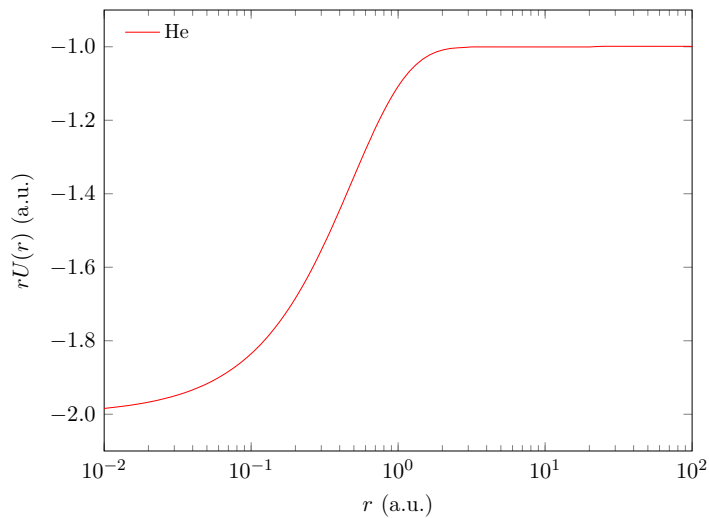


Figure 8.1: The effective one-electron pseudopotential $U(r)$ weighted by r for He.

Figure 8.1 shows the radial dependence of the effective potential $U(r)$ multiplied by radius r for the helium atom. Here $U(r)$ is the potential which is felt by any one of the electrons in the field produced by the nucleus and the remaining electron of the atom. As we can see the potential is attractive, and tends to the expected functional form of $-2/r$ near the origin and has the asymptotic $-1/r$ tail at large distances. The pseudopotential has a ground-state energy of -0.904 , corresponding exactly to the first ionisation energy of helium. In Tbl. 8.1 we compare the first few energy levels of helium calculated with the two-electron approach in Sect. 8.1.2 and the E1E approach with the experimentally measured values from Kramida *et al.* [200]. The ground-state energy from the E1E approach

is very close to the experimental value (by construction), whereas the two-electron structure leads to a ground-state energy that is about 3% different to the experimental value. However, the excited states have more accurate energies when constructed using the two-electron method.

Having obtained the effective one-electron pseudostates we use the three-body WP-CCC method from Ch. 3 to calculate the probability amplitudes for all one-electron processes. Compared to the two-electron method this approach is significantly faster to calculate, but at the cost of neglecting electron-exchange effects and electron-electron correlations in the scattering equations. We emphasise, however, that electron-electron correlations are not neglected in constructing the E1E wave functions.

Table 8.1: Comparison of calculated singlet-state energy levels of helium from two-electron and effective one-electron structures with experimentally measured values from Kramida *et al.* [200]. Labels in the first column are for one electron, the other is frozen in the $1s$ orbital.

Subshell	Two-electron energy (a.u.)	E1E energy (a.u.)	Exp. (a.u.)
$1s$	-0.8725	-0.9036	-0.9037
$2s$	-0.1434	-0.1574	-0.1460
$2p$	-0.1224	-0.1280	-0.1238
$3s$	-0.0606	-0.0644	-0.0613
$3p$	-0.0547	-0.0565	-0.0551
$3d$	-0.0555	-0.0556	-0.0556

8.3 Angular differential cross sections for p+He collisions

In this section we consider angular differential cross sections for elastic scattering, target excitation, and electron capture in p+He collisions. A number of methods have been applied to calculate differential cross sections for this system. The CTMC calculations of Schultz *et al.* [218] produced results in good agreement with the experiment of Martin *et al.* [219] for differential electron-capture cross sections into all projectile states at 100 keV. The classical static-potential scat-

tering (SPS) method employed by Kobayashi and Ishihara [220] was applied to elastic scattering at 25, 50, and 100 keV. Kobayashi and Ishihara [220] found a large discrepancy between the experimental data of Ref. [221] and their results at 100 keV. These authors also used the Glauber approximation to calculate the differential elastic-scattering cross section. This method gave better agreement with the experimental data in shape, however, the discrepancy in the magnitude remained.

Methods based on the first Born approximation by Ghanbari-Adivi [222], [220], and Mančev *et al.* [223] achieved some success in the narrow forward-scattering cone but displayed unphysical dips and disagreement with experiment at larger angles. In these works, the results for electron capture into all states were obtained from the calculations into only the $1s$ state by using the Oppenheimer scaling rule.

Other perturbative methods such as the CDW-EIS method of Abufager *et al.* [224], the four-body boundary-corrected continuum-intermediate-state (BCIS-4B) method of Mančev *et al.* [225], the symmetric eikonal (SE2) method of Rodríguez *et al.* [226], and the distorted-wave Hartree-Fock (DWHF) method of Wong *et al.* [58], have employed the distorted-wave formalism to calculate elastic scattering [58], electron capture into the $1s$ state [224, 225], and excitation into the $2p$ state [226]. All these methods resulted in good agreement with experiments for the particular processes they were applied to, except for the partial-wave method of Wong *et al.* [58] which gave reasonable agreement only after scaling by a factor of 0.1. No justification for such scaling was given.

The perturbative methods mentioned above are applicable at sufficiently high energies. In the intermediate energy range, various reaction channels are interdependent. Therefore, coupling between these channels is important. These effects can be accounted for in the close-coupling formalism. In a two-centre AOCC approach of [227], it was found that the effect of electron exchange has increasing importance with decreasing projectile impact energy. The approach is found to be

in good agreement with experimental data for electron capture into all projectile states [219] and excitation into $2s$ and $2p$ states of the target [228], but it showed poor agreement for elastic scattering [221] at a projectile energy of 100 keV. The basis-generator method (BGM) was applied to differential scattering in $p + \text{He}$ collisions by Zapukhlyak *et al.* [229]. Two different approaches were used to treat the two-electron target structure: the independent-event-model basis-generator method (IEM-BGM) and the one-active-electron basis-generator method (OAE-BGM). Both implementations of the method were used to calculate electron capture into all states of hydrogen over projectile energies ranging from 25 to 200 keV.

We now apply the two-electron and E1E WP-CCC methods to calculate angular differential cross sections for direct scattering and electron capture in $p + \text{He}$ collisions. The two-electron results are labelled as WP-CCC and results obtained using the effective one-electron method are labelled as E1E WP-CCC. The present calculations are compared with experimental data and other theoretical calculations where available. Results are presented in the centre-of-mass frame.

In both approaches the number of included negative- and positive-energy pseudostates are increased until adequate convergence is achieved in the predicted cross sections for the investigated collision processes. We found that a basis containing $n_{\text{neg}} = 5 - \ell$ bound states and 20 continuum bins on both the target and projectile centres was sufficient to obtain converged results. In all cases the maximum angular momentum required was $\ell_{\text{max}} = 3$.

In Fig. 8.2 we present our calculations of the angular differential cross sections for target excitation into all $n = 2$ states and electron capture into all projectile-atom states included in the basis for 75 keV $p + \text{He}$ collisions. As seen from the figure, both the two-electron and E1E WP-CCC results agree very well with the experimental data of Kvale *et al.* [228] for $n = 2$ excitation. For total electron capture, our results are in excellent agreement with the most recent measurements by Guo *et al.* [231]. The data by Schulz *et al.* [230] suggests a larger cross section

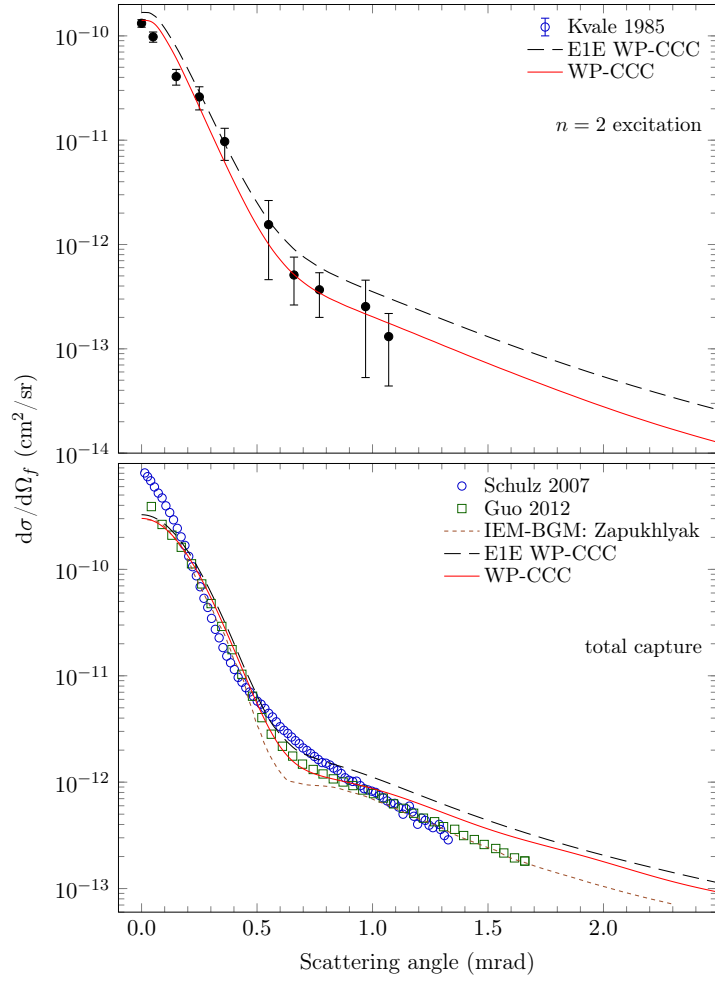


Figure 8.2: Angular differential cross sections (in the centre-of-mass frame) for excitation into the $n = 2$ target states, and electron capture summed over all projectile states in 75 keV p + He collisions. Experimental data are by Kvale *et al.* [228], Schulz *et al.* [230], and Guo *et al.* [231]. The theoretical results are: present two-electron and E1E WP-CCC methods and IEM-BGM by Zapukhlyak *et al.* [229].

in the forward direction which is not supported by the measurements by Guo *et al.* [231] or either the IEM-BGM results or our calculations. We generally find good agreement between our calculations and the IEM-BGM results by Zapukhlyak *et al.* [229], except between 0.5 to 0.8 mrad where the IEM-BGM underestimates the experiments.

Figure 8.3 shows our results at 100 keV. For $n = 2$ excitation, we find excellent agreement between the two-electron and E1E WP-CCC calculations and experimental data by Kvale *et al.* [228]. We also find very good agreement with the measurements by Schulz *et al.* [232]. For the total electron-capture cross section, we compare our results with the experiments of Martin *et al.* [219] and Guo *et al.*

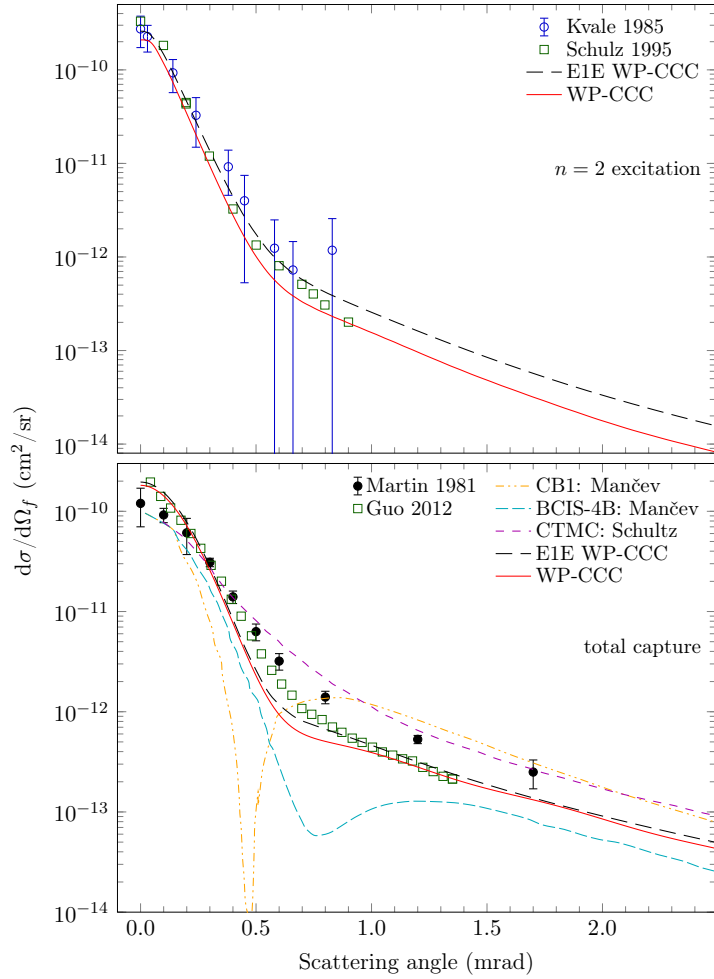


Figure 8.3: Angular differential cross sections (in the centre-of-mass frame) for excitation into the $n = 2$ target states, and electron capture summed over all projectile states in 100 keV $p + \text{He}$ collisions. Experimental data are by Kvale *et al.* [228], Schulz *et al.* [232], Martin *et al.* [219], and Guo *et al.* [231]. The theoretical results are: present two-electron and E1E WP-CCC methods, CB1 and BCIS-4B methods by Mančev *et al.* [225], and CTMC method by Schultz *et al.* [218].

[231] along with the CB1 and BCIS-4B calculations by Mančev *et al.* [225] and CTMC calculations by Schultz *et al.* [218]. In the forward direction we find both our methods agree very well with the data by Guo *et al.* [231], and slightly overestimate the data by Martin *et al.* [219]. At larger scattering angles the WP-CCC calculations underestimate the measurements of Martin *et al.* [219], but we find generally good agreement with those of Guo *et al.* [231]. The CB1 and BCIS-4B calculations by Mančev *et al.* [225] show unphysical dips and deviate significantly from the experimental results away from the forward direction. Meanwhile, the CTMC calculations by Schultz *et al.* [218] tend to agree with the data by Martin

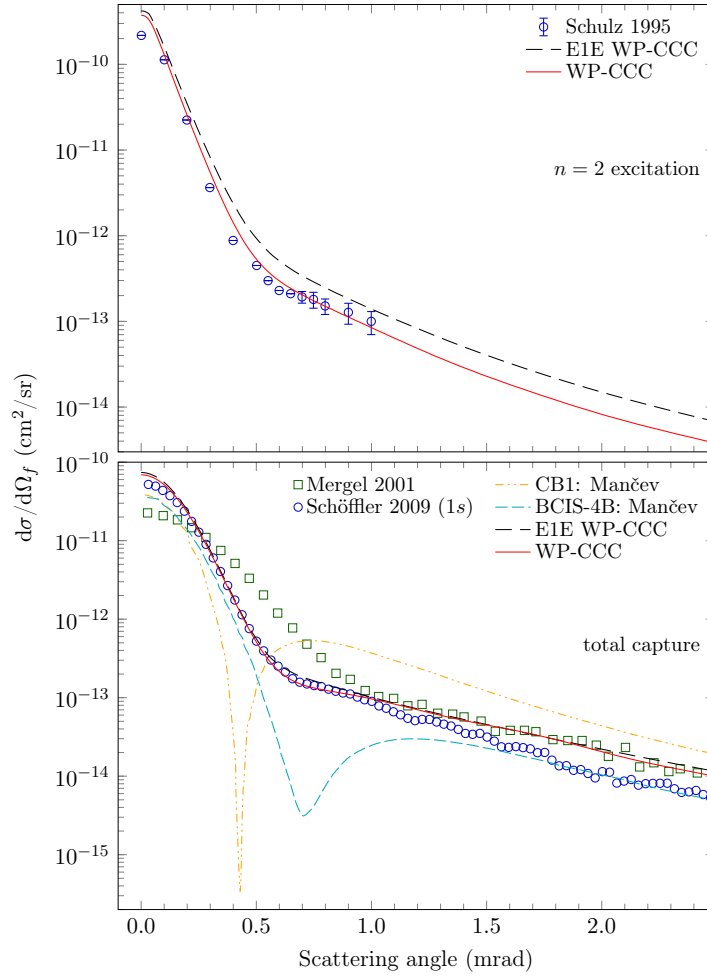


Figure 8.4: Angular differential cross sections (in the centre-of-mass frame) for excitation into the $n = 2$ target states, and electron capture summed over all projectile states in 150 keV $p + \text{He}$ collisions. Experimental data are by Schulz *et al.* [232], Mergel *et al.* [233], and Schöffler *et al.* [234]. The data from Schöffler *et al.* [234] is for capture into the $1s$ state only. The theoretical results are: present two-electron and E1E WP-CCC methods and CB1 and BCIS-4B methods by Mančev *et al.* [225].

et al. [219]. Overall we find that both the two-electron and E1E WP-CCC results more consistently describe the available experimental data.

Our results for 150 keV collisions are shown in Fig. 8.4. At this energy the present results for $n = 2$ excitation slightly overestimate the data of Schulz *et al.* [232] in the forward direction but agree well at larger scattering angles, especially the two-electron WP-CCC calculations. For electron capture, the CB1 and BCIS-4B calculations by Mančev *et al.* [225] again fail to accurately describe the available experimental data at this incident energy. At large scattering angles our results agree very well with the data of Mergel *et al.* [233], however significant

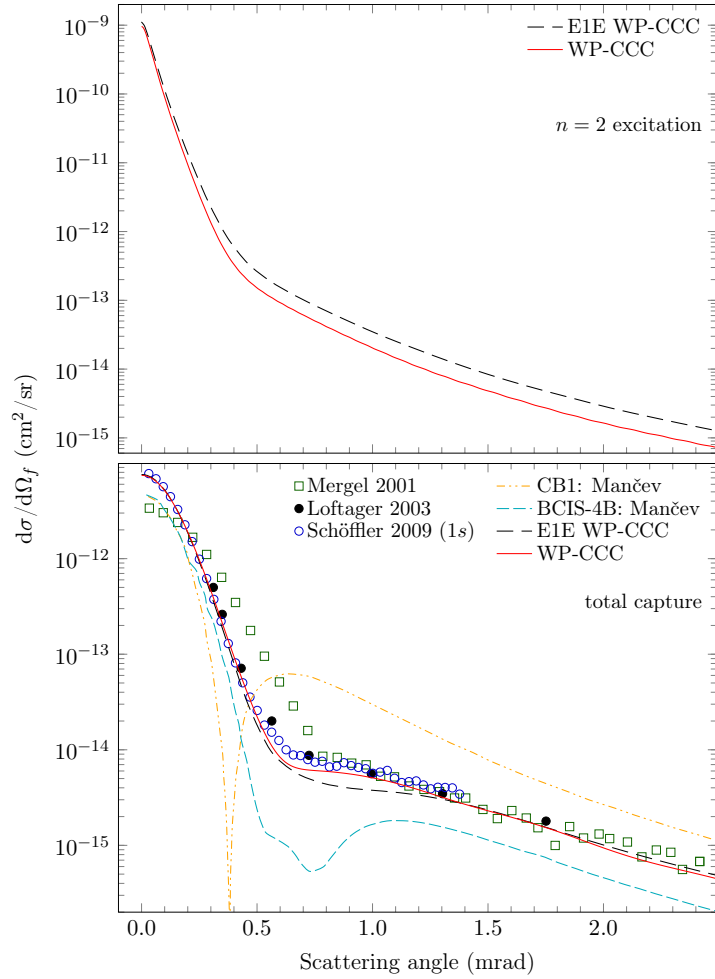


Figure 8.5: Angular differential cross sections (in the centre-of-mass frame) for excitation into the $n = 2$ target states, and electron capture summed over all projectile states in 300 keV $p + \text{He}$ collisions. Experimental data are by Mergel *et al.* [233], Loftager (from Ref. [223]), and Schöffler *et al.* [234]. The data from Schöffler *et al.* [234] is for capture into the $1s$ state only. The theoretical results are: present two-electron and E1E WP-CCC methods and CBI and BCIS-4B methods by Mančev *et al.* [225].

differences are seen for scattering angles less than 0.9 mrad. For comparison, we also include the more recent measurements for capture into the $1s$ state by Schöffler *et al.* [234]. From our calculations we find that capture into the $1s$ state is by far the dominant channel for charge exchange, contributing 80% of the total electron capture cross section. Interestingly, we observe significantly better agreement with the data of Schöffler *et al.* [234] than that of Mergel *et al.* [233]. The latter significantly underestimates the ground-state data in a narrow cone around the forward direction (that defines the integrated capture cross section) and predicts a different slope.

Figure 8.5 shows our results for 300 keV $p + \text{He}$ collisions. As far as we are aware, there are no data available for $n = 2$ excitation at this energy. For the total electron-capture cross section, we compare with the measurements by Mergel *et al.* [233] and Loftager. We again include the data for $1s$ capture by Schöffler *et al.* [234]. Here we find that our results agree very well with the Schöffler *et al.* [234] and Loftager data, but again differ from the measurements by Mergel *et al.* [233] at smaller scattering angles. This leads us to conclude that the data by Mergel *et al.* [233] may be inaccurate for small scattering angles. Once again, the perturbative methods used by Mančev *et al.* [225] consistently differ from the experimental data and our results.

Next, we calculate angular differential cross sections for elastic scattering, $2s$ and $2p$ target excitation, and electron capture into the $1s$, $2s$, and $2p$ states of the projectile atom. In Figs. 8.6–8.9 we show our results at 75, 100, 150, and 300 keV, respectively. We compare to the experimental data of Refs. [221, 228, 234, 235] and other calculations [58, 218, 220, 225–227, 229] where available.

For elastic scattering, presented in the upper-left panels of Figs. 8.6–8.9, we find the most significant differences between the two-electron and E1E WP-CCC results. The only experimental data available for this process are the measurements by Peacher *et al.* [221] at 100 keV. Here there are also a number of other theoretical results available. However, none of the calculations, including the present results, agree with the magnitude of the data of Peacher *et al.* [221]. Previously, the failure of the theoretical treatments to adequately account for the effects of the various inelastic channels, particularly ionisation and charge transfer, was suggested to be a possible source of this discrepancy. Therefore, we expected that including a sufficient number of negative-energy and positive-energy pseudostates would resolve the discrepancy as such a large basis correctly accounts for the polarisability of the target. However, as we can see from the figure, this is not the case. As Peacher *et al.* [221] mentioned, relative data from their experimental chamber, the interaction length of which was uncertain, were

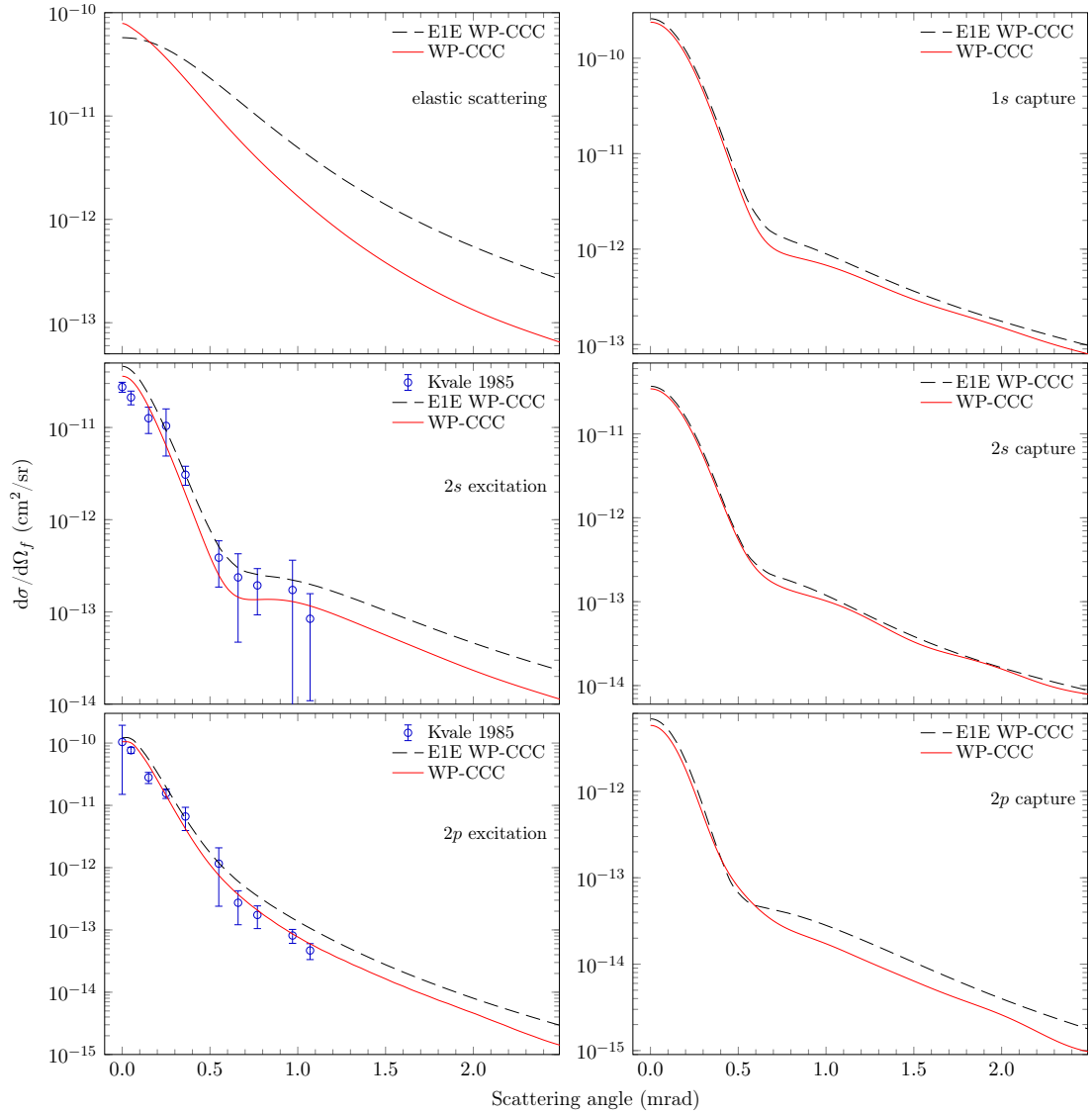


Figure 8.6: Angular differential cross sections (in the centre-of-mass frame) for elastic scattering, $2s$ and $2p$ target excitation, and electron capture into the $1s$, $2s$, and $2p$ projectile-atom states in 75 keV $p+\text{He}$ collisions. Experimental data are by Kvale *et al.* [228]. The theoretical results are: present two-electron and E1E WP-CCC methods.

normalised to the absolute differential cross sections using a single normalising constant. Given the two-electron WP-CCC method is based on the very accurate correlated two-electron target structure and the obtained results are convergent in terms of the included target- and projectile-centred states, one can cautiously suggest that there could be a normalisation error in the experiment. Indeed, agreement in shape between the experiment and the two-electron WP-CCC results is excellent. Note that there was no such disagreement in similar calculations for the proton-hydrogen system (see Sect. 5.1).

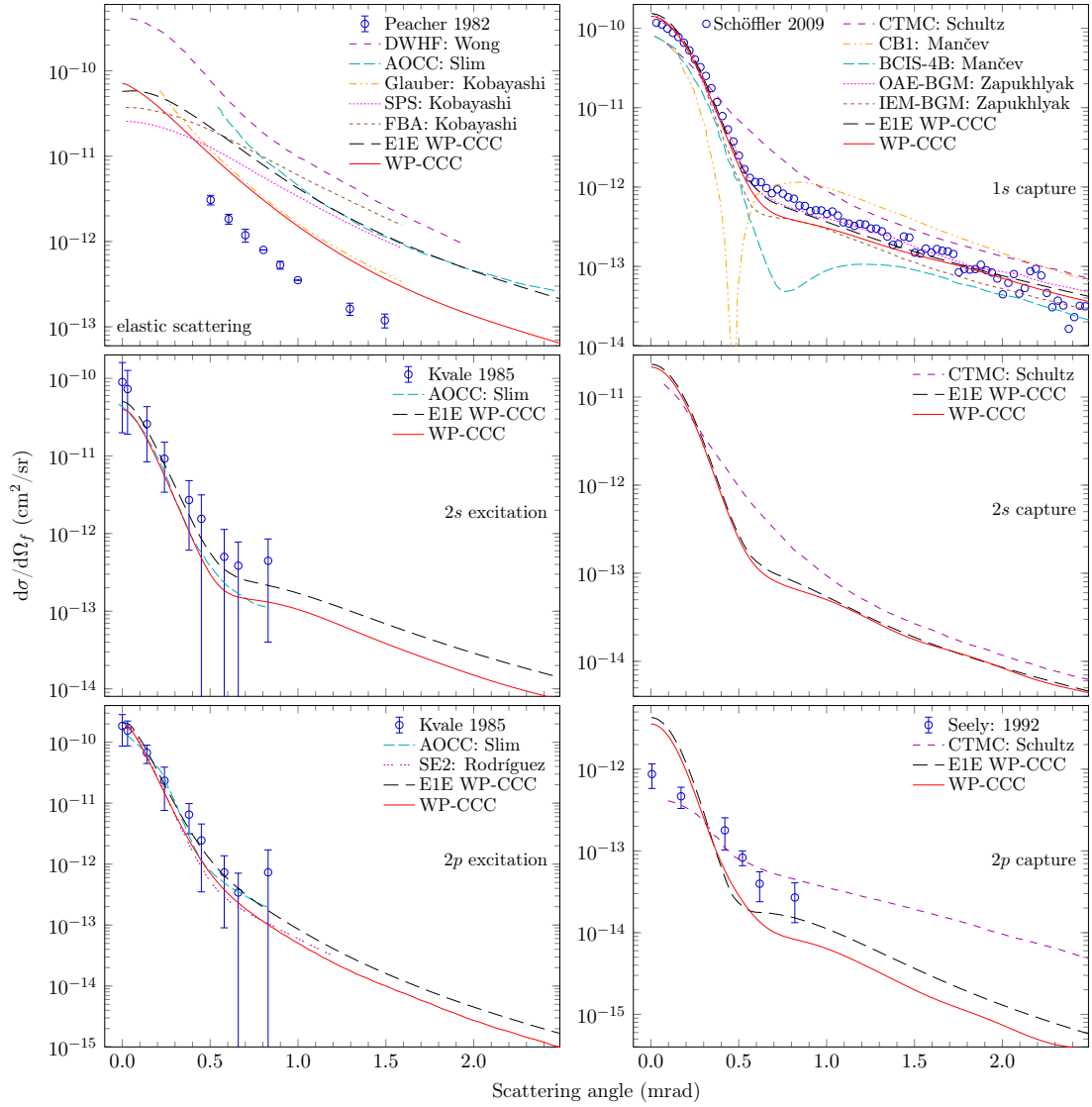


Figure 8.7: Angular differential cross sections (in the centre-of-mass frame) for elastic scattering, $2s$ and $2p$ target excitation, and electron capture into the $1s$, $2s$, and $2p$ projectile-atom states in 100 keV $p + \text{He}$ collisions. Experimental data are by Peacher *et al.* [221], Kvale *et al.* [228], Seely *et al.* [235], and Schöffler *et al.* [234]. The theoretical results are: present two-electron and E1E WP-CCC methods, DWHF method by Wong *et al.* [58], AOCC method by Slim *et al.* [227], Glauber approximation, SPS, and FBA by Kobayashi and Ishihara [220], CTMC method by Schultz *et al.* [218], CBI and BCIS-4B methods by Mančev *et al.* [225], OAE-BGM and IEM-BGM by Zapukhlyak *et al.* [229], and SE2 method by Rodríguez *et al.* [226].

For target excitation into the $2s$ and $2p$ states (centre-left and lower-left panels of Figs. 8.6–8.9, respectively) we find that the E1E WP-CCC results overestimate the two-electron WP-CCC calculations for larger scattering angles with the difference between the two methods decreasing as projectile energy increases. Nevertheless, both two-electron and E1E WP-CCC calculations agree very well with the experimental results by Kvale *et al.* [228] available at 75 and 100 keV

and for scattering angles up to 1.07 and 0.83 mrad, respectively. The AOCC calculation by Slim *et al.* [227] at 100 keV also agrees well with the experiment, following a very similar pattern as the two-electron WP-CCC method within the angular range where the data are available. The cross section for $2p$ excitation is the combination of the cross sections for excitation into the $2p_{-1}$, $2p_0$, and $2p_1$ states. Here, the situation is very similar to that of $2s$ excitation. Rodríguez *et al.* [226] performed SE2 calculations at 75 and 100 keV for scattering angles up to 0.5 mrad. Their results agree very well with our two-electron WP-CCC calculations. Again, the E1E WP-CCC $2p$ angular cross section is somewhat higher than the more accurate two-electron one away from the forward direction, but the difference between the E1E and two-electron results is still within the experimental uncertainties.

For angular differential cross sections for electron capture into the ground state of the projectile, (upper-right panels in Figs. 8.6–8.9) Schöffler *et al.* [234] reported data at 100, 150, and 300 keV using the accurate cold target recoil ion momentum spectroscopy (COLTRIMS) technique. The E1E and two-electron WP-CCC methods are in excellent agreement with their data over the entire angular range at all three energies, especially for small scattering angles less than 0.5 mrad. At very small scattering angles our results agree with the CTMC calculation of Schultz *et al.* [218] available at 100 keV. Agreement is reasonably good also at larger angles with some deviation between 0.4 and 1.2 mrad. The CB1 and the BCIS-4B methods of Mančev *et al.* [225], predict unphysical dips around 0.4 and 0.8 mrad, respectively, as they did for total capture. They agree with the data in the narrow forward cone which should ensure the resulting integrated cross section is accurate. The IEM-BGM and OAE-BGM results [229] are available for ground-state capture at 100 and 150 keV. They exhibit a similar level of agreement with the experimental data as the E1E WP-CCC results.

For capture into the $2s$ state of hydrogen, the two-electron and E1E WP-CCC results are very close to each other over the entire angular range. No

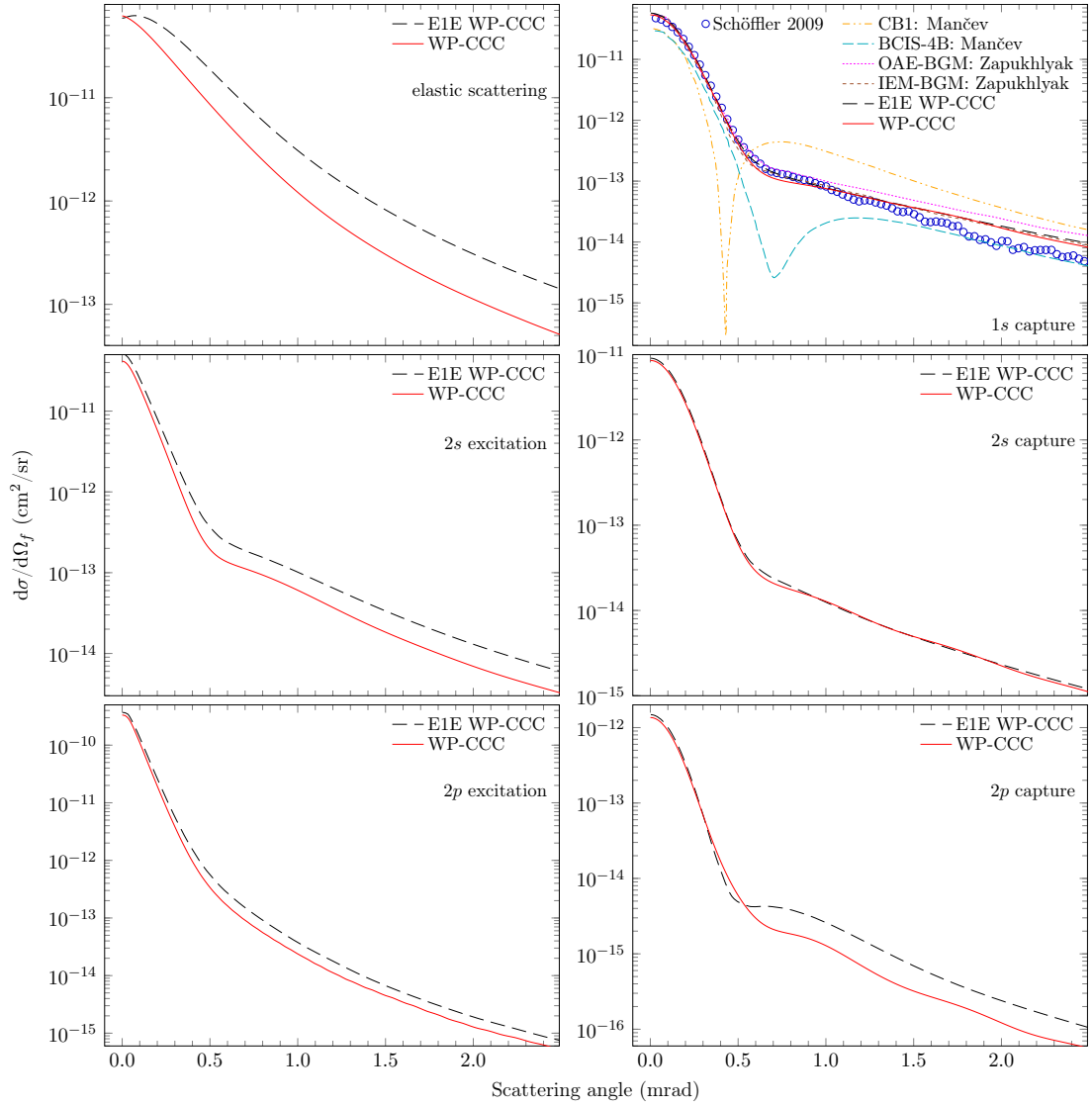


Figure 8.8: Angular differential cross sections (in the centre-of-mass frame) for elastic scattering, $2s$ and $2p$ target excitation, and electron capture into the $1s$, $2s$, and $2p$ projectile-atom states in 150 keV $p + \text{He}$ collisions. Experimental data are by Schöffler *et al.* [234]. The theoretical results are: present two-electron and E1E WP-CCC methods, CB1 and BCIS-4B methods by Mančev *et al.* [225], and OAE-BGM and IEM-BGM by Zapukhlyak *et al.* [229].

experimental data is available for this process. The CTMC calculations by Schultz *et al.* [218] are available at 100 keV. The difference between the CTMC results and the WP-CCC ones is somewhat similar to the situation with ground-state capture. For capture into the $2p$ state of hydrogen, the two-electron and E1E WP-CCC methods are in agreement for scattering angles less than ≈ 0.55 mrad after which they slightly deviate from each other. However, both methods disagree with the experiment conducted by Seely *et al.* [235] for 100 keV. The WP-CCC

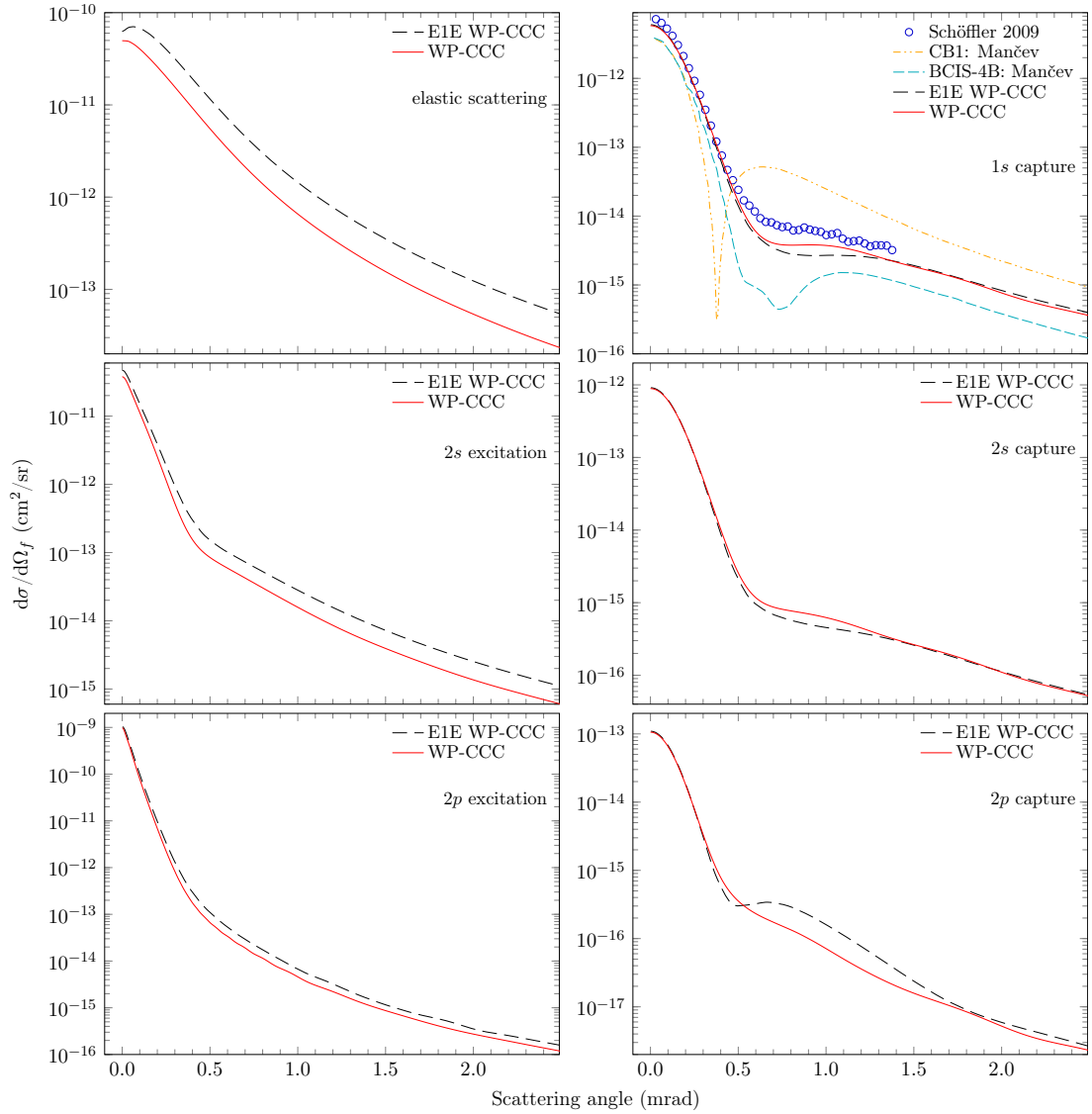


Figure 8.9: Angular differential cross sections (in the centre-of-mass frame) for elastic scattering, $2s$ and $2p$ target excitation, and electron capture into the $1s$, $2s$, and $2p$ projectile-atom states in 300 keV $p + \text{He}$ collisions. Experimental data are by Schöffler *et al.* [234]. The theoretical results are: present two-electron and E1E WP-CCC methods, CB1 and BCIS-4B methods by Mančev *et al.* [225], and OAE-BGM and IEM-BGM by Zapukhlyak *et al.* [229].

calculations overestimate it for scattering angles near the forward direction and underestimate it at larger angles. The CTMC results by Schultz *et al.* [218] are in somewhat better agreement with the experiment but still do not correctly reproduce the shape of the cross section, underestimating the experiment at small angles and overestimating it at larger angles. As a matter of fact, we note that the two-electron WP-CCC results at 25 keV are in very good agreement with the corresponding measurements by Seely *et al.* [235], but at 50 keV agreement is

already not good, just like at 100 keV (not shown).

Overall, we conclude that non-perturbative methods describe the experimental data well. We note that our method includes all interaction potentials. Some authors mentioned above solve the semiclassical Schrödinger equation without the internuclear potential and incorporate the latter in the form of a phase factor. The two-electron WP-CCC method is based on the full Schrödinger equation with the full four-body Hamiltonian. Finally, we remark that in all cases the differential cross sections display somewhat similar behaviour. They fall off fast at small angles. This changes around 0.5 mrad beyond which the fall off is slower. Larger scattering angles correspond to smaller impact parameters and vice versa. Accordingly, scattering into large angles is mostly due to the heavy-particle interaction at short distances while the electron interaction with the projectile and the target nucleus is responsible for scattering into small angles where collision takes place at relatively long distances.

8.4 Singly differential cross sections for ionisation in p+He collisions

We now turn our attention to the SDCS for single ionisation of helium. Using both the two-electron and E1E WP-CCC methods, we calculate all three types of singly differential cross sections for ionisation at 75, 100, 150, and 300 keV. Compared to p + H collisions, there is significantly more experimental and theoretical data available for the SDCS for ionisation in p + He collisions. Since ionisation is a challenging process to model, the majority of theoretical approaches are based on the FBA, such as the calculations by Manson *et al.* [236] and Salin [237]. Schulz *et al.* [238] also applied the first-order Born approximation with post-collision interaction (FBA-PCI) method and Fukuda *et al.* [239] used the partial-wave Born approximation (PWBA) to calculate the SDCS for ionisation in proton collisions with helium. The theoretical approaches based on the FBA typically

agree with experimental data for the TICS at high collision energies, but close quantitative agreement in differential ionisation has been weak, particularly for angular distributions.

Other perturbative methods applied to differential ionisation in $p + \text{He}$ collisions are the CDW method of Barna *et al.* [240], the CDW-EIS approaches of Bernardi *et al.* [241] and Barna *et al.* [240], and the eikonal distorted-wave method with static potential (DW-S) and eikonal distorted-wave method with Coulombic potential (DW-C) approaches of Fukuda *et al.* [239].

Calculations based on classical descriptions of the collision are also available for the different types of SDCS for ionisation in $p + \text{He}$ collisions. Reinhold and Olson [242] and Barna *et al.* [240] applied the CTMC method to the problem and Meng *et al.* [243] used the dynamical classical trajectory Monte Carlo (dCTMC) method. Results obtained with the binary-encounter free-fall (BE-FF) method of Gryziński [40, 244] are available for the SDCS for ionisation as a function of the emitted-electron energy.

As for the angular differential cross sections presented in Sect. 8.3, we found that a basis of $n_{\text{neg}} = 5 - \ell$ bound states and 20 discretisation bins, on both centres, was sufficient with $\ell_{\text{max}} = 3$. The value obtained by integrating the SDCS for ionisation agreed with the TICS calculated directly from the expansion coefficients within 99% for all results presented herein.

First, we present the SDCS differential in the energy of the emitted electron in Fig. 8.10. The results are presented in the laboratory frame in comparison with experiment [236, 238, 245–248] and other available calculations [40, 236, 238, 242, 244]. As seen from the figure, the two-electron and E1E WP-CCC results agree very well with all the available experimental data at 75, 100, and 300 keV, but only one set of measurements at 150 keV.

To be more specific, at 75 keV, the two-electron WP-CCC results are in excellent agreement with the experimental data by Schulz *et al.* [238] over the electron-energy range where the data are available. Noticeably, they also repro-

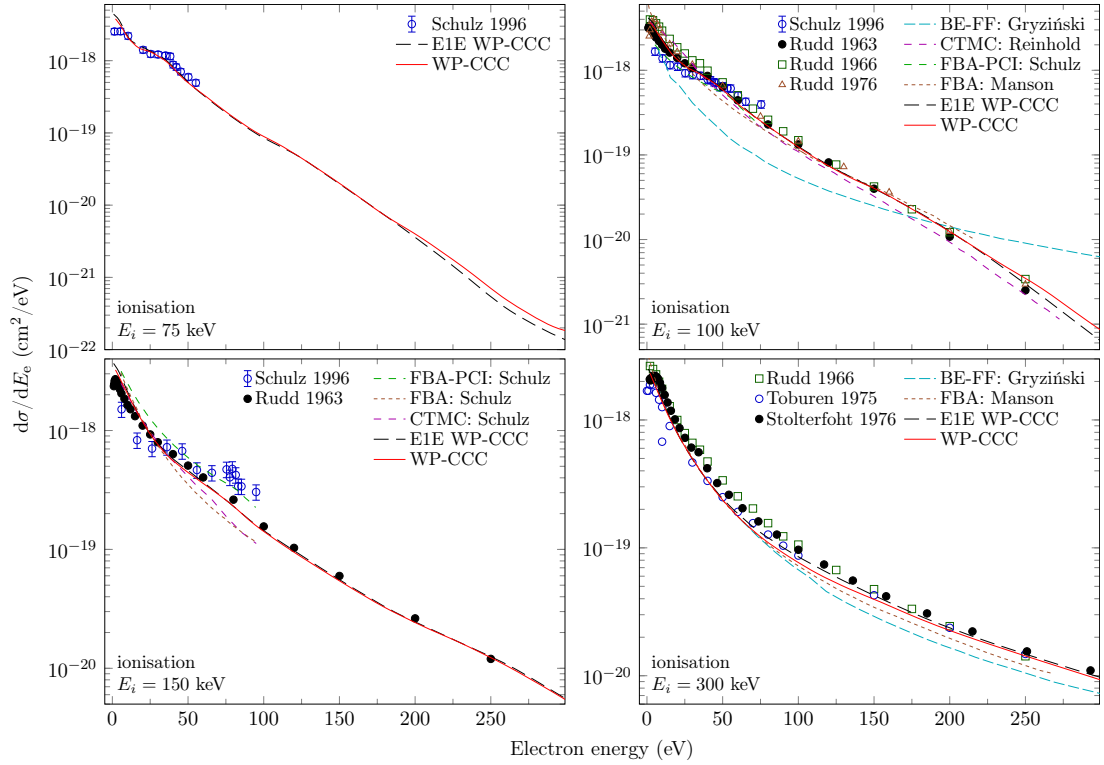


Figure 8.10: Singly differential cross sections (in the laboratory frame) for ionisation as functions of the electron energy for 75, 100, 150, and 300 keV $p + \text{He}$ collisions. Experimental data are by Schulz *et al.* [238], Rudd and Jorgensen [245], Rudd *et al.* [246], Rudd and Madison [247], Manson *et al.* [236] (labelled as Toburen), and Rudd *et al.* [248] (labelled as Stolterfoht). (Note: The raw data labelled in the figure as Rudd, Toburen and Stolterfoht are taken from Ref. [248]. As described in Ref. [248], the data from Refs. [246] and [245] were recalculated to remove certain experimental error, while the Toburen data came from Manson *et al.* [236] and was averaged to reduce the number of data points. The Stolterfoht data came from multiple sources. See Ref. [248] for details). The theoretical results are: present two-electron and E1E WP-CCC methods, BE-FF method by Gryziński [244], CTMC method by Reinhold and Olson [242], FBA, and FBA-PCI and CTMC methods by Schulz *et al.* [238], and FBA by Manson *et al.* [236].

duce the slight shoulder present in the experimental data. This feature occurs when the ejected-electron speed is approximately equal to that of the projectile. At the matching speed the ejected-electron energy is 40.8 eV, and that is exactly where is the shoulder of the SDCS obtained in the two-electron and E1E WP-CCC approach. Other calculations available at this energy are the FBA and FBA-PCI results of Schulz *et al.* [238]. The FBA-PCI results were originally presented with a scaling factor of 0.5 to compare with the experiment in shape. Figure 8.10 shows unscaled results. Though the FBA-PCI results overestimate the experimental data in magnitude, they are in better agreement in shape. On

the other hand, the simpler FBA results are in better agreement with the data in magnitude, however, they do not reproduce the shoulder structure around 40.8 eV.

The situation at 100 keV is somewhat similar. The WP-CCC results are in excellent agreement with all experimental data [238, 245–247] over the entire ejected-electron energy range. The FBA-PCI results of Schulz *et al.* [238] and FBA results of Manson *et al.* [236] fall below the experimental data of all experiments, though, somewhat surprisingly, agreement improves for the simple hydrogenic FBA [236] for ejected-electron energies larger than 100 eV. Of note is the fact that the present WP-CCC results again exhibit a slight but noticeable shoulder at 54.4 eV ejection energy which is the ejection energy where the speed of the electron matches that of the projectile. The CTMC results by Reinhold and Olson [242] also agree with the experimental data, particularly at small ejected-electron energies, though these calculations do not display the shoulder structure. The results of Reinhold and Olson [242] begin to slightly underestimate the experimental data and other methods as the ejected-electron energy increases. The classical BE-FF approach of Gryziński [40] does not agree with any experimental data at all, having too steep a slope initially and falling below and then flattening to overestimate the data at large ejected-electron energies.

At 150 keV, again the present WP-CCC results exhibit a slight but quite noticeable shoulder at 81.6 eV ejected-electron energy corresponding to the speed of the projectile. Our results agree perfectly with the experimental data of Rudd and Jorgensen [245] over the entire ejected-electron energy range. We also observe reasonably good agreement with the experiment of Schulz *et al.* [238] at the lower emission energies where these measurements were taken. The FBA-PCI and CTMC calculations of Schulz *et al.* [238] are in excellent agreement with both sets of experimental data as well as our results for ejection-energies below 40 eV, though they begin to underestimate the data after this point. These calculations also display a slight shoulder around 81.6 eV ejected-electron energy while the

FBA does not. The FBA-PCI approach tends to overestimate the experiment of Rudd and Jorgensen [245] and all other theoretical approaches across the energy range presented. However, for ejected-energies greater than 50 eV, the FBA-PCI method is in good agreement with the Schulz *et al.* [238] experiment. At these energies, this experiment slightly deviates from the other available experimental data [245].

By 300 keV projectile energy, the aforementioned shoulder structure, expected at 163.3 eV, has dissipated completely, a change that is reflected in our results. The present WP-CCC results are in excellent agreement with the experimental data of Refs. [236, 246, 248]. Agreement with the results from the hydrogenic FBA by Manson *et al.* [236] and classical BE-FF by Gryziński [40, 244] methods is very good for low ejected-electron energies, however, they slightly deviate from the experiment at emission energies greater than 100 eV.

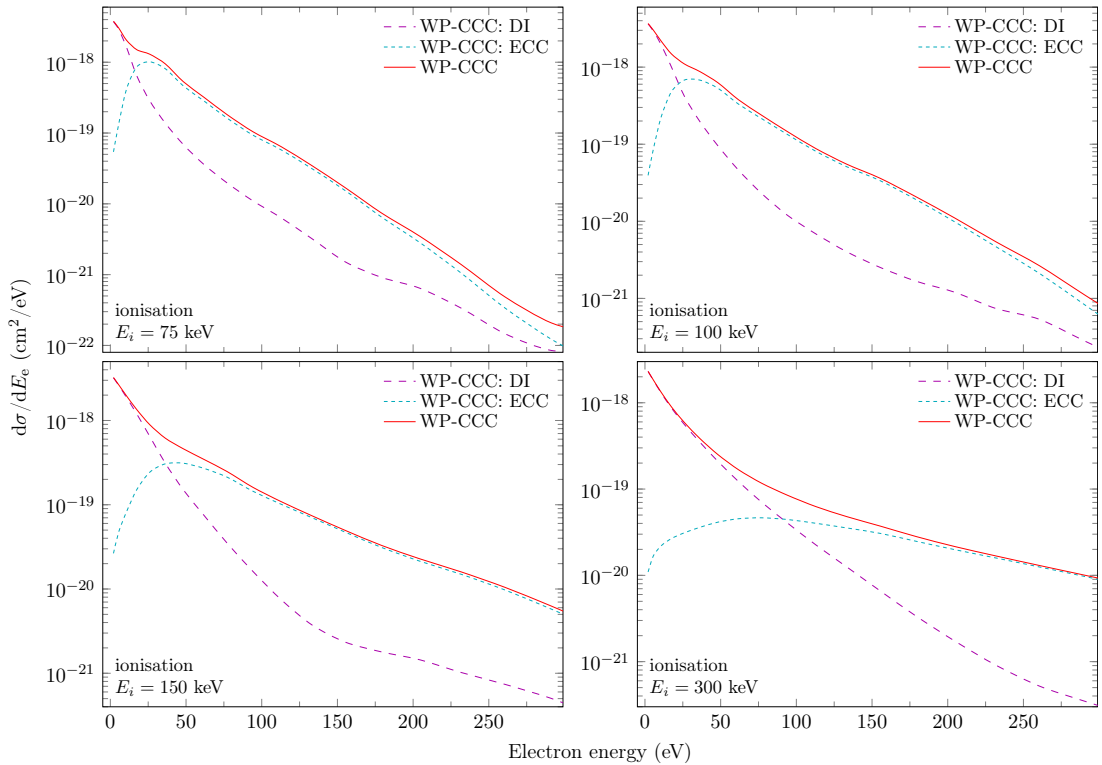


Figure 8.11: DI and ECC components for the two-electron WP-CCC result shown in Fig. 8.10.

In Fig. 8.11 we present the DI and ECC components of the two-electron WP-CCC results for the SDCS as functions of the emitted-electron energy. The

components of the SDCS obtained in the E1E WP-CCC approach are not shown here but are very similar. The effect of electron capture to the continuum changes depending on the ejected-electron energy. It can be seen that at collision energies of 75 and 100 keV, the ECC contribution constitutes most of the net differential cross section everywhere except for a narrow range of small ejected-electron energies. At 150 keV, the ECC component dominates the total SDCS at ejected-electron energies above 50 eV. By 300 keV, the low-energy region where the DI component dominates extends to about 80 eV. For low ejected-electron energies, the ECC component is negligible but becomes dominant beyond 80 eV, ensuring excellent agreement with the experiment. This demonstrates the importance of accounting for both the DI and ECC mechanisms in order to accurately describe the experimental data at intermediate collision energies.

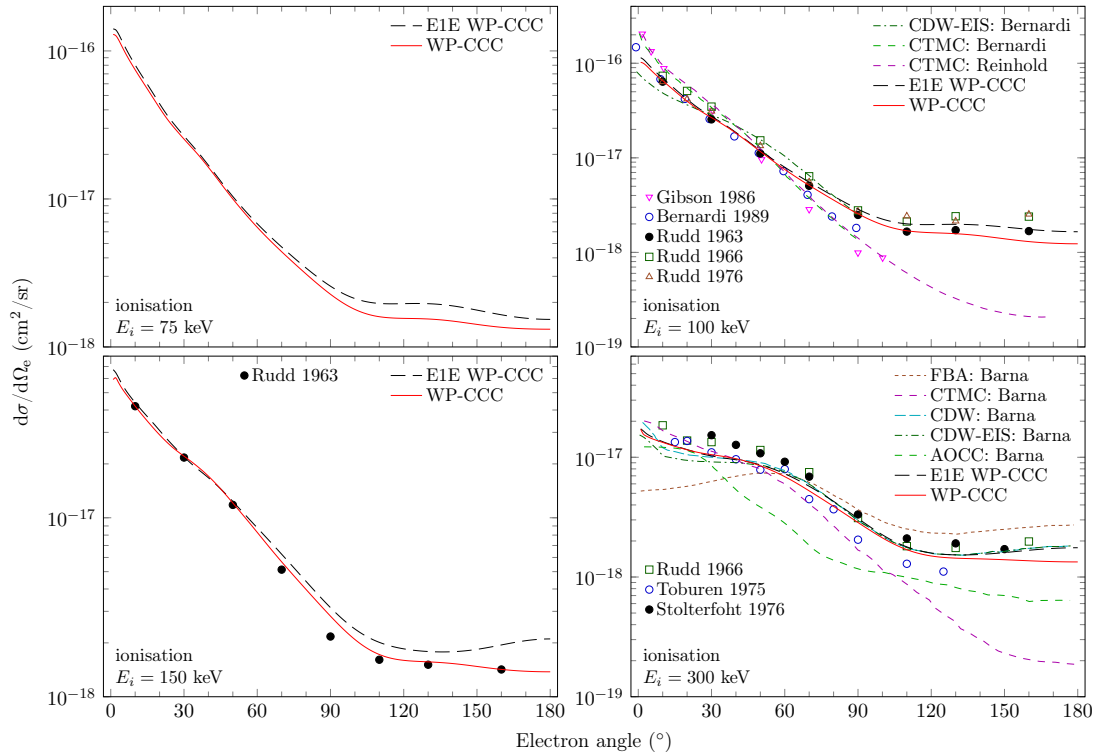


Figure 8.12: Singly differential cross sections (in the laboratory frame) for ionisation as functions of the electron angle for 75, 100, 150, and 300 keV $p + \text{He}$ collisions. Experimental data are by Gibson and Reid [249], Bernardi *et al.* [241], Rudd and Jorgensen [245], Rudd *et al.* [246], Rudd and Madison [247], Manson *et al.* [236] (labelled as Toburen), and Rudd *et al.* [248] (labelled as Stolterfoht). The theoretical results are: present two-electron and E1E WP-CCC methods, CDW-EIS and CTMC methods by Bernardi *et al.* [241], CTMC method by Reinhold and Olson [242], and FBA, CTMC, CDW, CDW-EIS, and AOCC methods by Barna *et al.* [240].

The two-electron and E1E WP-CCC results for the SDCS for ionisation as a function of the ejected-electron angle shown in Fig. 8.12, in comparison with experimental data [236, 241, 245–249] and other calculations [240–242]. Similar to the SDCS as a function of the ejected-electron energy, the results are presented in the laboratory frame. Generally, the WP-CCC calculations agree very well with experimental measurements, where available. For this type of SDCS we see some differences between the two-electron and E1E WP-CCC results. They are practically identical when the emission angle is less than 90° , but at higher ejection angles the E1E results tend to be slightly higher than the two-electron ones.

There are no experimental data available at 75 keV but we present our results for completeness. At 100 keV the WP-CCC results agree well with the experiments of Rudd and Jorgensen [245], Rudd *et al.* [246], and Rudd and Madison [247] over the entire ejected-electron angle range. However, they do not agree with the experimental data of Gibson and Reid [249] and Bernardi *et al.* [241]. Our results are lower at small angles, though at the same time they overestimate these experimental data at larger angles. Gibson and Reid [249] suggested that the data of Rudd and Jorgensen [245], Rudd *et al.* [246], and Rudd and Madison [247] were inaccurate due to the influence of electrons reflected by the chamber walls or multiple scattering in the target gas. The CTMC calculations of Reinhold and Olson [242] are in agreement with the Gibson and Reid [249] experiment, however, they do not conclude that this experiment is more accurate than the others. This is because their CTMC approach neglects the correlation effects between the two electrons. However, the present two-electron WP-CCC method uses a correlated two-electron description of the target. This could suggest that the Rudd and Jorgensen [245], Rudd *et al.* [246], and Rudd and Madison [247] measurements, with which the two-electron WP-CCC results agree, might be more accurate in the entire range of ejected-electron angles. The CDW-EIS method of Bernardi *et al.* [241] extends only to 90° , like the CTMC method of Reinhold and Olson

[242], but agrees better with the WP-CCC results within that region.

The two-electron WP-CCC results at 150 keV are in excellent agreement with the experimental data by Rudd and Jorgensen [245] over the entire range of ejected-electron angles. No other theoretical calculations are available at this collision energy. The E1E WP-CCC results are practically the same up until 90° after which they slightly overestimate the two-electron results and data of Rudd and Jorgensen [245].

Overall good agreement between the WP-CCC results and the experimental data [236, 246, 248] is again found at 300 keV. A comparative study of several different methods was performed by Barna *et al.* [240] at this energy. The study included the CTMC, FBA, CDW, CDW-EIS, and one-centre AOCC methods. The FBA results sharply deviate from the experimental data for small angles pointing at the importance of the (missing) Coulomb distortion. The CDW and CDW-EIS results of Barna *et al.* [240] that do include the Coulomb distortion indeed give significantly better agreement with the experiment. However, they deviate from each other, and from the experimental data, for angles less than 30° . Here the CDW results lie above the CDW-EIS ones and are closer to the experimental points. At angles greater than 30° both approaches agree with the experimental data. The CTMC results agree with the experimental data for angles below 90° but then significantly underestimate the data at larger angles. The single-centre AOCC results do not agree with the experimental data. This could be due to the small size of the expansion basis used and not due to the single-centre nature of the expansion since our calculations show that adding the second centre would give a negligible contribution to the SDCS in emission angle at 300 keV.

Figure 8.13 shows the DI and ECC components of the two-electron WP-CCC results for the SDCS for ionisation as functions of the emitted-electron angle. Our calculations reveal an interesting interplay between direct ionisation and electron capture into the continuum in the angular-differential cross section as well. They

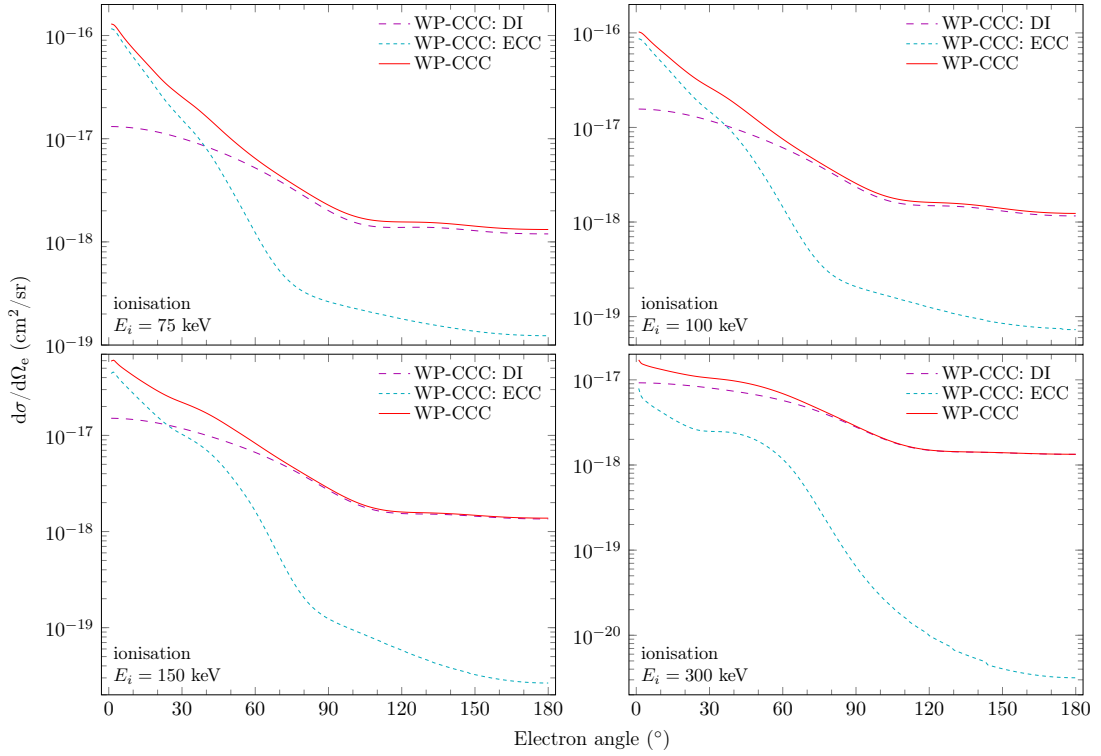


Figure 8.13: DI and ECC components for the two-electron WP-CCC result shown in Fig. 8.12.

clearly demonstrate that the ionisation cross section differential in the angle of the ejected electron is dominated by electron capture into the continuum for emission into small angles, while emission into large angles is purely due to direct ionisation.

The present results for the SDCS for ionisation as a function of the scattered-projectile angle are shown in Fig. 8.14. We compare the two-electron and E1E WP-CCC calculations to the available experimental data [243, 250, 251] and other calculations [237, 239, 243, 252]. To be consistent with the angular differential cross sections shown in Sect. 8.3, the results are presented in the centre-of-mass frame. Experimental results are available only at 300 keV. The present calculations are in particularly good agreement with the experimental data of Giese and Horsdal [250] and Kristensen and Horsdal-Pedersen [251], however, the measurements of Meng *et al.* [243] substantially deviate from them for scattering angles less than 1 mrad. The DW-S and DW-C approaches of Fukuda *et al.* [239] also exhibit good agreement with the experimental data of Giese and Horsdal

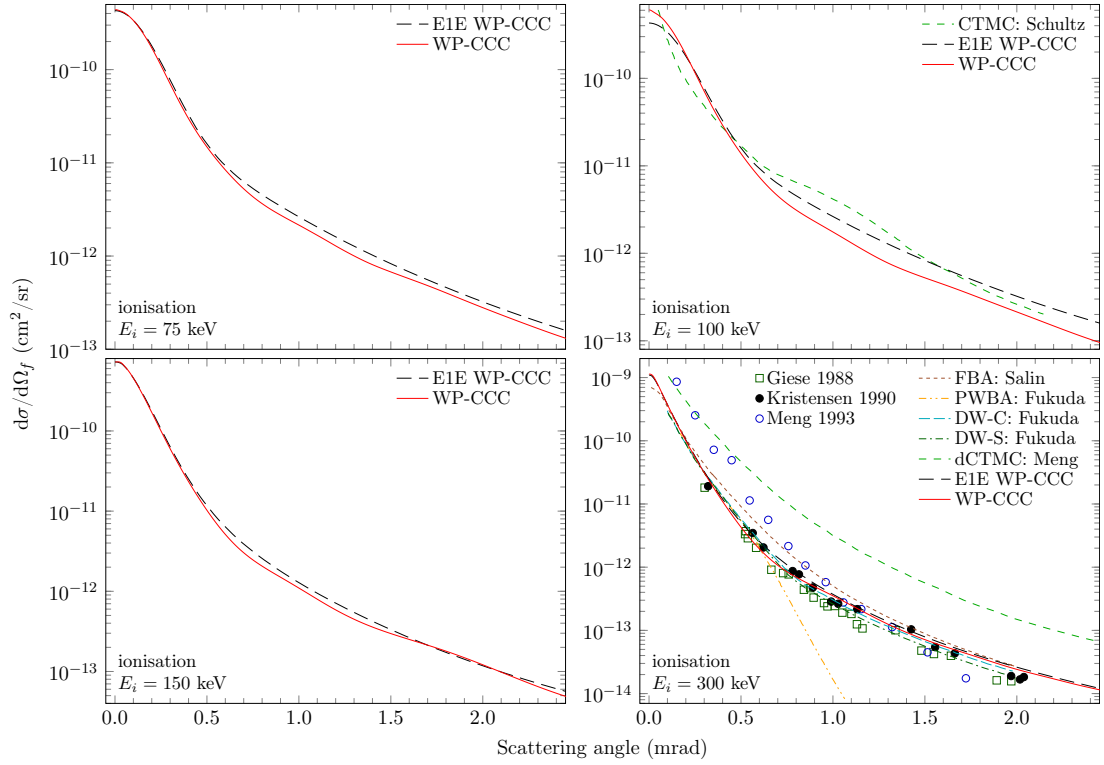


Figure 8.14: Singly differential cross sections (in the centre-of-mass frame) for ionisation as functions of the scattering angle of the projectile for 75, 100, 150, and 300 keV p + He collisions. Experimental data are by Giese and Horsdal [250], Kristensen and Horsdal-Pedersen [251], and Meng *et al.* [243]. The theoretical results are: present two-electron and E1E WP-CCC methods, CTMC method by Schultz and Olson [252], PWBA, DW-C, and DW-S methods by Fukuda *et al.* [239], and dCTMC, method by Meng *et al.* [243].

[250] and Kristensen and Horsdal-Pedersen [251]. The PWBA method by Fukuda *et al.* [239] demonstrates agreement with these experimental data for small angles, though their cross section falls off steeply to significantly underestimate all the other results for scattering angles greater than 0.6 mrad. The FBA of Salin [237] performed better due to its use of the Hartree-Fock-Slater wave function for the helium target. It is in agreement with our results in the forward direction though overestimates the experiments elsewhere. The dCTMC approach of Meng *et al.* [243] significantly overestimates the experimental data by Giese and Horsdal [250] and Kristensen and Horsdal-Pedersen [251] and all other theoretical results over the entire angular range considered. However, these authors agree with their own measurements below 0.5 mrad. The CTMC method of Schultz and Olson [252] was applied at 100 keV. The resulting cross section appears to have a somewhat

different shape to the WP-CCC one. However, there are no experimental data available at this energy to help resolve this discrepancy.

The DI and ECC components of the two-electron WP-CCC results for the SDCS as functions of the scattering angle of the projectile are shown in Fig. 8.15. At 75 keV collision energy, electron capture into the continuum dominates in the SDCS as a function of the scattered-projectile angle near the forward direction. However, as the collision energy increases the direct ionisation mechanism gradually becomes dominant. This finding reflects the fact that at 75 keV the cross section for electron capture into all bound states of the projectile atom is significantly large and comparable with the ionisation cross section, but falls sharply as the energy increases and becomes orders-of-magnitude smaller than the ionisation cross section at 300 keV (see Sect. 8.3).

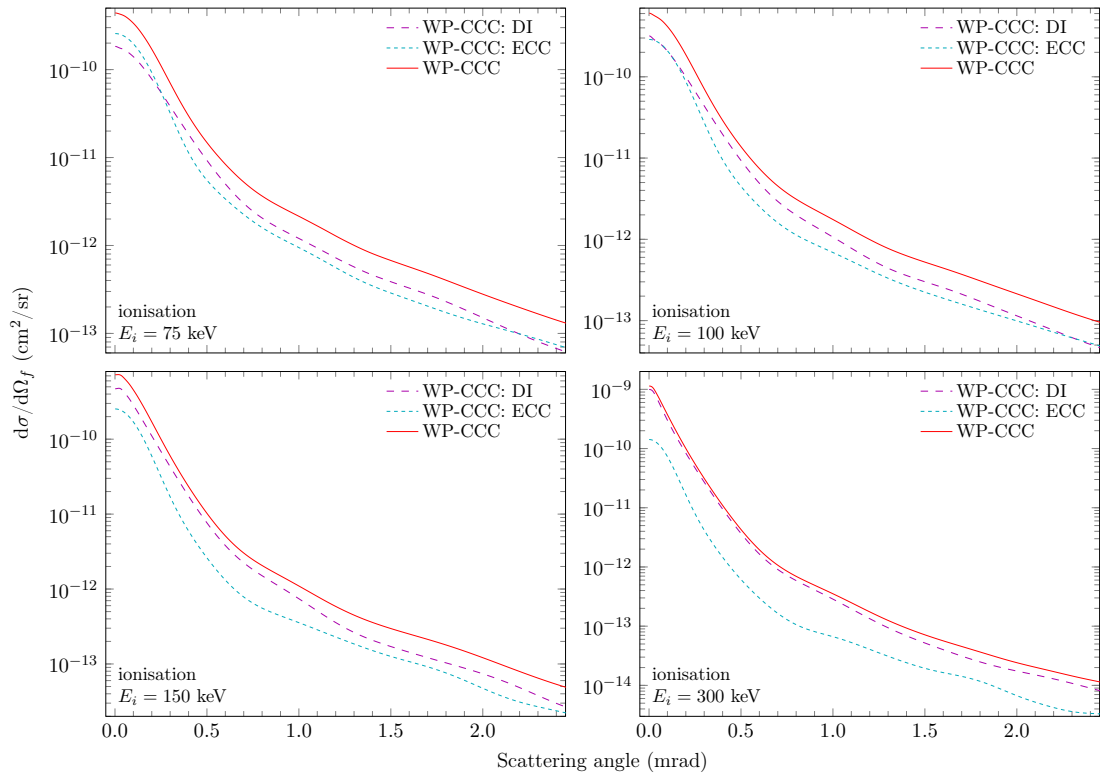


Figure 8.15: DI and ECC components for the two-electron WP-CCC result shown in Fig. 8.14.

In conclusion, we find that both the two-electron and E1E WP-CCC methods generally agree very well with the experimental data on the SDCS for ionisation in $p+\text{He}$ collisions. The present results are the first two-centre close-coupling cal-

culations of these cross sections available in the literature. We find improvement over perturbative methods which inconsistently describe the experimental data and the CTMC method which in some cases differs significantly from experiment. Furthermore, we are able to distinguish between the DI and ECC parts of our results, which allows us to analyse the relative contribution of each mechanism in different kinematic regimes. Overall, it is clear that both DI and ECC play essential roles in the collision dynamics at the considered energies. Finally, we see that the significantly simpler E1E WP-CCC method is capable of accurately reproducing the SDCS as a function of electron energy and the SDCS as a function of the scattering angle of the projectile. Only in the case of the SDCS as a function of ejected-electron angle for angles greater than 90° do we find that any significant differences between the present two-electron and E1E approaches.

8.5 Chapter summary

The two-centre wave-packet convergent close-coupling approach was applied to calculate singly differential cross sections for elastic scattering, target excitation, electron capture, and ionisation in proton-helium collisions at intermediate projectile energies. Results are presented using both the four-body WP-CCC approach based on the correlated two-electron treatment of the target and the three-body effective one-electron version based on the method developed in Ch. 7. Calculations for the angular differential cross sections of excitation and electron capture agree well with experiment. For elastic scattering, there is significant disagreement between the only available experiment at 100 keV and all available theories, though agreement in shape between the experiment and the two-electron WP-CCC results is excellent. We cannot explain the discrepancy. New experiments and independent calculations would shed more light on the situation. Overall, the results of the two-electron and effective one-electron methods agree with each other quite well indicating that the angular differential cross sections are not very sensitive to electron-electron correlations. We find that the differ-

ence between the E1E and two-electron WP-CCC results are largest for elastic scattering and for the ionisation cross section differential in the ejection angle of the electron.

We conclude that the WP-CCC method is a unique approach capable of providing a realistic differential picture of all interdependent and interconnected processes taking place in proton-helium collisions at intermediate energies where coupling between various channels is important. It does this in a unitary fashion by conserving the norm of the total scattering wave function throughout the collision process.

Chapter 9

Fully stripped helium-ion scattering on helium*

In this chapter we apply the two-electron and E1E WP-CCC methods described in Ch. 8 to collisions of He^{2+} ions with helium atoms. This is an example of a four-body scattering problem with the residual long-range Coulomb interaction in the rearrangement channel. We present cross sections for total electron-capture, excitation, and single ionisation for collision energies from 10 keV to 5 MeV. There are many experimental measurements and other theoretical calculations of the integrated cross sections for the considered processes and we make comparisons wherever available. Furthermore, we present state-selective electron-capture cross sections into the $1s$, $2s$, $2p$, $3s$, $3p$, and $3d$ states of the hydrogen-like He^+ ion formed after electron capture. However, for $\text{He}^{2+} + \text{He}$ collisions, after the electron is captured by the projectile, the formed and the residual ions become indistinguishable, which makes the state-selective measurements very challenging. Therefore, accurate calculations are required for state-selective cross sections to fill the gap where experimental data is unavailable. Collisional data for these processes is important for the ITER project.

* This chapter is adapted from work published by the candidate [253]. The publishers (the American Physical Society) provide the author with the right to use the articles, or parts thereof, in a thesis or dissertation without requesting permission.

9.1 Overview of previous work

There have been a number of experimental measurements of the total cross section for electron capture [254–258] and the total ionisation cross section [255, 257, 259–261] for $\text{He}^{2+} + \text{He}$ collisions. State-selective electron-capture cross sections were measured by Mergel *et al.* [262] and Alessi *et al.* [258], however, the experiments were unable to distinguish which He^+ ion is in the excited state in the final channel. This is because when the reaction products are symmetric their experimental separation becomes very challenging. Therefore, for $n = 2$ and 3 Refs. [258, 262] provide data for the sum of the cross sections for electron capture and residual target-ion excitation into the corresponding shell.

Depending on the projectile energy, a number of theoretical methods have been applied to the $\text{He}^{2+} + \text{He}$ scattering problem. At high energies, perturbative methods such as the four-body boundary-corrected first-order Born (CB1-4B) approximation by Mančev *et al.* [263] and the four-body CDW-EIS method by Abufager *et al.* [264] agree well with the experimental data. Terekhin *et al.* [265] used the three-body CDW-EIS method to study electron capture and ionisation in multiply charged ion collisions with helium. The results agreed well with the experimental data, especially at high impact energies. Very recently, Delibašić *et al.* [266] calculated total and state-selective cross sections for single-electron capture from the helium atom in its ground state by a number of multiply charged ions using the BCIS-3B method at intermediate and high projectile energies.

At sufficiently high energies, where the probability of electron capture is small in comparison with excitation and ionisation, single-centre close-coupling methods can produce accurate results. Barna *et al.* [267] and Pindzola *et al.* [268] applied the single-centre AOCC method to calculate the TICS at 600 keV/u, finding good agreement with the experimental data. Barna *et al.* [267] also applied the CTMC method to $\text{He}^{2+} + \text{He}$ collisions. They used two versions of the approach. In the non-equivalent electron classical trajectory Monte Carlo (NEE-

CTMC) method the four constituents of the collision system are treated explicitly, although the electron-electron interaction is neglected. The helium wave functions were built as products of two different single-particle wave functions. The second approach, called the equivalent electron classical trajectory Monte Carlo (EE-CTMC) method, is a three-body method consisting of the projectile, the active electron, and the remaining He^+ ion. The two-electron wave functions were constructed as products of two identical single-particle wave functions. The NEE-CTMC method was found to agree better with the experiment than the EE-CTMC one; however, both methods were not as successful as the AOCC method for the purpose of investigating the ionisation process.

Baxter and Kirchner [269] developed two methods for calculating ion collisions with helium based on the TDDFT. These are the time-dependent density-functional theory using the Wilken-Bauer correlation integral (TDDFT-WB) approach and the time-dependent density-functional theory using the independent-event-model (TDDFT-IEM) approach. Comparison with experimental data revealed that the former provides a more accurate prediction of the cross sections for electron capture and ionisation. In particular, the TDDFT-WB method significantly improved agreement between theory and experiment for the total electron-capture cross section in the problematic region below 100 keV/u.

The two-centre AOCC method was applied to study low- and intermediate-energy $\text{He}^{2+} + \text{He}$ collisions by Fritsch [270]. Their approach accounted for electron-electron correlations, which play an important role at lower incident energies. Particular attention was paid to obtaining partial cross sections for single transfer, transfer-excitation, and excitation of the target, which are sensitive to the target description.

9.2 Calculations of integrated cross sections

We now present our results for the integrated cross sections for $\text{He}^{2+} + \text{He}$ collisions. Using both the two-electron and E1E WP-CCC methods systematic calcu-

lations were performed. The convergence of the results was tested by gradually increasing the number of both target-centred and projectile-centred states. We found that a basis containing $n_{\text{neg}} = 5 - \ell$ bound states and $n_{\text{pos}} = 20$ to 30 bins, depending on the incident energy, with $\ell_{\text{max}} = 3$ was sufficient for the integrated cross sections to converge. Impact parameters up to $b_{\text{max}} = 15$ a.u. were found to be sufficient to obtain convergence and the maximum electron momentum varied from $\kappa_{\text{max}} = 4.0$ to 8.0 a.u. across the considered range of incident energies.

9.2.1 Single-electron-capture cross section

In Fig. 9.1 we present the two-electron and E1E WP-CCC total cross sections for single-electron capture for $\text{He}^{2+} + \text{He}$ collisions. The experimental data are only available below 1 MeV/u. In the lower panel we show the results for a wide energy range on a logarithmic scale. There is very good agreement between all the theoretical calculations and the experimental measurements above 200 keV/u. Thus, we can conclude that the high-energy electron-capture problem is fairly well understood as far as the integrated cross section is concerned. However, the situation is less clear in the intermediate-energy region highlighted in the upper panel of Fig. 9.1 using a linear scale. As one can see, there is significant deviation among the theoretical results. As expected, the high-energy perturbative methods [263, 264, 266] substantially overestimate the experimental data in this region. On the other hand, the non-perturbative methods [269] predict dumping of the cross section as energy decreases. The present results produce the maximum of the cross section to be around 35 keV/u, in agreement with the measurements. However, both two-electron and E1E WP-CCC methods overestimate the experimental data near the maximum of the cross section. Not surprisingly, the two-electron WP-CCC method performs better as it accounts for the electron-electron correlation and electron-exchange effects. The deviation from the data by Rudd *et al.* [254] is about 15% at most. This can be considered as reasonably good agreement given the fact that the deviation between the two sets of independent

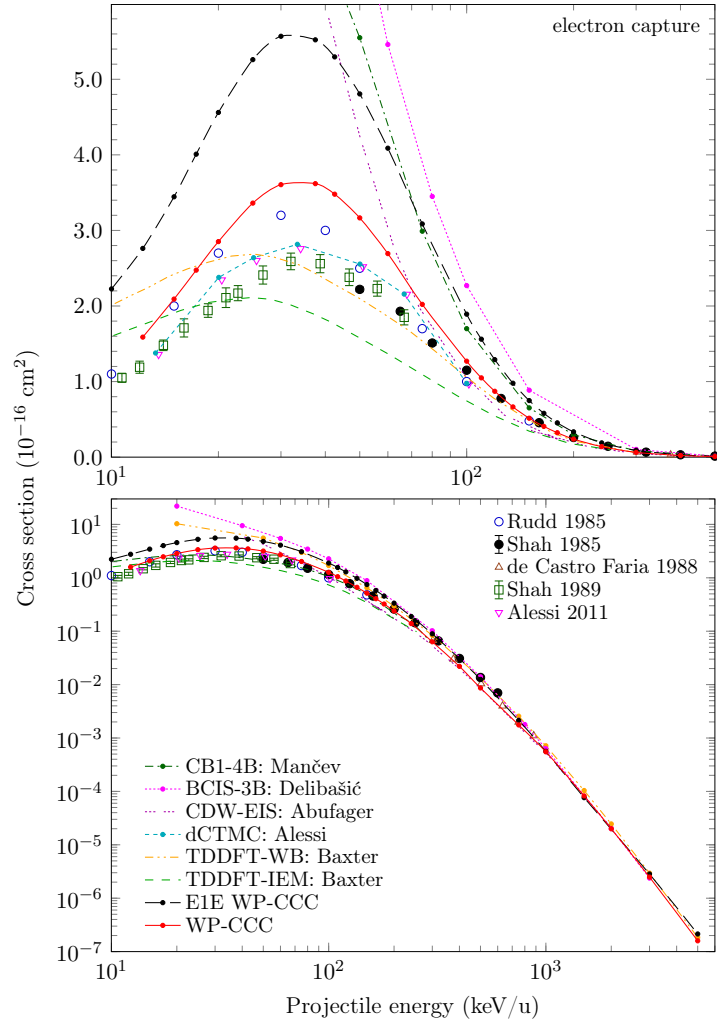


Figure 9.1: Single-electron-capture cross section for $\text{He}^{2+} + \text{He}$ collisions (upper and lower panels are in the linear and logarithmic scales, respectively). Experimental data are by Rudd *et al.* [254], Shah and Gilbody [255], de Castro Faria *et al.* [256], Shah *et al.* [257], and Alessi *et al.* [258]. The theoretical results are: present two-electron and E1E WP-CCC methods, CB1-4B method by Mančev *et al.* [263], BCIS-3B method by Delibašić *et al.* [266], CDW-EIS method by Abufager *et al.* [264], dCTMC method by Alessi *et al.* [258], and TDDFT-WB method and TDDFT-IEM method by Baxter and Kirchner [269]. The key in the lower panel applies to both panels.

measurements by Rudd *et al.* [254] and Shah *et al.* [257] reaches 25%. The two sets of results by Baxter and Kirchner [269] based on the TDDFT are similar in shape, with the TDDFT-WB method giving a systematically larger cross section than the TDDFT-IEM one, in better agreement with experiment, at all energies. The dCTMC calculations are in very good agreement with the experimental data of Shah and Gilbody [255] and Shah *et al.* [257] starting from 30 keV/u. Overall, we can see that the two-electron WP-CCC and TDDFT-WB calculations agree best with the experimental data in the entire energy range considered.

9.2.2 State-selective electron-capture cross sections

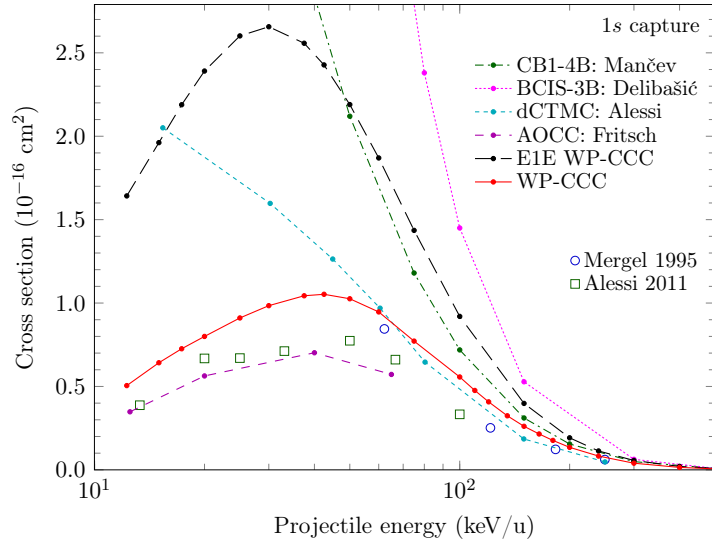


Figure 9.2: Partial $1s$ cross section for electron capture in $\text{He}^{2+} + \text{He}$ collisions. Experimental data are by Mergel *et al.* [262] and Alessi *et al.* [258]. The theoretical results are: present two-electron and E1E WP-CCC methods, CB1-4B method by Mančev *et al.* [263], BCIS-3B method by Delibašić *et al.* [266], dCTMC method by Alessi *et al.* [258], and AOCC method by Fritsch [270].

Figure 9.2 shows the cross sections for electron capture into the ground state of the He^+ ion. Our two-electron and E1E WP-CCC results are compared with the experimental data by Mergel *et al.* [262] and Alessi *et al.* [258], as well as the dCTMC [258], CB1-4B [263], BCIS-3B [266], and AOCC [270] calculations. The figure exposes a huge discrepancy between various theoretical methods for this important capture channel. The two-electron WP-CCC results are overall in fairly good agreement with the experimental data, while the E1E WP-CCC ones significantly overestimate the data near its maximum, highlighting the importance of accounting for the electron-electron correlation and electron-exchange effects. The AOCC method of Fritsch [270], which also takes the interaction of the electrons into account, is the only theory that agrees well with the experimental data of Alessi *et al.* [258]. However, the results are available only below 65 keV/u. The dCTMC calculations of Alessi *et al.* [258] overestimate the two-electron WP-CCC results at lower energies but are in good agreement above 60 keV/u.

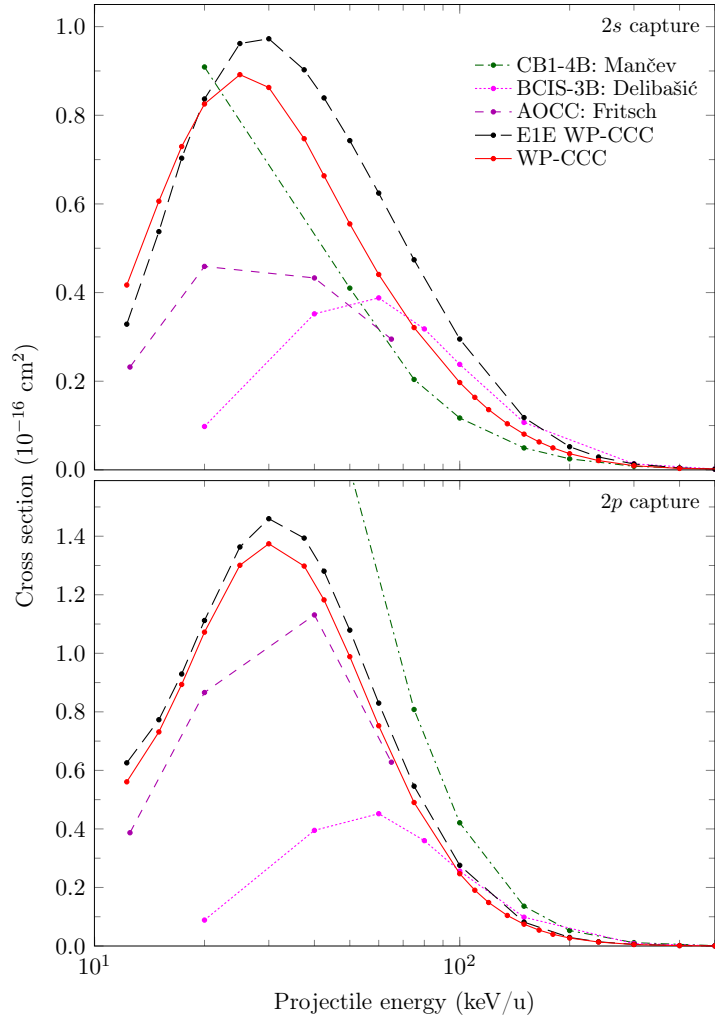


Figure 9.3: Partial 2ℓ cross sections for electron capture in $\text{He}^{2+} + \text{He}$ collisions. The theoretical results are: present two-electron and E1E WP-CCC methods, CB1-4B method by Mančev *et al.* [263], BCIS-3B method by Delibašić *et al.* [266], and AOCC method by Fritsch [270]. The key in the upper panel applies to both panels.

In Figs. 9.3 and 9.4 the two-electron and E1E WP-CCC calculations for capture into excited states are compared with the similar results based on the CB1-4B method by Mančev *et al.* [263] and the BCIS-3B method by Delibašić *et al.* [266]. The cross sections for the $2s$ and $2p$ states are shown in Fig. 9.3 and the results for the 3ℓ states are presented in Fig. 9.4, summed over the magnetic quantum numbers where applicable. Figure 9.3 reveals substantial discrepancy between various theoretical methods for these $n = 2$ capture channels at low energies. We emphasise, however, that all the methods are in excellent agreement with each other at high energies, not only for the total cross section (shown in Fig. 9.1) but also for practically all the state-selective cross sections (not shown). We can see

substantial deviations for the $n = 3$ capture channels as well, however the two-electron WP-CCC and the AOCC methods are in reasonably good agreement, except for capture into the $3s$ state where the WP-CCC results are much higher. It can be seen that the E1E cross sections somewhat overestimate the two-electron WP-CCC ones at intermediate energies, but the difference is not as high as it was for capture into the ground state. The results from all the methods merge as the incident energy increases above 200 keV/u. Another observation is that both two-electron and E1E WP-CCC calculations for electron capture into the $3d$ state show oscillatory behaviour at low energies, where there is no clear maximum.

Figure 9.5 shows the cross sections for electron capture into the $n = 2$ and 3 shells (summed over the orbital angular momentum and magnetic quantum numbers). We use the notation suggested by Mergel *et al.* [262] to denote the states of the ion formed by the projectile after electron capture and the residual target ion in the final channel. In this notation, (n, n') indicates the $\text{He}^{2+} + \text{He}(1s^2) \rightarrow \text{He}^+(n) + \text{He}^+(n')$ process. We contrast our results against the experimental data by Mergel *et al.* [262] and Alessi *et al.* [258] for the $(n, n') + (n', n)$ process, meaning that the experiments do not distinguish which He^+ ion is in which state. We emphasise that the dCTMC calculations by Alessi *et al.* [258] are for the $(n, n') + (n', n)$ process, however our results as well as the CB1-4B [263] and BCIS-3B [266] calculations ones correspond to the $(n, 1)$ case. As one can see from the figure, our E1E and two-electron WP-CCC results for the $(2, 1)$ channel agree with the experimental data for $(2, 1) + (1, 2)$ starting from 60 keV/u. Agreement with the experimental data for the $(3, 1) + (1, 3)$ process is seen starting from 100 keV/u. This allows us to conclude that above 60 and 100 keV/u the dominant contribution to the cross section of the $(2, 1) + (1, 2)$ and $(3, 1) + (1, 3)$ processes come from the $(2, 1)$ and $(3, 1)$ channels, respectively. We also note that there is fair agreement between our two approaches throughout the entire energy range, especially at high energies. The dCTMC results for the $(2, 1) + (1, 2)$ process roughly follow the experimental data even at low energies

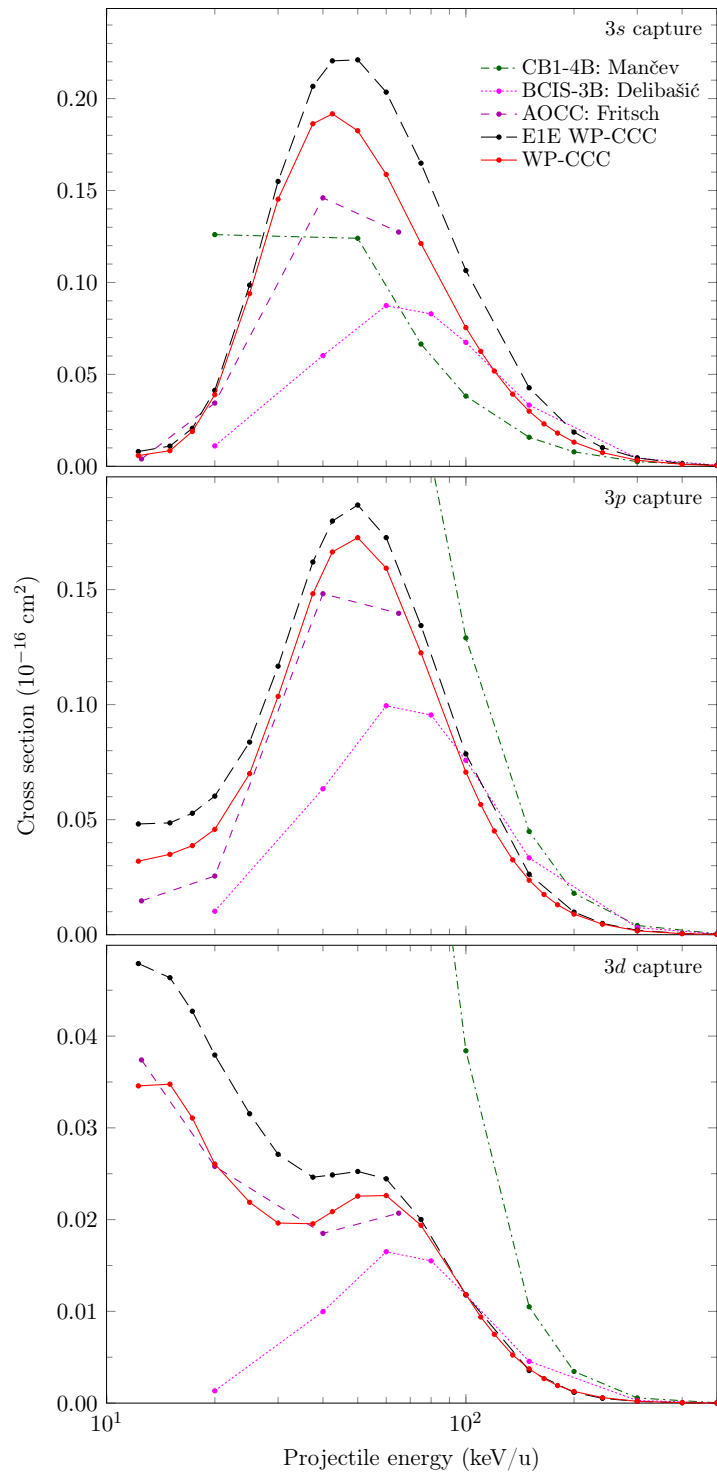


Figure 9.4: Partial 3ℓ cross sections for electron capture in $\text{He}^{2+} + \text{He}$ collisions. The theoretical results are: present two-electron and E1E WP-CCC methods, CB1-4B method by Mančev *et al.* [263], BCIS-3B method by Delibašić *et al.* [266], and AOCC method by Fritsch [270]. The key in the upper panel applies to all panels.

but they completely fail to reproduce the data for the $(3, 1) + (1, 3)$ process. The lower panel in Fig. 9.5 appears to suggest that the CB1-4B method of Mančev *et al.* [263] better describes the $(3, 1) + (1, 3)$ data at 20 and 50 keV/u. However,

the agreement is accidental since, first, the CB1-4B results are for the (3, 1) process only and, second, the method is known to significantly overestimate the state-selective electron-capture cross sections at these energies. Overall, there is clearly a need for better modelling for the $(n, n') + (n', n)$ process.

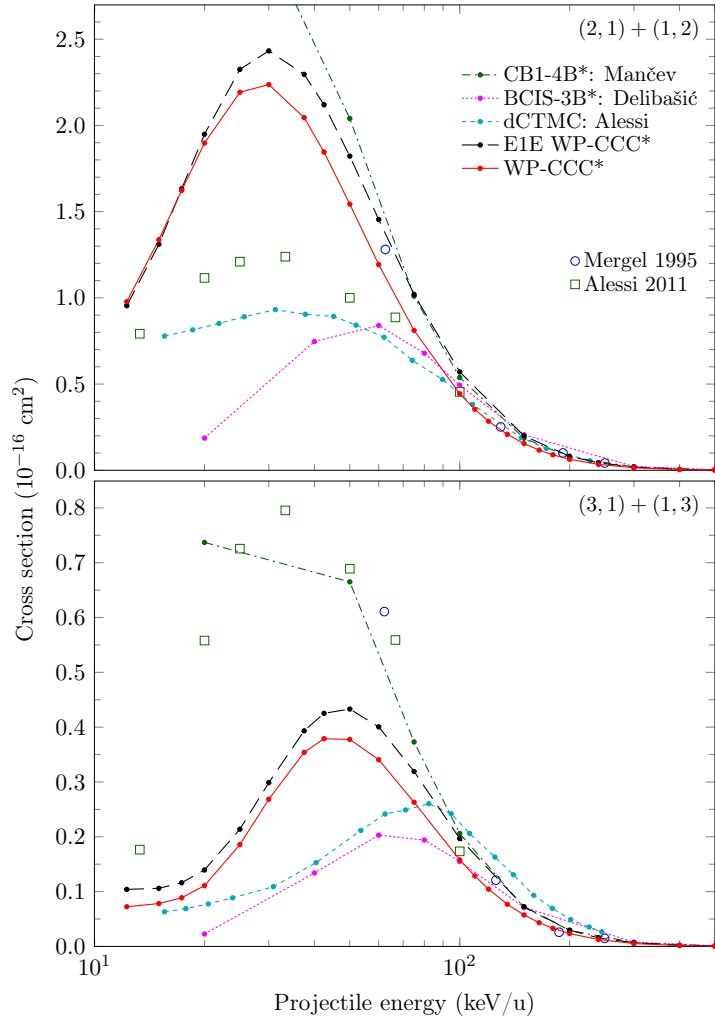


Figure 9.5: State-selective electron-capture cross sections for the $\text{He}^{2+} + \text{He}(1s^2) \rightarrow \text{He}^+(n) + \text{He}^+(n')$ processes for (2, 1) + (1, 2) (upper panel) and (3, 1) + (1, 3) (lower panel). Experimental data are by Mergel *et al.* [262] and Alessi *et al.* [258]. The measurements do not distinguish which He^+ ion is which state. The theoretical results are: present two-electron and E1E WP-CCC methods, dCTMC by Alessi *et al.* [258], BCIS-3B method by Delibašić *et al.* [266], and CB1-4B method by Mančev *et al.* [263]. The asterisk after the method name indicates that the corresponding calculations include the contributions from the $\text{He}^{2+} + \text{He}(1s^2) \rightarrow \text{He}^+(n) + \text{He}^+(n' = 1)$ channels only. The key in the upper panel applies to both panels.

9.2.3 Elastic-scattering cross section

The present results for elastic scattering are shown in Fig. 9.6. The E1E WP-CCC cross section is consistently larger than the two-electron WP-CCC one across the entire energy range considered. The E1E WP-CCC results appear to increasingly overestimate the elastic-scattering cross section as the projectile energy diminishes. To the best of our knowledge, there are no experimental data or other theoretical results for elastic scattering available in the literature.

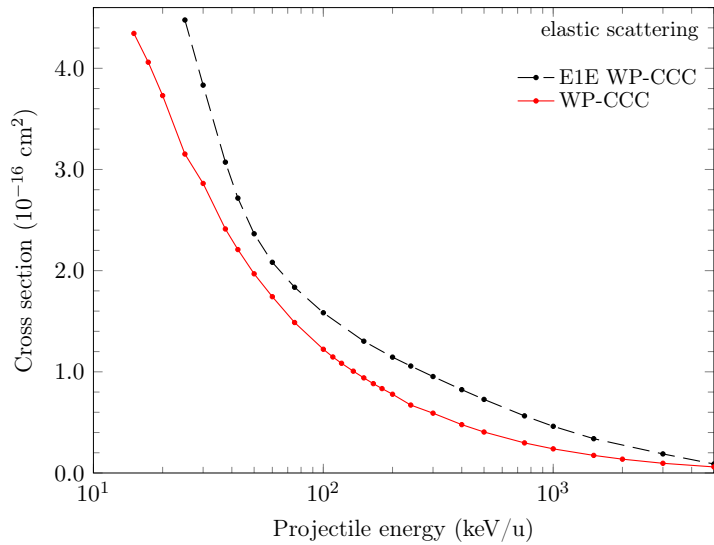


Figure 9.6: Elastic-scattering cross section for $\text{He}^{2+} + \text{He}$ collisions. The theoretical results are: present two-electron and E1E WP-CCC methods and AOCC method by Fritsch [270].

9.2.4 State-selective target-excitation cross sections

Figures 9.7 and 9.8 show our results for excitation into the 2ℓ and 3ℓ states of the target, respectively. The E1E WP-CCC results for excitation into the $3d$ subshell are shown only from 70 keV and above due to difficulties in reaching convergence while maintaining the unitarity of the norm of the total scattering wave function at lower energies. In both figures we also show the AOCC calculations of Fritsch [270]. Starting from 50 keV/u, the cross section for excitation into the 2ℓ state becomes larger than all the other excitation cross sections, making this channel the most probable target-excitation channel at higher energies.

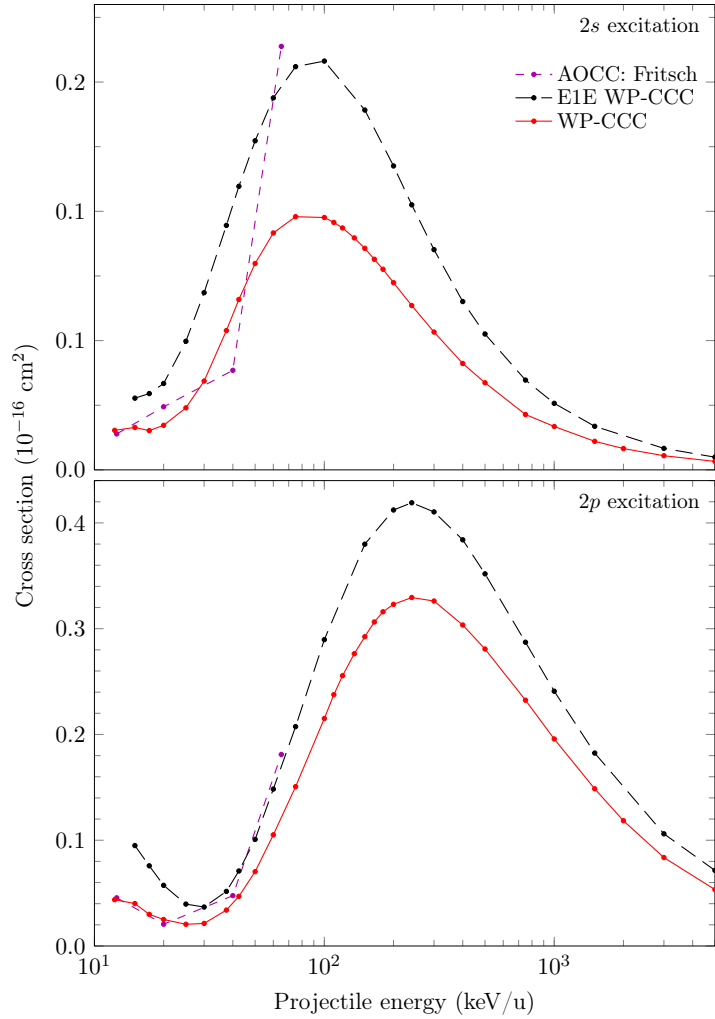


Figure 9.7: Partial 2ℓ cross sections for target excitation in $\text{He}^{2+} + \text{He}$ collisions. The theoretical results are: present two-electron and E1E WP-CCC methods and AOCC method by Fritsch [270]. The key in the upper panel applies to both panels.

We observe different levels of agreement between the three sets of calculations for different states. While below 40 keV/u the AOCC and WP-CCC partial excitation cross sections appear more or less to agree with the corresponding counterparts, at 65 keV/u they deviate substantially. For instance, the AOCC cross sections for $2s$ and $2p$ excitation are about 70% larger than the corresponding two-electron WP-CCC results. Disagreement is even bigger for $3p$ excitation. We note the present cross sections for excitation into states with the largest orbital angular momentum show a minimum at small energies. For $2p$ and $3d$ states, the minima can also be seen in the AOCC calculations, though the density of the energy points used by Fritsch [270] is not sufficient to exhibit this feature clearly.

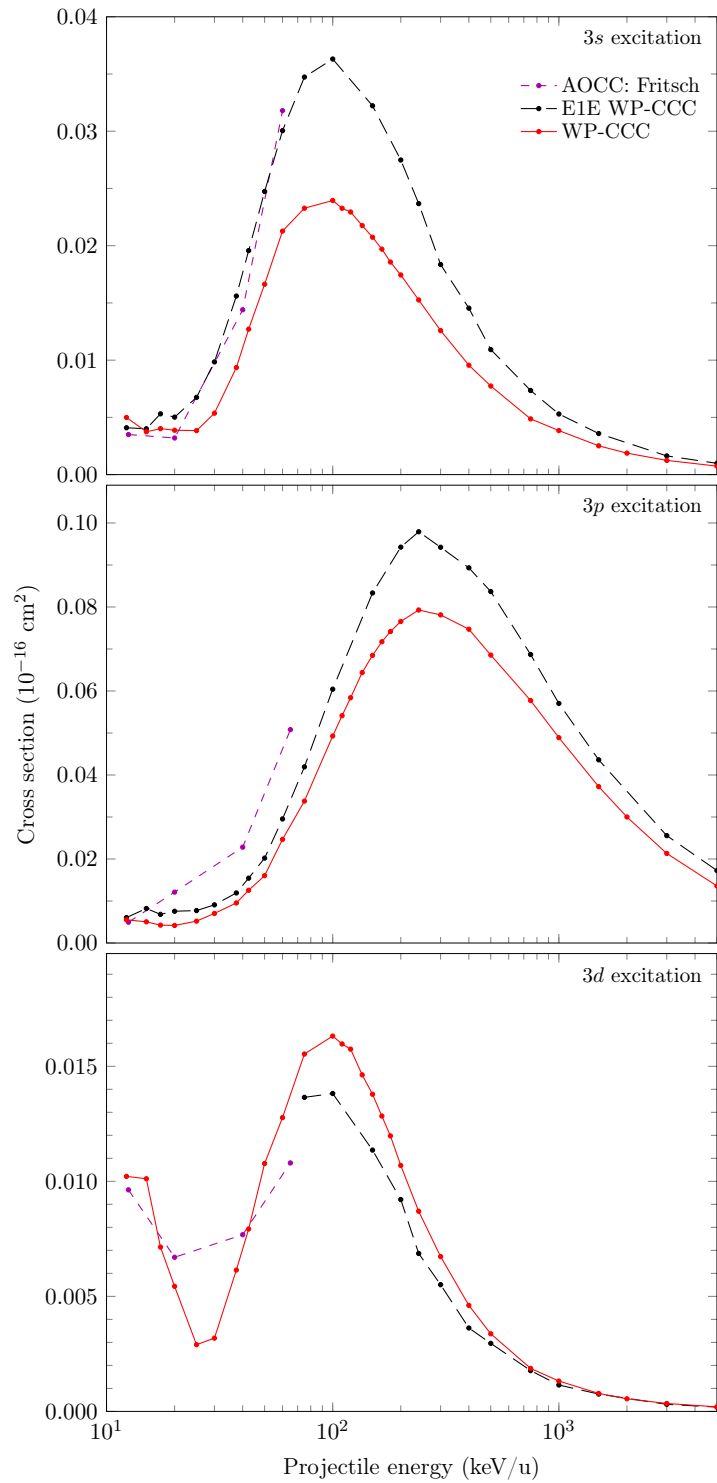


Figure 9.8: Partial 3ℓ cross sections for target excitation in $\text{He}^{2+} + \text{He}$ collisions. The theoretical results are: present two-electron and E1E WP-CCC methods and AOCC method by Fritsch [270]. The E1E WP-CCC results are shown only for energies where convergent results could be obtained. The key in the upper panel applies to all panels.

The E1E WP-CCC results are consistently larger than the corresponding two-electron calculations for all considered target-excitation channels except for $3d$. At the highest energies the two methods begin to converge, but the E1E WP-CCC

results are still larger for the $2p$ and $3p$ channels. Combined, Figs. 9.6–9.8 seem to suggest that electron-correlation effects are particularly important for direct-scattering channels. This makes sense as these cross sections are very sensitive to the accuracy of the target structure.

9.2.5 Single-ionisation cross section

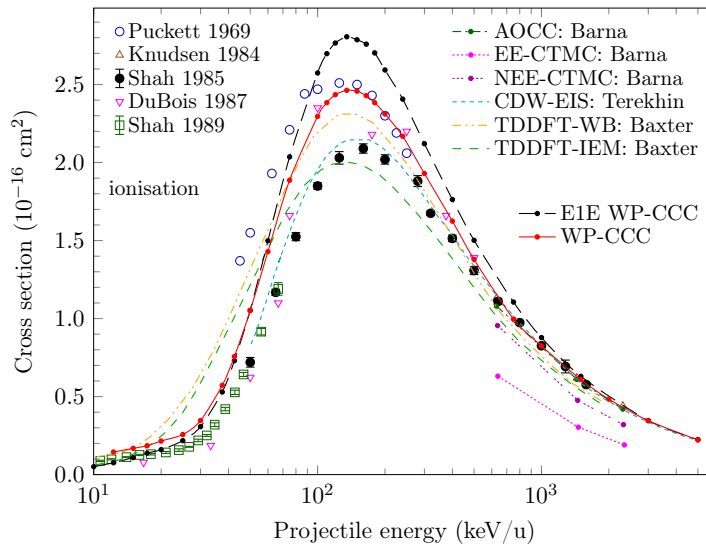


Figure 9.9: Single-ionisation cross section for $\text{He}^{2+} + \text{He}$ collisions. Experimental data are by Puckett *et al.* [259], Knudsen *et al.* [260], Shah and Gilbody [255], DuBois [261], and Shah *et al.* [257]. The theoretical results are: present two-electron and E1E WP-CCC methods, AOCC, EE-CTMC, and NEE-CTMC methods by Barna *et al.* [267], CDW-EIS method by Terekhin *et al.* [265], and TDDFT-WB and TDDFT-IEM methods by Baxter and Kirchner [269].

Finally, we consider ionisation of the helium target. Figure 9.9 shows the present two-electron and E1E WP-CCC results for the integrated cross section for single ionisation of helium in comparison with available experimental data and other calculations. We note that both our methods include not only direct ionisation of the target but also electron capture to the continuum of the projectile. The two-electron and E1E results agree well with each other at low- and high-energies. However, the E1E results somewhat overestimate the two-electron ones at the intermediate energies, the difference being especially noticeable around 150 keV/u, where the peak of the cross section is observed. Overall, the discrepancy between the two theories is within 15%.

Our results are generally similar in shape to the experimental data by Shah and Gilbody [255] and Shah *et al.* [257]. While they are in good agreement with the data at low and high energies, one can see a noticeable discrepancy at intermediate energies. Near the peak, the two-electron WP-CCC results overestimate the data from Shah and Gilbody [255] by about 20%. This appears to be a systematic problem in practically all close-coupling approaches to ionisation in ion-atom collisions (see Refs. [33, 173, 227, 271, 272]). The WP-CCC results are also in very good agreement with the experiment of Puckett *et al.* [259] in the energy range above 150 keV/u.

We note that our two-electron calculations agree very well with the experimental data of Knudsen *et al.* [260] available at three projectile energies (0.63, 1.44, and 2.31 MeV/u). At these energies, Barna *et al.* [267] provided the results of three distinct theoretical methods: the single-centre AOCC approach and the EE-CTMC and NEE-CTMC methods. The AOCC results are in excellent agreement with the experimental data and our calculations. However, both of the CTMC theories underestimate the experimental data, with the NEE-CTMC method agreeing better than the EE-CTMC one. Pindzola *et al.* [268] also performed single-centre AOCC calculations at high energies (not shown). As expected, their results were practically identical to those by Barna *et al.* [267]. The TDDFT-WB and TDDFT-IEM methods by Baxter and Kirchner [269] were also applied to calculate the single-ionisation cross section. We can see that the results obtained using the TDDFT-WB approach agree with the TDDFT-IEM calculations at low and high energies, but overestimate them in the intermediate-energy region. The TDDFT-WB calculations are in very good agreement with the available experimental data above 250 keV/u. The three-body CDW-EIS approach by Terekhin *et al.* [265] demonstrates very good agreement with the data of Shah and Gilbody [255] and Shah *et al.* [257].

9.3 Chapter summary

In this chapter we applied the two-electron and E1E WP-CCC methods to calculate the integrated cross sections for all single-electron processes occurring in $\text{He}^{2+} + \text{He}$ collisions. Results are presented over a wide range of incident energies from 10 keV/u to 5 MeV/u, where one-electron processes are expected to dominate. Attention is focussed on the intermediate-energy region where we find substantial deviations between various theoretical methods. Overall, our two approaches show fairly good consistency with each other for all considered processes, perhaps with the exception of capture into $\text{He}^+(1s)$. The cross sections for total and state-selective electron capture as well as for single ionisation show good agreement with the available experimental results and other theoretical calculations. For total electron capture, we observe generally good agreement between our results and the experimental data throughout the entire energy range considered. However, discrepancies between various theoretical results for the total and state-selective electron-capture cross sections below 100 keV/u require more investigation using independent methods. For single ionisation, excellent agreement with experiment is obtained at high and low energies, whereas at intermediate energies the agreement with the data remains somewhat unsatisfactory.

For electron capture and ionisation processes, the correlated two-electron calculations show much better agreement with the available experimental data than the effective single-electron ones. In particular, our results demonstrate that accurate description of state-selective electron capture and direct scattering at intermediate and low energies requires proper account of the electron-electron correlations in the target treatment and electron-exchange effects between the reaction products in the electron-transfer channels.

Chapter 10

Proton scattering on molecular hydrogen^{*}

Accurately modelling the various processes that take place in ion collisions with molecules is a challenging problem. The simplest homonuclear diatomic molecule is H_2 , but even for this system the development of accurate electronic wave functions is very difficult. In addition to the presence of two electrons, the multicentre nature of the molecule makes it difficult to accurately represent its structure, requiring complex theoretical descriptions and computationally demanding codes. However, as the most abundant molecule in nature and the simplest molecular target it represents a first step towards developing theories for scattering on more complex targets. One important reason for developing accurate methods for calculating ion collisions with molecules is to improve the quality of beam transport models used in hadron therapy treatment planning. Treatment plans for hadron therapy are developed using Monte Carlo simulations, which rely on accurate stopping power cross sections for collisions of the beam ions with biological molecules. The water molecule is used as a reference target in these simulations [21]. Hence, there is an urgent need for accurate stopping power

^{*} This chapter is adapted from works published by the candidate [273–277]. The publishers (Springer, the American Physical Society, and MDPI) provide the author with the right to use the articles, or parts thereof, in a thesis or dissertation without requesting permission.

cross sections on proton collisions with H_2O . The path to developing theories that can accurately calculate cross sections for ion collisions with water starts with the simpler H_2 molecule target.

In this chapter we extend the two-centre WP-CCC method to proton collisions with molecular hydrogen. To do this we use a spherically symmetric model potential to construct one-electron wave functions representing the state of one of the target electrons subject to the field of the remaining electron and two protons averaged over all orientations. The method is first applied to calculate the TICS for $\bar{p} + \text{H}_2$ collisions where accurate calculations that account for the electron correlations and multicentre nature of the target are available for comparison. Then, we apply the approach to calculate integrated cross sections for all single-electron processes in $p + \text{H}_2$ collisions. Next we calculate singly differential cross sections for elastic scattering, target excitation, electron capture, and ionisation. Finally, the method is applied to calculate the doubly differential cross sections for ionisation where currently available theory cannot describe the experimental data well.

10.1 Overview of previous work

The $p + \text{H}_2$ collision system has been extensively investigated. There are many experimental measurements available for integrated and differential cross sections. However, theoretical investigations have mainly focussed on integrated cross sections. Furthermore, calculations for H_2 are typically performed by multiplying the results for the atomic target by 2 or by using an empirical energy-scaling procedure [278, 279].

10.1.1 Experimental data

Electron-loss and electron-capture cross sections were measured by Stier and Barnett [280] as early as 1956. The total electron-capture cross section was also

measured by Refs. [168, 281, 282], without making distinction between capture that lead to dissociation of the residual H_2^+ ion or not. However, measurements by Shah *et al.* [283] and Shah and Gilbody [284] of the separate dissociative and non-dissociative capture channels showed that the contribution from capture events leading to dissociation are approximately an order of magnitude smaller than non-dissociative capture processes. Rudd *et al.* [285] made empirical calculations and estimated uncertainties by fitting an analytical formula to the range of available experimental data. Additionally, state-selective cross sections for electron capture have been measured for charge transfer into various states of the projectile atom [286–294].

Hooper *et al.* [279] and Toburen and Wilson [295] provided data for the TICS at high energies where the electron-capture contribution to total electron loss is negligible in comparison with ionisation. Later, measurements by Edwards *et al.* [296] and Shah *et al.* [283] showed that dissociative ionisation becomes negligible in comparison with non-dissociative ionisation above 20 keV.

The first and only measurements of the DCS for electron capture in $\text{p} + \text{H}_2$ collisions available in the literature are those by Sharma *et al.* [297] at energies of 25 and 75 keV. However, the differential cross sections for ionisation have been thoroughly investigated experimentally. The first comprehensive study of the SDCS for ionisation in $\text{p} + \text{H}_2$ collisions was performed by Kuyatt and Jorgensen [298]. They measured both the angular and energy distribution of emitted electrons at proton energies of 50, 75, and 100 keV. However, their integrated results were significantly larger than the accepted TICS. Rudd and Jorgensen [245] also measured the singly differential cross section for ionisation at 100 keV. They extended their work to a wider energy range (up to 300 keV) in Ref. [246]; however, their integrated cross sections also overestimated the TICS. Later, Rudd [299] measured the differential ionisation cross sections at small incident energies from 5 to 100 keV. Gealy *et al.* [12] used a new apparatus designed to minimise experimental error in measurements of the singly differential cross sections for

ionisation in low-energy collisions. They measured the SDCS as a function of ejected-electron energy and angle at projectile energies of 20, 48, 67, 95, and 114 keV. Additionally, the integrated ionisation cross sections from their SDCS agreed well with independent measurements of the TICS. An extensive review of experimental studies of the differential ionisation cross sections is given by Rudd *et al.* [300]. As far as we are aware, there are neither experimental nor theoretical data for the singly differential ionisation cross section as a function of the scattered-projectile angle.

The doubly differential cross section for ionisation was measured by Rudd and Jorgensen [245] at 100 keV over a wide range of ejected-electron energies and angles. Kuyatt and Jorgensen [298], Rudd *et al.* [246], and Gealy *et al.* [12] measured both the angular and energy distributions of the emitted electrons simultaneously. In fact, they obtained the SDCS data by integrating over one of the variables. In addition to this, Toburen and Wilson [295] independently measured the DDCS for ionisation from 300 keV up to 1.5 MeV. In general, their results agree well with those of Rudd *et al.* [246] at 300 keV. However, their data deviate from those of Rudd *et al.* [246] at ejection energies less than 50 eV for ejection angles greater than 30°. The most significant difference is seen at the highest measured ejection energies and for emission in the backward direction where the cross section is very small and the signal-to-noise ratio in their measurements is low. At the larger impact energies considered by Toburen and Wilson [295], the binary-encounter peak becomes visible for ejection of high-energy electrons at small emission angles. This secondary peak in the DDCS is the result of binary collisions between the projectile and the active electron.

Gibson and Reid [301] measured the DDCS for ionisation at 50 keV for ejection energies over a range from 5 to 150 eV and emission angles from 0 to 100°; however, the TICS found by integrating their results differed from direct measurements by 33%. Furthermore, subsequent experiments called into question the accuracy of their results due to potential spreading of their proton beam [302].

The DDCS for ionisation as a function of the scattering angle of the projectile and emission energy of the ejected electron for $p+H_2$ collisions was first measured by Alexander *et al.* [303] at 75 keV. Their data suggests the presence of some structure in the cross section around a scattering angle of 1.4 mrad at some emission energies considered. The authors suggested this may be due to two-centre interference resulting from the indistinguishability of which target centre the electron is emitted from. A further study was undertaken by Egodapitiya *et al.* [304] for the single emission energy of 14.6 eV. The results slightly underestimate the data of Ref. [303]. The most recent experimental measurements of this cross section were performed by Sharma *et al.* [305]. Compared to the data from Refs. [303] and [304], background signals were reduced, potentially increasing the accuracy. Unlike the other experimental data, the measurements by Sharma *et al.* [305] fall off smoothly at large scattering angles and show no evidence of additional structure in the DDCS.

10.1.2 Theoretical methods

Thus far, the majority of theoretical works on ion collisions with molecular hydrogen is limited to negatively charged projectiles such as antiprotons [37, 69, 94, 306]. This removes the possibility of charge-exchange processes, significantly simplifying the collisional problem. Accurate ionisation cross sections for antiproton scattering on H_2 were calculated by Abdurakhmanov *et al.* [37, 94] over a projectile energy range from 1 to 2000 keV. They used a full two-electron two-centre treatment of the target, constructing the electronic wave functions using a configuration-interaction (CI) expansion in terms of the product of two one-electron orbitals. While they obtained very good agreement with experiment, even at low energies where other theories deviate significantly, the treatment of the target structure significantly increased the complexity of the theory and computational implementation when compared to methods that use a spherically symmetric effective one-electron target description [69]. Lühr and Saenz [306]

also used a single-centre AOCC method to calculate ionisation cross sections for $\bar{p} + \text{H}_2$ scattering. However, the same caveats apply whereby the two-electron non-spherical treatment of the hydrogen molecule complicates the theory. Furthermore, this complicates the generalisation of these sophisticated single-centre approaches to include the second centre required for allowing capture of one or both electrons from the target.

For proton projectiles, Corchs *et al.* [307] applied the CB1 method to calculate cross sections for capture into the ground state of the projectile at collision energies from 100 to 1000 keV. The CDW-EIS and CDW-EFS methods were used by Busnengo *et al.* [308] to calculate cross sections for single-electron capture to all bound projectile states in $p + \text{H}_2$ collisions from 20 keV to 10 MeV [308] and state-selective cross sections for capture into the $2s$, $3s$, $2p$, $3p$, and $3d$ orbitals of the projectile [309]. While they found generally good agreement with experiment [287, 289–291, 291, 293, 294] at intermediate impact energies, the CDW approaches deviate from one another and some significantly overestimate the low-energy experimental data.

The single-ionisation cross section for $p + \text{H}_2$ collisions was calculated by Galassi *et al.* [310] using the CDW-EIS method. Two methods for determining the cross section were used. The first one is based on the simple Bragg additivity rule, which multiplies the CDW-EIS results for $p + \text{H}$ scattering by a factor of 2. The second one treats the target as two independent H atoms separated by the equilibrium internuclear distance of the H_2 molecule. The cross section for proton scattering on H_2 is then given by the integral over all orientations of the target and an orientation-dependent factor resulting from the two scattering centres. The authors refer to the latter approach as the continuum-distorted-wave eikonal-initial-state molecular-orbital (CDW-EIS-MO) method. Good agreement with the recommended data [285, 311] for the TICS was observed at high energies.

The CTMC method has also been applied to the $p + \text{H}_2$ scattering problem. Meng *et al.* [312] calculated single-ionisation and electron-capture cross sections

as well as the state-resolved cross sections for transfer into the $2s$, $2p$, $3s$, and $3p$ states of the projectile [313]. Results by Illescas and Riera [133] demonstrate good agreement with experimental ionisation and electron-capture cross sections from Refs. [279, 283, 295] over an energy range from 9 to 225 keV. Schultz *et al.* [28] used the CTMC approach to calculate total electron-capture and ionisation cross sections from 1 keV to 25 MeV. After applying a Born correction and normalising to recommended data from Ref. [314], their results agree well with the experimental results reported in Refs. [168, 281–285, 296].

The modified molecular-orbital (MMO) close-coupling method was employed by Kimura [315] to calculate the $1s$ -capture cross section for $p + H_2$ collisions from 1 to 20 keV. Shingal and Lin [316] calculated ground-state electron-capture cross sections using the travelling atomic-orbital expansion (AO) method. In this approach the close-coupling equations for proton scattering on atomic hydrogen are first solved. Then, the molecular wave function is constructed using a linear combination of atomic orbitals (LCAO) and the scattering amplitudes for the $p + H_2$ system are calculated from the amplitudes for scattering on the atomic target using perturbation theory.

The spherically symmetric model potential proposed by Vanne and Saenz [317] was used in the single-centre AOCC method to calculate total electron-loss cross sections for $p + H_2$ collisions from 10 keV to 4 MeV [318]. Elizaga *et al.* [319] calculated the electron-loss cross section using the travelling molecular-orbital (MO) method and the optimised dynamical-pseudostates (ODP) method. They also used a model potential in a CTMC approach. Their results agree closely with those of Lühr *et al.* [318], except below 30 keV where the CTMC results underestimate both the experimental data [285] and the other calculations. However, the aforementioned methods cannot give any information on electron capture.

The differential cross section for electron capture was calculated by Igarashi [320] for incident energies of 25, 75, and 300 keV. They used the DWB approxima-

tion and presented results obtained using a number of different structure models for the H_2 target. Agreement with the experimental data of Sharma *et al.* [297] is mixed. Their calculated angular differential cross sections for electron capture into the ground state agree well with the experimental data for scattering angles less than 0.5 mrad. However, at larger scattering angles discrepancies are seen between various approaches based on changing the target description. In particular, using a LCAO approach, they were able to deduce information about the final vibrational state of the residual ion; however, the angular differential cross sections for electron capture found using this model are very similar to results using a fixed-nuclei (FN) approximation. In fact, they find that using the two-effective-centre (TEC) method gives improved agreement with the experimental data despite a less detailed description of the molecular nature of the target. In the TEC approach the target is simply treated as two independent hydrogen-like atoms separated by the equilibrium internuclear distance of H_2 .

Adivi [321] also used an effective one-electron target description to calculate the differential cross section for electron capture at 300 keV using the CB1 method. Ghanbari-Adivi and Sattarpour [322] applied the four-body eikonal approximation (EA) at 100 and 300 keV. There is no experimental data available at these energies for comparison.

There are far fewer theoretical investigations of differential cross sections for ionisation. Rudd *et al.* [246] performed calculations of the SDCS differential in both ejected-electron angle and energy at 100, 200, and 300 keV using the FBA. They also compared the differential cross section in energy to that predicted by the classical Gryziński theory. Both the FBA and Gryziński binary-encounter method are only applicable at high incident energies, and while agreement with their experimental results was generally good, the latter deviates from the experimental points at large ejection energies. Lühr and Saenz [69] used their one-centre AOCC method to calculate the electron-loss cross section differential in ejected-electron energy at 48 keV. Comparison with the experimental results

of Gealy *et al.* [12] shows good agreement except around the region where the ejected electron has a similar speed to the incident projectile. Here, the inability of the one-centre AOCC method to distinguish between pure ionisation and electron capture results in an unphysical peak in the presented cross section. More recently, Schultz *et al.* [28] used the CTMC method to calculate cross sections for ionisation singly differential in electron angle and in energy. At 50 and 75 keV, their results for the ionisation cross section as a function of ejection energy are smaller than the experimental data of Refs. [246, 298, 299]. At 100 keV, their results agree with the FBA calculations and Gryziński approach for small ejection energies, but deviate further from the experimental points than the FBA calculations.

Calculating the doubly differential cross section for ionisation as a function of the ejected-electron energy and angle in $p + H_2$ collisions has proven to be a significant challenge. There are only a few attempts to calculate this cross section available in the literature. Moreover, most calculations have used the FBA that is only applicable at high projectile energies. A different approach was taken by Macek [90]. They used the first term in the Neuman expansion of Faddeev's equations for the final state of the projectile-electron-residual ion system to calculate the DDCS for ionisation. The calculations were performed at an incident energy of 300 keV. The results showed improved agreement with the measured cross section compared to the FBA calculations but still demonstrated significant deviation from the experimental data. In particular, the results of Macek [90] significantly overestimate the cross section near small ejection energies. This is possibly due to the fact that the Faddeev-equation approach is not valid for breakup in a system of three charged particles. In this case, the kernel of the Faddeev equations becomes non-compact.

The most recent calculations of the DDCS for ionisation as a function of ejected-electron energy and angle in $p + H_2$ collisions were performed by Galassi *et al.* [310]. Using the FBA and the CDW-EIS approach and they calculated the

DDCS at 114 keV and compared to the experimental data by Gealy *et al.* [12]. Their results show that Bragg's additivity rule is inadequate at providing accurate doubly differential cross sections for ionisation, overestimating the results of Ref. [12], particularly for ejection at angles greater than 90° . Nevertheless, overall, the CDW-EIS-MO calculations demonstrate improved agreement with experiment.

Since the first measurements of the DDCS as a function of the projectile-scattering angle and electron energy by Alexander *et al.* [303], there have been a number of attempts to calculate this cross section. The CDW-EIS approach to proton collisions with atomic hydrogen was used in Ref. [303] by introducing a two-centre interference factor to apply the results to the molecular target. The results agree well with their experimental data at the lowest emission energies but significant discrepancies are observed as the emission energy increases. Chowdhury *et al.* [323] used the molecular three-body distorted-wave-eikonal initial-state (M3DW-EIS) approach in which the molecular target is represented by orientation-averaged electronic wave functions [324], rather than averaging the orientation-dependent cross sections over all possible orientations of the molecule as is commonly done for diatomic molecular targets [306]. Quantitatively, the results were found to consistently underestimate the experimental data of Alexander *et al.* [303] but demonstrated improved agreement in shape compared to the previously available CDW-EIS results. Chowdhury *et al.* [323] also used the FBA to calculate this DDCS. The results significantly differ from the experimental data and all other calculations. The CDW-EIS-MO approach was used by Igarashi and Gulyás [325] to investigate the DDCS for ionisation in proton collisions with H_2 . They used a number of different approximations to represent the interaction potential between the projectile nucleus and residual target ion, resulting in significant differences between their various calculations. To account for the two-centre nature of the target nucleus they employ the TEC approximation. They compared their results to those for the $p + H$ collision system, i.e. without the

interference factor arising from the way in which they model the nuclei of the molecular target. Overall, it is shown that the inclusion of the two-centre factor does not significantly alter the shape of the DDCS. As with the other results based on the CDW formalism, the agreement is best for low emission energies and worst at the highest emission energy considered.

10.2 Effective one-electron description of H_2

There is currently no known method to determine of the exact electronic wave functions for H_2 . However, several approximate methods exist for constructing orthogonal sets of electronic states. Sophisticated approaches such as those based on the CI expansion in terms of one-electron orbitals are capable of generating two-electron wave functions for ground and excited states whose energies correspond closely with experimentally measured values. Application of such methods to collisions of antiprotons with H_2 has resulted in highly accurate calculations of the integrated ionisation cross section [37]. However, due to the mixing of the electrons in the two-electron state, it is not possible to determine which electron was ionised. This makes differential studies of ionisation impossible within the CI framework.

Simpler, effective one-electron descriptions have also been used to generate electronic wave functions for H_2 . These approaches typically reduce the problem to a spherically-symmetric model system. An analytical potential is then chosen such that the ground-state produced by solving the target Schrödinger equation with this interaction has an energy corresponding to the experimentally measured ground-state energy of H_2 . Although these methods are unable to distinguish between different orientations of the molecule, they have seen considerable success in application to scattering problems [69, 306, 326]. In practice, cross sections for scattering on molecular targets averaged over all orientations are of significant interest since they represent the usual situation where the molecules are randomly oriented.

One of the main aims of this work is to investigate differential ionisation in proton collisions with molecular hydrogen. To that end, in this section we describe an effective one-electron description of H_2 that can be used to generate orthonormal one-electron target states. Then, these states can be used in the one-electron WP-CCC framework, allowing us to utilise highly optimised codes already developed for one-electron atomic targets. In this method, the target is treated as a spherically-symmetric H_2^+ ionic ‘core’ with a single active electron subject to the effective potential of the two protons and other electron. To represent the interaction of the active electron with the effective H_2^+ ion we employ the model potential [317]

$$V_{\text{mod}}(r) = \frac{1}{r}(1 + e^{-\zeta r}). \quad (10.1)$$

The parameter, $\zeta = 5.4824$, is chosen such that the energy of the lowest-energy state is equal to -0.5976 a.u. This value corresponds to the difference in energy between the ground state of H_2 at the average internuclear distance of the hydrogen molecule, $\langle d \rangle = 1.45$ a.u., and the ground state of H_2^+ at the same internuclear distance. This effectively represents the hydrogen cation as a spherically symmetric system, so that there is no possibility of the residual ion existing in a vibrationally excited state. Thus, this ground-state energy is analogous to the adiabatic ionisation energy rather than the vertical ionisation energy of the hydrogen molecule.

Practically, employing the model potential given in Eq. (10.1) within the WP-CCC method consists of first writing the target Hamiltonian as

$$H_{\text{T}} = -\frac{1}{2}\nabla_{\mathbf{r}_{\text{T}}}^2 - Z_{\text{T}}V_{\text{mod}}(r_{\text{T}}). \quad (10.2)$$

Then, description of the target is reduced to that of a quasi one-electron atom. The effective charge is $Z_{\text{T}} = +1$ for the H_2^+ ion. To find bound-states, we solve the target Schrödinger equation using an iterative Numerov approach for negative

values of the energy. This results in a set of eigenstates for the (quasi-atomic) hydrogen-like system. To represent the continuum, we construct wave packets using the method outlined in Sect. 3.2. The pure Coulomb wave is replaced with the continuum wave solution obtained by solving the Schrödinger equation for positive values of the energy using the iterative Numerov approach.

10.2.1 Matrix elements in E1E approach to H_2

Using the effective one-electron description of H_2 , the interaction potential \bar{V}_T entering the matrix elements in Eq. (3.39) becomes

$$\bar{V}_T = Z_T Z_P V_{\text{mod}}(R) - \frac{Z_P}{|\mathbf{r}_T - \mathbf{R}|}, \quad (10.3)$$

where we choose to represent the interaction between the projectile nucleus and H_2^+ ion with the same model potential as the interaction between the electron and the H_2^+ ion.

First, consider the direct-scattering matrix elements in the $\alpha \rightarrow \alpha'$ channel. We substitute Eq. (10.3) into Eq. (3.41) and expand the potential of interaction between the projectile nucleus and active electron in terms of partial-waves as

$$\bar{V}_T = 4\pi \sum_{\lambda\mu} \frac{1}{2\lambda + 1} \mathcal{U}_\lambda(R, r_T) Y_{\lambda\mu}^*(\hat{\mathbf{R}}) Y_{\lambda\mu}(\hat{\mathbf{r}}_T), \quad (10.4)$$

where

$$\mathcal{U}_\lambda(R, r_T) = \begin{cases} \delta_{\lambda 0} Z_T Z_P V_{\text{mod}}(R) - \frac{Z_P R^\lambda}{r_T^{\lambda+1}}, & R \leq r_T, \\ \delta_{\lambda 0} Z_T Z_P V_{\text{mod}}(R) - \frac{Z_P r_T^\lambda}{R^{\lambda+1}}, & R > r_T. \end{cases} \quad (10.5)$$

The radial and angular parts of the integral over \mathbf{r}_T can then be separated and we obtain the same result as in the pure three-body Coulombic case in Sect. 3.3. The only difference is the functional form of $\mathcal{U}_\lambda(R, r_T)$.

For the $\beta \rightarrow \beta'$ channel, the total interaction potential is the sum of the

heavy-particle interaction and the interaction between the target H_2^+ core and the electron,

$$\bar{V}_P = Z_T Z_P V_{\text{mod}}(R) - Z_T V_{\text{mod}}(r_T). \quad (10.6)$$

There is an additional term here compared to \bar{V}_T with an exponential factor due to the model potential acting between the residual target ion and electron (but not between the projectile and electron). This additional term can be partial-wave expanded in terms of the product of the spherical Bessel and spherical Hankel functions [102], leading to

$$\bar{V}_P = 4\pi \sum_{\lambda\mu} \frac{(-1)^\lambda}{2\lambda + 1} \mathcal{U}'_\lambda(R, r_P) Y_{\lambda\mu}^*(\hat{\mathbf{R}}) Y_{\lambda\mu}(\hat{\mathbf{r}}_P). \quad (10.7)$$

The expansion coefficients are defined as

$$\mathcal{U}'_\lambda(R, r_P) = \mathcal{U}_\lambda(R, r_P) + \begin{cases} \zeta(2\lambda + 1) j_\lambda(i\zeta R) h_\lambda^{(1)}(i\zeta r_P), & R \leq r_P, \\ \zeta(2\lambda + 1) j_\lambda(i\zeta r_P) h_\lambda^{(1)}(i\zeta R), & R > r_P, \end{cases} \quad (10.8)$$

where j_λ and $h_\lambda^{(1)}$ denote the spherical Bessel and spherical Hankel functions of the first kind, respectively. Evaluating these special functions with complex arguments accurately is challenging. We used the COULCC subroutine from Thompson and Barnett [327]. Evaluating the direct matrix elements this way is more accurate compared to a purely numerical approach. This has a significant effect for low-energy projectile scattering where small inaccuracies can exaggerate the ill-conditioning caused by the lack of orthogonality between the two basis sets.

The overlap matrix elements are unchanged in the effective one-electron description of H_2 . Meanwhile, the interaction potential in the exchange matrix elements is replaced with the new form of \bar{V}_T or \bar{V}_P defined in Eqs. (10.3) and (10.6) as appropriate. Overlap and exchange matrix elements are then evaluated numerically in spheroidal coordinates the same way as described in Sect. 3.3.

10.2.2 Probabilities and cross sections for single-electron processes

In the three-body WP-CCC method the integrated ionisation cross section is given by Eq. (3.147). To calculate cross sections for scattering from the two-electron H₂ target, we can write the probability entering Eq. (3.147) in terms of the probability for a single-electron, $P_f^{\text{SE}}(b)$, as

$$P_f(b) = 2P_f^{\text{SE}}(b) \quad (10.9)$$

to account for the equivalent chance of either electron transitioning to the final state f in the physical two-electron collision system [318]. The reason for the factor of 2 is the fact that there are 2 electrons and both of them can be modelled in exactly the same way. In other words, the two-electron problem is cut into two equal effective single-electron halves. When the single-electron problem is solved, the two halves must be brought together, hence, the factor of 2.

An alternative method is to employ the independent-particle model (IPM) [328]. The IPM writes the probability of a single-electron process as

$$P_f^{\text{IPM}}(b) = 2P_f^{\text{SE}}(b)[1 - P_f^{\text{SE}}(b)]. \quad (10.10)$$

This corresponds to one electron occupying the state f while preventing the other electron from occupying the same state. A disadvantage of this approach is that the two-electron amplitudes cannot be calculated, only the probabilities. Therefore, it is impossible to calculate differential cross sections for ionisation. However, in the first approach, Eq. (10.9), the amplitudes for scattering on the two-electron target can be obtained simply by multiplying the one-electron amplitudes by a factor of $\sqrt{2}$ which follows from normalisation (to unity) of the two-electron target wave function.

10.3 Calculations of integrated cross sections

10.3.1 Electron loss in $\bar{p} + \text{H}_2$ collisions

Before considering $p + \text{H}_2$ collisions, we first apply the developed idea to antiproton projectiles. With no electron capture to consider, and the probability of protonium formation being negligible, we can test the target structure in the WP-CCC method without the additional complexities associated with positively charged projectiles. Therefore, a one-centre expansion is sufficient. In this case, the only surviving matrix elements in Eq. (3.39) are $\mathcal{D}_{\alpha'\alpha}^T$.

To obtain convergent results, the radial grid extended to 300 a.u., and the z -grid extended from -100 to $+100$ a.u. relative to the target nucleus with 400 points. A total of 32 impact-parameter points which ranged from 0 to 22 a.u. were used for antiproton scattering. The maximum momentum value for the continuum discretisation varied from 5 to 8 a.u. depending on the incident energy.

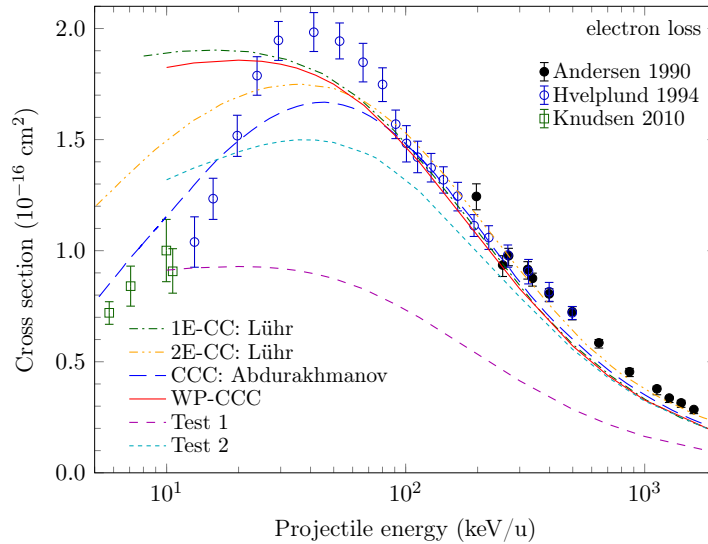


Figure 10.1: Single-electron-loss cross section for $\bar{p} + \text{H}_2$ collisions. Experimental data are by Andersen *et al.* [329], Hvelplund *et al.* [330], and Knudsen *et al.* [331]. The theoretical results are: WP-CCC method, WP-CCC method without the factor of 2 in Eq. (10.9) (Test 1), WP-CCC method using the IPM in Eq. (10.10) (Test 2), effective-one-electron AOCC method by Lühr and Saenz [69], two-electron AOCC method of Lühr and Saenz [306], and two-electron CI CCC approach by Abdurakhmanov *et al.* [37].

Figure 10.1 shows the total cross section for ionisation in $\bar{p} + \text{H}_2$ collisions as a function of the projectile energy. At high impact energies there is good agreement between our results and the experiments by Andersen *et al.* [329] and Hvelplund *et al.* [330]. Between 30 and 80 keV the WP-CCC results underestimate the experimental data which includes the region near the peak of the ionisation cross section. However, the same is true of the other theoretical results shown in Fig. 10.1. At low energies our results do not fall sufficiently to match the experimental data, as is also seen in the results of Ref. [69] which use the same model potential representation in a close-coupling formalism. We see small deviations from the results of Ref. [69]. These are due to different types of the pseudostates used. The theoretical works that use a full two-electron treatment of the target [37, 306] both fall in a similar fashion to the experiment at low energies. The calculations by Abdurakhmanov *et al.* [37] showed that the reduction of the ionisation cross section at low energies observed in experiment is due to the two-centre nature of the molecular target. It follows that theories which use spherically symmetric target structures would not replicate this so-called target structure-induced suppression of the ionisation cross section. This suggests that the simple effective potential cannot accurately model the properties of the hydrogen molecule in low-energy antiproton collisions. Proton collisions are fundamentally different, however, due to low-energy collisions being dominated by electron-capture processes.

In Fig. 10.1 we also compare our results with those obtained in two test calculations. In Test 1 the factor of 2 in Eq. (10.9) is dropped, while Test 2 is based on the IPM. Agreement with experiment is significantly worse in Test 1 at intermediate and high energies. The Test 2 results are not too bad, but clearly this approach does not change the low-energy behaviour of the cross section. That is because this disagreement with experiment is purely due to the single-electron spherical treatment of the target structure. Such an approximation cannot account for the target-structure induced suppression responsible for the shape of the

low-energy $\bar{p} + \text{H}_2$ ionisation cross section [37, 94]. We conclude that multiplying the single-electron probability by 2 confirms the widely-used approach. In addition, we should note that in our approach there is no need to explicitly prevent the second electron from occupying the same final state as there is effectively no second electron. We use Eq. (10.9) for all following results. Since our model cannot differentiate between one- and two-electron processes, to avoid confusion, we label our result as a single-electron one.

10.3.2 Integrated cross sections for $\text{p} + \text{H}_2$ collisions

Now we apply the two-centre WP-CCC method to calculate the integrated cross sections for elastic scattering, excitation, electron loss, single ionisation, and single electron capture in proton collisions with H_2 . Additionally, we present state-resolved capture cross sections for exchange into the $1s$, $2s$, $2p$, $3s$, $3p$, and $3d$ states of the projectile. To do this we switch the charge of the projectile to $+1$ and use a two-centre expansion of the total scattering wave function. With this we solve the full set of coupled equations given in Eq. (3.39). The single-electron-loss cross section is given by the sum of the single-ionisation and single-electron-capture cross sections. The required basis for converged results contained bound states with principal quantum numbers up to $n_{\text{neg}} = 10 - \ell$ and angular momentum up to $\ell_{\text{max}} = 4$. For incident energies below 25 keV the continuum was discretised with 15 bins up to a maximum electron momentum of $\kappa_{\text{max}} = 4$ a.u. Then, from 25 keV we used 20 bins and κ_{max} was increased up to 7 a.u. at a projectile energy of 500 keV. At the highest impact energies considered, 35 continuum bins were required to obtain sufficient continuum discretisation up to $\kappa_{\text{max}} = 11$ a.u. The z -grid extended from -300 to $+300$ a.u. with 600 to 1000 points depending on the incident energy. These parameters were sufficient for the elastic-scattering, total capture, and ionisation cross sections (and state-resolved capture cross sections), presented below, to reach 99% convergence. The net excitation cross section has converged to within 95%, with $n_{\text{neg}} = 10$, however,

adding additional states caused unitarity violations at low incident energies. A total of 32 impact parameters ranging from 0 to 22 a.u. were used at low impact energies, while 64 points from 0 up to 40 a.u. were required to obtain convergence in the results at high impact energies.

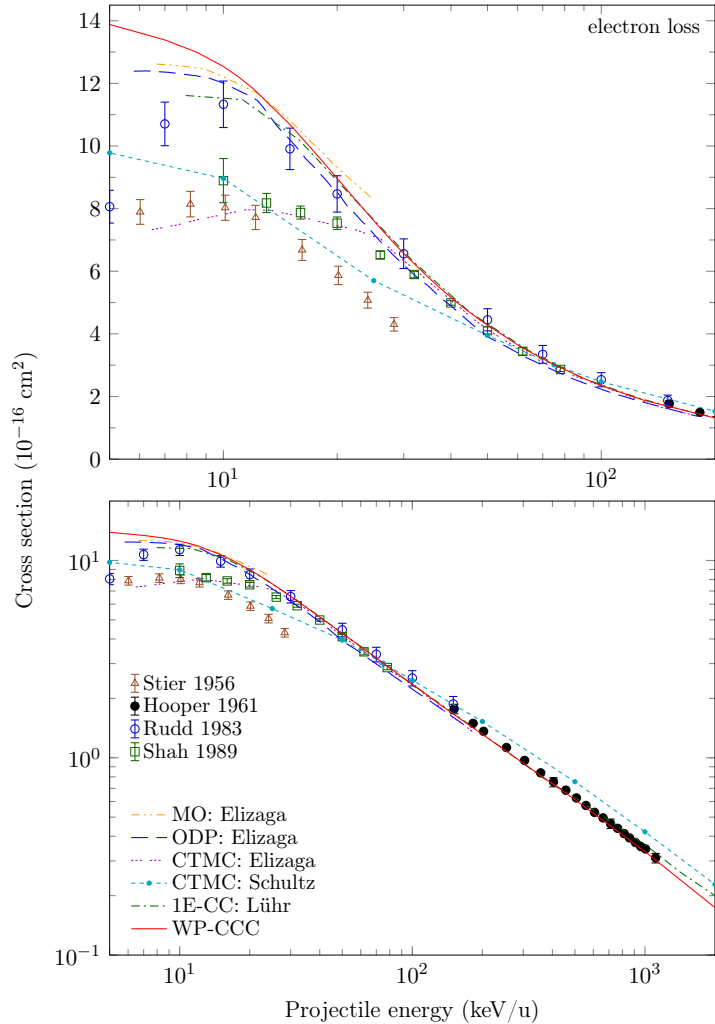


Figure 10.2: Single-electron-loss cross section for $p + H_2$ collisions (upper and lower panels are in the linear and logarithmic scales, respectively). Experimental data are by Stier and Barnett [280], Hooper *et al.* [279], Rudd *et al.* [285], and Shah *et al.* [283]. The theoretical results are: present WP-CCC method, MO and ODP methods by Elizaga *et al.* [319], CTMC approach by Elizaga *et al.* [319] and Schultz *et al.* [28], and single-centre AOCC approach by Lühr *et al.* [318]. The key in the lower panel applies to both panels.

Our results for the total single-electron-loss cross section for $p + H_2$ collisions are shown in Fig. 10.2. They agree well with available experimental data and single-centre close-coupling calculations by Lühr *et al.* [318] as well as MO and ODP results by Elizaga *et al.* [319] from 20 to 1000 keV. The CTMC results by

Schultz *et al.* [28] are shown as points connected with straight lines. They underestimate the experimental results by Rudd *et al.* [285] and Shah *et al.* [283] as well as the present ones below 70 keV, but are slightly larger than the experimental data by Stier and Barnett [280]. However, above 100 keV the CTMC calculations underestimate both the experiment by Hooper *et al.* [279] and our calculations. At lower incident energies, our results overestimate the cross section. The $1s$ -capture channel accounts for the majority of the total cross section for electron capture. As discussed below, the observed overestimation of the electron-loss cross section at low energies is due to an increasing contribution from capture into the $1s$ state of the projectile.

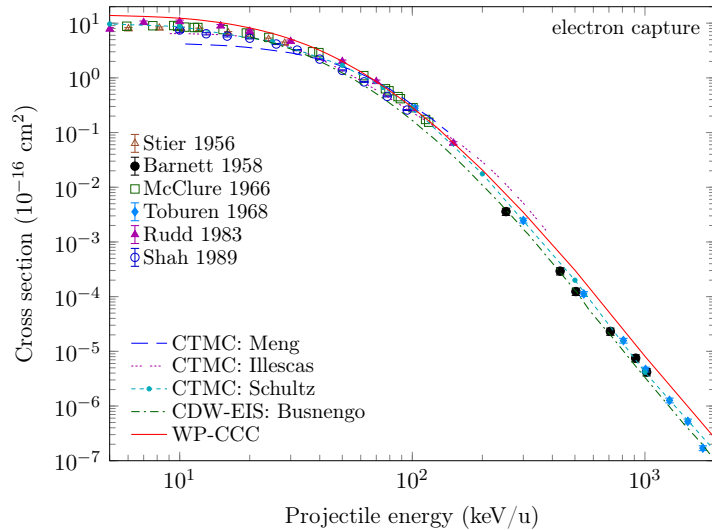


Figure 10.3: Single-electron-capture cross section for $p + H_2$ collisions. Experimental data are by Stier and Barnett [280], Barnett and Reynolds [281], McClure [168], Toburen *et al.* [282], Rudd *et al.* [285], and Shah *et al.* [283]. The theoretical results are: present WP-CCC method, CTMC approach by Meng *et al.* [312], Illescas and Riera [133], and Schultz *et al.* [28], and CDW-EIS method by Busnengo *et al.* [308].

Using our two-centre method, we are able to decompose the electron-loss cross section into electron-capture and single-ionisation contributions. The total electron-capture cross section is shown in Fig. 10.3. Our results overestimate the experiments of Shah *et al.* [283] and McClure [168] below 30 keV, but converge to their data above 60 keV. The empirical data from Rudd *et al.* [285] are higher than the other experimental results, and our calculation agrees more with these data. In the high-energy regime, our results are slightly larger than the experimental

data by Toburen *et al.* [282] and Barnett and Reynolds [281]. Across the entire energy range shown, the WP-CCC cross sections are larger than the CTMC results of Schultz *et al.* [28]. We also show the CDW-EIS calculations of Busnengo *et al.* [308]. Our calculations are larger than the latter across the entire energy range considered.

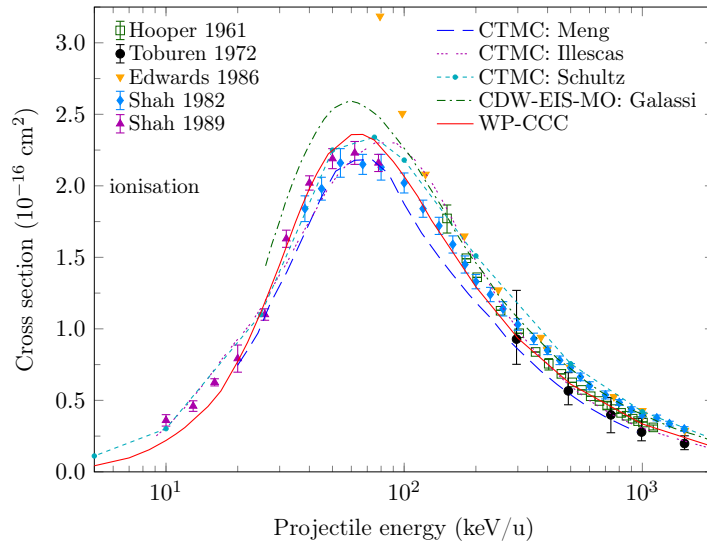


Figure 10.4: Single-ionisation cross section for $p + \text{H}_2$ collisions. Experimental data are by Hooper *et al.* [279], Toburen and Wilson [295], Edwards *et al.* [296], Shah and Gilbody [284], and Shah *et al.* [283]. The theoretical results are: present WP-CCC method, CTMC approach by Meng *et al.* [312], Illescas and Riera [133], and Schultz *et al.* [28], and CDW-EIS-MO method by Galassi *et al.* [310].

The results for the non-dissociative single-ionisation cross section are given in Fig. 10.4. This provides a good representation of the total cross section for single ionisation since the dissociative channel contributes significantly less [283]. The WP-CCC results agree very well with available experimental data from 30 to 1000 keV. This indicates that the ionisation cross section is less sensitive (than the electron-capture one) to the accuracy of the target wave function. At higher energies, our calculations fall between the experimental results of Toburen and Wilson [295] and Shah and Gilbody [284], very close to the data from Hooper *et al.* [279]. The results by Edwards *et al.* [296] overestimate the other experiments and theories around the peak in the ionisation spectrum but converge to those of Shah and Gilbody [284] at higher energies. Our results agree well with the CTMC calculations in the energy region below 100 keV. However, above 100

keV the calculations of Schultz *et al.* [28] are somewhat higher and those from Illescas and Riera [133] are lower than ours, with all three sets of results being within the experimental uncertainty. The CDW-EIS-MO calculations by Galassi *et al.* [310] produce larger cross sections than the WP-CCC method, especially at lower energies where the CDW approaches are less reliable. In particular, they overestimate the ionisation cross section in the region of its maximum around 100 keV, whereas our calculations agree well with the experimental results.

The total cross section for elastic scattering is shown in Fig. 10.5. The only other calculation available in the literature that we are aware of is the CTMC one by Schultz *et al.* [28]. Our results appear to significantly differ from the CTMC ones in the entire energy range. Experimental data and further theoretical calculations are required to resolve this discrepancy.

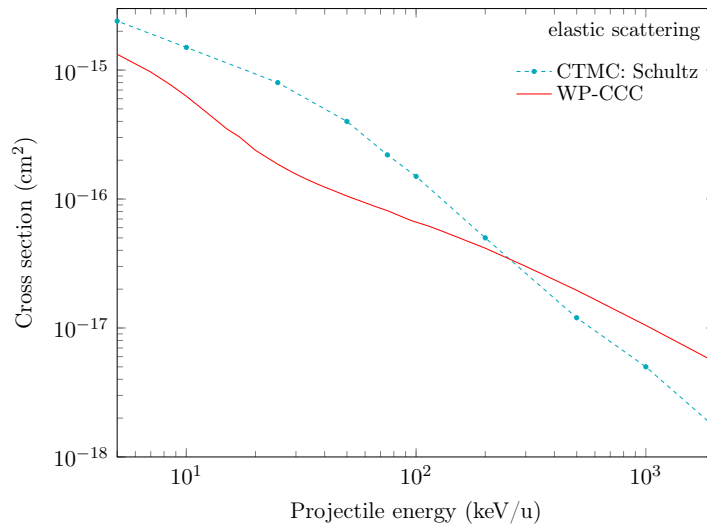


Figure 10.5: Elastic-scattering cross section for p+H₂ collisions. The theoretical results are: present WP-CCC method and CTMC approach by Schultz *et al.* [28].

Figure 10.6 presents the net cross section for excitation into all states included in the target-centred basis ($n_{\text{neg}} = 10$ and $\ell_{\text{max}} = 4$). The results of Schultz *et al.* [28] are also shown. Note that unlike their other results, the excitation cross section is not normalised to the experimental data from Ref. [314]. The CTMC results are larger than ours above 50 keV, generally agreeing in shape. Below 20 keV the shape of our results is different. However, we should note that this is the energy region where our model potential is expected to become less reliable.

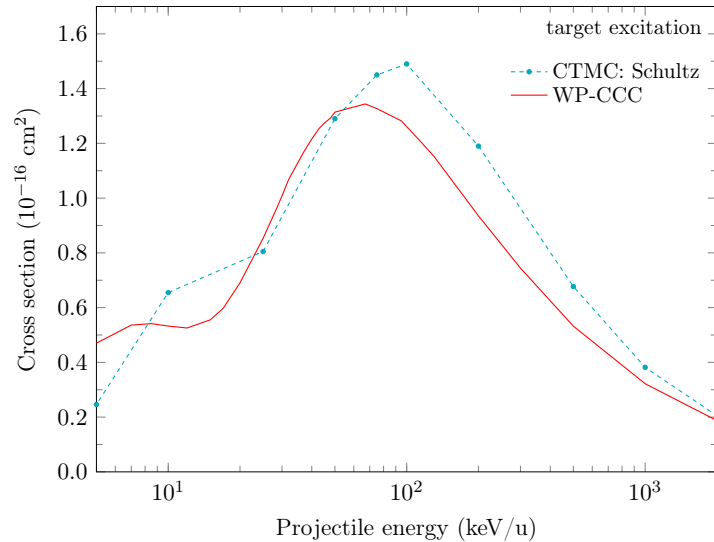


Figure 10.6: Net target-excitation cross section for $p + \text{H}_2$ collisions. The theoretical results are: present WP-CCC method and CTMC approach by Schultz *et al.* [28].

We also calculated the state-selective electron-capture cross sections for those channels for which experimental or theoretical data is available. Figure 10.7 shows capture into the ground state of the projectile. This is the dominant channel contributing to the total electron-capture cross section presented in Fig. 10.3. Our results are in good agreement with the CB1 calculations by Corchs *et al.* [307] at 100 keV and above. Below 30 keV, the WP-CCC results overestimate the MMO calculations of Kimura [315] and AOCC ones by Shingal and Lin [316]. Although above 40 keV the AOCC calculations are larger than both the CB1 calculations and our results.

In Fig. 10.8 we present results for capture into the 2ℓ states of the projectile in comparison with the available experimental data. Note that the experimental results of Shah *et al.* [292] are normalised absolutely, as are those from Andreev *et al.* [286]. However, the other experimental data are normalised to cross sections from other scattering systems (see Ref. [292] for a detailed discussion). For capture into the $2s$ state, our results describe the shape and magnitude of the experimental works [286–288, 292] at all energies, except for overestimating the data from Hughes *et al.* [290]. The lower panel of Fig. 10.8 shows the cross section for capture into the $2p$ projectile state. As with capture into the $2s$ state, here

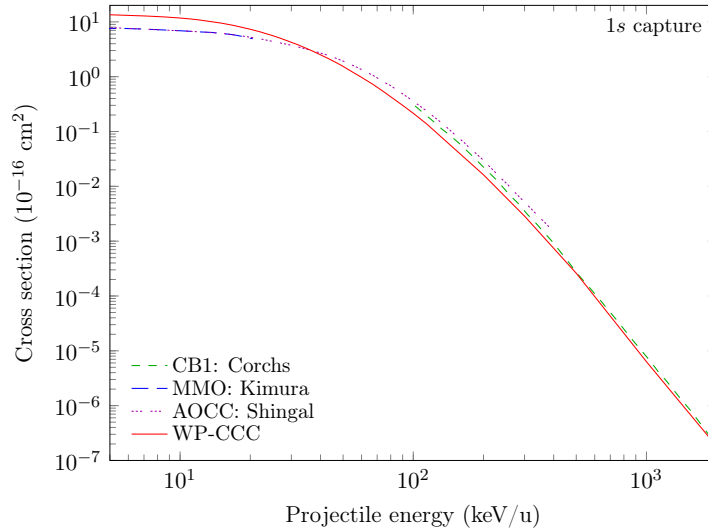


Figure 10.7: Partial $1s$ cross section for electron capture in $p + \text{H}_2$ collisions. The theoretical results are: present WP-CCC method, CB1 method by Corchs *et al.* [307], MMO method by Kimura [315], and AOCC method by Shingal and Lin [316].

we find that the WP-CCC results reproduce the magnitude and shape of the available experimental data very well.

Figure 10.9 shows the cross section for electron capture into the 3ℓ states of atomic hydrogen. Agreement between other theories and our results for electron capture into the $3s$ state (upper panel) is very similar to capture into the $2s$ state. Our calculations are consistently larger than the CDW-EIS calculations. The CTMC calculations agree fairly well with the WP-CCC results, but deviate below 40 keV. Our results agree well with the experiment of Williams *et al.* [293] above 20 keV, but underestimate it below this energy. Experimental data from Hughes *et al.* [289] are smaller than the WP-CCC results like for $2s$ capture.

In the middle panel of Fig. 10.9, we see that the WP-CCC results overestimate the experimental data from Hughes *et al.* [289] for capture into the $3p$ projectile state. However, at low energies our calculations agree with the data from Dawson and Loyd [294], although not in the same shape as their points suggest. The CDW-EIS and CTMC calculations agree well with our results above 50 keV.

We finally consider capture into the $3d$ state of atomic hydrogen in the lower panel of Fig. 10.9. Here, our result is slightly larger than the experimental data by Dawson and Loyd [294] below 10 keV while above 40 keV, we underestimate

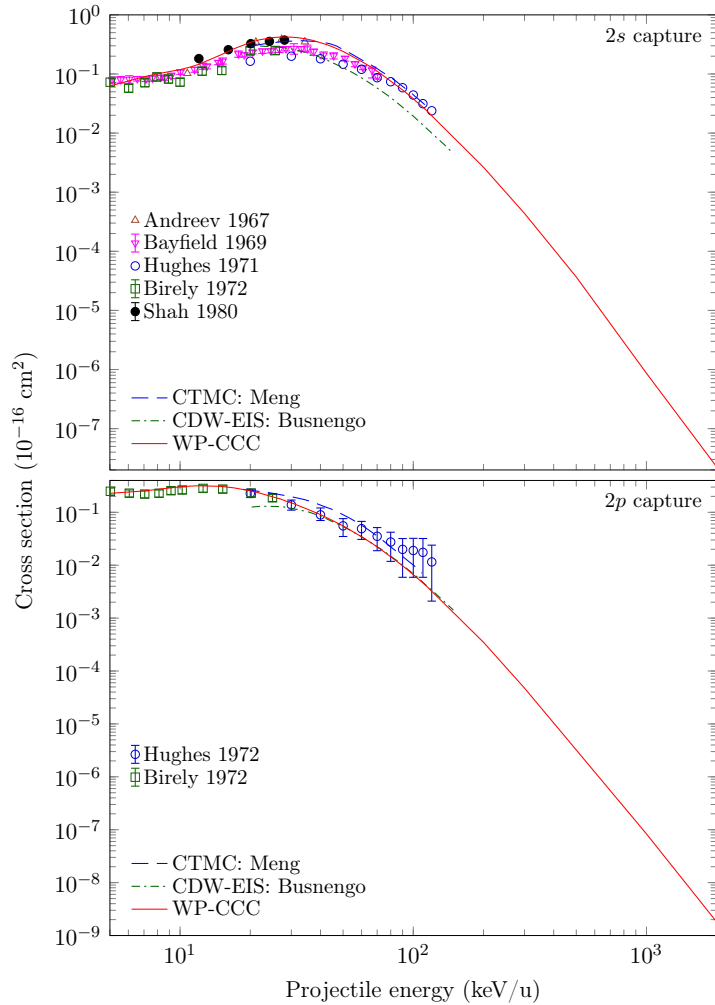


Figure 10.8: Partial 2ℓ cross sections for electron capture in $p + \text{H}_2$ collisions. Experimental data are by Andreev *et al.* [286], Bayfield [287], Hughes *et al.* [290], Birely and McNeal [288], Shah *et al.* [292], and Hughes *et al.* [291]. The theoretical results are: present WP-CCC method, CTMC approach by Meng *et al.* [313], and CDW-EIS method by Busnengo *et al.* [308].

the experimental points of Hughes *et al.* [289]. The CDW-EIS calculation of Busnengo *et al.* [308] is the same as ours above 50 keV but suggests a different shape to the experimental data at lower energies.

To summarise, we have presented the first two-centre coupled-channel calculations of the integrated cross sections for $p + \text{H}_2$ collisions. Agreement with the experimental data for the TICS is very good. For electron capture, the measurements of the total and state-selective cross sections are generally described well by our approach. Interestingly, our results significantly overestimate other theoretical calculations for charge transfer into the ground state yet generally agree well

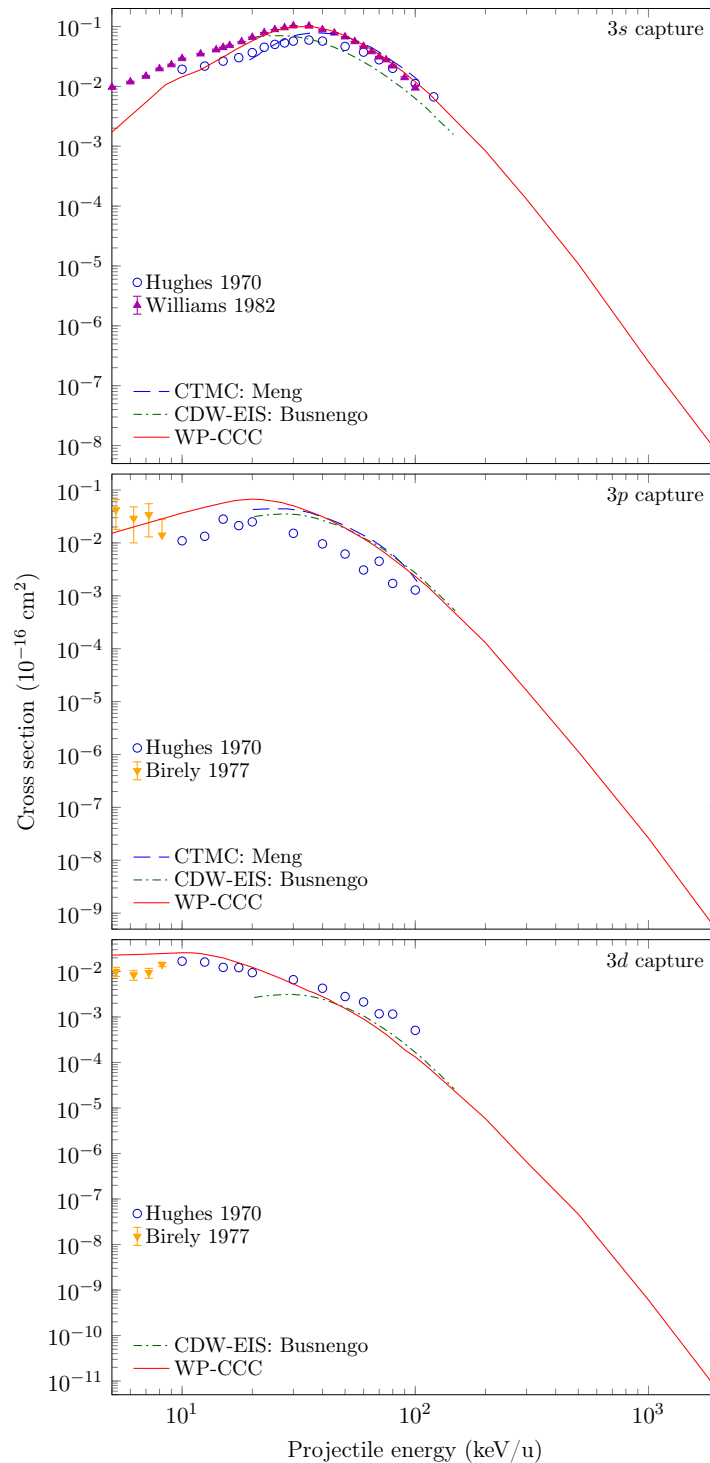


Figure 10.9: Partial 3ℓ cross sections for electron capture in $p + H_2$ collisions. Experimental data are by Hughes *et al.* [289], Williams *et al.* [293], and Dawson and Loyd [294]. The theoretical results are: present WP-CCC method, CTMC approach by Meng *et al.* [313], and CDW-EIS method by Busnengo *et al.* [308].

with experimental data for low energy capture into 2ℓ and 3ℓ states. A possible reason for the observed differences between the present results and experimental data at low projectile energies is the simple target structure. Electron-correlation

effects and the anisotropy of the target potential play a more important role in the collision dynamics for slower projectiles.

10.4 Angular differential cross sections for p+H₂ collisions

In this section we present singly differential cross sections for elastic scattering, target excitation, and electron capture. Differential cross sections provide a more detailed description of the collision processes and therefore represent a more stringent test on theoretical methods than integrated cross sections.

Our calculations for the elastic-scattering, total excitation, and total single-electron-capture cross sections for collision energies of 25, 75, 100, and 300 keV are presented in Figs. 10.10–10.13, respectively. In the upper panels, we compare the differential cross sections for these three processes. In the lower panel, we compare our results for electron capture to other theories and experimental data where available. To the best of our knowledge no experimental or theoretical data is available for the orientation-averaged elastic-scattering or excitation cross sections for p + H₂ collisions at intermediate energies.

The upper panels allow us to gauge comparative information about the values of these three cross sections. If we consider scattering into small angles, which practically define the integrated cross section, at 25 keV the dominant process is electron capture. However, as the collision energy grows, the excitation cross section grows, while the elastic-scattering and electron-capture cross sections diminish, so that at 75 keV and above, excitation becomes dominant. We can also see that the EC cross section diminishes faster, becoming smaller than the elastic-scattering cross section at 300 keV.

For the angular differential cross sections for electron capture there are a number of investigations with which we can compare our results. At 25 keV, we find that our calculations agree well with the data of Sharma *et al.* [297] up to 0.8

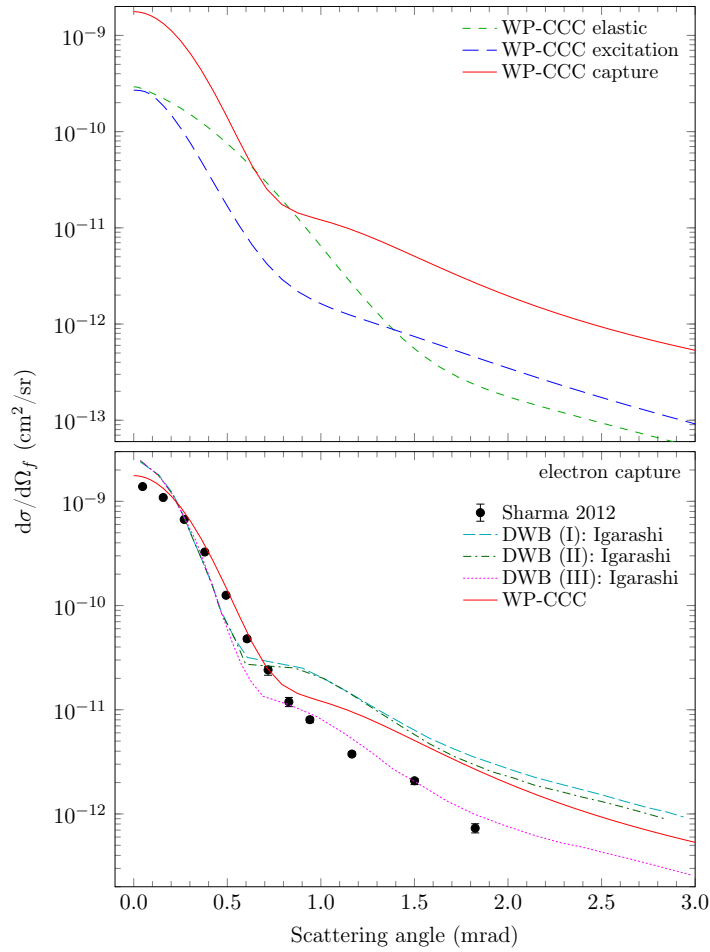


Figure 10.10: Angular differential cross sections (in the centre-of-mass frame) for elastic scattering, total excitation, and single-electron capture (upper panel) in 25 keV $p + \text{H}_2$ collisions. In the lower panel the present results for EC are compared with the experimental data by Sharma *et al.* [297] and other available calculations. The other theoretical results are: various DWB methods by Igarashi [320].

mrad, more closely following the experiment than other calculations. However, at larger scattering angles the WP-CCC method overestimates the experiment and more closely resembles the shape of the DWB (I) and DWB (II) models of Igarashi [320]. The DWB (I) result contains information about the vibrational state of the residual ion, while the DWB (II) calculation used the FN approximation. At larger angles, the DWB (III) method shows the best agreement with the experiment, despite describing the molecular target with the simple TEC treatment. This allows us to conclude that neglecting the vibrational motion of the target is not responsible for the discrepancy between our result and the experimental data.

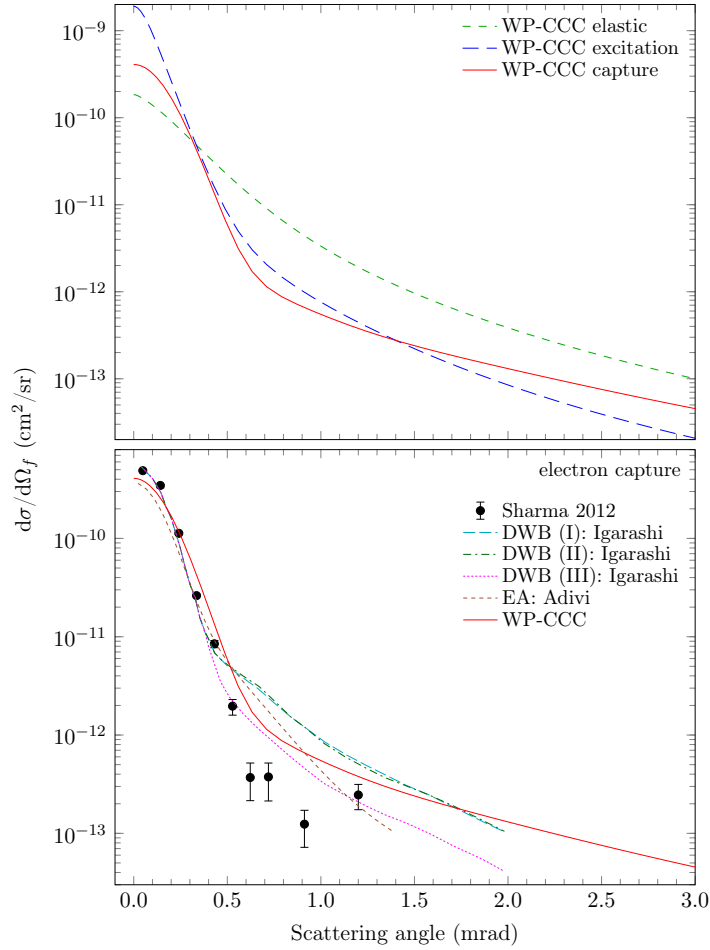


Figure 10.11: Angular differential cross sections (in the centre-of-mass frame) for elastic scattering, total excitation, and single-electron capture (upper panel) in 75 keV $p + H_2$ collisions. In the lower panel the present results for EC are compared with the experimental data by Sharma *et al.* [297] and other calculations. The other theoretical results are: various DWB methods by Igarashi [320] and EA by Ghanbari-Adivi and Sattarpour [322].

In Fig. 10.11 we present our calculations for 75 keV projectiles. The WP-CCC results generally agree with the experimental data quite well, except they do not suggest any dip around 0.9 mrad. The DWB methods of Igarashi [320] and the EA by Ghanbari-Adivi and Sattarpour [322] also do not show any local minimum. The DWB (III) method again agrees best with the experimental points.

The results for 100 keV collisions are shown in Fig. 10.12. Here we compare to the EA calculations of Ghanbari-Adivi and Sattarpour [322] and find that our results fall off less steeply at higher scattering angles where the nucleus-nucleus interaction dominates. There are no experimental data to compare to at this energy.

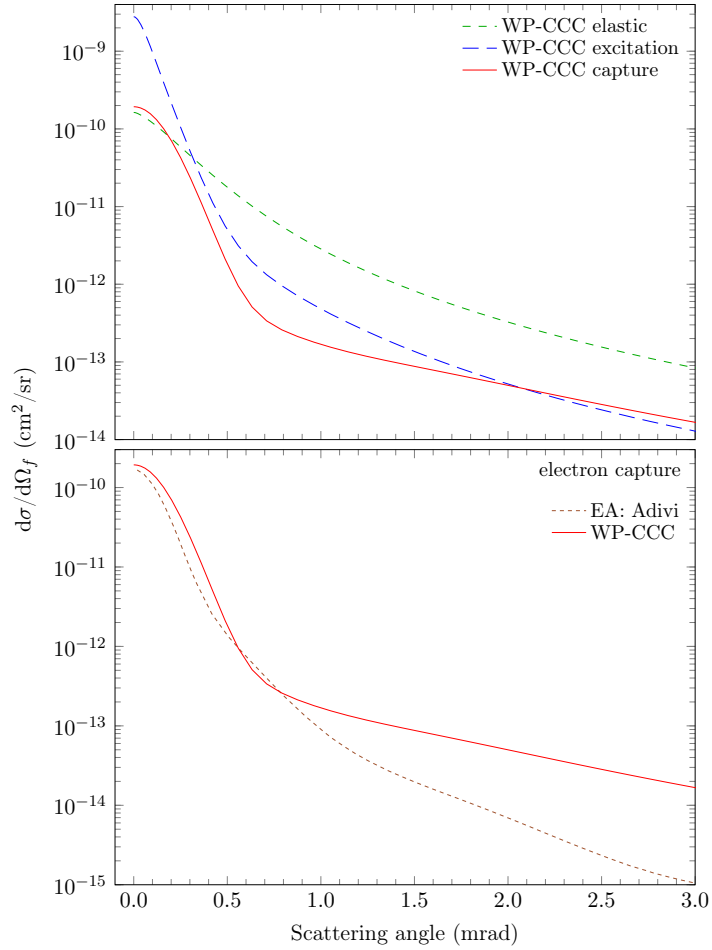


Figure 10.12: Angular differential cross sections (in the centre-of-mass frame) for elastic scattering, total excitation, and single-electron capture (upper panel) in 100 keV $p + H_2$ collisions. In the lower panel the present results for EC are compared with the EA results by Ghanbari-Adivi and Sattarpour [322].

The highest energy considered for the angular differential cross sections is 300 keV. Our results for this energy are shown in Fig. 10.13. Here the different methods based on the DWB approach by Igarashi [320] agree well with one another, while our calculation shows a somewhat different shape. Near the forward direction our cross section is slightly lower than the DWB ones, as it was the case at other projectile energies. Interestingly, we see a secondary peak around 1.2 mrad. While the CB1 results from Ref. [321] also show a secondary peak, this is due to the unphysical dip in the CB1 cross section resulting from cancellation of the projectile-electron and projectile-residual ion interaction terms in the first-order Born series. This unphysical feature is not present in our theory. The comparison between our results and the EA ones by Ghanbari-Adivi and Sattarpour [322] is

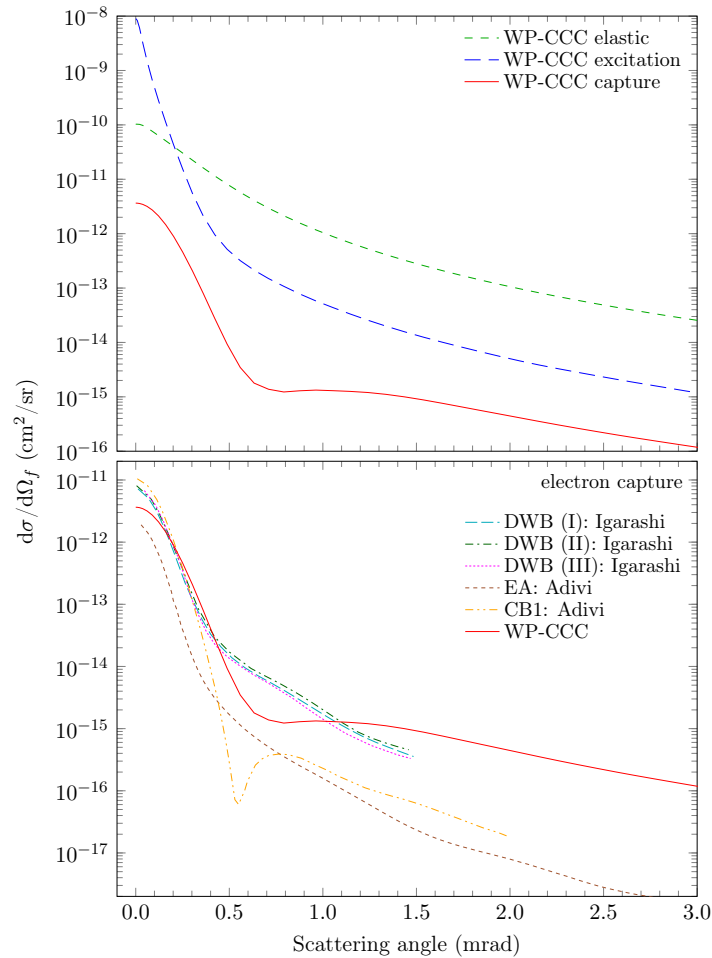


Figure 10.13: Angular differential cross sections (in the centre-of-mass frame) for elastic scattering, total excitation, and single-electron capture (upper panel) in 300 keV $p + H_2$ collisions. In the lower panel the present results for EC are compared with other available calculations. The other theoretical results are: various DWB methods by Igarashi [320], EA by Ghanbari-Adivi and Sattarpour [322], and CB1 method by Adivi [321].

similar to the 100-keV case. Both the WP-CCC and DWB calculations are larger than the EA and CB1 results.

One possible reason for the discrepancy between our calculations and the other models is that our results include electron capture into all projectile-atom states, not only the ground state. Furthermore, unlike the other available calculations, the WP-CCC method accounts for coupling effects between all the reaction channels.

10.5 Singly differential cross sections for ionisation in $p+H_2$ collisions

Next we consider the singly differential cross sections for single ionisation. We calculate all three types of SDCS for ionisation: the SDCS as a function of the electron energy, the SDCS as a function of the electron angle, and the SDCS as a function of the scattering angle of the projectile. We emphasise that the integration of each of the three singly differential cross sections reproduces the TICS in Fig. 10.4 calculated directly from the expansion coefficients using Eq. (3.147). The deviation is at most 1%. Results are presented in the laboratory frame.

In Fig. 10.14, we present our results for the singly differential cross section for ionisation as a function of ejected electron energy. There are experimental data at a number of incident projectile energies. The results are shown at 10 typical impact energies from 20 to 300 keV at which there are experimental data from multiple groups. There are also theoretical calculations to compare to at these energies.

In general, the obtained results agree very well with the experimental data by Gealy *et al.* [12]. They also agree with the data by Rudd *et al.* [246] available at projectile energies within the range 100–300 keV. However, our results slightly underestimate the data from Kuyatt and Jorgensen [298] and Rudd [299] available from 5 to 100 keV. The drop seen in the results of Kuyatt and Jorgensen [298] for low ejection energies at collision energies of 50, 75, and 100 keV was due to the inability of their apparatus to detect all of the low-energy electrons produced in the collision (see Ref. [12] for a detailed discussion of the various experimental results). We find that the WP-CCC calculations appear to better replicate experiment than the CTMC calculations by Schultz *et al.* [28] available at 50, 75, and 100 keV. At high impact energies, there is good agreement between our calculations and the FBA results by Rudd *et al.* [246].

At the lowest considered projectile energy, 20 keV, our results are slightly lower

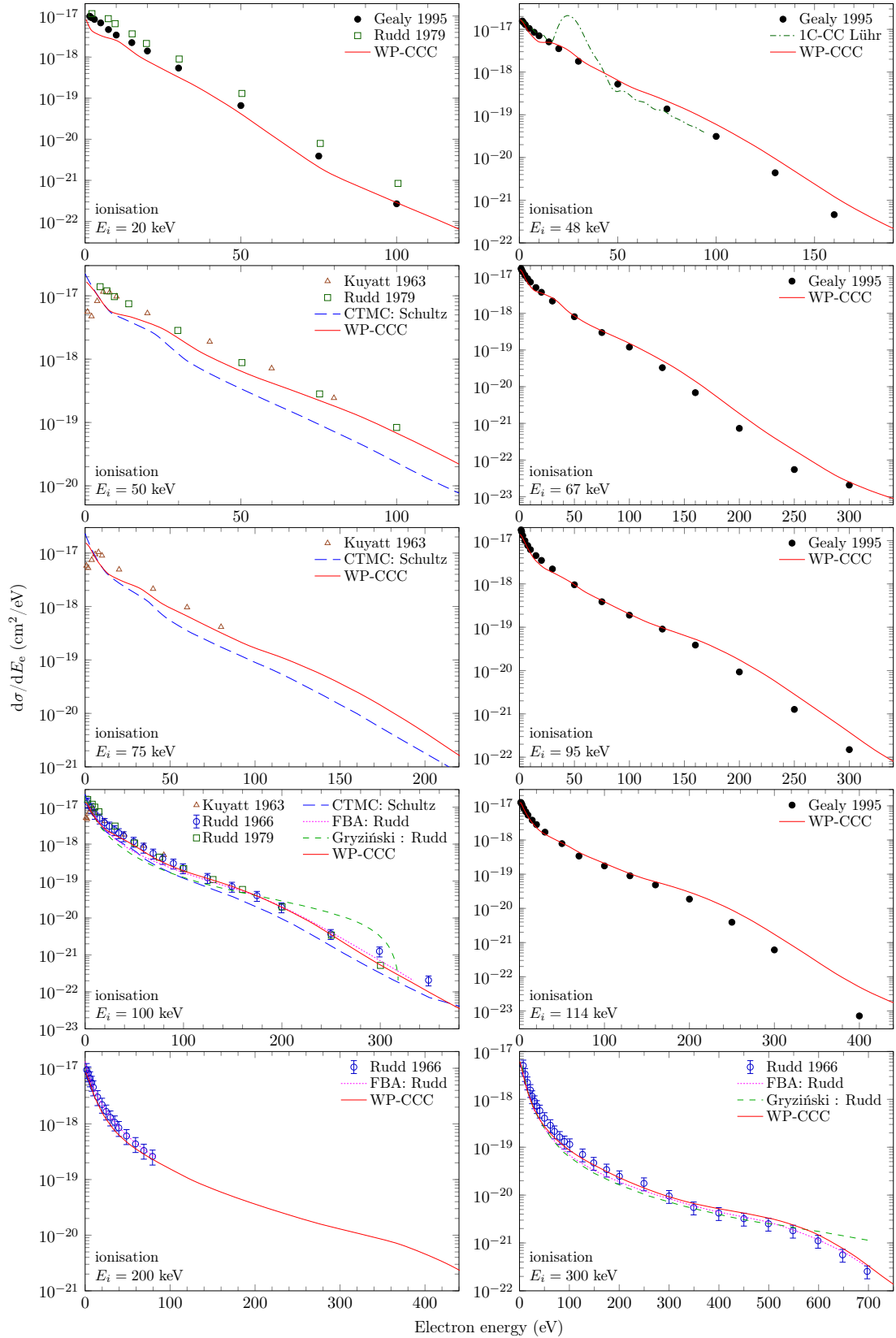


Figure 10.14: Singly differential cross sections for ionisation in $p + \text{H}_2$ collisions as functions of the electron energy. Experimental data are by Gealy *et al.* [12], Rudd [299], Kuyatt and Jorgensen [298], and Rudd *et al.* [246]. The theoretical results are: present WP-CCC approach, one-centre AOCC method by Lühr and Saenz [69], CTMC method by Schultz *et al.* [28], and FBA and Gryziński method by Rudd *et al.* [246].

than the experimental data by both Rudd [299] and Gealy *et al.* [12], at all ejected-electron energies, except for the last data point at 100 eV. At a projectile energy of 48 keV, we see excellent agreement with the experimental data from Gealy *et al.* [12] for low emission energies, but our results overestimate the experiment at high ejection energies. At this collision energy, Lühr and Saenz [69] used a one-centre effective one-electron close-coupling approach to calculate the singly differential ionisation cross section. Their cross section has a peak around 26 eV, the energy that is close to the region where the speed of the ejected electron matches that of the projectile making electron capture significantly more likely. The single-centre method cannot separate pure ionisation from electron capture leading to the unphysical peak. For 50 keV incident protons, we compare our results to the experimental data by Kuyatt and Jorgensen [298] and Rudd [299]. Similar to the 20-keV case, our calculations underestimate the data from Rudd [299] across the entire ejected-electron energy range considered. The WP-CCC results are systematically smaller than the data measured by Kuyatt and Jorgensen [298] for all but the smallest ejection energies where, as mentioned above, the experimental data are unreliable. Below 10 eV emission energy, our results are very close to the CTMC ones by Schultz *et al.* [28]. However, as the energy of the ejected electron increases, our results fall less steeply, better replicating the experimental data. At 67 keV, the WP-CCC results agree well with the data from Gealy *et al.* [12], especially at low emission energies. At 75 keV, our calculations again fall slightly below the data from Kuyatt and Jorgensen [298], except for their unphysical result at small ejection energies. Here we also see that our result falls less steeply than the CTMC calculations [28]. As the incident energy increases to 95 keV, we find very good agreement with the experimental results of Gealy *et al.* [12]. For an incident projectile energy of 100 keV, the WP-CCC results agree well with the experimental data by Rudd *et al.* [246], Kuyatt and Jorgensen [298], and Rudd [299]. We also see very good agreement with the FBA calculations by Rudd [299].

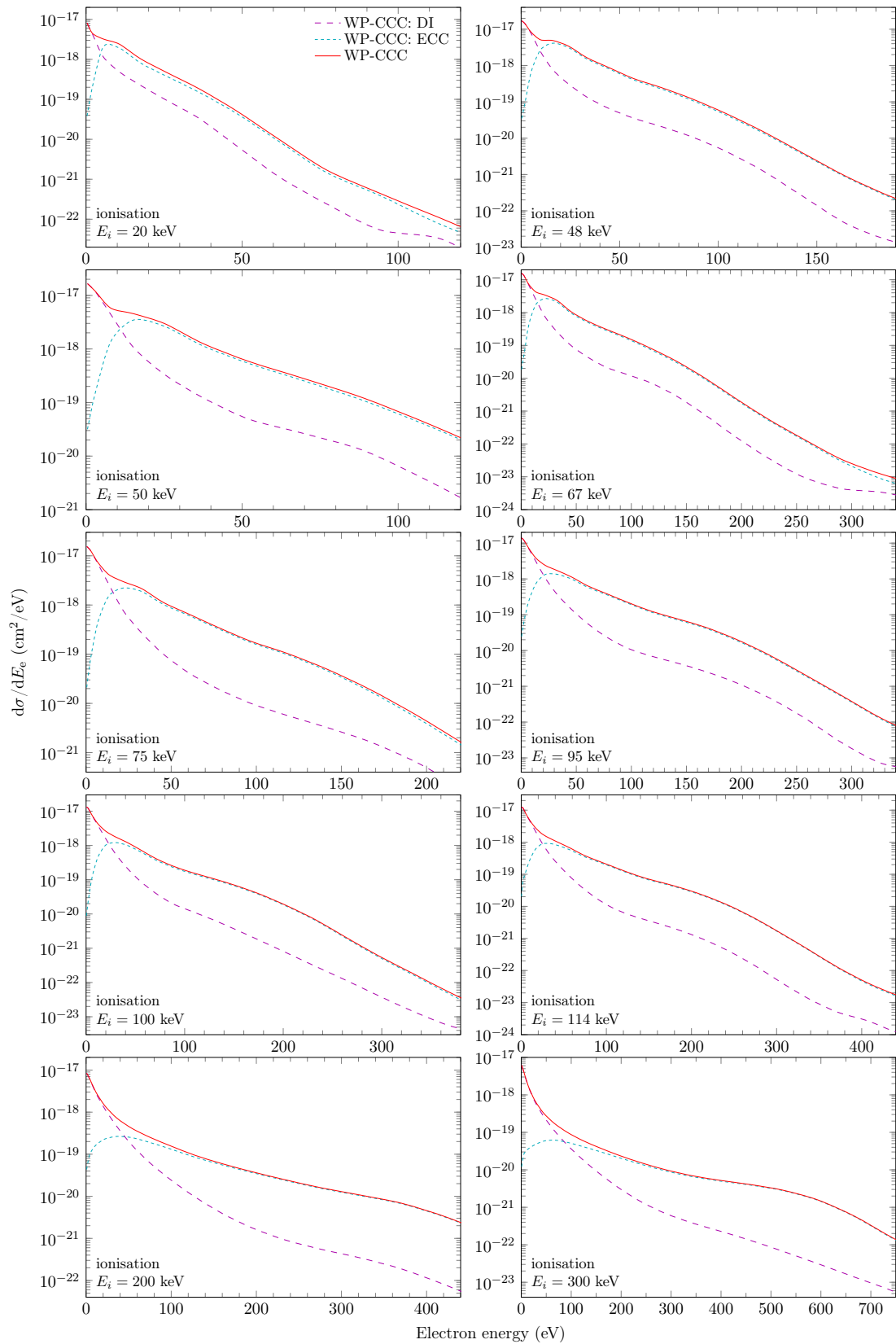


Figure 10.15: DI and ECC components for the WP-CCC results shown in Fig. 10.14. The key in the upper-left panel applies to all panels.

The classical Gryziński method produces a different shape to the experimental data, dipping slightly around 50–100 eV and then turning sharply down at 300 eV. Similar to lower impact energies, we find the WP-CCC results to be slightly larger than the CTMC ones by Schultz *et al.* [28], better agreeing with the experimental data. Our results again agree well with the experimental data by Gealy *et al.* [12] at 114 keV. At large ejection energies, our cross section overestimates the experiment. At 200 keV, agreement between the WP-CCC results and the data of Rudd *et al.* [246] is excellent. We also see good agreement with the FBA calculations. The largest impact energy considered is 300 keV. Here again our results agree very well with the experimental data across four orders of magnitude from the ionisation threshold up to an ejection energy of 700 eV. The FBA calculations from Rudd *et al.* [246] also agree well with the experimental data. The Gryziński method slightly underestimates the experiment between 100 and 300 eV and overestimates it above 600 eV. It appears that, somewhat surprisingly, the simple FBA suffices for the purpose of calculating the SDCS in the emission energy at projectile energy of 100 keV and above.

In Fig. 10.15 we show the DI and ECC components of the total WP-CCC results from Fig. 10.14. This allows us to analyse the relative contributions of these mechanisms. As one can see, the singly differential cross section for ionisation as a function of ejected-electron energy is dominated by DI, while energetic electrons are emitted purely due to ECC of the projectile. At the smaller impact energies considered, we see a slight shoulder in our results. This occurs when the contribution from electron capture into the continuum of the projectile peaks.

Figure 10.16 presents the singly differential cross section for ionisation as a function of the electron emission angle at the same projectile energies as in Fig. 10.14. Generally, we see very good agreement between the WP-CCC results and available experimental data at all collision energies considered, except for 20 keV. At 20 keV, our SDCS is systematically smaller than the experimental data by Rudd [299] and Gealy *et al.* [12] though agreeing in shape.

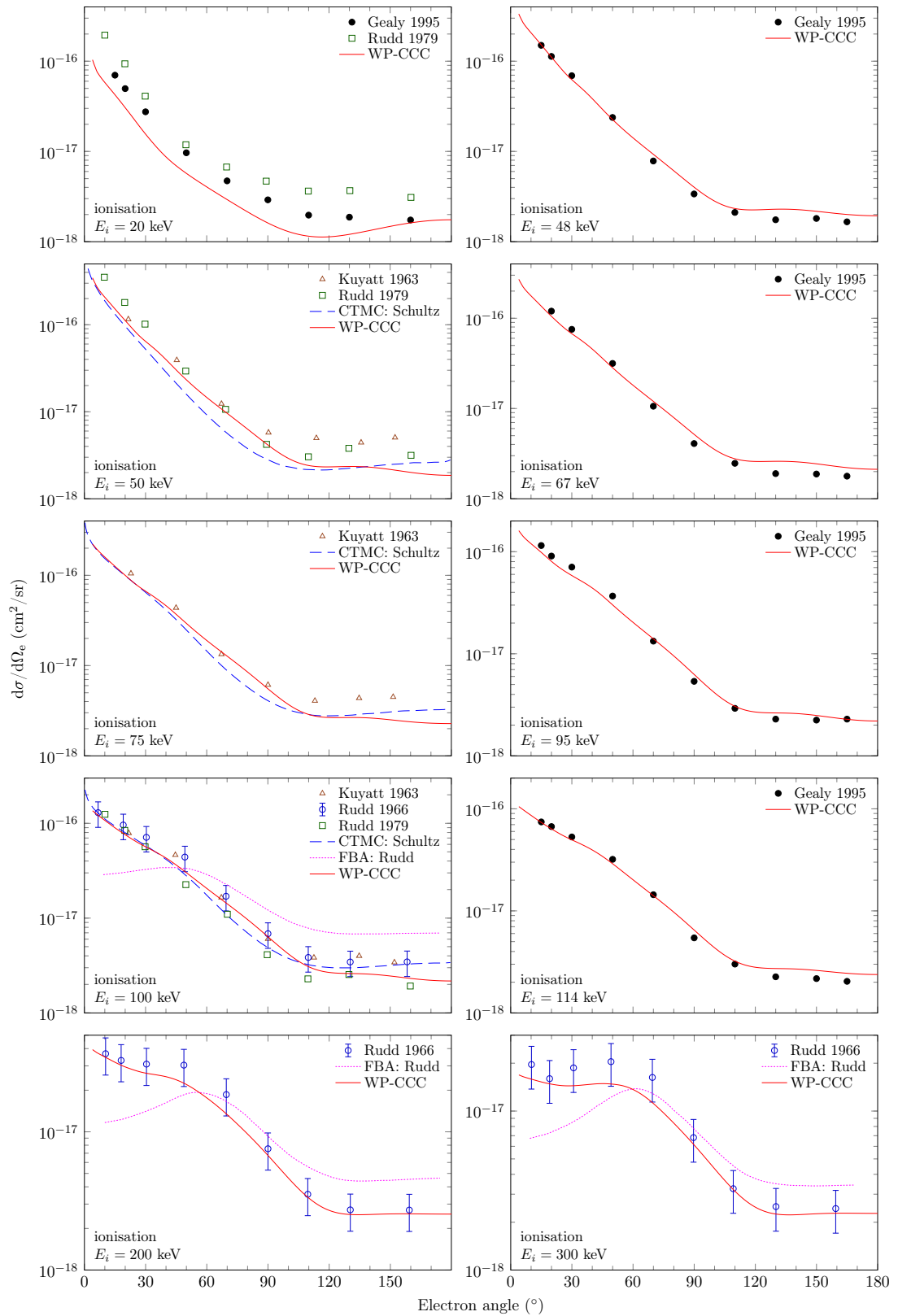


Figure 10.16: Singly differential cross sections for ionisation in $p + \text{H}_2$ collisions as functions of the electron angle. Experimental data are by Gealy *et al.* [12], Rudd [299], Kuyatt and Jorgensen [298], and Rudd *et al.* [246]. The theoretical results are: present WP-CCC approach, CTMC method by Schultz *et al.* [28], and FBA by Rudd *et al.* [246].

This is consistent with our results for the TICS where we found that the effective one-electron WP-CCC approach slightly underestimates the TICS for impact energies below about 20 keV. At 48, 67, 95 and 114 keV, our results agree very well with the experimental data from Gealy *et al.* [12] for the entire range of ejection angles. At 50 keV, we observe good agreement with the experiments of Kuyatt and Jorgensen [298] and Rudd [299] up to 110° . Above this angle, the WP-CCC method underestimates the experimental data. For an incident energy of 75 keV, our calculations agree well with the measurements from Kuyatt and Jorgensen [298] up to about 110° . Otherwise, the situation is similar to the 50-keV case. At 100, 200 and 300 keV, our results are in excellent agreement with the data from Rudd *et al.* [246].

The only other two theoretical approaches applied to calculate the SDCS in the emission angle are the FBA by Rudd *et al.* [246] and the CTMC method by Schultz *et al.* [28]. At 50, 75, and 100 keV, our results agree with the CTMC ones by Schultz *et al.* [28] reasonably well. As one can see, the FBA results by Rudd *et al.* [246], available at 100, 200, and 300 keV, fail to reproduce the experiment, significantly underestimating the data below 50° and overestimating at larger angles. Thus, our method provides significant improvement over the FBA.

The direct ionisation and electron capture to continuum components of the WP-CCC results for the SDCS for ionisation as functions of the ejected-electron angle are shown in Fig. 10.17. As one can see, at collision energies from 20 to 114 keV, the singly differential cross section for ionisation as a function of ejected electron angle is dominated by electron capture to continuum when electrons are emitted into a cone around the forward direction. Above 200 keV, the situation is opposite. Electrons emitted into large angles are purely due to direct ionisation regardless of the projectile energy.

In Fig. 10.18, we present the singly differential cross section for ionisation as a function of the scattering angle of the projectile. There are no experimental data or other theoretical calculations available in the literature to compare to.

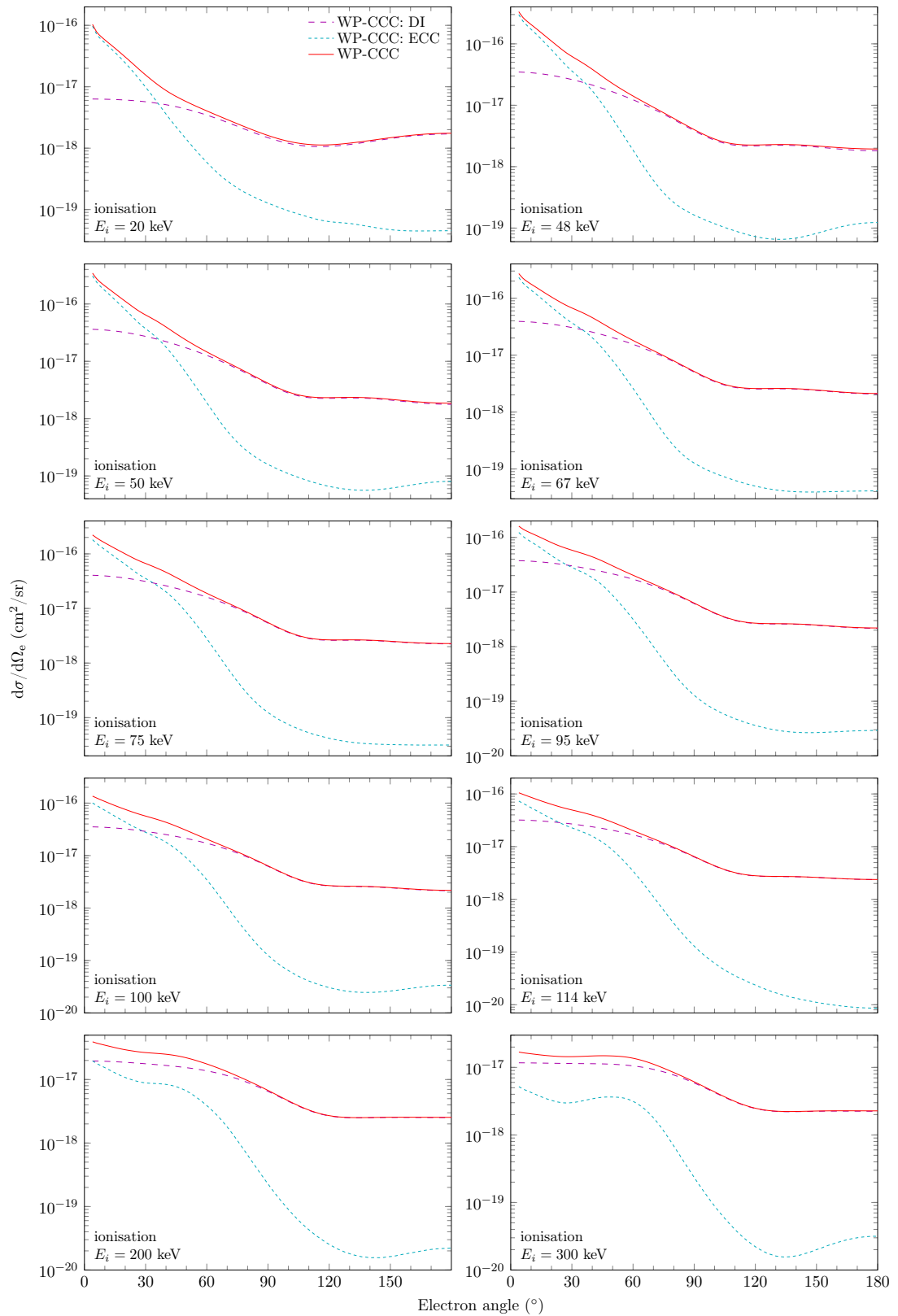


Figure 10.17: DI and ECC components for the WP-CCC results shown in Fig. 10.16. The key in the upper-left panel applies to all panels.

Therefore, the present WP-CCC results are compared with the present FBA ones. As one can see from the figure, the FBA is expected to fail at all collision energies,

even as high as 300 keV. It would be interesting to verify these results using other methods. The DI and ECC components of the WP-CCC results are also shown. At sufficiently low collision energies (50 keV and below), the dominant mechanism of ionisation is ECC if the projectile is scattered into small angles. At 67 and 75 keV, both DI and ECC mechanisms contribute equally. However, starting from 95 keV direct ionisation becomes the dominant channel for electron emission. If the projectile is scattered into large angles, electrons are ejected primarily through direct ionisation.

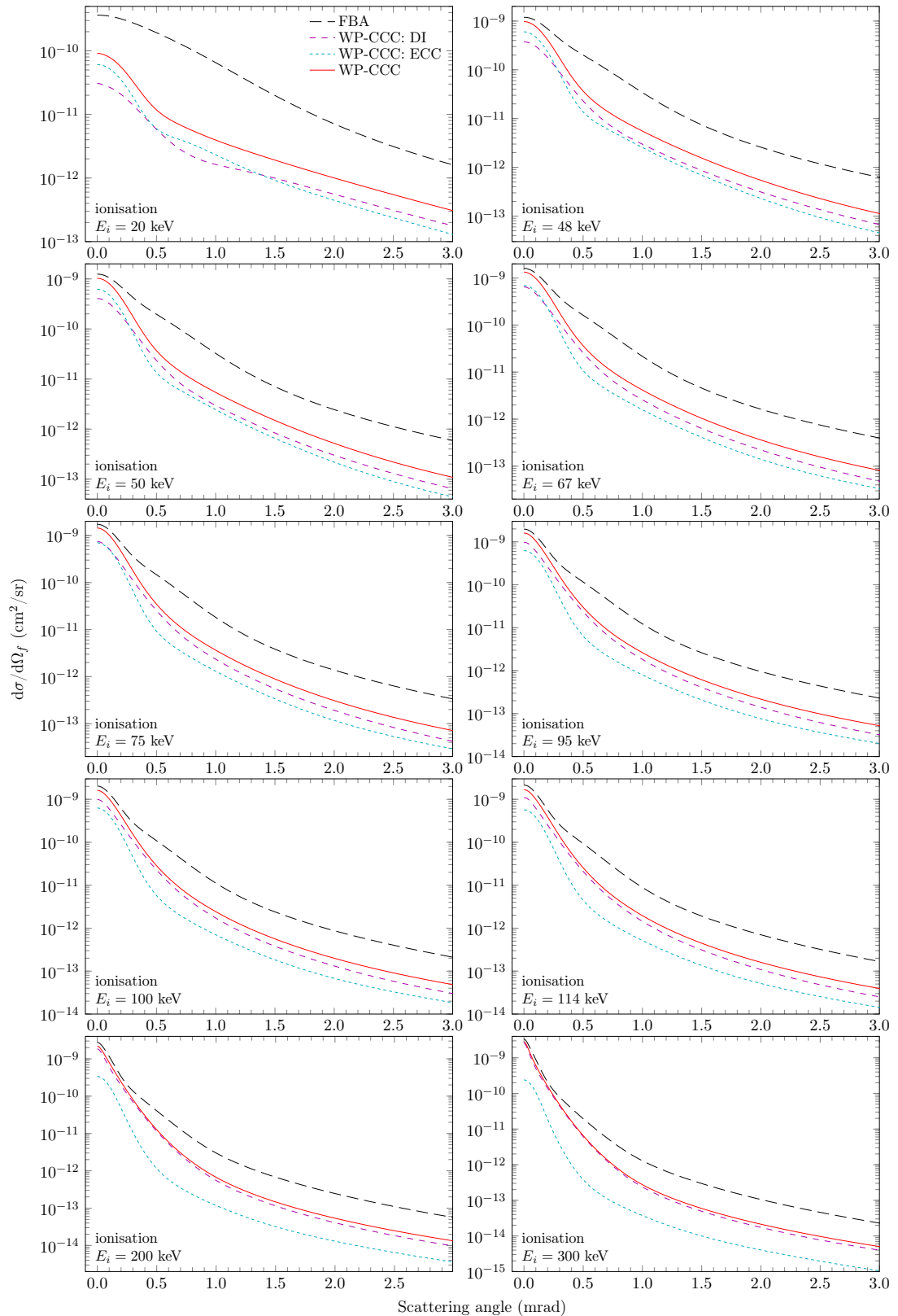


Figure 10.18: Singly differential cross sections for ionisation in $p + \text{H}_2$ collisions as functions of the scattering angle of the projectile. The theoretical results are: present WP-CCC approach and present FBA results. The DI and ECC components of the WP-CCC cross sections are also shown. The key in the upper-left panel applies to all panels.

10.6 Doubly differential cross sections for ionisation in $p + \text{H}_2$ collisions

Now we apply the WP-CCC method to calculate doubly differential cross sections for ionisation in $p + \text{H}_2$ collisions. There are three DDCS for single-electron ionisation. These are the DDCS as a function of the electron energy and electron angle, the DDCS as a function of the electron energy and scattering angle of the projectile, and the DDCS as a function of the electron angle and scattering angle of the projectile. Experimental data for the energy and angular distribution of electrons emitted in $p + \text{H}_2$ collisions has been available since the first measurements by Kuyatt and Jorgensen [298] in 1963. The DDCS as a function of projectile scattering angle and electron energy was first measured by Alexander *et al.* [303] relatively recently. We first focus on the former type of DDCS.

We find that a basis containing $10 - \ell$ bound states for each included orbital quantum number ℓ up to $\ell_{\max} = 7$ was sufficient to obtain converged results at all impact energies considered. The continuum was discretised with 25 bins and the electron-momentum cutoff κ_{\max} varied from 6.0 to 10.0 a.u., depending on the impact energy. The z -grid extended from -400 to $+400$ a.u.

10.6.1 DDCS as functions of the electron energy and the electron angle

There are many combinations of ejection angle and ejection energy at different incident energies for which experimental data exist. Here, we present the results for a wide range of electron energies and angles for impact energies from 48 to 300 keV, and compare these with the available experimental data. Where possible, we also compare to previous calculations existing in the literature. In most of the panels we also show the DI and ECC components of the cross section. These lines are omitted in the panels that contain other calculations to prevent crowding of

the figures. We calculated the DDCS by numerical integration of Eq. (3.141) and also directly using Eq. (3.142) as a self-consistency check for the method. In both cases the results were practically identical.

Our results for different impact energies are presented in Figs. 10.19–10.26. Within each figure, individual panels correspond to different emission angles. At the top of each panel we also show the speed of the ejected electron, v_e , in terms of the projectile speed. In the forward direction the ECC component peaks when $v_e/v_i = 1$. The smallest emission angle considered here is 10° . Nevertheless, the presence of the ECC peak is still observed, though to a lesser extent, even for 10° emission.

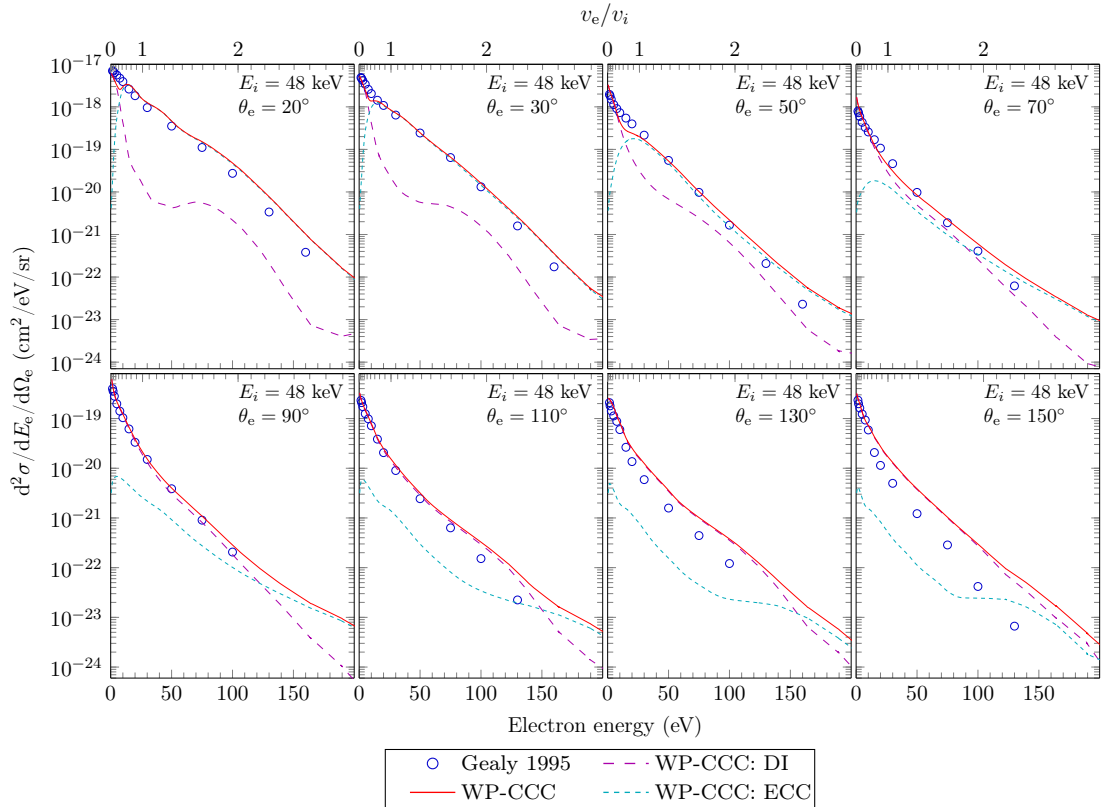


Figure 10.19: Doubly differential cross sections for ionisation in 48 keV $p + H_2$ collisions as functions of the electron energy at various emission angles. Experimental data are by Gealy *et al.* [12]. The theoretical results are: present WP-CCC approach. The DI and ECC components of the WP-CCC cross sections are also shown.

In Figs. 10.19 and 10.20 we present our calculations of the DDCS for ionisation at 48 and 67 keV. Here, the projectile speeds were $v_i = 1.386$ and 1.638 a.u., respectively. The only available data for the DDCS for ionisation at these

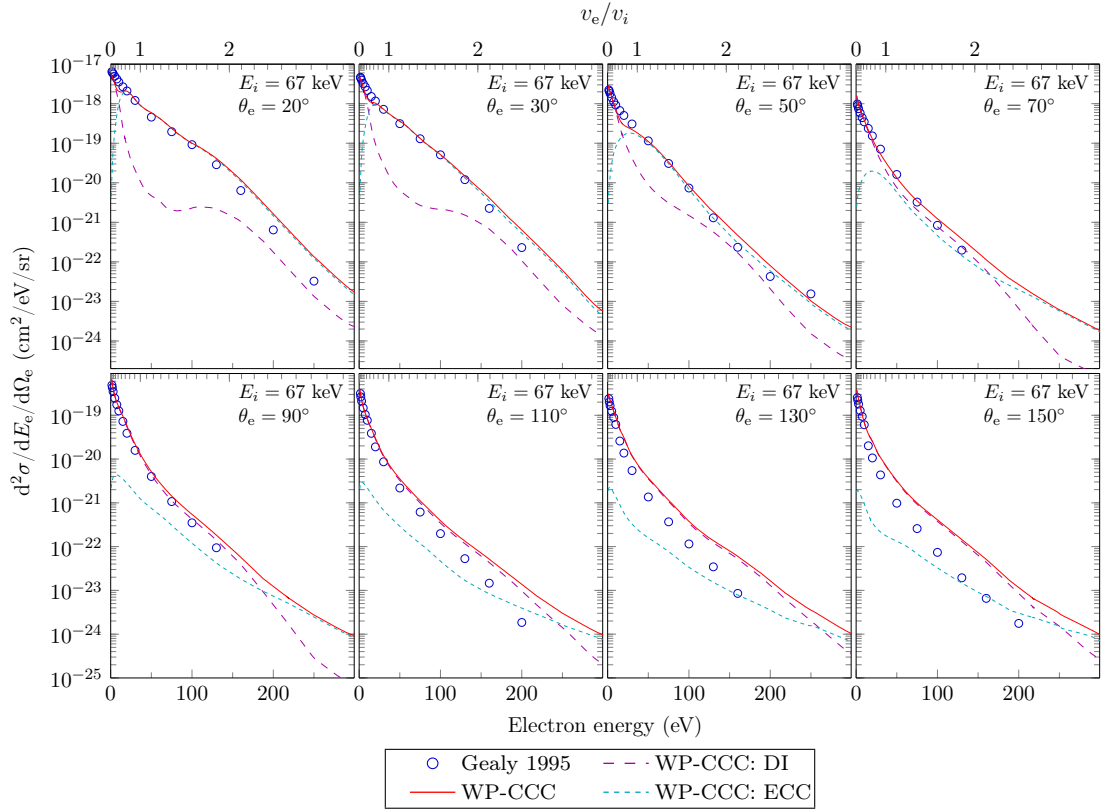


Figure 10.20: Doubly differential cross sections for ionisation in 67 keV $p + \text{H}_2$ collisions as functions of the electron energy at various emission angles. Experimental data are by Gealy *et al.* [12]. The theoretical results are: present WP-CCC approach. The DI and ECC components of the WP-CCC cross sections are also shown.

energies were the measurements by Gealy *et al.* [12]. To our best knowledge there are no other calculations at these collision energies either. For ejection angles of 110° and smaller, we observe excellent agreement between our results and the experimental data. At 130 and 150° our DDCS agree well with experiments for low-energy electrons but for high-energy electrons they overestimate the experimentally measured cross section at backward emission angles. There could be two possible explanations for this, one is experimental and the other theoretical. First, this is the region in which the DDCS is several orders of magnitude smaller than for low-energy electrons and, therefore, the experimental measurements have the greatest uncertainty due to low counting rates. Second, ionisation resulting in emission in the backward direction is dominated by the DI mechanism. The DI component of the ionisation cross section is given by the product of the amplitude for excitation into a positive-energy pseudostate and the overlap between the true

continuum wave and corresponding wave-packet pseudostate. The pseudostates and the continuum wave are found by numerically solving the Schrödinger equation with the model target potential. At asymptotically large distances this potential tends towards a Coulomb attraction with charge +1 a.u. However, in reality the electron would be on the opposite side of the residual target ion from the projectile proton, resulting in an effective Coulomb interaction at asymptotically large distances with charge +2 a.u. Hence, in our approach to calculating DI the emitted electron does not account for the additional attraction, due to the projectile proton. Therefore, the current approach may somewhat overestimate the probability of emission in the backward direction.

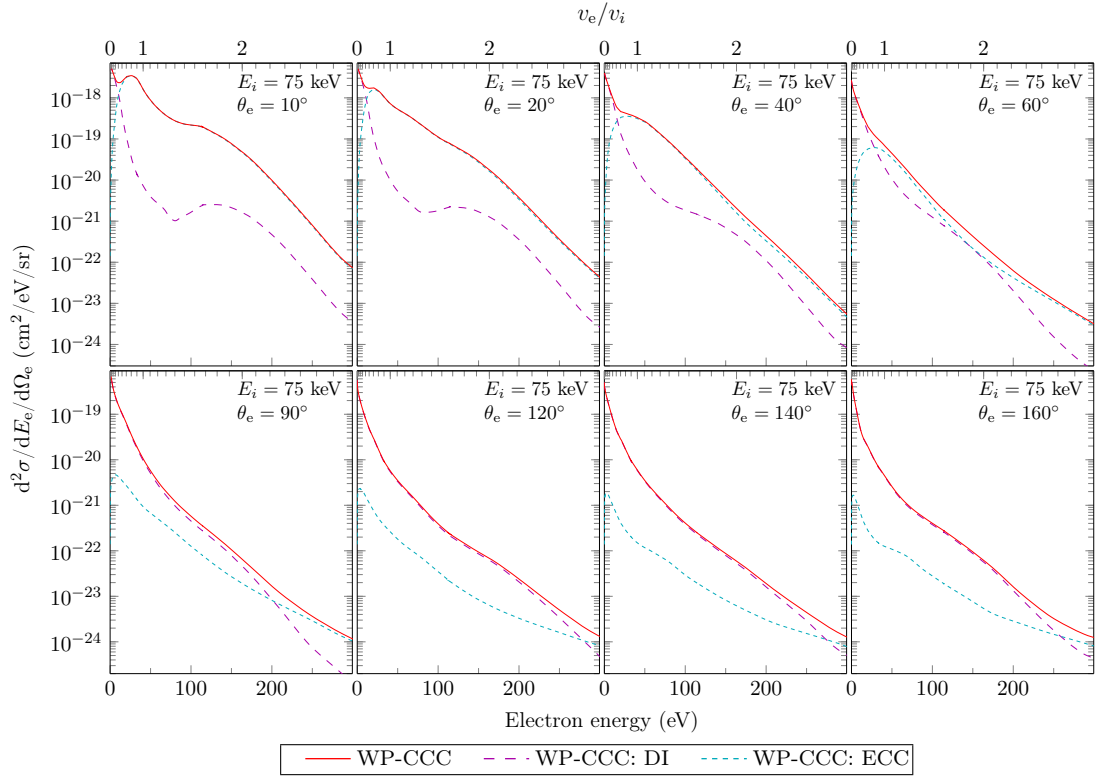


Figure 10.21: Doubly differential cross sections for ionisation in 75 keV $p + \text{H}_2$ collisions as functions of the electron energy at various emission angles. The theoretical results are: present WP-CCC approach. The DI and ECC components of the WP-CCC cross sections are also shown.

Figure 10.21 shows the DDCS for ionisation at 75 keV for ejection angles from 10 to 160°. For the smallest emission angle, we find that the ECC component of the DDCS peaks when the speed of the ejected electron is slightly less than that of

the projectile, meaning that the likelihood of the electron staying slightly behind the outgoing projectile is higher. The projectile speed is $v_i = 1.733$ a.u. at this impact energy. The ECC peak is strongest for emission at 0° . Our calculations suggest it has an influence on the cross section for electron emission, even at 10° . At 60° , the DI and ECC components are comparable for most of the considered electron energies. Then, for emission into angles of 90° and greater, DI becomes the dominant mechanism contributing to the total DDCS for ionisation. Only for very high electron energies does the ECC component have a significant effect on the overall results at 120° , 140° and 160° . For emission into the backwards direction the DDCS is entirely dominated by DI, as expected.

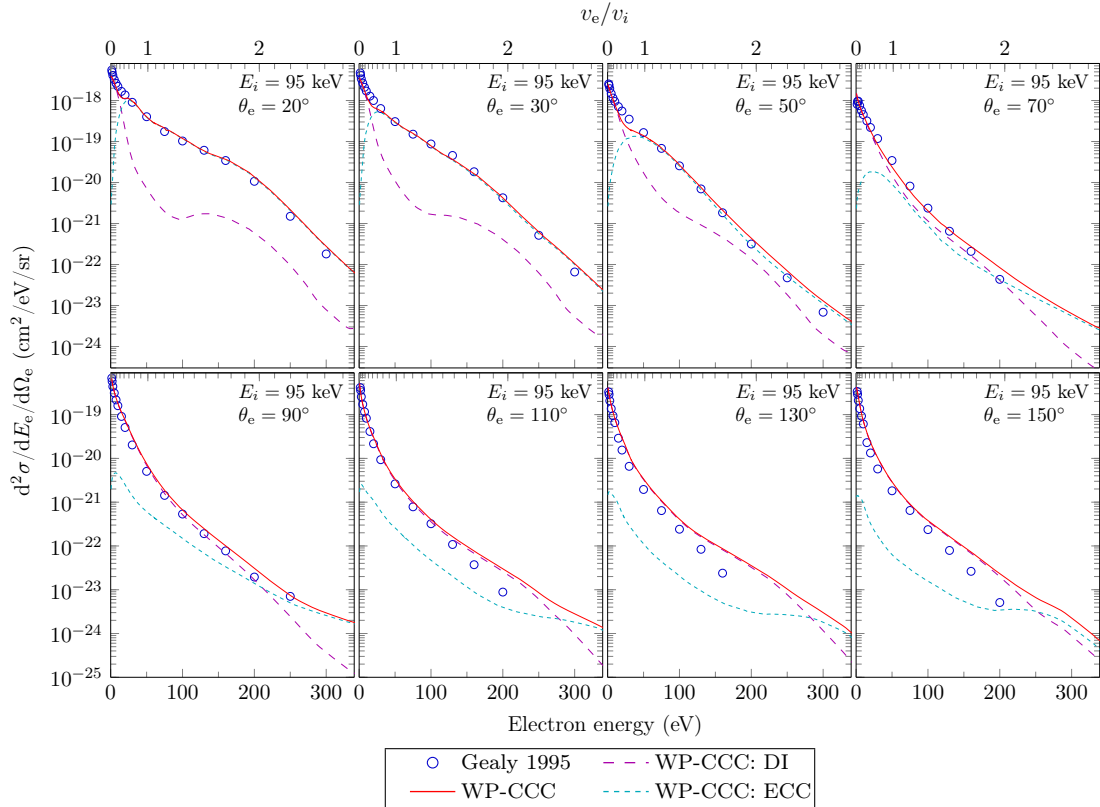


Figure 10.22: Doubly differential cross sections for ionisation in 95 keV $p + \text{H}_2$ collisions as functions of the electron energy at various emission angles. Experimental data are by Gealy *et al.* [12]. The theoretical results are: present WP-CCC approach. The DI and ECC components of the WP-CCC cross sections are also shown.

In Fig. 10.22 we present our DDCS for ionisation at 95 keV for ejection angles from 20 to 150° . The projectile speed at this energy is $v_i = 1.950$ a.u. Our results are compared with the experimental data of Gealy *et al.* [12]. To our

best knowledge there are no other experimental measurements or calculations at this collision energy. We observe very good agreement between the WP-CCC calculations and the experimental data. At the smallest considered ejection angle of 20° , the interplay between the DI and ECC contributions near the matching speed results in an overall smoother cross section that follows the experimental data more closely than observed at lower projectile energies. At this incident energy we also see improved agreement between our results and the experimental data for high-energy electrons emitted at 130 and 150° , compared to 48 and 67 keV.

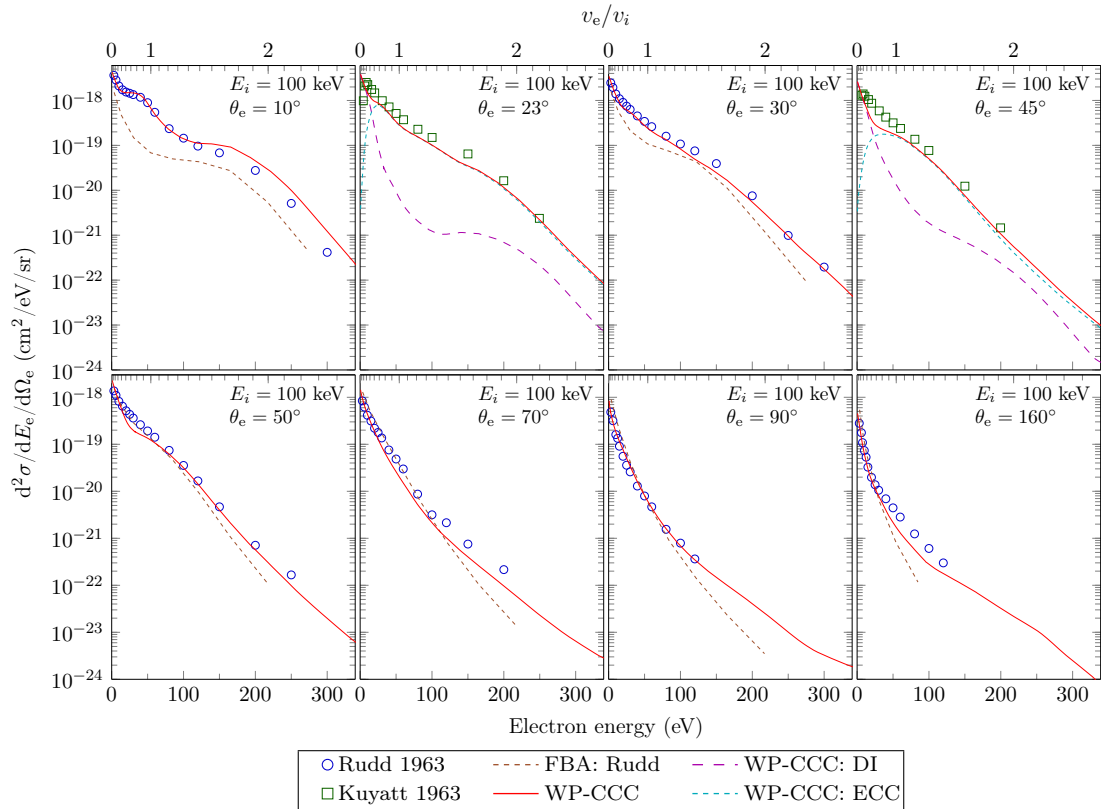


Figure 10.23: Doubly differential cross sections for ionisation in 100 keV $p+H_2$ collisions as functions of the electron energy at various emission angles. Experimental data are by Rudd and Jorgensen [245] and Kuyatt and Jorgensen [298]. The theoretical results are: present WP-CCC approach. The DI and ECC components of the WP-CCC cross sections are also shown. FBA by Rudd and Jorgensen [245].

In Fig. 10.23 we compare our results for 100 keV collisions with the experimental data of Rudd and Jorgensen [245] and Kuyatt and Jorgensen [298]. Rudd and Jorgensen [245] also performed the FBA calculations. The FBA results sig-

nificantly underestimate the cross section at an emission angle of 10° , whereas the WP-CCC calculations show excellent agreement with the experimental data across the entire measured energy range. We also see a clear shoulder, due to the ECC peak for emission at 10° , in both the experimental data and our calculations. At this impact energy, the matching speed is $v_i = 2.000$ a.u. At 23° , the WP-CCC results agree well with the experimental data of Kuyatt and Jorgensen [298], except for small energies of the emitted electrons. However, these experimental data were unreliable in that region, due to inefficiencies in the apparatus at detecting low-energy electrons [12]. In this energy region the DDCS is dominated by the DI mechanism. At energies above 30 eV, ECC is the most significant contributor to the ionisation cross section. At 30° , the FBA calculations continue to underestimate the experimental data, although less significantly, whereas the WP-CCC calculations follow the experiment very closely at all ejection energies. For emission into an angle of 45° , we find good agreement with the experimental results of Kuyatt and Jorgensen [298], except for the narrow region near the ejection energy of 30 eV, where the DI and ECC components contribute equally to the ionisation cross section. Here, our calculation underestimates the experiment. At an emission angle of 50° , we also observe a similar difference between our result and the experimental data of Rudd and Jorgensen [245]. However, the difference is smaller than at 45° . For ionisation resulting in electron emission at 70° , the WP-CCC results agree well with the experimental data, although as the ejection energy increases our results begin to underestimate the measured cross section. The FBA calculations by Rudd and Jorgensen [245] show similar behaviour, except beyond 100 eV, where they fall off more steeply, deviating from the experiment and the WP-CCC calculations. The FBA results show similar behaviour also at 90° , whereas the WP-CCC results display excellent agreement with the experiment at all emission energies. Lastly, for 160° emission the FBA overestimates the experimental cross section near the ionisation threshold and then falls off too steeply with increasing energy. Our calculations agree well with

the data of Rudd and Jorgensen [245] for low-energy electron emission, slightly underestimating the experimental data above 50 eV.

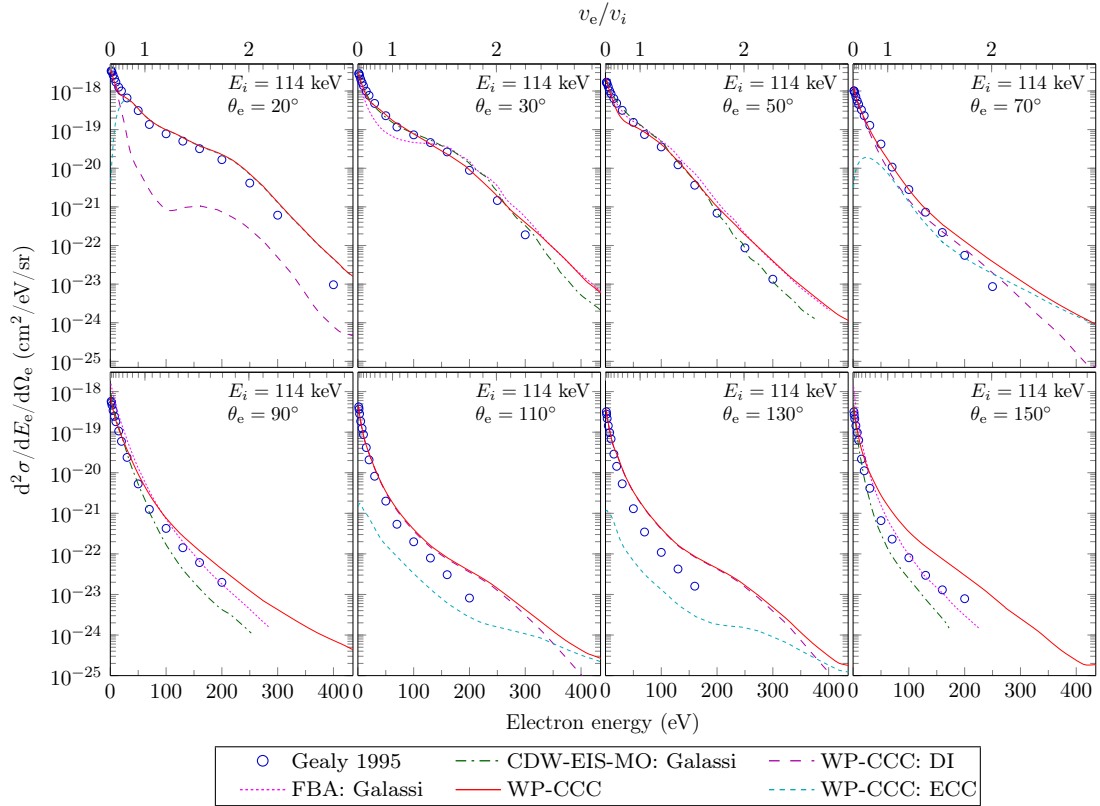


Figure 10.24: Doubly differential cross sections for ionisation in 114 keV $p+H_2$ collisions as functions of the electron energy at various emission angles. Experimental data are by Gealy *et al.* [12]. The theoretical results are: present WP-CCC approach and FBA and CDW-EIS-MO method by Galassi *et al.* [310]. The DI and ECC components of the WP-CCC cross sections are also shown.

Figure 10.24 shows the DDCS at an incident energy of 114 keV, along with the experimental data of Gealy *et al.* [12] and the FBA and CDW-EIS-MO calculations by Galassi *et al.* [310]. The projectile speed is $v_i = 2.136$ a.u. At an emission angle of 20° , the WP-CCC calculations agree very well with the experimental data below 250 eV emission energy. Above 250 eV, however, our results slightly overestimate the experiment. The same is observed at 30 and 50° . The FBA calculations of Galassi *et al.* [310] suggest a shoulder at 150 eV for 30° emission, which is not present in the other calculations or experimental data. At both 30 and 50° , the CDW-EIS-MO results agree well with the experiment. At 70° and above, the WP-CCC results agree well with the experimental data for

smaller ejection energies, then tend to overestimate the data as the emission angle and energy increases. At emission angles of 90 and 150°, the FBA results overestimate the cross section for low-energy electron emission, but agree well with the experimental data at high ejection energies. The CDW-EIS-MO calculations show the opposite behaviour, agreeing well with the experiment at small ejection energies, but underestimating it at larger emission energies. We conclude that the WP-CCC method describes the experimental cross section more consistently than the FBA and CDW-EIS-MO methods.

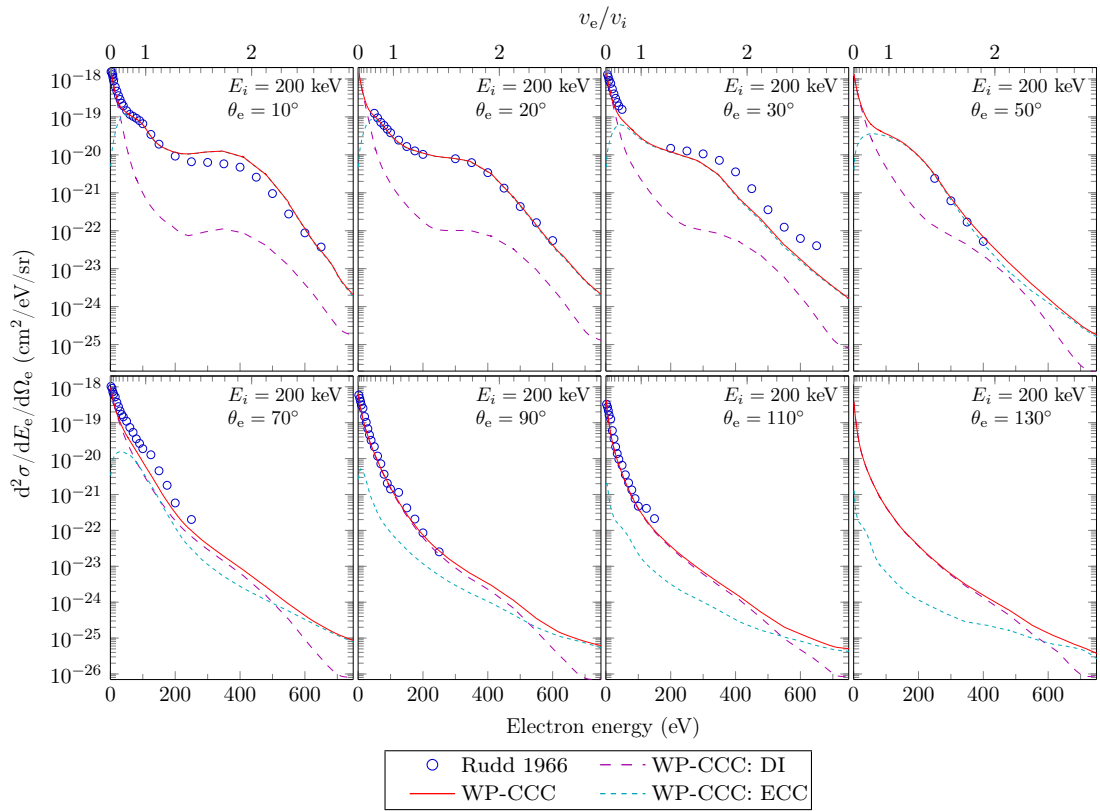


Figure 10.25: Doubly differential cross sections for ionisation in 200 keV $p+H_2$ collisions as functions of the electron energy at various emission angles. Experimental data are by Rudd *et al.* [246]. The theoretical results are: present WP-CCC approach. The DI and ECC components of the WP-CCC cross sections are also shown.

In Fig. 10.25 we present our results for a collision energy of 200 keV in comparison with the experimental data of Rudd *et al.* [246]. For emission into 10°, the experiment shows a clear shoulder near the matching speed of $v_i = 2.829$ a.u., which is perfectly reproduced by the WP-CCC results. We find good agreement between the WP-CCC results and experimental data across all ejection angles

and energies for which experimental data is available. At the emission angles of 10, 30 and 70°, our calculations slightly deviate from the experimental data when moderate-energy electrons are emitted. At this impact energy, we see the binary-encounter peak clearly resolved at small emission angles. In particular, at 10°, our calculations show a wide, but pronounced, peak at 350 eV, reproducing the shape of the measured cross section. There is no experiment at 130°. Here, the WP-CCC results are given for completeness.

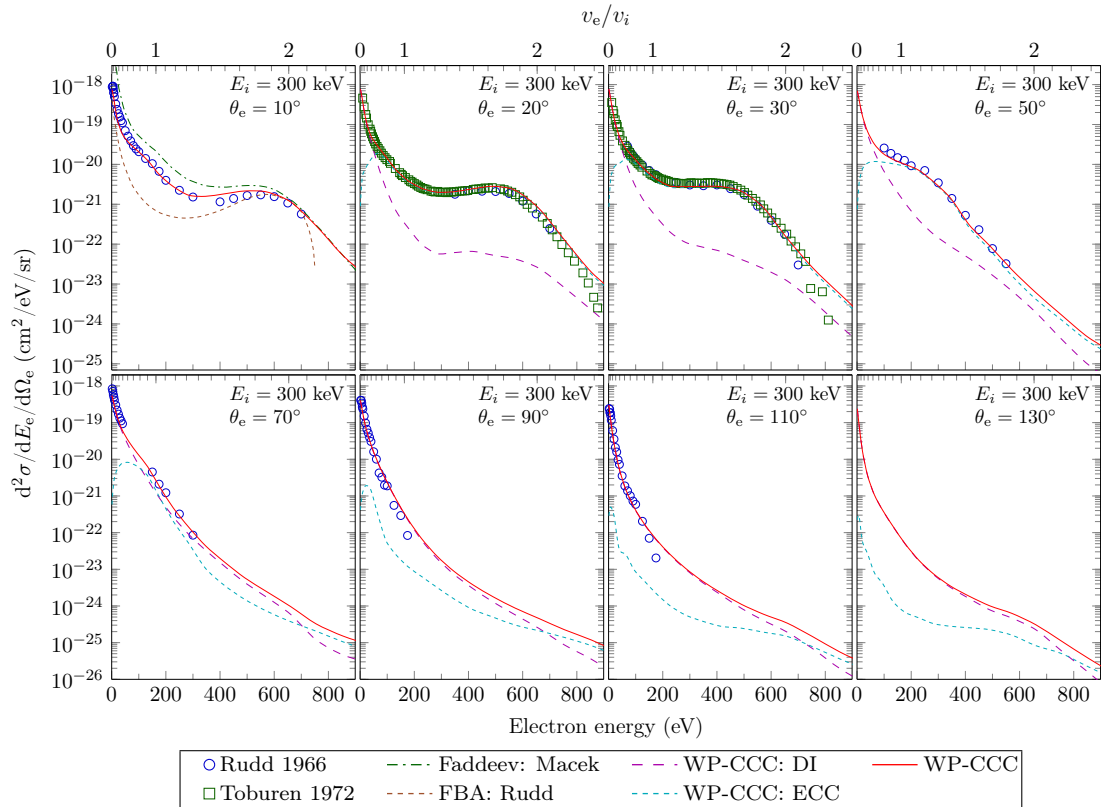


Figure 10.26: Doubly differential cross sections for ionisation in 300 keV $p+H_2$ collisions as functions of the electron energy at various emission angles. Experimental data are by Rudd *et al.* [246] and Toburen and Wilson [295]. The theoretical results are: present WP-CCC approach, FBA by Rudd *et al.* [246], and approach based on the first term in the Neuman expansion of the Faddeev equations by Macek [90]. The DI and ECC components of the WP-CCC cross sections are also shown.

Figure 10.26 shows the present results for the DDCS for ionisation at an incident energy of 300 keV as a function of the ejected electron energy for emission angles from 10 to 130°. We compare our calculations to the two independent sets of experimental data from Rudd *et al.* [246] and [295]. For emission at 10°, we can compare the present results to the FBA calculations by Rudd *et al.* [246] and

the calculations based on the first term in the Neuman expansion of the Faddeev equations by Macek [90]. There are no other calculations for other emission angles at this incident energy.

We find excellent agreement between our calculations and the experimental data of Rudd *et al.* [246]. The present results agree well with the measurements of Toburen and Wilson [295] as well, but only within the energy range where their data are in agreement with the data of Rudd *et al.* [246]. For emission into 10° , the FBA calculations by Rudd *et al.* [246] significantly deviate from the experimental results, underestimating the data from 0 up to 600 eV and then falling off sharply at higher emission angles. At this impact energy, the projectile speed is $v_i = 3.465$ a.u. It is sufficiently high for the FBA to be considered suitable for calculating the TICS. However, we see that the FBA fails to reproduce the underlying DDCS. The approach used by Macek [90] overestimates the experimental data significantly at small emission energies and then decreases to eventually agree at 650 and 700 eV. The reason is the same as indicated earlier.

The WP-CCC results reproduce both the main peak in the DDCS for the very low emission energies and the binary-encounter peak. Furthermore, we find that for small ejection angles the DDCS is dominated by DI for small energies and ECC for larger ejection energies. Near the emission angle of 70° , the DI and ECC components become comparable, except for very small ejection energies where the ECC part falls off steeply towards the ionisation threshold. At 90° and above, the DDCS is primarily made of the DI component, only for very large ejection energies does ECC contribute for backward ejection angles. This makes physical sense since ejection into angles greater than 90° will result in the electron being closer to the target nucleus while the projectile nucleus moves away from the scattering system in the forward direction.

The present results represent the first calculations of the DDCS for $p + H_2$ collisions in the intermediate-energy range, in particular, that are capable of describing the available experimental data. A wide range of experimental results

exist, spanning from the initial measurements of Kuyatt and Jorgensen [298] to the latest data of Gealy *et al.* [12]. However, theorists have struggled to accurately reproduce these experiments. All currently available theoretical results are obtained using perturbative approaches that are applicable only at sufficiently high projectile energies. The WP-CCC method is the only non-perturbative approach to differential ionisation that accounts for the strong coupling between the reaction channels. Additionally, we are able to distinguish between the DI and ECC mechanisms, providing further insight into the underlying physics.

Our results demonstrate excellent agreement with all available experimental data at projectile energies from 48 to 300 keV and electron emission angles less than 130° . We observed an overestimation of the experimental data for emission into backward angles greater than 130° . It is suggested that this may be due to the large uncertainty in the experimental data in this region. In part, this could also be due to the approach to calculating the total breakup amplitude used herein that assumes a weaker effective charge experienced by the emitted electron at asymptotically large distances from the origin than it actually might be in this particular kinematic regime. Our results agree particularly well with the most recent experiment by Gealy *et al.* [12] and the high projectile energy data by Rudd *et al.* [246]. At the highest impact energies considered the WP-CCC method reproduces both the main peak in the DDCS near the ionisation threshold and the binary-encounter peak.

Furthermore, we explicitly calculated the DI and ECC contributions to the total DDCS. We find that both mechanisms play important roles in the electron emission cross sections. This indicates that inclusion of the two-centre nature of the scattering system is essential for accurately calculating differential cross sections for ionisation. Additionally, the present results demonstrate that strong coupling between reaction channels plays an important role in determining the energy and angular distribution of emitted electrons.

10.6.2 DDCS as functions of the projectile scattering angle and the electron energy

Figure 10.27 shows the present calculations for the DDCS for ionisation as a function of the scattering angle of the projectile at selected electron-emission energies. Specifically, results are presented for electron energies of 14.6, 34.6, 37.6, 41.6, 49.6, and 54.6 eV, where experimental data are available. The projectile energy is 75 keV, which corresponds to a speed of 1.733 a.u. At the matching speed, the emitted electron would have an energy of 40.8 eV. In the upper-left panel we present results for an electron energy of 14.6 eV. The three sets of experimental data available at this emission energy agree well with one another for scattering angles less than 0.5 mrad. However, at larger scattering angles the data of Alexander *et al.* [303] and Egodapitiya *et al.* [304] suggest the presence of some structure around 1.0 mrad, whereas the measurements reported by Sharma *et al.* [305] do not. The CDW-EIS calculations by Alexander *et al.* [303] agree with the experimental data in the forward direction but from 0.4–0.9 mrad they overestimate the data from both Alexander *et al.* [303] and Egodapitiya *et al.* [304]. Above this the CDW-EIS calculations agree with the magnitude of data recorded by Alexander *et al.* [303], but don't reproduce the shape. As the scattering angle increases the CDW-EIS results fall off more slowly than all other results. The M3DW-EIS calculations by Chowdhury *et al.* [323] generally reproduce the shape of the experimental data, including the structure reported by Alexander *et al.* [303] around 1.0 mrad. However, they are consistently smaller across all scattering angles. The FBA results of Chowdhury *et al.* [323] demonstrate significant disagreement with all experimental and other theoretical results. In the forward direction the FBA vastly overestimates the DDCS, then falls off steeply and underestimates the other results at large scattering angles. The CDW-EIS-MO calculations by Igarashi and Gulyás [325] more closely follow the experimental data than the other available theoretical results. In particular they agree very

well with the measurements by Alexander *et al.* [303] at scattering angles less than 0.9 mrad, then continue to fall off smoothly, similarly to the data of Sharma *et al.* [305]. The present WP-CCC results agree very well with the experimental data of Alexander *et al.* [303] and Sharma *et al.* [305] in the forward direction, then from 0.4–0.9 mrad they continue to closely follow the data of Alexander *et al.* [303], slightly underestimating the measurements by Sharma *et al.* [305]. Our calculations show no evidence of any structure at large scattering angles, instead falling off smoothly in agreement with the more recent data by Sharma *et al.* [305] above 1.0 mrad.

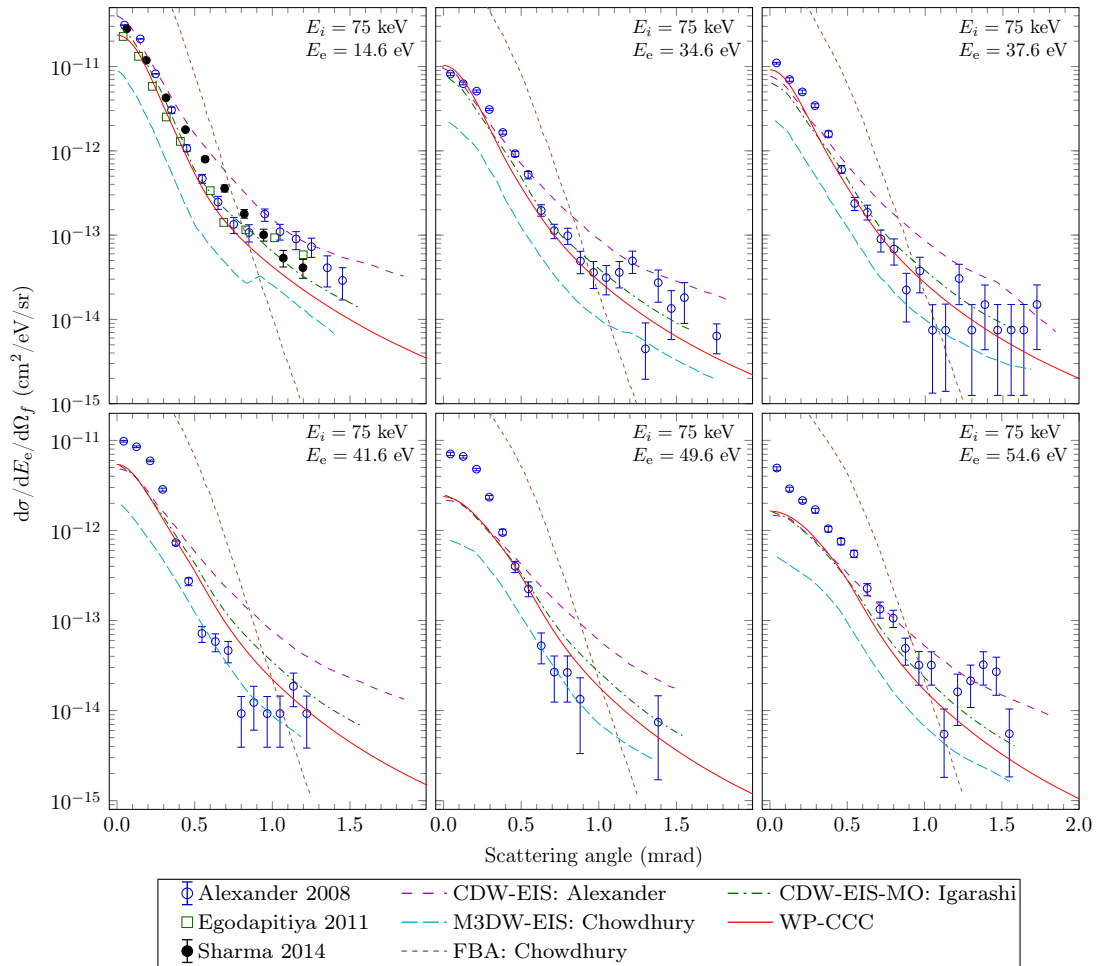


Figure 10.27: Doubly differential cross sections for ionisation in 75 keV $p + \text{H}_2$ collisions as functions of the scattering angle of the projectile at various ejected-electron energies. Experimental data are by Alexander *et al.* [303], Egodapitiya *et al.* [304], and Sharma *et al.* [305]. The theoretical results are: present WP-CCC approach, CDW-EIS method by Alexander *et al.* [303], M3DW-EIS method and FBA by Chowdhury *et al.* [323], and CDW-EIS-MO method by Igarashi and Gulyás [325].

The remaining panels in Fig. 10.27 show the DDCS results at the other emis-

sion energies where Alexander *et al.* [303] reported experimental data. At 34.6 eV, the situation is very similar to that at 14.6 eV. The WP-CCC results agree well with the experiment up to a scattering angle of 1.2 mrad. However, thereafter, the structure suggested by Alexander *et al.* [303] is not replicated by our calculations. In the forward direction our results are very similar to the CDW-EIS and CDW-EIS-MO calculations, but above 0.5 mrad the WP-CCC results decrease like the CDW-EIS-MO ones in agreement with the experimental data whereas the CDW-EIS calculation begins to fall off less steeply. The M3DW-EIS result is again in qualitative agreement with the experiment but underestimates the magnitude.

At 37.6, 41.6, and 49.6 eV, the measurements of Alexander *et al.* [303] suggest that the structure is less pronounced or absent. As a result, improved agreement between the WP-CCC results and the experiment is observed at large scattering angles. However, like in all other calculations, at small scattering angles significant discrepancies are observed when more energetic electrons are ejected. The CDW-EIS-MO ones also agree better with experiment. However, in the forward direction all available theoretical results underestimate the experimental measurements. The experimental data suggests a narrowing of the forward peak at emission energies near the 40.8 eV where the speed of the electron matches that of the projectile. However, our results agree with the CDW-EIS-MO prediction that the DDCS should continue to steadily decrease in magnitude, without significantly changing shape. At an emission energy of 54.6 eV the experimentally measured DDCS falls off at a similar rate to that recorded at 14.6 and 34.6 eV. The theoretical results are in better agreement with the experiment at this energy than at 37.6, 41.6, and 49.6 eV. However, the experimental data of Alexander *et al.* [303] again suggest some form of structure at large scattering angles which could not be resolved in the data at 49.6 eV. None of the available theoretical results support this observation at any of the emission energies considered.

To summarise, we find that the WP-CCC results demonstrate very good agreement with the CDW-EIS-MO calculations by Igarashi and Gulyás [325].

Both methods more consistently reproduce the experimental data than the other available theoretical approaches. The CDW-EIS calculations by Alexander *et al.* [303] show a similar level of agreement in the forward direction but overestimate the experiment and CDW-EIS-MO and WP-CCC results as the scattering angle increases. The M3DW-EIS calculations always underestimate the experimental data and other theoretical methods, although the shape is very similar to the CDW-EIS-MO and WP-CCC results qualitatively, except for the small peak present in the M3DW-EIS results for 14.6 eV electrons. With the exception of the not yet fully understood structure in the experimental data of Alexander *et al.* [303] and Egodapitiya *et al.* [304] at large scattering angles, the WP-CCC calculations demonstrate very good agreement with experiment at 14.6, 34.6, and 37.6 eV. At higher emission energies agreement is less satisfactory, in particular when the electron's speed is close to the projectile's. At both 41.6 and 49.6 eV the WP-CCC calculations fall off less steeply than the experimental data and underestimate the measured DDCS in the forward direction. Calculation of the DDCS for ionisation is easiest at the smallest scattering angles. Moreover, we find very close agreement between the CDW-EIS, CDW-EIS-MO, and WP-CCC results at all considered electron energies when the projectile is scattered into the forward direction. Therefore, the discrepancy between theory and experiment for small scattering angles observed in the lower three panels in Fig. 10.27 is somewhat puzzling. The experimental data by Sharma *et al.* [305] do not support the structure observed at large scattering angles by the other two experiments. However, improved data for large scattering angles is not available for other emission energies. Interestingly, the SDCS and TICS obtained by integrating our DDCS was consistent with our results presented in Sect. 10.3 and Sect. 10.5, respectively. Recall that at 75 keV it was found to slightly overestimate experiment. Consequently, we would expect our DDCS for ionisation to generally be slightly larger than experiment, but in fact we see the opposite.

A possible reason for the observed discrepancy between calculation and ex-

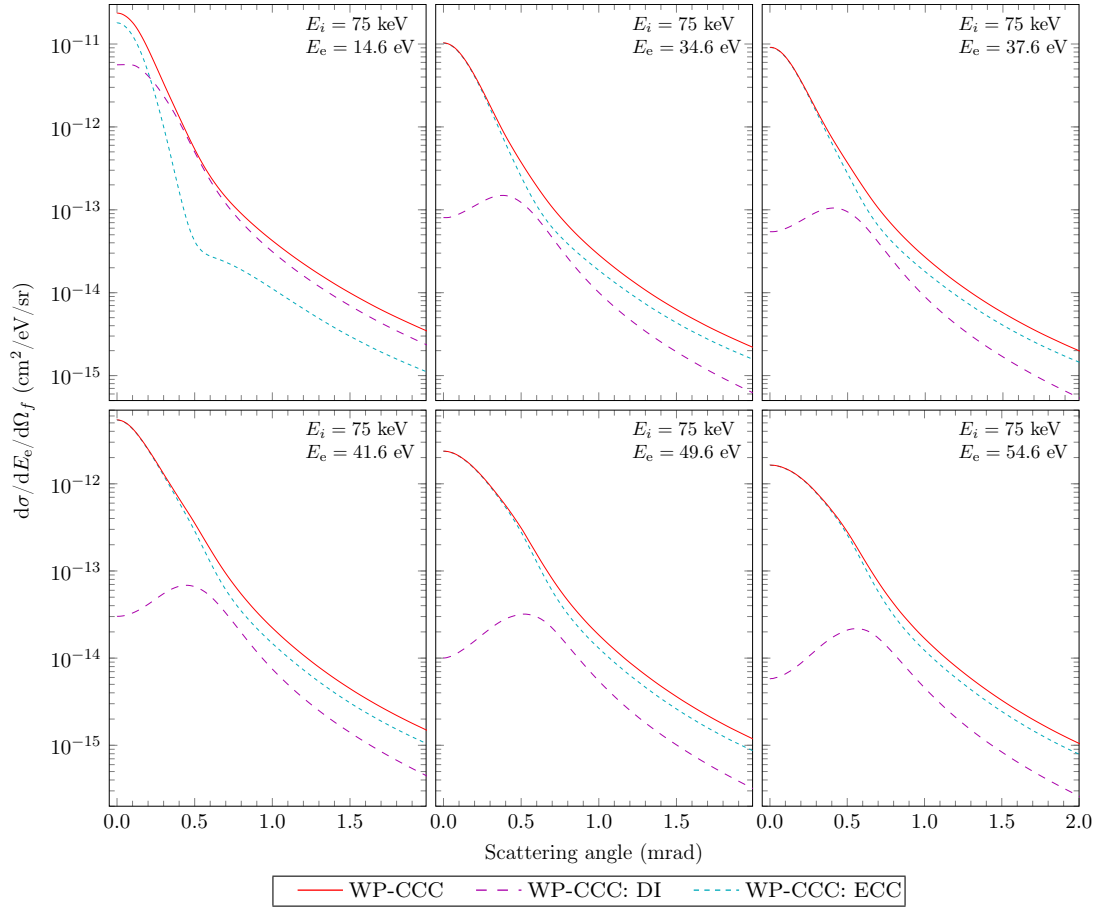


Figure 10.28: DI and ECC components for the WP-CCC results shown in Fig. 10.27.

periment for large electron energies could be the omission of electron-correlation effects in the theoretical models. However, this appears to be a reasonable approximation for calculating integrated and singly differential cross sections at intermediate projectile energies. Furthermore, the present approach gives excellent agreement with the experimental data for the DDCS as a function of the energy and angle of the ejected electrons. As seen in the lower three panels of Fig. 10.27, when more energetic electrons are emitted, the disagreement in the forward direction is as large as 70%. It is difficult to expect that electron-correlation effects can change the present results by that much. We should also mention that the WP-CCC approach to doubly differential ionisation in $p + \text{He}$ collisions with and without electron-correlation effects [332, 333] gave practically the same result in all domains including the forward-scattering angle. In any case, the reason for the discrepancy remains to be understood and warrants further investigation.

In Fig. 10.28 we show the same WP-CCC results as in Fig. 10.27, but this time together with the DI and ECC components. At all emission energies considered, except the smallest, we see that the forward scattering DDCS is dominated by the ECC mechanism. As the emission energy increases this becomes more pronounced. Physically this can be explained by the emitted electron being pulled along by the attractive charge of the projectile. Higher energy electrons are travelling faster, making it more likely for them to be closer to the projectile nucleus than the target nucleus if they are emitted into the forward cone. At larger scattering angles DI and ECC are generally of similar magnitude, with ECC dominating for low energy electrons and gradually becoming less significant as the energy increases. However, at all considered emission energies both DI and ECC play a significant role in determining the total DDCS for ionisation.

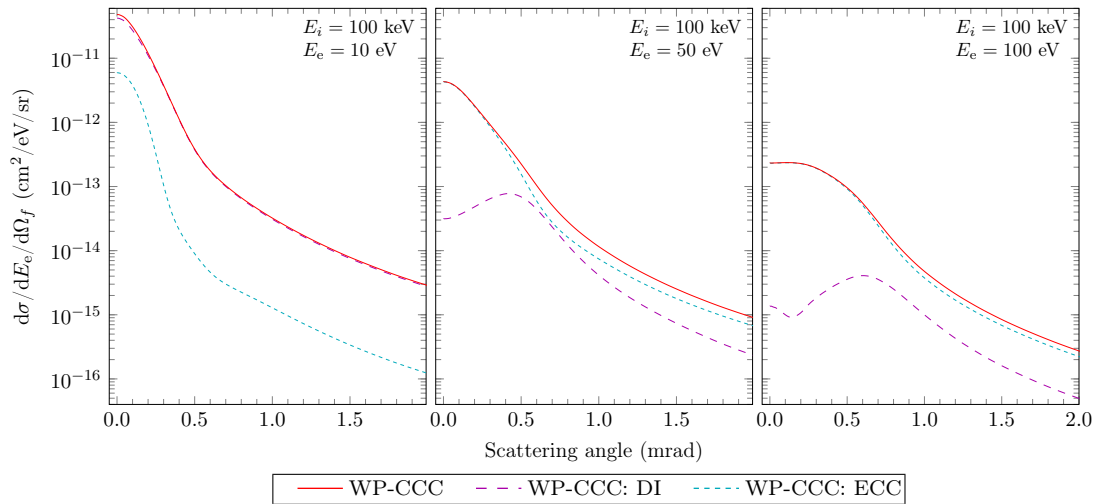


Figure 10.29: Doubly differential cross sections for ionisation in 100 keV $p+H_2$ collisions as functions of the scattering angle of the projectile at various ejected-electron energies. The theoretical results are: present WP-CCC approach. The DI and ECC components of the WP-CCC cross sections are also shown.

In Figs. 10.29 and 10.30 we present the DDCS for ionisation differential in the projectile scattering angle and electron energy at incident energies of 100 and 200 keV, respectively. We show the total DDCS and its DI and ECC components. The electron energy that corresponds to the matching speed is 54.4 and 114.3 eV for 100 and 200 keV projectiles, respectively. There are no experimental data available at these projectile energies. As one can see, DI and ECC both make

significant contributions to the total DDCS at all three emission energies. For 10 eV electrons, the DI component is dominant across all scattering angles, whereas at 50 eV the ECC one is two orders of magnitude larger in the forward direction. At 0.5 mrad both components are comparable, and DI contributes more at higher scattering angles. For 100 eV emission, ECC is the dominant mechanism from 0 to 2.0 mrad. Since this energy corresponds to an electron speed much larger than the projectile speed and electron emission near forward angles is most likely, this suggests that the majority of high-energy electrons leave the scattering system ahead of the projectile.

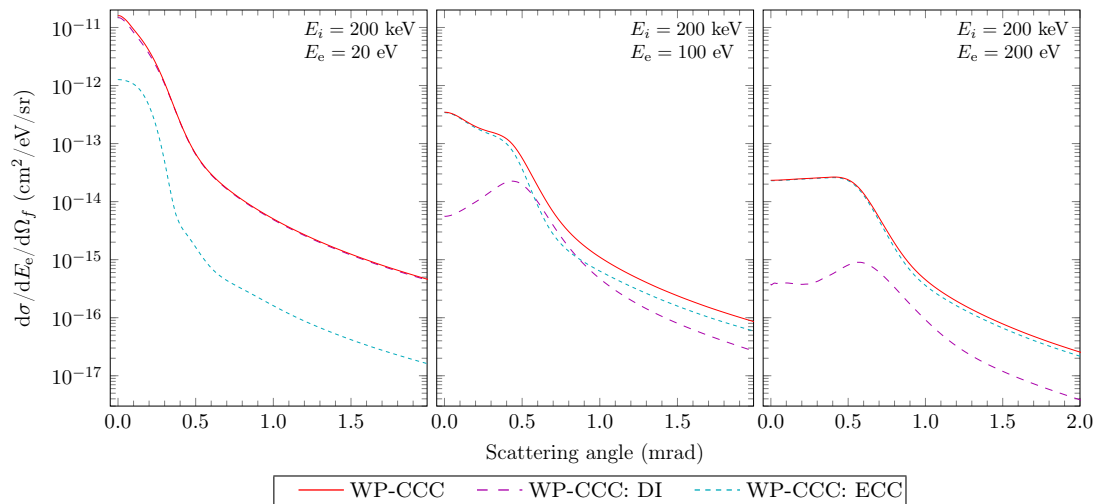


Figure 10.30: Doubly differential cross sections for ionisation in 200 keV $p+\text{H}_2$ collisions as functions of the scattering angle of the projectile at various ejected-electron energies. The theoretical results are: present WP-CCC approach. The DI and ECC components of the WP-CCC cross sections are also shown.

At an incident energy of 200 keV, we see that the DI component is less significant in the forward direction. For 100 eV electrons the results show a small shoulder around 0.5 mrad. For emission of 200 eV electrons the DDCS is almost constant from 0 to 0.5 mrad. This is similar to the behaviour observed for ejection of 100 eV electrons by 100 keV proton collisions in Fig. 10.29. The origin of this behaviour is unknown. However, it is reminiscent of the secondary-peak observed in angular differential cross sections for electron capture by positively charged ions at projectile energies in the MeV region. The secondary peak in electron capture DCS is attributed to the Thomas double-scattering mechanism [334].

According to this classical explanation, the projectile scatters the target electron by 60° , transferring energy and increasing the electron speed to approximately that of the projectile. Then, the electron elastically scatters from the residual target ion, altering its trajectory by 60° again such that it leaves the scattering system in approximately the same direction as the projectile. The momentum transfer required for this corresponds to a projectile scattering angle of 0.47 mrad. Therefore, the DCS for electron capture is increased at this angle. The structure observed in the present DDCS for ionisation occurs very close to the Thomas angle and is primarily caused by the ECC component. Perhaps it is possible that the Thomas mechanism is causing a secondary peak in the DDCS for ionisation by increasing the probability of ECC near 0.47 mrad. However, the projectile energies considered herein are significantly smaller than those typically associated with the Thomas mechanism. This feature is only observed in the DDCS for ionisation for emission of electrons with large energies and is not significant enough to have an effect on the SDCS for ionisation studied in Sect. 10.5. It should be noted however, that the rather pronounced peak structure in the DI channel is not due to the Thomas process. Rather, it can be explained as a simple effect of the kinematic conservation laws in a binary process.

10.6.3 DDCS as functions of the projectile scattering angle and the electron angle

Finally, for completeness, in Fig. 10.31 we present the DDCS for ionisation of H_2 by proton impact as a function of the scattering angle of the projectile and emission angle of the ejected electron. The azimuthal angle of the electron is measured relative to the scattering plane, i.e. $\varphi_f = 0$. Since the interaction between the particles is symmetric relative to the scattering plane, we include angles only for one hemisphere of the collision geometry. To the best of our knowledge there are no experimental measurements or calculations of this type of DDCS for $p + \text{H}_2$ collisions available in the literature. For comparison we

present FBA calculations as well. Each row in Fig. 10.31 shows our results for electrons emitted at a fixed polar angle θ_e with varying azimuthal angle, φ_e . Each column represents emission into a fixed azimuthal angle for different polar angles. For small scattering angles the FBA results are larger or comparable to the WP-CCC calculations across all considered collision geometries. Conversely, at the larger scattering angles the FBA results fall off much more rapidly. The overall magnitude of the WP-CCC calculations decreases with increasing θ_e for all considered azimuthal angles, suggesting emission in the forward direction is more likely. However, for a fixed polar angle, different values of φ_e have less of an effect on the magnitude of the cross section. Instead, we see that the shape of the DDCS is influenced by the azimuthal angle.

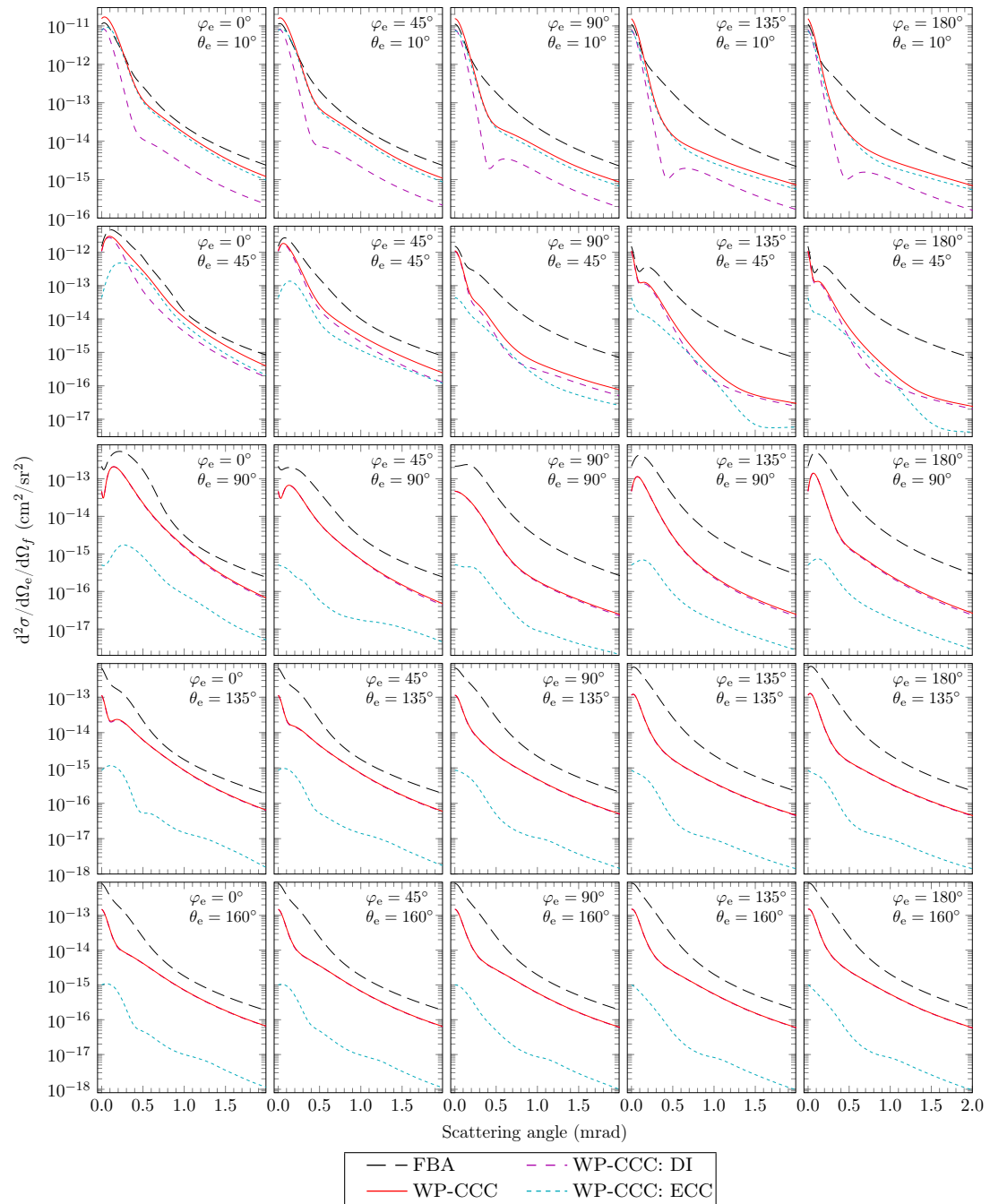


Figure 10.31: Doubly differential cross sections for ionisation in 75 keV $p + \text{H}_2$ collisions as functions of the scattering angle of the projectile at various emission angles. The theoretical results are: present WP-CCC approach and present FBA results. The DI and ECC components of the WP-CCC cross sections are also shown.

10.7 Chapter summary

In this chapter we developed an effective one-electron approach to $p + \text{H}_2$ collisions within the WP-CCC framework. This approach allows us to utilise the efficient computational techniques developed in our one-electron code and avoid signifi-

cant complexities associated with a two-electron target description. Despite the simplicity of the approach, the converged total cross sections for single-electron capture and ionisation show good agreement with experiment in a wide energy range. While previous close-coupling methods applied to this system used only a single-centre expansion, our two-centre method allows differentiation between ionisation and electron capture, providing a more detailed picture of the collision process. We also calculate state-resolved capture cross sections and find reasonably good agreement with experiment. Overall, our results improve over previous theoretical studies.

Next, we calculated the angular differential cross sections for elastic scattering, excitation and electron capture, and the singly differential ionisation cross sections as functions of the ejected-electron energy and angle, as well as projectile scattering angle. This is the first time that the close-coupling approach has been applied to the singly differential cross sections for $p + H_2$ collisions. We find significantly improved agreement with experiment compared to previously available classical and perturbative calculations, where available. Furthermore, we identify specific mechanisms responsible for electron emission in particular kinematic regimes by analysing the DI and ECC components of the total SDCS. The present results demonstrate that the effective one-electron WP-CCC approach to proton collisions with H_2 can provide an accurate description of the singly differential cross sections for all interconnected processes taking place in $p + H_2$ collisions.

Finally, we calculated all types of doubly differential cross sections for single-ionisation in $p+H_2$ collisions. A wide range of experimental results exist, spanning from the initial measurements of Kuyatt and Jorgensen [298] to the latest data of Sharma *et al.* [305]. However, theorists have struggled to accurately reproduce these experiments. All currently available theoretical results are obtained using perturbative approaches that are applicable only at sufficiently high projectile energies. The fundamental assumptions that these methods are based on become questionable at the incident energies considered in this work, where the orbital

speed of the target electrons is comparable to, or somewhat greater than, the projectile speed. The present WP-CCC method is the first non-perturbative approach to differential ionisation that is applicable at all considered incident energies. Furthermore, it is the only method applied to this collision problem that accounts for the strong coupling between reaction channels, including capture into the continuum. When electrons are emitted at angles less than 130° , our results demonstrate excellent agreement with all available experimental data for the DDCS as a function of the energy and emission angle of the electron over a wide range of projectile energies from 48 to 300 keV. At larger emission angles where the DDCS is very small, the present calculations systematically overestimate the experimental data. This may be the result of the large uncertainty in the experimental data in this region. Alternatively, it may be due a weaker effective charge the electron emitted in the backwards direction is assumed to experience at asymptotically large distances from the origin than it actually might be in this kinematic regime. Overall, we conclude that the present results provide the first accurate description of the experimental data for the energy and angular distribution of electrons emitted in $p + H_2$ collisions, resolving a long-standing theoretical challenge.

The present results for the DDCS for ionisation as a function of the projectile scattering angle and emitted electron energy generally agree well with experiment, although differences exist for some emission energies where the old measurements have not been updated.

Chapter 11

Conclusion and outlook

The two-centre WP-CCC approach to ion-atom and ion-molecule collisions was extended and applied to a number of collision systems and processes for which accurate collision data are required for practical applications. Integrated cross sections for all the interconnected processes occurring in collisions of Li^{3+} , Be^{4+} , and Ne^{10+} ions with $\text{H}(1s)$ were calculated over a wide energy range from several keV to several MeV. We also performed calculations for fully stripped beryllium-ion scattering on hydrogen in the $2\ell m$ states. The results provide the most comprehensive set of accurate collision data for these processes to date. The state-resolved cross sections for electron capture are of particular interest to the IAEA CRP on Data for Atomic Processes of Neutral Beams in Fusion Plasma [151]. The integrated cross sections generated in this work that are relevant to fusion plasma modelling have been made available world-wide in the IAEA online repositories.

Next we calculated all types of singly differential cross sections for $p + \text{H}$ collisions. The proton-hydrogen collision system has fundamental significance in scattering theory since it represents a genuine three-body problem where the interactions between all of the particles and the two-body bound-state wave functions in the reaction channels are analytically known. We find that the WP-CCC method gives a complete differential picture of all the interconnected processes

at once, subject to the unitary principle. Results for elastic scattering, target excitation, and electron capture agree well with the available experimental data. In particular, significant improvement over previously available calculations was observed for the SDCS for ionisation.

Computing the two-centre close-coupling equations is a computationally demanding task, especially for highly charged ions where a large number of basis states are required to obtain convergence in the results. Therefore, a novel technique was developed to extract probability amplitudes for electron capture from the single-centre WP-CCC method. Calculated cross sections for total and state-resolved electron capture agreed very well with results obtained using the two-centre version of the WP-CCC theory. The proposed method is simpler and faster than the full two-centre implementation. We also applied it to $p + \text{Li}$ collisions, using the independent-event model to account for the possibility of capture from either the L- or K-shell, finding very good agreement with the experimental data for electron capture.

The WP-CCC method was extended to multielectron atomic targets through development of an effective one-electron structure model. This method allows the calculation of single-ionisation and single-electron-capture cross sections taking into account the effect of all the inner- and outer-shell target electrons without making distinction between which of the many target electrons is captured or ionised. In this approach the scattering calculations are of the same level of complexity as those for three-body systems, significantly simplifying the many body problem. Application to proton collisions with alkali metal atoms showed that accounting for both the inner- and outer-shell electrons is essential for accurate description of the experimental data on the electron-capture cross section at high energies. Our calculations are the only ones for capture in $p + \text{Na}$ and $p + \text{K}$ collisions above 100 keV.

We also performed a comprehensive investigation of the four-body proton-helium differential scattering problem. Using the four-body WP-CCC method

that takes into account electron-exchange and electron-correlation effects we calculated the SDCS for all single-electron processes occurring in $p + \text{He}$ collisions. The results agree well with experimental data, where available. For comparison, calculations were also performed using the E1E method. Somewhat unexpectedly, the results of the effective one-electron method exhibit a very good level of agreement with the full two-electron ones. Therefore, we also conclude that, at least for the purpose of calculating the singly differential cross sections, an effective one-electron treatment of the target suffices. This provides a promising avenue for consideration of targets with more electrons by using an effective one-electron model since the four-body WP-CCC method is significantly more complex than the three-body version, making extension to systems with more active electrons very difficult within the current framework.

The two-electron version of the WP-CCC approach was generalised to multiply charged ion collisions with helium and applied to calculate integrated cross sections for all single-electron processes occurring in $\text{He}^{2+} + \text{He}$ collisions. Results were presented from 10 keV/u to 5 MeV/u, finding good agreement with the experimental data and other calculations where available. Comparison with the E1E WP-CCC method showed good agreement at high energies, but differences were observed as the projectile energy was decreased, especially for direct-scattering processes. These findings suggest that cross sections for ion scattering on He are more sensitive to the accuracy of the target structure when the projectile charge is higher.

Finally, the two-centre WP-CCC method was extended to proton collisions with molecular hydrogen. A model potential was used to construct effective one-electron wave functions representing one active electron in the orientation-averaged field of the two protons and remaining electron. With this we performed the first two-centre coupled-channel calculations of the integrated cross sections for all single-electron non-dissociative processes in $p + \text{H}_2$ collisions. Calculated cross sections for total and state-selective electron capture and ionisation

agreed well with the available experimental data, improving on previous theoretical studies which consider different collision outcomes in isolation. Next, we calculated the differential cross sections for elastic scattering, net target excitation, and single-electron capture. Good agreement was found with the only available measurements for total electron capture. The present results are the first data for the orientation-averaged DCS for elastic scattering and target excitation in intermediate-energy $p + H_2$ collisions. We also calculated all types of singly differential cross section for ionisation over a wide energy range from 20 to 300 keV. Consistent agreement with the experimental data was observed. Moreover, significant improvement is found over previously available calculations that rely on perturbative or classical methods. The present calculations of the SDCS for ionisation as a function of the scattering angle of the projectile are the first available for this system.

Until now accurate description of the energy and angular distribution of electrons emitted in $p + H_2$ collisions has presented a major theoretical challenge. We have provided the first solution to this problem. The results for the DDCS as a function of the energy and angle of the ejected electron agreed very well with the experimental data, providing significant improvement over sparsely available previous calculations.

Although a number of calculations exist for the DDCS for ionisation as a function of the scattering angle of the projectile and energy of the ejected electron for proton collisions with H_2 , discrepancies still exist between different theories and the experimental data. We applied the present method to calculate this type of DDCS, finding good agreement with the experimental data in the forward direction when the electron energy is small. However, at larger scattering angles and for higher-energy electrons our results agreed more closely with previously available calculations, therefore disagreeing with the measurements. Lastly, we presented calculations for the DDCS for ionisation in $p+H_2$ collisions as a function of the scattering angle of the projectile and emission angle of the ejected electron.

These are the first available data for this quantity.

For the ionisation process, our approach also allows for the distinction between direct ionisation and electron capture into the continuum of the projectile. We show the separate DI and ECC components for all singly and doubly differential cross sections for ionisation calculated herein. This provides insight into which mechanism is most responsible for the production of free electrons in the different kinematic regions considered. Our calculations reveal an interesting interplay between DI and ECC. In particular, we demonstrate that the ionisation cross section differential in the angle of the ejected electron is dominated by electron capture into the continuum for ejection into small angles, while ejection into large angles is purely due to direct ionisation.

The work done in this thesis lays the foundations for detailed theoretical studies of numerous collision systems and processes of practical importance. Convergent cross sections for total and state-selective processes in multiply charged ion collisions with hydrogen calculated over a wide energy range demonstrate that the WP-CCC method is uniquely positioned to provide accurate collisional data for collisions involving impurity ions in fusion plasmas. An obvious area for consideration is extension to other projectile species important for fusion plasma modelling, such as N^{7+} [335] and Ar^{18+} [336]. Furthermore, the present calculations for $Be^{4+} + H(2\ell m)$ collisions show that the approach is capable of producing accurate data for scattering of multiply charged ions on initially excited states of hydrogen. Collisions of other types of impurity ions with initially excited hydrogen presents another possible avenue for future research.

In Ch. 9 we applied the three-body and four-body versions of the WP-CCC method to $He^{2+} + He$ collisions. Collisions of other types of multiply charged ions with helium could be readily calculated with these methods. Impurity ions in the ITER tokamak are expected to interact with helium as well as hydrogen. Data for these collision systems is also in demand for fusion plasma modelling [36].

The two-centre calculations for state-selective electron-capture cross sections

required very large bases and numerical parameters to obtain convergence. Only through offloading computation to GPU accelerators was this possible. Moreover, as the charge of the projectile increases the calculations become more demanding. Therefore, modelling electron transfer in collisions of ions like Ar^{18+} may require alternative methods, such as the single-centre approach to rearrangement developed in Ch. 6. This technique effectively reduces the two-centre problem to a single-centre one, significantly simplifying description of rearrangement processes. This method could also be used to treat positronium formation in positron collisions with atoms and molecules as an alternative to the two-centre approach [337] to help avoid the complicated theoretical treatment of the Ps-formation channels. This could be especially useful when the positron collides with charged targets, as well as multielectron targets [338]. One of the main challenges in the two-centre treatment of positron scattering on multielectron targets is the necessity to deal with electron exchange between the formed Ps and the residual target ion explicitly.

The effective one-electron description of multielectron atoms presented in Ch. 7 was successfully applied to proton collisions with alkali metal atoms. In particular, the new approach has the potential to simplify stopping-power calculations for many electron targets. At the moment, sufficiently accurate two-centre calculations of the stopping power of hydrogen for protons are possible [339], however, these are significantly more challenging than the corresponding one-centre calculations for antiprotons [340, 341]. Furthermore, the single-centre approach presented herein should also work for quasi-one-electron alkali-like ions and quasi-two-electron alkaline-earth atoms and alkaline-earth-like ions with one or two electrons in their valence shell. Application of the present theory and computer code to such atoms is straightforward.

The present results for the differential cross sections for ionisation demonstrate the potential of the two-centre WP-CCC method to investigate the ionisation process further and calculate the fully differential cross sections for ionisation

of H, H₂, and He by proton impact. We recently calculated doubly differential cross sections for ionisation in proton-helium collisions and obtained excellent agreement with the available experimental data [332, 333]. Currently, there is no theory that can describe the experimental data for the fully differential cross section at 75 keV, recently measured by Schulz *et al.* [342] and Dhital *et al.* [57] in all kinematic regimes. Existing theoretical methods deviate from one another significantly and cannot reproduce the experiment well. The single-centre version of the WP-CCC method has already been applied to the fully differential cross sections for ionisation in proton-helium collisions [188, 343] at sufficiently high impact energies where the electron-capture channels are believed to be negligible. The results agreed very well with the recent high-resolution experiment by Gassert *et al.* [344]. However, the approach predicted a slight, but unexpected, shift in the position of the binary peak compared to the experimental data. Furthermore, recent measurements of the FDCS for ionisation in p + H₂ collisions in various geometries also demonstrate significant differences with currently available distorted-wave theories [57]. Application of the two-centre WP-CCC method to calculate the FDCS for these collision systems should reveal if higher-order effects, resulting from the presence of the second centre, are able to explain the aforementioned discrepancies.

Lastly, the H₂ molecule is a two-centre target. In principle, the waves scattered from the two centres may interfere. One can expect that this may affect the cross sections. However, this effect is explicitly excluded in the present E1E method and we found good agreement with the experimental data for the SDCS and DDCS for ionisation. Nevertheless, experiments by Hossain *et al.* [345] and Stolterfoht *et al.* [346] suggest that interference becomes important at significantly higher projectile energies and for highly charged ions. At the same time, interference could also be important for the DDCS as a function of the projectile-scattering angle and electron energy where some discrepancies between theory and experiment still remain. Furthermore, the FDCS provides the most detailed

description of the ionisation process and therefore may be more sensitive to this effect. The possibility of two-centre interference influencing the ionisation cross section remains a controversial topic. Development of a more detailed target structure that accounts for the two-centre nature of the H_2 molecule within the two-centre WP-CCC method may provide insight into this situation.

Summarising, the two-centre WP-CCC method was extended to multielectron targets, including H_2 , through the development of effective one-electron target-structure models. Then, both three- and four-body versions of the approach were applied to calculate integrated and differential cross sections for a number of different projectile and target species. In most cases the results agree very well with the available experimental data over a wide energy range, providing significant improvement over previously available theoretical data. The effective one-electron approach is particularly promising since it readily facilitates application of the WP-CCC method to more complex multielectron targets, provided suitable model potentials can be constructed and the collision energy is sufficiently large that electron-electron correlations play a negligible role in the collision dynamics. The method accounts for the coupling effects between the many competing reaction channels that play important roles in the intermediate energy region. All present calculations were performed in a unitary manner, preserving the norm of the total scattering wave function throughout the collisions. This paves the way for applying the approach to other types of collision systems of practical interest and calculating the fully differential cross section for ionisation which remains a challenging problem.

Appendix A

Momentum-transfer algebra

A.1 $\alpha \rightarrow \alpha'$ channel

Energy conservation requires that

$$\frac{q_\alpha^2}{2\mu_T} + \varepsilon_\alpha^T = \frac{q_{\alpha'}^2}{2\mu_T} + \varepsilon_{\alpha'}^T. \quad (\text{A.1})$$

This can be written as

$$q_\alpha - q_{\alpha'} = \frac{2\mu_T(\varepsilon_{\alpha'}^T - \varepsilon_\alpha^T)}{q_\alpha + q_{\alpha'}}. \quad (\text{A.2})$$

Then making the assumption that $q_{\alpha'} \approx q_\alpha \approx \mu_T v$, Eq. (A.2) reduces to

$$q_\alpha - q_{\alpha'} = \frac{\varepsilon_{\alpha'}^T - \varepsilon_\alpha^T}{v}. \quad (\text{A.3})$$

Since the scattering angle of the projectile is very small, we can approximate the parallel component of the momentum transfer vector as $q_T^\parallel \approx q_\alpha - q_{\alpha'}$. Combining this with Eq. (A.3) we can write Eq. (3.22) as

$$\mathbf{q}_T \cdot \mathbf{R} = (\varepsilon_{\alpha'}^T - \varepsilon_\alpha^T)t + \mathbf{q}_T^\perp \cdot \mathbf{b}. \quad (\text{A.4})$$

A.2 $\beta \rightarrow \beta'$ channel

Following the same ideas as for the $\alpha \rightarrow \alpha'$ channel we use the fact that

$$\frac{\mathbf{q}_\beta^2}{2\mu_P} + \varepsilon_\beta^P = \frac{\mathbf{q}_{\beta'}^2}{2\mu_P} + \varepsilon_{\beta'}^P \quad (\text{A.5})$$

to obtain

$$q_\beta - q_{\beta'} = \frac{2\mu_T(\varepsilon_{\beta'}^P - \varepsilon_\beta^P)}{q_\beta + q_{\beta'}} \quad (\text{A.6})$$

and

$$q_\beta - q_{\beta'} = \frac{\varepsilon_{\beta'}^P - \varepsilon_\beta^P}{v}. \quad (\text{A.7})$$

In the small-angle approximation we have $q_P^\parallel \approx q_\beta - q_{\beta'}$. Therefore,

$$\mathbf{q}_P \cdot \mathbf{R} = (\varepsilon_{\beta'}^P - \varepsilon_\beta^P)t + \mathbf{q}_P^\perp \cdot \mathbf{b}. \quad (\text{A.8})$$

A.3 $\beta \rightarrow \alpha'$ channel

Using the definitions,

$$\begin{cases} \boldsymbol{\sigma}_T = \mathbf{R} - \mathbf{r}_T(1 - \gamma_T), \\ \boldsymbol{\sigma}_P = \mathbf{R} + \mathbf{r}_P(1 - \gamma_P), \end{cases} \quad (\text{A.9})$$

we write

$$\mathbf{q}_\beta \cdot \boldsymbol{\sigma}_P - \mathbf{q}_{\alpha'} \cdot \boldsymbol{\sigma}_T = \mathbf{R} \cdot (\mathbf{q}_\beta \gamma_P - \mathbf{q}_{\alpha'}) + \mathbf{r}_T \cdot (\mathbf{q}_\beta - \mathbf{q}_\beta \gamma_P + \mathbf{q}_{\alpha'} - \mathbf{q}_{\alpha'} \gamma_T). \quad (\text{A.10})$$

Then we define \mathbf{p}_β and $\mathbf{p}_{\alpha'}$ according to Eq. (3.24), and obtain

$$\mathbf{q}_\beta \cdot \boldsymbol{\sigma}_P - \mathbf{q}_{\alpha'} \cdot \boldsymbol{\sigma}_T = \mathbf{p}_\beta \cdot \mathbf{R} + (\mathbf{p}_{\alpha'} - \mathbf{p}_\beta) \cdot \mathbf{r}_T. \quad (\text{A.11})$$

The second term can be simplified. For this first we write

$$\begin{aligned}\mathbf{p}_{\alpha'} - \mathbf{p}_{\beta} &= \mathbf{q}_{\beta} - \gamma_{\text{T}}\mathbf{q}_{\alpha'} - \gamma_{\text{P}}\mathbf{q}_{\beta} + \mathbf{q}_{\alpha'} \\ &= \mathbf{q}_{\beta}(1 - \gamma_{\text{P}}) + \mathbf{q}_{\alpha'}(1 - \gamma_{\text{T}}).\end{aligned}\tag{A.12}$$

Then, assuming the velocity of the projectile is approximately constant throughout the collision we have that $\mathbf{q}_{\beta} \approx \mu_{\text{P}}\mathbf{v}$ and $\mathbf{q}_{\alpha'} \approx \mu_{\text{T}}\mathbf{v}$. Using the reduced masses,

$$\begin{cases} \mu_{\text{T}} = \frac{M_{\text{T}}M_{\text{P}}}{M_{\text{T}} + M_{\text{P}}}, \\ \mu_{\text{P}} = \frac{(M_{\text{T}} - 1)(M_{\text{P}} + 1)}{M_{\text{T}} + M_{\text{P}}}, \end{cases}\tag{A.13}$$

and Eq. (3.25) we get

$$\begin{aligned}\mathbf{q}_{\beta}(1 - \gamma_{\text{P}}) + \mathbf{q}_{\alpha'}(1 - \gamma_{\text{T}}) &= \mu_{\text{P}}\mathbf{v}(1 - \gamma_{\text{P}}) + \mu_{\text{T}}\mathbf{v}(1 - \gamma_{\text{T}}) \\ &= \frac{M_{\text{T}} + M_{\text{P}} - 1}{M_{\text{T}} + M_{\text{P}}}\mathbf{v} \\ &\approx \mathbf{v},\end{aligned}\tag{A.14}$$

where we made the assumption that $M_{\text{T}} + M_{\text{P}} - 1 \approx M_{\text{T}} + M_{\text{P}}$ since M_{T} and $M_{\text{P}} \gg 1$. Therefore, Eq. (A.12) is simply

$$\mathbf{p}_{\alpha'} - \mathbf{p}_{\beta} \approx \mathbf{v},\tag{A.15}$$

which allows us to write Eq. (A.11) as

$$\mathbf{q}_{\beta} \cdot \boldsymbol{\sigma}_{\text{P}} - \mathbf{q}_{\alpha'} \cdot \boldsymbol{\sigma}_{\text{T}} = p_{\beta}^{\parallel}z + \mathbf{p}_{\beta}^{\perp} \cdot \mathbf{b} + \mathbf{v} \cdot \mathbf{r}_{\text{T}},\tag{A.16}$$

since $\mathbf{R} = \mathbf{b} + \mathbf{v}t$. In the small-angle approximation, the parallel component of \mathbf{p}_β is given by

$$p_\beta^\parallel = \gamma_P q_\beta - q_{\alpha'}. \quad (\text{A.17})$$

Additionally, energy conservation requires that

$$\frac{q_{\alpha'}^2}{2\mu_T} + \varepsilon_{\alpha'}^T = \frac{q_\beta^2}{2\mu_P} + \varepsilon_\beta^P, \quad (\text{A.18})$$

which implies

$$q_{\alpha'} = q_\beta \sqrt{\frac{\mu_T}{\mu_P}} \sqrt{1 + \frac{2\mu_P(\varepsilon_\beta^P - \varepsilon_{\alpha'}^T)}{q_\beta^2}}. \quad (\text{A.19})$$

The Maclaurin series for the function $(x + 1)^{\frac{1}{2}}$ is

$$(1 + x)^{\frac{1}{2}} = 1 + \frac{1}{2}x - \frac{1}{8}x^2 + \dots. \quad (\text{A.20})$$

Setting $x = 2\mu_P(\varepsilon_\beta^P - \varepsilon_{\alpha'}^T)/q_\beta^2$ we obtain

$$\left(1 + \frac{2\mu_P(\varepsilon_\beta^P - \varepsilon_{\alpha'}^T)}{q_\beta^2}\right)^{\frac{1}{2}} = 1 + \frac{1}{2}\left(\frac{2\mu_P(\varepsilon_\beta^P - \varepsilon_{\alpha'}^T)}{q_\beta^2}\right) - \frac{1}{8}\left(\frac{2\mu_P(\varepsilon_\beta^P - \varepsilon_{\alpha'}^T)}{q_\beta^2}\right)^2 + \dots. \quad (\text{A.21})$$

Since the energy difference, $\varepsilon_\beta^P - \varepsilon_{\alpha'}^T$, is small, we keep only the first two terms.

With this we can express Eq. (A.19) as

$$q_{\alpha'} \approx q_\beta \sqrt{\frac{\mu_T}{\mu_P}} \left(1 + \frac{\mu_P(\varepsilon_\beta^P - \varepsilon_{\alpha'}^T)}{q_\beta^2}\right). \quad (\text{A.22})$$

Therefore, Eq. (A.17) is written as

$$p_\beta^\parallel \approx \gamma_P q_\beta - q_\beta \sqrt{\frac{\mu_T}{\mu_P}} \left(1 + \frac{\mu_P(\varepsilon_\beta^P - \varepsilon_{\alpha'}^T)}{q_\beta^2}\right). \quad (\text{A.23})$$

Also note that

$$\begin{aligned}\sqrt{\frac{\mu_{\text{T}}}{\mu_{\text{P}}}} &= \sqrt{\left(\frac{M_{\text{T}}}{M_{\text{T}}-1}\right)\left(\frac{M_{\text{P}}}{M_{\text{P}}+1}\right)} \\ &= \frac{1}{\sqrt{1-\frac{1}{M_{\text{T}}}}}\frac{1}{\sqrt{1+\frac{1}{M_{\text{P}}}}}.\end{aligned}\quad (\text{A.24})$$

Now we use $1/\sqrt{1+x} \approx 1-x/2$ and set $x = -1/M_{\text{T}}$ and $x = 1/M_{\text{P}}$, to get

$$\sqrt{\frac{\mu_{\text{T}}}{\mu_{\text{P}}}} = \left(1 + \frac{1}{2M_{\text{T}}}\right)\left(1 - \frac{1}{2M_{\text{P}}}\right) \approx 1 + \frac{1}{2M_{\text{T}}} - \frac{1}{2M_{\text{P}}}.\quad (\text{A.25})$$

Additionally, we write

$$\gamma_{\text{P}} = \frac{1}{1 + \frac{1}{M_{\text{P}}}} \approx 1 - \frac{1}{M_{\text{P}}}.\quad (\text{A.26})$$

With Eqs. (A.25) and (A.26) the parallel component of \mathbf{p}_{β} from Eq. (A.23) is

$$\begin{aligned}p_{\beta}^{\parallel} &= q_{\beta}\left(1 - \frac{1}{M_{\text{P}}}\right) - q_{\beta}\left(1 + \frac{1}{2M_{\text{T}}} - \frac{1}{2M_{\text{P}}}\right)\left(1 + \frac{\mu_{\text{P}}(\varepsilon_{\beta}^{\text{P}} - \varepsilon_{\alpha'}^{\text{T}})}{q_{\beta}^2}\right) \\ &= -q_{\beta}\left(\frac{q_{\beta}}{2M_{\text{T}}} + \frac{q_{\beta}}{2M_{\text{P}}}\right) - \left(1 + \frac{1}{2M_{\text{T}}} - \frac{1}{2M_{\text{P}}}\right)\left(\frac{\mu_{\text{P}}(\varepsilon_{\beta}^{\text{P}} - \varepsilon_{\alpha'}^{\text{T}})}{q_{\beta}}\right).\end{aligned}\quad (\text{A.27})$$

Since M_{T} and $M_{\text{P}} \gg 1$, we find that

$$\frac{1}{2M_{\text{P}}} - \frac{1}{2M_{\text{T}}} = \frac{M_{\text{P}} - M_{\text{T}}}{2M_{\text{T}}M_{\text{P}}} \approx 0,\quad (\text{A.28})$$

and

$$\left(\frac{1}{2M_{\text{T}}} + \frac{1}{2M_{\text{P}}}\right) = \frac{M_{\text{T}} + M_{\text{P}}}{2M_{\text{P}}M_{\text{T}}} \approx \frac{1}{2\mu_{\text{P}}}.\quad (\text{A.29})$$

Finally, recalling $q_{\beta} = v\mu_{\text{P}}$ we get

$$p_{\beta}^{\parallel} = -\frac{v}{2} - \frac{(\varepsilon_{\beta}^{\text{P}} - \varepsilon_{\alpha'}^{\text{T}})}{v}.\quad (\text{A.30})$$

A.4 $\alpha \rightarrow \beta'$ channel

Using the definitions in Eq. (A.9) we write

$$\begin{aligned} \mathbf{q}_\alpha \cdot \boldsymbol{\sigma}_T - \mathbf{q}_{\beta'} \cdot \boldsymbol{\sigma}_P &= \mathbf{R} \cdot (\mathbf{q}_\alpha \gamma_T - \mathbf{q}_{\beta'}) \\ &+ \mathbf{r}_P \cdot (-\mathbf{q}_\alpha + \mathbf{q}_\alpha \gamma_T - \mathbf{q}_{\beta'} + \mathbf{q}_{\beta'} \gamma_P). \end{aligned} \quad (\text{A.31})$$

Then we define \mathbf{p}_α and $\mathbf{p}_{\beta'}$ according to Eq. (3.34) and obtain

$$\mathbf{q}_\alpha \cdot \boldsymbol{\sigma}_T - \mathbf{q}_{\beta'} \cdot \boldsymbol{\sigma}_P = \mathbf{p}_\alpha \cdot \mathbf{R} + (\mathbf{p}_\alpha - \mathbf{p}_{\beta'}) \cdot \mathbf{r}_P. \quad (\text{A.32})$$

The second term can be simplified by considering that

$$\begin{aligned} \mathbf{p}_\alpha - \mathbf{p}_{\beta'} &= \gamma_T \mathbf{q}_\alpha - \mathbf{q}_{\beta'} - \mathbf{q}_\alpha + \gamma_P \mathbf{q}_{\beta'} \\ &= \mathbf{q}_\alpha (\gamma_T - 1) + \mathbf{q}_{\beta'} (\gamma_P - 1). \end{aligned} \quad (\text{A.33})$$

Then, following a similar procedure as for the $\beta \rightarrow \alpha'$ channel we get

$$\mathbf{p}_\alpha - \mathbf{p}_{\beta'} \approx -\mathbf{v}, \quad (\text{A.34})$$

which allows us to write Eq. (A.32) as

$$\mathbf{p}_\alpha \cdot \mathbf{R} + (\mathbf{p}_\alpha - \mathbf{p}_{\beta'}) \cdot \mathbf{r}_P = p_\alpha^\parallel z + \mathbf{p}_\alpha^\perp \cdot \mathbf{b} - \mathbf{v} \cdot \mathbf{r}_P, \quad (\text{A.35})$$

since $\mathbf{R} = \mathbf{b} + \mathbf{v}t$. The parallel component of \mathbf{p}_α is given by

$$p_\alpha^\parallel = \gamma_T q_\alpha - q_{\beta'}. \quad (\text{A.36})$$

Then, following the same procedure as in Sect. A.3 we get

$$p_\alpha^\parallel = -\frac{v}{2} - \frac{(\varepsilon_\alpha^T - \varepsilon_{\beta'}^P)}{v}. \quad (\text{A.37})$$

Appendix B

Frames of reference transformations

B.1 Rotating molecular frame

To evaluate the matrix elements in Sect. 3.3 we make use of the rotating molecular frame illustrated in Fig. 3.3. In this frame the origin is positioned halfway between the target and projectile nuclei and the z' -axis is directed along the vector \mathbf{R} . Thus, the orientation of the primed axes is dependent on the relative position of the projectile, i.e. the angle $\theta_{\mathbf{R}}$.

Rotation from the laboratory frame to the molecular frame is characterised by the Euler angles α , β , and γ , given by

$$\begin{cases} \alpha = \varphi_{\mathbf{b}} \\ \beta = \theta_{\mathbf{R}} \\ \gamma = 0. \end{cases} \quad (\text{B.1})$$

We use the convention that the rotation is performed by the following sequence:

1. Rotation about the z -axis through an angle γ in the direction such that the positive x -axis rotates towards the positive y -axis.
2. Rotation about the original y -axis through an angle β in the direction such that the positive z -axis rotates towards the positive x -axis.

3. Rotation about the original z -axis through an angle α in the direction such that the positive x -axis rotates towards the positive y -axis.

In this scheme the inverse transformation is given by the angles

$$\begin{cases} \alpha \rightarrow -\gamma, \\ \beta \rightarrow -\beta, \\ \gamma \rightarrow -\alpha. \end{cases} \quad (\text{B.2})$$

The polar angle of the projectile in the laboratory frame is straightforwardly given by

$$\theta_{\mathbf{R}} = \arcsin\left(\frac{b}{R}\right) = \arccos\left(\frac{vt}{R}\right). \quad (\text{B.3})$$

The Cartesian coordinates of the active electron are written as (x_e, y_e, z_e) and (x'_e, y'_e, z'_e) in the laboratory and molecular frames, respectively. The magnitudes of $\mathbf{r}_{\mathbf{T}}$, $\mathbf{r}_{\mathbf{P}}$, and \mathbf{r} remain unchanged under rotation of the coordinate axes. We can write these in terms of the Cartesian coordinates of the electron according to

$$\begin{cases} r_{\mathbf{T}} = r'_{\mathbf{T}} = \sqrt{x_e'^2 + y_e'^2 + (z'_e + R/2)^2}, \\ r_{\mathbf{P}} = r'_{\mathbf{P}} = \sqrt{x_e'^2 + y_e'^2 + (z'_e - R/2)^2}, \\ r = r' = \sqrt{x_e'^2 + y_e'^2 + z_e'^2}. \end{cases} \quad (\text{B.4})$$

The cosines of the polar angle of the electron in the rotating molecular frame are given by

$$\begin{cases} \cos \theta'_{\mathbf{T}} = \frac{z'_e + R/2}{r'_{\mathbf{T}}}, \\ \cos \theta'_{\mathbf{P}} = \frac{z'_e - R/2}{r'_{\mathbf{P}}}, \\ \cos \theta'_e = \frac{z'_e}{r'}. \end{cases} \quad (\text{B.5})$$

In the rotating molecular frame, we move from spherical to prolate spheroidal coordinates. Figure B.1 shows the orthogonal isosurfaces used to construct the

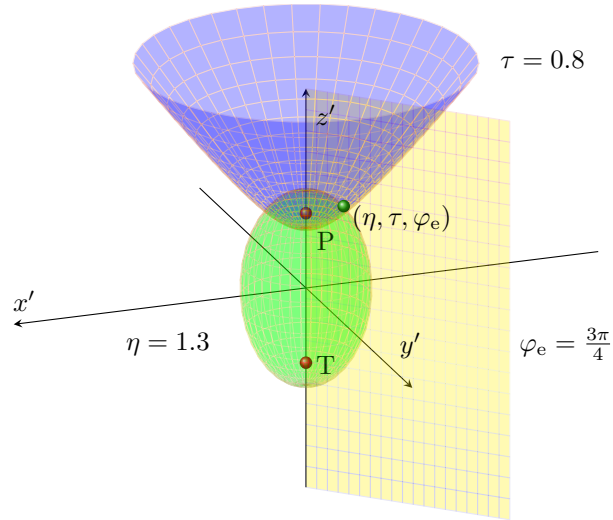


Figure B.1: Definition of the prolate spheroidal coordinate system used in this work. The foci of the hyperboloids and ellipsoids are positioned at the target and projectile nuclei. In this example the electron is located at $\eta = 1.3$, $\tau = 0.8$, $\varphi_e = 3\pi/4$.

basis vectors in spheroidal coordinates. Surfaces of constant η are confocal ellipsoids of revolution, surfaces of constant τ are hyperboloids of revolution, and φ_e is defined the same way as in spherical coordinates. The domains of η , τ , and φ_e are

$$\begin{cases} \eta \in [1, \infty], \\ \tau \in [-1, 1], \\ \varphi \in [0, 2\pi]. \end{cases} \quad (\text{B.6})$$

The transformation between the Cartesian and prolate spheroidal coordinates is given by

$$\begin{cases} x'_e = \frac{R}{2} \sqrt{(\eta^2 - 1)(1 - \tau^2)} \cos \varphi'_e, \\ y'_e = \frac{R}{2} \sqrt{(\eta^2 - 1)(1 - \tau^2)} \sin \varphi'_e, \\ z'_e = \frac{R}{2} \eta \tau. \end{cases} \quad (\text{B.7})$$

To find r'_T , r'_P , and r' in spheroidal coordinates we substitute the expressions in Eq. (B.7) into the equations in Eq. (B.4). First consider the term, $x_e'^2 + y_e'^2$, which

is common to each expression in Eq. (B.4),

$$\begin{aligned} x_e'^2 + y_e'^2 &= \left(\frac{R}{2}\right)^2 (\eta^2 - 1)(1 - \tau^2) \cos^2 \varphi_e' + \left(\frac{R}{2}\right)^2 (\eta^2 - 1)(1 - \tau^2) \sin^2 \varphi_e' \\ &= \left(\frac{R}{2}\right)^2 (\eta^2 - 1)(1 - \tau^2). \end{aligned} \quad (\text{B.8})$$

Using this result, the magnitudes in Eq. (B.4) are

$$\begin{aligned} r_T' &= \frac{R}{2} \sqrt{(\eta^2 - 1)(1 - \tau^2) + (\eta\tau + 1)^2} \\ &= \frac{R}{2} \sqrt{\eta^2 - \eta^2\tau^2 - 1 + \tau^2 + \eta^2\tau^2 + 2\eta\tau + 1} \\ &= \frac{R}{2} \sqrt{\eta^2 + \tau^2 + 2\eta\tau} \\ &= \frac{R}{2} (\eta + \tau), \end{aligned} \quad (\text{B.9})$$

and

$$\begin{aligned} r_P' &= \frac{R}{2} \sqrt{(\eta^2 - 1)(1 - \tau^2) + (\eta\tau - 1)^2} \\ &= \frac{R}{2} \sqrt{\eta^2 - \eta^2\tau^2 - 1 + \tau^2 + \eta^2\tau^2 - 2\eta\tau + 1} \\ &= \frac{R}{2} \sqrt{\eta^2 + \tau^2 - 2\eta\tau} \\ &= \frac{R}{2} (\eta - \tau), \end{aligned} \quad (\text{B.10})$$

and

$$\begin{aligned} r' &= \frac{R}{2} \sqrt{(\eta^2 - 1)(1 - \tau^2) + (\eta\tau)^2} \\ &= \frac{R}{2} \sqrt{\eta^2 - \eta^2\tau^2 - 1 + \tau^2 + \eta^2\tau^2} \\ &= \frac{R}{2} \sqrt{\eta^2 + \tau^2 - 1}. \end{aligned} \quad (\text{B.11})$$

Now consider the cosines of the polar angles of the electron position vectors.

Substituting for z'_e and r'_T we have¹

$$\begin{aligned}\cos \theta'_T &= \frac{\frac{R}{2}\eta\tau + \frac{R}{2}}{\frac{R}{2}(\eta + \tau)} \\ &= \frac{\eta\tau + 1}{\eta + \tau},\end{aligned}\tag{B.12}$$

and

$$\begin{aligned}\cos \theta'_P &= \frac{\frac{R}{2}\eta\tau - \frac{R}{2}}{\frac{R}{2}(\eta - \tau)} \\ &= \frac{\eta\tau - 1}{\eta - \tau},\end{aligned}\tag{B.13}$$

and

$$\begin{aligned}\cos \theta'_e &= \frac{\frac{R}{2}\eta\tau}{\frac{R}{2}\sqrt{\eta^2 + \tau^2 - 1}} \\ &= \frac{\eta\tau}{\sqrt{\eta^2 + \tau^2 - 1}}.\end{aligned}\tag{B.14}$$

The scalar product of the velocity and electron position vector is evaluated as follows. First, we write²

$$\mathbf{v}' \cdot \mathbf{r}' = v' r' \cos \theta_{\mathbf{v}'\mathbf{r}'},\tag{B.15}$$

where $\theta_{\mathbf{v}\mathbf{r}}$ is the angle between \mathbf{v} and \mathbf{r} . The cosine of the angle between two vectors, $\mathbf{r}_1 = (r_1, \theta_1, \varphi_1)$ and $\mathbf{r}_2 = (r_2, \theta_2, \varphi_2)$, in \mathbb{R}^3 is given by

$$\cos \theta_{\mathbf{r}_1\mathbf{r}_2} = \cos \theta_1 \cos \theta_2 + \sin \theta_1 \sin \theta_2 \cos(\varphi_1 - \varphi_2).\tag{B.16}$$

Since $\varphi'_v = 0$ we have

$$\mathbf{v}' \cdot \mathbf{r}' = v' r' [\cos \theta'_e \cos \theta'_v + \sin \theta'_e \sin \theta'_v \cos \varphi'_e].\tag{B.17}$$

¹Recall that $R' = R$.

²The scalar product is invariant under rotation of coordinates, therefore $\mathbf{v} \cdot \mathbf{r} = \mathbf{v}' \cdot \mathbf{r}'$.

The vector \mathbf{v}' makes an angle of $2\pi - \theta_{\mathbf{R}}$ to the z' -axis. Therefore,

$$\begin{cases} \cos \theta_{v'} = \cos(2\pi - \theta_{\mathbf{R}}) = \cos \theta_{\mathbf{R}} = \frac{vt}{R}, \\ \sin \theta_{v'} = \sin(2\pi - \theta_{\mathbf{R}}) = -\sin \theta_{\mathbf{R}} = -\frac{b}{R}. \end{cases} \quad (\text{B.18})$$

Lastly, using Eq. (B.14) and Pythagoras' Theorem we find that

$$\begin{aligned} \sin \theta'_e &= \frac{\sqrt{\eta^2 + \tau^2 - 1 - \eta^2\tau^2}}{\sqrt{\eta^2 + \tau^2 - 1}} \\ &= \frac{\sqrt{(\eta^2 - 1)(1 - \tau^2)}}{\sqrt{\eta^2 + \tau^2 - 1}}. \end{aligned} \quad (\text{B.19})$$

Substituting Eqs. (B.14), (B.18), and (B.19) into Eq. (B.17) yields

$$\begin{aligned} \mathbf{v}' \cdot \mathbf{r}' &= v' r' \left[\frac{\eta\tau}{\sqrt{\eta^2 + \tau^2 - 1}} \frac{vt}{R} - \frac{\sqrt{(\eta^2 - 1)(1 - \tau^2)}}{\sqrt{\eta^2 + \tau^2 - 1}} \frac{b}{R} \cos \varphi'_e \right] \\ &= \frac{v^2 t}{2} \eta\tau - \frac{vb}{2} \sqrt{(\eta^2 - 1)(1 - \tau^2)} \cos \varphi'_e. \end{aligned} \quad (\text{B.20})$$

Finally, we note that in spheroidal coordinates, the differential element of volume, $d\mathbf{r}'$, is written as

$$d\mathbf{r}' = \left(\frac{R}{2}\right)^3 (\eta^2 - \tau^2) d\eta d\tau d\varphi_e. \quad (\text{B.21})$$

B.2 The laboratory and centre-of-mass frames of reference

The cross sections differential in the scattering angle of the projectile are calculated in the centre-of-mass (CoM) frame. However, in some cases we convert the results to the laboratory (Lab) frame for comparison with experimental data. Here we derive the relation of the scattering angle and angular differential cross section in the centre-of-mass and laboratory frames.

In the CoM frame the projectile moves along the z -axis in the positive direction

while the target moves in the negative direction. Consider that the motion of the CoM itself is purely along the z -axis. This implies that azimuthal angles are unchanged under transformation between the Lab and CoM frames, $\varphi_{\text{Lab}} = \varphi_{\text{CoM}}$. The component of the projectile velocity in the Lab frame is given by

$$v_{\text{Lab}} \cos \theta_{\text{Lab}} = v_{\text{CoM}} \cos \theta_{\text{CoM}} + V, \quad (\text{B.22})$$

where V is the speed of the motion of the CoM, θ_{Lab} and θ_{CoM} are the scattering angle in the Lab and CoM frames of reference, respectively, and v_{Lab} and v_{CoM} are the speed of the projectile in the Lab and CoM frames, respectively. We also have

$$v_{\text{Lab}} \sin \theta_{\text{Lab}} = v_{\text{CoM}} \sin \theta_{\text{CoM}}. \quad (\text{B.23})$$

Dividing Eq. (B.23) by Eq. (B.22) we obtain

$$\tan \theta_{\text{Lab}} = \frac{\sin \theta_{\text{CoM}}}{\cos \theta_{\text{CoM}} + \tau}, \quad (\text{B.24})$$

where $\tau \equiv V/v_{\text{CoM}} = M_{\text{P}}/M_{\text{T}}$. We can also derive an expression for $\cos \theta_{\text{Lab}}$ which will be useful when considering how differential cross sections transform between these frames. To do this we use the expression $\tan^2 x \equiv \sec^2 x - 1$ on the LHS of Eq. (B.24) to get

$$\cos \theta_{\text{Lab}} = \frac{\cos \theta_{\text{CoM}} + \tau}{(1 + 2\tau \cos \theta_{\text{CoM}} + \tau^2)^{1/2}}. \quad (\text{B.25})$$

The relationship between the cross section differential in the scattering angle of the projectile in the Lab and CoM frames can be found by considering that the integrated cross section is frame-invariant, $\sigma_{\text{Lab}} = \sigma_{\text{CoM}}$, and that the flux of projectile particles scattered through Ω_{Lab} is the same as the number that pass

through Ω_{CoM} . Hence,

$$\begin{aligned} \frac{d\sigma_{\text{Lab}}}{d\Omega_{\text{Lab}}} d\Omega_{\text{Lab}} &= \frac{d\sigma_{\text{CoM}}}{d\Omega_{\text{CoM}}} d\Omega_{\text{CoM}} \\ \frac{d\sigma_{\text{Lab}}}{d\Omega_{\text{Lab}}} \sin \theta_{\text{Lab}} d\theta_{\text{Lab}} d\varphi_{\text{Lab}} &= \frac{d\sigma_{\text{CoM}}}{d\Omega_{\text{CoM}}} \sin \theta_{\text{CoM}} d\theta_{\text{CoM}} d\varphi_{\text{CoM}} \\ \therefore \frac{d\sigma_{\text{Lab}}}{d\Omega_{\text{Lab}}} &= \frac{d(\cos \theta_{\text{CoM}})}{d(\cos \theta_{\text{Lab}})} \frac{d\sigma_{\text{CoM}}}{d\Omega_{\text{CoM}}}, \end{aligned} \quad (\text{B.26})$$

since $d(\cos x) = -\sin x dx$, and $d\varphi_{\text{Lab}}/d\varphi_{\text{CoM}} = 1$. Thus, all that remains is to find the derivative of the cosine of the polar angle in the Lab frame with respect to the cosine of the polar angle in the CoM frame. Let's first consider the inverse relation since we already have an expression for $\cos \theta_{\text{Lab}}$ in terms of $\cos \theta_{\text{CoM}}$ in Eq. (B.25),

$$\begin{aligned} \frac{d(\cos \theta_{\text{Lab}})}{d(\cos \theta_{\text{CoM}})} &= \frac{d}{d(\cos \theta_{\text{CoM}})} \left(\frac{\cos \theta_{\text{CoM}} + \tau}{(1 + 2\tau \cos \theta_{\text{CoM}} + \tau^2)^{1/2}} \right), \\ &= \frac{1}{[1 + 2\tau \cos \theta_{\text{CoM}} + \tau^2]^{1/2}} - \frac{\tau [\cos \theta_{\text{CoM}} + \tau]}{[1 + 2\tau \cos \theta_{\text{CoM}} + \tau^2]^{3/2}} \\ &= \frac{1 + \tau \cos \theta_{\text{CoM}}}{[1 + 2\tau \cos \theta_{\text{CoM}} + \tau^2]^{3/2}}. \end{aligned} \quad (\text{B.27})$$

Therefore, the differential cross sections in the laboratory frame of reference can be recovered from the calculated cross section in the centre-of-mass frame of reference using

$$\frac{d\sigma_{\text{Lab}}}{d\Omega_{\text{Lab}}} = \frac{[1 + 2\tau \cos \theta_{\text{CoM}} + \tau^2]^{3/2}}{1 + \tau \cos \theta_{\text{CoM}}} \frac{d\sigma_{\text{CoM}}}{d\Omega_{\text{CoM}}}. \quad (\text{B.28})$$

Appendix C

Statements of contribution to published works

This appendix contains signed statements by all co-authors specifying my contribution to each peer-reviewed article that arose from the work contained within this thesis. Publications are arranged in reverse-chronological order.

Statements are not included for publications [347], [332], and [333] as these are not claimed towards completion of this PhD.

To whom it may concern,

I, Corey Plowman, contributed to the development of research methodology and computer code, performed the calculations, and prepared the first draft of the manuscript for the following publication:

C. T. Plowman, K. H. Spicer, M. Schulz, and A. S. Kadyrov, “Scattering-angle dependence of doubly differential cross sections for ionization in proton collisions with molecular hydrogen”, [Phys. Rev. A **108**, 052809 \(2023\)](#)

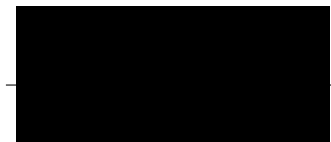
 _____

I, as co-author, endorse that this level of contribution by the candidate indicated above is appropriate.

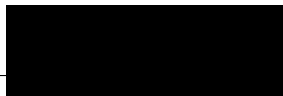
Kade Spicer

 _____

Michael Schulz

 _____

Alisher Kadyrov

 _____

To whom it may concern,

I, Corey Plowman, contributed to the development of research methodology and computer code, performed the calculations, and prepared the first draft of the manuscript for the following publication:

C. T. Plowman, K. H. Spicer, and A. S. Kadyrov, “Calculation of energy and angular distributions of electrons produced in intermediate-energy $p + H_2$ collisions”, [Atoms](#) **11**, 112 (2023)


 _____

I, as co-author, endorse that this level of contribution by the candidate indicated above is appropriate.

Kade Spicer

 _____

Alisher Kadyrov

 _____

To whom it may concern,

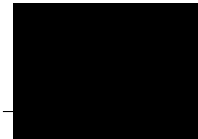
I, Corey Plowman, contributed to the development of research methodology and computer code, performed the calculations, and prepared the first draft of the manuscript for the following publication:

C. T. Plowman, I. B. Abdurakhmanov, I. Bray, and A. S. Kadyrov, “Energy and angular distributions of electrons emitted in proton collisions with molecular hydrogen”, [Phys. Rev. A **107**, 032824 \(2023\)](#)

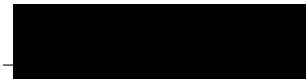


I, as co-author, endorse that this level of contribution by the candidate indicated above is appropriate.

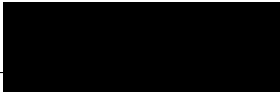
Ilkhom Abdurakhmanov



Igor Bray



Alisher Kadyrov



To whom it may concern,

I, Corey Plowman, contributed to the development of research methodology and computer code, performed the effective one-electron calculations, and contributed to editing and review of the manuscript for the following publication:

Sh. U. Alladustov, C. T. Plowman, I. B. Abdurakhmanov, I. Bray, and A. S. Kadyrov, “Wave-packet continuum discretization approach to He^{2+} -He collisions”, [Phys. Rev. A **106**, 062819 \(2022\)](#)

 _____

I, as co-author, endorse that this level of contribution by the candidate indicated above is appropriate.

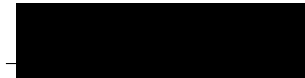
Shukhrat Alladustov

 _____

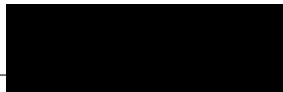
Ilkhom Abdurakhmanov

 _____

Igor Bray

 _____

Alisher Kadyrov

 _____

To whom it may concern,

I, Corey Plowman, contributed to the development of computer code and editing and review of the manuscript for the following publication:

A. M. Kotian, C. T. Plowman, I. B. Abdurakhmanov, I. Bray, and A. S. Kadyrov, “Electron capture and ionisation in collisions of Ne^{10+} and Li^{3+} with atomic hydrogen”, [Atoms](#) **10**, 144 (2022)

[Redacted signature]

I, as co-author, endorse that this level of contribution by the candidate indicated above is appropriate.

Aks Kotian

[Redacted signature]

Ilkhom Abdurakhmanov

[Redacted signature]

Igor Bray

[Redacted signature]

Alisher Kadyrov

[Redacted signature]

To whom it may concern,

I, Corey Plowman, contributed to the development of computer code and editing and review of the manuscript for the following publication:

N. W. Antonio, C. T. Plowman, I. B. Abdurakhmanov, I. Bray, and A. S. Kadyrov, “Fully-stripped beryllium-ion collisions with $2\ell m$ states of atomic hydrogen: target excitation and ionisation cross sections”, [Atoms](#) **10**, 137 (2022)

[Redacted signature]

I, as co-author, endorse that this level of contribution by the candidate indicated above is appropriate.

Nicholas Antonio

[Redacted signature]

Ilkhom Abdurakhmanov

[Redacted signature]

Igor Bray

[Redacted signature]

Alisher Kadyrov

[Redacted signature]

To whom it may concern,

I, Corey Plowman, contributed to the development of computer code and editing and review of the manuscript for the following publication:

N. W. Antonio, C. T. Plowman, I. B. Abdurakhmanov, I. Bray, and A. S. Kadyrov, “Fully-stripped-beryllium-ion collisions with $2\ell m$ states of atomic hydrogen: Total and state-selective electron-capture cross sections”, [Phys. Rev. A **106**, 012822 \(2022\)](#)



I, as co-author, endorse that this level of contribution by the candidate indicated above is appropriate.

Nicholas Antonio



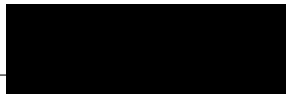
Ilkhom Abdurakhmanov



Igor Bray



Alisher Kadyrov



To whom it may concern,

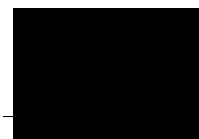
I, Corey Plowman, contributed to the development of research methodology and computer code, performed the calculations, and prepared the first draft of the manuscript for the following publication:

C. T. Plowman, I. B. Abdurakhmanov, I. Bray, and A. S. Kadyrov,
“Differential scattering in proton collisions with molecular hydrogen”,
[Eur. Phys. J. D **76**, 129 \(2022\)](#)

 _____

I, as co-author, endorse that this level of contribution by the candidate indicated above is appropriate.

Ilkhom Abdurakhmanov

 _____

Igor Bray

 _____

Alisher Kadyrov

 _____

To whom it may concern,

I, Corey Plowman, contributed to the development of computer code and editing and review of the manuscript for the following publication:

A. M. Kotian, C. T. Plowman, I. B. Abdurakhmanov, I. Bray, and A. S. Kadyrov, "State-selective electron capture in collisions of fully stripped neon ions with ground-state hydrogen", *J. Phys. B* **55**, 115201 (2022)

[Redacted signature]

I, as co-author, endorse that this level of contribution by the candidate indicated above is appropriate.

Aks Kotian

[Redacted signature]

Ilkhom Abdurakhmanov

[Redacted signature]

Igor Bray

[Redacted signature]

Alisher Kadyrov

[Redacted signature]

To whom it may concern,

I, Corey Plowman, contributed to the development of research methodology and computer code, performed the calculations, and prepared the first draft of the manuscript for the following publication:

C. T. Plowman, I. B. Abdurakhmanov, I. Bray, and A. S. Kadyrov,
“Effective one-electron approach to proton collisions with molecular hydrogen”,
[Eur. Phys. J. D **76**, 31 \(2022\)](#)



I, as co-author, endorse that this level of contribution by the candidate indicated above is appropriate.

Ilkhom Abdurakhmanov



Igor Bray



Alisher Kadyrov



To whom it may concern,

I, Corey Plowman, contributed to the development of research methodology, computer code, and editing and review of the manuscript for the following publication:

K. H. Spicer, C. T. Plowman, I. B. Abdurakhmanov, Sh. U. Alladustov, I. Bray, and A. S. Kadyrov, "Proton-helium collisions at intermediate energies: Singly differential ionization cross sections", [Phys. Rev. A **104**, 052815 \(2021\)](#)

[Redacted signature]

I, as co-author, endorse that this level of contribution by the candidate indicated above is appropriate.

Kade Spicer

[Redacted signature]

Ilkhom Abdurakhmanov

[Redacted signature]

Shukhrat Alladustov

[Redacted signature]

Igor Bray

[Redacted signature]

Alisher Kadyrov

[Redacted signature]

To whom it may concern,

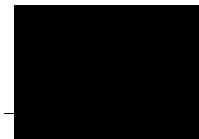
I, Corey Plowman, contributed to the development of computer code and editing and review of the manuscript for the following publication:

I. B. Abdurakhmanov, C. T. Plowman, K. H. Spicer, I. Bray, and A. S. Kadyrov, “Effective single-electron treatment of ion collisions with multielectron targets without using the independent-event model”, [Phys. Rev. A](#) **104**, 042820 (2021)

 _____

I, as co-author, endorse that this level of contribution by the candidate indicated above is appropriate.

Ilkhom Abdurakhmanov

 _____

Kade Spicer

 _____

Igor Bray

 _____

Alisher Kadyrov

 _____

To whom it may concern,

I, Corey Plowman, contributed to the development of computer code and editing and review of the manuscript for the following publication:

N. W. Antonio, C. T. Plowman, I. B. Abdurakhmanov, I. Bray, and A. S. Kadyrov, “Integrated total and state-selective cross sections for bare beryllium ion collisions with atomic hydrogen”, *J. Phys. B* **54**, 175201 (2021)

[Redacted signature]

I, as co-author, endorse that this level of contribution by the candidate indicated above is appropriate.

Nicholas Antonio

[Redacted signature]

Ilkhom Abdurakhmanov

[Redacted signature]

Igor Bray

[Redacted signature]

Alisher Kadyrov

[Redacted signature]

To whom it may concern,

I, Corey Plowman, contributed to the development of research methodology, computer code and editing and review of the manuscript for the following publication:

K. H. Spicer, C. T. Plowman, I. B. Abdurakhmanov, Sh. U. Alladustov, A. S. Kadyrov, and I. Bray, “Differential study of proton-helium collisions at intermediate energies: Elastic scattering, excitation, and electron capture”, [Phys. Rev. A **104**, 032818 \(2021\)](#)

[Redacted signature]

I, as co-author, endorse that this level of contribution by the candidate indicated above is appropriate.

Kade Spicer	[Redacted signature]
Ilkhom Abdurakhmanov	[Redacted signature]
Shukhrat Alladustov	[Redacted signature]
Alisher Kadyrov	[Redacted signature]
Igor Bray	[Redacted signature]

To whom it may concern,

I, Corey Plowman, contributed to the development of research methodology and computer code, performed the calculations, and prepared the first draft of the manuscript for the following publication:

C. T. Plowman, K. H. Spicer, I. B. Abdurakhmanov, A. S. Kadyrov, and I. Bray, “Singly differential cross sections for direct scattering, electron capture, and ionization in proton-hydrogen collisions”, [Phys. Rev. A **102**, 052810 \(2020\)](#)

[Redacted signature]

I, as co-author, endorse that this level of contribution by the candidate indicated above is appropriate.

Kade Spicer

[Redacted signature]

Ilkhom Abdurakhmanov

[Redacted signature]

Alisher Kadyrov

[Redacted signature]

Igor Bray

[Redacted signature]

To whom it may concern,

I, Corey Plowman, contributed to the development of computer code and editing and review of the manuscript for the following publication:

I. B. Abdurakhmanov, C. T. Plowman, A. S. Kadyrov, I. Bray, and A. M. Mukhamedzhanov, “One-center close-coupling approach to two-center rearrangement collisions”, *J. Phys. B* **53**, 145201 (2020)

 _____

I, as co-author, endorse that this level of contribution by the candidate indicated above is appropriate.

Ilkhom Abdurakhmanov

 _____

Alisher Kadyrov

 _____

Igor Bray

 _____

Akram Mukhamedzhanov

 _____

Appendix D

Abbreviations

Abbreviation	Description
AA	advanced adiabatic
AO	travelling atomic-orbital expansion
AOCC	atomic-orbital close-coupling
B2B0	second-order boundary-corrected Born approximation with simplified Green's functions
BCIS-3B	three-body boundary-corrected continuum-intermediate-state
BCIS-4B	four-body boundary-corrected continuum-intermediate-state
BE-FF	binary-encounter free-fall
BGM	basis-generator method
CB1	first-order boundary-corrected Born
CB1-4B	four-body boundary-corrected first-order Born
CB2	second-order boundary-corrected Born

Abbreviation	Description
CCC	convergent close-coupling
CDW	continuum-distorted-wave
CDW-EFS	continuum-distorted-wave eikonal-final-state
CDW-EIS	continuum-distorted-wave eikonal-initial-state
CDW-EIS-MO	continuum-distorted-wave eikonal-initial-state molecular-orbital
CI	configuration-interaction
COLTRIMS	cold target recoil ion momentum spectroscopy
CoM	centre-of-mass
CPU	central processing unit
CRP	Coordinated Research Project
CTMC	classical trajectory Monte Carlo
CXS	charge-exchange spectroscopy
DCS	differential cross section
dCTMC	dynamical classical trajectory Monte Carlo
DDCS	doubly differential cross section
DI	direct ionisation
DS	direct scattering
DW-C	eikonal distorted-wave method with Coulombic potential
DW-S	eikonal distorted-wave method with static potential
DWB	distorted-wave Born
DWHF	distorted-wave Hartree-Fock
E1E	effective one-electron
EA	eikonal approximation

Abbreviation	Description
EC	electron capture
ECC	electron capture into the continuum
EE-CTMC	equivalent electron classical trajectory Monte Carlo
EIA	eikonal impulse approximation
FBA	first-order Born approximation
FBA-PCI	first-order Born approximation with post-collision interaction
FDCS	fully differential cross section
FHBS	finite Hilbert basis set
FN	fixed-nuclei
GPU	graphics processing unit
GTDSE	numerical grid approach to solving the time-dependent Schrödinger equation for the total scattering wave function
GTO	Gaussian-type orbitals
hCTMC	hydrogenic classical trajectory Monte Carlo
HF	Hartree-Fock
IAEA	International Atomic Energy Agency
IEM	independent-event model
IEM-BGM	independent-event-model basis-generator method
IPFA	impact-parameter Faddeev approach
IPM	independent-particle model

Abbreviation	Description
ITER	formerly the International Thermonuclear Experimental Reactor
Lab	laboratory
LCAO	linear combination of atomic orbitals
LTDSE	lattice numerical solution to the time-dependent Schrödinger equation
M3DW-EIS	molecular three-body distorted-wave-eikonal initial-state
MC	Monte Carlo
MCSCF	multiconfigurational self-consistent field
mCTMC	microcanonical classical trajectory Monte Carlo
MMO	modified molecular-orbital
MO	molecular-orbital
MOCC	molecular-orbital close-coupling
MOM	multichannel optical-model
NEE-CTMC	non-equivalent electron classical trajectory Monte Carlo
OAE-BGM	one-active-electron basis-generator method
OBK	Oppenheimer-Brinkman-Kramers
ODP	optimised dynamical-pseudostates
OEDM	one-electron diatomic molecular
OP	optical potential
PW	partial-wave

Abbreviation	Description
PWBA	partial-wave Born approximation
QTMC-KW	quasi-classical trajectory Monte Carlo
SDCS	singly differential cross section
SE2	symmetric eikonal
SPS	static-potential scattering
TBEA	three-body eikonal approach
TC-AOCC	two-centre atomic-orbital close-coupling
TC-BGM	two-centre basis generator method
TDCC	time-dependent close-coupling
TDDFT	time-dependent density-functional theory
TDDFT-IEM	time-dependent density-functional theory using the independent-event-model
TDDFT-WB	time-dependent density-functional theory using the Wilken-Bauer correlation integral
TDSE	time-dependent Schrödinger equation
TEC	two-effective-centre
TECS	total electron-capture cross section
TEL	total electron loss
TICS	total ionisation cross section
WP-CCC	wave-packet convergent close-coupling

Bibliography

- [1] E. Rutherford, *Phys. Scr.* **21**, 669 (1911).
- [2] J. Chadwick, *Proc. Phys. Soc. (London)* **136**, 692 (1932).
- [3] K. Birkeland, *The Norwegian Aurora Polaris Expedition 1902–1903* (H. Aschehoug & Co. out-of-print, full text online, 1908).
- [4] J. T. Clarke, G. E. Ballester, J. Trauger, R. Evans, J. E. Connerney, K. Stapelfeldt, D. Crisp, P. D. Feldman, C. J. Burrows, S. Casertano, *et al.*, *Sci.* **274**, 404 (1996).
- [5] N. Ozak, T. Cravens, and D. Schultz, *Geophys. Res. Lett.* **40**, 4144 (2013).
- [6] O. Marchuk, *Phys. Scr.* **89**, 114010 (2014).
- [7] R. Wilson, *Radiol.* **47**, 487 (1946).
- [8] W. H. Bragg, *Philos. Mag.* **8**, 719 (1904).
- [9] R. Mohan and D. Grosshans, *Adv. Drug Deliv. Rev.* **109**, 26 (2017).
- [10] E. Schrödinger, *Phys. Rev.* **28**, 1049 (1926).
- [11] J. R. Oppenheimer, *Phys. Rev.* **31**, 349 (1928).
- [12] M. W. Gealy, G. W. Kerby, Y.-Y. Hsu, and M. E. Rudd, *Phys. Rev. A* **51**, 2247 (1995).
- [13] M. Schulz, ed., *Ion-Atom Collisions: The Few-Body Problem in Dynamic Systems* (De Gruyter, 2019).

- [14] Dž. Belkić, I. Bray, and A. Kadyrov, eds., *State-of-the-Art Reviews on Energetic Ion-Atom and Ion-Molecule Collisions* (World Scientific, Singapore, 2019).
- [15] ITER Organisation, “[Advantages of fusion](#),” (n.d.), Accessed: August 2023.
- [16] R. Hemsworth, H. Decamps, J. Graceffa, B. Schunke, M. Tanaka, M. Dremel, A. Tanga, H. De Esch, F. Geli, J. Milnes, *et al.*, *Nucl. Fusion* **49**, 045006 (2009).
- [17] E. Speth, *Rep. Prog. Phys.* **52**, 57 (1989).
- [18] A. Golubev, M. Basko, A. Fertman, A. Kozodaev, N. Mesheryakov, B. Sharkov, A. Vishnevskiy, V. Fortov, M. Kulish, V. Gryaznov, *et al.*, *Phys. Rev. E* **57**, 3363 (1998).
- [19] ITER Organisation, “[Neutral beam system](#),” (08/04/2019), Accessed: August 2023.
- [20] A. J. Sykes, P. A. Burt, N. J. Slevin, R. Stout, and J. E. Marrs, *Radiother. Oncol.* **48**, 15 (1998).
- [21] I. Abril, R. Garcia-Molina, P. de Vera, I. Kyriakou, and D. Emfietzoglou, *Adv. Quantum Chem.* **65**, 129 (2013).
- [22] J. E. Munzenrider and N. J. Liebsch, *Strahlentherapie und Onkologie* **175**, 57 (1999).
- [23] M. Durante, J. Debus, and J. S. Loeffler, *Nat. Rev. Phys.* **3**, 777 (2021).
- [24] J. W. Norbury, G. Battistoni, J. Besuglow, L. Bocchini, D. Boscolo, A. Botvina, M. Cloudsley, W. de Wet, M. Durante, M. Giraud, *et al.*, *Front. Phys.* **8**, 565954 (2020).
- [25] German Cancer Research Centre (DKFZ), “[matRad: Blaise v2.10.1](#),” (2020).

- [26] H. Bethe and J. Ashkin, in *Experimental Nuclear Physics*, edited by E. Segré (New York: Wiley, 1953-59).
- [27] B. Boudaiffa, P. Cloutier, D. Hunting, M. A. Huels, and L. Sanche, *Sci.* **287**, 1658 (2000).
- [28] D. Schultz, H. Gharibnejad, T. E. Cravens, and S. Houston, *At. Data Nucl. Data Tables* **132**, 101307 (2020).
- [29] K. Heng and R. A. Sunyaev, *Astron. Astrophys.* **481**, 117 (2008).
- [30] A. Wilson, *ESA Achievements*, 3rd ed. (ESA Publications Division, full text online, 2005).
- [31] T. E. Cravens, *Geophys. Res. Lett.* **24**, 105 (1997).
- [32] B. Mauk, D. Haggerty, S. Jaskulek, C. Schlemm, L. Brown, S. Cooper, R. Gurnee, C. Hammock, J. Hayes, G. Ho, *et al.*, *Space Sci. Rev.* **213**, 289 (2017).
- [33] Sh. U. Alladustov, I. Abdurakhmanov, A. Kadyrov, I. Bray, and K. Bartschat, *Phys. Rev. A* **99**, 052706 (2019).
- [34] J. Faulkner, I. Abdurakhmanov, Sh. U. Alladustov, A. Kadyrov, and I. Bray, *Plasma Phys. Control. Fusion* **61**, 095005 (2019).
- [35] I. Abdurakhmanov, K. Massen-Hane, Sh. U. Alladustov, J. Bailey, A. Kadyrov, and I. Bray, *Phys. Rev. A* **98**, 062710 (2018).
- [36] C. Hill, *Summary Report of the Second Research Coordination Meeting, Data for Atomic Processes of Neutral Beams in Fusion Plasma, 18–20 February 2019, Report INDC(NDS)-0780* (IAEA, 2019).
- [37] I. Abdurakhmanov, A. Kadyrov, D. Fursa, and I. Bray, *Phys. Rev. Lett.* **111**, 173201 (2013).

- [38] G. W. F. Drake, *Springer handbook of atomic, molecular, and optical physics* (Springer Nature, 2006).
- [39] R. Abrines and I. Percival, *Proc. Phys. Soc.* **88**, 861 (1966).
- [40] M. Gryziński, *Phys. Rev.* **115**, 374 (1959).
- [41] L. D. Landau and E. M. Lifshitz, *Quantum mechanics: non-relativistic theory*, 3rd ed., Vol. 3 (Elsevier, 2000).
- [42] Dž. Belkić, *Quantum Theory of High-Energy Ion-Atom Collisions* (CRC Press, 2008).
- [43] H. C. Brinkman and H. A. Kramers, *Proc. Acad. Sci.(Amsterdam)* **33**, 973 (1930).
- [44] D. R. Bates, *Proc. Phys. Soc. (London)* **247**, 294 (1958).
- [45] J. D. Jackson and H. Schiff, *Phys. Rev.* **89**, 359 (1953).
- [46] D. R. Bates and A. Dalgarno, *Proc. Phys. Soc. (London)* **66**, 972 (1953).
- [47] B. H. Bransden and M. R. C. McDowell, *Charge Exchange and the Theory of Ion-Atom Collisions* (Clarendon, Oxford, 1992).
- [48] D. Dewangan and J. Eichler, *J. Phys. B* **18**, L65 (1985).
- [49] Dž. Belkić, S. Saini, and H. S. Taylor, *Phys. Rev. A* **36**, 1601 (1987).
- [50] Dž. Belkić, *Phys. Rev. A* **43**, 4751 (1991).
- [51] D. P. Dewangan and B. H. Bransden, *J. Phys. B* **21**, L353 (1988).
- [52] Dž. Belkić, *Europhys. Lett.* **7**, 323 (1988).
- [53] F. Decker and J. Eichler, *J. Phys. B* **22**, L95 (1989).
- [54] I. Cheshire, *Proc. Phys. Soc. (London)* **84**, 89 (1964).
- [55] D. Dewangan, *J. Phys. B* **8**, L119 (1975).

- [56] A. Hasan, T. Arthanayaka, B. Lamichhane, S. Sharma, S. Gurung, J. Remolina, S. Akula, D. H. Madison, M. F. Ciappina, R. D. Rivarola, *et al.*, [J. Phys. B](#) **49**, 04LT01 (2016).
- [57] M. Dhital, S. Bastola, A. Silvus, J. Davis, B. Lamichhane, E. Ali, M. Ciappina, R. Lomsadze, A. Hasan, D. H. Madison, *et al.*, [Phys. Rev. A](#) **102**, 032818 (2020).
- [58] T. G. Wong, M. Foster, J. Colgan, and D. H. Madison, [Eur. Phys. J.](#) **30**, 447 (2009).
- [59] R. Kosloff, *Dyn. Mol. and Chem. React.* , 185 (1996).
- [60] M. Kimura and N. Lane, [Phys. Rev. A](#) **35**, 70 (1987).
- [61] C. Harel, H. Jouin, and B. Pons, [At. Data Nucl. Data Tables](#) **68**, 279 (1998).
- [62] L. Errea, C. Harel, H. Jouin, L. Méndez, B. Pons, and A. Riera, [J. Phys. B](#) **31**, 3527 (1998).
- [63] L. Errea, C. Illescas, L. Méndez, B. Pons, A. Riera, and J. Suárez, [J. Phys. B](#) **37**, 4323 (2004).
- [64] C. Lin, S. Soong, and L. Tunnell, [Phys. Rev. A](#) **17**, 1646 (1978).
- [65] W. Fritsch and C. D. Lin, [Phys. Rev.](#) **202**, 1 (1991).
- [66] T. G. Winter, [Phys. Rev. A](#) **56**, 2903 (1997).
- [67] A. Ford, J. Reading, and K. Hall, [J. Phys. B](#) **26**, 4537 (1993).
- [68] N. Toshima, [Phys. Scr.](#) **1997**, 144 (1997).
- [69] A. Lühr and A. Saenz, [Phys. Rev. A](#) **78**, 032708 (2008).
- [70] I. Bray and A. T. Stelbovics, [Phys. Rev. A](#) **46**, 6995 (1992).

- [71] I. Abdurakhmanov, A. Kadyrov, I. Bray, and A. Stelbovics, *J. Phys. B* **44**, 075204 (2011).
- [72] I. Cheshire, D. Gallaher, and A. J. Taylor, *J. Phys. B* **3**, 813 (1970).
- [73] T. G. Winter and C. C. Lin, *Phys. Rev. A* **10**, 2141 (1974).
- [74] D. Gallaher and L. Wilets, *Phys. Rev.* **169**, 139 (1968).
- [75] R. Shakeshaft, *J. Phys. B* **8**, 1114 (1975).
- [76] N. Toshima and J. Eichler, *Phys. Rev. Lett.* **66**, 1050 (1991).
- [77] A. S. Kadyrov, I. B. Abdurakhmanov, I. Bray, and A. T. Stelbovics, *Phys. Rev. A* **80**, 022704 (2009).
- [78] O. Kroneisen, H. Lüdde, T. Kirchner, and R. Dreizler, *J. Phys. A* **32**, 2141 (1999).
- [79] M. Zapukhlyak, T. Kirchner, H. Lüdde, S. Knoop, R. Morgenstern, and R. Hoekstra, *J. Phys. B* **38**, 2353 (2005).
- [80] A. C. Leung and T. Kirchner, *Atoms* **10**, 11 (2022).
- [81] A. Henne, H. Lüdde, A. Toepfer, T. Gluth, and R. Dreizler, *J. Phys. B* **26**, 3815 (1993).
- [82] R. Potvliege, F. Furtado, and C. Joachain, *J. Phys. B* **20**, 1771 (1987).
- [83] L. Faddeev and Z. Eksperim, *Sov. Phys. JETP* **12**, 1014 (1961).
- [84] G. Avakov, A. Ashurov, L. Blokhinstev, A. Mukhamedzhanov, and M. Poletayeva, *J. Phys. B* **23**, 2309S (1990).
- [85] G. Avakov, A. Ashurov, L. Blokhintsev, A. Kadyrov, A. Mukhamedzhanov, and M. Poletayeva, *J. Phys. B* **23**, 4151 (1990).
- [86] G. Avakov, L. Blokhintsev, A. Kadyrov, and A. Mukhamedzhanov, *J. Phys. B* **25**, 213 (1992).

- [87] E. Alt, P. Grassberger, and W. Sandhas, [Nucl. Phys. B **2**, 167 \(1967\)](#).
- [88] E. Alt and W. Sandhas, [Phys. Rev. C **21**, 1733 \(1980\)](#).
- [89] E. Alt, G. Avakov, L. Blokhintsev, A. Kadyrov, and A. Mukhamedzhanov, [J. Phys. B **27**, 4653 \(1994\)](#).
- [90] J. Macek, [Phys. Rev. A **1**, 235 \(1970\)](#).
- [91] I. Bray and A. T. Stelbovics, [Phys. Rev. Lett. **70**, 746 \(1993\)](#).
- [92] I. Abdurakhmanov, A. Kadyrov, I. Bray, and A. Stelbovics, [J. Phys. B **44**, 165203 \(2011\)](#).
- [93] I. Abdurakhmanov, A. Kadyrov, D. Fursa, I. Bray, and A. Stelbovics, [Phys. Rev. A **84**, 062708 \(2011\)](#).
- [94] I. Abdurakhmanov, A. Kadyrov, D. Fursa, S. Avazbaev, and I. Bray, [Phys. Rev. A **89**, 042706 \(2014\)](#).
- [95] I. Abdurakhmanov, A. Kadyrov, and I. Bray, [Phys. Rev. A **94**, 022703 \(2016\)](#).
- [96] A. S. Kadyrov, I. Bray, A. M. Mukhamedzhanov, and A. T. Stelbovics, [Ann. Phys. **324**, 1516 \(2009\)](#).
- [97] S. Avazbaev, A. Kadyrov, I. Abdurakhmanov, D. Fursa, and I. Bray, [Phys. Rev. A **93**, 022710 \(2016\)](#).
- [98] I. Abdurakhmanov, J. Bailey, A. Kadyrov, and I. Bray, [Phys. Rev. A **97**, 032707 \(2018\)](#).
- [99] I. Abdurakhmanov, Sh. U. Alladustov, J. Bailey, A. Kadyrov, and I. Bray, [Plasma Phys. Control. Fusion **60**, 095009 \(2018\)](#).
- [100] M. R. C. McDowell and J. P. Coleman, *Introduction to the theory of ion-atom collisions* (North-Holland Pub. Co., Amsterdam, 1970).

- [101] A. Messiah, *Quantum Mechanics*, 1st ed. (North-Holland Publishing, Amsterdam, 1965).
- [102] D. A. Varshalovich, A. N. Moskalev, and V. K. Khersonskii, *Quantum theory of angular momentum*, 1st ed. (World Scientific Pub., Philadelphia, 1988).
- [103] G. Arfken and H. Weber, *Mathematical Methods for Physicists*, 6th ed. (Academic Press, New York, 2005).
- [104] A. S. Kadyrov, I. Bray, A. M. Mukhamedzhanov, and A. T. Stelbovics, *Phys. Rev. Lett.* **101**, 230405 (2008).
- [105] M. Flannery and K. McCann, *Phys. Rev. A* **8**, 2915 (1973).
- [106] *CuSolver Library* (NVIDIA Corporation, full text online, Santa Clara, CA, 2022).
- [107] W. L. Anderson, *ACM Transactions on Mathematical Software (TOMS)* **8**, 344 (1982).
- [108] N. Antonio, C. Plowman, I. Abdurakhmanov, I. Bray, and A. Kadyrov, *J. Phys. B* **54**, 175201 (2021).
- [109] A. M. Kotian, C. T. Plowman, I. Abdurakhmanov, I. Bray, and A. Kadyrov, *J. Phys. B* **55**, 115201 (2022).
- [110] N. W. Antonio, C. T. Plowman, I. B. Abdurakhmanov, I. Bray, and A. Kadyrov, *Phys. Rev. A* **106**, 012822 (2022).
- [111] N. W. Antonio, C. T. Plowman, I. B. Abdurakhmanov, I. Bray, and A. S. Kadyrov, *Atoms* **10**, 137 (2022).
- [112] A. M. Kotian, C. T. Plowman, I. B. Abdurakhmanov, I. Bray, and A. S. Kadyrov, *Atoms* **10**, 144 (2022).
- [113] R. Isler, *Plasma Phys. Control. Fusion* **36**, 171 (1994).

- [114] M. Shah, T. Goffe, and H. Gilbody, *J. Phys. B* **11**, L233 (1978).
- [115] W. Seim, A. Muller, I. Wirkner-Bott, and E. Salzborn, *J. Phys. B* **14**, 3475 (1981).
- [116] M. Shah and H. Gilbody, *J. Phys. B* **15**, 413 (1982).
- [117] M. Panov, A. Basalaev, and K. Lozhkin, *Phys. Scr.* **1983**, 124 (1983).
- [118] F. Meyer, A. Howald, C. Havener, and R. Phaneuf, *Phys. Rev. A* **32**, 3310 (1985).
- [119] C. Hill, D. Dipti, K. Heinola, A. Dubois, N. Sisourat, A. Taoutioui, H. Agueny, K. Tőkési, I. Ziaeeian, C. Illescas, *et al.*, *Nucl. Fusion* **63**, 125001 (2023).
- [120] D. Delibašić, N. Milojević, I. Mančev, and Dž. Belkić, *At. Data Nucl. Data Tables* **139**, 101417 (2021).
- [121] S. Datta, C. Mandal, S. Mukherjee, and N. Sil, *Phys. Rev. A* **26**, 2551 (1982).
- [122] D. Crothers and J. McCann, *J. Phys. B* **16**, 3229 (1983).
- [123] A. Jorge, C. Illescas, J. E. Miraglia, and M. S. Gravielle, *J. Phys. B* **48**, 235201 (2015).
- [124] W. Fritsch and C. Lin, *J. Phys. B* **15**, L281 (1982).
- [125] W. Fritsch and C. Lin, *Phys. Rev. A* **29**, 3039 (1984).
- [126] N. Toshima, *Phys. Rev. A* **50**, 3940 (1994).
- [127] N. Toshima and H. Tawara, *Excitation, ionization, and electron capture cross sections of atomic hydrogen in collisions with multiply charged ions* (U.S. Department of Energy, 1995).

- [128] K. Igenbergs, *Calculations of cross sections relevant for diagnostics of hot fusion plasmas*, Ph.D. thesis, Vienna University of Technology (2011).
- [129] L. Liu, X. Li, J. Wang, and R. Janev, *Phys. Plasmas* **21**, 062513 (2014).
- [130] K. Igenbergs, J. Schweinzer, and F. Aumayr, *J. Phys. B* **42**, 235206 (2009).
- [131] H. Agueny, J. P. Hansen, A. Dubois, A. Makhoute, A. Taoutioui, and N. Sisourat, *At. Data Nucl. Data Tables* **129**, 101281 (2019).
- [132] L. Liu, Y. Wu, J. Wang, and R. Janev, *At. Data Nucl. Data Tables* **143**, 101464 (2022).
- [133] C. Illescas and A. Riera, *Phys. Rev. A* **60**, 4546 (1999).
- [134] I. Ziaeian and K. Tórkési, *Atoms* **8**, 27 (2020).
- [135] G. Maynard, R. Janev, and K. Katsonis, *J. Phys. B* **25**, 437 (1992).
- [136] J. Perez, R. Olson, and P. Beiersdorfer, *J. Phys. B* **34**, 3063 (2001).
- [137] T. Minami, M. Pindzola, T. Lee, and D. R. Schultz, *J. Phys. B* **39**, 2877 (2006).
- [138] A. Jorge, J. Suárez, C. Illescas, L. Errea, and L. Méndez, *Phys. Rev. A* **94**, 032707 (2016).
- [139] R. Janev, E. Solov'ev, and Y. Wang, *J. Phys. B* **29**, 2497 (1996).
- [140] R. Isler and R. Olson, *Phys. Rev. A* **37**, 3399 (1988).
- [141] A. Jorge, C. Illescas, and L. Méndez, *Phys. Rev. A* **105**, 012811 (2022).
- [142] I. Ziaeian and K. Tórkési, *Eur. Phys. J. D* **75**, 138 (2021).
- [143] R. Hoekstra, H. Anderson, F. Blik, M. Von Hellermann, C. Maggi, R. Olson, and H. Summers, *Plasma Phys. Control. Fusion* **40**, 1541 (1998).

- [144] N. Shimakura, N. Kobayashi, M. Honma, T. Nakano, and H. Kubo, in *J. Phys. Conf. Ser.*, Vol. 163 (IOP Publishing, 2009) p. 012045.
- [145] I. Abdurakhmanov, O. Erkilic, A. Kadyrov, I. Bray, S. Avazbaev, and A. Mukhamedzhanov, *J. Phys. B* **52**, 105701 (2019).
- [146] D. R. Schultz, C. O. Reinhold, and P. S. Krstić, *Phys. Rev. Lett.* **78**, 2720 (1997).
- [147] R. E. Olson, *Phys. Rev. A* **24**, 1726 (1981).
- [148] R. Olson and A. Salop, *Phys. Rev. A* **16**, 531 (1977).
- [149] D. Schultz and P. Krstic, *Elastic, excitation, ionization and charge transfer cross sections of current interest in fusion energy research* (U.S. Department of Energy, 1997).
- [150] A. Salin, *J. Phys. France* **45**, 671 (1984).
- [151] IAEA, “IAEA Coordinated Research Project: Data for Atomic Processes of Neutral Beams in Fusion Plasma,” (2022), Accessed: October 2023.
- [152] C. T. Plowman, K. H. Spicer, I. B. Abdurakhmanov, A. S. Kadyrov, and I. Bray, *Phys. Rev. A* **102**, 052810 (2020).
- [153] E. Rille, J. L. Peacher, E. Redd, T. J. Kvale, D. G. Seely, D. Blankenship, R. E. Olson, and J. T. Park, *Phys. Rev. A* **29**, 521 (1984).
- [154] J. T. Park, J. E. Aldag, J. Peacher, and J. M. George, *Phys. Rev. A* **21**, 751 (1980).
- [155] P. J. Martin, D. M. Blankenship, T. J. Kvale, E. Redd, J. L. Peacher, and J. T. Park, *Phys. Rev. A* **23**, 3357 (1981).
- [156] V. Rodriguez, *J. Phys. B* **24**, L205 (1991).
- [157] E. O. Alt, A. S. Kadyrov, and A. M. Mukhamedzhanov, *Phys. Rev. A* **60**, 314 (1999).

- [158] N. Milojević, I. Mančev, D. Delibašić, and Dž. Belkić, *Phys. Rev. A* **102**, 012816 (2020).
- [159] V. Y. Lazur, V. Aleksiy, M. Karbovanets, M. Khoma, and S. Myhalyna, *Semicond. Phys. Quantum Electron. & Optoelectron.* **22**, 171 (2019).
- [160] G. Kerby III, M. Gealy, Y.-Y. Hsu, M. E. Rudd, D. Schultz, and C. Reinhold, *Phys. Rev. A* **51**, 2256 (1995).
- [161] J. Fu, *FHBS calculation of ionized electron angular and energy distribution following the $p+H$ collision at 20 keV*, Ph.D. thesis, Texas A&M University (2004).
- [162] J. F. Reading, J. Fu, and M. J. Fitzpatrick, *Phys. Rev. A* **70**, 032718 (2004).
- [163] J. Fu, M. J. Fitzpatrick, J. F. Reading, and R. Gayet, *J. Phys. B* **34**, 15 (2001).
- [164] I. B. Abdurakhmanov, C. T. Plowman, A. S. Kadyrov, I. Bray, and A. M. Mukhamedzhanov, *J. Phys. B* **53**, 145201 (2020).
- [165] I. Bray, *Phys. Rev. A* **49**, 1066 (1994).
- [166] A. V. Lugovskoy, A. S. Kadyrov, I. Bray, and A. T. Stelbovics, *Phys. Rev. A* **82**, 062708 (2010).
- [167] A. B. Wittkower, G. Ryding, and H. B. Gilbody, *Proc. Phys. Soc. (London)* **89**, 541 (1966).
- [168] G. W. McClure, *Phys. Rev.* **148**, 47 (1966).
- [169] J. E. Bayfield, *Phys. Rev.* **185**, 105 (1969).
- [170] P. Hvelplund and A. Andersen, *Phys. Scr.* **26**, 375 (1982).
- [171] M. B. Shah and H. B. Gilbody, *J. Phys. B* **14**, 2361 (1981).

- [172] M. B. Shah, D. S. Elliot, and H. B. Gilbody, *J. Phys. B* **20**, 2481 (1987).
- [173] N. Toshima, *Phys. Rev. A* **59**, 1981 (1999).
- [174] J. Kuang and C. D. Lin, *J. Phys. B* **29**, 1207 (1996).
- [175] J. Kuang and C. D. Lin, *J. Phys. B* **29**, 5443 (1996).
- [176] I. B. Abdurakhmanov, A. S. Kadyrov, and I. Bray, *J. Phys. B* **49**, 03LT01 (2016).
- [177] J. T. Park, J. E. Aldag, J. M. George, and J. L. Peacher, *Phys. Rev. A* **14**, 608 (1976).
- [178] B. A. D'yachkov, *Zh. Tekhn. Fiz.* **38**, 1259 (1968).
- [179] R. N. Il'in, V. A. Oparin, E. S. Solov'ev, and N. V. Fedorenko, *Zh. Tekhn. Fiz.* **36**, 1241 (1966).
- [180] W. Grüebler, P. A. Schmelzbach, V. König, and P. Marmier, *Helvetica Physica Acta* **43**, 254 (1970).
- [181] S. L. Varghese, G. Bissinger, J. M. Joyce, and R. Laubert, *Phys. Rev. A* **31**, 2202 (1985).
- [182] F. Aumayr, M. Fehringer, and H. Winter, *J. Phys. B* **17**, 4201 (1984).
- [183] F. Aumayr, G. Lakits, W. Husinsky, and H. Winter, *J. Phys. B* **18**, 2493 (1985).
- [184] M. B. Shah, D. S. Elliott, and H. B. Gilbody, *J. Phys. B* **18**, 4245 (1985).
- [185] R. D. DuBois and L. H. Toburen, *Phys. Rev. A* **31**, 3603 (1985).
- [186] R. DuBois, *Phys. Rev. A* **32**, 3319 (1985).
- [187] I. Mančev, N. Milojević, D. Delibašić, and Dž. Belkić, *Phys. Scr.* **95**, 065403 (2020).

- [188] I. Abdurakhmanov, A. Kadyrov, I. Bray, and K. Bartschat, *Phys. Rev. A* **96**, 022702 (2017).
- [189] J. Schweinzer, R. Brandenburg, I. Bray, R. Hoekstra, F. Aumayr, R. Janev, and H. Winter, *At. Data Nucl. Data Tables* **72**, 239 (1999).
- [190] M. McCartney and D. Crothers, *J. Phys. B* **26**, 4561 (1993).
- [191] F. Aumayr, M. Fehring, and H. Winter, *J. Phys. B* **17**, 4185 (1984).
- [192] M. S. Pindzola, *Phys. Rev. A* **60**, 3764 (1999).
- [193] C. Stary, H. Ludde, and R. Dreizler, *J. Phys. B* **23**, 263 (1990).
- [194] R. Brandenburg, J. Schweinzer, F. Aumayr, and H. P. Winter, *J. Phys. B* **31**, 2585 (1998).
- [195] T.-G. Lee and M. S. Pindzola, *Phys. Rev. A* **84**, 052712 (2011).
- [196] A. Ermolaev, *J. Phys. B* **17**, 1069 (1984).
- [197] I. B. Abdurakhmanov, C. T. Plowman, K. H. Spicer, I. Bray, and A. S. Kadyrov, *Phys. Rev. A* **104**, 042820 (2021).
- [198] M. Klapisch, *Comp. Phys. Comm.* **2**, 239 (1971).
- [199] A. Lühr and A. Saenz, *Phys. Rev. A* **77**, 052713 (2008).
- [200] A. Kramida, Yu. Ralchenko, J. Reader, and NIST ASD Team, “NIST Atomic Spectra Database (ver. 5.10),” (2022), Accessed: September 2023.
- [201] F. Aumayr, G. Lakits, and H. Winter, *J. Phys. B* **20**, 2025 (1987).
- [202] U. Müller, H. Meijer, N. Holme, M. Kmit, J. Lauritsen, J. Pedersen, C. Richter, J. Thomsen, N. Andersen, and S. Nielsen, *Z. Phys. D At. Mol. Clust.* **33**, 187 (1995).
- [203] F. Ebel and E. Salzborn, *J. Phys. B* **20**, 4531 (1987).

- [204] B. O'Hare, R. McCullough, and H. Gilbody, *J. Phys. B* **8**, 2968 (1975).
- [205] T. Morgan, R. Olson, A. Schlachter, and J. Gallagher, *J. Phys. Chem. Ref. Data* **14**, 971 (1985).
- [206] C. Anderson, A. Howald, and L. Anderson, *Nucl. Instr. and Meth.* **165**, 583 (1979).
- [207] Z. Wang, M. Li, W. Xiang, and D. Fu, *Nucl. Instr. and Meth. B* **450**, 77 (2019).
- [208] M. Gieler, P. Ziegelwanger, F. Aumayr, H. Winter, and W. Fritsch, *J. Phys. B* **24**, 647 (1991).
- [209] A. Dubois, S. Nielsen, and J. Hansen, *J. Phys. B* **26**, 705 (1993).
- [210] M. Pindzola, T. Lee, and J. Colgan, *J. Phys. B* **44**, 205204 (2011).
- [211] R. DuBois, *Phys. Rev. A* **34**, 2738 (1986).
- [212] C. Lundy and R. Olson, *J. Phys. B* **29**, 1723 (1996).
- [213] A. Jain and T. G. Winter, *Phys. Rev. A* **51**, 2963 (1995).
- [214] D. Elliott, M. Shah, and H. Gilbody, *J. Phys. B* **19**, 3277 (1986).
- [215] K. H. Spicer, C. T. Plowman, I. B. Abdurakhmanov, A. S. Kadyrov, I. Bray, and Sh. U. Alladustov, *Phys. Rev. A* **104**, 032818 (2021).
- [216] K. H. Spicer, C. T. Plowman, I. B. Abdurakhmanov, Sh. U. Alladustov, I. Bray, and A. S. Kadyrov, *Phys. Rev. A* **104**, 052815 (2021).
- [217] Sh. Alladustov, *Wave-Packet Convergent Close-Coupling Approach to Ion-Atom Collisions*, Ph.D. thesis, Curtin University (2019).
- [218] D. Schultz, C. Reinhold, R. Olson, and D. Seely, *Phys. Rev. A* **46**, 275 (1992).

- [219] P. J. Martin, K. Arnett, D. Blankenship, T. J. Kvale, J. Peacher, E. Redd, V. Sutcliffe, J. T. Park, C. Lin, and J. H. McGuire, *Phys. Rev. A* **23**, 2858 (1981).
- [220] K.-y. Kobayashi and T. Ishihara, *Phys. Rev. A* **29**, 3417 (1984).
- [221] J. Peacher, T. J. Kvale, E. Redd, P. J. Martin, D. Blankenship, E. Rille, V. Sutcliffe, and J. T. Park, *Phys. Rev. A* **26**, 2476 (1982).
- [222] E. Ghanbari-Adivi, *J. Phys. B* **44**, 165204 (2011).
- [223] I. Mančev, V. Mergel, and L. Schmidt, *J. Phys. B* **36**, 2733 (2003).
- [224] P. Abufager, P. Fainstein, A. Martínez, and R. Rivarola, *J. Phys. B* **38**, 11 (2004).
- [225] I. Mančev, N. Milojević, and Dž. Belkić, *Phys. Rev. A* **91**, 062705 (2015).
- [226] V. Rodríguez, C. Ramírez, R. Rivarola, and J. Miraglia, *Phys. Rev. A* **55**, 4201 (1997).
- [227] H. Slim, E. Heck, B. Bransden, and D. Flower, *J. Phys. B* **24**, L421 (1991).
- [228] T. J. Kvale, D. G. Seely, D. Blankenship, E. Redd, T. J. Gay, M. Kimura, E. Rille, J. Peacher, and J. T. Park, *Phys. Rev. A* **32**, 1369 (1985).
- [229] M. Zapukhlyak, T. Kirchner, A. Hasan, B. Tooke, and M. Schulz, *Phys. Rev. A* **77**, 012720 (2008).
- [230] M. Schulz, T. Vajnai, and J. Brand, *Phys. Rev. A* **75**, 022717 (2007).
- [231] D. Guo, X. Ma, S. Zhang, X. Zhu, W. Feng, R. Zhang, B. Li, H. Liu, S. Yan, P. Zhang, *et al.*, *Phys. Rev. A* **86**, 052707 (2012).
- [232] M. Schulz, W. Htwe, A. Gaus, J. Peacher, and T. Vajnai, *Phys. Rev. A* **51**, 2140 (1995).

- [233] V. Mergel, R. Dörner, K. Khayyat, M. Achler, T. Weber, O. Jagutzki, H. Lüdde, C. Cocks, and H. Schmidt-Böcking, *Phys. Rev. Lett.* **86**, 2257 (2001).
- [234] M. Schöffler, J. Titze, L. P. H. Schmidt, T. Jahnke, N. Neumann, O. Jagutzki, H. Schmidt-Böcking, R. Dörner, and I. Mančev, *Phys. Rev. A* **79**, 064701 (2009).
- [235] D. G. Seely, S. Bross, A. Gaus, J. W. Edwards, D. R. Schultz, T. J. Gay, J. T. Park, and J. Peacher, *Phys. Rev. A* **45**, R1287 (1992).
- [236] S. T. Manson, L. H. Toburen, D. H. Madison, and N. Stolterfoht, *Phys. Rev. A* **12**, 60 (1975).
- [237] A. Salin, *J. Phys. B* **22**, 3901 (1989).
- [238] M. Schulz, T. Vajnai, A. Gaus, W. Htwe, D. H. Madison, and R. E. Olson, *Phys. Rev. A* **54**, 2951 (1996).
- [239] H. Fukuda, I. Shimamura, L. Vegh, and T. Watanabe, *Phys. Rev. A* **44**, 1565 (1991).
- [240] I. F. Barna, A. Gagy-Palfy, L. Gulyas, K. Tókési, and J. Burgdörfer, *Nucl. Instr. and Meth. B* **233**, 176 (2005).
- [241] G. Bernardi, S. Suárez, P. Fainstein, C. Garibotti, W. Meckbach, and P. Focke, *Phys. Rev. A* **40**, 6863 (1989).
- [242] C. Reinhold and R. Olson, *Phys. Rev. A* **39**, 3861 (1989).
- [243] L. Meng, R. Olson, R. Dörner, J. Ullrich, and H. Schmidt-Böcking, *J. Phys. B* **26**, 3387 (1993).
- [244] M. Gryziński, *J. Phys. B* **20**, 4741 (1987).
- [245] M. E. Rudd and T. Jorgensen, *Phys. Rev.* **131**, 666 (1963).

- [246] M. E. Rudd, C. A. Sautter, and C. L. Bailey, *Phys. Rev.* **151**, 20 (1966).
- [247] M. E. Rudd and D. H. Madison, *Phys. Rev. A* **14**, 128 (1976).
- [248] M. Rudd, L. Toburen, and N. Stolterfoht, *At. Data Nucl. Data Tables* **18**, 413 (1976).
- [249] D. Gibson and I. Reid, *J. Phys. B* **19**, 3265 (1986).
- [250] J. Giese and E. Horsdal, *Phys. Rev. Lett.* **60**, 2018 (1988).
- [251] F. Kristensen and E. Horsdal-Pedersen, *J. Phys. B* **23**, 4129 (1990).
- [252] D. Schultz and R. Olson, *Phys. Rev. A* **38**, 1866 (1988).
- [253] Sh. U. Alladustov, C. Plowman, I. Abdurakhmanov, I. Bray, and A. Kadyrov, *Phys. Rev. A* **106**, 062819 (2022).
- [254] M. E. Rudd, T. Goffe, and A. Itoh, *Phys. Rev. A* **32**, 2128 (1985).
- [255] M. Shah and H. Gilbody, *J. Phys. B* **18**, 899 (1985).
- [256] N. de Castro Faria, F. Freire Jr, and A. De Pinho, *Phys. Rev. A* **37**, 280 (1988).
- [257] M. Shah, P. McCallion, and H. Gilbody, *J. Phys. B* **22**, 3037 (1989).
- [258] M. Alessi, S. Otranto, and P. Focke, *Phys. Rev. A* **83**, 014701 (2011).
- [259] L. Puckett, G. Taylor, and D. Martin, *Phys. Rev.* **178**, 271 (1969).
- [260] H. Knudsen, L. Andersen, P. Hvelplund, G. Astner, H. Cederquist, H. Danared, L. Liljeby, and K.-G. Rensfelt, *J. Phys. B* **17**, 3545 (1984).
- [261] R. DuBois, *Phys. Rev. A* **36**, 2585 (1987).
- [262] V. Mergel, R. Dörner, J. Ullrich, O. Jagutzki, S. Lencinas, S. Nüttgens, L. Spielberger, M. Unverzagt, C. L. Cocke, R. E. Olson, *et al.*, *Phys. Rev. Lett.* **74**, 2200 (1995).

- [263] I. Mančev, N. Milojević, and Dž. Belkić, *At. Data Nucl. Data Tables* **102**, 6 (2015).
- [264] P. Abufager, A. Martínez, R. Rivarola, and P. Fainstein, *J. Phys. B* **37**, 817 (2004).
- [265] P. Terekhin, P. R. Montenegro, M. A. Quinto, J. M. Monti, O. A. Fojon, and R. D. Rivarola, *Nucl. Instr. and Meth. B* **408**, 150 (2017).
- [266] D. Delibašić, N. Milojević, I. Mančev, and Dž. Belkić, *At. Data Nucl. Data Tables* **148**, 101530 (2022).
- [267] I. F. Barna, K. Tőkési, and J. Burgdörfer, *J. Phys. B* **38**, 1001 (2005).
- [268] M. Pindzola, F. Robicheaux, and J. Colgan, *J. Phys. B* **40**, 1695 (2007).
- [269] M. Baxter and T. Kirchner, *Phys. Rev. A* **93**, 012502 (2016).
- [270] W. Fritsch, *J. Phys. B* **27**, 3461 (1994).
- [271] T. G. Winter, *Phys. Rev. A* **44**, 4353 (1991).
- [272] I. Abdurakhmanov, A. Kadyrov, S. Avazbaev, and I. Bray, in *J. Phys. Conf. Ser.*, Vol. 635 (IOP Publishing, 2015) p. 022100.
- [273] C. T. Plowman, I. B. Abdurakhmanov, I. Bray, and A. S. Kadyrov, *Eur. Phys. J. D* **76**, 31 (2022).
- [274] C. T. Plowman, I. B. Abdurakhmanov, I. Bray, and A. S. Kadyrov, *Eur. Phys. J. D* **76**, 129 (2022).
- [275] C. T. Plowman, I. B. Abdurakhmanov, I. Bray, and A. S. Kadyrov, *Phys. Rev. A* **107**, 032824 (2023).
- [276] C. T. Plowman, K. H. Spicer, and A. S. Kadyrov, *Atoms* **11**, 112 (2023).
- [277] C. T. Plowman, K. H. Spicer, M. Schulz, and A. S. Kadyrov, *Phys. Rev. A* **108**, 052809 (2023).

- [278] D. R. Bates and G. Griffing, *Proc. Phys. Soc. (London)* **66**, 961 (1953).
- [279] J. Hooper, E. McDaniel, D. Martin, and D. Harmer, *Phys. Rev.* **121**, 1123 (1961).
- [280] P. M. Stier and C. F. Barnett, *Phys. Rev.* **103**, 896 (1956).
- [281] C. Barnett and H. Reynolds, *Phys. Rev.* **109**, 355 (1958).
- [282] L. H. Toburen, M. Y. Nakai, and R. A. Langley, *Phys. Rev.* **171**, 114 (1968).
- [283] M. Shah, P. McCallion, and H. Gilbody, *J. Phys. B* **22**, 3983 (1989).
- [284] M. Shah and H. Gilbody, *J. Phys. B* **15**, 3441 (1982).
- [285] M. E. Rudd, R. DuBois, L. Toburen, C. Ratcliffe, and T. Goffe, *Phys. Rev. A* **28**, 3244 (1983).
- [286] E. P. Andreev, V. A. Ankudinov, S. V. Bobashev, and V. B. Matveev, *Sov. Phys. JETP* **25**, 232 (1967).
- [287] J. E. Bayfield, *Phys. Rev.* **182**, 115 (1969).
- [288] J. H. Birely and R. J. McNeal, *Phys. Rev. A* **5**, 692 (1972).
- [289] R. Hughes, C. Stigers, B. Doughty, and E. D. Stokes, *Phys. Rev. A* **1**, 1424 (1970).
- [290] R. Hughes, E. Stokes, S.-S. Choe, and T. King, *Phys. Rev. A* **4**, 1453 (1971).
- [291] R. Hughes, T. King, and S.-S. Choe, *Phys. Rev. A* **5**, 644 (1972).
- [292] M. Shah, J. Geddes, and H. Gilbody, *J. Phys. B* **13**, 4049 (1980).
- [293] I. Williams, J. Geddes, and H. Gilbody, *J. Phys. B* **15**, 1377 (1982).
- [294] H. Dawson and D. Loyd, *Phys. Rev. A* **15**, 43 (1977).

- [295] L. H. Toburen and W. E. Wilson, *Phys. Rev. A* **5**, 247 (1972).
- [296] A. Edwards, R. Wood, and R. Ezell, *Phys. Rev. A* **34**, 4411 (1986).
- [297] S. Sharma, A. Hasan, K. N. Egodapitiya, T. Arthanayaka, G. Sakhelashvili, and M. Schulz, *Phys. Rev. A* **86**, 022706 (2012).
- [298] C. E. Kuyatt and T. Jorgensen, *Phys. Rev.* **130**, 1444 (1963).
- [299] M. E. Rudd, *Phys. Rev. A* **20**, 787 (1979).
- [300] M. E. Rudd, Y. K. Kim, D. H. Madison, and T. J. Gay, *Rev. Mod. Phys.* **64**, 441 (1992).
- [301] D. K. Gibson and I. D. Reid, *Double Differential Cross Sections for Electrons Ejected from H₂, O₂, N₂, CO₂, CH₄, H₂O and Ar by 50 keV Protons* (Australian Atomic Energy Commission, 1984).
- [302] W.-Q. Cheng, M. E. Rudd, and Y.-Y. Hsu, *Phys. Rev. A* **40**, 3599 (1989).
- [303] J. S. Alexander, A. C. LaForge, A. Hasan, Z. Machavariani, M. Ciappina, R. Rivarola, D. H. Madison, and M. Schulz, *Phys. Rev. A* **78**, 060701 (2008).
- [304] K. N. Egodapitiya, S. Sharma, A. Hasan, A. C. Laforge, D. H. Madison, R. Moshhammer, and M. Schulz, *Phys. Rev. Lett.* **106**, 153202 (2011).
- [305] S. Sharma, T. Arthanayaka, A. Hasan, B. Lamichhane, J. Remolina, A. Smith, and M. Schulz, *Phys. Rev. A* **89**, 052703 (2014).
- [306] A. Lühr and A. Saenz, *Phys. Rev. A* **81**, 010701 (2010).
- [307] S. Corchs, R. Rivarola, J. McGuire, and Y. Wang, *Phys. Rev. A* **47**, 201 (1993).
- [308] H. Busnengo, S. Corchs, and R. Rivarola, *Phys. Rev. A* **57**, 2701 (1998).

- [309] H. Busnengo, S. Corchs, and R. Rivarola, *Nucl. Instr. and Meth. B* **146**, 52 (1998).
- [310] M. Galassi, R. Rivarola, and P. Fainstein, *Phys. Rev. A* **70**, 032721 (2004).
- [311] M. E. Rudd, Y.-K. Kim, D. H. Madison, and J. W. Gallagher, *Rev. Mod. Phys.* **57**, 965 (1985).
- [312] L. Meng, C. Reinhold, and R. Olson, *Phys. Rev. A* **40**, 3637 (1989).
- [313] L. Meng, C. Reinhold, and R. Olson, *Phys. Rev. A* **42**, 5286 (1990).
- [314] H. T. Hunter, M. I. Kirkpatrick, I. Alvarez, C. Cisneros, R. A. Phaneuf, and C. F. Barnett, *Atomic data for fusion volume 1 collisions of H, H₂, He and Li atoms and ions with atoms and molecules* (Oak Ridge National Laboratory, 1990).
- [315] M. Kimura, *Phys. Rev. A* **32**, 802 (1985).
- [316] R. Shingal and C. D. Lin, *Phys. Rev. A* **40**, 1302 (1989).
- [317] Y. V. Vanne and A. Saenz, *J. Mod. Opt.* **55**, 2665 (2008).
- [318] A. Lühr, Y. V. Vanne, and A. Saenz, *Phys. Rev. A* **78**, 042510 (2008).
- [319] D. Elizaga, L. Errea, J. Gorfinkiel, C. Illescas, L. Méndez, A. Macías, A. Rivera, A. Rojas, O. Kroneisen, T. Kirchner, *et al.*, *J. Phys. B* **32**, 857 (1999).
- [320] A. Igarashi, *J. Phys. B* **53**, 225205 (2020).
- [321] E. G. Adivi, *J. Phys. B* **42**, 095207 (2009).
- [322] E. Ghanbari-Adivi and S. Sattarpour, *Mol. Phys.* **113**, 3336 (2015).
- [323] U. Chowdhury, M. Schulz, and D. H. Madison, *Phys. Rev. A* **83**, 032712 (2011).
- [324] J. Gao, J. L. Peacher, and D. H. Madison, *J. Chem. Phys.* **123**, 204302 (2005).

- [325] A. Igarashi and L. Gulyás, *J. Phys. B* **51**, 035201 (2018).
- [326] A. Ermolaev, *Hyperfine Interact.* **44**, 375 (1989).
- [327] I. Thompson and A. Barnett, *Comp. Phys. Comm.* **36**, 363 (1985).
- [328] H. Ludde and R. Dreizler, *J. Phys. B* **18**, 107 (1985).
- [329] L. Andersen, P. Hvelplund, H. Knudsen, S. Möller, J. Pedersen, S. Tang-Petersen, E. Uggerhoj, K. Elsener, and E. Morenzoni, *J. Phys. B* **23**, L395 (1990).
- [330] P. Hvelplund, H. Knudsen, U. Mikkelsen, E. Morenzoni, S. Möller, E. Uggerhoj, and T. Worm, *J. Phys. B* **27**, 925 (1994).
- [331] H. Knudsen, H. Torii, M. Charlton, Y. Enomoto, I. Georgescu, C. Hunniford, C. Kim, Y. Kanai, H.-P. Kristiansen, N. Kuroda, *et al.*, *Phys. Rev. Lett.* **105**, 213201 (2010).
- [332] K. Spicer, C. Plowman, M. Schulz, and A. Kadyrov, *Phys. Rev. A* **108**, 022803 (2023).
- [333] K. H. Spicer, C. T. Plowman, Sh. U. Alladustov, I. B. Abdurakhmanov, I. Bray, and A. S. Kadyrov, *Eur. Phys. J. D* **77**, 31 (2023).
- [334] L. H. Thomas, *Proc. R. Soc. A* **114**, 561 (1927).
- [335] A. Field, I. Balboa, P. Drewelow, J. Flanagan, C. Guillemaut, J. Harrison, A. Huber, V. Huber, B. Lipschultz, G. Matthews, *et al.*, *Plasma Phys. Control. Fusion* **59**, 095003 (2017).
- [336] L. Errea, C. Illescas, L. Méndez, B. Pons, A. Riera, and J. Suarez, *J. Phys. B* **39**, L91 (2006).
- [337] A. S. Kadyrov and I. Bray, *J. Phys. B* **33**, L635 (2000).
- [338] C. Rawlins, A. Kadyrov, and I. Bray, *Phys. Rev. A* **97**, 012707 (2018).

- [339] J. Bailey, I. Abdurakhmanov, A. Kadyrov, I. Bray, and A. Mukhamedzhanov, *Phys. Rev. A* **99**, 042701 (2019).
- [340] J. Bailey, A. Kadyrov, I. Abdurakhmanov, D. Fursa, and I. Bray, *Phys. Rev. A* **92**, 022707 (2015).
- [341] J. Bailey, A. Kadyrov, I. Abdurakhmanov, D. Fursa, and I. Bray, *Phys. Rev. A* **92**, 052711 (2015).
- [342] M. Schulz, A. Hasan, N. Maydanyuk, M. Foster, B. Tooke, and D. H. Madison, *Phys. Rev. A* **73**, 062704 (2006).
- [343] I. Abdurakhmanov, A. Kadyrov, Sh. U. Alladustov, I. Bray, and K. Bartschat, *Phys. Rev. A* **100**, 062708 (2019).
- [344] H. Gassert, O. Chuluunbaatar, M. Waitz, F. Trinter, H.-K. Kim, T. Bauer, A. Laucke, C. Müller, J. Voigtsberger, M. Weller, *et al.*, *Phys. Rev. Lett.* **116**, 073201 (2016).
- [345] S. Hossain, A. Alnaser, A. Landers, D. Pole, H. Knutson, A. Robison, B. Stamper, N. Stolterfoht, and J. Tanis, *Nucl. Instr. and Meth. B* **205**, 484 (2003).
- [346] N. Stolterfoht, B. Sulik, V. Hoffmann, B. Skogvall, J.-Y. Chesnel, J. Rangama, F. Frémont, D. Hennecart, A. Cassimi, X. Husson, *et al.*, *Phys. Rev. Lett.* **87**, 023201 (2001).
- [347] A. M. Kotian, C. T. Plowman, and A. S. Kadyrov, *Eur. Phys. J. D* **77**, 163 (2023).

Every reasonable effort has been made to acknowledge the owners of copyright material. I would be pleased to hear from any copyright owner who has been omitted or incorrectly acknowledged.